

Cadmium abundances and isotope compositions in Earth and chondrites

Gabriel Devos

▶ **To cite this version:**

Gabriel Devos. Cadmium abundances and isotope compositions in Earth and chondrites. Earth Sciences. Université Paris Cité, 2024. English. ⟨NNT : 2024UNIP7004⟩. ⟨tel-04773999⟩

HAL Id: tel-04773999

https://theses.hal.science/tel-04773999v1

Submitted on 8 Nov 2024

HAL is a multi-disciplinary open access archive for the deposit and dissemination of scientific research documents, whether they are published or not. The documents may come from teaching and research institutions in France or abroad, or from public or private research centers.

L'archive ouverte pluridisciplinaire **HAL**, est destinée au dépôt et à la diffusion de documents scientifiques de niveau recherche, publiés ou non, émanant des établissements d'enseignement et de recherche français ou étrangers, des laboratoires publics ou privés.



HAL Authorization

Thèse préparée à l'Institut de Physique du Globe de Paris

Université Paris Cité

École doctorale Sciences de la Terre et de l'Environnement et Physique de l'Univers de Paris, STEP'UP 560

Cadmium abundances and isotope compositions in Earth and chondrites

par Gabriel Devos

Thèse de doctorat de Sciences de la Terre et de l'Environnement

Octobre 2020 – Avril 2024

- Dirigée par
  Frédéric Moynier
  et Martin Bizzarro

- Présentée et soutenue publiquement le 29 Avril 2024

- Devant un jury composé de

  Arnaud Agranier, maître de conférence, Université de Bretagne occidentale

  Pierre Beck, maître de conférence, université de Grenoble, rapporteur

  Ingrid Blanchard, chargée de recherche CNRS, Sorbonne université

  Alexandra Gourlan, maîtresse de conférence, université de Grenoble

  Julien Siebert, professeur des universités, Institut de Physique du globe de Paris

  Nathalie Vigier, directrice de recherches CNRS, Sorbonne université, rapporteuse

C'était il y a très très longtemps.

A gauche du ciel, il y avait la planète Shadok.

A droite du ciel, il y avait la planète Gibi.

Au centre du ciel, il y avait la Terre

"Les Shadoks", Jacques Rouxel, 1968

STEP'UP ÉCOLE DOCTORALE

Funded by the European Union

European Research Council
Established by the European Commission

Contents

Abstract *7*

Résumé court *9*

Résumé étendu *11*

References **21**

Chapter 1 – General introduction *26*

1. Solar system objects **27**

1.1. On the origin of things 27

1.2. The formation of the solar system 28

1.3. Composition and structure of the Solar system 31

1.4. Meteorites and the records of primitive Solar system 32

1.4.1. Differentiated and undifferentiated 32

1.4.2. The chondrites classification 34

2. The moderately volatile elements problem **36**

2.1. What is a moderately volatile element? 36

2.2. The moderately volatile elements depletion 37

3. Cadmium: risks and opportunities **42**

3.1. What is cadmium? 42

3.2. Toxicity of cadmium 43

3.3. Applications and pollution 45

4. The geochemical method applied to Cd **47**

4.1. Obstacles to Cd analysis 47

4.1.1. Scarcity 47

4.1.2. Interferences 49

4.2. Cadmium isotope composition and isotope fractionation 52

4.3. Purification of Cd 53

4.4. Mass spectrometry 54

4.4.1. TIMS 54

4.4.2. ICPMS 55

4.4.3. The double spike method 56

5. Cd stable isotopes studies 59

5.1. The geological fractionating processes 59

5.1.1. Vaporization 59

5.1.2. Alteration 60

5.1.3. Precipitation and adsorption 61

5.1.4. Biological uptake 61

5.1.5. Debate on igneous fractionation processes 62

5.2. Uses of Cd 64

5.2.1. Anthropogenic pollution 64

5.2.2. In the oceans 65

5.2.3. In the silicate Earth 66

5.2.4. Extraterrestrial samples 70

6. The PhD project 72

6.1. Objectives of the PhD 72

6.2. Challenges 73

7. References 75

Chapter 2 – Methods *108*

1. Preparation of the samples **109**

1.1. Sample pre-processing 109

1.2. The acid digestion 110

1.3. Double spiking 111

2. Cadmium purification **115**

3. Sample analyses **120**

4. The data treatment **124**

4.1. Deconvolution 124

4.2. The interferences 124

5. References **132**

Chapter 3 – Cadmium isotope composition of the Earth's mantle inferred from analysis of oceanic basalts and komatiites **136**

Abstract **138**

1. Introduction **140**

2. Samples **148**

3. Analytical techniques **151**

3.1. Laboratories, tools and reagents 151

3.2. Sample digestion 151

3.3. Double spiking 152

3.4. Cadmium purification by anion exchange chromatography 152

3.5. Mass spectrometry and data reduction 154

3.6. Interference assessment and correction 155

3.7. Analyzed SRM – determination of the method's validity 156

4. Results 158

5. Discussion 169

5.1. Standard samples – validation of the method 169

5.2. The mid-oceanic ridge basalts 173

5.3. Ocean island basalts 175

5.4. Cadmium in komatiites: alteration and the Archean signature 176

5.5. Comparison between the literature estimations 182

5.6. The effects of partial melting 183

5.7. Determination of the Cd isotope composition of the Earth's mantle 183

5.8. From the mantle to the Bulk Earth 184

6. Conclusions 185

7. References 187

Chapter 4 – Cadmium isotope fractionation during fractional crystallization 204

1. Introduction 205

2. Samples 209

3. Results 216

4. Discussion 219

4.1. What caused the outliers compositions? 219

4.2. Cadmium during fractional crystallization 221

4.2.1. Forming the basalts and the rhyolites 221

4.2.2. From the basaltic andesites to the dacites 222

5. Conclusion 224

6. References 226

Chapter 5 – Cadmium composition of chondrites, a window to the primitive Solar System 230

1. Introduction 231

2. Samples 239

3. Methods 240

4. Results 242

5. Discussion 244

5.1. Impact glasses, a study of Cd volatilization 244

5.2. Cadmium compositions of chondrites 249

5.2.1. Compositional and isotopic heterogeneities in chondrites 249

5.2.2. Carbonaceous chondrites 254

5.2.3. Ordinary chondrites 267

5.2.4. Enstatite chondrites 277

6. Conclusion 281

6.1. Using tektites to assess Cd isotope fractionation during volatilization 281

6.2. Fall versus find chondrites, a sample's validity discussion 282

6.3. Chondrite's compositions 283

7. References 286

Chapter 5 – Synthesis 298

1. Conclusion 299

2. Future directions 304

Articles as co-author 306

Barium isotopes in ocean island basalts as tracers of mantle processes 307

Rubidium isotopic fractionation during magmatic processes and the composition of the bulk silicate Earth 319

Abstract

While cadmium stable isotopes studies have proven to be useful to characterize a number of natural or anthropic processes, the number of analyses of geological samples is still very limited. This scarcity is mainly due to Cd low concentrations in igneous rocks and important interferences. In this work, we present Cd concentrations and isotope compositions of geological and biological samples measured on MC-ICP-MS, using a newly developed ^{106}Cd-^{111}Cd double spike.

The first part of this project focused on proposing a new estimate of isotope composition for the Earth mantle. We analyzed 14 mid-oceanic ridge basalts (MORB), as well as 12 komatiites. The MORB are characterized by excellent isotopic homogeneity, regardless of their origin, with a mean $\delta^{114/110}Cd_{MORB}$ of 0.07 ± 0.10 ‰ (2SD, n = 23, including 10 datapoints from the literature). Komatiites Cd compositions are more diverse, with isotope compositions ranging from -0.33 ‰ to +0.26 ‰. There are correlations between the komatiites Cd concentrations as well as isotope compositions and their degree of secondary alteration, with preferential leaching of the heaviest Cd isotopes. Because of this, we only considered the least altered komatiites to determine their pristine isotope composition, which gave a $\delta^{114/110}$Cd of 0.14 ± 0.18 ‰ (2SD, n = 5, including one literature datapoint). Based on MORB and komatiites, we determined a Cd isotope composition of 0.11 ± 0.10 ‰ (2SD, n = 28) for the mantle, which is significantly heavier than what previous works proposed.

In a second part, we characterized the potential Cd isotope fractionation occurring during fractional crystallization. To this end, we analyzed a set of 18 lavas from the Hekla volcano, Iceland, ranging from basalts to rhyolites. Cadmium behaves as an incompatible element during magmatic differentiation. Basalts share a constant $\delta^{114/110}$Cd value of 0.32 ± 0.06 ‰ (2SD, n = 6) that is significantly heavier than the dacites ($\delta^{114/110}$Cd = 0.12 ± 0.06 ‰) and rhyolites while

samples from basaltic andesites to dacites have intermediary Cd. The most likely model is that intermediary compositions are produced by the mixing of the basaltic and dacitic melts. In this model, fractional crystallization does not produce any significant isotope variation for Cd. We also propose that the isotopically heavy basaltic composition reflects the preferential collection of the heavier Cd isotopes by the magmas produced by low degrees of partial melting.

Thirdly, we analyzed two Australasian tektites and two Atacama Desert impact glasses to better constrain Cd isotope fractionation occurring during volatilization. The samples are Cd-depleted and isotopically heavy, with $\delta^{114/110}$Cd values ranging from 1.03 to 4.01 ‰. These compositions can be accounted for by a Rayleigh distillation process. The measured isotope compositions, however, are significantly lighter than what theoretical distillation would produce. This because the molten tektites are not perfectly homogenized during the evaporation process and because the evaporation is likely not purely kinetic. The homogenization of the molten tektite following surficial evaporation is partly controlled by the diffusion of Cd from the center to the rim. We determined that, in Australasian tektites melt, the diffusivity order is as follow: $Cu > Zn \geq Cd > Sn$.

Finally, we analyzed a set of 17 chondrites (8 carbonaceous, 7 ordinary and 2 enstatite). We observed that about half of chondrites from each group are significantly heterogeneous, with replicates analyses finding significant variability in their Cd concentrations and / or isotope compositions. We observe a weak correlation between the carbonaceous chondrites' Cd isotope compositions and their Cd concentrations, with the Cd-richest samples being also isotopically the heaviest. This most likely reflects various mixing proportions between isotopically light chondrules and heavy matrix. No similar correlation is found for OC or EC falls.

Keywords: cadmium, stable isotopes, MORB, komatiites, tektites, chondrites, magmatic differentiation, vaporization, mantle

Résumé court

Cette thèse s'est concentrée sur le développement d'une méthode d'analyse isotopique basée sur le Cd, un système isotopique encore peu utilisé en géochimie. Dans ce cadre, un nouveau double spike, un protocole de purification chimique par chromatographie sur résine, ainsi qu'une méthode d'analyse isotopique par spectrométrie de masse à plasma à couplage inductif ont été proposés et évalués. L'objectif est d'utiliser ce nouvel outil pour caractériser des échantillons rocheux terrestres et extra-terrestres afin de mieux comprendre l'histoire du système solaire. Les corps rocheux du système solaire sont appauvris en éléments modérément volatils (MVE) comparé à sa composition moyenne. L'intensité de cet appauvrissement est liée à la volatilité de l'élément étudié. A ce jour, aucun modèle n'a permis de rendre compte à la fois des concentrations et compositions isotopiques reportées pour ces corps. Cela a poussé la communauté géochimique à se tourner vers de nouveaux systèmes isotopiques en quête de contraintes supplémentaires. Le Cd peut aider dans ce mouvement car il s'agit d'un des MVE les plus volatils, permettant l'étude de vaporisations peu intenses. De plus, le Cd est un élément sidérophile (attiré par le fer métallique lors de la fusion partielle) et chalcophile (attiré par les phases riches en S), impliquant une présence importante dans le noyau et donc la possibilité d'étudier sa formation.

Afin de valider nos données, nous avons analysé des échantillons standards déjà caractérisés. Nos résultats sont similaires à ceux obtenus par d'autres équipes de recherches, ce qui valide les méthodes employées. Nous avons ensuite analysé des basaltes de dorsales et des laves Archéennes (komatiites). Ces échantillons sont similaires isotopiquement. Nous en avons déduit une nouvelle composition isotopique pour la Terre silicatée : delta 114Cd = 0.11 ± 0.10 (2SD, n = 28) (où delta 114Cd est la déviation pour le rapport 114Cd / 110Cd entre un échantillon et le standard). Cette composition est significativement enrichie en isotope lourds

par rapport à une autre proposition, basée sur des péridotites. Ce travail fait l'objet d'une publication acceptée dans Chemical Geology.

Nous avons aussi voulu caractériser les fractionnements isotopiques affectant le Cd au cours de la différenciation d'un magma basaltique ainsi que durant un appauvrissement par vaporisation. Pour le premier sujet, nous avons étudié des laves provenant du volcan Hekla allant des basaltes aux rhyolites. Aucun fractionnement isotopique n'a été observé dans les basaltes, ce qui indique que le Cd reste alors principalement dans le magma. A l'inverse, les laves plus évoluées (des andésites basaltiques aux rhyolites) sont d'autant plus enrichies en isotopes légers qu'elles sont différenciées chimiquement. Cela suggère le mélange avec un basalte dacitique.

L'impact de la vaporisation a été caractérisé sur des verres d'impacts, lesquels ont montrés une perte préférentielle des isotopes légers du Cd conduisant à un fractionnement isotopique intense. Les compositions obtenues sont toutefois largement moins fractionnées qu'attendu dans le cas d'une distillation de Rayleigh parfaite, comme observé précédemment pour d'autres MVE (le Zn par exemple).

Enfin, une étude des compositions de chondrites a été conduite afin de mieux comprendre système solaire précoce. Nos résultats montrent que les chondrites sont hétérogènes car de nombreux réplicats sont caractérisés par des concentrations et/ou des compositions isotopiques significativement distinctes. Il y a une faible corrélation entre concentration en Cd et composition isotopique pour les chondrites carbonées, avec des compositions lourdes pour les échantillons riches en Cd.

Mots-clés : cadmium, isotopes stables, MORB, komatiites, tectites, chondrites, différenciation magmatique, vaporisation, manteau

Résumé étendu

Introduction

Les éléments chimiques peuvent être répartis en plusieurs catégories selon leurs volatilités sous les conditions de la nébuleuse solaire, exprimées par leurs T_{50} (température pour laquelle 50% de la masse disponible de l'élément existe sous forme condensée). Les éléments ayant une T_{50} supérieure à 1287 K sont dits réfractaires tandis que ceux dont la T_{50} est inférieure à 200 K sont dits hautement volatils. Entre les deux se trouve la catégorie des éléments modérément volatils (EMV). L'une des caractéristiques les plus notables des EMV est leur relative rareté dans les corps rocheux du système solaire comparé à la composition moyenne du Soleil (donc du système solaire), approximée par la composition des chondrites carbonées de type CI. Chacun de ces corps rocheux présente un appauvrissement en EMV croissant avec la volatilité de l'élément étudié. La cause de cet appauvrissement n'est, à ce jour, pas encore déterminée et fait l'objet de nombreuses publications utilisant souvent des systèmes isotopiques inhabituels pour apporter un nouvel éclairage au problème. Le présent document détaille les travaux conduits dans le cadre d'un projet doctoral ayant pour but l'étude de ce phénomène par le biais des isotopes du cadmium (Cd), un EMV dont l'emploi en géochimie est encore peu développé. Le Cd est caractérisé par une T_{50} de 502 K (Wood et al., 2019), ce qui en fait l'un des EMV les plus volatils. Il est aussi sidérophile et chalcophile (Kubik et al., 2021; Mahan et al., 2017; Marin et al., 2013; Steenstra et al., 2020), ce qui en fait un bon candidat pour étudier le stockage potentiel d'EMV dans le noyau terrestre.

L'utilisation des isotopes du Cd dans le cadre d'études géochimiques est encore assez marginale, et cela malgré ses nombreuses applications. Au cours des 50 dernières années, différentes équipes de recherche ont en effet employé les isotopes de cet élément dans des études variées, allant du traçage de la source de pollutions industrielles ou minières dans des

rivières (Cloquet et al., 2006; Robson et al., 2014; Wen et al., 2015; Zhu et al., 2018) à l'étude de l'histoire du système solaire par la caractérisation d'échantillons extraterrestres (Baker et al., 2010; Palk et al., 2018; Rosman et al., 1980b, 1980a; Rosman and De Laeter, 1988, 1978, 1976; Sands et al., 2001; Schediwy et al., 2006), en passant par l'analyse des cycles des nutriments phosphatés dans les océans (Conway and John, 2015; Ripperger and Rehkämper, 2007). Ce relatif manque d'études peut être expliqué par la très faible concentration en Cd de la plupart des roches ignées (aux alentours de 100 ng/g – ppb) ainsi que par l'existence d'interférences isobariques et polyatomiques massives sur la plupart de ses isotopes. Ce dernier point est particulièrement critique car les éléments interférents sont, pour la plupart, présents dans les échantillons géologiques à des concentrations supérieures à celle du Cd par plusieurs ordres de grandeur.

La présence de telles quantités de matrice et de matériel interférant implique que l'échantillon doit subir une purification chimique poussée afin d'obtenir une solution de Cd presque pure. Ce genre de solution est obtenu par chromatographie en phase liquide utilisant une résine à échange d'anion. L'obtention d'une solution de Cd suffisamment pure pour être analysée nécessite souvent la répétition de plusieurs étapes successives de chromatographie. Il est possible qu'une part du Cd de l'échantillon soit perdue au cours de ce processus, ce qui cause un fractionnement isotopique dans la part collectée. Afin de corriger cet effet potentiel, de nombreuses études utilisent la technique du double marquage isotopique, ou double spike (DS). Dans le cadre de cette thèse, nous avons développé un nouveau protocole de purification du Cd et utilisé un DS ^{106}Cd-^{111}Cd pour corriger tout potentiel fractionnement isotopique chimique ou instrumental dépendant de la masse.

Détermination de la composition isotopique en Cd du manteau

La première partie de ce projet a conduit à la publication d'un article scientifique dans le journal *Chemical Geology* en Avril 2024. Cette partie s'est focalisée sur l'évaluation de la justesse des données obtenues grâce à notre protocole puis à la détermination d'une composition isotopique de la Terre silicatée (Bulk Silicate Earth – BSE) pour le Cd. A cette fin, nous avons analysé deux solutions pures de Cd, ainsi qu'un ensemble de 9 échantillons standards (dont 8 roches et un échantillon biologique). Bien que les compositions isotopiques que nous avons obtenues sont généralement dans la limite haute des estimations de la littérature, nous observons généralement un recouvrement des barres d'erreur. Cette similarité entre nos résultats et ceux de la littérature nous pousse à valider notre protocole comme donnant des résultats satisfaisants.

Avant notre étude, deux articles ont proposé une composition isotopique du Cd pour la BSE, les deux étant d'accord sur un $\delta^{114/110}$Cd de -0,06 ± 0,03 ‰ (2SD) par rapport au standard NIST 3108 Cd (Pickard et al., 2022; Schmitt et al., 2009). Le premier article s'appuie sur une combinaison de lœss, de basaltes de dorsales (mid-oceanic ridge basalts – MORB) et de basaltes d'îles volcaniques (ocean island basalts – OIB) tandis que le second se base sur l'analyse de 4 lherzolites à spinelle, supposées représenter le manteau fertile. L'utilisation de roches magmatiques comme proxys de la composition isotopique du manteau repose sur l'hypothèse selon laquelle, pour les taux de fusion partielle associés aux roches étudiées, aucun fractionnement isotopique important ne se produit entre la roche initiale et le magma dérivé. Ainsi la composition isotopique du magma est supposée similaire à celle de la roche initiale. En nous basant sur les compositions d'OIB publiées à ce jour, nous argumentons que ces échantillons ne sont probablement pas représentatifs de leur source mantellique pour le Cd et donc qu'ils ne doivent pas être pris en compte pour déterminer la composition de la BSE.

Reprenant la démarche utilisée dans Schmitt et al. (2009), nous avons analysé 13 MORB des océans Atlantique, Indien et Pacifique et 12 komatiites (des laves archéennes formées par

un fort taux de fusion partielle) des ceintures de roches vertes d'Abitibi, de Barberton et de Kostomuksha. Ce jeu de données est complété par des analyses de MORB et komatiites détaillées dans (Pickard et al., 2022). Les compositions isotopiques des MORB sont extrêmement homogènes et donnent une valeur moyenne de 0.07 ± 0.10‰ (2SD, n = 23), composition que nous attribuons aussi à leur source mantellique. A l'inverse, les komatiites ont des concentrations et composition isotopiques très variables pour le Cd. Il existe une corrélation négative entre leur concentration en Cd et leur degré d'altération déterminé par la perte au feu (loss on ignition – LOI). De manière similaire, les compositions isotopiques des komatiites à basse LOI sont relativement constantes alors que celles des échantillons à haute LOI sont caractérisées par un éparpillement vers des compositions isotopiquement légères. Ces observations sont cohérentes avec les données publiées qui indiquent que les fluides altérants collectent préférentiellement les isotopes lourds du Cd. Nous avons déterminé une composition isotopique moyenne pour les komatiites les moins altérées (celles avec une LOI < 6 %) de 0.14 ± 0.18 ‰ (2SD, n = 5). De nombreuses komatiites plus altérées, de chaque région étudiée, ont une composition isotopique similaire, ce qui indique une bonne résistance de la composition isotopique du Cd à l'altération. De plus, les komatiites présentant cette composition isotopique sont datées de 3549 ± 99 millions d'années (Ma) à 2713 ± 29 Ma, ce qui indique que le manteau terrestre est homogène isotopiquement pour le Cd depuis au moins 3,5 milliards d'années.

En nous basant sur les compositions isotopiques des MORB et des komatiites, nous proposons une composition isotopique en Cd pour la BSE de 0.11 ± 0.10 ‰ (2SD, n = 28). Une telle valeur est significativement plus lourde isotopiquement que les compositions proposées dans la littérature.

Fractionnement isotopique du Cd durant la cristallisation fractionnée

Dans une seconde partie, nous avons étudié le potentiel fractionnement isotopique affectant le Cd durant des épisodes de cristallisation fractionnée. Pour cela, nous nous sommes basés sur un ensemble de 18 échantillons de laves provenant du système magmatique du volcan Hekla en Islande. Ce volcan est connu pour sa production de roches très distinctes chimiquement, allant des basaltes aux rhyolites. Bien qu'il n'existe pas encore de consensus sur les processus à l'œuvre au cours de la différentiation magmatique de ce système, certaines étapes sont acceptées par la plupart des chercheurs. Cet accord porte sur la différentiation des basaltes en andésites basaltiques ainsi que sur celle transformant les dacites en rhyolites. Ces deux processus sont supposés résulter principalement d'épisodes de cristallisation fractionnée. En revanche, la formation des andésites basaltiques, andésites et dacites fait l'objet de différentes théories. Certains spécialistes estiment que cette différentiation peut se faire simplement par cristallisation fractionnée (Geist et al., 2021) tandis que d'autres (Chekol et al., 2011; Sigmarsson et al., 1992) considèrent nécessaire d'assimiler un magma dacitique par fusion de la croûte encaissant la chambre magmatique (couplé ou non à de la cristallisation fractionnée).

Nous observons dans nos échantillons que la différentiation magmatique s'accompagne d'un enrichissement important en Cd, et ce dans toutes les phases de différenciation. Cela indique que Cd se comporte en élément incompatible, même lors d'épisodes de cristallisation fractionnée. Une rupture de pente est visible entre les basaltes et les échantillons plus différentiés sur une représentation de la concentration en Cd en fonction du degré de différentiation. Ainsi, les basaltes sont enrichis plus rapidement en fonction de leur degré de différenciation que les andésites basaltiques, andésites ou dacites. Nous pouvons expliquer ce constat par la cristallisation d'une phase porteuse de Cd ou par un mélange avec un magma moins riche en Cd que le magma basaltique le plus évolué.

Les compositions isotopiques en Cd des échantillons diffèrent significativement : les basaltes sont caractérisés par une valeur constante de δ^{114}Cd égale à 0.32 ± 0.06 ‰ (2SD, n = 6) alors que les dacites sont isotopiquement plus légères, avec un δ^{114}Cd de 0.12 ± 0.06 ‰. Tous les échantillons intermédiaires (andésites basaltiques, andésites et dacites peu évoluées) ont des compositions isotopiques comprises entre ces deux valeurs, avec une corrélation linéaire décroissante claire liant leurs valeurs de δ^{114}Cd et leurs concentrations en Cd. En détail, les andésites basaltiques les moins évoluées ont une composition similaire à celle des basaltes les plus différentiés tandis que les andésites les plus différentiées sont isotopiquement identiques aux dacites. Enfin la rhyolite analysée a une composition isotopique similaire à celle des dacites. Ces observations indiquent que les processus de cristallisation fractionnée ne causent pas de variabilité isotopique significative du Cd, au moins pour les basaltes et les rhyolites. Les compositions en Cd des échantillons intermédiaires peuvent être aisément expliqués par le mélange de magmas basaltiques et dacitiques. Dans ce cas de figure, l'éventuelle cristallisation fractionnée se produisant en parallèle du mélange ne devrait pas s'accompagner de fractionnement isotopique significatif pour le Cd. En revanche, dans le cas d'une explication par cristallisation fractionnée seule, nos résultats suggèrent la précipitation d'une phase enrichie en isotopes lourds du Cd pour des compositions entre les basaltes et les dacites. La différence de compositions isotopiques entre les basaltes et les dacites est expliquée par une production des basaltes caractérisée par un faible taux de fusion partielle. Cela indique que les magmas produits par de tels taux collectent préférentiellement les isotopes les plus lourds du Cd, comme c'est le cas pour le Zn (Day et al., 2022).

Caractérisation de la vaporisation du Cd, le cas des tectites

Nous nous sommes ensuite intéressés aux compositions isotopiques pour le Cd de verres d'impacts (tectites et atacamaites) dans le but de mieux caractériser le fractionnement isotopique se produisant dans le cadre d'une vaporisation de Cd dans l'atmosphère terrestre.

Cette caractérisation nous permettra de mieux appréhender l'impact de la formation d'une croûte de fusion sur la composition isotopique moyenne d'une météorite rocheuse.

Les deux tectites que nous avons analysé proviennent du champs de débris australasiatique, tout comme la seule tectite caractérisée précédemment pour le Cd (Wombacher et al., 2003). Les compositions de ces trois échantillons appartiennent à une même corrélation liant compositions isotopiques et concentrations. Cette corrélation est décrite mathématiquement par une distillation de Rayleigh dépendante d'un facteur cinétique α :

$$\delta^{114}Cd_{tectite} - \delta^{114}Cd_{initial} = 10^3 \times \left(\frac{[Cd]_{tectite}}{[Cd]_{initial}}\right)^{\alpha-1} - 10^3$$

Si le facteur α est élevé, alors l'échantillon a subi peu de fractionnement isotopique en perdant son Cd par vaporisation tandis qu'un α faible implique un fractionnement isotopique très important pour une évaporation similaire.

En prenant une composition initiale similaire à celle de la croûte continentale supérieure (90 ± 40 ppb; 0,06 ± 0,14 ‰) (Pickard et al., 2022; Rudnick and Gao, 2014), l'on obtient $\alpha_{tectites\ australasiatique} = 0{,}9984$ et $\alpha_{atacamaites} = 0{,}9995$. Ces deux valeurs sont bien supérieures à celles obtenues dans le cas d'une distillation théorique utilisant un facteur de fractionnement isotopique purement cinétique : $\alpha_{Cd} = 0{,}9823$ et $\alpha_{CdO} = 0{,}9845$. La principale différence repose sur le fait que dans une distillation théorique, l'échantillon fondu est en permanence parfaitement homogène et la vaporisation est contrôlée de manière purement cinétique par la volatilité de l'espèce chimique étudiée. Dans la réalité, le processus de vaporisation est principalement contrôlé par la diffusivité de l'espèce étudiée dans l'échantillon fondu depuis un cœur riche en volatils vers une bordure qui en est totalement dépourvue (Moynier et al., 2010, 2009).

Ce modèle prédit que les éléments chimiques diffusant le plus aisément dans le liquide silicaté seront aussi ceux pour lesquels les compositions isotopiques sont le plus fractionnées dans les verres d'impact. Grâce à ce critère, nous proposons l'ordre suivant, allant des éléments diffusant le plus aisément dans le liquide des tectites australasiatiques à ceux diffusant avec le plus de difficultés : $Cu > Zn \geq Cd > Sn$. Cet ordre semble être principalement dicté par les propriétés chimiques des éléments, avec Cu faisant partie du groupe 11, Zn et Cd du groupe 12 et Sn du groupe 14. Cela est en agrément avec nos connaissances concernant l'influence de la charge électrique et la diffusivité des ions, nous retrouvons l'ordre détaillé précédemment : $Cu^{+/2+}$, Zn^{2+} and Cd^{2+}, $Sn^{2+/4+}$.

Analyse de chondrites

Nous avons analysé un total de 17 chondrites, avec 8 carbonées, 7 ordinaires et 2 à enstatite. Parmi ces météorites, les concentrations et compositions isotopiques en Cd de 14 n'avaient pas encore été mesurées. Au final, notre ensemble de données double presque le nombre de chondrites ordinaires et de chondrites carbonées complètement décrites (concentrations et compositions isotopiques) pour le Cd.

Une des observations principales que nous avons faites est que presque la moitié des échantillons dans ce travail ou dans la littérature présentent des hétérogénéités importantes pour le Cd. Ainsi, la moitié des réplicats mesurés sont caractérisés par des concentrations ou compositions isotopiques en Cd différentes. Relevons notamment les points suivants :

- Les mesure de la concentration en Cd d'Allende s'accordent sur une répartition bimodale, avec une première composition à 232 ± 43 ppb et une seconde à 468 ± 11 ppb. Le fait qu'aucune valeur intermédiaire n'a été rapportée à ce jour montre que cette météorite est probablement composée de deux chondrites carbonées de composition différentes soudées.

- Les compositions isotopiques d'Allende, de Bjurböle et de Sahara 97096 sont variables mais ne présentent aucune corrélation avec leurs concentrations en Cd respectives. Notre interprétation est que ces compositions reflètent l'hétérogénéité isotopique qui régnait dans les zones de formation de ces échantillons dans la nébuleuse solaire.
- La chondrite carbonée NWA 13689 possède une composition isotopique en Cd stable. Elle est, en revanche, caractérisée par une grande variabilité de sa concentration en Cd, ce qui indique une dilution de la phase porteuse de Cd.
- Les deux réplicats de la chondrite Olivenza présentés dans cette étude ont des concentrations en Cd et des compositions isotopique très distinctes. Le réplica le plus riche en Cd est aussi isotopiquement le plus lourd, ce qui ne peut être expliqué par de la volatilisation. Puisque ces réplicats ont échantillonné la même poudre, nous proposons que l'échantillon le plus concentré a échantillonné une « pépite » de cadmium, c'est-à-dire une particule très riche en Cd et isotopiquement lourde, qui a altéré significativement la composition moyenne de l'échantillon.
- Enfin, dans le cas de la chondrite à enstatite Indarch, l'un de nos réplicats est moins riche en Cd et isotopiquement plus léger que la valeur de la littérature. L'autre réplica est plus riche en Cd et isotopiquement compris entre les deux valeurs précédentes (sans superposition). Dans ce cas nous proposons que différentes parties de la météorite aient subi une injection de Cd isotopiquement lourd en différentes proportions. La décorrélation entre concentrations et compositions isotopiques laisse penser que plusieurs mécanismes contradictoires pourraient être à l'œuvre.

Ces observations rendent primordiales l'échantillonnage de grandes masses pour assurer une homogénéité de résultats. Un autre point critique est le mode de trouvaille de l'échantillon.

Dans la plupart des cas, nous trouvons que les échantillons « trouvés » ont des concentrations en Cd et / ou des compositions isotopiques différentes des échantillons dont la chute a été observée. Les compositions de tous les échantillons « trouvés » ne peuvent pas être expliquées par les mécanismes connus d'altération à la surface de la Terre, dans lesquels un fluide collecte préférentiellement les isotopes lourds du Cd. Nous observons notamment que certaines météorites « trouvées » sont appauvries en isotopes léger du Cd, conformément à ce qui se produirait dans le cas d'une vaporisation de Cd. L'occurrence d'un tel processus à la surface de la Terre pour ces échantillons est néanmoins improbable, ce qui pourrait pointer vers des modes d'altération encore inconnus.

Dans le cas des chondrites carbonées, nous observons une corrélation peu intense entre la composition isotopique en Cd et la concentration en celui-ci. Cela se traduit par un enrichissement en isotopes lourds dans les échantillons les plus riches en Cd. Les chondrites CO et CI sont hors de cette tendance. La corrélation entre concentration et composition isotopique pour le Cd peut être expliquée par un mélange entre une matrice riche en Cd et isotopiquement lourde et des chondres pauvres en Cd et isotopiquement légers. Nous n'avons pas trouvé trace de corrélations similaires dans le cas des chondrites ordinaires ou à enstatite, lesquelles sont caractérisées par une intense variabilité isotopique et chimique.

References

Baker, R.G.A., Schönbächler, M., Rehkämper, M., Williams, H.M., Halliday, A.N., 2010. The thallium isotope composition of carbonaceous chondrites — New evidence for live 205Pb in the early solar system. Earth Planet. Sci. Lett. 291, 39–47. https://doi.org/10.1016/j.epsl.2009.12.044

Chekol, T.A., Kobayashi, K., Yokoyama, T., Sakaguchi, C., Nakamura, E., 2011. Timescales of magma differentiation from basalt to andesite beneath Hekla Volcano, Iceland: Constraints from U-series disequilibria in lavas from the last quarter-millennium flows. Geochim. Cosmochim. Acta 75, 256–283. https://doi.org/10.1016/j.gca.2010.10.001

Cloquet, C., Carignan, J., Libourel, G., Sterckeman, T., Perdrix, E., 2006. Tracing source pollution in soils using cadmium and lead isotopes. Environ. Sci. Technol. 40, 2525–2530. https://doi.org/10.1021/es052232+

Conway, T.M., John, S.G., 2015. Biogeochemical cycling of cadmium isotopes along a high-resolution section through the North Atlantic Ocean. Geochim. Cosmochim. Acta 148, 269–283. https://doi.org/10.1016/j.gca.2014.09.032

Day, J.M.D., Moynier, F., Ishizuka, O., 2022. A partial melting control on the Zn isotope composition of basalts. Geochem. Perspect. Lett. 23, 11–16. https://doi.org/10.7185/geochemlet.2230

Geist, D., Harpp, K., Oswald, P., Wallace, P., Bindeman, I., Christensen, B., 2021. Hekla Revisited: Fractionation of a Magma Body at Historical Timescales. J. Petrol. 62, egab001. https://doi.org/10.1093/petrology/egab001

Kubik, E., Siebert, J., Blanchard, I., Agranier, A., Mahan, B., Moynier, F., 2021. Earth's volatile accretion as told by Cd, Bi, Sb and Tl core–mantle distribution. Geochim. Cosmochim.

Acta 306, 263–280. https://doi.org/10.1016/j.gca.2021.02.017

Mahan, B., Siebert, J., Pringle, E.A., Moynier, F., 2017. Elemental partitioning and isotopic fractionation of Zn between metal and silicate and geochemical estimation of the S content of the Earth's core. Geochim. Cosmochim. Acta 196, 252–270. https://doi.org/10.1016/j.gca.2016.09.013

Marin, N., Righter, K., Danielson, L., Pando, K., Lee, C., 2013. Metal-silicate partitioning of Bi, In, and Cd as a function of temperature and melt composition. Presented at the 44th Lunar and Planetary Science Conference.

Moynier, F., Beck, P., Jourdan, F., Yin, Q.-Z., Reimold, U., Koeberl, C., 2009. Isotopic fractionation of zinc in tektites. Earth Planet. Sci. Lett. 277, 482–489. https://doi.org/10.1016/j.epsl.2008.11.020

Moynier, F., Koeberl, C., Beck, P., Jourdan, F., Telouk, P., 2010. Isotopic fractionation of Cu in tektites. Geochim. Cosmochim. Acta 74, 799–807. https://doi.org/10.1016/j.gca.2009.10.012

Palk, E., Andreasen, R., Rehkämper, M., Stunt, A., Kreissig, K., Coles, B., Schönbächler, M., Smith, C., 2018. Variable Tl, Pb, and Cd concentrations and isotope compositions of enstatite and ordinary chondrites—Evidence for volatile element mobilization and decay of extinct ^{205} Pb. Meteorit. Planet. Sci. 53, 167–186. https://doi.org/10.1111/maps.12989

Pickard, H., Palk, E., Schönbächler, M., Moore, R.E.T., Coles, B.J., Kreissig, K., Nilsson-Kerr, K., Hammond, S.J., Takazawa, E., Hémond, C., Tropper, P., Barfod, D.N., Rehkämper, M., 2022. The cadmium and zinc isotope compositions of the silicate Earth – Implications for terrestrial volatile accretion. Geochim. Cosmochim. Acta 338, 165–180. https://doi.org/10.1016/j.gca.2022.09.041

Ripperger, S., Rehkämper, M., 2007. Precise determination of cadmium isotope

fractionation in seawater by double spike MC-ICPMS. Geochim. Cosmochim. Acta 71, 631–642. https://doi.org/10.1016/j.gca.2006.10.005

Robson, T.C., Braungardt, C.B., Rieuwerts, J., Worsfold, P., 2014. Cadmium contamination of agricultural soils and crops resulting from sphalerite weathering. Environ. Pollut. 184, 283–289. https://doi.org/10.1016/j.envpol.2013.09.001

Rosman, Barnes, I.L., Moore, L.J., Gramlich, J.W., 1980a. Isotope composition of Cd, Ca and Mg in the Brownfield chondrite. Geochem. J. 14, 269–277. https://doi.org/10.2343/geochemj.14.269

Rosman, De Laeter, J.R., 1988. Cadmium mass fractionation in unequilibrated ordinary chondrites. Earth Planet. Sci. Lett. 89, 163–169. https://doi.org/10.1016/0012-821X(88)90168-9

Rosman, De Laeter, J.R., 1978. A survey of cadmium isotopic abundances. J. Geophys. Res. 83, 1279. https://doi.org/10.1029/JB083iB03p01279

Rosman, De Laeter, J.R., 1976. Isotopic fractionation in meteoritic cadmium. Nature 261, 216–218. https://doi.org/10.1038/261216a0

Rosman, De Laeter, J.R., Gorton, M.P., 1980b. Cadmium isotope fractionation in fractions of two H3 chondrites. Earth Planet. Sci. Lett. 48, 166–170. https://doi.org/10.1016/0012-821X(80)90179-X

Rudnick, R.L., Gao, S., 2014. Composition of the continental crust, in: Holland, H.D., Turekian, K.K. (Eds.), Treatise on Geochemistry. Elsevier, pp. 1–51. https://doi.org/10.1016/B978-0-08-095975-7.00301-6

Sands, D.G., Rosman, K.J.R., De Laeter, J.R., 2001. A preliminary study of cadmium mass fractionation in lunar soils. Earth Planet. Sci. Lett. 186, 103–111. https://doi.org/10.1016/S0012-821X(01)00233-3

Schediwy, S., Rosman, K.J.R., de Laeter, J.R., 2006. Isotope fractionation of cadmium in lunar material. Earth Planet. Sci. Lett. 243, 326–335. https://doi.org/10.1016/j.epsl.2006.01.007

Schmitt, A.-D., Galer, S.J.G., Abouchami, W., 2009. Mass-dependent cadmium isotopic variations in nature with emphasis on the marine environment. Earth Planet. Sci. Lett. 277, 262–272. https://doi.org/10.1016/j.epsl.2008.10.025

Sigmarsson, O., Condomines, M., Fourcade, S., 1992. A detailed Th, Sr and O isotope study of Hekla: differentiation processes in an Icelandic Volcano. Contrib. Mineral. Petrol. 112, 20–34. https://doi.org/10.1007/BF00310953

Steenstra, E.S., Seegers, A.X., Putter, R., Berndt, J., Klemme, S., Matveev, S., Bullock, E.S., van Westrenen, W., 2020. Metal-silicate partitioning systematics of siderophile elements at reducing conditions: A new experimental database. Icarus 335, 113391. https://doi.org/10.1016/j.icarus.2019.113391

Wen, H., Zhang, Y., Cloquet, C., Zhu, C., Fan, H., Luo, C., 2015. Tracing sources of pollution in soils from the Jinding Pb–Zn mining district in China using cadmium and lead isotopes. Appl. Geochem. 52, 147–154. https://doi.org/10.1016/j.apgeochem.2014.11.025

Wombacher, F., Rehkämper, M., Mezger, K., Münker, C., 2003. Stable isotope compositions of cadmium in geological materials and meteorites determined by multiple-collector ICPMS. Geochim. Cosmochim. Acta 67, 4639–4654. https://doi.org/10.1016/S0016-7037(03)00389-2

Wood, B.J., Smythe, D.J., Harrison, T., 2019. The condensation temperatures of the elements: A reappraisal. Am. Mineral. 104, 844–856. https://doi.org/10.2138/am-2019-6852CCBY

Zhu, C., Wen, H., Zhang, Y., Yin, R., Cloquet, C., 2018. Cd isotope fractionation during sulfide mineral weathering in the Fule Zn-Pb-Cd deposit, Yunnan Province, Southwest China.

Sci. Total Environ. 616–617, 64–72. https://doi.org/10.1016/j.scitotenv.2017.10.293

Chapter 1 – General introduction

1. Solar system objects

1.1. On the origin of things

In 1965, the cosmic microwave background (CMB) was described for the first time (Penzias and Wilson, 1965). This discovery would eventually lead to the acceptation of the idea of a Universe expanding from a theoretical single point containing all its energy and matter. Observations have allowed to describe a stage of utmost heat and density, thought to have occurred instants after this theoretical singularity, giving up an age of 13.8 billion years (Ga) for the Universe (Planck Collaboration et al., 2020). During the following minutes, intense nucleosynthesis occurred as the original plasma cooled down (Coc and Vangioni, 2017), allowing for proton-proton and proton-neutron bonds to survive. Nuclear fusion of hydrogen nuclei and capture of surrounding neutrons produced atoms for the very first time. Thus, were formed the first atoms of D and He alongside small amounts of Li and unstable ^{7}Be.

This event resulted in the formation of large cold molecular clouds composed mainly of H and He. Such clouds are often described as “stellar nurseries”, as they give birth to stars when local gas density gets high enough to trigger nuclear fusion. The mechanisms triggering the constitution of such high-density pockets are not well understood yet (Chambers and Halliday, 2014). Collapse of parts of the molecular cloud under its own gravity have been proposed (Heitsch and Hartmann, 2008) as well as formation of high densities at the intersection of two colliding supernovae bubbles (Williams, 2010). These high-density zones collapse in multiple protostars, forming clusters of young stars.

Stars are the reactors in which the whole periodic table is elaborated by different nuclear fusion reactions occurring successively in their core (Woosley and Janka, 2006). During most of their lifetime, H fusion produces He while He fusion produces C and O nuclei. Fusion of these heavier elements occur during the last stages of the star life, ending with the brief burning

of Si, days before the star death. During this step, He nuclei fuse with increasingly heavy elements until forming iron, which is the final stable product of stellar fusion processes. Alongside the fusion reactions, stars produce elements heavier than iron by neutron capture.

The rest of the known elements is formed by neutron and proton capture during explosive nucleosynthesis processes, occurring during supernovae or in a neutron star. Thus, the poetic saying describing humans as "stardust" is generally correct as we are made of elements forged in dying stars. Moreover, the current elemental and isotopic abundances in the solar system are directly determined by the genealogy of stars from which the solar system matter is derived.

1.2. The formation of the solar system

The formation of the solar system as we know it has long been the subject of conjectures and discussions. For most of human history, these explanations were tainted by religious dogma or mythological notions. The first proto-scientific discussions regarding its constitution occurred during the enlightenments, with René Descartes developing in 1633 a first qualitative model for how the planets accrete, based on observations of the movement of liquids. According to it, planets were suspended in an undetermined fluid and accreted in its eddies, smaller vortexes would accrete less material and form satellites (Descartes, 1633). The discussion was furthered by the count of Buffon one century later, who proposed that all the matter constituting planets originated in the Sun and was ejected from it by a catastrophic impact with a comet, which were then thought to be massive bodies (Buffon, 1745). Although these theories were mostly speculative, it is amusing to see fortuitous similarities with current cosmological models, as planet material do originate from stars (although not from the Sun) and accretion does involve vortexes driving matter to the accreting body. Immanuel Kant, in a pioneering philosophical work, was the first to propose that the planets were produced by processes inside a nebula (Kant, 1755). However, it's with Herschel's first description of stars surrounded by a nebula (Herschel, 1791) that the idea of the formation of stars in nebulae really started to be

considered. Shortly after this observation, the first model for Solar system formation based on the evolution of a proto-Solar nebula and later a proto-planetary disk was formulated (Laplace, 1796), really starting the scientific discussion.

As understood today, at the origin of the Solar system lies a wide, dense and cold molecular cloud, spanning a few light years in diameter (Portegies Zwart, 2009) and formed of H and He gas and fine solid material called hereafter "dust". Parts of this cloud collapsed and formed a cluster of stars with a collective mass superior or equal to 500 solar masses ($M_{\odot}$) (Portegies Zwart, 2009). Many of these stars still survive and are similar to the Sun, however the abundance of the short-lived radioisotope ^{60}Fe in the Solar system potentially indicate that it was injected by a neighboring supernova around 1 million year (Ma) after formation of the Sun (Hester et al., 2004). Such observation requires the presence of massive (15-25 $M_{\odot}$) short-lived (6-12 Ma) stars in the cluster (Portegies Zwart, 2009). These supernovae might also have triggered the formation of star-spawning high density pockets (Cameron and Truran, 1977; Williams, 2010). Thus, the Sun might have spent its first 100 Ma of existence in an open cluster of stars before it broke apart (Kaib and Quinn, 2008). After the cluster dissolved, the Sun remained isolated, surrounded by a disk of gas and dust called the protosolar nebula, from which the current Solar system bodies will eventually emerge. At this point, the Sun is characterized as a T-Tauri star, meaning that it was then too cold to trigger nuclear reactions in its core. Its heat resulted from the dissipation of gravitational energy during the viscous accretion of gas and the contraction of the Sun (Chambers and Halliday, 2014). The inner protosolar nebula was also heated by the viscous accretion of material toward the star via its median plane, allowing for temperatures to rise to 1500 K there (Chambers and Halliday, 2014), while the surface of the disk was cooled by radiating. On the other hand, the more diffuse outer disk was less heated by viscous accretion and so, was probably colder.

The starting point of the Solar system history is usually defined by the formation of its first solid, occurring 4.567 Ga before the present (Amelin et al., 2002; Connelly et al., 2012). These solids, the calcium-aluminum inclusions (CAI), were formed when the nebula cooled down enough to allow for refractory elements condensation to occur. Most CAIs are millimeter to centimeter-sized fine-grained condensates, they are thought to have formed from a gas of solar composition at temperatures higher than 1400K and pressures below 10^{-4} bar (Grossman, 1972). Simultaneously were formed similar-sized spherules characterized by igneous textures, with igneous minerals caught in glass, called chondrules (Bollard et al., 2017; Connelly et al., 2012). Chondrules may have been produced by a variety of processes. A first population could have been formed by nebular melting and quenching of aggregates of condensed dust (Ciesla, 2002; Connolly and Desch, 2004; Connolly and Love, 1998; Desch and Connolly, 2002), possibly caused by shock waves in the disk, while secondary populations may have been splashing debris resulting from low velocity impacts between big molten bodies (Asphaug et al., 2011; Faure et al., 2012; Florentin et al., 2017; Sanders and Scott, 2012).

These refractory inclusions and chondrules accreted in bigger bodies, called planetesimals, alongside with fine-grained matrix. Such bodies would not have any radial internal structure yet as they were composed of a rather homogeneous mix of chondrules, refractory inclusions and dust. However, during their growth, they accumulated short-live radioactive isotopes (^{26}Al being the most significant), heating their insides (Van Kooten et al., 2016). Some planetesimals underwent rapid and early growth, leading to an object rich in radioisotopes and with a big volume over surface ratio. In such a scenario, intense heat production inside the body occurred, outpacing its dissipation by radiation at the surface. The planetesimal became unable to maintain a cool core and melted (Hevey and Sanders, 2006). Under such conditions it underwent a planetary differentiation, meaning that it acquired a radial structure formed by a metallic core surrounded by a silicate mantle and a crust. However, some planetesimals never

experienced such melting, either because they accreted late and thus lacked short-lived radioisotopes, because they grew slowly which ended in the same scenario or because they never grew big enough to have sufficient volume over surface ratio. Accretion of planetesimals onto each other formed the planets and moons we know today. Asteroids are fragments or remains of these planetesimals.

1.3. Composition and structure of the Solar system

The Solar system is constituted by every object caught in orbit by its star, the Sun. It is composed of the eight planets and their over 200 moons, five dwarf planets, an asteroid belt standing between Mars and Jupiter, the Kuiper belt, beyond Neptune's orbit, the scattered disc and finally the Oort cloud, forming the outer rim of the Solar system. Despite the great number of objects forming this system, the Sun accounts for more than 99 % of its mass (Woolfson, 2000). Thus, the mean elemental composition of the Solar system can be defined as the mean composition of the Sun, determined from its photosphere (the Sun's outer shell, from which light is radiated). The Sun is primarily composed of H (74 wt.%) and He (25 wt.%), with heavier elements representing around 1 wt.% (Asplund et al., 2009). This composition is found again in the rest of the solar system, as the remaining mass is dominated by the gas giants (Jupiter and Saturn) and the ice giants (Uranus and Neptune), all composed mainly of H and He.

These four bodies are designated as outer planets, contrasting with the inner planets, as they are situated beyond the asteroid belt. They are also located beyond the current water ice line (the isotherm line past which a volatile specie exists under solid form in space rather than under gaseous state), which coincides with the asteroid belt (Jewitt et al., 2007). Beyond this line, asteroids and planets are "wet", understood as rich in ices. Inversely, inner bodies are called "dry" as they cannot maintain volatiles under solid state and loose them to space unless they are massive enough to maintain an atmosphere. Inner planets are also known as terrestrial or

rocky planets as they are significantly depleted in volatile species compared with the outer ones, being composed at 90 % of O, Mg, Si and Fe (Chambers and Halliday, 2014).

1.4.Meteorites and the records of primitive Solar system

1.4.1. Differentiated and undifferentiated

Meteorites are defined as larger than 10 µm natural bodies that fragmented from a celestial object and fell by natural means on a body larger than itself (Rubin and Grossman, 2010), be it natural or artificial. They are widely regarded as fragments of asteroids, ejected by impacts, and so are studied as proxy for the compositions of their parent body. This is of paramount interest as asteroids are remnants of planetesimals and thus hold records of accretion processes in the protoplanetary disk. Because the "meteorite" label only provides information on the recent history of the object (namely that it travelled through space and fell on another body) and not on its composition, its texture or its thermal history; it is expected that it would cover multiple object categories. Thus, intense efforts have been dedicated to their classification. Here, we will review the main categories used in geochemistry studies.

Meteorites can be divided between undifferentiated and differentiated. This categorization relies on the meteorite parent body thermal history, meaning whether it underwent total melting accompanied by planetary differentiation. Undifferentiated meteorites, also known as chondrites, form the majority of the known meteoritic ensemble as they represent more than two third of it (Grady, 2022). They never experienced total melting and thus, their compositions and textures reflect mostly that of the accreted material. They are composed of a heterogenous mix of chondrules (or remnants of it), refractory inclusions and matrix in varying proportions. Although they are thought to have formed later than achondrites (see paragraph on planetesimals earlier), they are the most primitive samples from the Solar system as their components were among the first objects to condense from the nebula. Moreover, the fact that

they never melted allows for study of individual components, unlike differentiated meteorites which were homogenized. Thus, they are widely used to constrain the conditions occurring in the nebula during the first Ma of the Solar system. Chondrites also have similar ratios of refractory elements than the Sun photosphere.

Differentiated meteorites, however, did experience melting and planetary differentiation. This altered their chemical compositions, as iron and siderophile (Fe-loving) elements were extracted from the silicate phase and segregated in a metallic core. The "differentiated" label covers three categories defined by their chemical composition and their origin reservoir: iron meteorites (54 % of all differentiated), stony-iron meteorites (around 7 %) and achondrites (39%). Iron meteorites (also known as siderites) are almost entirely composed of an iron-nickel alloy, they are thought to be fragments of the metallic core of their parent asteroid (Weisberg et al., 2006). Achondrites are differentiated stony meteorites, they do not conserve traces of chondrules, refractory inclusions or matrix as all of it was melted away and chemically homogenized. They are thought to originate from the mantle and crusts of their parent bodies. Most known achondrites originated from an asteroidal parent body, however, around 30 were determined to have originated from Mars or from the Moon (Grady, 2022) and one is even thought to be from the Earth (Gattacceca et al., 2023). Finally, stony-iron meteorites (or siderolites) are composed in comparable amounts of metal (Fe-Ni) and silicates (mostly olivine). They are often understood as representing the contact between a metallic core and a silicate mantle. This can result from collisional extraction of the core-mantle boundary of an asteroid or from two differentiated objects colliding and one core being injected through the mantle.

Finally, primitive achondrites are intermediary samples located somewhere between chondrites and other achondrites as they display clear signs of partial melting but maintained

traces of their chondritic past (relic chondrules for example) and maintained significant part of their parent rock unmelted (Pilski et al., 2011; Prinz et al., 1983).

1.4.2. The chondrites classification

Although they are fundamentally composed of the same objects, chondrites can be divided in 3 main categories based on their textures and their chemical, mineralogical and isotopic compositions (Weisberg et al., 2006):

- *Carbonaceous chondrites (CC):* These meteorites were originally characterized by the presence of a carbon-rich matrix. However, discovery of new C-poor subcategories reframed this definition. They are currently defined by abundances of refractory elements that equals or exceed that of Ivuna-type CC (CI) and by specific isotope compositions for oxygen (Scott and Krot, 2014). These CI chondrites are known for having similar abundances than the Sun for most element, and are used oftentimes to determine the bulk Solar system elemental composition. Carbonaceous chondrites represent 4% of total known chondrites (Grady, 2022) and are subdivided in many subgroups named after the type chondrite. These subgroups are characterized by multiple factors, among which the matrix abundance, ranging from almost 100 vol.% (CI) to less than 1 % (CB); the chondrules sizes, that can go from less than 0.1 mm in diameter (CH) to more than 1 mm (CV, CK); the metal content, ranging from 0 to almost 80 vol.% or the refractory inclusions abundance, with CH being generally depleted (around 0.1 vol%) while CO, CV and CK have more than 10 vol.%.
- *Ordinary chondrites (OC):* They are by far the most common type of meteorites as they represent about 63% of all meteorites and 94% of chondrites (Grady, 2022). They are characterized by high abundances of large (mm-sized) chondrules, relatively low matrix content (10-15 vol%) and almost no refractory inclusions. Their Mg-normalized refractory lithophile (rock-loving) elements concentrations are slightly inferior to CI

reference and their oxygen isotope compositions plot above the terrestrial fractionation line, which allow determination from CC (Sears and Weeks, 1983). These chondrites are divided in 3 sub-groups, originally based on their Fe content:

- H chondrites ("high iron content"): they are characterized by Fe-rich compositions (25 to 31 wt.%) and higher metal content (8 vol.%) than L and LL chondrites. They also contain smaller chondrules. The Co content of their fayalite and kamacite phases allows distinction with L sub-group (Rubin, 1990).
- L chondrites ("low iron content"): L chondrites contain much less metal (around 4 vol.%) and iron (20-25 wt.%). It can be distinguished from H and LL by their siderophile elements content (Sears and Weeks, 1983).
- LL chondrites ("low iron content, low metal content"): These samples contain even less metal (around 2 vol.%) and have Fe content that are similar to lower than that of L chondrites (19-22 wt.%).

- *Enstatite chondrites (EC):* As their name reflect, they are rich in enstatite. These are the least common chondrite, representing only 1% of the known chondrites (Grady, 2022). They formed under reducing conditions, which are reflected by their chemistry. Unlike the other chondrites, their minerals contain almost no iron oxide as all of their iron is reduced in metal grains. Two categories are drawn depending on the compositions of their sulfides and on their Fe content:
  - EH ("high iron content"): They contain tinier chondrules than EL, have more iron and are characterized by the presence of niningerite sulfides.
  - EL ("low iron content"): They contain characteristic alabandite sulfides.

Chondrites are also grouped by petrologic type in six categories, based on their metamorphism and alteration history. Type 1 and 2 samples are characterized by extensive aqueous alteration while types 4 to 6 chondrites have textures and compositions determined

mainly by thermic metamorphism. Type 3 chondrites are regarded as the most pristine type. This classification has been significantly modified since its proposal (Van Schmus and Wood, 1967), as it was originally thought that type 1 chondrites were the pristine ones (Wiik, 1956), and that type 2 to 6 underwent increasing intensity of thermal metamorphism. These assumptions were based on the fact that type 1 chondrites are generally chemically the most pristine although they lost their original texture due to recrystallization. Type 3 have the closest mineralogy to their parent asteroid (McSween, 1979) and as such, took the "most pristine chondrites" role.

2. The moderately volatile elements problem

2.1. What is a moderately volatile element?

Volatility is the quality of a chemical element or compound which describes its tendency to vaporize. In cosmochemistry, it is usually determined under solar nebula conditions at a distance of 1 astronomical unit from the Sun, and a total pressure around 10^{-4} bar (Fegley, Jr., 2000; Lewis, 1974). Two different values can be used to compare volatilities: the condensation temperature T_c and the 50% condensation temperature T_{50}. The condensation temperature corresponds to that at which the element starts to condense from the Solar nebula gas. The 50% condensation temperature differs in that, at this temperature, half of the available mass is sequestered in condensates and the other half is in gaseous form. The T_{50} is often preferred as it better describes the reality of the elements' behavior. For example, Ni and Ge have similar T_c but distinct T_{50} ($T_{50\text{-Ni}} > T_{50\text{-Ge}}$), indicating that when half of the Ni mass is condensed, Ge is mainly in gaseous form. Thus, Ge has a more volatile behavior than Ni (Lodders, 2003). It must be noted that these condensation temperatures depend in good part of the nature of the condensate phase and can be determined by using thermodynamical models (Lodders, 2003; Wood et al., 2019).

Depending on their T_{50}, chemical elements can be sorted in three families: refractories, moderately volatiles and highly volatiles. Refractory elements are defined as condensing at high temperatures ($T_{50} > 1287$ K), with phosphorus being the most volatile refractory element (Wood et al., 2019). By contrast, highly volatile elements have such a low T_{50} (inferior to 200 K) that they exist as gas on the surface of the Earth, this group contains C, N, O and noble gases (Lodders, 2003). Hence, the moderately volatile elements (MVE) are more volatile than the refractory elements but are not usually found in gaseous form in the Earth atmosphere (with the exceptions of F and Cl).

Three other categories are defined by the behavior of the elements during metal-silicate partitioning experiments: lithophile, siderophile and highly siderophile elements. Lithophile elements tend to remain in the silicate phase, while siderophile elements go mainly in the iron phase (but are, most of the time, still present in significant amounts in the silicates). During planetary differentiation, oxidized iron gets reduced into high-density metallic blebs that converge downward to form the planetary core. Siderophile elements are then collected by the iron, leading to enrichment in the core and depletion in the mantle. Highly siderophile elements (HSE) are so efficiently retrieved by the metal phase that they can basically be considered absent from the mantle (O'Neill, 1991; Varas-Reus et al., 2019; Wang and Becker, 2013). Their current abundance in the silicate Earth results from a post-differentiation input from meteoritic materials, during an event called the "Late Veneer".

2.2. The moderately volatile elements depletion

Study of the lithophile elements abundances in the silicate Earth and in other terrestrial object of the Solar system (chondritic, lunar or Martian samples) has revealed the existence of a so-called MVE depletion trend when compared to the mean composition of the Solar system. This trend is best described by plotting elemental abundances normalized to CI chondrite refractory content (usually Mg) vs. their respective T_{50} (see Figure 1) (Wood et al., 2019). In

such figure, refractory lithophile elements are clustered in a plateau, with normalized abundances being close to 1. By contrast, lithophile MVE form a depletion trend with a positive correlation between normalized abundances and T_{50}. Generally speaking, the most volatile elements are also the most depleted in terrestrial samples. There is still debates surrounding the shape of the overall trend, as some works have proposed that it looks like a hockey stick (Braukmüller et al., 2019, 2018; Krähenbühl et al., 1973), with a low concentration plateau for the most volatile MVE. However, this relies on abundances for a few elements like In, for which the effective T_{50} have been debated (Liu et al., 2022). Refractory and moderately volatile elements were defined on this trend, with all non-depleted lithophile elements being called refractory while depleted lithophile samples were defined as moderately volatile. Siderophile elements do not belong on these trends, as they are depleted in the silicate Earth, probably due to their segregation into the core.

This MVE depletion is observed in every terrestrial body (with the exception of CI chondrites), with differing intensities depending on the object. As an example, most chondrite types have specific MVE depletion (Braukmüller et al., 2018), the Earth is more depleted than chondrites (Jochum et al., 1983; Palme and O'Neill, 2014; Ringwood, 1966; Siebert et al., 2018; Tuller-Ross et al., 2019; Urey, 1954; Wänke and Dreibus, 1988), and Mars and the Moon are even more depleted (Albarède et al., 2015; Ganapathy and Anders, 1974; Paniello et al., 2012).

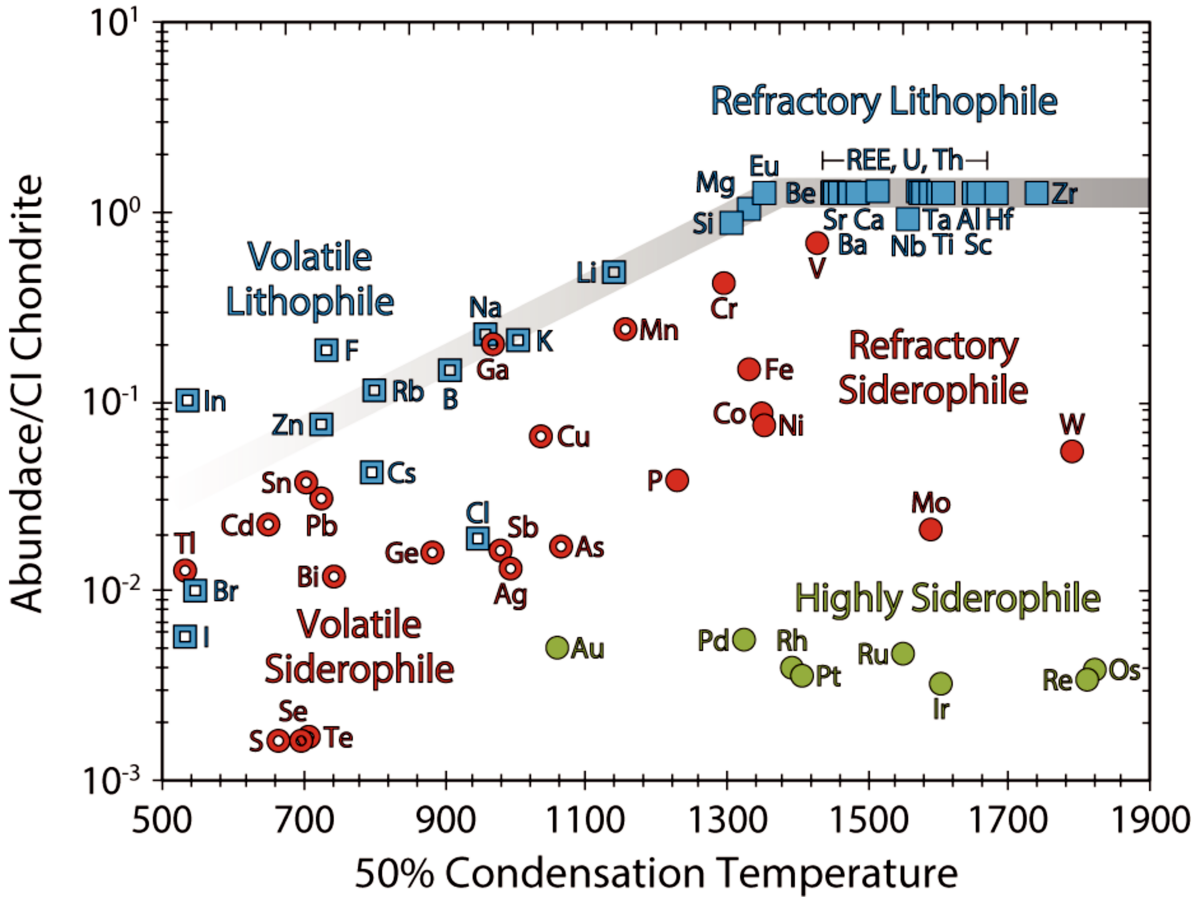


Figure 1: Elemental abundances in the silicate Earth, relative to those in CI chondrites (Clay et al., 2017; Palme and O'Neill, 2014), normalized to Mg vs. their respective T_{50} temperatures (in K) (Wood et al., 2019). Condensation temperatures were calculated for a gas of solar composition at 10^{-4} bars. Figure from Wood et al. (2019). Siderophile elements are depleted compared to the lithophile ones because a significant part of their total amount is segregated in the core. Highly siderophile elements are characterized by chondritic ratios because their current budget in the BSE was established by chondritic input after the differentiation occurred.

Many hypotheses have been proposed to explain the origin of this depletion pattern. One of the first and most intuitive one is certainly the vaporization hypothesis (Urey, 1954). In this model, MVE were lost to space during local or global melting events. Proposed models range from superficial melting coupled with collisional accretion caused by a steady bombardment by small-sized objects (O'Neill and Palme, 2008) to global melting of the body caused by short-lived radioactivity or major impacts (Norris and Wood, 2017; O'Neill, 1991; Pringle et al., 2014). In these models, refractory elements would not have been significantly vaporized while MVE would have been depleted with a magnitude depending on their T_{50}. This mechanism is

expected to produce isotope fractionation through Rayleigh distillation (Rayleigh, 1902, 1896), due to a preferential loss of the lightest isotopes, at the same time as a significant alteration of MVE abundances ratios.

Such modifications of MVE abundances ratios exists for Mars, the Moon and some meteorites parent bodies (Siebert et al., 2018) while the Bulk Earth (BE) is much closer to the chondritic range, indicating a limited influence of vaporization. Similarly, although some isotopic traces of vaporization have been found on Earth (Hin et al., 2017; Young et al., 2019), other studies point out the lack of such traces for many isotope systems that should be sensitive to vaporization events (Day et al., 2020; Humayun and Clayton, 1995; Sossi et al., 2019, 2018; Tuller-Ross et al., 2019; Wang and Jacobsen, 2016; Wombacher et al., 2008). However, consistent isotope fractionation coupled to MVE depletion was found in the lunar rocks (Baedecker et al., 1971; Kato et al., 2015; Paniello et al., 2012), comforting the hypothesis of a formation by accretion of molten terrestrial material ejected by a giant-impact. Authors have proposed that, even if this impact would have caused the formation of a magma ocean on Earth that could have triggered a significant vaporization event, Earth mass and the MVE behavior in silicate and atmosphere limited their loss to space (Chen et al., 2019). Vaporized MVE would have mostly condensed back on Earth, restoring its initial isotope composition. Alternatively, equilibrium-driven processes rather than kinetic-driven ones may have prevented significant isotope fractionation during vaporization (Sossi et al., 2018), which would revive the MVE vaporization model.

Another explanation for the MVE depletion can be found in the so-called “wet” and “dry accretion” models. Wet accretion theory states that the Earth MVE depletion trend reflects the composition of its building blocks (often understood as chondrites or chondritic components) (Righter et al., 2017). However, despite the best efforts of the cosmochemical community, no fitting building block has yet been found.

Alternatively, dry accretion model proposes that primitive terrestrial compositions were not CI-like and then depleted but rather that they were already almost totally MVE-depleted during accretion. Such composition would reflect that of the accreted material, which is proposed to have condensed with such composition already established due to incomplete condensation (Humayun and Clayton, 1995; Vollstaedt et al., 2020; Wasson and Chou, 1974). This process would allow for the formation of MVE-poor but isotopically unfractionated terrestrial building blocks. Volatile elements could be brought to the Earth during the Late Veneer (Albarede et al., 2013; Albarède, 2009). However, there is contradiction between the amount of meteoritical input needed to account for the BSE (Bulk Silicate Earth) HSE budget (less than 1 % mass. of the final Earth mass) (O'Neill, 1991; Varas-Reus et al., 2019; Wang and Becker, 2013) or for the volatile elements (up to 4 % mass.) (Albarede et al., 2013).

This last model has evolved into what is known as the "heterogeneous accretion" model (Liu et al., 2022; Pringle and Moynier, 2017; Schonbachler et al., 2010; Sossi et al., 2019; Wang et al., 2016). It states that the Earth building blocks were at first mostly dry objects and that the Earth's MVE budget is accounted for by a shift in the nature of accreted bodies. Thus, it is thought that the last 10 to 20 mass.% of accretion (Braukmüller et al., 2019; Kubik et al., 2021) mobilized volatile-rich CI-like material. Variants of the model involve a dry proto-Earth, collided by a volatile-rich planetesimal during the Moon-forming event (Morbidelli et al., 2020; O'Neill, 1991), adding the last 35-40 mass.% to the proto-Earth. The greater mass of the impactor implies that it was less volatile-rich than CI chondrites, which are the model used for determining the 10-20 % input. This model reflects the two-components theory for the formation of chondrite, involving mixing between a dry component (often understood as chondrules and refractory inclusions) and a volatile-rich one (the matrix) (Pringle et al., 2017). These models couples well with the "pebble accretion" one, which overcomes accretion regime problems by using small objects ("pebbles") accretion rather than inefficient stochastic

collisions (Amsellem et al., 2017; Burkhardt et al., 2021; Johansen et al., 2021). These pebbles are thought to be mostly chondrules, which would create a parallel between chondrites and terrestrial planets (both being a mix of chondrules and MVE-rich component).

In any case, the study of MVE depletion in terrestrial bodies has been the source of significant inputs to better constrain their accretion and histories. Siderophile and chalcophile (S-loving) MVE can especially help tracking the influences of vaporization events and of planetary differentiation, as well as the nature of planetary building blocks. When applied to chondrites, it can provide insights in the nebular processes at stake in the formation of primitive solids.

3. Cadmium: risks and opportunities

3.1. What is cadmium?

Discovered in 1817 as an impurity in smithsonite (Zn carbonates) (Stromeyer, 1818), Cd was named after the traditional name of the mineral: “kadmeia”. It is a scarce element, rarely being more concentrated than a few hundreds of ng / g (part per billion, ppb) in silicates (Arevalo and McDonough, 2010; Greaney et al., 2017; Pickard et al., 2022; Schmitt et al., 2009a; Yi et al., 2000). Thus, native cadmium is extremely rare and almost all of the historical production relied on extracting Cd as coproduct of Zn, Pb or phosphates extraction. This is possible because Cd is concentrated in such ores, with abundances in Pb-Zn ores ranging from a few hundreds to more than a few thousands of µg / g (part per million, ppm) (Rosman and De Laeter, 1974a; Wen et al., 2015) while it reaches a few ppm in phosphates (Schmitt et al., 2009a). It is a malleable and ductile metal, resistant to corrosion, which easily form complex compounds (Holleman et al., 1985).

With 48 protons in the nucleus, Cd is a group 12 transitional metal, which means its d electronic sub-shell is only partially filled, allowing it to form Cd^{2+} cations. Being part of the

Zinc group, it shares similar behaviors as it is moderately volatile with a T_{50} of 502 K (Wood et al., 2019), incompatible during mantle melting (Yi et al., 2000), siderophile and chalcophile under core forming conditions (Kiseeva and Wood, 2013; Kubik et al., 2021; Mahan et al., 2017; Marin et al., 2013; Steenstra et al., 2020; Wood et al., 2014). This chalcophile behavior also shows in the significant Cd enrichment in continental (403 - 1404 ppm) and oceanic (122 – 409 ppm) sulfides (Schmitt et al., 2009a) compared to silicates.

Cadmium has a total of 38 isotopes, with masses ranging from 95 to 132 atomic mass units (amu) (Audi et al., 2003). Among these, only six are stable (^{106}Cd, ^{108}Cd, ^{110}Cd, ^{111}Cd, ^{112}Cd and ^{114}Cd). Two isotopes (^{113}Cd and ^{116}Cd) are primordial long-lived radioisotopes with half-lives of 7.7 petayears (10^{15} years) and 30 exayears (10^{18} years) respectively. These extremely long half-lives have caused the characterization of these isotopes as almost stable. The other isotopes are characterized by short half-lives (the longest one being of 461.4 days for ^{109}Cd) and thus are basically extinct in nature. The terrestrial Cd content is dominated by ^{114}Cd (28.73 %) and ^{112}Cd (24.13 %) (Berglund and Wieser, 2011; Böhlke et al., 2005; Pritzkow et al., 2007), leading to a mean atomic mass of Cd is 112.411 amu (Loss, 2003).

3.2. Toxicity of cadmium

Cadmium is known to be a very potent toxic element, affecting numerous organs and metabolic reactions, which provoked a wide discussion regarding its danger (Bernhoft, 2013; Genchi et al., 2020; Godt et al., 2006). Although it is currently thought to serve no purpose in human metabolism, it is found bound to proteins and transport complexes in the place of other cations (mainly Mg^{2+}, Ca^{2+}, Zn^{2+}, Cu^{2+}, $Fe^{2+/3+}$) and is concentrated in the guts and kidneys (Moulis, 2010; Satarug, 2018; Tinkov et al., 2018). Excretion by natural means is not efficient, leading to accumulation, with the estimated half-life in kidneys for non-smokers being estimated to be of 30 years (Elinder et al., 1976).

The main inputs of Cd in a human body are through food and drink and micro-particles inhalation. Alimentation represents an input of 30-35 µg Cd per day in Europe, of which only 5 % are absorbed by the organism (Genchi et al., 2020; Godt et al., 2006). Meat, fish, fruits and vegetables are usually characterized by low Cd concentrations, culminating at 10-20 ppb (Jorhem et al., 1986). However, some aliments display higher concentrations, as can be seen for cattle livers (70 ppb) and kidneys (350 ppb), seeds (up to 840 ppb) or oysters (9 ppm) (Jorhem et al., 1986; Nielsen, 1975). Similarly, a product as fundamental for many populations as rice can contain between 5 and 69 ppb depending on the local pollution (Shi et al., 2020). Intoxication via the respiratory system, however, is the most efficient intake process, as up to 56 % of the inhaled Cd is absorbed by the blood (Elinder et al., 1976). Here, the main Cd source is cigarette ash, as it has been shown that long-term smokers have twice as much Cd in their kidneys than non-smokers (Elinder et al., 1976). Industry-related exposure can also happen, notably by inhalation of welding fumes (Barbee and Prince, 1999). Smaller amounts can also be ingested by dermal absorption (Lansdown and Sampson, 1996), although it is not thought to be a major cause for intoxication.

Once in the organism, Cd disrupts numerous processes, leading to poisoning from multiple causes. Ionized cadmium (Cd^{2+}) bonds to ionic sites of molecules usually handling other elements, leading to abnormal metabolism (Moulis, 2010). Calcium is notably affected (Kazantzis, 1979) as its absorption is prevented by high Cd concentrations (Hamilton and Smith, 1978), which also trigger Ca releasing from the bones (Ando et al., 1978). Furthermore, it has been shown that Cd intake is promoted when other metals are lacking (Ca, Fe) (Flanagan et al., 1978; Scheuhammer, 1996), disrupting even more their metabolism. The poisoning also kickstart independent and nefarious processes such as oxidative stress of the cells (Matović et al., 2011; Patra et al., 2011), impairment of mitochondria (Cannino et al., 2009), protein

misfolding (Tamás et al., 2018) and even epigenetic modification of the DNA expression (Luparello et al., 2011; Wang et al., 2012).

All these metabolic disturbances provoke diversified symptoms, reflecting the wide variety of processes impacted. Because of the accumulation of Cd in the kidneys, renal disorders are common, with increased risks of kidney stones and permanent damages to the tubules (Barbier et al., 2005; Kazantzis, 1979; Larison et al., 2000), which can lead to cancer (Ilyasova and Schwartz, 2005). Lungs are also affected, causing pneumonia (Seidal et al., 1993) and acute respiratory distress syndrome (Barbee and Prince, 1999). Finally, Cd tampering with the Ca metabolism can lead to serious bone diseases, caused by intense decalcification (Staessen et al., 1999). When the kidneys become too damaged to fulfill their metabolic duties, the subject develops osteomalacia, a painful condition characterized by the softening of the skeleton and caused by inadequate bone mineralization, usually linked to a lack of kidney-produced vitamin D_3 (Kazantzis, 1979; Larison et al., 2000). This illness has also been known as the "itai-itai disease" (literally "it hurts-it hurts disease") in Japan during the XX^{th} century, where it caused around 600 victims because of intense Cd poisoning of the river by local mining activities (Ogawa et al., 2004). Simultaneously, the loss of bone Ca triggered by Cd intoxication can lead to osteoporosis: reduced bone density increasing the fracture risk (Buha et al., 2019; Jarup et al., 1998).

3.3. Applications and pollution

Cadmium is not a commonly used material in industry; however, it has been employed for some specific needs along the years. Because of its resistance to corrosion, cadmium-based coatings are found in aeronautical, mining or electronical materials. It is also used in alloys, with Cu, Pb, Ag, Sn or Zn to reinforce hardness and improve resistance to mechanical stress as well as lowering the melting point of soldering material or enhancing the alloy castability. It is found in infrared detectors (in combination with Hg and Te), in photovoltaic cells (forming a

stable semiconductor when combined with Te), and in Ni-Cd industrial batteries ("Cadmium Applications," 2021) as well. However, its most iconic application is as a pigment with yellow (CdS) or red (CdSe) crystals being used for example by Van Gogh for his sunflowers.

Despite these applications, Cd toxicity has incited lawmakers to limit its use as much as possible, leading to a relative stagnation in worldwide production between 1990 and 2010 before a new rise in production occurred, driven by a renewed need for batteries. Current global production attained 25 600t per annum in 2019 ("Cadmium.org," 2021), with 2 500t being used in the European Union (EU) despite increasingly strict regulations. In 2019, worldwide Cd consumption was dominated by jewelry alloys (57 % mass.), mainly in China and India. However, this number is hard to come by as it is most of the time an illegal usage, made by small unregistered artisans. First among the other applications are NiCd batteries (23 % of global total, 80 % of EU28 total), despite limiting Cd content in electronics to 0.002 % in the EU (*Directive 2006/66/EC of the European Parliament and of the Council of 6 September 2006 on batteries and accumulators and waste batteries and accumulators and repealing Directive 91/157/EEC*, 2006). The remaining 20 % being split between PVC stabilizers (8 % global, banned from the EU), coating (4 % global, < 4 % in EU), technical alloys (4 % both globally and in the EU) and pigments (3 % global and 12 % in the EU) ("Cadmium.org," 2021).

These activities have led to a worldwide contamination of soils and waters by Cd particles. This pollution has multiple sources, be it from mining industry, refining activity, hydrocarbon burning or agriculture. Cadmium can be released by the weathering of ores or Cd-bearing minerals, especially in active or decommissioned mines (Robson et al., 2014; Zhang et al., 2016; Zhu et al., 2018). Ore refining activities can also contaminate the surroundings with Cd-concentrated ashes (1 431 to 12 195 ppm) (Cloquet et al., 2005) and slag (13 – 765 ppm) from the smelters (Cloquet et al., 2006, 2005; Gao et al., 2013; Jacquet et al., 2022; Wen et al., 2015). Such contaminations can concern very wide areas around active and closed industrial sites,

enriching local soils from normal concentration of less than 1 ppm up to more than 500 ppm (Cloquet et al., 2006, 2005; Li et al., 2018; Wen et al., 2015). It can also contaminate all the land downstream via local rivers (Gao et al., 2013; Larison et al., 2000). The burning of hydrocarbons, especially coal (Cui et al., 2019), and of city wastes (Cloquet et al., 2005) can also release Cd-enriched ashes in the atmosphere. However, one of the main source of land contamination is not related to such industrial activity as phosphates-based agriculture fertilizers bear significant amounts of Cd (Cloquet et al., 2006). The extent of these pollutions and the potential hazard it represents for human health have prompted researchers to find innovative ways to extract Cd from soils, among which phytoextraction is a promising option (Ghosh and Singh, 2005; Imseng et al., 2018; Jacquet et al., 2022; Zhang et al., 2010).

4. The geochemical method applied to Cd

As a volatile, siderophile and chalcophile element, Cd could provide significant insights into the Earth accretion and differentiation alongside its thermal history. Its presence in Pb-Zn ores and its release during refining could also serve to study potential ore deposits or to monitor environmental contamination by extractive industries. However, even though such studies have been conducted, they constitute only a small ensemble as Cd is often regarded as a niche element and its usefulness has not yet received wide recognition. The fact that the Cd community is still quite small can be explained by at least two elements: the scarcity of Cd in most igneous samples and the issues of isobaric interferences during the measurements. These two difficulties are not insurmountable but do complexify the conception of Cd-based works.

4.1. Obstacles to Cd analysis

4.1.1. Scarcity

Despite the fact that the previously mentioned biological tissues, industrial ores, slags and ashes or polluted soils record high Cd concentrations of dozens or hundreds of ppm, most

geological samples have lower Cd content. Some non-silicate rocks like oceanic manganese nodules or sediments present concentrations comprised between 7 and 23 ppm (Cloquet et al., 2005; Li et al., 2018; Liu et al., 2020; Lu et al., 2021). However, this is still unusually high when looking at the wider picture, as Earth silicates usually have Cd compositions of less than a few hundred ppb (Dostal et al., 1979; Pickard et al., 2022; Rosman and De Laeter, 1974a; Schmitt et al., 2009a; Vincent and Bilefield, 1960; Yi et al., 2000). This leads to a composition for bulk continental crust of 80 ppb (Rudnick and Gao, 2014) and of 126 ppb for oceanic crust (Devos et al., 2024). Earth mantle is thought to be even less concentrated as Cd is incompatible (Yi et al., 2000), with proposed values being close to 40 ppb (Wang et al., 2018), confirmed by recent peridotites data (5 – 43 ppb) (Pickard et al., 2022). Igneous samples having experienced significant Cd vaporization are even more depleted, with concentrations of a few tens of ppb for aerial basalts (Yi et al., 2000) or even less than 25 ppb for tektites and impact glasses (Wombacher et al., 2003; This work). Oceanic waters are even poorer, as they only have 28 to 109 ng per kg (part per trillion, ppt). Despite this, ocean-centered works constitute one of the most dynamic field of Cd isotopic studies.

Extraterrestrial samples span over a wide range of compositions. As an example, surficial lunar rocks range from less than 1 ppb for the rocks having experience the most complete vaporization, to more than 1 ppm for samples that are thought to have absorbed vaporized Cd on their surfaces (Sands et al., 2001b; Schediwy et al., 2006). Differentiated meteorites have generally low concentrations, with iron meteorites rarely being richer than 10 ppb and achondrites having no more than 30 ppb (Rosman and De Laeter, 1974b). This stands in stark contrast with chondrites, as these samples span a wide range of concentrations, the poorest chondrites having Cd contents of less than 1 ng per gram (Palk et al., 2018; Rosman and De Laeter, 1974b; Wang and Lipschutz, 2007) while Cd-rich chondrites frequently have concentrations of a few hundreds of ppb (Braukmüller et al., 2018; Krähenbühl et al., 1973;

Loss et al., 1984; Palk et al., 2018; Rosman and De Laeter, 1988, 1974b; Wang and Lipschutz, 2007, 2005) or even over than one ppm (Rosman and De Laeter, 1988, 1974b; Wang and Lipschutz, 2007).

These concentrations of often no more than 100 or 200 ppb in most terrestrial and extraterrestrial silicate rocks call for digestion of one or more grams of sample to have enough Cd for multiple optimal measurements. This can disqualify or complexify Cd analyses in the cases of samples for which only limited masses are available, be it because of their inherent rarity (asteroidal samples, lunar rocks, some rare meteorites), or because individual samples are small objects that contain little Cd, like chondritic components (individual CAI or chondrules), tektites and impact glasses (Creech et al., 2019; Devouard et al., 2014; Koeberl, 1992; Koeberl et al., 1997; Morgan, 1978; Moynier et al., 2009, 2010; Rochette et al., 2014; Watt et al., 2011; Wombacher et al., 2003). Moreover, some samples combine strong Cd depletion with small individual masses, preventing efficient analyses. This is especially obvious for tektites or nuclear explosion-related rocks like trinitites (Chen et al., 2019; Day et al., 2020, 2017; Eby et al., 2010) or Hiroshima glasses (Wannier et al., 2019). For the most favorable of these cases, for example tektites, often only one or two measurements will be possible because of the low Cd content.

These concentrations also imply high matrix / Cd ratios, which could result in problematic matrix effects and interferences during analysis. This calls for extensive matrix elimination, which could cause Cd isotope fractionation if the purification yield is not close enough to 100 %. This will be discussed in more details in the next paragraphs.

4.1.2. Interferences

Another hindrance to the implementation of Cd stable isotopes studies lies in the intensity of isobaric and polyatomic interferences on its isotopes. Although dealing with interferences is common for most isotope systems, it is rendered more difficult in this case by the fact that Cd

is often less concentrated than its interferents by a few orders of magnitude. Table 1 lists all the isobaric interferences as well as the most common polyatomic ones that may be encountered during ICP (inductively coupled plasma) mass spectrometry, which is the method that will be used in this work.

As an example, typical basalt (approximated here by BHVO-2 standard material) contains around 100 ppb of Cd (Braukmüller et al., 2020; Chang et al., 2023; Du and Hu, 2015; Liu et al., 2020; Lu et al., 2021; Pickard et al., 2022; Wang et al., 2015), 100 ppb of In, less than 10 ppb of Pd and 1 800 ppb of Sn (Jochum et al., 2005). Our work have shown that Cd isotope measurements were not affected by such interferences for Cd / Pd > 500, Cd / Sn > 1 000 and Cd / In > 10 000 (Devos et al., 2024 and see section below). Thus, Sn is the main source of interferences in this set up. To obtain quality data, it is necessary to divide Sn concentration by more than a 10 000 factor. In other samples, mainly chondrites, Pd is roughly as abundant as Cd (Braukmüller et al., 2018; Horan et al., 2003), causing important interferences. These difficulties can be overturned by extensive Cd purification and / or effective correction of individual influences. In last resort, it is possible to eliminate problematic data by checking their mass dependence. Indeed, interferences create apparent mass-independent isotope compositions, unlike most natural isotope fractionation processes.

Table 1: Main isobaric and polyatomic interferences on stable Cd isotopes for MC-ICPMS analysis

Mass number	Cd	Pd	In	Sn	Polyatomic					
106	0.13%	27.33%			$^{66}Zn^{40}Ar^{+}$ 27.73%	$^{90}Zr^{16}O$ 51.45%				
108	0.89%	26.46%			$^{68}Zn^{40}Ar^{+}$ 18.45%	$^{92}Mo^{16}O^{+}$ 14.53%	$^{92}Zr^{16}O^{+}$ 17.15%			
110	12.49%	11.72%			$^{70}Ge^{40}Ar^{+}$ 20.57%	$^{70}Zn^{40}Ar^{+}$ 0.61%	$^{39}K_2{}^{16}O^{+}$ 93.26%	$^{94}Mo^{16}O^{+}$ 9.15%	$^{94}Zr^{16}O^{+}$ 17.38%	
111	12.80%				$^{71}Ga^{40}Ar^{+}$ 39.89%	$^{39}K_2{}^{16}O_2H^{+}$ 93.26%	$^{95}Mo^{16}O^{+}$ 15.84%	$^{94}Zr^{16}OH^{+}$ 17.38%		
112	24.13%			0.97%	$^{40}Ar_2{}^{16}O_2$ 99.60%	$^{72}Ge^{40}Ar^{+}$ 27.45%	$^{40}Ca_2{}^{16}O_2$ 96.94%	$^{96}Mo^{16}O^{+}$ 16.67%	$^{96}Ru^{16}O^{+}$ 5.54%	$^{96}Zr^{16}O^{+}$ 2.80%
113	12.22%		4.29%		$^{73}Ge^{40}Ar^{+}$ 7.75%	$^{40}Ar_2{}^{16}O_2H$ 99.60%	$^{40}Ca_2{}^{16}O_2H$ 96.94%	$^{97}Mo^{16}O^{+}$ 9.60%	$^{96}Ru^{17}O^{+}$ 5.54%	$^{96}Zr^{16}OH^{+}$ 2.80%
114	28.73%			0.66%	$^{74}Ge^{40}Ar^{+}$ 36.50%	$^{98}Mo^{16}O^{+}$ 24.39%	$^{98}Ru^{16}O^{+}$ 1.89%			
116	7.49%			14.54%	$^{76}Ge^{40}Ar^{+}$ 7.73%	$^{76}Se^{40}Ar^{+}$ 9.37%	$^{100}Mo^{16}O^{+}$ 9.82%	$^{100}Ru^{16}O^{+}$ 12.60%		

Isotopic proportions are from Berglund and Wieser (2011) and Böhlke et al. (2005). Polyatomic interferences are from May and Wiedmeyer (1998) and Rehkämper et al. (2012).

4.2. Cadmium isotope composition and isotope fractionation

As exposed previously, Cd has a few radioactive isotopes. They can be sorted in two categories: almost stable (half-lives superior to 10^{15} years) and short-lived (half-lives under 2 years) radioactive isotopes (Audi et al., 2003). In the absence of a production of Cd short-lived radioisotopes on Earth, these isotopes are currently insignificant fractions of the total Cd. On the other hand, almost stable radioisotopes have such long half-lives that their proportions in the total Cd amount are not significantly influenced by radioactive decay. Moreover, the Earth magnetic field and atmosphere prevent most production of Cd isotope by neutron capture. Thus, the only source of significant Cd isotope variations on Earth should be mass-dependent stable isotope fractionation.

Extraterrestrial samples, however, can present mass-independent isotope compositions caused by neutron capture when interacting with cosmic rays as they are not shielded by any atmosphere or magnetosphere. Most Cd isotopes have thermal cross sections for neutron capture contained under 1 barn, with only ^{110}Cd and ^{112}Cd being characterized by bigger cross sections (10.999 and 2.198 barns respectively) (Gicking et al., 2019). The ^{113}Cd isotope, however, stands out with a large thermal cross section of about 20 615 ± 400 barns (Mughabghab, 2006). This indicates that ^{113}Cd can readily capture cosmic ray neutrons and produce ^{114}Cd, creating mass-independent isotope compositions. Such compositions have been found on some lunar samples and meteorites (Sands et al., 2001b, 2001a; Schediwy et al., 2006; Wombacher et al., 2008). However, such observation was only made on long-exposed samples, with no significant trace of such a process occurring for lunar samples as old as 30 Ma (Arvidson et al., 1975; Schediwy et al., 2006).

Cadmium isotope compositions are usually reported using the ε or δ notations, which can be expressed as follow for the ^{114}Cd / ^{110}Cd isotope ratio:

$$\varepsilon^{114}Cd = \left[\frac{\left({}^{114}Cd/_{110}Cd \right)_{sample}}{\left({}^{114}Cd/_{110}Cd \right)_{standard}} - 1 \right] \times 10\,000$$

$$\delta^{114}Cd = \left[\frac{\left({}^{114}Cd/_{110}Cd \right)_{sample}}{\left({}^{114}Cd/_{110}Cd \right)_{standard}} - 1 \right] \times 1\,000$$

Both notations provide the same deviation of the isotope composition for a sample relative to a reference material (called standard in the equations), but they differ in sensitivity by a factor 10.

4.3. Purification of Cd

As detailed previously, Cd isotopic analyses are impaired by a high matrix / Cd ratio and by the presence of multiple isobaric and polyatomic interferences. Thus, extensive Cd purification needs to be conducted in order to limit as much as possible the potential influences of these two factors. Nevertheless, extensive purification processes can create isotope fractionation if the protocol yield is not close to 100 % (Cloquet et al., 2005; Schmitt et al., 2009b; Wombacher et al., 2003). Usage of a Double Spike (DS) method (discussed later) can correct for any mass-dependent isotope fractionation occurring during purification. However, near total recovery of Cd is desirable as the available Cd mass is often the limiting parameter for analysis.

Cadmium is usually purified by anion exchange chromatography using resin-filled columns. This methods are favorable since Cd get strongly bound by most anion exchange resins from HCl or HBr (Marsh et al., 1978; Strelow, 1978) and can be eluted with diluted HNO_3 acid (Faris and Buchanan, 1964).

The most common Cd purification protocols rely on a one step purification using concentrated HCl solutions to load the samples and to elute the matrix before collecting Cd fraction in diluted HCl (Cloquet et al., 2005) or in nitric acid (Liu et al., 2020; Wombacher et al., 2003). Later development of these techniques led to the addition of a supplementary step following similar protocol to further eliminate the matrix (Ripperger and Rehkämper, 2007). This protocol is mostly used for separation of Cd from ocean water, as the matrix over Cd ratio is especially unfavorable in this case. Another supplementary purification step has been experimented in order to eliminate the remaining traces of Sn using specific Eichrom TRU resin (Ripperger and Rehkämper, 2007; Wombacher et al., 2003). Numerous variations thereupon have been proposed (Liu et al., 2020; Pickard et al., 2022). Here we will propose a new purification protocol based on an HBr loading and matrix removing and on a nitric acid-based collection of Cd.

4.4. Mass spectrometry

4.4.1. TIMS

The first mass spectrometer (MS) technology used to investigate Cd isotope compositions was TIMS (thermal-ionization mass spectrometer), in a seminal work by Rosman and De Laeter (1975). This kind of MS obtains ionization of a determined mass of sample by heating it with a filament. The study revealed significant deviations of a few permil (‰) per amu for Cd-bearing sphalerite and galena from the laboratory standard. After this first work focusing on terrestrial minerals, the authors published a series of studies providing isotope compositions for meteorites (Rosman et al., 1980b, 1980a; Rosman and De Laeter, 1988, 1978, 1976), proving the existence of significant mass-dependent isotope variations in these samples (-2.1 to +2.8 ‰ per amu). These studies also used a ^{106}Cd-^{111}Cd DS to correct for instrumental bias, which improved the precision of the measurements (see Table 2). While the first works with TIMS only had a single electron multiplier to collect signal, later improvements on the technology

allowed for more Faraday cups and the simultaneous collection of multiple isotope signals (Schediwy et al., 2006). Similarly to chondrites, significant mass-dependent isotope variations were observed in Cd-depleted lunar soils (Sands et al., 2001b; Schediwy et al., 2006). Most recent TIMS-based Cd studies have brought significant insights in its oceanic cycle (Abouchami et al., 2014), its precipitation in sulfides (Guinoiseau et al., 2018; Schmitt et al., 2009a), the isotope composition of the BSE (Schmitt et al., 2009a) or simply focused on improving the quality of measurements to allow for better discrimination between isotope compositions (Schmitt et al., 2009b).

4.4.2. ICPMS

In 2003, Cd isotopic studies were introduced to a new MS design, with the multiple-collector inductively coupled plasma mass spectrometer (MC-ICPMS) (Wombacher et al., 2003). The main difference with TIMS is the ionization method, as here the liquid sample is continuously injected in a plasma where it is ionized. This allows for easier analysis of Cd by overcoming its high first ionization potential, which was limiting TIMS efficiency (Rehkämper et al., 2001). However, this comes with new challenges, as the high ionization efficiency of the plasma does not allow for discrimination between Cd and its interferents. Thus, the Cd solution must be extremely pure and / or potential interferents must be monitored with dedicated collectors. The mass spectrometer is also more sensitive to matrix effects if the measurements are carried out using the standard sampler bracketing (SSB) or the external normalization methods (Rehkämper et al., 2001). These matrix effects can result in unsystematic mass bias than are not corrected by either method, leading to poor accuracy and / or precision (Shiel et al., 2009; Wombacher et al., 2003). Despite this, the use of MC-ICPMS did develop swiftly for Cd isotope studies, and represent today the main method used for these.

4.4.3. The double spike method

The DS method involves the spiking of a sample with a previously characterized solution significantly enriched in two isotopes of the studied element compared with natural abundances. During mass spectrometry, three isotopic ratios sharing a similar denominator are measured. The two spiked isotopes are measured as numerators in these three ratios. A post-analysis deconvolution step allows for the determination of the sample initial isotope composition (Creech and Paul, 2015; Dodson, 1963; Galer, 1999; Hofmann, 1971; Rudge et al., 2009; Wetherill, 1964). One of the main benefits of DS usage is that any mass-dependent isotope fractionation occurring after spiking can be corrected during the deconvolution. Thus, one can overcome both purification fractionation and instrumental bias while also increasing the overall precision of the measurements (Schmitt et al., 2009b). Moreover, one of the byproducts of spiking is the determination of precise concentrations. However, this procedure cannot be applied to any element as it need at least four stable isotopes. As the DS is characterized by an optimal spike / sample ratio, it is also necessary to already know the sample Cd content, which introduces a supplementary step in the analytic process. Finally, it is generally more complicated to handle than other normalization methods as the necessary deconvolution step prevent on-the-fly assessment of the quality of data while it is produced.

The choice of the isotopes used for spiking and their ratio is one of the critical parameters for an optimal efficiency of the DS method. For an element with as many isotopes as Cd, the definition of the best DS can be an overwhelming process, as there is a multitude of possible DS formulas. Some studies have used numerical methods to answer this issue, determining the combination with the most favorable uncertainties (Galer, 1999; Rudge et al., 2009). However, other parameters are important to choose a DS system: (1) the lack of significant interferences on the chosen DS masses; (2) the absence of isotopic fractionation causing mass-independent isotopic variations on the spiked isotopes such as cosmogenic anomalies (Gicking et al., 2019;

Grinyer et al., 2005; Sands et al., 2001a) or odd masses related problems encountered with TIMS (Manhès and Göpel, 2003, 2007; Schmitt et al., 2009b); (3) limitations imposed by the number and possible positions of the MS collectors.

Table 2: Reproducibility of Cd isotope measurements in different studies

Reference	Method	instrument	2 SD (‰ per amu)	
			min	max
Rosman and De Laeter (1975)	Constant run conditions	TIMS	0.800	1.600
Rosman et al. (1980) a	$^{106-111}$ DS	TIMS	0.060	0.400
Rosman et al. (1980) b	$^{106-111}$ DS	TIMS	0.300	1.000
Rosman and De Laeter (1988)	$^{106-111}$ DS	TIMS	0.200	2.900
Sands et al. (2001)	$^{106-111}$ DS	TIMS	0.200	0.800
Wombacher et al. (2003)	Ag-; Sb-normalization	ICPMS	0.040	0.130
Cloquet et al. (2005)	SSB	ICPMS	0.010	0.110
Schediwy et al. (2006)	$^{106-111}$ DS	TIMS	0.200	15.000
*	*	*	*	0.900
Ripperger and Rehkämper (2007)	Ag normalization	ICPMS	0.038	0.038
Ripperger and Rehkämper (2007)	$^{110-111}$ DS	ICPMS	0.013	0.050
Schmitt et al. (2009) a	$^{106-108}$ DS	TIMS	0.006	0.028
Schmitt et al. (2009) b	$^{106-108}$ DS	TIMS	0.003	0.011
Horner et al. (2010)	$^{111-113}$ DS	ICPMS	0.010	0.100
Horner et al. (2011)	$^{111-112}$ DS	ICPMS	0.033	0.070
Abouchami et al. (2014)	$^{106-108}$ DS	TIMS	0.004	0.017
Pallavicini et al. (2014)	SSB	ICPMS	0.004	0.027
Wasylenki et al. (2014)	$^{111-116}$ DS	ICPMS	0.015	0.045
Li et al. (2018)	$^{111-113}$ DS	ICPMS	0.008	0.058
Tan et al. (2020)	$^{111-113}$ DS	ICPMS	0.002	0.021
Borovicka et al. (2020)	$^{106-116}$ DS	TIMS	0.003	0.018
Liu et al. (2020)	$^{111-113}$ DS	ICPMS	0.001	0.019
Druce et al. (2022) a	$^{110-111}$ DS	ICPMS	0.014	0.090
Pickard et al. (2022)	$^{111-113}$ DS	ICPMS	0.008	0.035
Chang et al. (2023)	$^{111-113}$ DS	ICPMS	0.003	0.015
Chang et al. (2023)	$^{111-113}$ DSSA - single	ICPMS	0.006	0.062
Chang et al. (2023)	$^{111-113}$ DSSA - multi	ICPMS	0.006	0.050
Peng et al. (2023)	$^{111-113}$ DS	ICPMS	0.003	0.050
Pickard et al. (2023)	$^{111-113}$ DS	ICPMS	0.010	0.020
Devos et al. (2024)	$^{106-111}$ DS	ICPMS	0.001	0.031

*Reproducibilities are based on the reported 2SD for multiple measurements of pure standards or of samples. They are quoted in permil per atomic mass unit (amu). DS: double spike; SSB: standard sample bracketing; DSSA: double spike-standard addition. *Schediwy very high maximum 2SD was obtained at suboptimal concentrations for a very depleted sample (0.4 ppb); its second worst 2SD gives a 0.900 ‰ per amu. (Abouchami et al., 2014; Borovička et al., 2021; Chang et al., 2023; Cloquet et al., 2005; Devos et al., 2024; Druce et al., 2022a; Horner et al., 2010, 2011; Li et al., 2018; Liu et al., 2020; Pallavicini et al., 2014; Peng et al., 2023; Pickard et al., 2022, 2023; Ripperger and Rehkämper, 2007; Rosman et al., 1980b, 1980a; Rosman*

and De Laeter, 1975, 1988; Sands et al., 2001b; Schediwy et al., 2006; Schmitt et al., 2009b, 2009a; Tan et al., 2020; Wasylenki et al., 2014; Wombacher et al., 2003)

Use of DS in Cd isotope studies is as old as the field, as the very first study determining Cd isotope compositions on terrestrial minerals did employ a ^{106}Cd-^{111}Cd DS (Rosman and De Laeter, 1975). Other works have since used new DS systems to avoid interferences and undesirable effects on specific isotopes (see Table 2). As a matter of facts, DS have become almost ubiquitous in recent Cd studies. In this work, we use a ^{106}Cd-^{111}Cd double spike with a ^{106}Cd / ^{110}Cd ratio of 349.531 and a ^{111}Cd / ^{110}Cd ratio of 228.392, which is a composition close to the numerically determined optimal one (Rudge et al., 2009). The deconvolution will use ^{110}Cd and ^{114}Cd (or ^{113}Cd to check for mass dependence). This setting should allow for better precision and accuracy but will be sensible to potential Pd, Sn, Ga, Ge, Mo, Ru, Zn and Zr interferences.

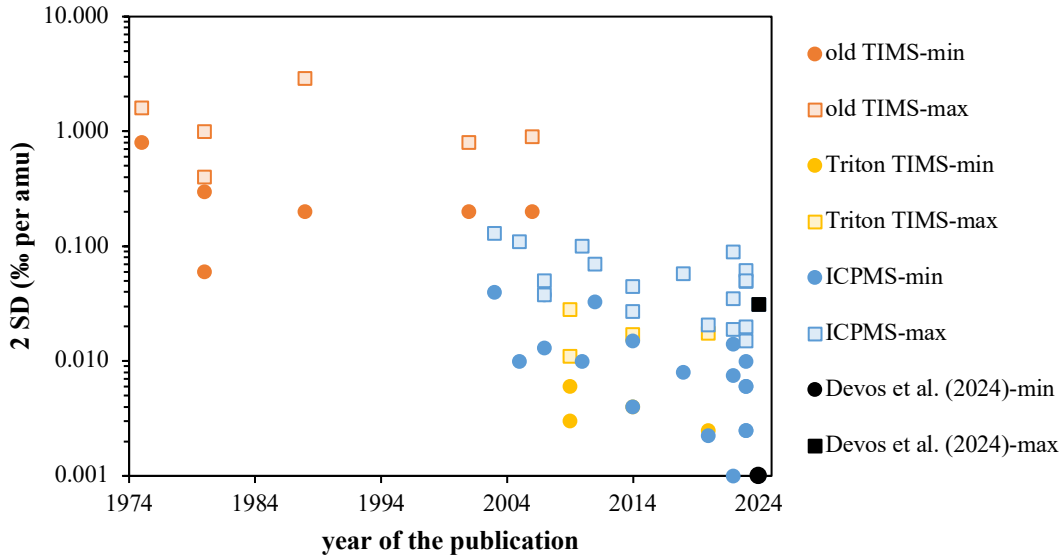


Figure 2: Evolution of the uncertainties reported in Cd isotope studies. The data represented here coincide with the one reported in Table 2. All uncertainties are normalized 2SD to obtain permil per amu deviations. The data are divided between three categories, depending on the mass spectrometer design utilized in the study. The introduction of a new mass spectrometer design usually coincides with a precision increase of at least one order of magnitude. "Min" datapoints represent the best reported 2SD in the work while "max" ones figure the worst uncertainties.

Measurement precision on Cd isotope ratios, provided by normalized uncertainties and expressed in ‰ per amu in Table 2, significantly increased during the last 50 years (see Figure 2). For the existing data, two disruptions can be observed in 2003 (at the introduction of ICPMS) and in 2009 (first studies using the new generation of TIMS) respectively. Each of these introductions of new material allowed for a precision increase of at least one order of magnitude. Table 2 shows that the method used in this work produced data with uncertainties that are in line with the best works published until now.

5. Cd stable isotopes studies

In this part, we will give a brief overview of the processes that are known to produce isotope fractionation for Cd. In a second time, we will detail the main uses that have been developed for Cd isotopic studies.

5.1. The geological fractionating processes

5.1.1. Vaporization

Cadmium being a MVE (Wood et al., 2019), it is expected to undergo extensive vaporization at high temperatures. This should cause significant isotope fractionation, following Rayleigh distillation (Rayleigh, 1902, 1896). Such process has been shown to occur during industrial smelting of Cd-bearing ores, creating isotopically light fumes and ashes and isotopically heavy slag and metal (Cloquet et al., 2006; Martinková et al., 2016; Shiel et al., 2010). These products often display strongly fractionated compositions, with δ^{114}Cd ranging from -0.52 ± 0.02 ‰ (2SD, n = 3) for the fumes to +0.52 ± 0.19 ‰ (2SD, n = 3) for the final Cd metal. For comparison, the starting isotope composition for the ores vary from -0.13 ± 0.24 ‰ (2SD, n = 3) to -0.18 ± 0.27 ‰ (2SD, n = 3) (Shiel et al., 2009). Some industrial dusts were even found to have isotopic compositions as light as -0.86 ± 0.02 ‰ (Martinková et al., 2016).

These observations confirm the hypothesis of an easily vaporized Cd and indicated that its lightest isotopes are the one that are preferentially extracted during evaporation.

Similar observations were conducted on natural samples, as a tektite was found to be simultaneously Cd-depleted (11 ppb) and isotopically heavy, with a δ^{114}Cd up to 2.94 ± 0.52 ‰ (n = 1, 2SD was obtain as the worst reproducibility obtain in the study) (Wombacher et al., 2003), compared to crustal rocks characterized by higher concentration (90 ± 20 ppb) (Rudnick and Gao, 2014) and rather unfractionated isotope compositions, with δ^{114}Cd generally around 0.10 ‰ (Pickard et al., 2022). Similar Cd vaporization during aerial volcanism has been shown to occur on Earth (Yi et al., 2000), although no isotope composition was determined on the vapor or on the residue. Finally, loss of isotopically light Cd has been reported in hydrothermal systems, during vapor-liquid fractionation (Wang et al., 2020). The Rayleigh distillation parameters determining the extent of isotope fractionation during Cd vaporization/condensation have been characterized by evaporation experiments conducted in a vacuum chamber over pure Cd metal (Wombacher et al., 2004).

5.1.2. Alteration

Alteration is the process by which rocks and minerals are deteriorated through reactions with the environment (notably water). A significant part of this process is the extraction of ions from the rock by reacting fluids. Cadmium being significantly incompatible in silicates, it is easily leached by fluids (be it melts or altering water). Thus, the alteration of Cd-bearing minerals releases significant amounts of Cd in the environment (Shiel et al., 2012; Wiggenhauser et al., 2016). This release of Cd is probably coupled to an isotopic fractionation, as isotopes have different affinities with fluids. Studies have shown that alteration residues are depleted in heavy Cd isotopes, leading to light compositions (Zhang et al., 2016; Zhu et al., 2018). The heavier isotopes are leached out preferentially by the altering fluids. While the magnitude of the isotope fractionation between the leachate and the residue depends on the

extent of the alteration and on the conditions under which it takes place, it was found that it is typically close to 0.1 ‰ per amu (Zhang et al., 2016)

5.1.3. Precipitation and adsorption

Precipitation of Cd-bearing minerals from Cd-rich fluids is occurring in seawater and in weathering fluids. Recent studies have revealed that theses minerals are generally enriched in light Cd isotopes compared to the fluid, regardless of their natures. This is coherent with the previous point, confirming that the heavier Cd isotopes remain preferentially in fluids. Significant isotope fractionation was found to occur during the precipitation of Cd in calcite (Horner et al., 2011) and in sulfides (Guinoiseau et al., 2018; Xie et al., 2019). Multiple factors seem to intervene in the determination of the extent of the isotope fractionation occurring between the fluid and the formed mineral: notably the proportion of crystallized Cd, its mineralogy and the ionic strength of the fluid. It was shown that the isotope deviation occurring between the fluid and mineral can be as high as 0.025 ‰ per amu for chloride, 0.087 ‰ per amu for sulfide (Guinoiseau et al., 2018), or more than 0.6 ‰ per amu for calcite (Druce et al., 2022a).

Another input mechanism for Cd is adsorption onto particles surfaces. Such a mechanism has been shown to occur in marine environment, on Mn oxyhydroxides (Wasylenki et al., 2014) and on calcite particles (Peng et al., 2023). Again, the isotopes preferentially retrieved by the solid are the lightest ones, while the heavy isotopes remain in solution. The isotope deviation between the fluid and the solid stabilize around 0.06 ‰ per amu for Mn oxyhydroxides and up to 0.17 ‰ per amu for calcite.

5.1.4. Biological uptake

Biological processes are well-known to produce important isotope fractionation. Such processes do occur with Cd, and are significant in the establishment of the ocean’s isotope

compositions. This is observable by comparing the superficial Cd-depleted water layers, characterized by heavy isotope compositions, with the Cd-rich intermediate layers that have lighter compositions (Abouchami et al., 2014; Conway and John, 2015; Ripperger and Rehkämper, 2007; Xie et al., 2019). The depleted layer corresponds to depths for which the phytoplanktonic activity is intense, mainly close to the surface where the solar energy is the most concentrated. There, the plankton uptakes preferentially light Cd isotopes from the water, which are later re-mineralized in lower water layers. Planktonic organisms can produce highly fractionated isotope compositions (up to -5 ‰ per amu compared with the medium) for their tissues (Lacan et al., 2006). Other marine organisms can produce significant isotope variations between their metabolic products and their surrounding waters. As an example, bivalve tissues can be characterized by isotope compositions as light as - 0.3 ‰ per amu (Shiel et al., 2012).

In more complex organisms, significant isotope variations can occur between organs. As an example, from a bulk composition of δ^{114}Cd = 0.09 ‰ for the whole plant, wheat grains can be characterized by isotope compositions of 0.59 ‰ (Wiggenhauser et al., 2016). Similarly, barley harvest can present an isotope composition that is roughly 0.25 ‰ per amu heavier than the related soil, and 0.05 ‰ per amu heavier than the seepage water (Imseng et al., 2018). Natural biological samples isotope compositions range from -0.19 ‰ per amu to +0.25 ‰ per amu (Borovička et al., 2021; Chang et al., 2023; Imseng et al., 2018; Lu et al., 2021; Pallavicini et al., 2014).

5.1.5. Debate on igneous fractionation processes

Other processes are known to produce significant isotope variations for other elements and so are likely to isotopically fractionate Cd as well. However, the influence of these processes has not yet been characterized for Cd. Characterization of isotope fractionation occurring during these steps will be significantly improving the discussions surrounding Cd isotope studies as it will allow for finer discussion of the Cd isotopic variations causes. Three mechanisms can be

regarded as the most important to investigate because of their ubiquity and overall significance in the establishment of BSE isotope composition: magma differentiation, partial melting and metal-silicate partitioning.

Magmatic differentiation is the process by which magmatic chemical compositions evolve from Si-poor to Si-rich. This is mainly caused by the fractional crystallization of Si-poor minerals (olivine for example) in the magma chamber, driving the melt composition toward viscous Si-rich compositions. This chemical evolution is reflected in the progression of volcanic dynamisms from effusive toward explosive, if the magma chamber is not refilled by fresh magma. Numerous studies have shown that this chemical evolution is coupled to an isotope composition modification of the melt caused by isotope fractionation during the minerals crystallization (Chen et al., 2013; Inglis et al., 2019; Savage et al., 2011; Teng et al., 2008). Characterization of the intensity of such a process for Cd would be necessary for further discussion of igneous processes.

Production of magmas rarely results from total melting of the parent sample. This can occur during the accretion phase of a planetary body, with total melting caused by energetic impacts or by short-lived radioactivity heating. However, apart from these cases, magmas are formed by only partial melting of their precursor. If the melting rate is low and the studied element is not strongly incompatible, a significant fraction of the element remains in the residue, producing potentially important isotope fractionation between the melt and the residue (Savage et al., 2011). Because of this, characterization of the mantle isotope composition often relies on samples with high melting rates, to overcome any potential isotope fractionation (Sossi et al., 2018). The determination of the Cd isotope fractionation occurring during partial melting would allow for better use of igneous samples to constrain the mantle isotope composition.

Although there is, to our knowledge, no study exploring in depth the effects of these igneous processes on the isotope compositions of magmatic samples, some recorded significant isotopic

variations between such samples (Liu et al., 2020; Pickard et al., 2022). This suggests that isotopically fractionating processes play a role in the histories of these different rocks.

Finally, isotope fractionation can occur during metal-silicate partitioning. This is particularly pertinent for the determination of the Bulk Earth (BE) isotope composition, as we have no way to sample the Earth core to determine its isotope composition. The only way to determine an isotope composition for the BE is to experimentally investigate isotope fractionation occurring during metal-silicate partition and to apply the conclusions to the planetary differentiation process. Since the Earth core is thought to contain around 68 wt. % of Earth total Cd budget (calculated from reservoir masses and Cd concentrations) (Rudnick and Gao, 2014; Wang et al., 2018; Yoder, 1995), even the slightest isotope fractionation occurring during the core formation would produce significant isotope variations between the core and the mantle (and thus, between the BSE and the BE). A recent study did suggest that no detectable isotope fractionation occurred during the core formation (Pickard et al., 2023), however the complexity of the subject calls for more studies before it can be put to rest.

5.2. Uses of Cd

5.2.1. Anthropogenic pollution

Cadmium isotope studies have been used to trace man-made contamination based on its scarcity in nature and on the intense isotope fractionation that are obtained in industrially refined materials (Cloquet et al., 2006; Gao et al., 2013; Martinková et al., 2016; Shiel et al., 2010). Sampling in rivers (Gao et al., 2013) and soils (Cloquet et al., 2006; Wen et al., 2015) allows for determination of the contamination source depending on the sampled isotope compositions since refined Cd-bearing products have very fractionated isotope compositions compared to natural ores (Martinková et al., 2016; Shiel et al., 2010). Thus, Cd isotope studies

constitute an efficient mean to monitor anthropogenic contamination by Cd-releasing activities like ore refining, coal burning or agricultural fertilization.

5.2.2. In the oceans

A significant part of all Cd studies focused on the oceanic environment as Cd concentrations are a good proxy for major nutrients concentrations like nitrates or phosphates (Boyle et al., 1976; Bruland, 1980). In the oceanic water column, Cd concentration can be best described as starting from an almost Cd-deprived surface layer, only to rise rapidly with depth and reach a maximum concentration at around 1000m depth. It then stabilizes or slightly decreases over the next vertical 1000m (Abouchami et al., 2014; Boyle et al., 1976; Bruland, 1980; Conway and John, 2015; Lacan et al., 2006; Schmitt et al., 2009a). Interestingly, this pattern does fit much closer to nutrients contents than to silicate ones (Boyle et al., 1976; Bruland, 1980). This can be explained by the fact that Cd concentrations are mostly driven by biological uptake at the surface, re-mineralization of this biological Cd at higher depths and circulation within the oceans.

A particular interest of Cd for paleo-oceanographers is that seawater phosphates are rarely recorded in oceanic sediments (Henderson, 2002). However, Cd used in the formation of foraminifera tests is conserved in sediments and the recorded Cd/Ca ratio is depending on the Cd (hence the nutrients) seawater concentration at the moment of intake (Boyle, 1981). Reconstructions of paleo-oceanic Cd distribution are used both to trace changes in oceanic circulation (Boyle, 1992, 1988) and to constrain nutrients levels (Elderfield and Rickaby, 2000; Rickaby and Elderfield, 1999). These last constraints also provide indications about the biological productivity of the ocean and thus about its role as a storage for C (Druce et al., 2022b, 2022a).

This concentration profile is coupled with an isotope composition one, in which the Cd-depleted surface layer is characterized by heavy compositions. The general trend for deeper

layers is that the Cd isotope composition of the water gets lighter in the first 1000m and then stabilizes (Abouchami et al., 2014; Conway and John, 2015; Lacan et al., 2006; Schmitt et al., 2009a). Such isotope compositions profiles also indicate that potential Cd sulfide precipitation is likely to occur in low-oxygen waters (Conway and John, 2015). These studies allow for the reconstruction of the Cd cycle in oceans from inputs to sinks. Such knowledge is necessary to permit study of paleo-oceans conditions (notably the nutrient use) and biogeochemical cycling from the sediments.

5.2.3. In the silicate Earth

Most of our current data set concerning terrestrial silicates results from analyses of a few geological standard reference materials (SRM). These are rock samples that are produced and distributed in great quantities to laboratories, most of the time by state agencies like the U.S. geological Survey (USGS) or the National Institute of Standards and technology (NIST). This allows for results comparison between different teams and thus confirmation of the accuracy of different methods. Thus, many studies include some SRM analyses to prove their relevance (Borovička et al., 2021; Chang et al., 2023; Cloquet et al., 2005; Horner et al., 2010; Li et al., 2018; Liu et al., 2020; Lu et al., 2021; Pallavicini et al., 2014; Pickard et al., 2022; Tan et al., 2020; Wombacher et al., 2003). However, these results do not provide much insight in the geological processes or in the isotope compositions of geological reservoirs as the SRM are not chosen for their representativity but for their availability and homogeneity. Moreover, some studies have proven that they can be contaminated due to their batch processing, which would render them unusable for any comparison with uncontaminated samples (Willbold et al., 2016; Willbold and Elliott, 2017), although no such effect has yet been proven (nor tested) to occur for Cd. Despite these concerns, some authors have used geological SRM as reference isotope compositions for natural Earth minerals in order to discuss highly fractionated samples like

meteorites (Chang et al., 2023; Pickard et al., 2022; Wombacher et al., 2003) or industry-derived products and pollutants (Chang et al., 2023; Cloquet et al., 2005).

Only a few studies have provided isotope compositions for non-SRM terrestrial silicates, either to characterize isotope fractionation occurring during vaporization events, with tektites (Wombacher et al., 2003), or to determine a BSE isotope composition (Pickard et al., 2022; Schmitt et al., 2009a). In this last case, coherent results were obtained with two different set of samples. The first study proposed a $\delta^{114}Cd_{BSE}$ = -0.04 ± 0.02 ‰ (2SD, n = 7) deviation (Schmitt et al., 2009a) to the NIST SRM 3108 Cd standard isotopic solution (Abouchami et al., 2013). This estimation was calculated as the weighted mean isotope composition for a set of 2 MORB (Mid-Oceanic Ridge Basalts), 2 OIB (Ocean Island Basalts) and 3 loesses. These compositions are the first proposed for such samples. The second study, by Pickard et al. (2022), presents the first Cd isotope compositions for peridotites and komatiites, alongside a set of 10 MORB, 5 OIB and 13 loesses. It proposes a $\delta^{114}Cd_{BSE}$ of -0.06 ± 0.03 ‰ (2SD, n = 4) based on four supposed pristine spinel lherzolites compositions.

Although the proposed BSE isotope compositions of the two studies are similar, some problems emerge when comparing their datasets. Despite the good agreement between individual data points from the two studies, which demonstrate the quality of Schmitt et al. (2009a) data, it appears that most of the data from Pickard et al. (2022) study are significantly heavier than the BSE isotope composition proposed by Schmitt (see Figure 3). Thus, this proposed BSE value seems to have been stirred toward light isotopic compositions by a combination of wide uncertainties and unrepresentative data set. This last point is especially visible for OIB, which seems to be characterized by very diverse, and sometime very heavy, compositions which are not correctly accounted for by the two light values reported by the study. Thus, we argue that the BSE isotope composition proposed in Schmitt et al. (2009a) is likely to be not accurate because of a lack of data. Using the same method (a mean of loess,

OIB and MORB values) with a more complete dataset (Pickard et al., 2022) provides a significantly distinct BSE composition: $\delta^{114}Cd_{BSE}$ = 0.11 ± 0.14 ‰ (2SD, n = 28). This new value does not overlap with Pickard et al. (2022) preferred composition, determined on four supposedly pristine spinel lherzolites. It is, however, similar to a discarded plagioclase lherzolite isotope composition reported by Pickard et al. (2022), as well as to the mean harzburgite composition reported in the same study. Since the published compositions for peridotites are quite scattered, with a $\delta^{114}Cd$ ranging from -0.29 ± 0.05 ‰ to 0.10 ± 0.05 ‰ (with even a discarded extreme sample at 0.87 ± 0.03 ‰), and since this diversity is reflected in all investigated peridotite category (dunites, harzburgites and lherzolites), it appears that we may need more data regarding these kinds of samples and the processes affecting them before being able to derive a satisfactory BSE isotope composition from it.

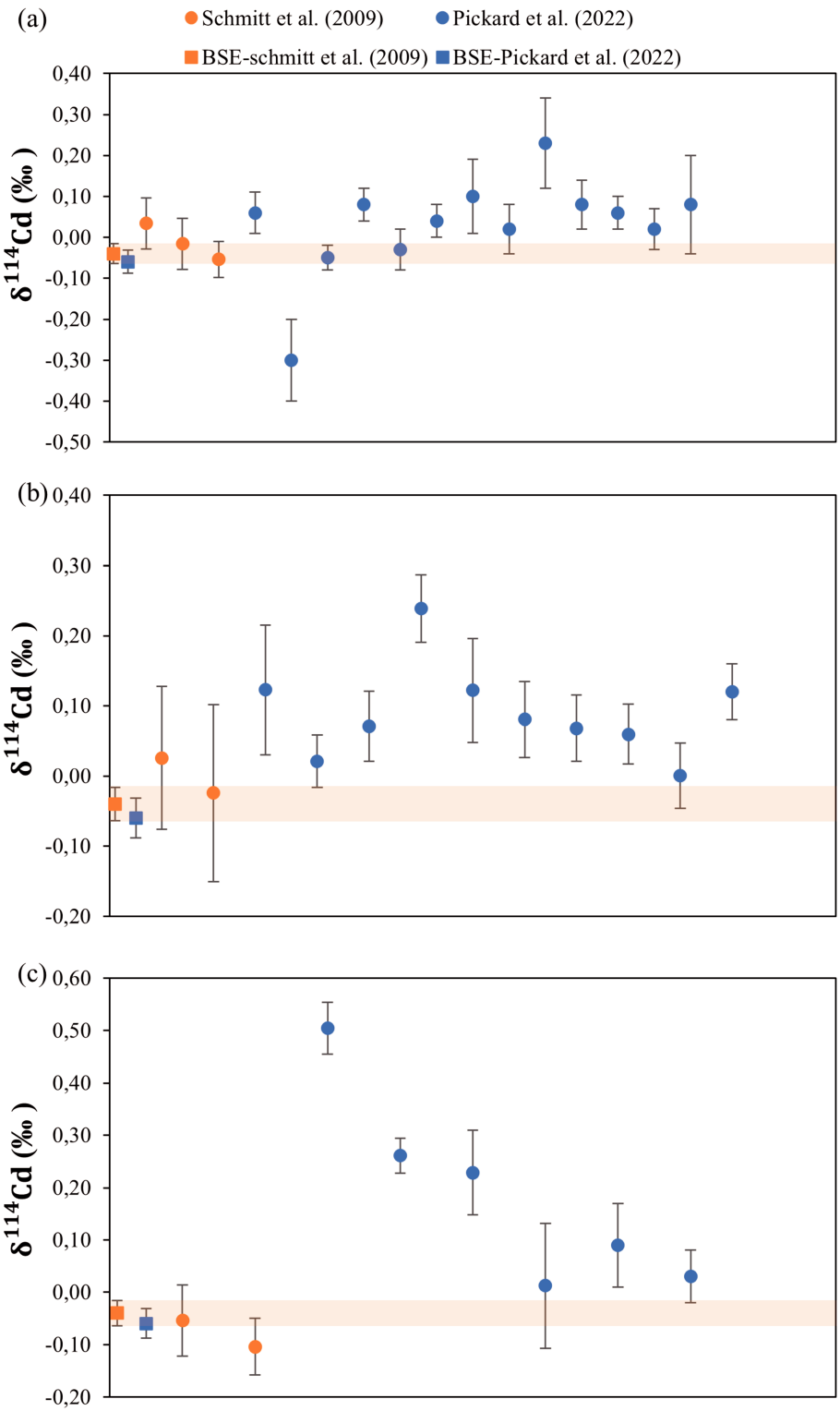


Figure 3: Comparison between the data sets from the studies by Schmitt et al. (2009) (orange shapes) and Pickard et al. (2022) (blue shapes). Squares represent the proposed isotope compositions for the BSE while circles represent individual data point. Uncertainties are expressed as 2SD. Orange fields represent the BSE isotope composition proposed by Schmitt et al. (2009).

(a) displays the data for loesses, (b) for MORB and (c) for OIB. Although the individual data points for both studies do overlap, demonstrating the quality of the work by Schmitt et al., the more extensive data set by Pickard et al. (2022) shows that the proposed BSE value does not fit with the samples it is supposed to represent (MORB, OIB and loesses). This is probably due to an unrepresentative sampling, especially for OIB, which are characterized by very diverse compositions.

5.2.4. Extraterrestrial samples

Extraterrestrial samples have been the subject of numerous studies because of their often very fractionated isotope compositions, which were easier to characterize at times when the attainable precision was still too bad for discrimination of less fractionated compositions like terrestrial minerals.

Chondrites isotope compositions were the subject of the 2nd isotopic study of Cd (Rosman and De Laeter, 1976), denoting an early interest in such samples. Since then, numerous articles have investigated their isotope compositions, especially for ordinary chondrites (Palk et al., 2018; Rosman et al., 1980b, 1980a; Rosman and De Laeter, 1976, 1978, 1988; Schediwy et al., 2006; Wombacher et al., 2003, 2008) and carbonaceous chondrites (Baker et al., 2010; Rosman and De Laeter, 1978; Wombacher et al., 2003, 2008). Enstatite chondrites (Palk et al., 2018; Wombacher et al., 2008) have received less interest, probably due to their lower availability. Alongside these samples, a small set of more unusual meteorites (Rumuruti chondrites, iron meteorites, eucrites, ureilites, winonaites, Martian and lunar meteorites) has been characterized (Rosman and De Laeter, 1978; Wombacher et al., 2003, 2008).

Chondrites present diversified compositions, with Cd concentrations ranging from a few ppb to almost 1 ppm for CC and EC and to a few ppm for OC. Isotope compositions can also be very fractionated, especially for OC and EC. Carbonaceous chondrites mostly have rather unfractionated isotope compositions, as 13 out of the 18 characterized CC have δ^{114}Cd comprised between -1 and +1 ‰ (Baker et al., 2010; Wombacher et al., 2003, 2008). Many of these compositions are roughly comparable to that of Earth materials. The most heavily

fractionated CC are mainly (4 out of 5) finds, which could indicate a terrestrial contamination. Their δ^{114}Cd compositions range from -1.08 ± 0.43 to 4.42 ± 0.43 ‰, but we lack concentration data to discuss potential vaporization or input processes. Interestingly, different studies produced significantly distinct isotope compositions for similar samples (Baker et al., 2010; Wombacher et al., 2003, 2008), this does not occur for OC or EC. This could indicate that CC are significantly heterogeneous for Cd.

Ordinary and enstatite chondrites have much more variable isotope compositions, as around 65 % of samples from both categories have a δ^{114}Cd higher than 1 ‰ or lower than -1 ‰ (most samples are isotopically heavy but a few OC are significantly light). These fractionated samples are composed equally of falls and finds, which seem to indicate that the fractionating process for these samples is not terrestrial in nature. No obvious correlation was found between isotope compositions and Cd concentrations. Interestingly, OC and EC have much more fractionated compositions than CC, with δ^{114}Cd reaching compositions as fractionated as 15.92 ‰ or -7.88 ‰.

One study (Wombacher et al., 2008) did compare isotope compositions for bulk chondrites and for isolated components (matrix, CAI, chondrules, fusion crust). These analyses indicate that the matrixes have generally similar to heavier isotope compositions than the bulk chondrite, while CAI, chondrules and fusion crusts are isotopically lighter than the bulk composition. Since these last elements are often considered as MVE-depleted (Hezel et al., 2018) compared to the matrix, such a result is surprising. Indeed, a vaporization scenario would imply a depletion of the residue in light isotopes. Thus, such compositions seem to indicate that the volatile depletion of chondrules is not caused by any kinetic vaporization event but probably by interaction with an isotopically light gas (Wombacher et al., 2008).

A few achondrites were analyzed, but they do constitute a set that is probably too small for any meaningful conclusion. To our knowledge, only two iron meteorites have been analyzed

(Rosman and De Laeter, 1978). Both exhibits fractionated but distinct isotope compositions, with one δ^{114}Cd value around -2.4 ‰ and one around +2 ‰. These results could indicate that significant isotope fractionation occur during the formation of planetary cores, but more complete analyses would be needed to confirm such an assumption. Among achondrites, eucrites and winonaites seem to be isotopically light while ureilites are isotopically heavy (Wombacher et al., 2008), but again these observations rely on exceedingly low number of samples.

Finally, 3 Martian meteorites and 13 lunar samples (2 lunar meteorites and 11 lunar surface samples) were analyzed (Rosman and De Laeter, 1978; Sands et al., 2001a; Schediwy et al., 2006; Wombacher et al., 2008). Martian samples (2 shergottites and 1 nakhlite) are characterized by lowly fractionated isotope compositions, with δ^{114}Cd under 1 ‰. To the contrary, lunar samples display most of the time isotope compositions that are strongly fractionated toward heavy compositions. This is coherent with the formation of the Moon by a giant impact as well as the constant meteoritical bombardment that melts parts of its surface.

6. The PhD project

6.1. Objectives of the PhD

As shown in previous sections, Cd isotopic studies are still a developing field. It is our belief that it is still an understudied research topic and that it could produce significant insights for numerous geochemical issues. The high volatility of Cd, for example, could be used to investigate potential vaporization events on Earth or for extraterrestrial samples. Moreover, Cd siderophility and chalcophility should result in the segregation of a significant fraction (up to two third) of Earth total Cd budget in the core (Wang et al., 2018; Yoder, 1995). This could produce important isotope fractionation between the BSE and BE, if Cd partitioning in metal is an isotope fractionating process. Thus, comparing isotope compositions of the BSE and

meteorites (iron and chondrites) should allow us to better describe the terrestrial differentiation process.

The goal of this PhD was to develop a new method for purification and high precision analysis of Cd isotopes, using MC-ICPMS. Although a Cd DS was previously developed in the team in prevision of such work, this PhD was our first attempt at measuring Cd isotope compositions in geological samples. Thus, the first objective of the project was to prove the efficiency and accuracy of the new Cd purification process as well as the new Cd DS formula. An important part of this objective has been to prove the reliability of the new method for low concentrations (a few ppb) samples. The second objective was to determine a new isotope composition for the BSE and to compare it to the previously published ones. The third goal of this work was to investigate Cd isotope fractionation occurring during fractional crystallization. The fourth purpose of this work was to describe MVE isotope fractionation occurring during vaporization events. Finally, we aimed at expanding the knowledge of Cd isotope compositions in chondrites to discuss Earth accretion as well as the early processes occurring during the first Ma of the solar system.

6.2.Challenges

Since this work represents a major challenge in developing high precision isotope analyses of Cd in various samples containing very low amount of Cd, several difficulties were expected. The main encountered difficulty has certainly been the development of the Cd purification method, as it appeared to lack efficiency for Sn and Pd elimination, thus requiring multiple runs as well as monitoring and correcting remaining interferences. Working with highly depleted samples, like tektites, has also proven challenging as it allowed only for a limited number of mass spectrometer analyses. Some samples, like iron meteorites, were in fact too Cd-poor to be analyzed for this element. Finally, an unexpected hurdle emerged from the study of chondrites,

as some of these samples were characterized by distinct isotope compositions between replicates, potentially indicating a very heterogeneous nature for Cd.

7. References

Abouchami, W., Galer, S.J.G., de Baar, H.J.W., Middag, R., Vance, D., Zhao, Y., Klunder, M., Mezger, K., Feldmann, H., Andreae, M.O., 2014. Biogeochemical cycling of cadmium isotopes in the southern ocean along the zero meridian. Geochim. Cosmochim. Acta 127, 348–367. https://doi.org/10.1016/j.gca.2013.10.022

Abouchami, W., Galer, S.J.G., Horner, T.J., Rehkämper, M., Wombacher, F., Xue, Z., Lambelet, M., Gault-Ringold, M., Stirling, C.H., Schönbächler, M., Shiel, A.E., Weis, D., Holdship, P.F., 2013. A common reference material for cadmium isotope studies - NIST SRM 3108. Geostand. Geoanalytical Res. 37, 5–17. https://doi.org/10.1111/j.1751-908X.2012.00175.x

Albarède, F., 2009. Volatile accretion history of the terrestrial planets and dynamic implications. Nature 461, 1227–1233. https://doi.org/10.1038/nature08477

Albarède, F., Albalat, E., Lee, C.A., 2015. An intrinsic volatility scale relevant to the Earth and Moon and the status of water in the Moon. Meteorit. Planet. Sci. 50, 568–577. https://doi.org/10.1111/maps.12331

Albarede, F., Ballhaus, C., Blichert-Toft, J., Lee, C.-T., Marty, B., Moynier, F., Yin, Q.-Z., 2013. Asteroidal impacts and the origin of terrestrial and lunar volatiles. Icarus 222, 44–52. https://doi.org/10.1016/j.icarus.2012.10.026

Amelin, Y., Krot, A.N., Hutcheon, I.D., Ulyanov, A.A., 2002. Lead Isotopic Ages of Chondrules and Calcium-Aluminum-Rich Inclusions. Science 297, 1678–1683. https://doi.org/10.1126/science.1073950

Amsellem, E., Moynier, F., Pringle, E.A., Bouvier, A., Chen, H., Day, J.M.D., 2017. Testing the chondrule-rich accretion model for planetary embryos using calcium isotopes. Earth

Planet. Sci. Lett. 469, 75–83. https://doi.org/10.1016/j.epsl.2017.04.022

Ando, M., Sayato, Y., Osawa, T., 1978. Studies on the disposition of calcium in bones of rats after continuous oral administration of cadmium. Toxicol. Appl. Pharmacol. 46, 625–632. https://doi.org/10.1016/0041-008X(78)90308-3

Arevalo, R., McDonough, W.F., 2010. Chemical variations and regional diversity observed in MORB. Chem. Geol. 271, 70–85. https://doi.org/10.1016/j.chemgeo.2009.12.013

Arvidson, R., Crozaz, G., Drozd, R.J., Hohenberg, C.M., Morgan, C.J., 1975. Cosmic ray exposure ages of features and events at the apollo landing sites. The Moon 13, 259–276. https://doi.org/10.1007/BF00567518

Asphaug, E., Jutzi, M., Movshovitz, N., 2011. Chondrule formation during planetesimal accretion. Earth Planet. Sci. Lett. 308, 369–379. https://doi.org/10.1016/j.epsl.2011.06.007

Asplund, M., Grevesse, N., Sauval, A.J., Scott, P., 2009. The chemical composition of the Sun. https://doi.org/10.48550/ARXIV.0909.0948

Audi, G., Bersillon, O., Blachot, J., Wapstra, A.H., 2003. The Nubase evaluation of nuclear and decay properties. Nucl. Phys. A 729, 3–128. https://doi.org/10.1016/j.nuclphysa.2003.11.001

Baedecker, P.A., Schaudy, R., Elzie, J.L., Kimberlin, J., Wasson, J.T., 1971. Trace element studies of rocks and soils from Oceanus Procellarum and Mare Tranquillitatis. Lunar Planet. Sci. Conf. Proc. 2, 1037–1061.

Baker, R.G.A., Schönbächler, M., Rehkämper, M., Williams, H.M., Halliday, A.N., 2010. The thallium isotope composition of carbonaceous chondrites — New evidence for live 205Pb in the early solar system. Earth Planet. Sci. Lett. 291, 39–47. https://doi.org/10.1016/j.epsl.2009.12.044

Barbee, J.Y., Prince, T.S., 1999. Acute respiratory distress syndrome in a welder exposed to metal fumes: South. Med. J. 92, 510–512. https://doi.org/10.1097/00007611-199905000-00012

Barbier, O., Jacquillet, G., Tauc, M., Cougnon, M., Poujeol, P., 2005. Effect of Heavy Metals on, and Handling by, the Kidney. Nephron Physiol. 99, p105–p110. https://doi.org/10.1159/000083981

Berglund, M., Wieser, M.E., 2011. Isotopic compositions of the elements 2009 (IUPAC Technical Report). Pure Appl. Chem. 83, 397–410. https://doi.org/10.1351/PAC-REP-10-06-02

Bernhoft, R.A., 2013. Cadmium toxicity and treatment. Sci. World J. 2013, 1–7. https://doi.org/10.1155/2013/394652

Böhlke, J.K., de Laeter, J.R., De Bièvre, P., Hidaka, H., Peiser, H.S., Rosman, K.J.R., Taylor, P.D.P., 2005. Isotopic compositions of the elements, 2001. J. Phys. Chem. Ref. Data 34, 57–67. https://doi.org/10.1063/1.1836764

Bollard, J., Connelly, J.N., Whitehouse, M.J., Pringle, E.A., Bonal, L., Jørgensen, J.K., Nordlund, Å., Moynier, F., Bizzarro, M., 2017. Early formation of planetary building blocks inferred from Pb isotopic ages of chondrules. Sci. Adv. 3, e1700407. https://doi.org/10.1126/sciadv.1700407

Borovička, J., Ackerman, L., Rejšek, J., 2021. Cadmium isotopic composition of biogenic certified reference materials determined by thermal ionization mass spectrometry with double spike correction. Talanta 221, 121389. https://doi.org/10.1016/j.talanta.2020.121389

Boyle, E.A., 1992. Cadmium and δ^{13}C paleochemical ocean distributions during the stage 2 glacial maximum. Annu. Rev. Earth Planet. Sci. 20, 245–287. https://doi.org/10.1146/annurev.ea.20.050192.001333

Boyle, E.A., 1988. Cadmium: Chemical tracer of deepwater paleoceanography. Paleoceanography 3, 471–489. https://doi.org/10.1029/PA003i004p00471

Boyle, E.A., 1981. Cadmium, zinc, copper, and barium in foraminifera tests. Earth Planet. Sci. Lett. 53, 11–35. https://doi.org/10.1016/0012-821X(81)90022-4

Boyle, E.A., Sclater, F., Edmond, J.M., 1976. On the marine geochemistry of cadmium. Nature 263, 42–44. https://doi.org/10.1038/263042a0

Braukmüller, N., Wombacher, F., Bragagni, A., Münker, C., 2020. Determination of Cu, Zn, Ga, Ag, Cd, In, Sn and Tl in geological reference materials and chondrites by isotope dilution ICP-MS. Geostand. Geoanalytical Res. 44, 733–752. https://doi.org/10.1111/ggr.12352

Braukmüller, N., Wombacher, F., Funk, C., Münker, C., 2019. Earth's volatile element depletion pattern inherited from a carbonaceous chondrite-like source. Nat. Geosci. 12, 564–568. https://doi.org/10.1038/s41561-019-0375-x

Braukmüller, N., Wombacher, F., Hezel, D.C., Escoube, R., Münker, C., 2018. The chemical composition of carbonaceous chondrites: Implications for volatile element depletion, complementarity and alteration. Geochim. Cosmochim. Acta 239, 17–48. https://doi.org/10.1016/j.gca.2018.07.023

Bruland, K.W., 1980. Oceanographic distributions of cadmium, zinc, nickel, and copper in the North Pacific. Earth Planet. Sci. Lett. 47, 176–198. https://doi.org/10.1016/0012-821X(80)90035-7

Buffon, G.-L., 1745. Réflexions sur la loi de l'attraction. Histoire de l'Académie royale des sciences de Paris.

Buha, A., Jugdaohsingh, R., Matovic, V., Bulat, Z., Antonijevic, B., Kerns, J.G., Goodship, A., Hart, A., Powell, J.J., 2019. Bone mineral health is sensitively related to environmental

cadmium exposure- experimental and human data. Environ. Res. 176, 108539. https://doi.org/10.1016/j.envres.2019.108539

Burkhardt, C., Spitzer, F., Morbidelli, A., Budde, G., Render, J.H., Kruijer, T.S., Kleine, T., 2021. Terrestrial planet formation from lost inner solar system material. Sci. Adv. 7, eabj7601. https://doi.org/10.1126/sciadv.abj7601

Cadmium Applications [WWW Document], 2021. . Int. Cadmium Assoc. URL https://www.cadmium.org/#

Cadmium.org [WWW Document], 2021. . Int. Cadmium Assoc. URL https://www.cadmium.org

Cameron, A.G.W., Truran, J.W., 1977. The supernova trigger for formation of the solar system. Icarus 30, 447–461. https://doi.org/10.1016/0019-1035(77)90101-4

Cannino, G., Ferruggia, E., Luparello, C., Rinaldi, A.M., 2009. Cadmium and mitochondria. Mitochondrion 9, 377–384. https://doi.org/10.1016/j.mito.2009.08.009

Chambers, J.E., Halliday, A.N., 2014. The Origin of the Solar System, in: Encyclopedia of the Solar System. Elsevier, pp. 29–54. https://doi.org/10.1016/B978-0-12-415845-0.00002-5

Chang, H., Zhu, J.-M., Wang, X., Gao, T., 2023. High-precision measurement of Cd isotopes in ultra-trace Cd samples using double spike-standard addition MC-ICP-MS. J. Anal. At. Spectrom. 38, 950–962. https://doi.org/10.1039/D3JA00047H

Chen, H., Meshik, A.P., Pravdivtseva, O.V., Day, J.M.D., Wang, K., 2019. Potassium isotope fractionation during high-temperature evaporation determined from the Trinity nuclear test. Chem. Geol. 522, 84–92. https://doi.org/10.1016/j.chemgeo.2019.04.028

Chen, H., Savage, P.S., Teng, F.-Z., Helz, R.T., Moynier, F., 2013. Zinc isotope fractionation during magmatic differentiation and the isotopic composition of the bulk Earth.

Earth Planet. Sci. Lett. 369–370, 34–42. https://doi.org/10.1016/j.epsl.2013.02.037

Ciesla, F., 2002. The Nebular Shock Wave Model for Chondrule Formation: Shock Processing in a Particle–Gas Suspension. Icarus 158, 281–293. https://doi.org/10.1006/icar.2002.6895

Clay, P.L., Burgess, R., Busemann, H., Ruzié-Hamilton, L., Joachim, B., Day, J.M.D., Ballentine, C.J., 2017. Halogens in chondritic meteorites and terrestrial accretion. Nature 551, 614–618. https://doi.org/10.1038/nature24625

Cloquet, C., Carignan, J., Libourel, G., Sterckeman, T., Perdrix, E., 2006. Tracing source pollution in soils using cadmium and lead isotopes. Environ. Sci. Technol. 40, 2525–2530. https://doi.org/10.1021/es052232+

Cloquet, C., Rouxel, O., Carignan, J., Libourel, G., 2005. Natural cadmium isotopic variations in eight geological reference materials (NIST SRM 2711, BCR 176, GSS-1, GXR-1, GXR-2, GSD-12, Nod-P-1, Nod-A-1) and anthropogenic samples, measured by MC-ICP-MS. Geostand. Geoanalytical Res. 29, 95–106. https://doi.org/10.1111/j.1751-908X.2005.tb00658.x

Coc, A., Vangioni, E., 2017. Primordial nucleosynthesis. https://doi.org/10.48550/ARXIV.1707.01004

Connelly, J.N., Bizzarro, M., Krot, A.N., Nordlund, A., Wielandt, D., Ivanova, M.A., 2012. The absolute chronology and thermal processing of solids in the solar protoplanetary disk. Science 338, 651–655. https://doi.org/10.1126/science.1226919

Connolly, H.C., Desch, S.J., 2004. On the origin of the “kleine Kügelchen” called Chondrules. Geochemistry 64, 95–125. https://doi.org/10.1016/j.chemer.2003.12.001

Connolly, H.C., Love, S.G., 1998. The Formation of Chondrules: Petrologic Tests of the Shock Wave Model. Science 280, 62–67. https://doi.org/10.1126/science.280.5360.62

Conway, T.M., John, S.G., 2015. Biogeochemical cycling of cadmium isotopes along a high-resolution section through the North Atlantic Ocean. Geochim. Cosmochim. Acta 148, 269–283. https://doi.org/10.1016/j.gca.2014.09.032

Creech, J.B., Moynier, F., Koeberl, C., 2019. Volatile loss under a diffusion-limited regime in tektites: Evidence from tin stable isotopes. Chem. Geol. 528, 119279. https://doi.org/10.1016/j.chemgeo.2019.119279

Creech, J.B., Paul, B., 2015. IsoSpike: improved double-spike inversion software. Geostand. Geoanalytical Res. 39, 7–15. https://doi.org/10.1111/j.1751-908X.2014.00276.x

Cui, W., Meng, Q., Feng, Q., Zhou, L., Cui, Y., Li, W., 2019. Occurrence and release of cadmium, chromium, and lead from stone coal combustion. Int. J. Coal Sci. Technol. 6, 586–594. https://doi.org/10.1007/s40789-019-00281-4

Day, J.M.D., Moynier, F., Meshik, A.P., Pradivtseva, O.V., Petit, D.R., 2017. Evaporative fractionation of zinc during the first nuclear detonation. Sci. Adv. 3, e1602668. https://doi.org/10.1126/sciadv.1602668

Day, J.M.D., Moynier, F., Sossi, P.A., Wang, K., Meshik, A.P., Pravdivtseva, O.V., Pettit, D.R., 2020. Moderately volatile element behaviour at high temperature determined from nuclear detonation. Geochem. Perspect. Lett. 35, 54–60. https://doi.org/10.7185/geochemlet.2014

Descartes, R., 1633. Le Monde ou traité de la lumière, 1974th ed, Les classiques des sciences sociales.

Desch, S.J., Connolly, H.C., 2002. A model of the thermal processing of particles in solar nebula shocks: Application to the cooling rates of chondrules. Meteorit. Planet. Sci. 37, 183–207. https://doi.org/10.1111/j.1945-5100.2002.tb01104.x

Devos, G., Moynier, F., Creech, J., Liu, D., Puchtel, I.S., Bizzarro, M., 2024. Cadmium

isotope composition of the Earth's mantle inferred from analysis of oceanic basalts and komatiites. Chem. Geol. 650, 121996. https://doi.org/10.1016/j.chemgeo.2024.121996

Devouard, B., Rochette, P., Gattacceca, J., Valenzuela, E.M., Alard, O., Balestrieri, M.L., Santos, E.D., Gounelle, M., Jambon, A., Laridhi, N., Shuster, D.L., Warner, M., Warner, M., 2014. A new tektite strewnfield in Atacama, Chile. Presented at the 77th Annual Meteoritical Society Meeting.

Directive 2006/66/EC of the European Parliament and of the Council of 6 September 2006 on batteries and accumulators and waste batteries and accumulators and repealing Directive 91/157/EEC, 2006.

Dodson, M.H., 1963. A theoretical study of the use of internal standards for precise isotopic analysis by the surface ionization technique: Part I - General first-order algebraic solutions. J. Sci. Instrum. 40, 289–295. https://doi.org/10.1088/0950-7671/40/6/307

Dostal, J., Elson, C., Dupuy, C., 1979. Distribution of lead, silver and cadmium in some igneous rocks and their constituent minerals. Can. Mineral. 17, 561–567.

Druce, M., Stirling, C.H., Bostock, H.C., Rolison, J.M., 2022a. Cadmium isotope systematics in sedimentary carbonate: Extending the utility of the cadmium isotope palaeo-productivity proxy. Geochim. Cosmochim. Acta 339, 80–96. https://doi.org/10.1016/j.gca.2022.10.041

Druce, M., Stirling, C.H., Bostock, H.C., Rolison, J.M., 2022b. Examining the effects of chemical cleaning, leaching, and partial dissolution on zinc and cadmium isotope fractionation in marine carbonates. Chem. Geol. 592, 120738. https://doi.org/10.1016/j.chemgeo.2022.120738

Du, C., Hu, S., 2015. Accurate determination of trace cadmium in geological reference materials by closed vessel acid digestion ETAAS. At. Spectrosc. 36, 141–145.

https://doi.org/10.46770/AS.2015.03.005

Eby, N., Hermes, R., Charnley, N., Smoliga, J.A., 2010. Trinitite-the atomic rock. Geol. Today 26, 180–185. https://doi.org/10.1111/j.1365-2451.2010.00767.x

Elderfield, H., Rickaby, R.E.M., 2000. Oceanic Cd/P ratio and nutrient utilization in the glacial Southern Ocean. Nature 405, 305–310. https://doi.org/10.1038/35012507

Elinder, C.-G., Kjellström, T., Friberg, L., Linnman, B.L.L., 1976. Cadmium in Kidney Cortex, Liver, and Pancreas from Swedish Autopsies. Arch. Environ. Health Int. J. 31, 292–302. https://doi.org/10.1080/00039896.1976.10667239

Faris, J.P., Buchanan, R.F., 1964. Anion exchange characteristics of the elements in nitric acid medium. Anal. Chem. 36, 1157–1158. https://doi.org/10.1021/ac60212a067

Faure, F., Tissandier, L., Libourel, G., Mathieu, R., Welsch, B., 2012. Origin of glass inclusions hosted in magnesian porphyritic olivines chondrules: Deciphering planetesimal compositions. Earth Planet. Sci. Lett. 319–320, 1–8. https://doi.org/10.1016/j.epsl.2011.12.013

Fegley, Jr., B., 2000. Kinetics of gas-grain reactions in the Solar nebula. Space Sci. Rev. 92, 177–200. https://doi.org/10.1023/A:1005286910756

Flanagan, P.R., McLellan, J.S., Haist, J., Cherian, G., Chamberlain, M.J., Valberg, L.S., 1978. Increased dietary cadmium absorption in mice and human subjects with iron deficiency. Gastroenterology 74, 841–846.

Florentin, L., Faure, F., Deloule, E., Tissandier, L., Gurenko, A., Lequin, D., 2017. Origin of Na in glass inclusions hosted in olivine from Allende CV3 and Jbilet Winselwan CM2: Implications for chondrule formation. Earth Planet. Sci. Lett. 474, 160–171. https://doi.org/10.1016/j.epsl.2017.06.038

Galer, S.J.G., 1999. Optimal double and triple spiking for high precision lead isotopic

measurement. Chem. Geol. 157, 255–274. https://doi.org/10.1016/S0009-2541(98)00203-4

Ganapathy, R., Anders, E., 1974. Bulk composition of the moon and earth, estimated from meteorites. Lunar Planet. Sci. Conf. Proc. 2, 1181–1206.

Gao, B., Zhou, H., Liang, X., Tu, X., 2013. Cd isotopes as a potential source tracer of metal pollution in river sediments. Environ. Pollut. 181, 340–343. https://doi.org/10.1016/j.envpol.2013.05.048

Gattacceca, J., Debaille, V., Devouard, B., leya, I., Jourdan, F., Braucher, R., Roland, J., Pourkhorsandi, H., Goderis, S., Jambon, A., 2023. Northwest Africa 13188: a possible meteorite ... from Earth! Presented at the Goldschmidt 2023 Conference.

Genchi, G., Sinicropi, M.S., Lauria, G., Carocci, A., Catalano, A., 2020. The Effects of Cadmium Toxicity. Int. J. Environ. Res. Public. Health 17, 3782. https://doi.org/10.3390/ijerph17113782

Ghosh, M., Singh, S.P., 2005. A comparative study of cadmium phytoextraction by accumulator and weed species. Environ. Pollut. 133, 365–371. https://doi.org/10.1016/j.envpol.2004.05.015

Gicking, A.M., Takahashi, K., Krane, K.S., 2019. Neutron capture cross sections of stable Cd isotopes. Eur. Phys. J. A 55, 52. https://doi.org/10.1140/epja/i2019-12721-7

Godt, J., Scheidig, F., Grosse-Siestrup, C., Esche, V., Brandenburg, P., Reich, A., Groneberg, D.A., 2006. The toxicity of cadmium and resulting hazards for human health. J. Occup. Med. Toxicol. 1, 1–6. https://doi.org/10.1186/1745-6673-1-22

Grady, M., 2022. Catalogue of Meteorites. https://doi.org/10.5519/TQFUWLE7

Greaney, A.T., Rudnick, R.L., Helz, R.T., Gaschnig, R.M., Piccoli, P.M., Ash, R.D., 2017. The behavior of chalcophile elements during magmatic differentiation as observed in Kilauea

Iki lava lake, Hawaii. Geochim. Cosmochim. Acta 210, 71–96. https://doi.org/10.1016/j.gca.2017.04.033

Grinyer, J., Byun, S.H., Chettle, D.R., 2005. In vivo prompt gamma neutron activation analysis of cadmium in the kidney and liver. Appl. Radiat. Isot. 63, 475–479. https://doi.org/10.1016/j.apradiso.2005.05.046

Grossman, L., 1972. Condensation in the primitive solar nebula. Geochim. Cosmochim. Acta 36, 597–619. https://doi.org/10.1016/0016-7037(72)90078-6

Guinoiseau, D., Galer, S.J.G., Abouchami, W., 2018. Effect of cadmium sulphide precipitation on the partitioning of Cd isotopes: Implications for the oceanic Cd cycle. Earth Planet. Sci. Lett. 498, 300–308. https://doi.org/10.1016/j.epsl.2018.06.039

Hamilton, D.L., Smith, M.W., 1978. Inhibition of intestinal calcium uptake by cadmium and the effect of a low calcium diet on cadmium retention. Environ. Res. 15, 175–184. https://doi.org/10.1016/0013-9351(78)90094-4

Heitsch, F., Hartmann, L., 2008. Rapid Molecular Cloud and Star Formation: Mechanisms and Movies. Astrophys. J. 689, 290–301. https://doi.org/10.1086/592491

Henderson, G.M., 2002. New oceanic proxies for paleoclimate. Earth Planet. Sci. Lett. 203, 1–13. https://doi.org/10.1016/S0012-821X(02)00809-9

Herschel, W., 1791. IV. On nebulous stars, properly so called. Philos. Trans. R. Soc. Lond. 81, 71–88. https://doi.org/10.1098/rstl.1791.0006

Hester, J.J., Desch, S.J., Healy, K.R., Leshin, L.A., 2004. The Cradle of the Solar System. Science 304, 1116–1117. https://doi.org/10.1126/science.1096808

Hevey, P.J., Sanders, I.S., 2006. A model for planetesimal meltdown by ^{26}Al and its implications for meteorite parent bodies. Meteorit. Planet. Sci. 41, 95–106.

https://doi.org/10.1111/j.1945-5100.2006.tb00195.x

Hezel, D.C., Harak, M., Libourel, G., 2018. What we know about elemental bulk chondrule and matrix compositions: Presenting the ChondriteDB database. Geochemistry 78, 1–14. https://doi.org/10.1016/j.chemer.2017.05.003

Hin, R.C., Coath, C.D., Carter, P.J., Nimmo, F., Lai, Y.-J., Pogge von Strandmann, P.A.E., Willbold, M., Leinhardt, Z.M., Walter, M.J., Elliott, T., 2017. Magnesium isotope evidence that accretional vapour loss shapes planetary compositions. Nature 549, 511–515. https://doi.org/10.1038/nature23899

Hofmann, A., 1971. Fractionation corrections for mixed-isotope spikes of Sr, K, and Pb. Earth Planet. Sci. Lett. 10, 397–402. https://doi.org/10.1016/0012-821X(71)90087-2

Holleman, A.F., Wiberg, E., Wiberg, N., 1985. Lehrbuch der anorganischen Chemie, 91.-100., verb. und stark erw. Aufl. von Nils Wiberg. ed. de Gruyter, Berlin.

Horan, M.F., Walker, R.J., Morgan, J.W., Grossman, J.N., Rubin, A.E., 2003. Highly siderophile elements in chondrites. Chem. Geol. 196, 27–42. https://doi.org/10.1016/S0009-2541(02)00405-9

Horner, T.J., Rickaby, R.E.M., Henderson, G.M., 2011. Isotopic fractionation of cadmium into calcite. Earth Planet. Sci. Lett. 312, 243–253. https://doi.org/10.1016/j.epsl.2011.10.004

Horner, T.J., Schönbächler, M., Rehkämper, M., Nielsen, S.G., Williams, H., Halliday, A.N., Xue, Z., Hein, J.R., 2010. Ferromanganese crusts as archives of deep water Cd isotope compositions: DATA BRIEF. Geochem. Geophys. Geosystems 11, n/a-n/a. https://doi.org/10.1029/2009GC002987

Humayun, M., Clayton, R.N., 1995. Potassium isotope cosmochemistry: Genetic implications of volatile element depletion. Geochim. Cosmochim. Acta 59, 2131–2148. https://doi.org/10.1016/0016-7037(95)00132-8

Ilyasova, D., Schwartz, G., 2005. Cadmium and renal cancer. Toxicol. Appl. Pharmacol. 207, 179–186. https://doi.org/10.1016/j.taap.2004.12.005

Imseng, M., Wiggenhauser, M., Keller, A., Müller, M., Rehkämper, M., Murphy, K., Kreissig, K., Frossard, E., Wilcke, W., Bigalke, M., 2018. Fate of Cd in agricultural soils: a stable isotope approach to anthropogenic impact, soil formation, and soil-plant cycling. Environ. Sci. Technol. 52, 1919–1928. https://doi.org/10.1021/acs.est.7b05439

Inglis, E.C., Moynier, F., Creech, J., Deng, Z., Day, J.M.D., Teng, F.-Z., Bizzarro, M., Jackson, M., Savage, P., 2019. Isotopic fractionation of zirconium during magmatic differentiation and the stable isotope composition of the silicate Earth. Geochim. Cosmochim. Acta 250, 311–323. https://doi.org/10.1016/j.gca.2019.02.010

Jacquet, J., Benizri, E., Echevarria, G., Sirguey, C., 2022. New insights on glass industry wasteland ecosystems. Environ. Pollut. 315, 120431. https://doi.org/10.1016/j.envpol.2022.120431

Jarup, L., Alfven, T., Persson, B., Toss, G., Elinder, C.G., 1998. Cadmium may be a risk factor for osteoporosis. Occup. Environ. Med. 55, 435–439. https://doi.org/10.1136/oem.55.7.435

Jewitt, D., Chizmadia, L., Grimm, R., Prialnik, D., 2007. Water in the small bodies of the Solar system, in: Reipurth, B., Jewitt, D., Keil, K. (Eds.), Protostars and Planets V, The University of Arizona Space Science Series. University of Arizona Press ; In collaboration with Lunar and Planetary Institute, Tucson : Houston, pp. 863–878.

Jochum, K.P., Hofmann, A.W., Ito, E., Seufert, H.M., White, W.M., 1983. K, U and Th in mid-ocean ridge basalt glasses and heat production, K/U and K/Rb in the mantle. Nature 306, 431–436. https://doi.org/10.1038/306431a0

Jochum, K.P., Nohl, U., Herwig, K., Lammel, E., Stoll, B., Hofmann, A.W., 2005.

GeoReM: A New Geochemical Database for Reference Materials and Isotopic Standards. Geostand. Geoanalytical Res. 29, 333–338. https://doi.org/10.1111/j.1751-908X.2005.tb00904.x

Johansen, A., Ronnet, T., Bizzarro, M., Schiller, M., Lambrechts, M., Nordlund, Å., Lammer, H., 2021. A pebble accretion model for the formation of the terrestrial planets in the Solar System. Sci. Adv. 7, eabc0444. https://doi.org/10.1126/sciadv.abc0444

Jorhem, L., Mattsson, P., Slorach, S., 1986. Lead, cadmium, zinc and certain other metals in foods on the Swedish market. J. Environ. Pathol. Toxicol. Oncol. Off. Organ Int. Soc. Environ. Toxicol. Cancer 6, 195–256.

Kaib, N., Quinn, T., 2008. The formation of the Oort cloud in open cluster environments. Icarus 197, 221–238. https://doi.org/10.1016/j.icarus.2008.03.020

Kant, I., 1755. Universal natural history and theory of heaven, 2023rd ed. Newcomb Livraria Press.

Kato, C., Moynier, F., Valdes, M.C., Dhaliwal, J.K., Day, J.M.D., 2015. Extensive volatile loss during formation and differentiation of the Moon. Nat. Commun. 6, 7617. https://doi.org/10.1038/ncomms8617

Kazantzis, G., 1979. Renal tubular dysfunction and abnormalities of calcium metabolism in cadmium workers. Environ. Health Perspect. 28, 155–159. https://doi.org/10.1289/ehp.7928155

Kiseeva, E.S., Wood, B.J., 2013. A simple model for chalcophile element partitioning between sulphide and silicate liquids with geochemical applications. Earth Planet. Sci. Lett. 383, 68–81. https://doi.org/10.1016/j.epsl.2013.09.034

Koeberl, C., 1992. Geochemistry and origin of Muong Nong-type tektites. Geochim. Cosmochim. Acta 56, 1033–1064. https://doi.org/10.1016/0016-7037(92)90046-L

Koeberl, C., Bottomley, R., Glass, B.P., Storzer, D., 1997. Geochemistry and age of Ivory Coast tektites and microtektites. Geochim. Cosmochim. Acta 61, 1745–1772. https://doi.org/10.1016/S0016-7037(97)00026-4

Krähenbühl, U., Morgan, J.W., Ganapathy, R., Anders, E., 1973. Abundance of 17 trace elements in carbonaceous chondrites. Geochim. Cosmochim. Acta 37, 1353–1370. https://doi.org/10.1016/0016-7037(73)90066-5

Kubik, E., Siebert, J., Blanchard, I., Agranier, A., Mahan, B., Moynier, F., 2021. Earth's volatile accretion as told by Cd, Bi, Sb and Tl core–mantle distribution. Geochim. Cosmochim. Acta 306, 263–280. https://doi.org/10.1016/j.gca.2021.02.017

Lacan, F., Francois, R., Ji, Y., Sherrell, R.M., 2006. Cadmium isotopic composition in the ocean. Geochim. Cosmochim. Acta 70, 5104–5118. https://doi.org/10.1016/j.gca.2006.07.036

Lansdown, A.B., Sampson, B., 1996. Dermal toxicity and percutaneous absorption of cadmium in rats and mice. Lab. Anim. Sci. 46, 549–554.

Laplace, P.S., 1796. Exposition du système du monde, 1835th ed. Artheme Fayard.

Larison, J.R., Likens, G.E., Fitzpatrick, J.W., Crock, J.G., 2000. Cadmium toxicity among wildlife in the Colorado Rocky Mountains. Nature 406, 181–183. https://doi.org/10.1038/35018068

Lewis, J.S., 1974. The Temperature Gradient in the Solar Nebula. Science 186, 440–443. https://doi.org/10.1126/science.186.4162.440

Li, D., Li, M.-L., Liu, W.-R., Qin, Z.-Z., Liu, S.-A., 2018. Cadmium isotope ratios of standard solutions and geological reference materials measured by MC-ICP-MS. Geostand. Geoanalytical Res. 42, 593–605. https://doi.org/10.1111/ggr.12236

Liu, D., Moynier, F., Siebert, J., Sossi, P.A., Hu, Y., Kubik, E., 2022. Origin of moderately

volatile element depletion on differentiated bodies: Insights from the evaporation of indium from silicate melts. Geochim. Cosmochim. Acta 339, 46–57. https://doi.org/10.1016/j.gca.2022.09.043

Liu, M., Zhang, Q., Zhang, Y., Zhang, Z., Huang, F., Yu, H., 2020. High-precision Cd isotope measurements of soil and rock reference materials by MC-ICP-MS with double spike correction. Geostand. Geoanalytical Res. 44, 169–182. https://doi.org/10.1111/ggr.12291

Lodders, K., 2003. Solar system abundances and condensation temperatures of the elements. Astrophys. J. 591, 1220–1247. https://doi.org/10.1086/375492

Loss, R.D., 2003. Atomic weights of the elements 2001 (IUPAC Technical Report). Pure Appl. Chem. 75, 1107–1122. https://doi.org/10.1351/pac200375081107

Loss, R.D., Rosman, K.J.R., De Laeter, J.R., 1984. Mass spectrometric isotope dilution analyses of palladium, silver, cadmium and tellurium in carbonaceous chondrites. Geochim. Cosmochim. Acta 48, 1677–1681. https://doi.org/10.1016/0016-7037(84)90336-3

Lu, Z., Zhu, J., Tan, D., Wang, X., Zheng, Z., 2021. $\delta^{114/110}$ Cd values of a suite of different reference materials. Geostand. Geoanalytical Res. 45, 565–581. https://doi.org/10.1111/ggr.12380

Luparello, C., Sirchia, R., Longo, A., 2011. Cadmium as a transcriptional modulator in human cells. Crit. Rev. Toxicol. 41, 73–80. https://doi.org/10.3109/10408444.2010.529104

Mahan, B., Siebert, J., Pringle, E.A., Moynier, F., 2017. Elemental partitioning and isotopic fractionation of Zn between metal and silicate and geochemical estimation of the S content of the Earth's core. Geochim. Cosmochim. Acta 196, 252–270. https://doi.org/10.1016/j.gca.2016.09.013

Manhès, G., Göpel, C., 2007. Mass-independant fractionationation during TIMS measurements: Evidence of nuclear shift effect. Geochim. Cosmochim. Acta 71, A618.

https://doi.org/10.1016/j.gca.2007.06.021

Manhès, G., Göpel, C., 2003. Heavy stable isotope measurements with thermal ionization mass spectrometry : non mass-dependent fractionation effects between even and uneven isotopes. Presented at the EGS - AGU - EUG Joint Assembly, Nice, p. 10936.

Marin, N., Righter, K., Danielson, L., Pando, K., Lee, C., 2013. Metal-silicate partitioning of Bi, In, and Cd as a function of temperature and melt composition. Presented at the 44th Lunar and Planetary Science Conference.

Marsh, S.F., Alarid, J.E., Hammond, C.F., McLeod, M.J., Roensch, F.R., Rein, J.E., 1978. Anion exchange of 58 elements in hydrobromic acid and in hydriodic acid (No. LA-7084, 5149421). https://doi.org/10.2172/5149421

Martinková, E., Chrastný, V., Francová, M., Šípková, A., Čuřík, J., Myška, O., Mižič, L., 2016. Cadmium isotope fractionation of materials derived from various industrial processes. J. Hazard. Mater. 302, 114–119. https://doi.org/10.1016/j.jhazmat.2015.09.039

Matović, V., Buha, A., Bulat, Z., Đukić-Ćosić, D., 2011. Cadmium Toxicity Revisited: Focus on Oxidative Stress Induction and Interactions with Zinc and Magnesium. Arch. Ind. Hyg. Toxicol. 62, 65–76. https://doi.org/10.2478/10004-1254-62-2011-2075

May, T.W., Wiedmeyer, R.H., 1998. A table of polyatomic interferences in ICP-MS. At. Spectrosc. 19, 150–155.

McSween, H.Y., 1979. Are carbonaceous chondrites primitive or processed? A review. Rev. Geophys. 17, 1059–1078. https://doi.org/10.1029/RG017i005p01059

Morbidelli, A., Libourel, G., Palme, H., Jacobson, S.A., Rubie, D.C., 2020. Subsolar Al/Si and Mg/Si ratios of non-carbonaceous chondrites reveal planetesimal formation during early condensation in the protoplanetary disk. Earth Planet. Sci. Lett. 538, 116220. https://doi.org/10.1016/j.epsl.2020.116220

Morgan, J.W., 1978. Lonar crater glasses and high-magnesium australites: trace element volatilization and meteoritic contamination. Lunar Planet. Sci. Conf. Proc. 2, 2713–2730.

Moulis, J.-M., 2010. Cellular mechanisms of cadmium toxicity related to the homeostasis of essential metals. BioMetals 23, 877–896. https://doi.org/10.1007/s10534-010-9336-y

Moynier, F., Beck, P., Jourdan, F., Yin, Q.-Z., Reimold, U., Koeberl, C., 2009. Isotopic fractionation of zinc in tektites. Earth Planet. Sci. Lett. 277, 482–489. https://doi.org/10.1016/j.epsl.2008.11.020

Moynier, F., Koeberl, C., Beck, P., Jourdan, F., Telouk, P., 2010. Isotopic fractionation of Cu in tektites. Geochim. Cosmochim. Acta 74, 799–807. https://doi.org/10.1016/j.gca.2009.10.012

Mughabghab, S.F., 2006. Atlas of Neutron Resonnances: Resonnance Parameters and Thermal Cross Sections Z=1-100, 5th ed. Elsevier.

Nielsen, S.A., 1975. Cadmium in New Zealand Dredge Oysters: Geographic Distribution. Int. J. Environ. Anal. Chem. 4, 1–7. https://doi.org/10.1080/03067317508071096

Norris, C.A., Wood, B.J., 2017. Earth's volatile contents established by melting and vaporization. Nature 549, 507–510. https://doi.org/10.1038/nature23645

Ogawa, T., Kobayashi, E., Okubo, Y., Suwazono, Y., Kido, T., Nogawa, K., 2004. Relationship among prevalence of patients with Itai-itai disease, prevalence of abnormal urinary findings, and cadmium concentrations in rice of individual hamlets in the Jinzu River basin, Toyama prefecture of Japan. Int. J. Environ. Health Res. 14, 243–252. https://doi.org/10.1080/09603120410001725586

O'Neill, H.St.C., 1991. The origin of the moon and the early history of the earth—A chemical model. Part 2: The earth. Geochim. Cosmochim. Acta 55, 1159–1172. https://doi.org/10.1016/0016-7037(91)90169-6

O'Neill, H.St.C., Palme, H., 2008. Collisional erosion and the non-chondritic composition of the terrestrial planets. Philos. Trans. R. Soc. Math. Phys. Eng. Sci. 366, 4205–4238. https://doi.org/10.1098/rsta.2008.0111

Palk, E., Andreasen, R., Rehkämper, M., Stunt, A., Kreissig, K., Coles, B., Schönbächler, M., Smith, C., 2018. Variable Tl, Pb, and Cd concentrations and isotope compositions of enstatite and ordinary chondrites—Evidence for volatile element mobilization and decay of extinct ^{205} Pb. Meteorit. Planet. Sci. 53, 167–186. https://doi.org/10.1111/maps.12989

Pallavicini, N., Engström, E., Baxter, D.C., Öhlander, B., Ingri, J., Rodushkin, I., 2014. Cadmium isotope ratio measurements in environmental matrices by MC-ICP-MS. J Anal Spectrom 29, 1570–1584. https://doi.org/10.1039/C4JA00125G

Palme, H., O'Neill, H.St.C., 2014. Cosmochemical estimates of mantle composition, in: Holland, H.D., Turekian, K.K. (Eds.), Treatise on Geochemistry. Elsevier, pp. 1–39. https://doi.org/10.1016/B978-0-08-095975-7.00201-1

Paniello, R.C., Day, J.M.D., Moynier, F., 2012. Zinc isotopic evidence for the origin of the Moon. Nature 490, 376–379. https://doi.org/10.1038/nature11507

Patra, R.C., Rautray, A.K., Swarup, D., 2011. Oxidative Stress in Lead and Cadmium Toxicity and Its Amelioration. Vet. Med. Int. 2011, 1–9. https://doi.org/10.4061/2011/457327

Peng, H., Liu, P., Zheng, H., Belshaw, N.S., Hu, S., Zhu, Z., 2023. Cadmium isotope fractionation during adsorption onto calcite. Chem. Geol. 620, 121341. https://doi.org/10.1016/j.chemgeo.2023.121341

Penzias, A.A., Wilson, R.W., 1965. A Measurement of Excess Antenna Temperature at 4080 Mc/s. Astrophys. J. 142, 419. https://doi.org/10.1086/148307

Pickard, H., Palk, E., Schönbächler, M., Moore, R.E.T., Coles, B.J., Kreissig, K., Nilsson-Kerr, K., Hammond, S.J., Takazawa, E., Hémond, C., Tropper, P., Barfod, D.N., Rehkämper,

M., 2022. The cadmium and zinc isotope compositions of the silicate Earth – Implications for terrestrial volatile accretion. Geochim. Cosmochim. Acta 338, 165–180. https://doi.org/10.1016/j.gca.2022.09.041

Pickard, H., Palk, E., Wood, B.J., Rehkämper, M., 2023. Cadmium isotope fractionation during metal-silicate partitioning – Results and implications for Earth's volatile accretion. Chem. Geol. 618, 121293. https://doi.org/10.1016/j.chemgeo.2022.121293

Pilski, A.S., Przylibski, T.A., Łuszczek, K., 2011. Primitive enstatite chondrites. Meteorites 0, 9–21.

Planck Collaboration, Aghanim, N., Akrami, Y., Ashdown, M., Aumont, J., Baccigalupi, C., Ballardini, M., Banday, A.J., Barreiro, R.B., Bartolo, N., Basak, S., Battye, R., Benabed, K., Bernard, J.-P., Bersanelli, M., Bielewicz, P., Bock, J.J., Bond, J.R., Borrill, J., Bouchet, F.R., Boulanger, F., Bucher, M., Burigana, C., Butler, R.C., Calabrese, E., Cardoso, J.-F., Carron, J., Challinor, A., Chiang, H.C., Chluba, J., Colombo, L.P.L., Combet, C., Contreras, D., Crill, B.P., Cuttaia, F., De Bernardis, P., De Zotti, G., Delabrouille, J., Delouis, J.-M., Di Valentino, E., Diego, J.M., Doré, O., Douspis, M., Ducout, A., Dupac, X., Dusini, S., Efstathiou, G., Elsner, F., Enßlin, T.A., Eriksen, H.K., Fantaye, Y., Farhang, M., Fergusson, J., Fernandez-Cobos, R., Finelli, F., Forastieri, F., Frailis, M., Fraisse, A.A., Franceschi, E., Frolov, A., Galeotta, S., Galli, S., Ganga, K., Génova-Santos, R.T., Gerbino, M., Ghosh, T., González-Nuevo, J., Górski, K.M., Gratton, S., Gruppuso, A., Gudmundsson, J.E., Hamann, J., Handley, W., Hansen, F.K., Herranz, D., Hildebrandt, S.R., Hivon, E., Huang, Z., Jaffe, A.H., Jones, W.C., Karakci, A., Keihänen, E., Keskitalo, R., Kiiveri, K., Kim, J., Kisner, T.S., Knox, L., Krachmalnicoff, N., Kunz, M., Kurki-Suonio, H., Lagache, G., Lamarre, J.-M., Lasenby, A., Lattanzi, M., Lawrence, C.R., Le Jeune, M., Lemos, P., Lesgourgues, J., Levrier, F., Lewis, A., Liguori, M., Lilje, P.B., Lilley, M., Lindholm, V., López-Caniego, M., Lubin, P.M., Ma, Y.-Z., Macías-Pérez, J.F., Maggio, G., Maino, D., Mandolesi, N., Mangilli, A., Marcos-

Caballero, A., Maris, M., Martin, P.G., Martinelli, M., Martínez-González, E., Matarrese, S., Mauri, N., McEwen, J.D., Meinhold, P.R., Melchiorri, A., Mennella, A., Migliaccio, M., Millea, M., Mitra, S., Miville-Deschênes, M.-A., Molinari, D., Montier, L., Morgante, G., Moss, A., Natoli, P., Nørgaard-Nielsen, H.U., Pagano, L., Paoletti, D., Partridge, B., Patanchon, G., Peiris, H.V., Perrotta, F., Pettorino, V., Piacentini, F., Polastri, L., Polenta, G., Puget, J.-L., Rachen, J.P., Reinecke, M., Remazeilles, M., Renzi, A., Rocha, G., Rosset, C., Roudier, G., Rubiño-Martín, J.A., Ruiz-Granados, B., Salvati, L., Sandri, M., Savelainen, M., Scott, D., Shellard, E.P.S., Sirignano, C., Sirri, G., Spencer, L.D., Sunyaev, R., Suur-Uski, A.-S., Tauber, J.A., Tavagnacco, D., Tenti, M., Toffolatti, L., Tomasi, M., Trombetti, T., Valenziano, L., Valiviita, J., Van Tent, B., Vibert, L., Vielva, P., Villa, F., Vittorio, N., Wandelt, B.D., Wehus, I.K., White, M., White, S.D.M., Zacchei, A., Zonca, A., 2020. *Planck* 2018 results: VI. Cosmological parameters. Astron. Astrophys. 641, A6. https://doi.org/10.1051/0004-6361/201833910

Portegies Zwart, S.F., 2009. The lost siblings of the Sun. Astrophys. J. 696, L13–L16. https://doi.org/10.1088/0004-637X/696/1/L13

Pringle, E.A., Moynier, F., 2017. Rubidium isotopic composition of the Earth, meteorites, and the Moon: Evidence for the origin of volatile loss during planetary accretion. Earth Planet. Sci. Lett. 473, 62–70. https://doi.org/10.1016/j.epsl.2017.05.033

Pringle, E.A., Moynier, F., Beck, P., Paniello, R., Hezel, D.C., 2017. The origin of volatile element depletion in early solar system material: Clues from Zn isotopes in chondrules. Earth Planet. Sci. Lett. 468, 62–71. https://doi.org/10.1016/j.epsl.2017.04.002

Pringle, E.A., Moynier, F., Savage, P.S., Badro, J., Barrat, J.-A., 2014. Silicon isotopes in angrites and volatile loss in planetesimals. Proc. Natl. Acad. Sci. 111, 17029–17032. https://doi.org/10.1073/pnas.1418889111

Prinz, M., Nehru, C.E., Delaney, J.S., Weisberg, M., 1983. Silicates in IAB and IIICD Irons, Winonaites, Lodranites an Brachina: a Primitive and Modified-Primitive Group 616–617.

Pritzkow, W., Wunderli, S., Vogl, J., Fortunato, G., 2007. The isotope abundances and the atomic weight of cadmium by a metrological approach. Int. J. Mass Spectrom. 261, 74–85. https://doi.org/10.1016/j.ijms.2006.07.026

Rayleigh, Lord, 1902. LIX. *On the distillation of binary mixtures*. Lond. Edinb. Dublin Philos. Mag. J. Sci. 4, 521–537. https://doi.org/10.1080/14786440209462876

Rayleigh, Lord, 1896. L. *Theoretical considerations respecting the separation of gases by diffusion and similar processes*. Lond. Edinb. Dublin Philos. Mag. J. Sci. 42, 493–498. https://doi.org/10.1080/14786449608620944

Rehkämper, M., Schönbächler, M., Stirling, C.H., 2001. Multiple Collector ICP-MS: Introduction to Instrumentation, Measurement Techniques and Analytical Capabilities. Geostand. Newsl. 25, 23–40. https://doi.org/10.1111/j.1751-908X.2001.tb00785.x

Rehkämper, M., Wombacher, F., Horner, T.J., Xue, Z., 2012. Natural and anthropogenic Cd isotope variations, in: Baskaran, M. (Ed.), Handbook of Environmental Isotope Geochemistry, Advances in Isotope Geochemistry. Springer Berlin Heidelberg, Berlin, Heidelberg, pp. 125–154. https://doi.org/10.1007/978-3-642-10637-8_8

Rickaby, R.E.M., Elderfield, H., 1999. Planktonic foraminiferal Cd/Ca: Paleonutrients or paleotemperature? Paleoceanography 14, 293–303. https://doi.org/10.1029/1999PA900007

Righter, K., Nickodem, K., Pando, K., Danielson, L., Boujibar, A., Righter, M., Lapen, T.J., 2017. Distribution of Sb, As, Ge, and In between metal and silicate during accretion and core formation in the Earth. Geochim. Cosmochim. Acta 198, 1–16. https://doi.org/10.1016/j.gca.2016.10.045

Ringwood, A.E., 1966. Chemical evolution of the terrestrial planets. Geochim. Cosmochim. Acta 30, 41–104. https://doi.org/10.1016/0016-7037(66)90090-1

Ripperger, S., Rehkämper, M., 2007. Precise determination of cadmium isotope fractionation in seawater by double spike MC-ICPMS. Geochim. Cosmochim. Acta 71, 631–642. https://doi.org/10.1016/j.gca.2006.10.005

Robson, T.C., Braungardt, C.B., Rieuwerts, J., Worsfold, P., 2014. Cadmium contamination of agricultural soils and crops resulting from sphalerite weathering. Environ. Pollut. 184, 283–289. https://doi.org/10.1016/j.envpol.2013.09.001

Rochette, P., Moustard, F., Gattacceca, J., Devouard, B., 2014. Magnetic properties of tektites and related glasses: discriminating among different fields and impactor component. Presented at the 77th Annual Meeting of the Meteoritical Society, p. 5040.

Rosman, Barnes, I.L., Moore, L.J., Gramlich, J.W., 1980a. Isotope composition of Cd, Ca and Mg in the Brownfield chondrite. Geochem. J. 14, 269–277. https://doi.org/10.2343/geochemj.14.269

Rosman, De Laeter, J.R., 1988. Cadmium mass fractionation in unequilibrated ordinary chondrites. Earth Planet. Sci. Lett. 89, 163–169. https://doi.org/10.1016/0012-821X(88)90168-9

Rosman, De Laeter, J.R., 1978. A survey of cadmium isotopic abundances. J. Geophys. Res. 83, 1279. https://doi.org/10.1029/JB083iB03p01279

Rosman, De Laeter, J.R., 1976. Isotopic fractionation in meteoritic cadmium. Nature 261, 216–218. https://doi.org/10.1038/261216a0

Rosman, De Laeter, J.R., 1975. The isotopic composition of cadmium in terrestrial minerals. Int. J. Mass Spectrom. Ion Phys. 16, 385–394. https://doi.org/10.1016/0020-7381(75)85027-3

Rosman, De Laeter, J.R., 1974a. Mass spectrometric isotope dilution analyses of cadmium in standard rocks. Chem. Geol. 13, 69–74. https://doi.org/10.1016/0009-2541(74)90051-5

Rosman, De Laeter, J.R., 1974b. The abundance of cadmium and zinc in meteorites. Geochim. Cosmochim. Acta 38, 1665–1677. https://doi.org/10.1016/0016-7037(74)90184-7

Rosman, De Laeter, J.R., Gorton, M.P., 1980b. Cadmium isotope fractionation in fractions of two H3 chondrites. Earth Planet. Sci. Lett. 48, 166–170. https://doi.org/10.1016/0012-821X(80)90179-X

Rubin, A.E., 1990. Kamacite and olivine in ordinary chondrites: Intergroup and intragroup relationships. Geochim. Cosmochim. Acta 54, 1217–1232. https://doi.org/10.1016/0016-7037(90)90148-E

Rubin, A.E., Grossman, J.N., 2010. Meteorite and meteoroid: new comprehensive definitions. Meteorit. Planet. Sci. https://doi.org/10.1111/j.1945-5100.2009.01009.x

Rudge, J.F., Reynolds, B.C., Bourdon, B., 2009. The double spike toolbox. Chem. Geol. 265, 420–431. https://doi.org/10.1016/j.chemgeo.2009.05.010

Rudnick, R.L., Gao, S., 2014. Composition of the continental crust, in: Holland, H.D., Turekian, K.K. (Eds.), Treatise on Geochemistry. Elsevier, pp. 1–51. https://doi.org/10.1016/B978-0-08-095975-7.00301-6

Sanders, I.S., Scott, E.R.D., 2012. The origin of chondrules and chondrites: Debris from low-velocity impacts between molten planetesimals?: Origin of chondrules and chondrites. Meteorit. Planet. Sci. 47, 2170–2192. https://doi.org/10.1111/maps.12002

Sands, D.G., De Laeter, J.R., Rosman, K.J.R., 2001a. Measurements of neutron capture effects on Cd, Sm and Gd in lunar samples with implications for the neutron energy spectrum. Earth Planet. Sci. Lett. 186, 335–346. https://doi.org/10.1016/S0012-821X(01)00231-X

Sands, D.G., Rosman, K.J.R., De Laeter, J.R., 2001b. A preliminary study of cadmium mass fractionation in lunar soils. Earth Planet. Sci. Lett. 186, 103–111. https://doi.org/10.1016/S0012-821X(01)00233-3

Satarug, S., 2018. Dietary Cadmium Intake and Its Effects on Kidneys. Toxics 6, 15. https://doi.org/10.3390/toxics6010015

Savage, P.S., Georg, R.B., Williams, H.M., Burton, K.W., Halliday, A.N., 2011. Silicon isotope fractionation during magmatic differentiation. Geochim. Cosmochim. Acta 75, 6124–6139. https://doi.org/10.1016/j.gca.2011.07.043

Schediwy, S., Rosman, K.J.R., de Laeter, J.R., 2006. Isotope fractionation of cadmium in lunar material. Earth Planet. Sci. Lett. 243, 326–335. https://doi.org/10.1016/j.epsl.2006.01.007

Scheuhammer, A.M., 1996. Influence of reduced dietary calcium on the accumulation and effects of lead, cadmium, and aluminum in birds. Environ. Pollut. 94, 337–343. https://doi.org/10.1016/S0269-7491(96)00084-X

Schmitt, A.-D., Galer, S.J.G., Abouchami, W., 2009a. Mass-dependent cadmium isotopic variations in nature with emphasis on the marine environment. Earth Planet. Sci. Lett. 277, 262–272. https://doi.org/10.1016/j.epsl.2008.10.025

Schmitt, A.-D., Galer, S.J.G., Abouchami, W., 2009b. High-precision cadmium stable isotope measurements by double spike thermal ionisation mass spectrometry. J. Anal. At. Spectrom. 24, 1079. https://doi.org/10.1039/b821576f

Schonbachler, M., Carlson, R.W., Horan, M.F., Mock, T.D., Hauri, E.H., 2010. Heterogeneous accretion and the moderately volatile Element budget of Earth. Science 328, 884–887. https://doi.org/10.1126/science.1186239

Scott, E.R.D., Krot, A.N., 2014. Chondrites and Their Components, in: Treatise on Geochemistry. Elsevier, pp. 65–137. https://doi.org/10.1016/B978-0-08-095975-7.00104-2

Sears, D.W.G., Weeks, K.S., 1983. Chemical and physical studies of type 3 chondrites: 2. Thermoluminescence of sixteen type 3 ordinary chondrites and relationships with oxygen isotopes. J. Geophys. Res. Solid Earth 88. https://doi.org/10.1029/JB088iS01p0B301

Seidal, K., Jorgensen, N., Elinder, C., Sjogren, B., Vahter, M., 1993. Fatal cadmium-induced pneumonitis. Scand. J. Work. Environ. Health 19, 429–431. https://doi.org/10.5271/sjweh.1450

Shi, Z., Carey, M., Meharg, C., Williams, P.N., Signes-Pastor, A.J., Triwardhani, E.A., Pandiangan, F.I., Campbell, K., Elliott, C., Marwa, E.M., Jiujin, X., Farias, J.G., Nicoloso, F.T., De Silva, P.M.C.S., Lu, Y., Norton, G., Adomako, E., Green, A.J., Moreno-Jiménez, E., Zhu, Y., Carbonell-Barrachina, Á.A., Haris, P.I., Lawgali, Y.F., Sommella, A., Pigna, M., Brabet, C., Montet, D., Njira, K., Watts, M.J., Hossain, M., Islam, M.R., Tapia, Y., Oporto, C., Meharg, A.A., 2020. Rice Grain Cadmium Concentrations in the Global Supply-Chain. Expo. Health 12, 869–876. https://doi.org/10.1007/s12403-020-00349-6

Shiel, A.E., Barling, J., Orians, K.J., Weis, D., 2009. Matrix effects on the multi-collector inductively coupled plasma mass spectrometric analysis of high-precision cadmium and zinc isotope ratios. Anal. Chim. Acta 633, 29–37. https://doi.org/10.1016/j.aca.2008.11.026

Shiel, A.E., Weis, D., Orians, K.J., 2012. Tracing cadmium, zinc and lead sources in bivalves from the coasts of western Canada and the USA using isotopes. Geochim. Cosmochim. Acta 76, 175–190. https://doi.org/10.1016/j.gca.2011.10.005

Shiel, A.E., Weis, D., Orians, K.J., 2010. Evaluation of zinc, cadmium and lead isotope fractionation during smelting and refining. Sci. Total Environ. 408, 2357–2368. https://doi.org/10.1016/j.scitotenv.2010.02.016

Siebert, J., Sossi, P.A., Blanchard, I., Mahan, B., Badro, J., Moynier, F., 2018. Chondritic Mn/Na ratio and limited post-nebular volatile loss of the Earth. Earth Planet. Sci. Lett. 485,

130–139. https://doi.org/10.1016/j.epsl.2017.12.042

Sossi, P.A., Klemme, S., O'Neill, H.St.C., Berndt, J., Moynier, F., 2019. Evaporation of moderately volatile elements from silicate melts: experiments and theory. Geochim. Cosmochim. Acta 260, 204–231. https://doi.org/10.1016/j.gca.2019.06.021

Sossi, P.A., Nebel, O., O'Neill, H.St.C., Moynier, F., 2018. Zinc isotope composition of the Earth and its behaviour during planetary accretion. Chem. Geol. 477, 73–84. https://doi.org/10.1016/j.chemgeo.2017.12.006

Staessen, J.A., Roels, H.A., Emelianov, D., Kuznetsova, T., Thijs, L., Vangronsveld, J., Fagard, R., 1999. Environmental exposure to cadmium, forearm bone density, and risk of fractures: prospective population study. The Lancet 353, 1140–1144. https://doi.org/10.1016/S0140-6736(98)09356-8

Steenstra, E.S., Seegers, A.X., Putter, R., Berndt, J., Klemme, S., Matveev, S., Bullock, E.S., van Westrenen, W., 2020. Metal-silicate partitioning systematics of siderophile elements at reducing conditions: A new experimental database. Icarus 335, 113391. https://doi.org/10.1016/j.icarus.2019.113391

Strelow, F.W.E., 1978. Distribution coefficients and anion exchange behavior of some elements in hydrobromic-nitric acid mixtures. Anal. Chem. 50, 1359–1361. https://doi.org/10.1021/ac50031a041

Stromeyer, 1818. Ueber das Kadmium. Ann. Phys. 60, 193–210. https://doi.org/10.1002/andp.18180601004

Tamás, M.J., Fauvet, B., Christen, P., Goloubinoff, P., 2018. Misfolding and aggregation of nascent proteins: a novel mode of toxic cadmium action in vivo. Curr. Genet. 64, 177–181. https://doi.org/10.1007/s00294-017-0748-x

Tan, D., Zhu, J.-M., Wang, X., Han, G., Lu, Z., Xu, W., 2020. High-sensitivity

determination of Cd isotopes in low-Cd geological samples by double spike MC-ICP-MS. J. Anal. At. Spectrom. 35, 713–727. https://doi.org/10.1039/C9JA00397E

Teng, F.-Z., Dauphas, N., Helz, R.T., 2008. Iron Isotope Fractionation During Magmatic Differentiation in Kilauea Iki Lava Lake. Science 320, 1620–1622. https://doi.org/10.1126/science.1157166

Tinkov, A.A., Gritsenko, V.A., Skalnaya, M.G., Cherkasov, S.V., Aaseth, J., Skalny, A.V., 2018. Gut as a target for cadmium toxicity. Environ. Pollut. 235, 429–434. https://doi.org/10.1016/j.envpol.2017.12.114

Tuller-Ross, B., Marty, B., Chen, H., Kelley, K.A., Lee, H., Wang, K., 2019. Potassium isotope systematics of oceanic basalts. Geochim. Cosmochim. Acta 259, 144–154. https://doi.org/10.1016/j.gca.2019.06.001

Urey, H.C., 1954. On the Dissipation of Gas and Volatilized Elements from Protoplanets. Astrophys. J. Suppl. Ser. 1, 147. https://doi.org/10.1086/190006

Van Kooten, E.M.M.E., Wielandt, D., Schiller, M., Nagashima, K., Thomen, A., Larsen, K.K., Olsen, M.B., Nordlund, Å., Krot, A.N., Bizzarro, M., 2016. Isotopic evidence for primordial molecular cloud material in metal-rich carbonaceous chondrites. Proc. Natl. Acad. Sci. 113, 2011–2016. https://doi.org/10.1073/pnas.1518183113

Van Schmus, W.R., Wood, J.A., 1967. A chemical-petrologic classification for the chondritic meteorites. Geochim. Cosmochim. Acta 31, 747–765. https://doi.org/10.1016/S0016-7037(67)80030-9

Varas-Reus, M.I., König, S., Yierpan, A., Lorand, J.-P., Schoenberg, R., 2019. Selenium isotopes as tracers of a late volatile contribution to Earth from the outer Solar System. Nat. Geosci. 12, 779–782. https://doi.org/10.1038/s41561-019-0414-7

Vincent, E.A., Bilefield, L.I., 1960. Cadmium in rocks and minerals from the Skaergaard

intrusion, East Greenland. Geochim. Cosmochim. Acta 19, 63–69. https://doi.org/10.1016/0016-7037(60)90126-5

Vollstaedt, H., Mezger, K., Alibert, Y., 2020. Carbonaceous Chondrites and the Condensation of Elements from the Solar Nebula. Astrophys. J. 897, 82. https://doi.org/10.3847/1538-4357/ab97b4

Wang, B., Li, Y., Shao, C., Tan, Y., Cai, L., 2012. Cadmium and Its Epigenetic Effects. Curr. Med. Chem. 19, 2611–2620. https://doi.org/10.2174/092986712800492913

Wang, D., Zheng, Y., Mathur, R., Yu, M., 2020. Fractionation of cadmium isotope caused by vapour-liquid partitioning in hydrothermal ore-forming system: A case study of the Zhaxikang Sb–Pb–Zn–Ag deposit in Southern Tibet. Ore Geol. Rev. 119, 103400. https://doi.org/10.1016/j.oregeorev.2020.103400

Wang, H.S., Lineweaver, C., Ireland, T., 2018. The elemental abundances (with uncertainties) of the most Earth-like planet. Icarus 299, 460–474. https://doi.org/10.1016/j.icarus.2017.08.024

Wang, K., Jacobsen, S.B., 2016. Potassium isotopic evidence for a high-energy giant impact origin of the Moon. Nature 538, 487–490. https://doi.org/10.1038/nature19341

Wang, M.-S., Lipschutz, M.E., 2007. Trace elements in primitive meteorites—VII Antarctic unequilibrated ordinary chondrites. Geochim. Cosmochim. Acta 71, 1062–1073. https://doi.org/10.1016/j.gca.2006.10.009

Wang, M.-S., Lipschutz, M.E., 2005. Thermal metamorphism of primitive meteorites—XII. The enstatite chondrites revisited. Environ. Chem. 2, 215–226. https://doi.org/10.1071/EN04075

Wang, Z., Becker, H., 2013. Ratios of S, Se and Te in the silicate Earth require a volatile-rich late veneer. Nature 499, 328–331. https://doi.org/10.1038/nature12285

Wang, Z., Becker, H., Wombacher, F., 2015. Mass fractions of S, Cu, Se, Mo, Ag, Cd, In, Te, Ba, Sm, W, Tl and Bi in geological reference materials and selected carbonaceous chondrites determined by isotope dilution ICP-MS. Geostand. Geoanalytical Res. 39, 185–208. https://doi.org/10.1111/j.1751-908X.2014.00312.x

Wang, Z., Laurenz, V., Petitgirard, S., Becker, H., 2016. Earth's moderately volatile element composition may not be chondritic: Evidence from In, Cd and Zn. Earth Planet. Sci. Lett. 435, 136–146. https://doi.org/10.1016/j.epsl.2015.12.012

Wänke, Dreibus, 1988. Chemical composition and accretion history of terrestrial planets. Philos. Trans. R. Soc. Lond. Ser. Math. Phys. Sci. 325, 545–557. https://doi.org/10.1098/rsta.1988.0067

Wannier, M.M.A., de Urreiztieta, M., Wenk, H.-R., Stan, C.V., Tamura, N., Yue, B., 2019. Fallout melt debris and aerodynamically-shaped glasses in beach sands of Hiroshima Bay, Japan. Anthropocene 25, 100196. https://doi.org/10.1016/j.ancene.2019.100196

Wasson, J.T., Chou, C., 1974. Fractionation of moderately volatile elements in ordinary chondrites. Meteoritics 9, 69–84. https://doi.org/10.1111/j.1945-5100.1974.tb00063.x

Wasylenki, L.E., Swihart, J.W., Romaniello, S.J., 2014. Cadmium isotope fractionation during adsorption to Mn oxyhydroxide at low and high ionic strength. Geochim. Cosmochim. Acta 140, 212–226. https://doi.org/10.1016/j.gca.2014.05.007

Watt, N., Bouchet, R.A., Lee, C.-T.A., 2011. Exploration of tektite formation processes through water and metal content measurements: Water and metal in tektites. Meteorit. Planet. Sci. 46, 1025–1032. https://doi.org/10.1111/j.1945-5100.2011.01207.x

Weisberg, M.K., McCoy, T.J., Krot, A.N., 2006. Systematics and evaluation of meteorite classification, in: Lauretta, D.S., McSween, H.Y. (Eds.), Meteorites and the Early Solar System II. pp. 19–52.

Wen, H., Zhang, Y., Cloquet, C., Zhu, C., Fan, H., Luo, C., 2015. Tracing sources of pollution in soils from the Jinding Pb–Zn mining district in China using cadmium and lead isotopes. Appl. Geochem. 52, 147–154. https://doi.org/10.1016/j.apgeochem.2014.11.025

Wetherill, G.W., 1964. Isotopic composition and concentration of molybdenum in iron meteorites. J. Geophys. Res. 69, 4403–4408. https://doi.org/10.1029/JZ069i020p04403

Wiggenhauser, M., Bigalke, M., Imseng, M., Müller, M., Keller, A., Murphy, K., Kreissig, K., Rehkämper, M., Wilcke, W., Frossard, E., 2016. Cadmium Isotope Fractionation in Soil–Wheat Systems. Environ. Sci. Technol. 50, 9223–9231. https://doi.org/10.1021/acs.est.6b01568

Wiik, H.B., 1956. The chemical composition of some stony meteorites. Geochim. Cosmochim. Acta 9, 279–289. https://doi.org/10.1016/0016-7037(56)90028-X

Willbold, M., Elliott, T., 2017. Molybdenum isotope variations in magmatic rocks. Chem. Geol. 449, 253–268. https://doi.org/10.1016/j.chemgeo.2016.12.011

Willbold, M., Hibbert, K., Lai, Y.-J., Freymuth, H., Hin, R.C., Coath, C., Vils, F., Elliott, T., 2016. High-precision mass-dependent molybdenum isotope variations in magmatic rocks determined by double-spike MC-ICP-MS. Geostand. Geoanalytical Res. n/a-n/a. https://doi.org/10.1111/ggr.12109

Williams, J.P., 2010. The astrophysical environment of the solar birthplace. Contemp. Phys. 51, 381–396. https://doi.org/10.1080/00107511003764725

Wombacher, F., Rehkämper, M., Mezger, K., 2004. Determination of the mass-dependence of cadmium isotope fractionation during evaporation. Geochim. Cosmochim. Acta 68, 2349–2357. https://doi.org/10.1016/j.gca.2003.12.013

Wombacher, F., Rehkämper, M., Mezger, K., Bischoff, A., Münker, C., 2008. Cadmium stable isotope cosmochemistry. Geochim. Cosmochim. Acta 72, 646–667.

https://doi.org/10.1016/j.gca.2007.10.024

Wombacher, F., Rehkämper, M., Mezger, K., Münker, C., 2003. Stable isotope compositions of cadmium in geological materials and meteorites determined by multiple-collector ICPMS. Geochim. Cosmochim. Acta 67, 4639–4654. https://doi.org/10.1016/S0016-7037(03)00389-2

Wood, B.J., Kiseeva, E.S., Mirolo, F.J., 2014. Accretion and core formation: The effects of sulfur on metal–silicate partition coefficients. Geochim. Cosmochim. Acta 145, 248–267. https://doi.org/10.1016/j.gca.2014.09.002

Wood, B.J., Smythe, D.J., Harrison, T., 2019. The condensation temperatures of the elements: A reappraisal. Am. Mineral. 104, 844–856. https://doi.org/10.2138/am-2019-6852CCBY

Woolfson, M., 2000. The origin and evolution of the solar system. Astron. Geophys. 41, 12. https://doi.org/10.1046/j.1468-4004.2000.00012.x

Woosley, S., Janka, H.-T., 2006. The Physics of Core-Collapse Supernovae. https://doi.org/10.48550/ARXIV.ASTRO-PH/0601261

Xie, R.C., Rehkämper, M., Grasse, P., Van De Flierdt, T., Frank, M., Xue, Z., 2019. Isotopic evidence for complex biogeochemical cycling of Cd in the eastern tropical South Pacific. Earth Planet. Sci. Lett. 512, 134–146. https://doi.org/10.1016/j.epsl.2019.02.001

Yi, W., Halliday, A.N., Alt, J.C., Lee, D.-C., Rehkämper, M., Garcia, M.O., Langmuir, C.H., Su, Y., 2000. Cadmium, indium, tin, tellurium, and sulfur in oceanic basalts: Implications for chalcophile element fractionation in the Earth. J. Geophys. Res. Solid Earth 105, 18927–18948. https://doi.org/10.1029/2000JB900152

Yoder, C.F., 1995. Astrometric and geodetic properties of Earth and the solar system, in: Ahrens, T.J. (Ed.), Global Earth Physics - A Handbook of Physical Constants, AGU Reference

Shelf. American geophysical union, Washington, D. C., pp. 1–31. https://doi.org/10.1029/RF001p0001

Young, E.D., Shahar, A., Nimmo, F., Schlichting, H.E., Schauble, E.A., Tang, H., Labidi, J., 2019. Near-equilibrium isotope fractionation during planetesimal evaporation. Icarus 323, 1–15. https://doi.org/10.1016/j.icarus.2019.01.012

Zhang, S., Chen, M., Li, T., Xu, X., Deng, L., 2010. A newly found cadmium accumulator—Malva sinensis Cavan. J. Hazard. Mater. 173, 705–709. https://doi.org/10.1016/j.jhazmat.2009.08.142

Zhang, Y., Wen, H., Zhu, C., Fan, H., Luo, C., Liu, J., Cloquet, C., 2016. Cd isotope fractionation during simulated and natural weathering. Environ. Pollut. 216, 9–17. https://doi.org/10.1016/j.envpol.2016.04.060

Zhu, C., Wen, H., Zhang, Y., Yin, R., Cloquet, C., 2018. Cd isotope fractionation during sulfide mineral weathering in the Fule Zn-Pb-Cd deposit, Yunnan Province, Southwest China. Sci. Total Environ. 616–617, 64–72. https://doi.org/10.1016/j.scitotenv.2017.10.293

Chapter 2 – Methods

1. Preparation of the samples

1.1.Sample pre-processing

While most samples were already available in powdered form, some (the Hekla suite and tektites) were provided as chunky rock pieces. These samples needed to be powdered to homogenize their individual compositions and ease their acid digestion. This processing was conducted at the IPGP facility, in two steps for the volcanic rocks and in one step for the smaller tektites.

The first step of the general procedure, called crushing, consists in the reduction of the initial block to a set of small chips that can be easily grounded. Crushing of the bulk rocks was conducted using a Retsch BB51 jaw crusher. The crusher was extensively cleaned with ethanol between each sample, in order to eliminate dust and prevent cross contamination between them. This step allowed for reduction of multi-cm sized blocks to a mix of pluri-mm sized particles.

The second step of the pre-processing, grinding, aims at reducing these particles to a homogeneous powder. Grinding was conducted using a Retsch PM200 planetary ball mill, which is comprised of agate balls rolling in a closed agate jar. Agate is used because of its pure silica nature, which prevents contamination in the case of Cd, and its resilience to erosion, which allows for a durable instrument. The grinding jars are submitted to high centrifugal forces by a double rotation movement. The movement of the balls in the jars will pulverize the rock fragments and cause attrition, which transforms coarse particles in small-grained powder. Another effect of grinding is the mechanical mixing and homogenization of the powder, which is primordial for representative bulk analyses. The apparatus was cleaned with alcohol between each sample.

Tektites were powdered using a different process as they would be too small to be effectively crushed but too big to be grounded by the ball mill. Moreover, their very Cd-depleted nature and small masses make them especially sensitive to any potential contamination, unlike bulkier samples for which such potential contamination would be rendered insignificant by dilution. Thus, tektites samples and impact glasses were powdered by hand, using a clean agate (same reasons as before) mortar and pestle.

1.2. The acid digestion

Sample digestion and following chemical treatment were conducted in a class 100 clean room, at the IPGP facility. Used acids (6 mol/L HCl, 16 mol/L HNO_3, and 27 mol/L HF) were obtained from commercial-grade solutions by sub-boiling distillation. Additionally, Optima™ quality 8.8 mol/L HBr was purchased from Fischer Scientific. Almost all the samples analyzed in this work were silicates and thus, were prepared following a common protocol. However, a few SRM were biological (dried and powdered pork kidneys), and thus, required a different digestion method.

Silicates were first digested in Teflon beakers by a mixture of concentrated HF and HNO_3. Samples were then heated in a box-type hotplate at 120°C for 2 to 4 days until total digestion of the sample was obtained and then dried at temperatures close to 90°C. Concentrated HCl was employed to convert the fluorides into chloride form by refluxing the samples at 100 °C for a week. Ultrasonic bath was widely used to ease fluorides breakdown.

Biological matrixes were digested using a mix of concentrated (16 mol/L) nitric acid (HNO_3) and oxygenated water (H_2O_2). This solution allowed for the oxidation of the organic matter into CO_2. After this step, the solution was regarded as mainly mineral and was subjected to the same digestion processes than the rest of the samples (starting with the hydrochloric acid digestion). Although the obtained solutions were characterized by slightly viscous behaviors,

indicating that some organic matter probably remained, the results did not differ from geological samples.

Usage of HF, required specific safety precautions because of its high toxicity (Bertolini, 1992). Exposition to HF produces common acid-burns symptoms like dehydration and tissues corrosion because of reacting hydrogen, although these are limited because of the low amount of H^+ ions. Thus, the initial pain may be limited and the acid burn might go unnoticed for a time, allowing F^- ions to penetrate deep before treatment is provided. Fluoride ions complex divalent cations (primarily Ca^{2+} and Mg^{2+}) to form insoluble ionic solids. This interferes greatly with Ca metabolism, causing cells and bones destruction and finally chemical toxicity by hypocalcemia and/or hypomagnesemia. Thus, handling of this acid was conducted with nitrile gloves or multiple latex gloves and HF-resistant sleeves. Calcium gluconate gel was also available for immediate treatment of localized burns.

1.3.Double spiking

For this work, we employed the double spike (DS) technique as a way to improve data quality and to correct for potential mass-dependent isotope fractionation occurring during the purification or the mass spectrometric analysis. Our DS is a ^{106}Cd-^{111}Cd solution characterized by a ^{106}Cd / ^{110}Cd isotopic ratio of 350 and a ^{111}Cd / ^{110}Cd ratio of 228. To ensure the quality of the obtained data, we must aim for the optimal spike / sample proportion defined as follow: $\left(\frac{m_{Cd\ spike}}{m_{Cd\ sample} + m_{Cd\ spike}}\right) = 0.35$ (Rudge et al., 2009). Thus, to spike correctly our samples, we need to previously know their individual Cd concentrations. These concentrations were obtained by analyzing an aliquot of the sample using an Agilent quadrupole ICPMS (Q-ICPMS) at the IPGP. The remaining samples, dissolved in HCl, were then mixed to different amounts of the DS solution, depending on their Cd concentrations, and were refluxed for two days on a hotplate to ensure comprehensive sample-spike isotopic homogenization.

Cadmium concentrations determined by Q-ICPMS were often significantly more important than what was determined later by the DS deconvolution. This could be explained by the absence of chemical purification for the aliquot. Thus, matrix effects and isobaric interferences could add to the Cd signal and produce an artificially high Cd concentration.

Many samples, appeared to be spiked with non-optimal proportions, ranging from a deficit of 40% to a surplus of 43% compared to the optimum. This can be explained by the uncertainty surrounding the concentration measurement, but also by the scale precision during spiking or sampling. Since suboptimal spiking is unavoidable, we investigated whether it created important isotope variations or whether it lowered the overall precision of the measurement. To test for this, we used a ChemLab standard solution (Lot n° CL01.0301.0100), which is characterized by a similar isotope composition than NIST 3108 Cd. We spiked this solution with different amounts of DS (with deviations from the optimal spike over sample ratio ranging from -60% to +30%) and measured its isotope composition. The Table 1 lists the obtained isotope compositions for these experiments. We found no correlation between the deviation to optimal spike proportion and the measured isotope composition or the overall precision (see Figure 1).

Table 1: Influence of under- or overspiking on isotope compositions

sample	spike proportion		δ^{113}Cd (‰)	2SD	δ^{114}Cd (‰)	2SD	n
	ratio	deviation					
ChemLab	0.37	6%	0.03	0.03	0.02	0.02	202
1	0.14	-60%	-0.02	0.10	0.06	0.06	6
2	0.17	-52%	-0.01	0.08	0.06	0.06	6
3	0.18	-49%	0.00	0.07	0.04	0.06	6
4	0.20	-43%	0.01	0.06	0.04	0.06	6
5	0.21	-39%	-0.02	0.07	0.02	0.05	6
6	0.23	-35%	0.01	0.08	0.03	0.03	6
7	0.24	-31%	-0.01	0.07	0.02	0.06	6
8	0.26	-27%	0.01	0.07	0.02	0.08	6
9	0.28	-21%	0.02	0.05	0.04	0.07	6
10	0.30	-15%	0.02	0.07	0.04	0.06	6
11	0.31	-12%	0.01	0.05	0.02	0.05	6
12	0.32	-8%	0.03	0.06	0.04	0.04	6
13	0.34	-4%	0.01	0.05	0.02	0.05	6
14	0.36	4%	0.02	0.07	0.03	0.05	6
15	0.37	6%	0.03	0.03	0.05	0.04	6
16	0.39	11%	0.02	0.02	0.02	0.04	6
17	0.40	15%	0.02	0.03	0.03	0.06	6
18	0.42	20%	0.01	0.06	0.02	0.05	6
19	0.46	30%	0.01	0.06	0.02	0.05	6

We find no significant influence of over- or under-spiking on the obtained isotope compositions or on the precision. This conclusion is valid only for deviations ranging from -60% to +30%, it does not preclude the existence of a significant influence of this parameter for bigger deviations.

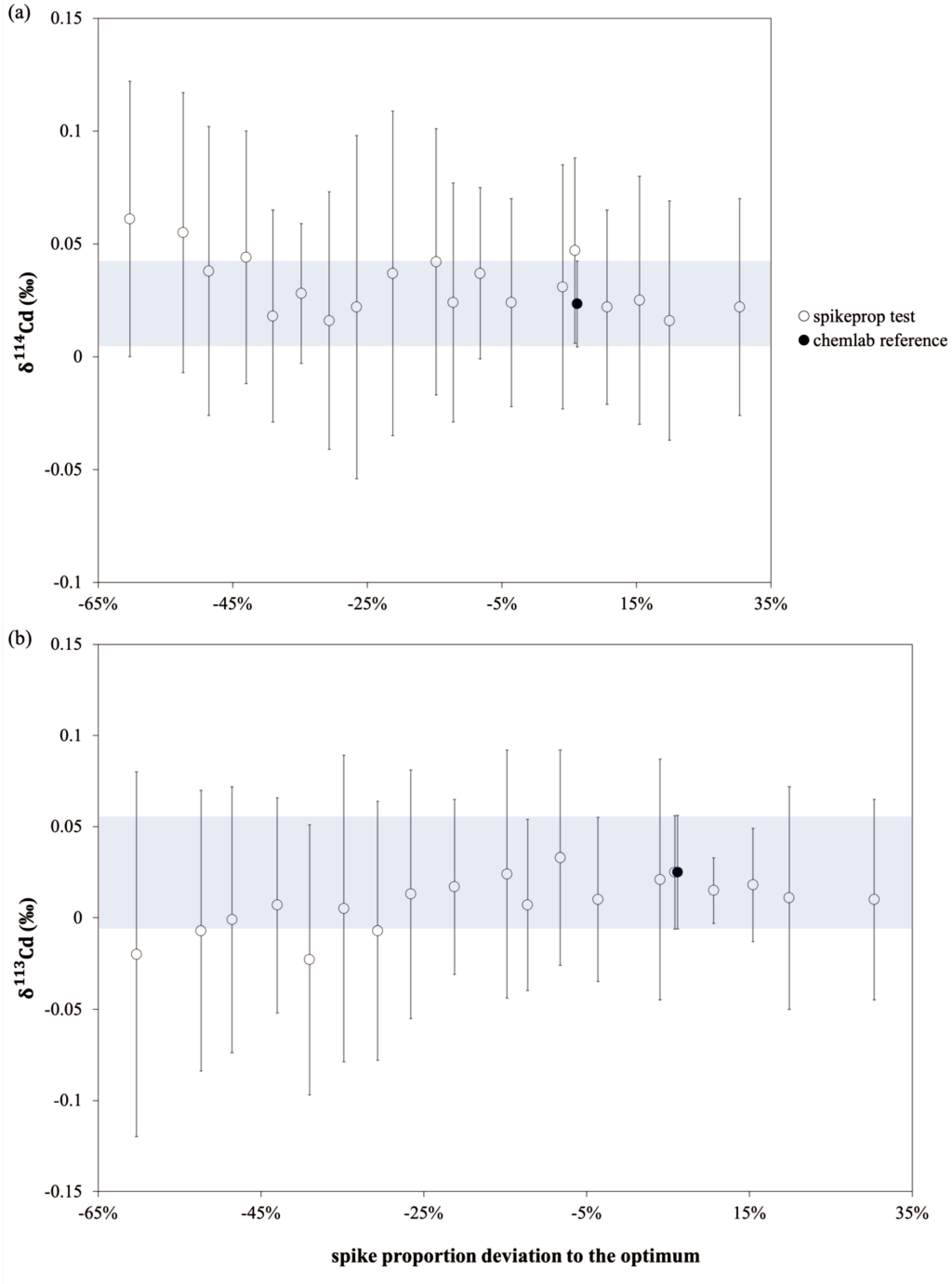


Figure 1: Visualization of the data presented in Table 1. No significant correlation was observed between the deviation to the spike optimum and the overall precision or the measured isotope composition.

2. Cadmium purification

As showed previously, silicates matrixes contain numerous potential isobaric and polyatomic interferents to Cd (the main ones being Sn and In). To prevent interferences and matrix effects that could jeopardize the quality of the measurements, we extensively purified the Cd fraction following an anion exchange resin chromatography protocol adapted from already existing ones. We took inspiration from published protocols for the purification of Cd (Schmitt et al., 2009), of Zn (Moynier and Le Borgne, 2015; Van Kooten and Moynier, 2019) and In (Liu et al., 2023) as one of the initial goals of the elaborated protocol was to allow for the collection of the In fraction as well. This part of the project was abandoned later because of a lack of time. The purification uses custom-made Teflon columns composed of a three to four mL containing reservoirs connected to a tube of 3 to 4 mm in diameter that contain the resin.

The Cd purification protocol relies on an anion exchange, chloride form, resin (Bio-Rad AG 1X8 200-400 mesh) and requires five successive purification runs to efficiently remove Sn. Before loading the samples on the resin, we eliminated any remaining solid by centrifugation

The Table 2 gives the detail of the purification protocol. The first run differs from the other ones as the amount of matter to be dissolved is higher. Thus, we used more concentrated acid (1.5 mol/L HBr rather than 0.1 mol/L HBr) and started to remove matrix during the sample loading step with 0.1 mol/L HBr to prevent columns to clog due to the important masses that flow through the resin. This did not impact the elution of Cd as Cd's distribution coefficients remain very high with both molarities (Marsh et al., 1978) (see the elution data reported in Table 3, Table 4 and Figure 2). Based on our elution data, we retrieve most of the available Cd while eliminating efficiently Sn. Thus, the succession of multiple purification protocols like these should logically allow us to retain almost all of Cd while discarding more than 99% of the total Sn fraction. The Cd fraction was dried down at 80°C and refluxed in concentrated

nitric acid at 110°C in order to destroy any remaining resin residue. Obtained Cd blanks ranged between 7 and 55 pg, with a median 15 pg value. This represents less than 1 wt. % of the total Cd amount for the most depleted samples.

Table 2: Details of the Cd purification protocol

	Procedure step	Reagent	Volume (mL)
Every run	Resin introduction	AG 1x8 200-400mesh	0.2
	Resin cleaning	Mili-Q water	3
		0.5 M HNO_3	3
		Mili-Q water	3
1st run only	Conditioning	1.5 M HBr	3
	Sample load*	1.5 M HBr	5
	Matrix removing*	0.1 M HBr	5
Every run except 1st	Conditioning	0.1 M HBr	3
	Sample load	0.1 M HBr	2
Every run	Matrix removing	0.1 M HBr	12
	Cd elution	0.1 M HNO_3	12

*The table outlines the detailed procedure used to purify Cd and eliminate Sn from the matrix. In reagent column, M notation stands for mol/L. Samples were purified 5 times, with introduction and cleaning of the resin in the Teflon column being similar at every iteration. The first run for each sample differed from the other four runs as a more concentrated solution of HBr (1.5 mol/L) was used for the dissolution of the sample due to the high matrix content. *During the first run, the sample was introduced 0.5mL at a time, followed by 0.5mL HBr 0.1 mol/L to remove matrix and prevent column clogging. The other four purifications did not require this precaution as most matrix had already been discarded and so the sample could be directly dissolved in HBr 0.1 mol/L.*

Table 3: Elution data for the major elements, Cd and Sn during the first purification run.

Purification phase	Chemistry phase	Acid	Volume (mL)	Cumulated volume (mL)	Major elements elution (%)						Traces elements elution (%)	
					Na	Mg	Al	K	Ca	Fe	Cd	Sn
First Cd purification	Sample introduction	HBr 1.5N + HBr 0.1N	2	2	20%	20%	20%	20%	20%	19%	0%	5%
			2	4	20%	20%	20%	19%	19%	19%	0%	17%
			2	6	19%	19%	19%	19%	19%	19%	0%	15%
			2	8	19%	19%	19%	19%	19%	19%	0%	20%
			2.5	10.5	18%	18%	19%	19%	19%	19%	0%	20%
	Matrix removing	HBr 0.1N	2	12.5	1%	1%	1%	1%	1%	0%	0%	4%
			2	14.5	4%	4%	4%	4%	4%	5%	0%	14%
			2	16.5	0%	0%	0%	0%	0%	0%	0%	4%
			2	18.5	0%	0%	0%	0%	0%	0%	0%	1%
			2	20.5	0%	0%	0%	0%	0%	0%	0%	0%
			2	22.5	0%	0%	0%	0%	0%	0%	0%	0%
	Cd collecting	HNO3 0.1N	2	24.5	0%	0%	0%	0%	0%	0%	0%	0%
			2	26.5	0%	0%	0%	0%	0%	0%	0%	0%
			2	28.5	0%	0%	0%	0%	0%	0%	98%	0%
			2	30.5	0%	0%	0%	0%	0%	0%	2%	0%
			2	32.5	0%	0%	0%	0%	0%	0%	0%	0%
			2	34.5	0%	0%	0%	0%	0%	0%	0%	0%
	efficiency (wt.% collected in the final product)				0.01%	0.01%	0.00%	0.00%	0.07%	0.00%	99.62%	0.54%

The percentages are calculated as the ratio of collected element over the total amount collected. The efficiency is determined as the sum of the collected amounts in the Cd fraction. We have a very high yield for Cd (99.6 wt. %) and the protocol is quite specific as we collect no more than 0.6 wt.% of any other measured element. Measurements were conducted on Q-ICPMS on a BCR-2 sample.

Table 4: Elution data for the major elements, Cd and Sn during the second purification protocol (used for runs 2 to 5).

Purification phase	Chemistry phase	Acid	Volume (mL)	Cumulated volume (mL)	Major elements elution (%)						Traces elements elution (%)	
					Na	Mg	Al	K	Ca	Fe	Cd	Sn
Second to fifth Cd purification	Sample introduction	HBr 0.1N	2	2	0%	33%	5%	0%	5%	27%	0%	33%
	Matrix removing	HBr 0.1N	4	6	0%	2%	2%	0%	4%	8%	0%	34%
			4	10	4%	8%	6%	0%	11%	8%	0%	0%
			4	14	86%	16%	28%	25%	15%	7%	0%	28%
	Cd collecting	HNO3 0.1N	2	16	6%	12%	7%	74%	11%	4%	0%	3%
			2	18	0%	5%	6%	0%	5%	13%	98%	0%
			2	20	0%	3%	5%	0%	5%	0%	2%	1%
			2	22	4%	2%	5%	0%	4%	5%	0%	1%
			2	24	0%	17%	32%	0%	31%	19%	0%	0%
			2	26	0%	3%	4%	0%	7%	9%	0%	0%
	efficiency (wt.% collected in the final product)				9.53%	41.42%	58.34%	74.59%	63.91%	50.25%	99.99%	4.90%

The data is obtained similarly than for the previous table. Although this protocol is less efficient at major elements removal, it is still very good at removing Sn. Moreover, the Cd yield is still very high. Thus, we expect no significant loss of Cd during the purification process. Measurements were conducted on Q-ICPMS on a BCR-2 sample.

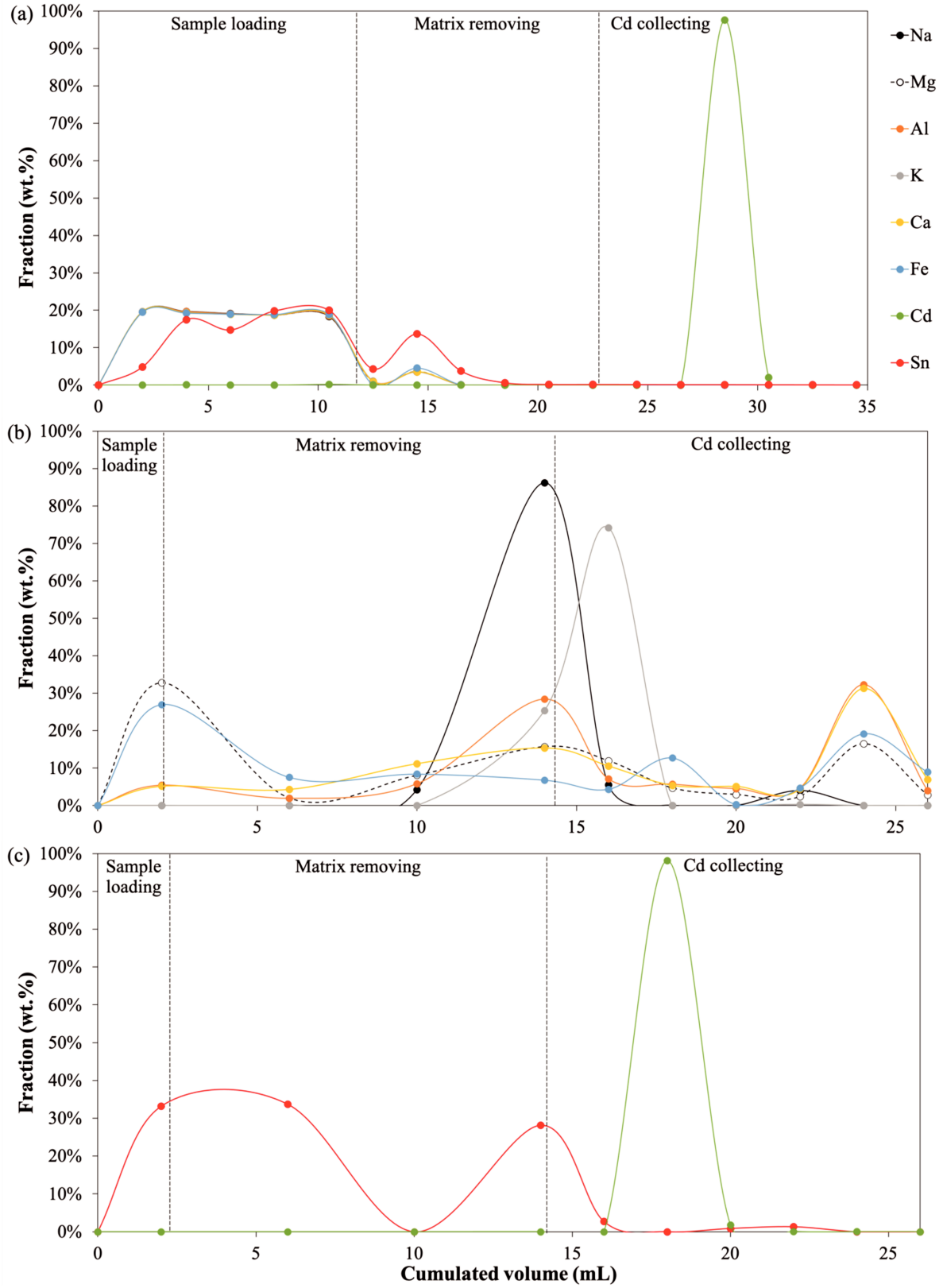


Figure 2: Visualization of the elution data reported in Table 3 and Table 4. (a) First purification protocol. All the investigated elements are represented. Apart from Cd, all elements are mainly eluted during the sample loading or matrix removing phases. (b) Second purification protocol (second to fifth run). For clarity, only the major elements were represented. We retrieve more

of them than with the first purification protocol, however, these elements should not produce interferences on Cd. (c) Same protocol as (b). We represented only Sn and Cd. The protocol is very efficient at retrieving Cd; however, we retrieve a small portion of Sn as well. Measurements were conducted on Q-ICPMS on a BCR-2 sample.

If these elution data are reliable (i.e., if the Sn removal is similar for second to fifth runs), then a MORB sample with a starting Sn concentration around 1ppm (compatible with She et al. (2023)) should end up (after purification) with a Sn concentration that would just represent the Sn analytical blank.

3. Sample analyses

Samples were analyzed using a multi-collector ICPMS (MC-ICPMS), either a *ThermoFischer Neptune* or a *ThermoFischer Neptune Plus*, at the IPGP. The MC-ICPMS was equipped with nickel Jet and H skimmer cones and coupled to an ESI IR Apex desolvation system to increase stability and sensitivity. The Apex system was configurated with a hot sector at 120°C and a cold one at 2°C. The samples, dissolved in HNO_3 0.5 mol/L, were injected in the system by a probe with an uptake rate of 100 μL/min.

We monitored six Cd isotope on the Neptune Plus (^{106}Cd, ^{110}Cd, ^{111}Cd, ^{113}Cd, ^{114}Cd and ^{116}Cd) and only five on the Neptune (^{106}Cd, ^{110}Cd, ^{111}Cd, ^{113}Cd and ^{114}Cd), due to limitations in the number and possible positions of collectors. The ^{116}Cd isotope was disregarded for Neptune analyses because it is exposed to potentially significant isobaric interferences by ^{116}Sn (14.54 molar % of the total Sn content) (Berglund and Wieser, 2011). Thus, it could not have been reliably used to determine Cd isotope composition for samples susceptible to have important Sn fractions. Isobaric interferences could also be significant for four other studied Cd isotopes, as ^{106}Cd and ^{110}Cd could be affected by ^{106}Pd (27.33 molar %) and ^{111}Pd (11.72 molar %), ^{113}In (4.29 molar %) could affect the ^{113}Cd signal and ^{114}Sn (0.66 molar %) could interfere with ^{114}Cd (Berglund and Wieser, 2011). However, Pd and In should be present in similar or smaller amounts than Cd in terrestrial silicates, with concentrations in MORB being roughly of 1 ppb

and 50 ppb respectively (Yang et al., 2014; Yi et al., 2000). Thus, the purification process should be able to reduce these interferences to insignificant levels. Since In is generally more concentrated than Pd in the terrestrial igneous samples, we chose to monitor ^{115}In to correct for its potential interferences. Similarly, Sn is often more concentrated than Cd in igneous samples and thus, ^{118}Sn signals was measured to correct Sn interferences on ^{114}Cd.

Samples were analyzed at Cd concentrations of 25 ppb whenever possible, but Cd-poor ones had to be analyzed at concentrations as low as 10, 5 or 1 ppb, although precision is significantly lower for such measurements. We generally measured between 50 and 80 V per ppm on the ^{114}Cd signal. Individual data points were produced by integration of values obtained for a block of 50 measurements. This integration excluded measurements that deviated from the mean value by more than 2SD. Sample blocks were bracketed by standard solutions, to ensure optimal results. In order to assess the correctness of the produced data, we always analyzed NIST 3108 (as standard reference), and ChemLab (lot# CL01.0301.0100) and AAS (Lot# 1797541, obtained from the University of Science and Technology, Hefei, China) solutions. The AAS solution, notably, is very isotopically fractionated for Cd, with a reported δ^{114}Cd of -0.69 ± 0.04‰ (2SD, n = 57) (Liu et al., 2022), which should allow noticing any instrumental bias. With this method, we attained precisions ranging from 0.001 to 0.037 ‰ per amu, which is similar to what other works report.

Some experiments were conducted to determine the influence of concentration mismatch over the measured isotope compositions. For this, we used a spiked AAS solution as well as a NIST SRM 2711 soil sample (in case some matrix effects intervene). These solutions were analyzed at different Cd concentrations versus a 25 ppb NIST 3108 Cd standard. The concentrations ranged from 15 to 36 ppb for AAS and from 22 to 32 ppb for NIST SRM 2711. Results are given in Table 5 and displayed in Figure 3. No significant correlation was observed between concentration mismatch and isotope compositions or related uncertainties. To remain

as conservative as possible, we made sure that all of our analyzed samples remained below 10 % concentration mismatch.

Table 5: Determination of the Cd concentration mismatch influence over measured isotope compositions

sample	Concentration mismatch		δ^{113}Cd (‰)	2SD	δ^{114}Cd (‰)	2SD	n
	Cd (ppb)	deviation					
AAS ref	**25**		**-0.51**	**0.03**	**-0.67**	**0.04**	**124**
AAS 1	15	-41%	-0.53	0.05	-0.69	0.04	5
AAS 2	18	-29%	-0.53	0.02	-0.68	0.02	5
AAS 3	20	-20%	-0.53	0.05	-0.68	0.03	5
AAS 4	21	-14%	-0.51	0.05	-0.68	0.02	5
AAS 5	23	-7%	-0.51	0.06	-0.68	0.05	5
AAS 6	24	-5%	-0.51	0.05	-0.67	0.04	5
AAS 7	27	6%	-0.53	0.04	-0.71	0.02	5
AAS 8	29	16%	-0.53	0.03	-0.72	0.04	5
AAS 9	30	18%	-0.52	0.02	-0.72	0.02	5
AAS 10	30	21%	-0.53	0.03	-0.70	0.02	5
AAS 11	33	33%	-0.54	0.02	-0.70	0.02	5
AAS 12	36	45%	-0.53	0.03	-0.69	0.02	5
NIST 2711 ref	**25**		**0.50**	**0.01**	**0.67**	**0.04**	**10**
NIST 2711 1	22	-11%	0.50	0.03	0.67	0.02	3
NIST 2711 2	23	-7%	0.53	0.02	0.71	0.02	3
NIST 2711 3	24	-3%	0.52	0.05	0.68	0.04	3
NIST 2711 4	26	4%	0.50	0.05	0.68	0.03	3
NIST 2711 5	28	10%	0.51	0.05	0.68	0.03	3
NIST 2711 6	29	14%	0.52	0.02	0.69	0.03	3
NIST 2711 7	30	21%	0.49	0.05	0.67	0.01	3
NIST 2711 8	32	27%	0.52	0.07	0.69	0.02	3
NIST 2711 9	32	28%	0.51	0.05	0.68	0.02	3

No significant correlation is found between isotope composition, or uncertainties over this value and concentration mismatch.

To remain conservative, the effective Cd concentration mismatch between satndard and samples was kept below 10 %.

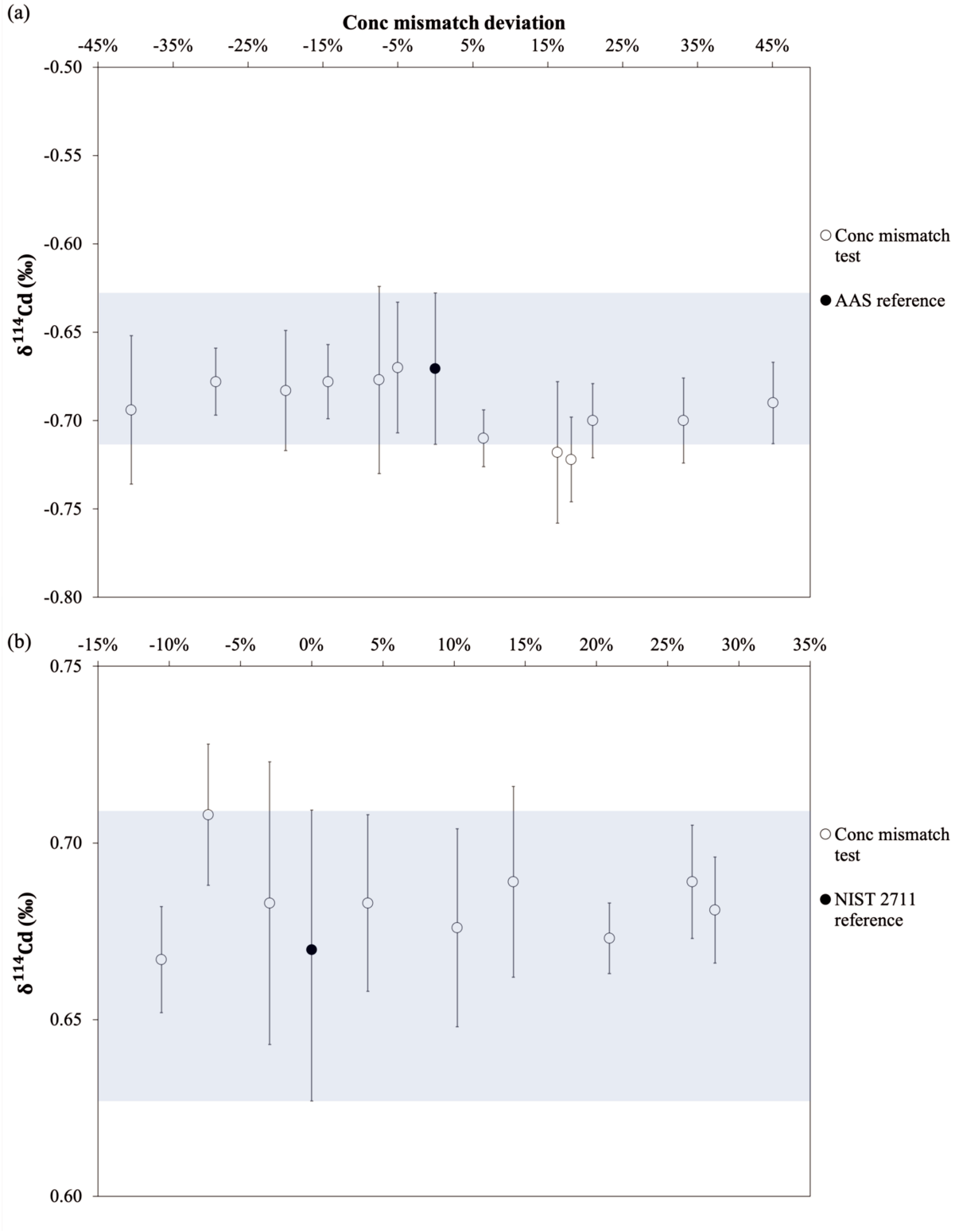


Figure 3: Illustration of the data exposed in the Table 5. (a) present results for AAS experiments while (b) displays that for NIST 2711 ones. The blue fields materialize the reference isotope compositions for the sample. Despite important mismatches,

all the measured isotope compositions remain coherent with the reference values. No significant change in uncertainties is noticeable.

4. The data treatment

4.1. Deconvolution

Double spike technique requires the measurement of signals from at least four isotopes because the deconvolution step needs three isotope ratios sharing the same denominator. We focused primarily on the ^{106}Cd / ^{110}Cd, ^{111}Cd / ^{110}Cd and ^{114}Cd / ^{110}Cd ratios. The deconvolution was performed using the *IsoSpike* integration-by-integration algorithm (Creech and Paul, 2015). We chose to exclude any point that deviates of more than 2SD from the mean isotope composition. As an output of the algorithm, we obtained a value for the $\left(\frac{m_{Cd\ spike}}{m_{Cd\ sample} + m_{Cd\ spike}}\right)$ ratio and an isotope composition estimation, given as $\delta^{114}Cd$. The $\delta^{113}Cd$ value was also determined (on the ^{106}Cd / ^{110}Cd, ^{111}Cd / ^{110}Cd and ^{113}Cd / ^{110}Cd ratios) as a way to evaluate the validity of the $\delta^{114}Cd$ value (this point is detailed later). The spike over total Cd ratio, combined to the knowledge of the mass of spike Cd introduced in the sample, allows for precise determination of the sample Cd concentration.

The 2SD uncertainties on isotope compositions were determined by the deconvolution algorithm whenever more than 2 measurements were available for a same sample. Otherwise, we attributed to the sample the biggest uncertainties that were produced during the analysis sequence for same concentration samples.

4.2. The interferences

As stated previously, the ^{106}Cd, ^{110}Cd, ^{111}Cd, ^{113}Cd, and ^{114}Cd are not free of isobaric and polyatomic interferences. Main interferences come from Sn, In, Pd for the isobaric and Mo, Zn and Zr for the isobaric ones. Palladium is, most of the time, not a significant interferent as it is

less concentrated than Cd even before purification. However, in the case of chondrites, Pd concentrations are most of the time higher than 500 ppb (Horan et al., 2003), which is often slightly more than Cd (Baker et al., 2010; Braukmüller et al., 2020, 2018; Krähenbühl et al., 1973; Loss et al., 1984; Rosman and De Laeter, 1988, 1974; Wang et al., 2015; Wombacher et al., 2003). Thus, we monitored preferentially Sn (^{118}Sn) and In (^{115}In). With these signals, and assuming mass dependency and natural isotopic ratios of ^{114}Sn/^{118}Sn = 0.02725 and ^{113}In / ^{115}In = 0.04482 (Berglund and Wieser, 2011), one can determine the expected interferences on ^{113}Cd and ^{114}Cd and correct it. Such correction was applied to all samples to obtain the most accurate isotope compositions possible.

Table 6: Assessment of the interference-correction efficiency for Sn and In isobaric interferences

Sample	Cd/X	X conc (ppb)	Uncorrected				Corrected				n
			δ^{113}Cd (‰)	2SD	δ^{114}Cd (‰)	2SD	δ^{113}Cd (‰)	2SD	δ^{114}Cd (‰)	2SD	
Sn 1	4159	0.006	-0.01	0.06	-0.02	0.06	-0.01	0.05	-0.04	0.06	6
Sn 2	1288	0.02	0.01	0.07	0.03	0.05	0.01	0.07	0.00	0.05	6
Sn 3	450	0.06	0.01	0.05	0.09	0.06	0.01	0.06	0.01	0.06	6
Sn 4	138	0.2	0.04	0.03	0.25	0.05	0.03	0.03	0.00	0.05	6
Sn 5	46	0.5	0.03	0.04	0.80	0.04	-0.01	0.04	0.04	0.04	6
Sn 6	14	1.8	0.01	0.07	2.63	0.09	-0.14	0.07	0.04	0.04	6
Sn 7	5	5.4	-0.03	0.05	7.89	0.18	-0.47	0.06	0.01	0.04	6
Sn 8	3	9.4	0.17	0.07	265.10	5.00	-14.05	0.23	250.00	4.70	6
In 1	16517	0.002	0.02	0.07	-0.03	0.06	-0.01	0.07	-0.04	0.06	6
In 2	4373	0.006	0.15	0.04	0.02	0.03	0.03	0.04	0.01	0.03	6
In 3	2283	0.01	0.28	0.04	0.00	0.07	0.04	0.04	0.00	0.07	6
In 4	478	0.05	1.22	0.04	-0.02	0.03	0.02	0.05	-0.02	0.03	6
In 5	241	0.1	2.42	0.06	0.02	0.10	0.02	0.05	0.02	0.10	6
In 6	48	0.5	12.08	0.22	0.04	0.01	0.02	0.03	0.05	0.01	5
In 7	24	1.0	24.13	0.43	-0.03	0.02	-0.03	0.04	-0.02	0.02	6
In 8	11	2.3	120.30	1.30	-0.04	0.05	66.40	0.90	-0.02	0.05	6

Sn interferences are efficiently corrected for Cd/Sn over 5. At Cd/Sn = 3, the corrected value reaches 250 ‰. We do not understand this result, however, it is not problematic as no sample reaches such Cd/Sn ratio. In interferences are corrected until Cd/In reached less than 24.

To determine the limits of this correction, we conducted experiments in which a spiked NIST 3108 Cd solution was contaminated by Sn or In with Cd / Sn ranging from 3 to more than

4000 (or from 11 to more than 16 000 for Cd / In). Isotope compositions were measured with and without correction to determine the efficiency of the correction. The results are listed in the Table 6 and displayed in Figure 4 and Figure 5. It appears that the correction scheme is highly efficient until the interferent concentration reaches 1 / 10 of the Cd one. All of our samples have higher Cd over interferent ratios, guaranteeing efficient interferences corrections.

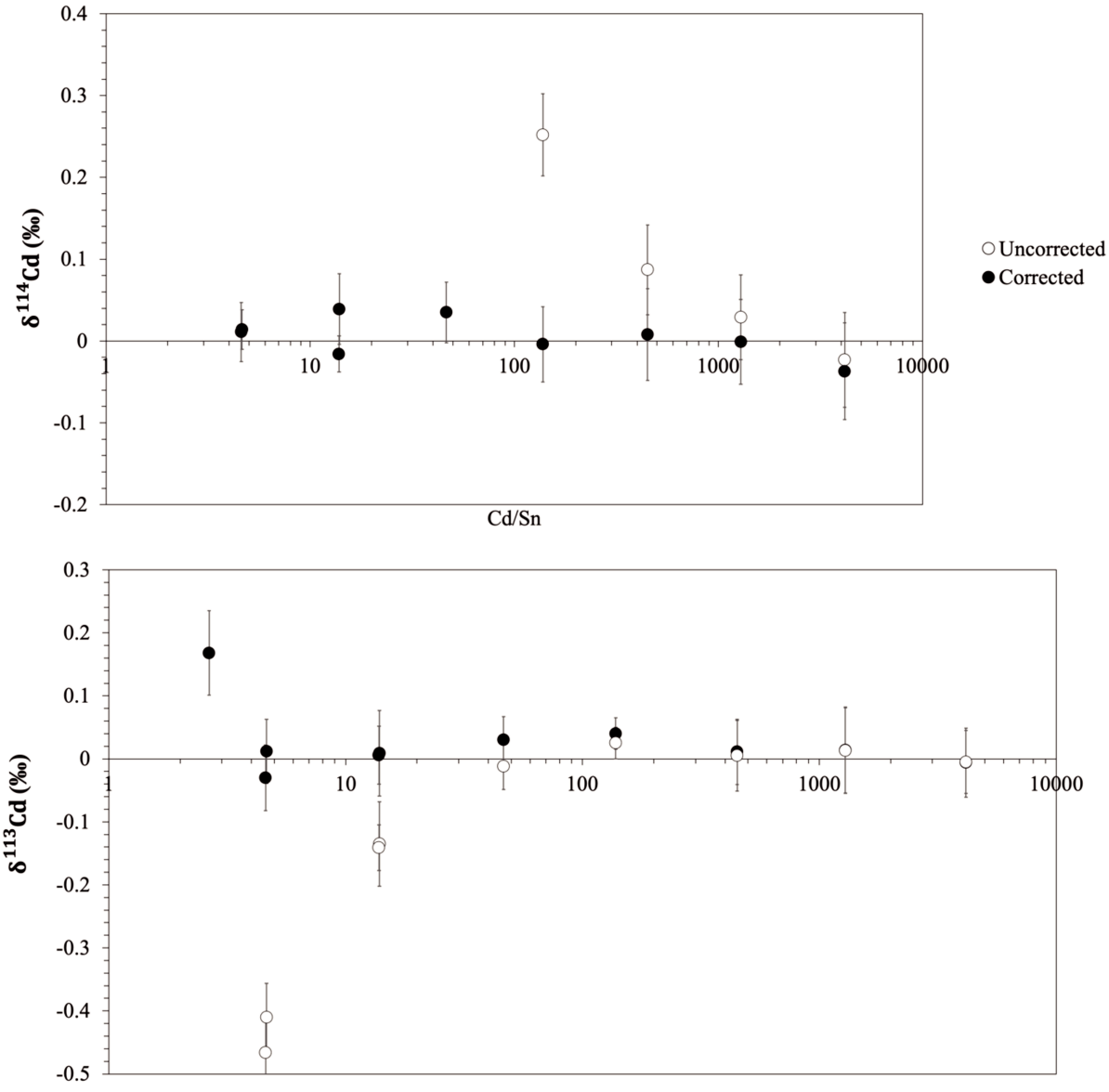


Figure 4: Tin interferences correction experiments. The top panel shows $\delta^{114}Cd$ isotope compositions while the bottom one displays $\delta^{113}Cd$ composition. High concentrations of Sn produce heavier $\delta^{114}Cd$, with a significant effect starting at Cd/Sn

around 1000, and lighter $\delta^{113}Cd$ compositions, starting at Cd/Sn below 40. The correction is efficient until Cd/Sn reaches 4, below this value it does not mitigate efficiently the interferences.

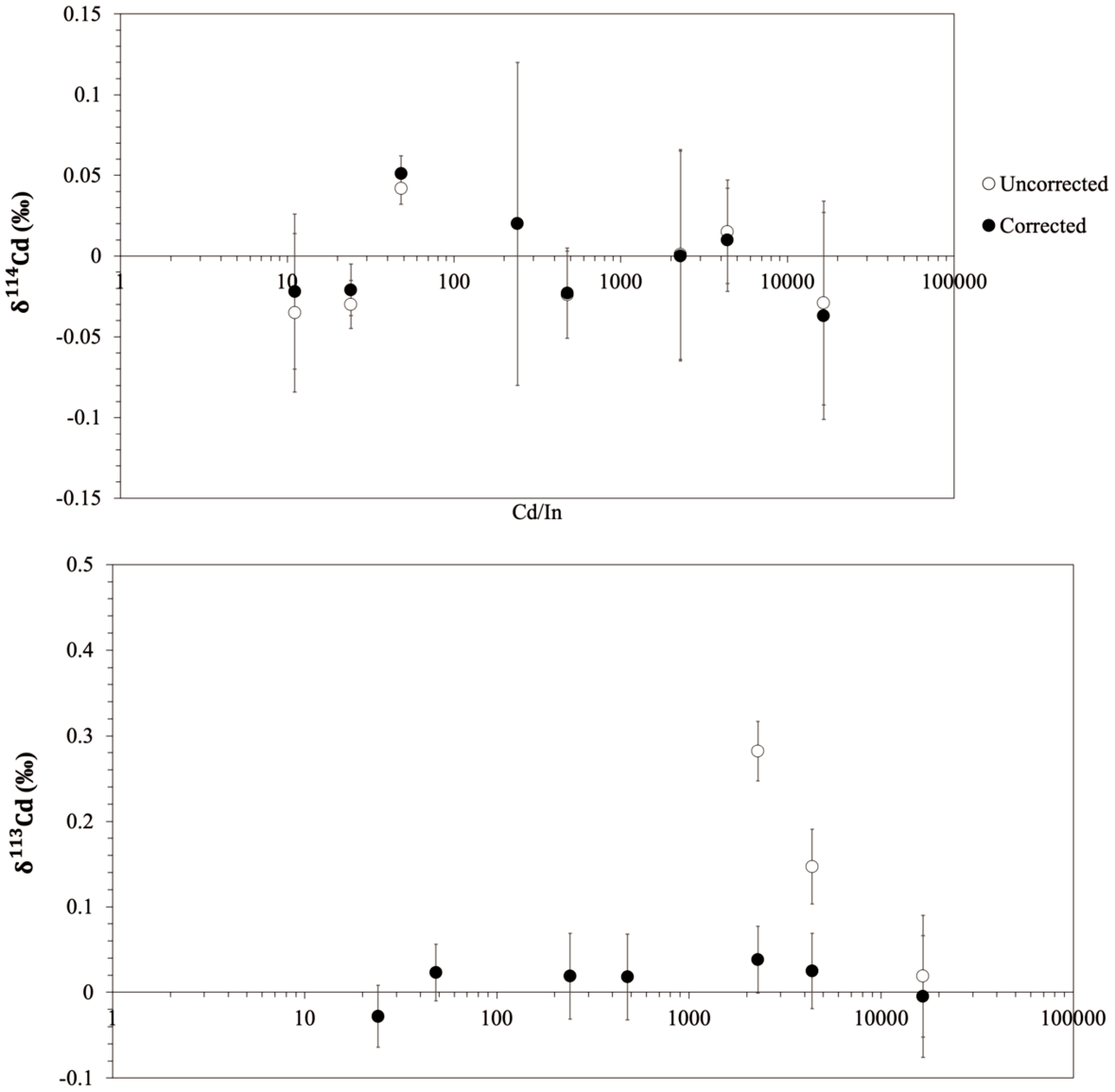


Figure 5: Indium interferences correction experiments. The top panel shows $\delta^{114}Cd$ isotope compositions while the bottom one displays $\delta^{113}Cd$ composition. High concentrations of In do net produce $\delta^{114}Cd$ deviation, while $\delta^{113}Cd$ become isotopically heavier with increasing In concentrations, starting at Cd/In below 10 000. The correction is efficient until Cd/In reaches 11, below this value it does not mitigate efficiently the interferences. The $\delta^{114}Cd$ compositions show two points significantly distinct

from the 0 ‰ reference. We believe this is because unrepresentatively low uncertainties. Typical 0.05‰ 2SD would resolve this problem, thus, we assess that it is not significant.

Palladium isobaric interferences were also characterized, with Cd over Pd ratios ranging from more than 4000 to 1. Significant interferences, driving the measured Cd isotope compositions toward light compositions, are noticed for samples with Cd/Pd being below 472 (δ^{114}Cd) or 3995 (δ^{113}Cd) (see Table 7 and Figure 6). The interference is significantly more intense for isotope compositions calculated using ^{113}Cd than for that based on ^{114}Cd. Moreover, when Cd/Pd is close to unity, the Pd influence seem to change directions for δ^{114}Cd, with an apparent isotope composition drifting toward heavier compositions. Thus, Pd could be the source of important interferences, even at low concentrations.

Finally, we characterized the polyatomic interferences caused by Mo, Zn and Zr compounds. Zinc produces no significant interference at the studied concentrations. Molybdenum produces some interferences at high concentrations, for which the Cd/Mo ratio is below 5. For higher Mo concentrations, the measured Cd isotope compositions drift toward light compositions, with similar intensities for both δ^{113}Cd and δ^{114}Cd. Finally, Zr causes important interferences whenever the Cd/Zr ratio falls below 264. It has contrary effects on δ^{113}Cd (deriving toward light compositions) and δ^{114}Cd (which drifts toward heavier isotopes-enriched compositions) (see Figure 6 and Table 7).

Most of our samples have post-purification compositions such as no significant interference is expected from the investigated elements. Nevertheless, we made sure that interferences are indeed insignificant by comparing the Cd isotope compositions determined with ^{113}Cd to that relying on ^{114}Cd. Since almost all Cd isotopes fractionating processes are mass-dependent (i.e., the isotope fractionation extent is correlated to the mass difference of the isotopes), interference-free samples should fall on a line of slope 4/3 when their δ^{114}Cd is plotted against their δ^{113}Cd. Compositions for which interferences are significant would plot outside of this

trend and thus, are easy to spot. The only known exception to this rule for Cd is caused by neutron capture on ^{113}Cd, transmutating it into ^{114}Cd (Gicking et al., 2019; Sands et al., 2001; Wisshak et al., 2002). This process, occurring mainly in space by reaction with the solar flux of neutron, significantly alter the sample isotope composition by reducing its δ^{113}Cd and enhancing its δ^{114}Cd. However, this process does not occur on the Earth because of the atmosphere; thus, for terrestrial samples we will consider mass-independent isotope compositions to be caused exclusively by interferences and remove the corresponding samples.

Table 7: Assessment of the interference intensity caused by different amounts of Mo, Pd, Zn or Zr on δ^{114}Cd or δ^{113}Cd

Sample	X conc (ppb)	Cd/X	δ^{114}Cd (‰)	2SD	n	2SD	δ^{113}Cd (‰)	n
Mo 1	0.01	3678	0.01	0.06	4	0.03	0.01	4
Mo 2	0.03	937	0.02	0.09	4	0.02	0.08	4
Mo 3	0.05	510	0.03	0.07	4	0.02	0.01	4
Mo 4	0.26	97	-0.01	0.04	4	0.02	0.05	4
Mo 5	0.52	48	0.01	0.02	4	0.02	0.03	4
Mo 6	2.6	10	-0.03	0.03	4	-0.01	0.05	4
Mo 7	5.0	5	-0.02	0.03	4	-0.02	0.03	4
Mo 8	26	1	-0.15	0.04	4	-0.14	0.04	4
Pd 1	0.01	4257	-0.01	0.03	5	0.04	0.05	5
Pd 2	0.01	3995	0.02	0.05	5	0.01	0.03	5
Pd 3	0.01	2029	0.03	0.08	5	-0.04	0.08	5
Pd 4	0.05	472	0.00	0.05	5	-0.07	0.06	5
Pd 5	0.34	74	-0.05	0.03	5	-0.44	0.03	5
Pd 6	0.77	32	-0.07	0.05	5	-1.10	0.04	5
Pd 7	4.4	6	-0.43	0.03	5	-6.80	0.11	5
Pd 8	26	1	0.88	0.14	5	-34.70	0.46	5
Zn 1	0.14	184	-0.02	0.06	4	0.03	0.10	4
Zn 2	0.23	110	0.04	0.05	4	0.04	0.03	4
Zn 3	0.47	53	0.03	0.07	4	0.05	0.02	4
Zn 4	0.53	47	-0.01	0.03	4	0.01	0.05	4
Zn 5	0.94	27	-0.01	0.04	4	-0.01	0.07	4
Zn 6	3.8	7	-0.01	0.04	4	0.02	0.07	4
Zn 7	7.3	3	-0.01	0.03	4	-0.01	0.06	4
Zn 8	36	1	0.01	0.04	4	0.00	0.07	4
Zr 1	0.01	4890	-0.01	0.02	5	0.04	0.05	5
Zr 2	0.01	3336	0.02	0.05	5	-0.04	0.10	5
Zr 3	0.01	2799	0.05	0.06	5	0.03	0.03	5
Zr 4	0.03	806	0.02	0.03	5	-0.02	0.02	5
Zr 5	0.09	264	0.02	0.08	5	-0.04	0.08	5
Zr 6	0.88	28	0.71	0.05	5	-0.69	0.05	5
Zr 7	19	1	4.08	0.16	5	-4.27	0.30	5

Molybdenum causes significant isobaric interferences for Mo concentrations close to that of Cd and drives the measured isotope compositions to drift toward light compositions. The presence of Pd is determined to create significant interferences whenever the Cd/Pd ratio is inferior to 450 for δ^{114}Cd and to 3900 for δ^{113}Cd. These interferences generally cause the apparent Cd isotope composition to be lighter than the real one; however, at Cd/Pd close to unity, the influence over δ^{114}Cd is reversed

and the measured Cd isotope composition drifts toward heavier compositions. Zinc does not cause any significant interference at the investigated concentrations. Finally, Zr causes significant interferences when Cd/Zr is below 250. The $\delta^{114}Cd$ composition is then driven toward heavier compositions while the $\delta^{113}Cd$ one drifts toward lighter ones.

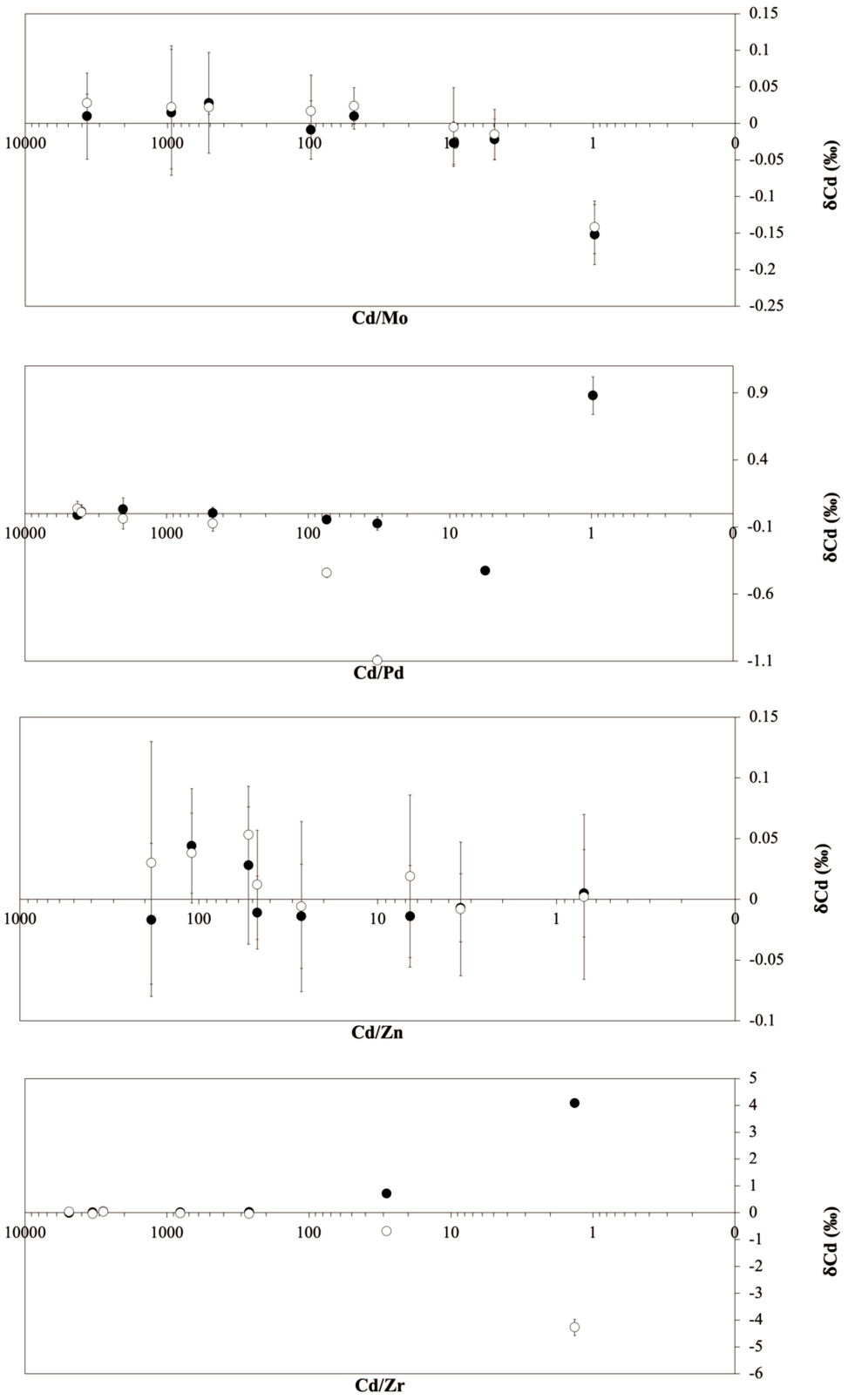


Figure 6: Graphical illustration of the influences of Mo, Pd, Zn and Zr interferences on the measured Cd isotope compositions. Data are detailed in the table 7. Black points correspond to $\delta^{114}Cd$ compositions while white ones refer to $\delta^{113}Cd$ ones.

5. References

Baker, R.G.A., Schönbächler, M., Rehkämper, M., Williams, H.M., Halliday, A.N., 2010. The thallium isotope composition of carbonaceous chondrites — New evidence for live 205Pb in the early solar system. Earth Planet. Sci. Lett. 291, 39–47. https://doi.org/10.1016/j.epsl.2009.12.044

Berglund, M., Wieser, M.E., 2011. Isotopic compositions of the elements 2009 (IUPAC Technical Report). Pure Appl. Chem. 83, 397–410. https://doi.org/10.1351/PAC-REP-10-06-02

Bertolini, J.C., 1992. Hydrofluoric acid: A review of toxicity. J. Emerg. Med. 10, 163–168. https://doi.org/10.1016/0736-4679(92)90211-B

Braukmüller, N., Wombacher, F., Bragagni, A., Münker, C., 2020. Determination of Cu, Zn, Ga, Ag, Cd, In, Sn and Tl in geological reference materials and chondrites by isotope dilution ICP-MS. Geostand. Geoanalytical Res. 44, 733–752. https://doi.org/10.1111/ggr.12352

Braukmüller, N., Wombacher, F., Hezel, D.C., Escoube, R., Münker, C., 2018. The chemical composition of carbonaceous chondrites: Implications for volatile element depletion, complementarity and alteration. Geochim. Cosmochim. Acta 239, 17–48. https://doi.org/10.1016/j.gca.2018.07.023

Creech, J.B., Paul, B., 2015. IsoSpike: improved double-spike inversion software. Geostand. Geoanalytical Res. 39, 7–15. https://doi.org/10.1111/j.1751-908X.2014.00276.x

Gicking, A.M., Takahashi, K., Krane, K.S., 2019. Neutron capture cross sections of stable Cd isotopes. Eur. Phys. J. A 55, 52. https://doi.org/10.1140/epja/i2019-12721-7

Horan, M.F., Walker, R.J., Morgan, J.W., Grossman, J.N., Rubin, A.E., 2003. Highly

siderophile elements in chondrites. Chem. Geol. 196, 27–42. https://doi.org/10.1016/S0009-2541(02)00405-9

Krähenbühl, U., Morgan, J.W., Ganapathy, R., Anders, E., 1973. Abundance of 17 trace elements in carbonaceous chondrites. Geochim. Cosmochim. Acta 37, 1353–1370. https://doi.org/10.1016/0016-7037(73)90066-5

Liu, D., Moynier, F., Siebert, J., Sossi, P.A., Hu, Y., Kubik, E., 2022. Origin of moderately volatile element depletion on differentiated bodies: Insights from the evaporation of indium from silicate melts. Geochim. Cosmochim. Acta 339, 46–57. https://doi.org/10.1016/j.gca.2022.09.043

Liu, D., Moynier, F., Sossi, P.A., Pik, R., Halldórsson, S.A., Inglis, E., Day, J.M.D., Siebert, J., 2023. The indium isotopic composition of the bulk silicate Earth. Geochim. Cosmochim. Acta 352, 24–35. https://doi.org/10.1016/j.gca.2023.04.018

Loss, R.D., Rosman, K.J.R., De Laeter, J.R., 1984. Mass spectrometric isotope dilution analyses of palladium, silver, cadmium and tellurium in carbonaceous chondrites. Geochim. Cosmochim. Acta 48, 1677–1681. https://doi.org/10.1016/0016-7037(84)90336-3

Marsh, S.F., Alarid, J.E., Hammond, C.F., McLeod, M.J., Roensch, F.R., Rein, J.E., 1978. Anion exchange of 58 elements in hydrobromic acid and in hydriodic acid (No. LA-7084, 5149421). https://doi.org/10.2172/5149421

Moynier, F., Le Borgne, M., 2015. High Precision Zinc Isotopic Measurements Applied to Mouse Organs. J. Vis. Exp. 52479. https://doi.org/10.3791/52479

Rosman, De Laeter, J.R., 1988. Cadmium mass fractionation in unequilibrated ordinary chondrites. Earth Planet. Sci. Lett. 89, 163–169. https://doi.org/10.1016/0012-821X(88)90168-9

Rosman, De Laeter, J.R., 1974. The abundance of cadmium and zinc in meteorites.

Geochim. Cosmochim. Acta 38, 1665–1677. https://doi.org/10.1016/0016-7037(74)90184-7

Rudge, J.F., Reynolds, B.C., Bourdon, B., 2009. The double spike toolbox. Chem. Geol. 265, 420–431. https://doi.org/10.1016/j.chemgeo.2009.05.010

Sands, D.G., De Laeter, J.R., Rosman, K.J.R., 2001. Measurements of neutron capture effects on Cd, Sm and Gd in lunar samples with implications for the neutron energy spectrum. Earth Planet. Sci. Lett. 186, 335–346. https://doi.org/10.1016/S0012-821X(01)00231-X

Schmitt, A.-D., Galer, S.J.G., Abouchami, W., 2009. Mass-dependent cadmium isotopic variations in nature with emphasis on the marine environment. Earth Planet. Sci. Lett. 277, 262–272. https://doi.org/10.1016/j.epsl.2008.10.025

She, J.-X., Kubik, E., Li, W., Moynier, F., 2023. Stable Sn isotope signatures of mid-ocean ridge basalts. Chem. Geol. 622, 121347. https://doi.org/10.1016/j.chemgeo.2023.121347

Van Kooten, E., Moynier, F., 2019. Zinc isotope analyses of singularly small samples (<5 ng Zn): Investigating chondrule-matrix complementarity in Leoville. Geochim. Cosmochim. Acta 261, 248–268. https://doi.org/10.1016/j.gca.2019.07.022

Wang, Z., Becker, H., Wombacher, F., 2015. Mass fractions of S, Cu, Se, Mo, Ag, Cd, In, Te, Ba, Sm, W, Tl and Bi in geological reference materials and selected carbonaceous chondrites determined by isotope dilution ICP-MS. Geostand. Geoanalytical Res. 39, 185–208. https://doi.org/10.1111/j.1751-908X.2014.00312.x

Wisshak, K., Voss, F., Käppeler, F., Kazakov, L., 2002. Neutron capture cross sections for stellar Cd production. Phys. Rev. C 66, 025801. https://doi.org/10.1103/PhysRevC.66.025801

Wombacher, F., Rehkämper, M., Mezger, K., Münker, C., 2003. Stable isotope compositions of cadmium in geological materials and meteorites determined by multiple-collector ICPMS. Geochim. Cosmochim. Acta 67, 4639–4654. https://doi.org/10.1016/S0016-7037(03)00389-2

Yang, A.Y., Zhou, M.-F., Zhao, T.-P., Deng, X.-G., Qi, L., Xu, J.-F., 2014. Chalcophile elemental compositions of MORBs from the ultraslow-spreading Southwest Indian Ridge and controls of lithospheric structure on S-saturated differentiation. Chem. Geol. 382, 1–13. https://doi.org/10.1016/j.chemgeo.2014.05.019

Yi, W., Halliday, A.N., Alt, J.C., Lee, D.-C., Rehkämper, M., Garcia, M.O., Langmuir, C.H., Su, Y., 2000. Cadmium, indium, tin, tellurium, and sulfur in oceanic basalts: Implications for chalcophile element fractionation in the Earth. J. Geophys. Res. Solid Earth 105, 18927–18948. https://doi.org/10.1029/2000JB900152

Chapter 3 – Cadmium isotope composition of the Earth's mantle inferred from analysis of oceanic basalts and komatiites

Cadmium isotope composition of the Earth's mantle inferred from analysis of oceanic basalts and komatiites

Gabriel Devos [a], Frederic Moynier [a], John Creech [a], Deze Liu [b],

Igor S. Puchtel [c], and Martin Bizzarro [a,d]

[a] Université Paris Cité, Institut de physique du globe de Paris, CNRS, F-75005 Paris, France

[b] Department of Earth sciences, University of Oxford, South Parks Road, Oxford OX1 3AN, UK

[c] Department of Geology, University of Maryland, College Park, MD 20742, USA

[d] Centre for Star and Planet Formation, Globe Institute, University of Copenhagen, Øster Voldgade 5–7, Copenhagen DK-1350, Denmark

Published in *Chemical Geology*

Vol 650, p 121996

DOI: https://doi.org/10.1016/j.chemgeo.2024.121996

Keywords: Cadmium stable isotopes; Cadmium double spike; MC-ICP-MS; Bulk Silicate Earth; mid-oceanic ridge basalts, komatiites

Abstract:

Cadmium stable isotope ratios can serve as valuable tracers for biological and geological processes, including nutrients sampling from the surrounding medium, volatilization events, and terrestrial differentiation. However, studies of the isotope fractionation occurring during geological processes require the characterization of the isotope compositions of the different terrestrial reservoirs. Notably, the cadmium isotopic composition of the Bulk Silicate Earth (BSE) is still a matter of debate. To address this issue, we present high-precision cadmium isotope data from a diverse set of samples, including mid-oceanic ridge basalts (MORB) and komatiites obtained using a ^{106}Cd-^{111}Cd double spike system. We processed nine biological and geological reference materials (AGV-2, BCR-2, BHVO-2, BIR-1, COQ 1, GSP-2, NIST 2711, NOD-A-1, ERM BB 186) and two pure Cd solutions (AAS and ChemLab) to assess the accuracy and precision of the method.

Our study revealed that twenty-three MORB samples (including ten analyses from the literature) from the Atlantic, Indian, and Pacific oceans have a homogeneous cadmium isotopic composition. The weighted mean isotope composition for these samples, expressed as $\delta^{114}Cd$ (the permil deviation of the $^{114}Cd/^{110}Cd$ ratio from the NIST SRM 3108 Cd standard), is 0.07 ± 0.10 ‰ (2SD, n = 23). We also studied twelve komatiite samples from the Abitibi (Superior Craton, Canada), Barberton (Kaapvaal Craton, South Africa), and Kostomuksha (Baltic Shield, Fennoscandia) greenstone belts to characterize the deep Archean mantle isotope composition. These samples, combined with four analyses from the literature (Pickard et al., 2022) exhibited isotopic compositions ranging from -0.33 ± 0.04 ‰ to 0.26 ± 0.08 ‰. We observed a negative correlation between cadmium abundances and the degree of secondary alteration (measured by loss on ignition-LOI). For samples with low LOI (≤ 6 wt.%), the isotope compositions of komatiites are quite consistent. On the other hand, the samples with higher LOI (between 6 and

8.4 wt.%) tend to be more scattered and can have lighter isotope compositions. These correlations suggest that, although Cd isotope compositions in komatiites are quite resilient to alteration, heavier Cd isotopes can be mobilized into secondary alteration fluids, driving altered samples toward isotopically lighter compositions. This implies that secondary alteration exerts an important control on the isotope compositions of komatiites. Therefore, only the Cd isotope compositions of the least altered komatiites (i.e., those with LOI ≤ 6 wt.%) have been used as proxies for their mantle source isotope composition. These samples (two from the Abitibi greenstone belt, one from the Barberton greenstone belt, one from the Baltic shield and one from the Belingwe greenstone belt) gave a weighted mean isotope composition of 0.14 ± 0.18 ‰ (2SD, n = 5). No significant isotope variation was found between the pristine samples from each region, despite ages ranging from 3549 ± 99 Ma to 2713 ± 29 Ma, indicating a possible isotopic homogeneity (within the currently achievable precision) of the Archean mantle for Cd starting as early as 3.55 billion years ago. We determined a Cd isotope composition for the mantle by combining the data for mean MORB and komatiites. This gave a δ^{114}Cd value of 0.11 ± 0.10 ‰ (2SD, n = 28) for the Bulk Silicate Earth. This value is significantly heavier than previously proposed.

1. Introduction

Cadmium (Cd) is classified as a moderately volatile element (MVE) due to its low T_{50} (50 % condensation temperature under solar nebula conditions) of 502 K (Wood et al., 2019). Moderately volatile elements are characterized by unique depletion patterns found in terrestrial objects (Earth, Moon, Mars, rocky meteorites), when compared to the average composition of the solar system, as determined by elemental composition of the Sun's photosphere (and approximated by CI carbonaceous chondrites) (Braukmüller et al., 2019; McDonough, 2014; Steenstra et al., 2019; Wang et al., 2016). Stable isotopes of MVE such as Cd (Sands et al., 2001; Wang et al., 2016; Wombacher et al., 2003), Cu (Luck et al., 2005, 2003), Zn (Luck et al., 2005; Pringle et al., 2017), or Rb (Pringle and Moynier, 2017) have been used to provide insights into the origin of these variations in their abundances.

Being a group 12 element (same as Zn), Cd is characterized by divalent cations and siderophile (Kubik et al., 2021; Mahan et al., 2017; Marin et al., 2013; Steenstra et al., 2020) and chalcophile (Kiseeva and Wood, 2013; Wood et al., 2014) behaviors under core-forming conditions. It is also among the MVE with the lowest T_{50} (for comparison, T_{50} of Zn is 704K: Wood et al., 2019).

The study of Cd isotope composition started in the early XX^{th} century (Aston, 1935, 1934; Nier, 1936; Stenvinkel and Svensson, 1935; Svensson, 1933). The development and improvement of thermal ionization mass spectrometers (TIMS) allowed the use of the Cd isotope system for elemental abundance determination by isotope dilution (Loss et al., 1984; Rosman and De Laeter, 1974a, 1974b) and for isotope composition determination using a ^{106}Cd-^{111}Cd double spike (DS) (Rosman and De Laeter, 1975). Following this seminal work, a number of studies explored Cd isotope compositions of meteorites (Rosman et al., 1980b, 1980a; Rosman and De Laeter, 1988, 1978, 1976), using the DS method. These studies

demonstrated that chondrites are characterized by significantly fractionated mass-dependent isotope compositions compared to terrestrial materials, ranging from -2.1 to +2.8 ‰ per atomic mass unit (amu). Similarly, significant isotope variations (-2.3 to +6.3 ‰ per amu) were observed in Cd-poor lunar soils (Sands et al., 2001; Schediwy et al., 2006). However, unlike these extraterrestrial samples, most terrestrial rocks are characterized by smaller isotope variations (often less than ± 0.075 ‰ per amu: Chang et al., 2023; Horner et al., 2011, 2010; Liu et al., 2022; Lu et al., 2021; Murphy et al., 2016; Pallavicini et al., 2014; Pickard et al., 2022; Tan et al., 2020; Wombacher et al., 2003). From the 1980s to the 2000s, the external reproducibility achieved with TIMS, expressed as 2 standard deviations (2SD), was ranging from 0.06 to 2.9 ‰ per atomic mass unit, amu, (see Table 1). Thus, the precision of the measurements was then insufficient to distinguish between many terrestrial materials. Although a new generation of TIMS has been available since the 2000s, it was employed for the first time in 2009 for Cd isotope studies and significantly improved the overall reproducibility (see Figure 1), making the study of such samples accessible.

Table 1: Reproducibility of Cd isotope measurements in different studies and comparison between instrumental design and double spike formulae

Reference	Method	instrument	2 SD (‰ per amu)	
			min	max
Rosman and De Laeter (1975)	Constant run conditions	TIMS	0.800	1.600
Rosman et al. (1980) a	$^{106-111}$ DS	TIMS	0.060	0.400
Rosman et al. (1980) b	$^{106-111}$ DS	TIMS	0.300	1.000
Rosman and De Laeter (1988)	$^{106-111}$ DS	TIMS	0.200	2.900
Sands et al. (2001)	$^{106-111}$ DS	TIMS	0.200	0.800
Wombacher et al. (2003)	Ag-; Sb-normalization	ICP-MS	0.040	0.130
Cloquet et al. (2005)	SSB	ICP-MS	0.010	0.110
Schediwy et al. (2006)	$^{106-111}$ DS	TIMS	0.200	15.000
*	*	*	*	0.900
Ripperger and Rehkämper (2007)	Ag normalization	ICP-MS	0.038	0.038
Ripperger and Rehkämper (2007)	$^{110-111}$ DS	ICP-MS	0.013	0.050
Schmitt et al. (2009) a	$^{106-108}$ DS	Triton TIMS	0.006	0.028
Schmitt et al. (2009) b	$^{106-108}$ DS	Triton TIMS	0.003	0.011
Horner et al. (2010)	$^{111-113}$ DS	ICP-MS	0.010	0.100
Horner et al. (2011)	$^{111-112}$ DS	ICP-MS	0.033	0.070
Abouchami et al. (2014)	$^{106-108}$ DS	Triton TIMS	0.004	0.017
Pallavicini et al. (2014)	SSB	ICP-MS	0.004	0.027
Wasylenki et al. (2014)	$^{111-116}$ DS	ICP-MS	0.015	0.045
Li et al. (2018)	$^{111-113}$ DS	ICP-MS	0.008	0.058
Tan et al. (2020)	$^{111-113}$ DS	ICP-MS	0.002	0.021
Borovicka et al. (2020)	$^{106-116}$ DS	Triton TIMS	0.003	0.018
Liu et al. (2020)	$^{111-113}$ DS	ICP-MS	0.001	0.019
Druce et al. (2022)	$^{110-111}$ DS	ICP-MS	0.014	0.090
Pickard et al. (2022)	$^{111-113}$ DS	ICP-MS	0.008	0.035
Chang et al. (2023)	$^{111-113}$ DS	ICP-MS	0.003	0.015
Chang et al. (2023)	$^{111-113}$ DSSA - single	ICP-MS	0.006	0.062
Chang et al. (2023)	$^{111-113}$ DSSA - multi	ICP-MS	0.006	0.050
Peng et al. (2023)	$^{111-113}$ DS	ICP-MS	0.003	0.050
Pickard et al. (2023)	$^{111-113}$ DS	ICP-MS	0.010	0.020
This work	$^{106-111}$ DS	ICP-MS	0.001	0.031

*Reproducibilities are based on the reported 2SD for multiple measurements of pure standards or of samples. They are quoted in permil per atomic mass unit. "Min" and "Max" list the best and worst 2SD reported in the work, respectively. DS: double spike; SSB: standard sample bracketing; DSSA: double spike-standard addition. *Schediwy very high maximum 2SD was obtained at suboptimal concentrations for a very depleted sample (0.4 ng/g); its second worst 2SD gives a 0.900 ‰ per amu, much more representative of the overall precision achieved then. (Abouchami et al., 2014; Borovička et al., 2021; Chang et al., 2023; Cloquet et al., 2005; Druce et al., 2022a, 2022b; Horner et al., 2011, 2010; Li et al., 2018; Liu et al., 2020; Pallavicini et al., 2014; Peng et al., 2023; Pickard et al., 2023, 2022; Ripperger and Rehkämper, 2007; Rosman et al., 1980b,*

1980a; Rosman and De Laeter, 1988, 1975; Sands et al., 2001; Schediwy et al., 2006; Schmitt et al., 2009a, 2009b; Tan et al., 2020; Wasylenki et al., 2014; Wombacher et al., 2003)

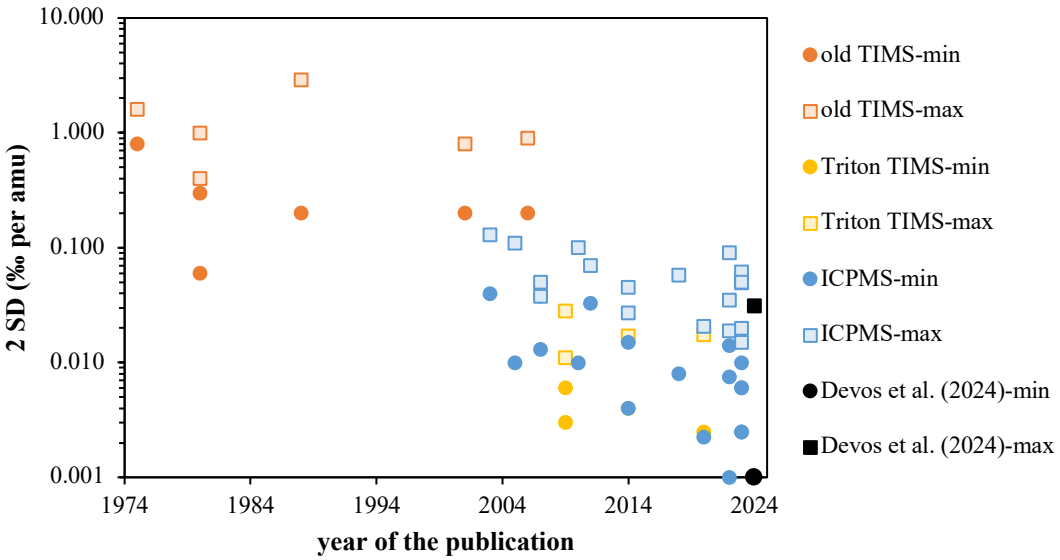


Figure 1: Evolution of the uncertainties reported in Cd isotope studies. The data represented here coincide with the one reported in Table 1. All uncertainties are normalized 2SD to obtain permil per amu deviations. The data are divided between three categories, depending on the mass spectrometer design utilized in the study. The introduction of a new mass spectrometer design usually coincides with a precision increase of at least one order of magnitude. "Min" and "Max" list the best and worst 2SD reported in the work, respectively. (Abouchami et al., 2014; Borovička et al., 2021; Chang et al., 2023; Cloquet et al., 2005; Druce et al., 2022a, 2022b; Horner et al., 2011, 2010; Li et al., 2018; Liu et al., 2020; Pallavicini et al., 2014; Peng et al., 2023; Pickard et al., 2023, 2022; Ripperger and Rehkämper, 2007; Rosman et al., 1980b, 1980a; Rosman and De Laeter, 1988, 1975; Sands et al., 2001; Schediwy et al., 2006; Schmitt et al., 2009a, 2009b; Tan et al., 2020; Wasylenki et al., 2014; Wombacher et al., 2003)

Many follow-up Cd studies employed these instruments (Abouchami et al., 2014, 2013; Borovička et al., 2021; Guinoiseau et al., 2018; Schmitt et al., 2009a) to analyze terrestrial samples, mostly using the ^{106}Cd-^{108}Cd DS (Schmitt et al., 2009b). Concurrently, other researchers developed analytical methods for Cd isotope studies using inductively-coupled plasma mass-spectrometry (ICP-MS), following the pioneering work by Wombacher (2003), as a solution to the problem of low ionization efficiency of Cd encountered with TIMS. This new technique allowed for a similar or better precision than what was then achievable using TIMS, with 2SD ranging from 0.04 to 0.13 ‰ per amu (Wombacher et al., 2003). More recent

TIMS (Borovička et al., 2021) and ICP-MS studies (Pickard et al., 2022) have demonstrated comparable precisions, with 2SD ranging from 0.01 to 0.02 ‰ per amu. The ICP-MS technique was employed in studies characterizing the Cd isotopic compositions of extraterrestrial samples (Wombacher et al., 2008), volatilization-related isotope fractionation (Wombacher et al., 2004), isotope fractionation occurring during biological processes (Chang et al., 2023), or seawater cycles (Conway and John, 2015; Ripperger and Rehkämper, 2007), for tracing pollution (Cloquet et al., 2006; Robson et al., 2014; Wen et al., 2015; Zhu et al., 2018), reconstruction of paleo-ocean characteristics (Druce et al., 2022a, 2022b; Horner et al., 2011; Peng et al., 2023; Wasylenki et al., 2014), and study of Earth accretion history (Pickard et al., 2023, 2022).

Until 2013, no isotopic standard material was available, leading to multiple in-house reference materials being used simultaneously. Most recent studies use the NIST SRM (the US National Institute of Standards and Technology standard reference material) 3108 Cd standard solution (Abouchami et al., 2013). We will hereafter express Cd isotope compositions against this NIST 3108 standard as $\delta^{114}Cd$, defined as:

$$\delta^{114}Cd = \left[\frac{\left({}^{114}Cd/{}^{110}Cd \right)_{sample}}{\left({}^{114}Cd/{}^{110}Cd \right)_{NIST\ SRM\ 3108}} - 1 \right] \times 10^3$$

One of the main hindrances to wider Cd-oriented research using ICP-MS is the low abundances of Cd in most igneous rocks, with concentrations generally under 100 ng/g (ppb). Such low concentrations mean that samples have a high matrix over Cd ratio, which can result in problematic matrix effects and interferences during the analysis. Hence, extensive purification is usually undertaken, which could potentially cause Cd loss and significant isotope fractionation if the chemical yield is not close to 100 %. As a result, many studies focused on developing DS methods to correct for potential chemical and instrumental isotope fractionation

(Ripperger and Rehkämper, 2007; Rosman and De Laeter, 1976; Schmitt et al., 2009b). With 6 stable isotopes (^{106}Cd, ^{108}Cd, ^{110}Cd, ^{111}Cd, ^{112}Cd and ^{114}Cd) and 2 long-lived radioactive isotopes (^{113}Cd and ^{116}Cd, $t_{1/2} > 10^{15}$ years) (Böhlke et al., 2005; Pritzkow et al., 2007), Cd is indeed highly suitable for double spike deconvolution, which requires at least four stable isotopes.

Despite this important analytical work, few widely available standard rock materials have been characterized for their Cd isotope compositions (Borovička et al., 2021; Chang et al., 2023; Cloquet et al., 2005; Horner et al., 2010; Li et al., 2018; Liu et al., 2020; Lu et al., 2021; Murphy et al., 2016; Pallavicini et al., 2014; Pickard et al., 2022; Tan et al., 2020; Wombacher et al., 2003), limiting inter-laboratory comparisons. Moreover, major processes affecting Cd isotope compositions have not yet been fully characterized. Notably, whether Cd isotopes are fractionated during igneous processes such as partial melting or fractional crystallization has never been tested, even though it is known to occur in some other isotopic systems, such as Zn, Ti, Fe, Zr, and Sn (Badullovich et al., 2017; Day et al., 2022; Inglis et al., 2019; Millet et al., 2016; Teng et al., 2008)

The Bulk Silicate Earth (BSE) is dominated (>99 wt. %) by the mantle (Yoder, 1995). Although the mantle Cd concentration is lower than that of the crust (38.3 ± 5.6 ppb, 80 ppb, and 126 ± 45 ppb for the mantle, continental crust, and oceanic crust, respectively: Rudnick and Gao, 2014; Wang et al., 2018; this study), it contains around 98 wt.% of the BSE Cd inventory. Thus, the Cd isotope composition of the BSE can be reliably approximated by that of the mantle.

The assumption of a well-mixed homogeneous mantle is known to be oversimplified, as the preservation of initial heterogeneities (Puchtel et al., 2018, 2016), and complex mixing processes of surficial materials in the deep mantle (Hofmann, 1997) contribute to present-day mantle heterogeneity (Helffrich and Wood, 2001; Lambart et al., 2019; Ohira et al., 2021; Van

Keken et al., 2002). Generally, two major mantle reservoirs are usually considered: a more heterogeneous lower mantle, which is the source of ocean island basalts (OIB) and a more homogeneous upper mantle. The latter reservoir is produced by the extraction of mid-oceanic ridge basalt (MORB) magmas enriched in incompatible trace elements and is, hence, called the DMM (depleted MORB mantle: Hirschmann and Stolper, 1996).

To date, only two estimates for the Cd isotope composition of the BSE are available, which are based on limited number of samples. These two estimates were obtained on three loesses (representing the continental crust), two MORB and two OIB (representing the DMM and the lower mantle respectively) (Schmitt et al., 2009a) ($\delta^{114}Cd_{BSE} = -0.04 \pm 0.02$ ‰, 2SD, n = 7) and on four spinel lherzolite samples (Pickard et al., 2022) ($\delta^{114}Cd_{BSE} = -0.06 \pm 0.03$ ‰, 2 SD, n = 4).

Using mantle-derived lavas to constrain the mantle isotope composition relies on the hypothesis that their isotope compositions mirror that of their source. This, however, may not always be the case as isotope fractionation during partial melting can make isotope compositions of melts drift away from that of their mantle sources. This may be especially so for compatible or moderately incompatible elements, for which a significant fraction of their original budgets remains in the mantle source during low degrees of partial melting. Such processes are known to produce small isotope fractionation for Zn, accounting for the isotope composition difference between OIB (2-10 % of melting), MORB (around 10 %), boninites (12-23 %) and komatiites (30 – 50 %) (Day et al., 2022). Cadmium is more incompatible than Zn, with MORB being 3 to 4 times Cd-richer than peridotites (Pickard et al., 2022; Wang et al., 2016; Witt-Eickschen et al., 2009; Yi et al., 2000) while they are only marginally enriched in Zn (Beunon et al., 2020; Day et al., 2022; Huang et al., 2018). Thus, we expect partial melting isotope fractionation to become insignificant at lower degrees of partial melting for Cd than for Zn. However, low degrees of melting should still affect the Cd isotope compositions

of the lavas. This is why we chose to focus on igneous rocks to obtain an independent estimate of the BSE isotopic composition for Cd to compare with the previous, peridotite-centered, value (Pickard et al., 2022).

Archean komatiites are lavas that sample from the heterogeneous deep mantle (Puchtel et al., 2022). They were chosen for this study because of the high degrees of partial melting that produced these melts (Herzberg, 1992), thus ensuring that no significant melting-related isotope fractionation occurs. The isotope compositions of the lavas can, however, be affected by olivine fractionation during magma differentiation, by Cd volatilization from the degassing melts (Yi et al., 2000) or by secondary processes. Since Cd has a low olivine-melt distribution coefficient (Righter et al., 2018), we do not expect that limited olivine fractionation would alter significantly the Cd isotope compositions of the melts. Moreover, the low viscosity of these magmas allows for a rapid ascent to the surface, with minimal magmatic differentiation before the eruption (Huppert et al., 1985).

The DMM composition can be determined by studying submarine-emplaced MORB. As submarine lavas are quenched upon emplacement, we do not expect significant Cd volatilization (Yi et al., 2000) or magma differentiation that could alter their original isotope compositions. Modern, unaltered samples of MORB are readily available. Thus, except if isotope fractionation is significant at the degrees of partial melting applicable to MORB formation, MORB isotope compositions should reflect that of the DMM.

The goal of this study is to obtain an accurate estimate of the Cd stable isotope composition of the BSE through the use of a ^{106}Cd-^{111}Cd DS system. To achieve this goal, we analyzed a diverse set of samples, including MORB to represent the modern depleted mantle and komatiites to represent the Archean deep mantle. We selected MORB samples from the Atlantic, Indian, and Pacific oceans and komatiites from three distinct regions: Fennoscandia (Baltic Shield), Kaapvaal Craton (South Africa), and Superior Craton (Canada). Additionally,

we included two Cretaceous Atlantic MORB samples to compare with their modern equivalents. The komatiite samples span an age range of 800 million years (Ma), allowing us to investigate the evolution of the Cd isotopic composition of the Archean deep mantle over time. Compositions of OIB samples from the literature (Pickard et al., 2022; Schmitt et al., 2009a) will be included in our discussion of the Cd isotope composition of the modern deep mantle.

2. Samples

Fourteen bulk MORB samples were analyzed, with their sampling locations displayed in Figure 2 (She et al., 2023; Wood et al., 1979) Nine of these samples were collected from the Atlantic region, with five of these originating from the North mid-Atlantic ridge (NAR) and one from the South mid-Atlantic ridge (SAR). These six samples have zero age. One sample, DSDP 409, was identified as a vesicular basalt from the Reykjanes ridge and determined to be 2.3 Ma old (Wood et al., 1979). The last two Atlantic MORB, DSDP 51A-417A and DSDP 52-417D, were collected from the Cretaceous oceanic crust located to the East of the Caribbean. Although, DSDP 417A was collected just 400 m away from DSDP 417D, it has undergone extensive alteration, unlike DSDP 417D (Emmermann and Puchelt, 1980). In addition to these samples, one MORB from the central Indian ridge (CIR) (MD57 D6-7), one from the South-West Indian ridge (SWIR) (MD34 D1) and three from the East Pacific rise (EPR) (CYP 78 12-34, Sea Rise 1 DR04 301, and Sea Rise 2 DR03) were analyzed. Samples from Indian and Pacific oceans are regarded as modern in age.

Twelve komatiite samples were analyzed in this study, originating from five distinct locations: Boston Creek and Pyke Hill from the Superior Craton, Canada; Kostomuksha from the Fennoscandian Shield in northern Europe, and Schapenburg and Weltevreden, from the Kaapvaal Craton, South Africa. These samples are thought to have been derived from

compositionally distinct mantle domains (Puchtel et al., 2022). Detailed descriptions, and major and trace element contents are available for all the samples, along with their ages (Byerly et al., 2017; Chauvel et al., 1993; Connolly et al., 2011; Corfu and Noble, 1992; Puchtel et al., 2018, 2016, 2013, 2009, 2004, 1998), which range from 2713 to 3549 Ma. All samples, except for SCH-1.9, which is an olivine cumulate, are spinifex-textured komatiites. Samples from Kostomuksha and Weltevreden were derived from several lava flows, while the Boston Creek, Pyke Hill, and Schapenburg samples were collected within the same lava flows for each locality. Additionally, all komatiite samples have undergone varying degrees of serpentinization and metamorphism.

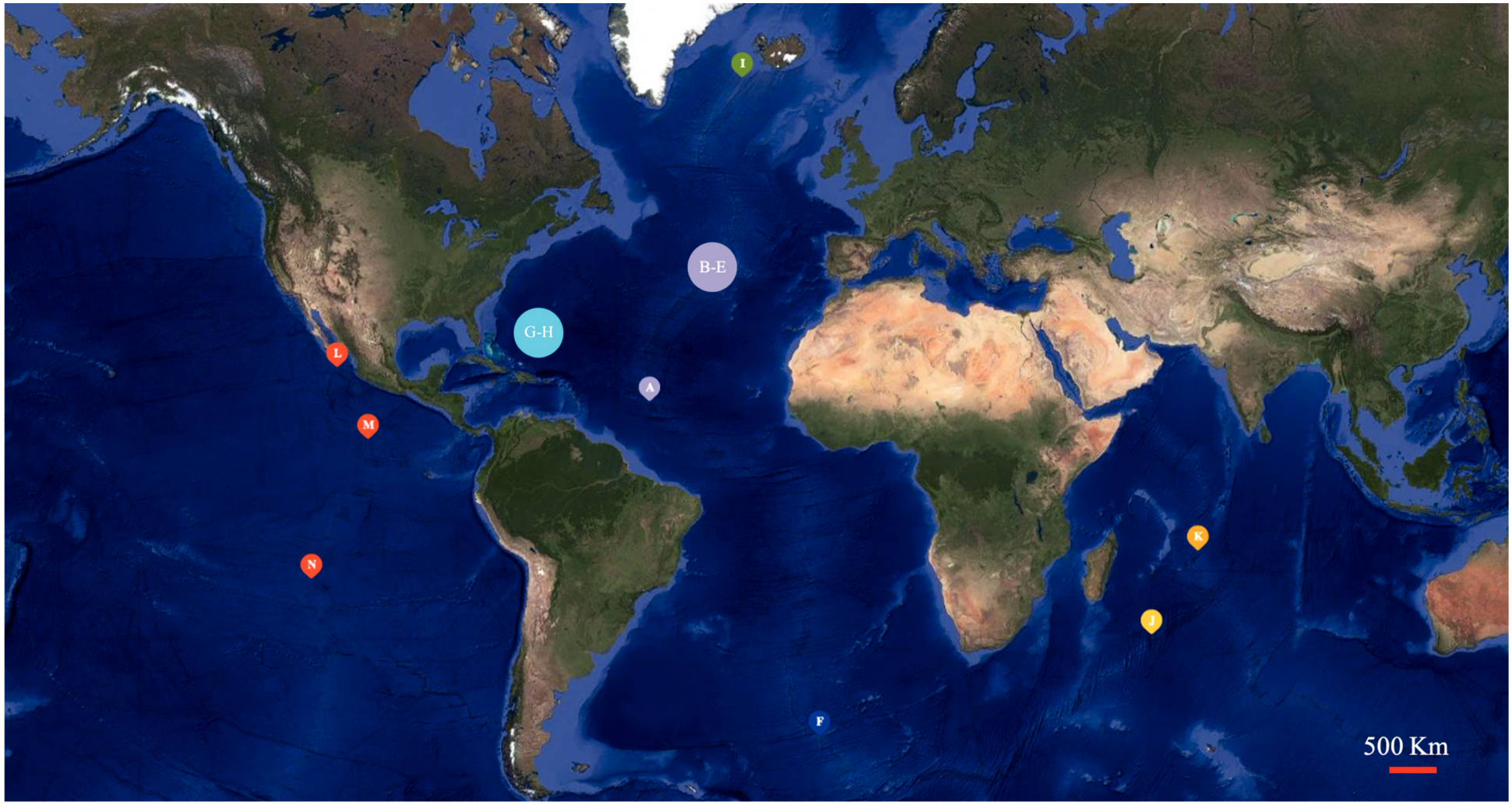

I
B-E
G-H
L
A
M
N
K
J
F
500 Km

Figure 2: Geographical locations of the sampled MORB. Each letter corresponds to an individual sample (details are provided in Table 4). The samples are grouped by the ridges they were obtained from: lavender points (A, B,C, D, E) represent samples from the Northern Mid-Atlantic Ridge (NAR), deep blue point (F) is for the Southern Mid-Atlantic Ridge (SAR), light blue points (G, H) indicate Cretaceous MORB from the NAR, green point (I) is from the Reykjanes ridge, yellow point (J) is from the South-West Indian Ridge (SWIR), orange point (K) is from the Central Indian Ridge (CIR) and red points (L, M, N) are from the East-Pacific Rise (EPR). Samples B, C, D and E are in close proximity and marked by a single point, as are G and H. The geographical positions were obtained from the literature (She et al., 2023; Wood et al., 1979) and this map was created using the Mapize online tool, with satellite imagery provided by Google resources.

3. Analytical techniques

3.1. Laboratories, tools and reagents

The samples were processed in a class 100 clean room at the Institut de Physique du Globe de Paris (IPGP), France. For purification purposes, the acids (6 mol/L HCl, 16 mol/L HNO_3, and 27 mol/L HF) were obtained by sub-boiling distillation of commercial-grade reagents. Optima™ quality 8.8 mol/L HBr was purchased from Fischer Scientific.

3.2. Sample digestion

For most terrestrial igneous rocks, about 1 to 2 g of powdered sample were weighted and then digested using a mixture of 5 mL concentrated HNO_3 and 5 mL concentrated HF in a closed screw-cap Teflon vial. Biological samples (ERM BB 186) were digested in a mixture of concentrated HNO_3 and H_2O_2 in order to breakdown organic compounds. Vials were heated at 120°C on a box-type hotplate for 3 to 4 days, until complete digestion was achieved. The samples were then evaporated to dryness at 100°C, and refluxed in 10 to 20 mL of 6 mol/L HCl at 100°C for one week, until complete conversion of the residue into the chloride form was achieved. During this phase, the samples were regularly placed in an ultrasonic bath to facilitate fluorides breakdown. Spiking was performed when the samples were dissolved in HCl.

3.3. Double spiking

In this work, we utilized the DS method to correct for experimental and instrumental isotope fractionation. To ensure the quality of the data, the spike/sample ratio, defined as $\left(\frac{m_{Cd\ spike}}{m_{Cd\ sample} + m_{Cd\ spike}}\right)$, was kept as close as possible to the optimum ratio of 0.35 (Rudge et al., 2009). Therefore, knowledge of the sample Cd concentration was essential. Prior to spiking, a small aliquot of the solution was analyzed using an Agilent quadrupole ICP-MS at the IPGP facility, to determine the Cd concentration. We mixed the remaining sample with a ^{106}Cd-^{111}Cd DS, characterized by a ^{106}Cd / ^{110}Cd isotopic ratio of 350 and a ^{111}Cd / ^{110}Cd ratio of 228, aiming at the optimal spike/sample ratio. After spiking, we refluxed the sample for 48h on a hotplate in order to ensure full sample-spike equilibration.

In order to assess the influence of the spike over sample ratio on the quality of the data, we analyzed a ChemLab pure Cd standard spiked with different amounts of DS. The table S1 and figure S1 synthetize the results of this experiment. We experimented with spike/sample ratios ranging from 0.14 (60 % deficit to the optimum) to 0.45 (30 % overabundance relative to the optimum ratio), which covers almost the entire range observed for our spiked samples (except for the two slightly overspiked komatiite samples SCH 1.9 and Welt 564-5 having spike/sample ratios of 0.48 and 0.50, respectively). No significant deviation from the reference value (see Table 3), nor significant change in the uncertainties, were observed within this range of spike/sample ratios.

3.4. Cadmium purification by anion exchange chromatography

Cadmium was separated from Sn and the sample matrix using a chemical protocol inspired by that used by Schmitt et al. (2009) for Cd separation and by established methods for Zn (Moynier and Le Borgne, 2015; Van Kooten and Moynier, 2019) and In (Liu et al., 2023) stable isotope measurements. This protocol uses an anion exchange, chloride form, resin (Bio-Rad

AG 1x8 200-400 mesh). The protocol requires five consecutive iterations of the purification of the Cd fraction to completely remove Sn, as detailed in Table 2. The first run was unique because it required the dissolution of a significant amount of sample. Therefore, a 1.5 mol/L HBr solution was used for the first run, while 0.1 mol/L HBr solutions were used for the four other runs. This did not impact the elution of Cd, as Cd's distribution coefficient with the anion exchange resin remains very high in both 1.5 mol/L or 0.1 mol/L HBr (see elution curves, calibrated on a BCR-2 basalt sample: Table S2, S3 and Figure S2). Based on our elution data, we retained only ~ 0.5 % of the initial Sn content after the first purification run. Then, with the second protocol (used from the second run to the fifth), we removed ~ 95 % of the Sn each time.

Thus, after the second purification run, only around 0.03 % of the initial Sn content remains, which becomes less than 0.01 % after the third run. After the fifth purification run, the initial Sn/Cd ratio should have been divided by a few thousands, while collecting 99.6 wt.% of the sample Cd. We then dried down the collected Cd solution cut on a hot plate, at 80°C, and refluxed it with concentrated nitric acid at 110°C for a day to destroy residual resin particles. Analytical Cd blanks ranged from 7 to 55 pg, with a median of 15 pg, representing less than 1 wt.% of the total Cd mass of the sample.

Table 2: Details of the Cd purification protocol

	Procedure step	Reagent	Volume (mL)
Every run	Resin introduction	AG 1x8 200-400mesh	0.2
	Resin cleaning	Mili-Q water	3
		0.5 M HNO_3	3
		Mili-Q water	3
1st run only	Conditioning	1.5 M HBr	3
	Sample load*	1.5 M HBr	5
	Matrix removing*	0.1 M HBr	5
Every run except 1st	Conditioning	0.1 M HBr	3
	Sample load	0.1 M HBr	2
Every run	Matrix removing	0.1 M HBr	12
	Cd elution	0.1 M HNO_3	12

The table outlines the detailed procedure used to purify Cd and eliminate Sn from the matrix. In reagent column, M notation stands for mol/L. Samples were purified 5 times, with introduction and cleaning of the resin in the Teflon column being similar at every iteration. The first run for each sample differed from the other four runs as a more concentrated solution of HBr (1.5

*mol/L) was used for the dissolution of the sample due to the high matrix content. *During the first run, the sample was introduced 0.5mL at a time, followed by 0.5mL HBr 0.1 mol/L to remove matrix and prevent column clogging. The other four purifications did not require this precaution as most matrix had already been discarded and so the sample could be directly dissolved in HBr 0.1 mol/L.*

3.5.Mass spectrometry and data reduction

Samples were analyzed either on a *ThermoFischer Neptune* or a *ThermoFischer Neptune Plus* multi-collector ICP-MS at the IPGP facility, equipped with nickel Jet and H skimmer cones. Sample introduction was carried out using an autosampler coupled to an ESI IR Apex desolvation system (hot sector at 120°C, cold sector at 2°C), with an uptake rate of 100 μL/min.

We monitored six cadmium isotopes, namely ^{106}Cd, ^{110}Cd, ^{111}Cd, ^{113}Cd, ^{114}Cd, and ^{116}Cd. However, due to potential major isobaric interferences from ^{116}Sn (14.3 molar % of the total Sn) on ^{116}Cd, only ^{106}Cd, ^{110}Cd, ^{111}Cd and ^{113}Cd or ^{114}Cd were used for deconvolution. There also may still be some interferences from Sn on mass 114, as ^{114}Sn makes up 0.6 molar % of the total Sn content. Indium interferences on ^{113}Cd were also corrected for. In order to evaluate and correct the intensity of interference from In and Sn isotopes, we also measured the ^{115}In and ^{118}Sn signals.

All measurements were conducted in 0.5 mol/L nitric acid, with Cd concentrations ranging from 10 to 25 ppb. Sample analyses were bracketed by spiked standard solutions to ensure accurate assessment of isotope variations. We usually attain sensitivities around 300 V/ppm on all cumulated Cd signals, or 80 V/ppm on ^{114}Cd. Individual data points were derived from a block of 50 individual measurements, roughly consuming 0.7 mL of the sample solution in 7 min. The precision attained in this work ranges from 0.01 to 0.03 ‰ per amu, which is similar to that of most recent studies (Pickard et al., 2022) (see Figure 1).

Some analyses were conducted to determine the influence of concentration mismatch over the $\delta^{114}Cd$ value. A standard AAS solution (AAS in the following) (Lot# 1797541), used in Liu et al. (2020), as well as the NIST SRM 2711 soil sample, were analyzed at different

concentrations against a 25 ppb NIST 3108 standard. The AAS solution and NIST SRM 2711 concentrations were ranging from 15 (-40 %) to 36 ppb (+44 %) and 22 (-12 %) to 32 ppb (+28 %), respectively. Results are summarized in Table S4 and Figure S3. No significant deviation from the reference value was observed in any cases. The Cd isotope compositions always overlapped with their reference value. Thus, our analysis method is resilient over 40 % of standard/sample intensity mismatch. In any case, during the analysis, sample and standard Cd concentrations were matched to be within 10 % intensity.

To obtain accurate DS isotopic data, we performed a deconvolution step using the *IsoSpike* integration-by-integration algorithm (Creech and Paul, 2015). Uncertainties for most samples were determined by calculating the 2SD obtained for repeated analyses of the sample. When the samples were analyzed only once or twice during the session, we used the largest 2SD uncertainties obtained for another sample analyzed under the same conditions and during the same analytical session. The Cd concentrations were determined using the spike proportion given as an output by the algorithm.

3.6. Interference assessment and correction

Tin is the main cause for interferences on the Cd isotopes used for data deconvolution. In order to correct any potential remaining isobaric interferences, we used the abundance of ^{118}Sn and assumed natural isotopic ratios of $^{114}Sn/^{118}Sn = 0.02725$, $^{116}Sn / ^{118}Sn = 0.60033$ and $^{117}Sn / ^{118}Sn = 0.31709$ (Berglund and Wieser, 2011). To determine the limits of this approach, we carried out further experiments using Sn-doped double-spiked NIST SRM 3108 Cd standard solutions. We varied the Cd/Sn ratios from 4000 to 2.5, with a Cd concentration of 25 ppb. Figure S4 displays the results of these experiments, detailed in table S5. Uncorrected Sn interferences produced a significant bias in the measured $\delta^{114}Cd$ values larger than our analytical error (0.087 ± 0.06 ‰) when Cd/Sn ≤ 450. After chemical purification, the Cd fraction has usually a Cd/Sn ratio > 500, and, therefore, the Sn interference should have a

negligible effect on the measured $\delta^{114}Cd$. In any case, the Sn interference was corrected for. This correction is effective for Cd/Sn as low 4.5, which is higher than in any of our samples after the chemical purification.

To assess the effect of the isobaric interference of ^{113}In on ^{113}Cd, we followed a similar protocol to that described above for Sn and the results are displayed in table S5. The δ^{113}Cd value is affected even for relatively low In concentrations (Cd/In < 16 500). However after chemical purification, most samples had Cd/In ratios over 20 000, and in any case, potential interferences were corrected for by using ^{115}In abundance and assuming a natural ^{113}In / ^{115}In ratio of 0.04482 (Berglund and Wieser, 2011). The correction algorithm is efficient for Cd/In $\geq$ 24.

The effect of isobaric interferences from ^{106}Pd and ^{110}Pd were tested using a similar approach. Significant effects (larger than our analytical uncertainty) were detected on δ^{114}Cd for Cd/Pd ratio lower than 472 and on δ^{113}Cd for Cd/Pd ratio lower than ~4000 (see table S6). Isobaric interferences would create apparent mass-independent isotope compositions. All the data reported fall on a straight line of slope 4/3 in the δ^{114}Cd vs. δ^{113}Cd space, as expected for a mass-dependent fractionation, further demonstrating the absence or efficient correction for any isobaric interferences.

Finally, polyatomic isobaric interferences can also affect some Cd isotopes (May and Wiedmeyer, 1998), notably from Mo or Zr. Significant effects on the δ^{114}Cd values were found when Cd/Mo was lower than 5 and Cd/Zr lower than 264 (see table S6). However, all of our samples have Cd/Mo and Cd/Zr ratios higher than 1804 and 428 respectively. Therefore, no significant effects are expected from these two elements.

3.7. Analyzed SRM – determination of the method's validity

We present a comprehensive dataset of Cd isotopic composition and concentration measurements for 11 standard materials, including two standard solutions of Cd. Calibration

of our analytical process was performed by analyzing two pure Cd ICP-MS standard solutions, ChemLab (lot# CL01.0301.0100) and AAS (Lot# 1797541), against the NIST SRM 3108 Cd standard solution. The AAS standard solution was obtained from the University of Science and Technology of China (USTC), in Hefei. It was previously characterized to have a $\delta^{114}Cd$ of -0.691 ± 0.041 ‰ (Liu et al., 2020).

We analyzed seven well-characterized United States Geological Survey (USGS) Geological Reference Materials (GRM): AGV-2 (andesite, Guano Valley, Oregon, USA), BCR-2 (basalt, Columbia River, Oregon, USA), BHVO-2 (basalt, Kilauea, Hawaii, USA), BIR-1a (basalt, Reykjavik region, Iceland), COQ-1 (carbonatite, Canada), GSP-2 (granodiorite, Silver Plume, Colorado, USA) and NOD-A-1 (manganese nodule powder from the Atlantic Ocean floor), as well as one biostandard (ERM BB 186, dried and powdered pork kidney, Institute for Reference Materials and Measurements, Geel, Belgium) and a standard reference material from the USA, NIST SRM 2711 (polluted soil from Montana, USA) that were selected based on their high Cd concentrations and heavy isotope compositions (Borovička et al., 2021; Cloquet et al., 2005; Liu et al., 2020; Pallavicini et al., 2014). While only a few of these reference materials were well characterized for cadmium isotope compositions until recently (Cloquet et al., 2005; Horner et al., 2010; Li et al., 2018; Murphy et al., 2016; Pallavicini et al., 2014; Wombacher et al., 2003), recent progress in high precision Cd isotope analyses has renewed interests in such studies, resulting in the reporting of additional geostandard Cd isotope compositions (Borovička et al., 2021; Chang et al., 2023; Liu et al., 2020; Lu et al., 2021; Pickard et al., 2022; Tan et al., 2020). However, only one study (Liu et al., 2020) report the Cd isotopic composition for COQ-1, and GSP-2.

4. Results

The Table 3displays the isotope compositions and Cd concentrations for the standard samples. All the discussed mean values, as well as results for Chemlab and AAS, are weighted means and standard deviations, defined as:

$$weighted\ mean = \delta_{mean} = \frac{\sum_i \delta_i \times w_i}{\sum_j w_j}$$

$$\text{and } weighted\ 2SD = 2 \times \sqrt{\frac{N \times \sum_i [w_i \times (\delta_i - \delta_{mean})]}{(N-1) \times \sum_j w_j}}$$

Where δ_i is the individual isotope composition measurement, w_i is the individual weight associated with this measurement and is defined as equal to 1/(2SD) and N is the number of separate isotope measurements taken into account in the calculation.

The ChemLab Cd standard and NIST 3108 Cd solution have similar isotopic compositions, with $\delta^{114}Cd_{chemlab} = 0.02 \pm 0.02$ ‰. On the other hand, the AAS solution has a significantly distinct isotope composition, with $\delta^{114}Cd_{AAS} = -0.67 \pm 0.04$ ‰. The USGS GRM AGV-2, BCR-2, BHVO-2, BIR-1a, COQ-1, GSP-2, and NOD-A-1 have less fractionated Cd isotope compositions, with $\delta^{114}Cd$ values ranging between -0.03 ± 0.07 ‰ (GSP-2) and 0.23 ± 0.02 ‰ (COQ-1, 2SD, n = 3). In contrast, the polluted soil NIST SRM 2711 and biostandard ERM BB 186 exhibit heavier isotopic compositions: $\delta^{114}Cd_{NIST\ 2711} = 0.67 \pm 0.04$ ‰ and $\delta^{114}Cd_{ERM\ BB\ 186} = 0.60 \pm 0.07$ ‰ (2SD, n = 2). Most SRM typically have Cd concentrations of a few hundred ppb. However, some standards, such as NOD-A-1, NIST 2711, COQ-1, and ERM-BB-186, are highly enriched in Cd, with concentrations as high as 37 ppm.

Basaltic samples collected from mid-oceanic ridges generally exhibit homogeneous Cd isotope compositions and concentrations (Table 4 and Figure 4). Regardless of their origin, their isotopic compositions fall within the range of 0.01 ± 0.10 ‰ to 0.13 ± 0.10 ‰, overlapping within uncertainties. Cadmium concentrations in these samples range from 91 to 151 ppb. Only

one sample (DSDP 51A 417A) shows significantly different characteristics. This sample is enriched in Cd and is isotopically light, with 386 ppb and $\delta^{114}Cd_{DSDP\ 51A\ 417A} = -0.42 \pm 0.04$ ‰ (compared with the 138 ppb and $\delta^{114}Cd_{DSDP\ 52\ 417D} = 0.09 \pm 0.08$ ‰, for the other Cretaceous Atlantic sample).

The Cd isotope compositions of komatiites exhibit much greater variability than those of MORB, ranging from -0.33 ± 0.04 to 0.26 ± 0.08 ‰ (see Table 5). They have low Cd concentrations, ranging from 27 to 92 ppb. Neither isotope compositions nor concentrations are correlated with locality. Most samples (except two) are isotopically similar or heavier than the mean MORB composition.

Table 3: Cd isotope compositions and concentration of standard reference materials

Sample	Description	Location	Spike proportion	δ^{113}Cd (‰)	2SD	n	δ^{114}Cd (‰)	2SD	n	References	Cd (ppb)	2SD	References
AAS	Reference solution		0.33	**-0.51**	**0.03**	**121**	**-0.67**	**0.04**	**124**	**This study**			
							-0.69	0.04	57	Liu et al. (2020)			
Chemlab	Reference solution		0.37	**0.03**	**0.03**	**200**	**0.02**	**0.02**	**202**	**This study**			
AGV-2	Andesite	Guano Valley, OR., USA	0.35	0.15	0.02	10	0.22	0.03	10		69		
			0.34	0.15	0.06	7	0.20	0.05	7		72		
Mean	**weighted**			**0.15**	**0.01**	**2**	**0.21**	**0.04**	**2**	**This study**	**71**	**4**	**This study**
											66	4	Du and Hu (2015)
											58	4	Xu et al. (2015)
											69		Braukmüller et al. (2020)**
							0.09	0.04	8	Liu et al. (2020)	70		Liu et al. (2020)**
							0.14	0.05	3	Pickard et al. (2022)	68		Pickard et al. (2022)**
BCR-2	Basalt	Columbia River, OR., USA	0.37	0.06	0.10	10	0.08	0.12	10		206		
			0.35	0.08	0.04	9	0.09	0.08	9		215		
			0.35	0.08	0.02	10	0.11	0.04	10		198		
Mean	**weighted**			**0.07**	**0.01**	**3**	**0.10**	**0.02**	**3**	**This study**	**206**	**17**	**This study**
											155	13	Du and Hu (2015)
											148	7	Xu et al. (2015)
											204		Braukmüller et al. (2020)**
							0.02	0.07	14	Liu et al. (2020)	209		Liu et al. (2020)**
							-0.03	0.06	4	Tan et al. (2020)	220		Tan et al.(2020)**
							0.01	0.07	6	Lu et al. (2021)	180		Lu et al. (2021)**
							0.01	0.04	4	Pickard et al. (2022)	207		Pickard et al. (2022)**
							-0.02	0.04	3	Chang et al. (2023)	180		Chang et al. (2023)**

Table 3 (continued)

Sample	Description	Location	Spike proportion	δ^{113}Cd (‰)	2SD	n	δ^{114}Cd (‰)	2SD	n	References	Cd (ppb)	2SD	References
BHVO-2	Basalt	Kilauea, Hawaii, USA	0.34	**0.10**	**0.04**	**11**	**0.15**	**0.03**	**11**	**This study**	**92**		**This study**
											107	8	Du and Hu (2015)
											93		Wang er al. (2015)**
											95		Braukmüller et al. (2020)**
							0.04	0.05	8	Liu et al. (2020)	88		Liu et al. (2020)**
							-0.03	0.08	4	Tan et al. (2020)	200		Tan et al. (2020)**
							0.02	0.07	6	Lu et al. (2021)	90		Lu et al. (2021)**
							0.09	0.08	6	Pickard et al. (2022)	88	6	Pickard et al. (2022)**
							0.02	0.05	42	Chang et al. (2023)	86		Chang et al. (2023)**
BIR-1a	Basalt	Iceland	0.36	0.14	0.07	10	0.22	0.07	10		94		
			0.39	0.12	0.01	5	0.15	0.02	5	*	78		
Mean	**weighted**			**0.12**	**0.02**	**2**	**0.17**	**0.09**	**2**	**This study**	**86**	**22**	**This study**
							0.14	0.52	6	Wombacher et al. (2003)			
											93	8	Du and Hu (2015)
											96		Braukmüller et al. (2020)**
							0.04	0.05	12	Liu et al. (2020)	98		Liu et al. (2020)**
							0.03	0.05	4	Pickard et al. (2022)	93		Pickard et al. (2022)**
COQ-1	Carbonatite	Canada	0.36	0.17	0.03	19	0.24	0.02	19		613		
			0.41	0.17	0.06	17	0.22	0.01	18	*	450		
			0.42	0.19	0.06	11	0.24	0.02	11	*	455		
Mean	**weighted**			**0.17**	**0.02**	**3**	**0.23**	**0.02**	**3**	**This study**	**506**	**185**	**This study**
											556	42	Du and Hu (2015)
							0.10	0.05	8	Liu et al. (2020)	600		Liu et al. (2020)**

Table 3 (continued)

Sample	Description	Location	Spike proportion	δ^{113}Cd (‰)	2SD	n	δ^{114}Cd (‰)	2SD	n	References	Cd (ppb)	2SD	References
ERM BB 186	Pork Kidney		0.37	**0.44**	**0.07**	**5**	**0.60**	**0.07**	**5**	**This study**	**979**		**This study**
							0.47	0.06	4	Pallavicini et al. (2014)	1040	100	Pallavicini et al. (2014)
							0.47	0.04	5	Borovicka et al. (2021)			
GSP-2	Granodiorite	Silver Plume, CO., USA	0.36	**-0.05**	**0.03**	**5**	**-0.03**	**0.07**	**5**	**This study**	**88**		**This study**
											106	8	Du and Hu (2015)
							-0.20	0.07	7	Liu et al. (2020)	91		Liu et al. (2020)**
NIST SRM 2711	Montana soil	Montana, USA	0.37	**0.50**	**0.01**	**10**	**0.67**	**0.04**	**10**	**This study**	**37363**		**This study**
							0.53	0.02	1	Cloquet et al. (2005)			
							0.76	0.13	16	Pallavicini et al. (2014)	41700		Pallavicini et al. (2014)
							0.63	0.04	14	Liu et al. (2020)			
NOD-A-1	Manganese nodule	Atlantic Ocean	0.36	0.18	0.08	10	0.23	0.04	10		7141		
			0.37	0.17	0.06	30	0.22	0.06	30		6914		
Mean	**weighted**			**0.17**	**0.01**	**2**	**0.22**	**0.02**	**2**	**This study**	**7027**	**322**	**This study**
							-0.05	0.23	1	Cloquet et al. (2005)	7500		Cloquet et al. 2005)
							0.23	0.08	2	Horner et al. (2010)	6810		Horner et al. (2010)
							0.09	0.03	4	Pallavicini et al. (2014)	7280	620	Pallavicini et al. (2014)
							0.17	0.05	6	Murphy et al. (2016)			
							0.16	0.10	4	Li et al. (2018)	7500		Li et al. (2018)**
							0.12	0.07	14	Tan et al. (2020)	6130		Tan et al. (2020)**
							0.12	0.01	5	Borovicka et al. (2021)			
							0.13	0.04	7	Lu et al. (2021)			
							0.13	0.03	15	Chang et al. (2023)	6170		Chang et al. (2023)**

*Separate rows indicate multiple digestions of the sample. n : number of mass spectrometer runs for a given digestion or number of independent digestions (for mean values). 2SD uncertainties for the Cd concentrations were calculated if multiples independent digestions of the same sample were available. Sample with * in the "References" field were spiked before HNO_3-HF digestion*

*to check for potential isotope fractionation during digestion. Literature concentrations with ** after the article reference were determined by isotope dilution. (Borovička et al., 2021; Braukmüller et al., 2020; Chang et al., 2023; Cloquet et al., 2005; Du and Hu, 2015; Horner et al., 2010; Li et al., 2018; Liu et al., 2020; Lu et al., 2021; Murphy et al., 2016; Pallavicini et al., 2014; Pickard et al., 2022; Tan et al., 2020; Wang et al., 2015; Wombacher et al., 2003; Xu et al., 2015)*

Table 4: Characterization of studied MORB

Sample	Corresponding letter on Figure 1	age (Ma)	Location	Spike proportion	δ^{113}Cd (‰)	2SD	n	δ^{114}Cd (‰)	2SD	n	References	Cd (ppb)
Atlantic Ocean												
2πD 44-1	A	0	North Atlantic Ridge (NAR)	0.279	0.04	0.04	10	0.07	0.03	10	This study	110
ARP 74 7 8 surface	B	0	North Atlantic Ridge (NAR)	0.246	-0.01	0.07	11	0.01	0.10	11	This study	151
ARP 74 9 13 C	C	0	North Atlantic Ridge (NAR)	0.293	0.03	0.01	13	0.06	0.02	13	This study	148
CH31 DR12 137	D	0	North Atlantic Ridge (NAR)	0.26	0.04	0.06	7	0.09	0.09	7	This study	101
CH30 DR17-03	E	0	North Atlantic Ridge (NAR)	0.281	0.08	0.03	8	0.13	0.10	8	This study	91
ERW 9309 2D-1g	F	0	South Atlantic Ridge (SAR)	0.372	0.01	0.06	3	0.01	0.05	3	This study	117
DSDP 51A-417A	G	109	Carbonaceous Atlantic Sample (CAS)	0.357	-0.34	0.01	8	-0.42	0.04	9	This study	386
DSDP 52-417D	H	109	Carbonaceous Atlantic Sample (CAS)	0.246	0.03	0.08	10	0.09	0.08	10	This study	138
DSDP LEG 49 409	I	2.3	Reykjanes Ridge	0.21	0.02	0.09	9	0.05	0.12	9	This study	133
Mean Atlantic Ocean MORB	**weighted**				**0.03**	**0.05**	**8**	**0.06**	**0.07**	**8**	**This study**	
POS 221 604 DS-1G			S.Kolbeinsey Ridge					0.12	0.09	2	Pickard et al. (2022)	152
M41/2 130 DS-3			Southern Mid Atlantic Ridge					0.02	0.04	2	Pickard et al. (2022)	71
M41/2 142 DS-2			Southern Mid Atlantic Ridge					0.07	0.05	2	Pickard et al. (2022)	115

Table 4 (continued)

Sample	Corresponding letter on Figure 1	age (Ma)	Location	Spike proportion	δ^{113}Cd (‰)	2SD	n	δ^{114}Cd (‰)	2SD	n	References	Cd (ppb)
A127 DR15			Azores Plateau					0.12	0.04	1	Pickard et al. (2022)	118
Mean Atlantic Ocean MORB	**weighted**							**0.06**	**0.08**	**12**	**This study and Pickard et al. (2022)**	
Indian Ocean												
MD34 D1	J	0	South West Indian Ridge (SWIR)	0.344	0.06	0.04	11	0.10	0.04	11	This study	133
MD57 D6-7	K	0	Central Indian Ridge (CIR)	0.231	0.09	0.01	7	0.11	0.04	7	This study	94
Mean Indian Ocean MORB	**weighted**				**0.07**	**0.04**	**2**	**0.10**	**0.02**	**2**	**This study**	
MD57 D10-1			Indian Ocean					0.24	0.05	1	Pickard et al. (2022)	132
Mean Indian Ocean MORB	**weighted**							**0.14**	**0.13**	**3**	**This study and Pickard et al. (2022)**	
Pacific Ocean												
CYP 78 12-34	L	0	East-Pacific Rise (EPR)	0.268	0.01	0.10	11	0.04	0.08	11	This study	130
Sea Rise 1 DR04 301	M	0	East-Pacific Rise (EPR)	0.272	0.02	0.07	11	0.04	0.08	11	This study	139

Table 4 (continued)

Sample	Corresponding letter on Figure 1	age (Ma)	Location	Spike proportion	δ^{113}Cd (‰)	2SD	n	δ^{114}Cd (‰)	2SD	n	References	Cd (ppb)
Sea Rise 2 DR03	N	0	East-Pacific Rise (EPR)	0.259	0.04	0.03	8	0.06	0.07	8	This study	121
Mean Pacific Ocean MORB	**weighted**				**0.02**	**0.03**	**3**	**0.05**	**0.02**	**3**	**This study**	
MW 87/2 87-6			East Pacific Rise					0.12	0.07	2	Pickard et al. (2022)	160
SO157 54 DS-1			Pacific Antarctic Rise					0.08	0.05	3	Pickard et al. (2022)	152
SO157 63 DS-1			Pacific Antarctic Rise					0.07	0.05	4	Pickard et al. (2022)	302
SO80 37 DS-1			Pukao Seamount					0.06	0.04	2	Pickard et al. (2022)	133
SO80 43 DS-1			Pukao Seamount					0.00	0.05	2	Pickard et al. (2022)	132
Mean Pacific Ocean MORB	**weighted**							**0.06**	**0.08**	**8**	**This study and Pickard et al. (2022)**	
Mean MORB	**weighted**							**0.07**	**0.10**	**23**	**This study and Pickard et al. (2022)**	

Ages and geographical positions are taken from Emmermann and Puchelt (1980), She et al. (2023), and Wood et al. (1979). Published data (in grey) are from Pickard et al. (2022).

Table 5: Description and isotope compositions of komatiites

Sample	Description	Locality	Region	age (Ma)	2SD	Loss on ignition (LOI) (wt.%)	Spike proportion	δ^{113}Cd (‰)	2SD	n	δ^{114}Cd (‰)	2SD	n	References	Cd (ppb)	References
BC 02	Px spinifex	Boston Creek	Abitibi greenstone belt. Canada	2720	2	3.0	0.23	0.16	0.09	3	0.26	0.08	3	This study	87	This study
BC 03	Px spinifex	Boston Creek	Abitibi greenstone belt. Canada	2720	2	1.6	0.23	0.12	0.09	4	0.18	0.08	3	This study	89	This study
Kost 9497	Ol spinifex	Kostomuksha	Baltic shield	2843	39	5.2	0.26	0.07	0.07	5	0.12	0.03	2	This study	74	This study
Kost 94123	Ol spinifex	Kostomuksha	Baltic shield	2843	39	6.1	0.36	-0.04	0.06	6	-0.04	0.05	2	This study	68	This study
PH 27	Ol spinifex	Pyke Hill	Abitibi greenstone belt. Canada	2713	29	6.7	0.33	0.14	0.06	8	0.20	0.05	2	This study	44	This study
PH 28	Ol spinifex	Pyke Hill	Abitibi greenstone belt. Canada	2713	29	6.1	0.31	0.01	0.09	9	0.08	0.08	1	This study	60	This study
SCH 1.1	Ol spinifex	Schapenburg	Barberton greenstone belt. South Africa	3549	99	4.2	0.30	0.14	0.09	10	0.23	0.08	3	This study	66	This study
SCH 1.5	Ol spinifex	Schapenburg	Barberton greenstone belt. South Africa	3549	99	2.8	0.26	0.00	0.03	11	0.02	0.04	5	This study	92	This study
SCH 1.9	Ol cumulate	Schapenburg	Barberton greenstone belt. South Africa	3549	99	7.1	0.48	0.07	0.08	12	0.08	0.05	1	This study	34	This study
Welt 12-2	Ol spinifex	Weltevereden	Barberton greenstone belt. South Africa	3266	8	8.1	0.26	-0.14	0.08	15	-0.19	0.09	3	This study	77	This study
Welt 564-4	Ol spinifex	Weltevereden	Barberton greenstone belt. South Africa	3266	8	7.9	0.22	0.11	0.08	16	0.14	0.05	1	This study	50	This study

Table 5 (continued)

Sample	Description	Locality	Region	age (Ma)	2SD	Loss on ignition (LOI) (wt.%)	Spike proportion	δ^{113}Cd (‰)	2SD	n	δ^{114}Cd (‰)	2SD	n	References	Cd (ppb)	References
Welt 564-5	Ol spinifex	Weltevereden	Barberton greenstone belt. South Africa	3266	8	8.4	0.50	0.05	0.08	17	0.10	0.08	2	This study	27	This study
MT 20	Ol spinifex	Munro Township	Abitibi greenstone belt. Canada	2714	2	7.9					-0.33	0.04	3		47	
M657	Ol spinifex	Alexo Mine	Abitibi greenstone belt. Canada	2690	15	6					0.12	0.03	2	Pickard et al. (2022)	48	Pickard et al. (2022)
KAL-1	Ol spinifex	Alexo Mine	Abitibi greenstone belt. Canada	2690	15	7.3					-0.12	0.1	1			
ZA-1	Ol spinifex	Belingwe	Belingwe greenstone belt. Zimbabwe	2690	13	3.37					0.03	0.05	2		77	
Pristine komatiites	**weighted**					**LOI < 6 wt. %**					**0.14**	**0.18**	**5**	**This study and Pickard et al. (2022)**		

Sample descriptions, locations, ages and LOI values are from existing literature (Byerly et al., 2017; Chauvel et al., 1993; Connolly et al., 2011; Corfu and Noble, 1992; Dupré et al., 1984; Lahaye and Arndt, 1996; Nisbet et al., 1987; Puchtel et al., 2018, 2016, 2013, 2009, 2004, 1998; Puchtel and Humayun, 2005; Rehkämper et al., 1999). Additional samples (in grey) from Munro Township, Alexo Mine (Abitibi greenstone belt, Canada) and Belingwe (Belingwe greenstone belt, Zimbabwe) are from Pickard et al. (2022). Ol stands for olivine, Px for pyroxene.

5. Discussion

5.1. Standard samples – validation of the method

Two standard solutions, ChemLab Cd solution and AAS, were used in this study. AAS had previously been analyzed to have a $\delta^{114}Cd$ of -0.69 ± 0.04 ‰ (Liu et al., 2020), which is consistent with the value of -0.67 ± 0.04 ‰ obtained in this study (see Table 3). Since AAS is a pure Cd solution, it was only spiked, diluted and analyzed, without being processed through the Cd purification protocol. Therefore, this result can only be used to ensure the correct calibration and the efficiency of the double spike system and that no problem occurs during analysis. With this agreement between our data and literature, we concluded that our ^{106}Cd-^{111}Cd double spike system was calibrated satisfactorily and that the analysis protocol produced correct results.

Several studies have reported Cd concentration data for the standard samples analyzed here (Braukmüller et al., 2020; Chang et al., 2023; Cloquet et al., 2005; Du and Hu, 2015; Horner et al., 2010; Li et al., 2018; Liu et al., 2020; Lu et al., 2021; Pallavicini et al., 2014; Pickard et al., 2022; Tan et al., 2020; Wang et al., 2015; Xu et al., 2015). Our measured Cd concentrations are consistent with these values, except for NIST 2711 for which we have a 10 % deficit compared to the published value (Pallavicini et al., 2014). For some samples (BIR-1a and COQ-1), the uncertainties (2SD) on our Cd concentrations are respectively 25 and 35 %. Some of these samples where spiked following digestion, and it is possible that some Cd was lost by evaporation prior to spiking. However, even if this is the case, the similarity of the isotope compositions of the samples spiked before or after digestion show that this process would not have significantly affected its isotopic composition. Alternatively, these differences in

concentration could also represent heterogenous distribution of Cd between different lots of the reference standards.

Most of our samples have a δ^{114}Cd that overlaps with at least one of the previously reported values (Borovička et al., 2021; Chang et al., 2023; Cloquet et al., 2005; Horner et al., 2010; Li et al., 2018; Liu et al., 2020; Lu et al., 2021; Murphy et al., 2016; Pallavicini et al., 2014; Pickard et al., 2022; Tan et al., 2020; Wombacher et al., 2003), although they are generally on the heavier side of the previous estimates (see Figure 3). For three samples, COQ-1, ERM BB 186 and GSP-2, our δ^{114}Cd is about 0.1 ‰ higher (Borovička et al., 2021; Liu et al., 2020; Pallavicini et al., 2014). It should be noted that there was only one previous measurement for COQ-1 and GSP-2 and two for ERM BB 186.

Given that the spiked AAS solution was analyzed at the same time as these samples and returned a similar δ^{114}Cd value to that obtained at USTC (Liu et al., 2020), it can be concluded that the DS calibration, the mass-spectrometry and the deconvolution step are not the source of potential shifts. We also tested whether Cd isotopes could have been fractionated prior to adding the double spike, i.e., at the sample dissolution stage. However, replicates of BIR-1a and COQ-1 that were double-spiked before or after digestion returned similar δ^{114}Cd values (see Table 3). This implies that no isotopic fractionation occurs at the digestion stage, as was previously also suggested (Vlastelic and Piro, 2022). Finally, as demonstrated above, we have tested that all reported data have δ^{114}Cd and δ^{113}Cd values that follow mass-dependency, refuting the presence of noticeable isobaric interferences. Moreover, all the MORB samples (except for the anomalous DSDP 51A-417A, which is discussed later) have isotope compositions that are consistent with that from the literature ($[0.01 \pm 0.05; 0.13 \pm 0.10$ ‰] in this work, versus $[0.00 \pm 0.05; 0.24 \pm 0.05$ ‰] in Pickard et al. (2022)). These MORB samples, as well as the AAS solution, were analyzed along with the geo- and biostandards.

Standard samples can potentially be affected by contamination due to their large-scale production, as previously demonstrated based on isotopically heterogeneous Mo between different batches (Willbold et al., 2016; Willbold and Elliott, 2017). It is, therefore, possible that some of the Cd isotopic variability observed here is due to contamination during processing; however, it has not been demonstrated that Cd was present in the grinding equipment used for the production of such samples. In any case, we consider that our results are representative of the isotope compositions of the samples.

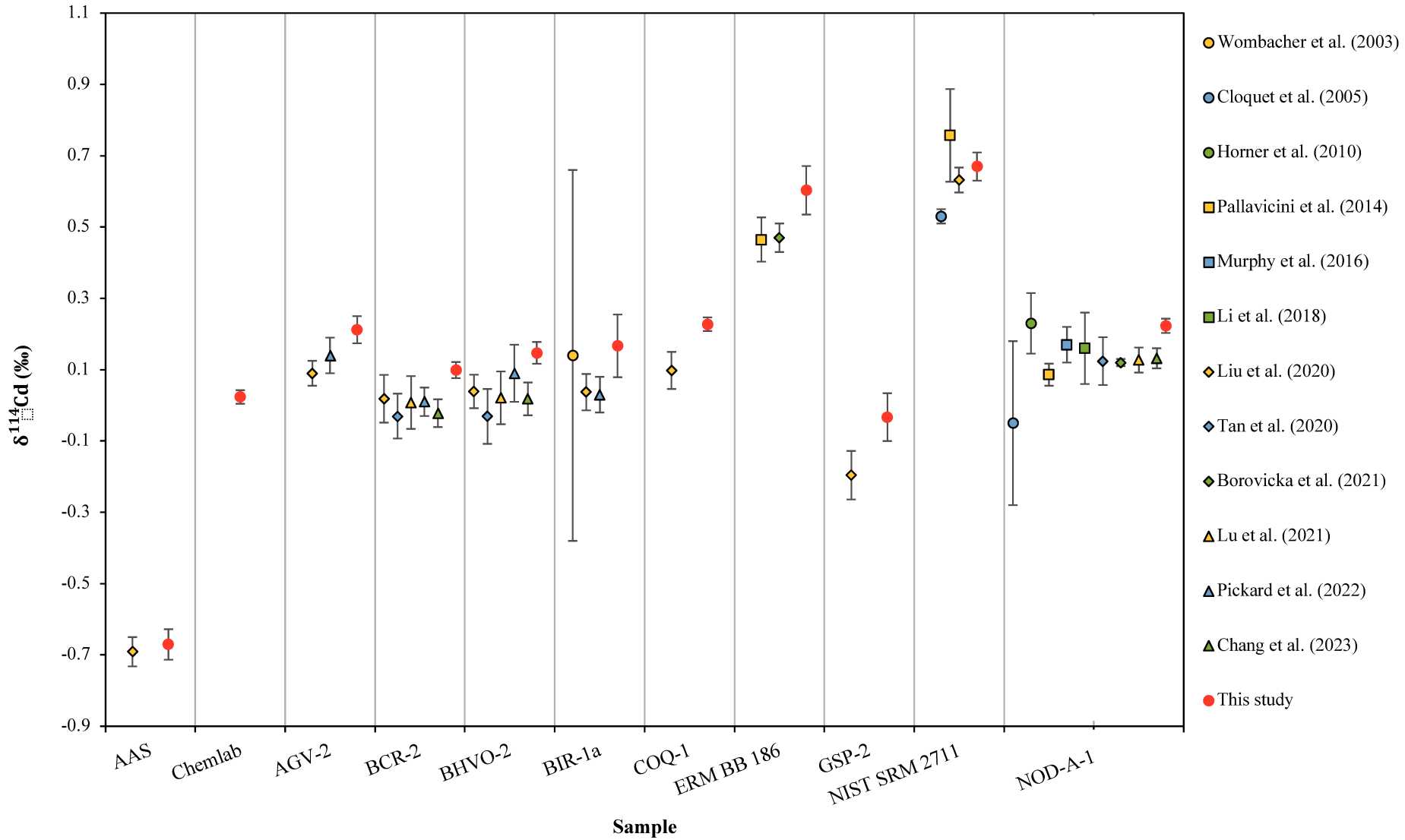

1.1
0.9
0.7
0.5
0.3
0.1
-0.1
-0.3
-0.5
-0.7
-0.9
δ114Cd (‰)
AAS
Chemlab
AGV-2
BCR-2
BHVO-2
BIR-1a
COQ-1
ERM BB 186
GSP-2
NIST SRM 2711
NOD-A-1
Sample
Wombacher et al. (2003)
Cloquet et al. (2005)
Horner et al. (2010)
Pallavicini et al. (2014)
Murphy et al. (2016)
Li et al. (2018)
Liu et al. (2020)
Tan et al. (2020)
Borovicka et al. (2021)
Lu et al. (2021)
Pickard et al. (2022)
Chang et al. (2023)
This study

Figure 3: Isotope compositions of geological and biological standard reference materials, compared with the literature data. Red circles correspond to the weighted values obtained in this study; the corresponding error bars represent weighted 2SD. Our results generally overlap with at least some estimations from the literature. However, in many cases it is at the isotopically heavier end of the previously proposed values. Since AAS pure Cd solution does not present such characteristic, we can assess that it does not reflect instrumental bias. All these samples have isotope compositions that fall on the 4/3 sloped mass dependency line in a $\delta^{114}Cd$ vs. $\delta^{113}Cd$ space, indicating that no interference is at play here. Such shift could result from geostandard contamination during processing. Sources of the data: (Borovička et al., 2021; Chang et al., 2023; Cloquet et al., 2005; Horner et al., 2010; Li et al., 2018; Liu et al., 2020; Lu et al., 2021; Murphy et al., 2016; Pallavicini et al., 2014; Pickard et al., 2022; Tan et al., 2020; Wombacher et al., 2003))

5.2. The mid-oceanic ridge basalts

The Cd concentration of MORB are homogeneous across the literature, regardless of their locality of origin, giving a mean Cd concentration of 119 ± 45 ppb (2SD, n = 31) (Yi et al., 2000), 129 ± 53 ppb (2SD, n = 9) (Pickard et al., 2022) or 124 ± 39 ppb (2SD, n = 13) (this work). This homogeneity indicates that Cd volatilization, which has been shown to be significant for sub-aerial basalts (Yi et al., 2000), is probably negligible for submarine MORB.

The Cd isotopic compositions of MORB also exhibit remarkable homogeneity both within and between the ridges (Figure 4). Our data show excellent agreement with those from the literature (Pickard et al., 2022). However, one outlier that stands out is sample DSDP 51A 417A. This outlier is one of the two Cretaceous basalts sampled from the Caribbean Sea, it has higher Cd concentration and is isotopically lighter than any other MORB. Previous studies (Emmermann and Puchelt, 1980; She et al., 2023) have described it as being more altered than DSDP 52 417D and also representing a unique Sn isotope composition among MORB. Exposure to seawater may have led to the enrichment of light Cd isotopes by Cd adsorption (Peng et al., 2023; Wasylenki et al., 2014), precipitation of calcite containing isotopically light Cd (Horner et al., 2011), although no anomalous amount of CaO was measured by She et al. (2023), crystallization of isotopically light CdS sulfides (Guinoiseau et al., 2018; Xie et al.,

2019) or by another, still unrecognized, mechanism. Each mechanism would contribute to the observed light Cd isotope composition by adding isotopically light Cd to the sample. Given this probable input, we consider DSDP 51A 417A to be non-representative of MORB and have excluded it from further discussion.

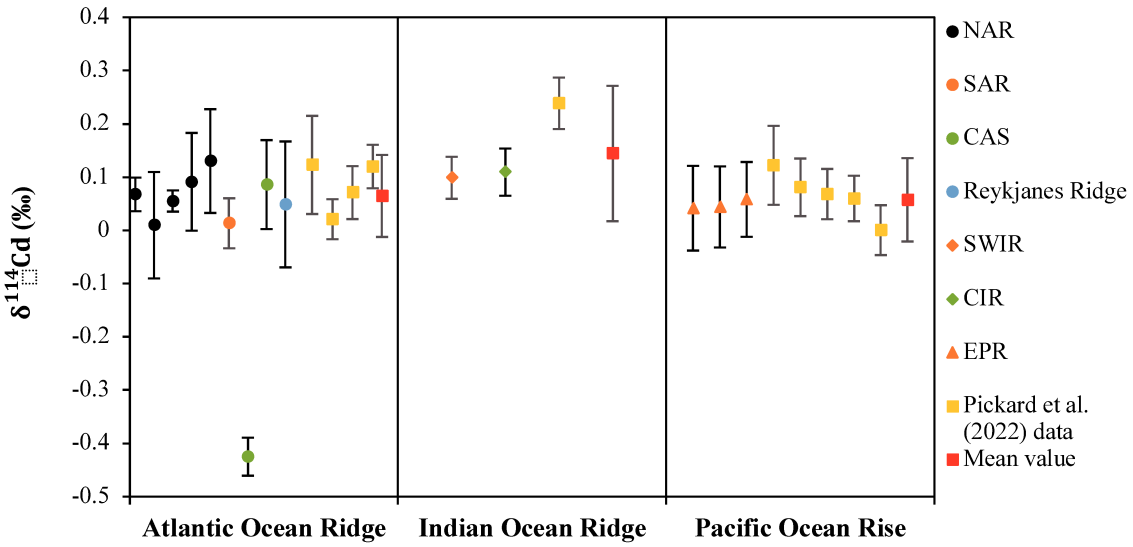


Figure 4: Isotope composition of MORB, arranged by locality. The localities include NAR: North Atlantic ridge, SAR: South Atlantic ridge, CAS: Cretaceous Atlantic sample, SWIR: South West Indian ridge, CIR: central Indian ridge, EPR: East Pacific rise. The error bars represent 2 weighted standard deviations. The mean isotope composition for each ocean is calculated using both our data and the literature data, with the exception of the isotopically fractionated CAS data point, which is discarded. Isotope compositions of the MORB samples are remarkably similar regardless of the ridge they originated from. This observation led us to propose that the depleted MORB mantle is isotopically homogeneous for Cd. Additional details are provided in Table 4.

To compare the Cd isotopic compositions of MORB between different ridge systems, mean values were calculated for each system. This was done first with our own data, literature data (Pickard et al., 2022), and finally with a combination of our own and literature data Pickard et al. (2022). For the Atlantic Ocean, the weighted mean isotope composition calculated using our data (0.06 ± 0.07 ‰, 2SD, n = 8), is similar to the literature weighted mean composition of 0.08 ± 0.10 ‰ (2SD, n = 4) and to the combined value of 0.06 ± 0.08 ‰ (2SD, n = 12).

Similarly, for the Pacific Ocean, our data (0.05 ± 0.02 ‰, 2SD, n = 3) are in good agreement with the literature data (0.06 ± 0.08 ‰, 2SD, n=5), resulting in a total weighted mean Cd isotope composition of 0.06 ± 0.08 ‰ (2SD, n = 8).

For the Indian Ocean, the isotope compositions of the three samples are more variable than in the other oceans. Thus, the weighted mean isotope composition of MORB from the Indian Ocean was calculated to be 0.10 ± 0.02 ‰ (2SD, n = 2) for our samples and 0.14 ± 0.13 ‰ (2SD, n = 3) when the MORB data from the literature are included. The weighted mean Cd isotope composition of each of the three oceanic systems significantly overlaps, with a mean MORB Cd isotope composition of 0.07 ± 0.10 ‰ (2SD, n = 23).

The Cd isotopic compositions of the MORB samples are remarkably consistent regardless of ages and locations. This suggests that, although processes such as variable degrees of partial melting, fractionated crystallization or volatilization may have affected the final Cd abundance of the different MORB samples, they did not generate significant Cd isotope variations within the currently achievable precision.

5.3. Ocean island basalts

Unlike MORB, OIB samples from the literature (Pickard et al., 2022; Schmitt et al., 2009a; Yi et al., 2000) are characterized by very diverse Cd concentrations, ranging from 43 to 324 ppb, and diverse isotope compositions, ranging from -0.10 ± 0.05 ‰ to 0.50 ± 0.05 ‰ (see Figure 5). These variations could reflect chemical heterogeneities in their mantle sources (caused by input of subducted material or primordial mantle heterogeneities), and/or igneous processes, such as variations in the degree of melting, volatilization, and fractional crystallization.

The Cd depletion, reported specifically for sub-aerial lavas (Pickard et al., 2022; Schmitt et al., 2009a; Yi et al., 2000), seems to confirm that significant Cd volatilization can occur for

lavas erupted sub-aerially. This volatilization could produce significant isotope fractionation even with relatively small Cd loss (Wombacher et al., 2004), with the residue drifting toward Cd-depleted and isotopically heavy compositions.

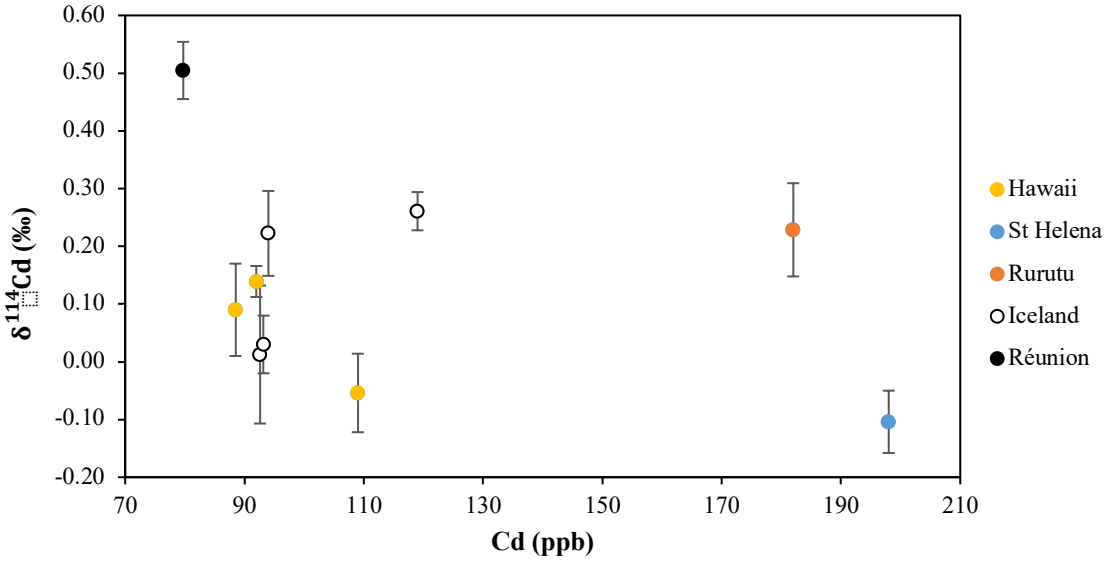


Figure 5: OIB compositions from five localities. No obvious correlation is visible that could indicate the main fractionating process. Isotope compositions could result from a mix of volatilization, light Cd isotopes input and alteration. It is also possible that some of these compositions are inheritors of isotopically fractionated specific mantle domains. (Pickard et al., 2022; Schmitt et al., 2009; This study)

Secondary processes, such as seawater alteration, could also alter the OIB isotope compositions. Studies have shown that alteration is a Cd-depleting process and that residues drift toward light isotope compositions (Zhang et al., 2016; Zhu et al., 2018). Thus, it could explain the depleted and light compositions observed for some OIBs from Hawaii and Iceland. Given that specific compositions could also be inherited from mantle source or by addition of subducted material, the interpretation of the OIB data is more complex than those for MORBs or komatiites.

5.4. Cadmium in komatiites: alteration and the Archean mantle signature

In contrast to the consistent isotopic compositions of the MORB samples, the isotopic compositions of komatiites are variable. One of the main differences that may explain such

variability is their degree of alteration. Other processes that could produce such variable isotope compositions would be Cd volatilization before cooling of the lava or other secondary processes, such as metamorphism or metasomatism.

Isotope fractionation through Cd volatilization is expected to produce a correlation between the Cd concentration and the isotope composition of the sample. Specifically, we expect Cd-rich samples to be isotopically lighter than the most depleted ones, which is not observed. To the contrary, the most Cd-rich samples are also among the isotopically heaviest. Thus, volatilization does not seem to explain the variability of komatiites Cd compositions. Similarly, metamorphism or metasomatism cannot be the cause for such variability, as we would expect processes like these to produce significant isotope variations between samples from different localities, which is not the case, as similar heavy isotope compositions are found in the samples from every locality.

Alteration has most probably affected the komatiites significantly. Samples located near the top of the lava flows have been exposed to seawater upon and after emplacement; this process may have affected the highly mobile Cd. Specifically, hydrothermal fluids may have preferentially leached out the heavy Cd isotopes, leading to lighter isotopic composition in the remaining residue (Zhang et al., 2016; Zhu et al., 2018).

We consider the loss on ignition (LOI) (Sueoka et al., 1985), which represents the amount of volatile species (primarily water and CO_2) in the sample, as an indicator of the degree of alteration. CO_2 constitutes only a small percentage of the LOI when it is under ~12 % (Cortiade et al., 2022; Tamblyn et al., 2023); thus LOI is considered a useful measure of hydration, for igneous rocks, particularly basalts (Arel and Tugrul, 2001; Irfan, 1999; Tugrul and Gurpinar, 1997). It has also been used as a proxy for the serpentinization rate (Cortiade et al., 2022; Mayhew and Ellison, 2020; Tamblyn et al., 2023; Zhou et al., 2022). The studied komatiites

underwent different degrees of serpentinization, which is reflected in the LOI values ranging from 1.6 to 8.4 wt. %.

There is a correlation between LOI and Cd concentrations, with a clear linear negative trend observed across all samples from our dataset and the literature, except for one noticeable outlier (Welt 12-2) (see Figure 6 (a)). This trend is consistent with our understanding of Cd mobility in hydrothermal fluids, where leaching can result in Cd loss. It also shows that alteration is the main process affecting Cd concentrations in komatiites.

The outlier, Welt 12-2, has a Cd content that is approximatively double that of other samples with similar LOI values. One explanation for this anomaly would be that its LOI value is artificially higher due to significant CO_2 amounts that were fixed in the sample by calcite precipitation. This would typically result in a higher CaO content, which is not observed (Puchtel et al., 2013). This suggests that the LOI value reflects hydration rather than carbonation, and that the outlier is due to anomalously high Cd content. It is possible that the sample was enriched in Cd after lava emplacement, via the previously discussed mechanisms (Guinoiseau et al., 2018; Wasylenki et al., 2014; Xie et al., 2019).

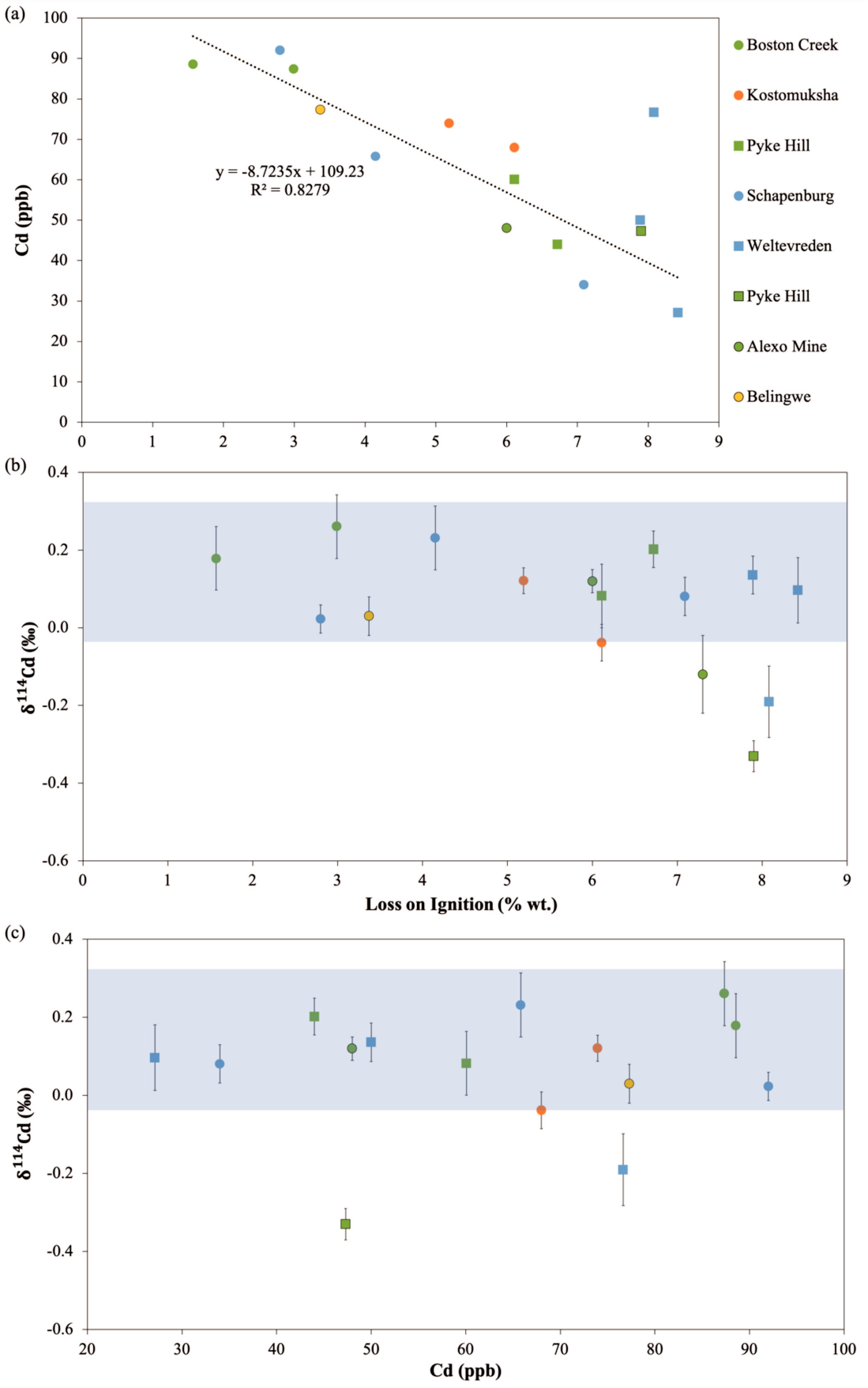

(a)
Cd (ppb)
y = -8.7235x + 109.23
R² = 0.8279
Boston Creek
Kostomuksha
Pyke Hill
Schapenburg
Weltevreden
Pyke Hill
Alexo Mine
Belingwe
(b)
δ114Cd (‰)
Loss on Ignition (% wt.)
(c)
δ114Cd (‰)
Cd (ppb)

Figure 6: Cadmium contents (a) and isotope compositions (b) of the komatiites plotted as a function of the Loss on Ignition (LOI). Panel (c) represents Cd isotope compositions of komatiites plotted as a function of their Cd content. Green circles and squares correspond to samples from the Abitibi Greenstone Belt (AGB), Canada, blue ones correspond to samples from the Barberton Greenstone Belt (BGB), South Africa, orange circles refer to samples from the Baltic Shield and yellow circle to sample from the Belingwe Greenstone Belt, Zimbabwe. Shapes with black rims refer to data from the literature (Pickard et al., 2022). (a) The Cd content follows a negative linear correlation with LOI, regardless of locality or age, except for one sample from Weltevreden and one from Schapenburg which are significantly enriched in Cd compared to other samples with similar LOI. (b) Although the non-anomalous komatiites are distributed along the LOI axis, their isotope compositions are very similar and often overlap, indicating that komatiite isotope compositions are quite resilient to alteration. The blue band embodies the mean isotope composition of the pristine komatiites (LOI < 6 wt. %).

The observed Cd depletion could result in significant isotope fractionation in the remaining komatiites, as heavy Cd isotopes loss can occur during alteration (Zhang et al., 2016; Zhu et al., 2018). Figure 6 (b) and (c), respectively, display isotope compositions of komatiites plotted as a function of their LOI and their Cd content. Although the heaviest compositions are similar regardless of LOI, there seems to be a trend toward lighter isotope enrichment when LOI is high and Cd content low, suggesting isotope fractionation during alteration.

In order to determine a reference isotope composition for pristine komatiites, we need to focus our analysis on the least altered samples. We will thereafter only consider samples below an arbitrary LOI threshold of 6 wt.%. Such value allows us to select only the least altered samples while having at least one komatiite from every geological region in our dataset. The isotope compositions of these samples are generally heavy, with two isotopically lighter outliers: SCH 1.5 and ZA-1. The previously mentioned outlier samples Welt 12-2 and SCH 1.5 present similarities, as both samples are enriched in Cd and are isotopically lighter than samples from the same location. This is contrary to what is expected from the general trend, in which Cd-rich samples are isotopically heavy. We propose that these samples have experienced a significant input of light isotopes of Cd from an unknown source. Furthermore, since their Cd contents and isotope compositions do not seem to be linked to the LOI (the Schapenburg

sample having low LOI when the Weltevreden one has high LOI), we assess that the enriching process is not coupled with hydration. Thus, SCH 1.5 is regarded as unrepresentative and not taken into account for determination of a pristine komatiites Cd isotope composition. We obtained a weighted mean isotope composition for pristine komatiites of $\delta^{114}Cd_{\text{pristine komatiites}}$ = 0.14 ± 0.18 ‰ (2SD, n = 5). This value is undistinguishable from the mean Cd isotope composition of MORB.

The ages of analyzed komatiite range from 3549 ± 99 Ma for Schapenburg (Puchtel et al., 2009) to 2690 ± 15 (Dupré et al., 1984) and 2690 ± 13 Ma (Chauvel et al., 1993) for Alexo and Belingwe, respectively (see Figure 7). Despite this large spread in age, pristine komatiite samples from different locations show identical isotope compositions. This suggests that the isotope composition of the Archean deep mantle likely remained largely constant 0.14 ± 0.18 ‰ (2SD, n = 5), and that this homogenization process occurred before the formation of the Schapenburg komatiites, at least 3549 ± 99 Ma ago. This conclusion, however, does not negate the potential existence of local Cd isotope heterogeneities.

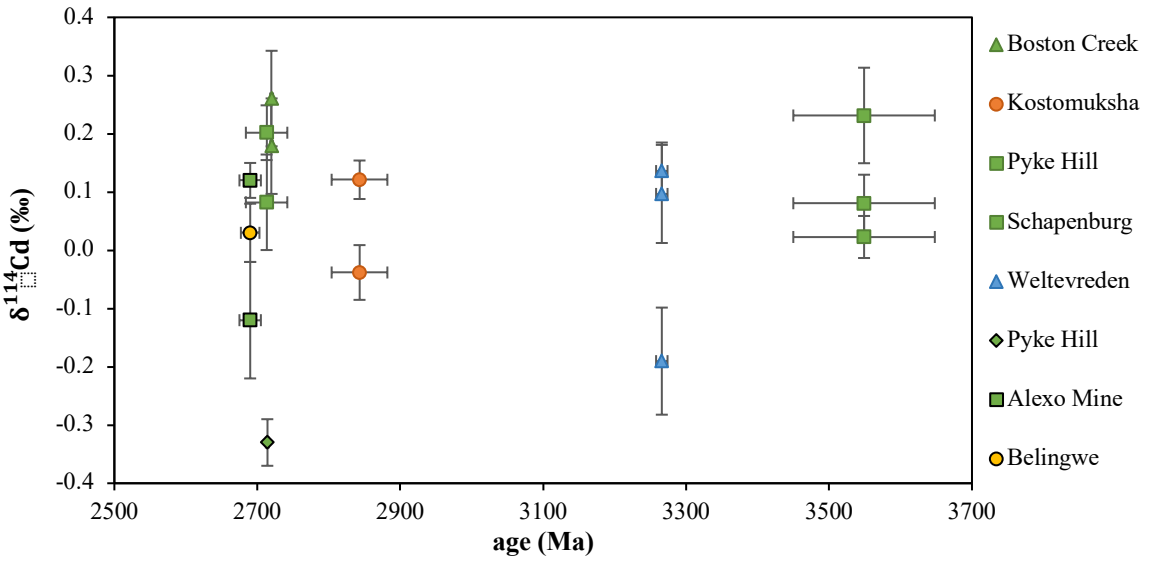


Figure 7: Cadmium isotope compositions of komatiites plotted against their individual ages. Green symbols represent samples from the Abitibi Greenstone Belt (AGB), Canada, blue ones correspond to samples from the Barberton Greenstone Belt (BGB), South Africa, orange circles refer to samples from the Baltic Shield and yellow circle to one sample from the Belingwe

Greenstone Belt, Zimbabwe. Markers with black rims represent data from the literature (Pickard et al., 2022). Despite being separated in time by almost one billion years, the isotope compositions of the BGB and AGB are similar. This suggests that the Cd isotope composition was homogeneous in the Archean mantle and that this homogeneity was established at least 3.5 billion years ago.

5.5. Comparison between the literature estimations

A previous study (Pickard et al., 2022) estimated that pristine komatiites are isotopically lighter than both MORB and OIB. Moreover, most of the peridotites analyzed in Pickard et al. (2022) are isotopically lighter than MORB and OIB but closer to some komatiitic compositions. The authors proposed a BSE isotope composition of -0.06 ± 0.03 ‰ (2SD, n = 4), based on the data for spinel lherzolites. Additionally, these conclusions suggest that magmas produced by the lower degrees of partial melting (e.g., OIB) are isotopically heavier than their mantle sources. This peridotite-based estimation is in agreement with the only other proposed BSE isotope composition for Cd, of -0.04 ± 0.02 ‰ (2SD, n = 7), which is based on analysis of loesses, MORB and OIB (Schmitt et al., 2009a).

Although the obtained BSE compositions are similar, comparison between the data sets does generate problems. Indeed, even if individual data points from both studies do overlap significantly, most MORB, OIB and loess samples from Pickard et al. (2022) are isotopically heavier than the BSE composition proposed by Schmitt et al. (2009), even though it is based on similar samples. If we apply Schmitt et al. (2009) approach (a mean of loesses, OIB and MORB compositions) to the larger dataset of Pickard et al. (2022), we obtain a BSE composition of 0.11 ± 0.14 ‰ (2SD, n = 28), which is significantly heavier than what was proposed by Pickard et al. (2022). Thus, it seems that both methods for BSE characterization (via peridotites or via igneous rocks) actually diverge.

Peridotite-based Cd isotope compositions for the BSE should be the most robust, as peridotites represent direct sampling from the mantle. However, peridotite xenoliths have been

affected by partial melting and secondary processes that could have caused significant isotope fractionation (Zhang et al., 2016; Zhu et al., 2018).

5.6. The effects of partial melting

We concluded that komatiites and MORB share similar Cd isotope compositions, indicating that the isotope fractionation of Cd occurring during partial melting is negligible for MORB and for samples formed by higher degrees of partial melting (komatiites). Thus, the compositions of these samples should reflect that of their mantle sources. On the other hand, OIB compositions are too scattered and potentially too affected by isotopic fractionation processes (partial melting, Cd volatilization and/or secondary processes) to propose a reliable isotope composition for their mantle source. Therefore, we propose that:

$$\delta^{114}Cd_{DMM} = \delta^{114}Cd_{MORB} = 0.07 \pm 0.10\ ‰\ (2SD, n = 23)$$

$$\delta^{114}Cd_{Archean\ mantle} = \delta^{114}Cd_{pristine\ komatiites} = 0.14 \pm 0.18\ ‰\ (2SD, n = 5)$$

These isotope compositions are much heavier than what was proposed for spinel lherzolites (-0.06 ± 0.03 ‰, 2SD, n = 4) (Pickard et al., 2022). This would be consistent with a significant loss of heavy Cd isotopes in these peridotites, possibly by alteration processes. In the absence of pristine peridotites or undegassed OIB isotope compositions, we cannot characterize the isotope fractionation occurring during low degrees of partial melting. Determination of Cd isotope compositions for submarine OIB that did not experience significant Cd loss by volatilization might be the way to resolve this problem.

5.7. Determination of the Cd isotope composition of the Earth's mantle

The Cd isotope composition of the mantle can be represented by a combination of isotope compositions of MORB and komatiites. However, since our sample set is dominated by MORB, calculating a mean value for all 28 samples would artificially skew the mantle isotope composition towards MORB value. To address this, we have chosen to consider the mantle

isotope composition as equally accounted for by the DMM and the Archean mantle, giving the following formula:

$$\delta^{114}Cd_{mantle} = \frac{\delta^{114}Cd_{DMM} + \delta^{114}Cd_{Archean\ mantle}}{2} = 0.11 \pm 0.10\ ‰\ (2SD,\ n = 28)$$

The fact that the isotope compositions of the DMM and Archean mantle, determined independently, are similar provides strong support for the conclusion that the mantle is significantly isotopically heavier than was proposed in the previous studies (Pickard et al., 2022; Schmitt et al., 2009a), as shown on Figure 8.

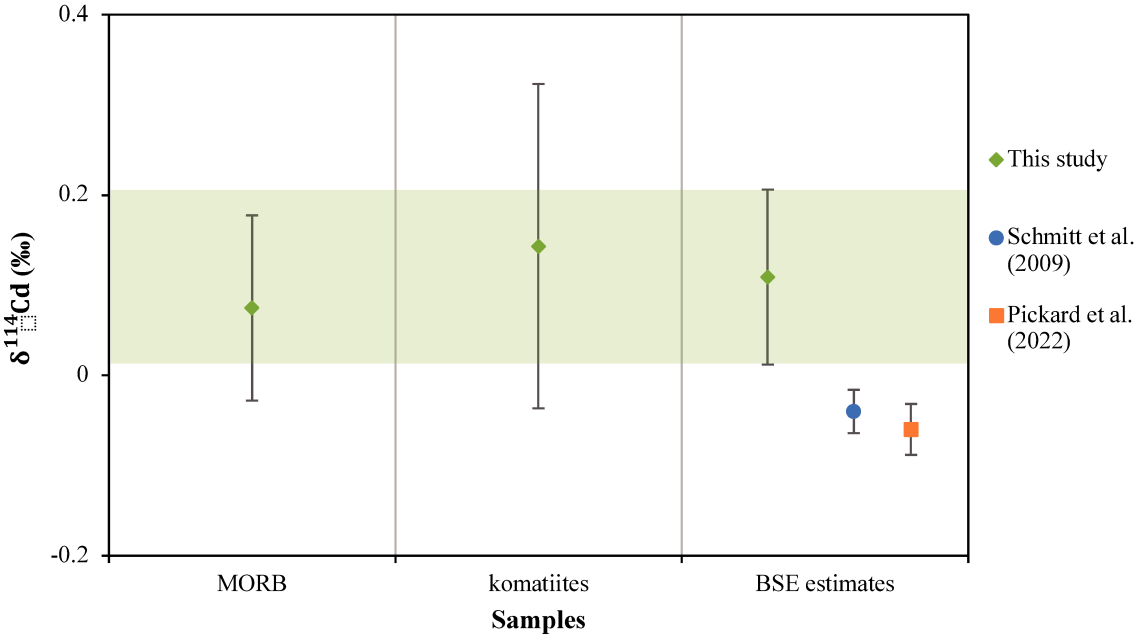


Figure 8: Comparison of the proposed Cd isotope composition of the mantle with the literature values and isotope compositions of different rock types. The green field represents the preferred proposed isotope composition for the mantle (based on the data for MORB and komatiites). There is no overlap with the previous isotope compositions proposed for the mantle (Pickard et al., 2022; Schmitt et al., 2009a).

5.8. From the mantle to the Bulk Earth

To assess the influence of the mantle on the Cd isotope composition of the Bulk Earth (BE), we need to estimate the distribution of Cd in the different reservoirs. The mass of the BE, including those of the mantle, core, and crust, are respectively estimated to be 5.9736×10^{24} Kg, 4.043×10^{24} Kg, 1.932×10^{24} Kg and 2.6×10^{22} Kg (Yoder, 1995). Thus, the BSE represents 68

wt.% of the BE. It is estimated that the continental crust constitutes 0.57 wt.% of the mantle mass (Rudnick, 1995), which amounts to 2.30×10^{22} Kg. This estimate leaves 2.95×10^{21} Kg for the oceanic crust.

Cadmium concentration of the BE has been determined to be 80 ± 20.8 ppb (Wang et al., 2018). The same study proposed that the core has a Cd concentration of 167 ± 63 ppb, while the BSE has a Cd concentration of 38.3 ± 5.6 ppb. The continental crust has a Cd concentration of 80 ppb (Rudnick and Gao, 2014). Here we propose a mean Cd concentration of 126 ± 45 ppb for the oceanic crust, based on the data for MORB glasses. Based on these data, the BE contains 4.78×10^{17} Kg of Cd, with 1.56×10^{17} Kg Cd in the BSE and 3.23×10^{17} Kg Cd in the core (67.5 wt.% of the total Cd content), consistent with Cd being both chalcophile and siderophile. As was seen previously, the rest of the Cd budget is dominated by the mantle.

The core's high Cd concentration makes it the most important reservoir to consider when studying the BE composition. Any isotopic variation between the core and the mantle would have a significant impact on the overall BE isotopic composition. Recent work suggests that Cd is unlikely to undergo any significant isotope fractionation during the formation of the Earth's core (Pickard et al., 2023). Therefore, the core and mantle should have similar Cd isotopic composition, leading to the following BE isotope composition:

$$\delta^{114}Cd_{BE} = \delta^{114}Cd_{BSE} = 0.11 \pm 0.10\ ‰ \text{ (2SD, n = 28)}$$

6. Conclusions

This study determined the Cd isotope compositions of a large set of terrestrial rocks to provide a new estimate of $\delta^{114}Cd_{BSE}$. The Cd isotope compositions of 9 available rocky and biological standards were characterized using a ^{106}Cd-^{111}Cd double spike method, and the new data showed general agreement with the previous results. The isotope composition of the MORB samples indicated a remarkable isotopic homogeneity within an individual ridge, as

well as a great similarity between different ridges, with a proposed mean $\delta^{114}Cd_{MORB}$ of 0.07 ± 0.10 ‰ (2SD, n = 23). The mean isotope composition for pristine komatiites shows a value of 0.14 ± 0.18 ‰ (2SD, n = 5), and indicates that the Archean mantle has had a homogeneous Cd isotope composition since at least 3549 ± 99 Ma ago. By coupling these results, the study defined a new value for $\delta^{114}Cd_{BSE}$ of 0.11 ± 0.10 ‰ (2SD, n = 28) that can also be used to approximate the bulk Earth Cd isotope composition.

Acknowledgements:

We thank Fang Huang for providing the USTC AAS internal Cd standard. We thank Dimitri Rigoussen, Pascale Louvat, Marine Paquet and Tu-Han Luu for their help with chemical preparation of samples and mass-spectrometry. The manuscript greatly benefited from comprehensive and constructive reviews by Frank Wombacher and two anonymous reviewers and from editorial handling by Sonja Aulbach. This work was supported by the ERC grant agreement No. 101001282 (METAL) (F.M.).

7. References

Abouchami, W., Galer, S.J.G., de Baar, H.J.W., Middag, R., Vance, D., Zhao, Y., Klunder, M., Mezger, K., Feldmann, H., Andreae, M.O., 2014. Biogeochemical cycling of cadmium isotopes in the southern ocean along the zero meridian. Geochim. Cosmochim. Acta 127, 348–367. https://doi.org/10.1016/j.gca.2013.10.022

Abouchami, W., Galer, S.J.G., Horner, T.J., Rehkämper, M., Wombacher, F., Xue, Z., Lambelet, M., Gault-Ringold, M., Stirling, C.H., Schönbächler, M., Shiel, A.E., Weis, D., Holdship, P.F., 2013. A common reference material for cadmium isotope studies - NIST SRM 3108. Geostand. Geoanalytical Res. 37, 5–17. https://doi.org/10.1111/j.1751-908X.2012.00175.x

Arel, E., Tugrul, A., 2001. Weathering and its relation to geomechanical properties of Cavusbasi granitic rocks in northwestern Turkey. Bull. Eng. Geol. Environ. 60, 123–133. https://doi.org/10.1007/s100640000091

Aston, F.W., 1935. The isotopic constitution and atomic weights of hafnium, thorium, rhodium, titanium, zirconium, calcium, gallium, silver, carbon, nickel, cadmium, iron and indium. Proc. R. Soc. Lond. Ser. - Math. Phys. Sci. 149, 396–405. https://doi.org/10.1098/rspa.1935.0070

Aston, F.W., 1934. Mass-spectra and Isotopes. J. Phys. Chem. 38, 713–713. https://doi.org/10.1021/j150356a016

Badullovich, N., Moynier, F., Creech, J., Teng, F.-Z., Sossi, P.A., 2017. Tin isotopic fractionation during igneous differentiation and Earth's mantle composition. Geochem. Perspect. Lett. 5, 24–28. https://doi.org/10.7185/geochemlet.1741

Berglund, M., Wieser, M.E., 2011. Isotopic compositions of the elements 2009 (IUPAC Technical Report). Pure Appl. Chem. 83, 397–410. https://doi.org/10.1351/PAC-REP-10-06-02

Beunon, H., Mattielli, N., Doucet, L.S., Moine, B., Debret, B., 2020. Mantle heterogeneity through Zn systematics in oceanic basalts: Evidence for a deep carbon cycling. Earth-Sci. Rev. 205, 103174. https://doi.org/10.1016/j.earscirev.2020.103174

Böhlke, J.K., de Laeter, J.R., De Bièvre, P., Hidaka, H., Peiser, H.S., Rosman, K.J.R., Taylor, P.D.P., 2005. Isotopic compositions of the elements, 2001. J. Phys. Chem. Ref. Data 34, 57–67. https://doi.org/10.1063/1.1836764

Borovička, J., Ackerman, L., Rejšek, J., 2021. Cadmium isotopic composition of biogenic certified reference materials determined by thermal ionization mass spectrometry with double spike correction. Talanta 221, 121389. https://doi.org/10.1016/j.talanta.2020.121389

Braukmüller, N., Wombacher, F., Bragagni, A., Münker, C., 2020. Determination of Cu, Zn, Ga, Ag, Cd, In, Sn and Tl in geological reference materials and chondrites by isotope dilution ICP-MS. Geostand. Geoanalytical Res. 44, 733–752. https://doi.org/10.1111/ggr.12352

Braukmüller, N., Wombacher, F., Funk, C., Münker, C., 2019. Earth's volatile element depletion pattern inherited from a carbonaceous chondrite-like source. Nat. Geosci. 12, 564–568. https://doi.org/10.1038/s41561-019-0375-x

Byerly, B.L., Kareem, K., Bao, H., Byerly, G.R., 2017. Early Earth mantle heterogeneity revealed by light oxygen isotopes of Archaean komatiites. Nat. Geosci. 10, 871–875. https://doi.org/10.1038/ngeo3054

Chang, H., Zhu, J.-M., Wang, X., Gao, T., 2023. High-precision measurement of Cd isotopes in ultra-trace Cd samples using double spike-standard addition MC-ICP-MS. J. Anal. At. Spectrom. 38, 950–962. https://doi.org/10.1039/D3JA00047H

Chauvel, C., Dupré, B., Arndt, N.T., 1993. Pb and Nd isotopic correlation in Belingwe komatiites and basalts, in: Bickle, M.J., Nisbet, E.G. (Eds.), The Geology of the Belingwe Greenstone Belt, Zimbabwe: A Study of the Evolution of Archaean Continental Crust. CRC

Press, p. 8. https://doi.org/10.1201/9781003077596

Cloquet, C., Carignan, J., Libourel, G., Sterckeman, T., Perdrix, E., 2006. Tracing source pollution in soils using cadmium and lead isotopes. Environ. Sci. Technol. 40, 2525–2530. https://doi.org/10.1021/es052232+

Cloquet, C., Rouxel, O., Carignan, J., Libourel, G., 2005. Natural cadmium isotopic variations in eight geological reference materials (NIST SRM 2711, BCR 176, GSS-1, GXR-1, GXR-2, GSD-12, Nod-P-1, Nod-A-1) and anthropogenic samples, measured by MC-ICP-MS. Geostand. Geoanalytical Res. 29, 95–106. https://doi.org/10.1111/j.1751-908X.2005.tb00658.x

Connolly, B.D., Puchtel, I.S., Walker, R.J., Arevalo, R., Piccoli, P.M., Byerly, G., Robin-Popieul, C., Arndt, N., 2011. Highly siderophile element systematics of the 3.3Ga Weltevreden komatiites, South Africa: Implications for early Earth history. Earth Planet. Sci. Lett. 311, 253–263. https://doi.org/10.1016/j.epsl.2011.09.039

Conway, T.M., John, S.G., 2015. Biogeochemical cycling of cadmium isotopes along a high-resolution section through the North Atlantic Ocean. Geochim. Cosmochim. Acta 148, 269–283. https://doi.org/10.1016/j.gca.2014.09.032

Corfu, F., Noble, S.R., 1992. Genesis of the southern Abitibi greenstone belt, Superior Province, Canada: Evidence from zircon Hf isotope analyses using a single filament technique. Geochim. Cosmochim. Acta 56, 2081–2097. https://doi.org/10.1016/0016-7037(92)90331-C

Cortiade, N., Delacour, A., Guillaume, D., Moine, B., Chevet, J., 2022. Serpentinization of mantle xenoliths in Kerguelen archipelago: A first petrographic and geochemical study. Lithos 428–429, 106796. https://doi.org/10.1016/j.lithos.2022.106796

Creech, J.B., Paul, B., 2015. IsoSpike: improved double-spike inversion software. Geostand. Geoanalytical Res. 39, 7–15. https://doi.org/10.1111/j.1751-908X.2014.00276.x

Day, J.M.D., Moynier, F., Ishizuka, O., 2022. A partial melting control on the Zn isotope composition of basalts. Geochem. Perspect. Lett. 23, 11–16. https://doi.org/10.7185/geochemlet.2230

Druce, M., Stirling, C.H., Bostock, H.C., Rolison, J.M., 2022a. Examining the effects of chemical cleaning, leaching, and partial dissolution on zinc and cadmium isotope fractionation in marine carbonates. Chem. Geol. 592, 120738. https://doi.org/10.1016/j.chemgeo.2022.120738

Druce, M., Stirling, C.H., Bostock, H.C., Rolison, J.M., 2022b. Cadmium isotope systematics in sedimentary carbonate: Extending the utility of the cadmium isotope palaeo-productivity proxy. Geochim. Cosmochim. Acta 339, 80–96. https://doi.org/10.1016/j.gca.2022.10.041

Du, C., Hu, S., 2015. Accurate determination of trace cadmium in geological reference materials by closed vessel acid digestion ETAAS. At. Spectrosc. 36, 141–145. https://doi.org/10.46770/AS.2015.03.005

Dupré, B., Chauvel, C., Arndt, N.T., 1984. Pb and Nd isotopic study of two archean komatiitic flows from Alexo, Ontario. Geochim. Cosmochim. Acta 48, 1965–1972. https://doi.org/10.1016/0016-7037(84)90378-8

Emmermann, R., Puchelt, H., 1980. Major and trace element chemistry of basalts from holes 417D and 418A, deep sea drilling project legs 51-53, in: Powell, R., Laughter, F. (Eds.), Initial Reports of the Deep Sea Drilling Project, 51/52/53. U.S. Government Printing Office, pp. 987–1000.

Guinoiseau, D., Galer, S.J.G., Abouchami, W., 2018. Effect of cadmium sulphide precipitation on the partitioning of Cd isotopes: Implications for the oceanic Cd cycle. Earth Planet. Sci. Lett. 498, 300–308. https://doi.org/10.1016/j.epsl.2018.06.039

Helffrich, G.R., Wood, B.J., 2001. The Earth's mantle. Nature 412, 501–507.

https://doi.org/10.1038/35087500

Herzberg, C., 1992. Depth and degree of melting of komatiites. J. Geophys. Res. 97, 4521–4540. https://doi.org/10.1029/91JB03066

Hirschmann, M.M., Stolper, E.M., 1996. A possible role for garnet pyroxenite in the origin of the "garnet signature" in MORB. Contrib. Mineral. Petrol. 124, 185–208. https://doi.org/10.1007/s004100050184

Hofmann, A.W., 1997. Mantle geochemistry: the message from oceanic volcanism. Nature 385, 219–229. https://doi.org/10.1038/385219a0

Horner, T.J., Rickaby, R.E.M., Henderson, G.M., 2011. Isotopic fractionation of cadmium into calcite. Earth Planet. Sci. Lett. 312, 243–253. https://doi.org/10.1016/j.epsl.2011.10.004

Horner, T.J., Schönbächler, M., Rehkämper, M., Nielsen, S.G., Williams, H., Halliday, A.N., Xue, Z., Hein, J.R., 2010. Ferromanganese crusts as archives of deep water Cd isotope compositions: DATA BRIEF. Geochem. Geophys. Geosystems 11, n/a-n/a. https://doi.org/10.1029/2009GC002987

Huang, J., Chen, S., Zhang, X., Huang, F., 2018. Effects of Melt Percolation on Zn Isotope Heterogeneity in the Mantle: Constraints From Peridotite Massifs in Ivrea-Verbano Zone, Italian Alps. J. Geophys. Res. Solid Earth 123, 2706–2722. https://doi.org/10.1002/2017JB015287

Huppert, H.E., Stephen, R., Sparks, J., 1985. Cooling and contamination of mafic and ultramafic magmas during ascent through continental crust. Earth Planet. Sci. Lett. 74, 371–386. https://doi.org/10.1016/S0012-821X(85)80009-1

Inglis, E.C., Moynier, F., Creech, J., Deng, Z., Day, J.M.D., Teng, F.-Z., Bizzarro, M., Jackson, M., Savage, P., 2019. Isotopic fractionation of zirconium during magmatic differentiation and the stable isotope composition of the silicate Earth. Geochim. Cosmochim. Acta 250, 311–323.

https://doi.org/10.1016/j.gca.2019.02.010

Irfan, T.Y., 1999. Characterization of weathered volcanic rocks in Hong Kong. Q. J. Eng. Geol. Hydrogeol. 32, 317–348.

Kiseeva, E.S., Wood, B.J., 2013. A simple model for chalcophile element partitioning between sulphide and silicate liquids with geochemical applications. Earth Planet. Sci. Lett. 383, 68–81. https://doi.org/10.1016/j.epsl.2013.09.034

Kubik, E., Siebert, J., Blanchard, I., Agranier, A., Mahan, B., Moynier, F., 2021. Earth's volatile accretion as told by Cd, Bi, Sb and Tl core–mantle distribution. Geochim. Cosmochim. Acta 306, 263–280. https://doi.org/10.1016/j.gca.2021.02.017

Lahaye, Y., Arndt, N., 1996. Alteration of a komatiite flow from Alexo, Ontario, Canada. J. Petrol. 37, 1261–1284. https://doi.org/10.1093/petrology/37.6.1261

Lambart, S., Koornneef, J.M., Millet, M.-A., Davies, G.R., Cook, M., Lissenberg, C.J., 2019. Highly heterogeneous depleted mantle recorded in the lower oceanic crust. Nat. Geosci. 12, 482–486. https://doi.org/10.1038/s41561-019-0368-9

Li, D., Li, M.-L., Liu, W.-R., Qin, Z.-Z., Liu, S.-A., 2018. Cadmium isotope ratios of standard solutions and geological reference materials measured by MC-ICP-MS. Geostand. Geoanalytical Res. 42, 593–605. https://doi.org/10.1111/ggr.12236

Liu, D., Moynier, F., Siebert, J., Sossi, P.A., Hu, Y., Kubik, E., 2022. Origin of moderately volatile element depletion on differentiated bodies: Insights from the evaporation of indium from silicate melts. Geochim. Cosmochim. Acta 339, 46–57. https://doi.org/10.1016/j.gca.2022.09.043

Liu, D., Moynier, F., Sossi, P.A., Pik, R., Halldórsson, S.A., Inglis, E., Day, J.M.D., Siebert, J., 2023. The indium isotopic composition of the bulk silicate Earth. Geochim. Cosmochim. Acta 352, 24–35. https://doi.org/10.1016/j.gca.2023.04.018

Liu, M., Zhang, Q., Zhang, Y., Zhang, Z., Huang, F., Yu, H., 2020. High-precision Cd isotope measurements of soil and rock reference materials by MC-ICP-MS with double spike correction. Geostand. Geoanalytical Res. 44, 169–182. https://doi.org/10.1111/ggr.12291

Loss, R.D., Rosman, K.J.R., De Laeter, J.R., 1984. Mass spectrometric isotope dilution analyses of palladium, silver, cadmium and tellurium in carbonaceous chondrites. Geochim. Cosmochim. Acta 48, 1677–1681. https://doi.org/10.1016/0016-7037(84)90336-3

Lu, Z., Zhu, J., Tan, D., Wang, X., Zheng, Z., 2021. $\delta^{114/110}$ Cd values of a suite of different reference materials. Geostand. Geoanalytical Res. 45, 565–581. https://doi.org/10.1111/ggr.12380

Luck, J.-M., Othman, D.B., Albarède, F., 2005. Zn and Cu isotopic variations in chondrites and iron meteorites: Early solar nebula reservoirs and parent-body processes. Geochim. Cosmochim. Acta 69, 5351–5363. https://doi.org/10.1016/j.gca.2005.06.018

Luck, J.M., Othman, D.B., Barrat, J.A., Albarède, F., 2003. Coupled 63Cu and 16O excesses in chondrites. Geochim. Cosmochim. Acta 67, 143–151. https://doi.org/10.1016/S0016-7037(02)01038-4

Mahan, B., Siebert, J., Pringle, E.A., Moynier, F., 2017. Elemental partitioning and isotopic fractionation of Zn between metal and silicate and geochemical estimation of the S content of the Earth's core. Geochim. Cosmochim. Acta 196, 252–270. https://doi.org/10.1016/j.gca.2016.09.013

Marin, N., Righter, K., Danielson, L., Pando, K., Lee, C., 2013. Metal-silicate partitioning of Bi, In, and Cd as a function of temperature and melt composition. Presented at the 44th Lunar and Planetary Science Conference.

May, T.W., Wiedmeyer, R.H., 1998. A table of polyatomic interferences in ICP-MS. At. Spectrosc. 19, 150–155.

Mayhew, L.E., Ellison, E.T., 2020. A synthesis and meta-analysis of the Fe chemistry of serpentinites and serpentine minerals. Philos. Trans. R. Soc. Math. Phys. Eng. Sci. 378, 20180420. https://doi.org/10.1098/rsta.2018.0420

McDonough, W.F., 2014. Compositional model for the Earth's core, in: Holland, H.D., Turekian, K.K. (Eds.), Treatise on Geochemistry. Elsevier, pp. 559–577. https://doi.org/10.1016/B978-0-08-095975-7.00215-1

Millet, M.-A., Dauphas, N., Greber, N.D., Burton, K.W., Dale, C.W., Debret, B., Macpherson, C.G., Nowell, G.M., Williams, H.M., 2016. Titanium stable isotope investigation of magmatic processes on the Earth and Moon. Earth Planet. Sci. Lett. 449, 197–205. https://doi.org/10.1016/j.epsl.2016.05.039

Moynier, F., Le Borgne, M., 2015. High Precision Zinc Isotopic Measurements Applied to Mouse Organs. J. Vis. Exp. 52479. https://doi.org/10.3791/52479

Murphy, K., Rehkämper, M., Kreissig, K., Coles, B., Van De Flierdt, T., 2016. Improvements in Cd stable isotope analysis achieved through use of liquid–liquid extraction to remove organic residues from Cd separates obtained by extraction chromatography. J. Anal. At. Spectrom. 31, 319–327. https://doi.org/10.1039/C5JA00115C

Nier, A.O., 1936. A mass-spectrographic study of the isotopes of argon, potassium, rubidium, zinc and cadmium. Phys. Rev. 30, 403–407. https://doi.org/10.1002/jms.1190300303

Nisbet, E.G., Arndt, N.T., Bickle, M.J., Cameron, W.E., Chauvel, C., Cheadle, M., Hegner, E., Kyser, T.K., Martin, A., Renner, R., Roedder, E., 1987. Uniquely fresh 2.7 Ga komatiites from the Belingwe greenstone belt, Zimbabwe. Geology 15, 1147–1150. https://doi.org/10.1130/0091-7613(1987)15<1147:UFGKFT>2.0.CO;2

Ohira, I., Jackson, J.M., Sturhahn, W., Finkelstein, G.J., Kawazoe, T., Toellner, T.S., Suzuki, A., Ohtani, E., 2021. The influence of δ-(Al,Fe)OOH on seismic heterogeneities in Earth's

lower mantle. Sci. Rep. 11, 12036. https://doi.org/10.1038/s41598-021-91180-9

Pallavicini, N., Engström, E., Baxter, D.C., Öhlander, B., Ingri, J., Rodushkin, I., 2014. Cadmium isotope ratio measurements in environmental matrices by MC-ICP-MS. J Anal Spectrom 29, 1570–1584. https://doi.org/10.1039/C4JA00125G

Peng, H., Liu, P., Zheng, H., Belshaw, N.S., Hu, S., Zhu, Z., 2023. Cadmium isotope fractionation during adsorption onto calcite. Chem. Geol. 620, 121341. https://doi.org/10.1016/j.chemgeo.2023.121341

Pickard, H., Palk, E., Schönbächler, M., Moore, R.E.T., Coles, B.J., Kreissig, K., Nilsson-Kerr, K., Hammond, S.J., Takazawa, E., Hémond, C., Tropper, P., Barfod, D.N., Rehkämper, M., 2022. The cadmium and zinc isotope compositions of the silicate Earth – Implications for terrestrial volatile accretion. Geochim. Cosmochim. Acta 338, 165–180. https://doi.org/10.1016/j.gca.2022.09.041

Pickard, H., Palk, E., Wood, B.J., Rehkämper, M., 2023. Cadmium isotope fractionation during metal-silicate partitioning – Results and implications for Earth's volatile accretion. Chem. Geol. 618, 121293. https://doi.org/10.1016/j.chemgeo.2022.121293

Pringle, E.A., Moynier, F., 2017. Rubidium isotopic composition of the Earth, meteorites, and the Moon: Evidence for the origin of volatile loss during planetary accretion. Earth Planet. Sci. Lett. 473, 62–70. https://doi.org/10.1016/j.epsl.2017.05.033

Pringle, E.A., Moynier, F., Beck, P., Paniello, R., Hezel, D.C., 2017. The origin of volatile element depletion in early solar system material: Clues from Zn isotopes in chondrules. Earth Planet. Sci. Lett. 468, 62–71. https://doi.org/10.1016/j.epsl.2017.04.002

Pritzkow, W., Wunderli, S., Vogl, J., Fortunato, G., 2007. The isotope abundances and the atomic weight of cadmium by a metrological approach. Int. J. Mass Spectrom. 261, 74–85. https://doi.org/10.1016/j.ijms.2006.07.026

Puchtel, I.S., Blichert-Toft, J., Horan, M.F., Touboul, M., Walker, R.J., 2022. The komatiite testimony to ancient mantle heterogeneity. Chem. Geol. 594, 120776. https://doi.org/10.1016/j.chemgeo.2022.120776

Puchtel, I.S., Blichert-Toft, J., Touboul, M., Horan, M.F., Walker, R.J., 2016. The coupled ^{182}W- ^{142}Nd record of early terrestrial mantle differentiation: Early mantle differentiation. Geochem. Geophys. Geosystems 17, 2168–2193. https://doi.org/10.1002/2016GC006324

Puchtel, I.S., Blichert-Toft, J., Touboul, M., Walker, R.J., 2018. 182W and HSE constraints from 2.7 Ga komatiites on the heterogeneous nature of the Archean mantle. Geochim. Cosmochim. Acta 228, 1–26. https://doi.org/10.1016/j.gca.2018.02.030

Puchtel, I.S., Blichert-Toft, J., Touboul, M., Walker, R.J., Byerly, G.R., Nisbet, E.G., Anhaeusser, C.R., 2013. Insights into early Earth from Barberton komatiites: Evidence from lithophile isotope and trace element systematics. Geochim. Cosmochim. Acta 108, 63–90. https://doi.org/10.1016/j.gca.2013.01.016

Puchtel, I.S., Hofmann, A.W., Mezger, K., Jochum, K.P., Shchipansky, A.A., Samsonov, A.V., 1998. Oceanic plateau model for continental crustal growth in the Archaean: A case study from the Kostomuksha greenstone belt, NW Baltic Shield. Earth Planet. Sci. Lett. 155, 57–74. https://doi.org/10.1016/S0012-821X(97)00202-1

Puchtel, I.S., Humayun, M., 2005. Highly siderophile element geochemistry of 187Os-enriched 2.8 Ga Kostomuksha komatiites, Baltic Shield. Geochim. Cosmochim. Acta 69, 1607–1618. https://doi.org/10.1016/j.gca.2004.09.007

Puchtel, I.S., Humayun, M., Campbell, A.J., Sproule, R.A., Lesher, C.M., 2004. Platinum group element geochemistry of komatiites from the Alexo and Pyke Hill areas, Ontario, Canada. Geochim. Cosmochim. Acta 68, 1361–1383. https://doi.org/10.1016/j.gca.2003.09.013

Puchtel, I.S., Walker, R.J., Anhaeusser, C.R., Gruau, G., 2009. Re–Os isotope systematics and HSE abundances of the 3.5 Ga Schapenburg komatiites, South Africa: Hydrous melting or prolonged survival of primordial heterogeneities in the mantle? Chem. Geol. 262, 355–369. https://doi.org/10.1016/j.chemgeo.2009.02.006

Rehkämper, M., Halliday, A.N., Fitton, J.G., Lee, D.-C., Wieneke, M., Arndt, N.T., 1999. Ir, Ru, Pt, and Pd in basalts and komatiites: new constraints for the geochemical behavior of the platinum-group elements in the mantle. Geochim. Cosmochim. Acta 63, 3915–3934. https://doi.org/10.1016/S0016-7037(99)00219-7

Righter, K., Pando, K., Marin, N., Ross, D.K., Righter, M., Danielson, L., Lapen, T.J., Lee, C., 2018. Volatile element signatures in the mantles of Earth, Moon, and Mars: Core formation fingerprints from Bi, Cd, In, and Sn. Meteorit. Planet. Sci. 53, 284–305. https://doi.org/10.1111/maps.13005

Ripperger, S., Rehkämper, M., 2007. Precise determination of cadmium isotope fractionation in seawater by double spike MC-ICPMS. Geochim. Cosmochim. Acta 71, 631–642. https://doi.org/10.1016/j.gca.2006.10.005

Robson, T.C., Braungardt, C.B., Rieuwerts, J., Worsfold, P., 2014. Cadmium contamination of agricultural soils and crops resulting from sphalerite weathering. Environ. Pollut. 184, 283–289. https://doi.org/10.1016/j.envpol.2013.09.001

Rosman, Barnes, I.L., Moore, L.J., Gramlich, J.W., 1980a. Isotope composition of Cd, Ca and Mg in the Brownfield chondrite. Geochem. J. 14, 269–277. https://doi.org/10.2343/geochemj.14.269

Rosman, De Laeter, J.R., 1988. Cadmium mass fractionation in unequilibrated ordinary chondrites. Earth Planet. Sci. Lett. 89, 163–169. https://doi.org/10.1016/0012-821X(88)90168-9

Rosman, De Laeter, J.R., 1978. A survey of cadmium isotopic abundances. J. Geophys. Res. 83, 1279. https://doi.org/10.1029/JB083iB03p01279

Rosman, De Laeter, J.R., 1976. Isotopic fractionation in meteoritic cadmium. Nature 261, 216–218. https://doi.org/10.1038/261216a0

Rosman, De Laeter, J.R., 1975. The isotopic composition of cadmium in terrestrial minerals. Int. J. Mass Spectrom. Ion Phys. 16, 385–394. https://doi.org/10.1016/0020-7381(75)85027-3

Rosman, De Laeter, J.R., 1974a. The abundance of cadmium and zinc in meteorites. Geochim. Cosmochim. Acta 38, 1665–1677. https://doi.org/10.1016/0016-7037(74)90184-7

Rosman, De Laeter, J.R., 1974b. Mass spectrometric isotope dilution analyses of cadmium in standard rocks. Chem. Geol. 13, 69–74. https://doi.org/10.1016/0009-2541(74)90051-5

Rosman, De Laeter, J.R., Gorton, M.P., 1980b. Cadmium isotope fractionation in fractions of two H3 chondrites. Earth Planet. Sci. Lett. 48, 166–170. https://doi.org/10.1016/0012-821X(80)90179-X

Rudge, J.F., Reynolds, B.C., Bourdon, B., 2009. The double spike toolbox. Chem. Geol. 265, 420–431. https://doi.org/10.1016/j.chemgeo.2009.05.010

Rudnick, R.L., 1995. Making continental crust. Nature 378, 571–578. https://doi.org/10.1038/378571a0

Rudnick, R.L., Gao, S., 2014. Composition of the continental crust, in: Holland, H.D., Turekian, K.K. (Eds.), Treatise on Geochemistry. Elsevier, pp. 1–51. https://doi.org/10.1016/B978-0-08-095975-7.00301-6

Sands, D.G., Rosman, K.J.R., De Laeter, J.R., 2001. A preliminary study of cadmium mass fractionation in lunar soils. Earth Planet. Sci. Lett. 186, 103–111. https://doi.org/10.1016/S0012-821X(01)00233-3

Schediwy, S., Rosman, K.J.R., de Laeter, J.R., 2006. Isotope fractionation of cadmium in lunar

material. Earth Planet. Sci. Lett. 243, 326–335. https://doi.org/10.1016/j.epsl.2006.01.007

Schmitt, A.-D., Galer, S.J.G., Abouchami, W., 2009a. Mass-dependent cadmium isotopic variations in nature with emphasis on the marine environment. Earth Planet. Sci. Lett. 277, 262–272. https://doi.org/10.1016/j.epsl.2008.10.025

Schmitt, A.-D., Galer, S.J.G., Abouchami, W., 2009b. High-precision cadmium stable isotope measurements by double spike thermal ionisation mass spectrometry. J. Anal. At. Spectrom. 24, 1079. https://doi.org/10.1039/b821576f

She, J.-X., Kubik, E., Li, W., Moynier, F., 2023. Stable Sn isotope signatures of mid-ocean ridge basalts. Chem. Geol. 622, 121347. https://doi.org/10.1016/j.chemgeo.2023.121347

Steenstra, E.S., Dankers, D., Berndt, J., Klemme, S., Matveev, S., van Westrenen, W., 2019. Significant depletion of volatile elements in the mantle of asteroid Vesta due to core formation. Icarus 317, 669–681. https://doi.org/10.1016/j.icarus.2018.08.020

Steenstra, E.S., Seegers, A.X., Putter, R., Berndt, J., Klemme, S., Matveev, S., Bullock, E.S., van Westrenen, W., 2020. Metal-silicate partitioning systematics of siderophile elements at reducing conditions: A new experimental database. Icarus 335, 113391. https://doi.org/10.1016/j.icarus.2019.113391

Stenvinkel, G., Svensson, E., 1935. Band Spectroscopic Observations of the Isotopes of Zinc and Cadmium. Nature 135, 955–955. https://doi.org/10.1038/135955a0

Sueoka, T.I.K.L., Lee, I.K., Muramatsu, M., Imamura, S., 1985. Geomechanical properties and engineering classification for decomposed granite soils in Kaduna district, Nigeria. Presented at the international conference on geomechanics in tropical lateritic and saprolitic soils, Brasilia, pp. 175–186.

Svensson, E., 1933. Isotope Effect in the Spectrum of Cadmium Hydride. Nature 131, 28–28. https://doi.org/10.1038/131028c0

Tamblyn, R., Hermann, J., Hasterok, D., Sossi, P., Pettke, T., Chatterjee, S., 2023. Hydrated komatiites as a source of water for TTG formation in the Archean. Earth Planet. Sci. Lett. 603, 117982. https://doi.org/10.1016/j.epsl.2022.117982

Tan, D., Zhu, J.-M., Wang, X., Han, G., Lu, Z., Xu, W., 2020. High-sensitivity determination of Cd isotopes in low-Cd geological samples by double spike MC-ICP-MS. J. Anal. At. Spectrom. 35, 713–727. https://doi.org/10.1039/C9JA00397E

Teng, F.-Z., Dauphas, N., Helz, R.T., 2008. Iron Isotope Fractionation During Magmatic Differentiation in Kilauea Iki Lava Lake. Science 320, 1620–1622. https://doi.org/10.1126/science.1157166

Tugrul, A., Gurpinar, O., 1997. The effect of chemical weathering on the engineering properties of eocene basalts in northeastern Turkey. Environ. Eng. Geosci. 3, 225–234. https://doi.org/10.2113/gseegeosci.III.2.225

Van Keken, P.E., Hauri, E.H., Ballentine, C.J., 2002. Mantle mixing: the generation, preservation, and destruction of chemical heterogeneity. Annu. Rev. Earth Planet. Sci. 30, 493–525. https://doi.org/10.1146/annurev.earth.30.091201.141236

Van Kooten, E., Moynier, F., 2019. Zinc isotope analyses of singularly small samples (<5 ng Zn): Investigating chondrule-matrix complementarity in Leoville. Geochim. Cosmochim. Acta 261, 248–268. https://doi.org/10.1016/j.gca.2019.07.022

Vlastelic, I., Piro, J., 2022. Volatilisation of trace elements during evaporation to dryness of HF-dissolved silicates (BHVO-2, AGV-1, BIR-1, UB-N): open- versus closed-system conditions. Geostand. Geoanalytical Res. 46, 519–534. https://doi.org/10.1111/ggr.12428

Wang, H.S., Lineweaver, C., Ireland, T., 2018. The elemental abundances (with uncertainties) of the most Earth-like planet. Icarus 299, 460–474. https://doi.org/10.1016/j.icarus.2017.08.024

Wang, Z., Becker, H., Wombacher, F., 2015. Mass fractions of S, Cu, Se, Mo, Ag, Cd, In, Te, Ba, Sm, W, Tl and Bi in geological reference materials and selected carbonaceous chondrites determined by isotope dilution ICP-MS. Geostand. Geoanalytical Res. 39, 185–208. https://doi.org/10.1111/j.1751-908X.2014.00312.x

Wang, Z., Laurenz, V., Petitgirard, S., Becker, H., 2016. Earth's moderately volatile element composition may not be chondritic: Evidence from In, Cd and Zn. Earth Planet. Sci. Lett. 435, 136–146. https://doi.org/10.1016/j.epsl.2015.12.012

Wasylenki, L.E., Swihart, J.W., Romaniello, S.J., 2014. Cadmium isotope fractionation during adsorption to Mn oxyhydroxide at low and high ionic strength. Geochim. Cosmochim. Acta 140, 212–226. https://doi.org/10.1016/j.gca.2014.05.007

Wen, H., Zhang, Y., Cloquet, C., Zhu, C., Fan, H., Luo, C., 2015. Tracing sources of pollution in soils from the Jinding Pb–Zn mining district in China using cadmium and lead isotopes. Appl. Geochem. 52, 147–154. https://doi.org/10.1016/j.apgeochem.2014.11.025

Willbold, M., Elliott, T., 2017. Molybdenum isotope variations in magmatic rocks. Chem. Geol. 449, 253–268. https://doi.org/10.1016/j.chemgeo.2016.12.011

Willbold, M., Hibbert, K., Lai, Y.-J., Freymuth, H., Hin, R.C., Coath, C., Vils, F., Elliott, T., 2016. High-precision mass-dependent molybdenum isotope variations in magmatic rocks determined by double-spike MC-ICP-MS. Geostand. Geoanalytical Res. n/a-n/a. https://doi.org/10.1111/ggr.12109

Witt-Eickschen, G., Palme, H., O'Neill, H.St.C., Allen, C.M., 2009. The geochemistry of the volatile trace elements As, Cd, Ga, In and Sn in the Earth's mantle: New evidence from in situ analyses of mantle xenoliths. Geochim. Cosmochim. Acta 73, 1755–1778. https://doi.org/10.1016/j.gca.2008.12.013

Wombacher, F., Rehkämper, M., Mezger, K., 2004. Determination of the mass-dependence of

cadmium isotope fractionation during evaporation. Geochim. Cosmochim. Acta 68, 2349–2357. https://doi.org/10.1016/j.gca.2003.12.013

Wombacher, F., Rehkämper, M., Mezger, K., Bischoff, A., Münker, C., 2008. Cadmium stable isotope cosmochemistry. Geochim. Cosmochim. Acta 72, 646–667. https://doi.org/10.1016/j.gca.2007.10.024

Wombacher, F., Rehkämper, M., Mezger, K., Münker, C., 2003. Stable isotope compositions of cadmium in geological materials and meteorites determined by multiple-collector ICPMS. Geochim. Cosmochim. Acta 67, 4639–4654. https://doi.org/10.1016/S0016-7037(03)00389-2

Wood, B.J., Kiseeva, E.S., Mirolo, F.J., 2014. Accretion and core formation: The effects of sulfur on metal–silicate partition coefficients. Geochim. Cosmochim. Acta 145, 248–267. https://doi.org/10.1016/j.gca.2014.09.002

Wood, B.J., Smythe, D.J., Harrison, T., 2019. The condensation temperatures of the elements: A reappraisal. Am. Mineral. 104, 844–856. https://doi.org/10.2138/am-2019-6852CCBY

Wood, D.A., Tarney, J., Varet, J., Saunders, A.D., Bougault, H., Joron, J.L., Treuil, M., Cann, J.R., 1979. Geochemistry of basalts drilled in the North Atlantic by IPOD Leg 49: Implications for mantle heterogeneity. Earth Planet. Sci. Lett. 42, 77–97. https://doi.org/10.1016/0012-821X(79)90192-4

Xie, R.C., Rehkämper, M., Grasse, P., Van De Flierdt, T., Frank, M., Xue, Z., 2019. Isotopic evidence for complex biogeochemical cycling of Cd in the eastern tropical South Pacific. Earth Planet. Sci. Lett. 512, 134–146. https://doi.org/10.1016/j.epsl.2019.02.001

Xu, Q., Guo, W., Jin, L., Guo, Q., Hu, S., 2015. Determination of cadmium in geological samples by aerosol dilution ICP-MS after inverse aqua regia extraction. J. Anal. At. Spectrom. 30, 2010–2016. https://doi.org/10.1039/C5JA00182J

Yi, W., Halliday, A.N., Alt, J.C., Lee, D.-C., Rehkämper, M., Garcia, M.O., Langmuir, C.H.,

Su, Y., 2000. Cadmium, indium, tin, tellurium, and sulfur in oceanic basalts: Implications for chalcophile element fractionation in the Earth. J. Geophys. Res. Solid Earth 105, 18927–18948. https://doi.org/10.1029/2000JB900152

Yoder, C.F., 1995. Astrometric and geodetic properties of Earth and the solar system, in: Ahrens, T.J. (Ed.), Global Earth Physics - A Handbook of Physical Constants, AGU Reference Shelf. American geophysical union, Washington, D. C., pp. 1–31. https://doi.org/10.1029/RF001p0001

Zhang, Y., Wen, H., Zhu, C., Fan, H., Luo, C., Liu, J., Cloquet, C., 2016. Cd isotope fractionation during simulated and natural weathering. Environ. Pollut. 216, 9–17. https://doi.org/10.1016/j.envpol.2016.04.060

Zhou, D., Cao, S., Liu, J., Li, X., Dong, Y., Neubauer, F., Bai, J., Li, H., 2022. Carbonation and serpentinization of diopsidite in the Altun Mountains, NW China. Sci. Rep. 12, 21361. https://doi.org/10.1038/s41598-022-25612-5

Zhu, C., Wen, H., Zhang, Y., Yin, R., Cloquet, C., 2018. Cd isotope fractionation during sulfide mineral weathering in the Fule Zn-Pb-Cd deposit, Yunnan Province, Southwest China. Sci. Total Environ. 616–617, 64–72. https://doi.org/10.1016/j.scitotenv.2017.10.293

Chapter 4 – Cadmium isotope fractionation during fractional crystallization

1. Introduction

Magmatic differentiation refers to the ensemble of processes modifying the bulk chemical composition of a magma. The main cause for this to happen are partial melting and fractional crystallization. The minerals precipitated during fractional crystallization are usually poorer in silica than the melt, leading the magma to evolve toward a SiO_2-enriched composition. This silica enrichment increases the melt viscosity and modifies the eruptive dynamism of connected volcanos, going from flows of fluid lava to explosive dynamism. Other mechanisms can alter magma bulk chemistry and cause magma differentiation, mainly mixing between two chemically distinct magmas and assimilation of material from the magmatic chamber walls. These last two mechanisms have predictable influences on the chemical and isotope compositions of the magma, as its final composition is determined by a simple mixing equation. Fractional crystallization, however, can have much more complex influence over the magma isotope and chemical compositions as the studied element is fractionated between numerous different minerals. Although it is theoretically possible to predict the influence of fractional crystallization by determining the partition coefficients of a given element or isotope for every mineral expected to crystallize, it would require to know the isotopic fractionation factors for all crystallizing phases, which is not the case for Cd. It is therefore more practical to analyze erupted lavas spanning the whole compositional field and to determine the element behavior from these.

A few volcanic systems allow for the study of a differentiating magma from basalts to rhyolites. Among these stands the Hekla volcano, a unique specimen in Iceland because of its important production of silicic lavas. Hekla is also characterized by a specific eruptive dynamism, as every eruption starts with rhyolitic material extruded in explosive phases and

ends with effusive expulsion of fluid basaltic andesites (Thorarinsson, 1967, 1950). Moreover, the initial silica content of the ejected lavas and the explosivity of individual eruptions increase with the repose time between eruptions (Thorarinsson, 1967).

Two families of model are in competition to explain this unusual dynamism as well as the wide range of chemical compositions found in Hekla lavas:

Models from the first group assess that all of the Hekla series can be formed with only fractional crystallization as a magma differentiating mechanism (Baldridge et al., 1973; Geist et al., 2021). According to Geist et al. (2021), a 30 % fractional crystallization, forming 4.2 % olivine, 12.8 % plagioclase, 6.1 % augite, 4 % magnetite, 2 % apatite and 1.1 % ilmenite would be enough to make Hekla basaltic andesites evolves into andesites. Similarly, dacites would be formed from andesites by a 12 % fractional crystallization (2.3 % olivine, 6.8 % plagioclase, 1.1 % augite, 1 % magnetite, 0.4 % apatite, 0.4 % ilmenite). Rhyolites would be then formed by fractional crystallization from dacites. The authors found no significant evidence for magma mixing or crustal assimilation. In this model, the silicic compositions of the first lavas erupted and the correlation between the repose duration and their silica content are explained by the unusual geometry of Hekla's magma chamber. Specifically, the magma is thought to be stored in a vertical macrodike, in which cooling by contact with the walls would favorize intense fractional crystallization, thus, important production of silicic lavas at the contact with the roof of the magma chamber.

The models from the other family argue that fractional crystallization cannot account on its own for all the observed compositions and propose that the silicic lavas extruded by Mt. Hekla are formed by assimilation of silica-rich material from the crust and mixing with a less evolved magma (Chekol et al., 2011; Lucic et al., 2016; Sigmarsson et al., 1992). One variation of this scenario, proposed in Sigmarsson et al. (1992), assesses that the fresh magma injected in the magmatic chamber is a Fe-Ti basalt. This basaltic melt already presents traces of magmatic

evolution, like low MgO and Ni contents, which are thought to be caused by an early crustal contamination. The basaltic magma evolves by fractional crystallization until it has a basaltic andesite composition. This new magma is then mixed with a dacitic melt assimilated from the chamber walls, leading to the formation of the andesitic lavas observed during eruptions. Eventually, some pockets of dacitic magma would remain unmixed with the rest. This dacitic melt is thought to evolve into a rhyolitic one by fractional crystallization.

Another model, proposed in 2011, modifies slightly the formation scenario for the andesitic lavas (Chekol et al., 2011). Similarly to the first model, the fresh magma is thought to be of basaltic composition. This magma evolves by fractional crystallization (13 % olivine, 40 % clinopyroxene, 32 % plagioclase and 15 % Fe-Ti oxides) until reaching the composition of the least evolved basaltic andesites. From the basaltic andesites to the most evolved andesites, fractional crystallization only is not enough to fit the observations. The main difference with the 1992 model lies in the fact that andesites are not formed by simple mixing with a dacitic melt but by a combination of mixing with a dacitic melt and fractional crystallization. The dacites are obtained by melting the crustal rocks surrounding the magma chamber. Finally, rhyolite compositions are formed by fractional crystallization from the dacitic magma. In these models, the longer the volcano remains dormant between two eruptions, the more dacitic melt will be obtained by assimilation of the crust and the more rhyolites will be formed by fractional crystallization; thus, the more silicic material will be extruded and the more explosive the eruptive dynamism will be.

Because of the importance of fractional crystallization in the establishment of the observed lavas compositions, samples from the Hekla volcano have been used to characterize the isotope fractionation accompanying this magma differentiation process for different elements. A majority of the investigated elements (Mo, Zn, K, Tl, Ba, Rb, Cl and Li) did not show any significant isotope fractionation correlated with fractional crystallization for Hekla samples

(Bai et al., 2022; Chen et al., 2013; Prytulak et al., 2017a; Ranta et al., 2021; Schuessler et al., 2009; Tuller-Ross et al., 2019; Wang et al., 2023; Yang et al., 2015). On the other hand, Ti, Zr, Fe, Si and V are characterized by evolving isotope compositions along the Hekla differentiation suite (Deng et al., 2019; Inglis et al., 2019; Prytulak et al., 2017b; Savage et al., 2011; Schuessler et al., 2009; Yuan et al., 2022), indicating influence from fractional crystallization processes.

Table 1: Comparison of the solid-liquid partition coefficients of Cd for different minerals

Mineral family	Mineral	D (solid-liquid)	Global chemistry	Source
Feldspar	Plagioclase - Albite 60%	9	Ferrogabbro	Vincent and Bilefield (1960)
	Plagioclase	0.7	Alkali basalt series	Dostal et al. (1979)
	Plagioclase	5.5	Ignimbrites	Dostal et al. (1979)
	K feldspar - Sanidine	2.95	Ignimbrites	Dostal et al. (1979)
Clinopyroxene	Pigeonite	27	Ferrogabbro	Vincent and Bilefield (1960)
	Clinopyroxene	0.2	Alkali basalt series	Dostal et al. (1979)
	Augite	0.34	Picrite (Kilauea Iki)	Greaney et al. (2017)
Olivine	Fayalite 60%	23	Ferrogabbro	Vincent and Bilefield (1960)
	Olivine	0.83	Picrite (Kilauea Iki)	Greaney et al. (2017)
Fe-Ti oxides	Titanomagnetite	19	Ferrogabbro	Vincent and Bilefield (1960)
	Titanomagnetite	0.05	Alkali basalt series	Dostal et al. (1979)
	Pseudobrookite	1.05	Picrite (Kilauea Iki)	Greaney et al. (2017)
	Ilmenite	8	Ferrogabbro	Vincent and Bilefield (1960)
	Ilmenite	0.97	Picrite (Kilauea Iki)	Greaney et al. (2017)
Sulfides	Cu-Fe Sulfides	<1	Ferrogabbro	Vincent and Bilefield (1960)
	Cu Sulfides*	380	Picrite (Kilauea Iki)	Greaney et al. (2017)

Depending on the overall chemistry of the rock, Cd is characterized by very distinct behaviors, oscillating between enrichment or depletion compared to the melt.

Few studies have focused on the behavior of Cd during fractional crystallization and all of these works only studied Cd concentrations (Dostal et al., 1979; Greaney et al., 2017; Vincent and Bilefield, 1960) and not its isotopic composition. The Cd behavior in magma seems to be strongly determined by the magma chemical composition, as the results of these 3 articles are sometimes at odds with each other. The two most recent studies provide us with solid-liquid partition coefficients ($D_{Cd\ solid/liquid} = \frac{[Cd]_{solid}}{[Cd]_{liquid}}$) while Vincent and Bilefield (1960) only provides concentrations. Nevertheless, we can determine D_{Cd} for this study, based on the Cd concentrations of minerals and on the knowledge that the minerals Cd content accounts for 60% of the whole rock Cd content. The partition coefficients are compared in Table 1 and show that

Cd behavior evolves greatly depending on the whole rock chemistry, as every listed mineral family is characterized by both <1 and >1 partition coefficients.

2. Samples

The Mt. Hekla is a 10 Km long edifice that has formed by ejection of lavas along a 5-6 Km long fissure within the last 3000 years. Eighteen eruptions have occurred in historic times, with the most recent in the year 2000. As discussed previously, the edifice is formed by accumulation of lavas ranging from basaltic andesites to rhyolites. Although the Mt. Hekla only erupted basaltic andesites or lavas that are more evolved, with no basalt known, sub-parallel surrounding fissures are known to have erupted significant amounts of basalts as recently as 1913. Despite being chemically distinct from Hekla lavas, these basalts are considered as related to Hekla magma based on their transitional alkalic character and on their geochemical likeness to the Hekla samples (Jakobsson, 1979; Sigmarsson et al., 1992). We used these basalts as a way to study the composition of the initial melt of Hekla, before it evolved into basaltic andesites by fractional crystallization.

For this work, we analyzed a set of 18 samples from the Hekla volcano as well as from the basaltic flows connected to the network of surrounding sub-parallel fissures. Most of our samples have already been described in published works (Bai et al., 2022; Wang et al., 2023), but we joined here their sampling locations and chemical compositions for major and trace elements nonetheless (see Table 2). All of our samples come from pre-historic formations. In detail, we analyzed 8 basalts, 5 basaltic andesites, 2 andesites, 2 dacites and one rhyolite. These samples span a wide range of compositions, with SiO_2 content ranging from 41 to 74 wt. % and MgO concentrations being comprised between 8 and 0 wt. %. The samples are generally fresh, showing little signs of secondary alteration (Chekol et al., 2011; Geist et al., 2021; Sigmarsson

et al., 1992), although some degassing might have occurred (Oskarsson et al., 1982), which could have influenced significantly Cd concentrations and isotope compositions.

Table 2: Location, description and chemical compositions of the samples

Sample	TAS rock type	Latitude (N)	Longitude (E)	SiO2 (wt.%)	TiO2 (wt.%)	Al2O3 (wt.%)	Fe2O3 (wt.%)	MgO (wt.%)	2SD (abs)	CaO (wt.%)	Na2O (wt.%)
ICE 20-31	Basalt	64.05244	-19.69265	43.58	2.26	17.73	13.63	8.04	0.099	11.32	2.61
ICE 20-28	Basalt	64.14758	-19.52250	42.42	4.02	14.84	16.96	7.06	0.054	10.38	3.02
ICE 20-27	Basalt	63.82916	-20.09704	40.67	3.78	15.79	18.35	6.96	0.069	9.83	3.31
ICE 20-37	Basalt	63.82597	-20.01850	41.93	3.73	15.54	17.68	6.83	0.096	9.79	3.18
ICE 20-41	Basalt	64.05266	-19.69201	42.67	4.28	14.67	17.35	6.57	0.007	10.06	3.01
ICE 20-22	Basalt	63.95842	-19.98367	45.07	3.75	13.96	18.14	5.48	0.041	9.41	2.88
ICE 20-36	Basalt	63.82633	-20.04412	48.13	3.51	13.45	17.20	4.89	0.016	8.84	2.77
ICE 20-45	Basalt	64.04855	-19.56473	47.66	3.04	15.48	15.02	4.52	0.012	8.12	4.02
ICE 20-40	Basaltic andesite	64.05257	-19.69198	51.34	1.98	16.29	13.24	3.39	0.03	6.91	4.27
				51.02	1.98	16.37	13.34	3.40	0.03	6.97	4.32
				51.18	1.98	16.33	13.29	3.39	0.00	6.94	4.29
ICE 20-44	Basaltic andesite	64.07573	-19.61344	50.87	2.04	16.10	13.49	3.38	0.03	6.94	4.54
				47.53	2.20	16.43	14.58	3.72	0.01	7.71	4.99
				49.20	2.12	16.27	14.04	3.55	0.48	7.33	4.76
ICE 20-34	Basaltic andesite	64.02565	-19.73649	51.19	1.94	16.40	13.04	3.24	0.016	6.99	4.58
ICE 20-19	Basaltic andesite	63.99697	-19.90464	51.30	1.88	16.29	13.27	3.24	0.006	6.73	4.64
ICE 20-23	Basaltic andesite	63.95866	-19.97375	51.98	1.82	16.00	13.09	3.04	0.02	6.57	4.87
				52.95	1.75	15.82	12.82	2.80	0.03	6.49	4.85
				52.47	1.79	15.91	12.95	2.92	0.34	6.53	4.86
ICE 20-24	Andesite	63.93778	-19.95694	54.61	1.72	14.90	12.65	2.85	0.02	6.19	4.57
				52.35	1.78	15.81	13.38	2.77	0.01	6.64	4.69
				53.48	1.75	15.35	13.01	2.81	0.12	6.42	4.63
ICE 20-35	Andesite	64.02916	-19.74244	54.50	1.32	17.18	11.36	2.25	0.022	5.78	5.19
ICE 20-39	Dacite	64.05267	-19.69190	65.77	0.38	16.53	5.36	0.28	0.01	2.97	5.99
				66.91	0.37	16.15	5.14	0.29	0.00	2.80	5.71
				66.34	0.37	16.34	5.25	0.29	0.01	2.89	5.85
ICE 20-32	Dacite	64.05200	-19.69698	66.56	0.31	16.73	4.87	0.28	0.005	2.76	5.88
ICE 20-33	Rhyolite	64.05246	-19.70048	74.42	0.13	13.23	2.37	0.02	0.001	1.24	5.61

The chemical compositions were obtained by Q-ICP-MS measurements. Silica content was calculated from the major elements' concentrations. The samples are ordained from the MgO-richest to the MgO-poorest. Analyses in grey are replicates for the same sample, a mean of these compositions is provided below when replicates were available.

Table 2 (continued)

Sample	TAS rock type	K2O (wt.%)	MnO (wt.%)	P2O5 (wt.%)	Li (ppm)	Be (ppm)	B (ppm)	Ti (ppm)	V (ppm)	Cr (ppm)	Co (ppm)	Ni (ppm)	Cu (ppm)	Zn (ppm)
ICE 20-31	Basalt	0.39	0.18	0.25	3.890	0.895	3.772	2.262	312.080	50.479	56.293	113.346	124.599	96.370
ICE 20-28	Basalt	0.55	0.24	0.50	6.930	1.437	3.905	4.020	375.748	55.215	52.748	45.977	78.594	146.565
ICE 20-27	Basalt	0.58	0.25	0.50	7.354	1.444	3.028	3.777	444.907	23.219	57.301	54.568	153.651	167.282
ICE 20-37	Basalt	0.58	0.24	0.51	7.140	1.485	3.586	3.725	414.126	23.381	54.919	55.294	120.924	155.679
ICE 20-41	Basalt	0.58	0.25	0.56	6.698	1.422	5.496	4.281	388.555	33.792	52.723	36.314	67.419	153.738
ICE 20-22	Basalt	0.57	0.24	0.49	6.999	1.487	2.597	3.755	464.646	25.232	58.081	60.929	168.011	165.428
ICE 20-36	Basalt	0.54	0.23	0.44	6.651	1.436	3.494	3.511	432.507	27.162	55.876	59.794	176.213	151.665
ICE 20-45	Basalt	0.95	0.28	0.90	10.368	2.460	3.668	3.041	160.493	0.369	27.521	0.636	8.844	188.089
ICE 20-40	Basaltic andesite	1.18	0.28	1.12	14.59	2.76	5.27	1.98	60.21	0.28	18.09	0.37	10.62	196.19
		1.19	0.28	1.13	14.85	2.89	5.74	1.98	60.91	3.16	18.02	0.30	10.68	195.79
		1.18	0.28	1.13	14.72	2.83	5.51	1.98	60.56	1.72	18.05	0.33	10.65	195.99
ICE 20-44	Basaltic andesite	1.26	0.29	1.10	13.57	2.92	5.78	2.04	63.88	0.21	16.52	0.25	9.65	203.89
		1.31	0.31	1.22	14.65	3.23	5.90	2.20	69.19	1.04	17.83	0.78	10.61	221.48
		1.28	0.30	1.16	14.11	3.07	5.84	2.12	66.53	0.62	17.17	0.52	10.13	212.69
ICE 20-34	Basaltic andesite	1.27	0.28	1.06	14.558	2.888	4.855	1.942	58.101	0.244	15.531	0.336	9.679	198.275
ICE 20-19	Basaltic andesite	1.29	0.28	1.07	13.228	2.957	5.438	1.882	50.480	0.260	15.242	0.346	9.816	210.407
ICE 20-23	Basaltic andesite	1.32	0.29	1.02	16.38	3.15	6.57	1.82	34.31	0.96	15.04	0.25	15.19	233.24
		1.26	0.27	0.99	16.33	3.09	5.54	1.75	39.81	0.26	14.38	0.33	11.70	195.56
		1.29	0.28	1.01	16.36	3.12	6.05	1.79	37.06	0.61	14.71	0.29	13.45	214.40
ICE 20-24	Andesite	1.24	0.27	0.99	14.93	3.15	5.39	1.72	32.48	0.99	14.26	0.52	16.06	217.51
		1.30	0.28	1.00	15.23	3.06	4.42	1.78	33.71	0.03	14.96	0.28	12.89	219.01
		1.27	0.28	1.00	15.08	3.11	4.91	1.75	33.09	0.51	14.61	0.40	14.47	218.26
ICE 20-35	Andesite	1.53	0.26	0.63	18.629	3.370	5.531	1.322	20.744	0.195	9.977	0.183	9.595	198.044
ICE 20-39	Dacite	2.50	0.15	0.07	30.58	4.59	4.91	0.38	0.81	15.57	1.18	0.09	14.38	141.19
		2.41	0.14	0.07	29.44	4.35	6.31	0.37	0.63	0.73	1.15	0.08	13.55	141.51
		2.46	0.14	0.07	30.01	4.47	5.61	0.37	0.72	8.15	1.16	0.09	13.96	141.35
ICE 20-32	Dacite	2.41	0.14	0.06	31.237	4.244	5.784	0.311	0.430	0.414	1.161	0.599	16.329	140.903
ICE 20-33	Rhyolite	2.88	0.07	0.03	36.366	4.966	5.585	0.129	0.470	0.323	0.158	0.170	12.041	128.263

Table 2 (continued)

Sample	TAS rock type	Ga (ppm)	Ge (ppm)	As (ppm)	Rb (ppm)	Sr (ppm)	Y (ppm)	Zr (ppm)	Nb (ppm)	Mo (ppm)	Ag (ppm)	Cd (ppm)	Sn (ppm)	Sb (ppm)	Cs (ppm)	Ba (ppm)
ICE 20-31	Basalt	21.234	1.487	0.475	8.327	396.710	22.170	127.281	18.228	0.893	0.069	0.213	1.280	0.247	0.113	100.571
ICE 20-28	Basalt	23.276	2.116	0.681	14.493	366.420	39.958	235.414	34.477	1.559	0.113	0.294	1.997	0.053	0.189	159.190
ICE 20-27	Basalt	25.413	2.227	0.808	15.706	387.076	40.828	252.442	32.328	1.498	0.119	0.236	2.064	0.050	0.221	160.477
ICE 20-37	Basalt	24.854	2.015	0.741	15.589	370.083	40.741	251.110	33.103	1.577	0.119	0.240	2.014	0.047	0.225	160.735
ICE 20-41	Basalt	24.471	2.113	0.861	14.894	368.709	42.197	254.043	36.697	1.584	0.121	0.259	2.031	0.050	0.198	166.251
ICE 20-22	Basalt	25.270	2.009	0.693	12.194	331.018	37.699	239.678	32.027	1.720	0.117	0.171	2.076	0.051	0.151	155.289
ICE 20-36	Basalt	24.336	1.839	0.743	11.247	296.323	35.857	224.617	29.941	1.814	0.116	0.171	1.963	0.040	0.134	147.944
ICE 20-45	Basalt	28.224	2.436	1.115	26.214	408.334	63.139	409.202	53.689	2.621	0.186	0.278	2.878	0.078	0.371	260.686
ICE 20-40	Basaltic andesite	31.14	2.80	1.55	34.80	412.48	75.48	469.23	61.34	3.07	0.21	0.32	3.64	0.11	0.52	299.57
		31.20	2.88	1.57	34.08	415.04	75.64	472.33	61.19	3.08	0.20	0.33	3.49	0.10	0.49	315.84
		31.17	2.84	1.56	34.44	413.76	75.56	470.78	61.26	3.07	0.21	0.32	3.57	0.10	0.50	307.71
ICE 20-44	Basaltic andesite	30.83	2.71	1.55	35.91	387.64	73.01	488.13	62.88	3.16	0.22	0.33	3.53	0.12	0.50	311.25
		33.57	2.92	1.60	28.74	349.70	79.77	532.04	67.92	3.55	0.23	0.36	3.90	0.11	0.54	345.79
		32.20	2.81	1.58	32.33	368.67	76.39	510.09	65.40	3.35	0.22	0.34	3.71	0.11	0.52	328.52
ICE 20-34	Basaltic andesite	30.649	2.625	1.396	37.019	411.886	74.942	486.411	62.401	3.100	0.228	0.293	3.540	0.098	0.532	338.337
ICE 20-19	Basaltic andesite	31.429	2.803	1.392	36.991	400.638	74.877	513.281	64.020	3.309	0.235	0.312	3.586	0.111	0.538	345.682
ICE 20-23	Basaltic andesite	32.29	2.57	1.62	31.90	400.08	74.71	537.20	65.97	3.58	0.24	0.35	4.15	0.13	0.58	352.09
		31.15	2.65	1.45	24.26	359.22	74.43	526.44	63.91	2.82	0.23	0.32	3.79	0.12	0.56	252.68
		31.72	2.61	1.53	28.08	379.65	74.57	531.82	64.94	3.20	0.24	0.34	3.97	0.12	0.57	302.38
ICE 20-24	Andesite	30.39	2.63	1.26	28.12	375.29	69.97	496.37	63.11	3.43	0.23	0.36	3.61	0.12	0.54	316.63
		32.07	2.68	1.51	29.10	406.39	78.20	517.02	65.30	0.00	0.23	0.39	3.75	0.11	0.49	380.42
		31.23	2.66	1.39	28.61	390.84	74.08	506.70	64.20	1.71	0.23	0.37	3.68	0.11	0.51	348.52
ICE 20-35	Andesite	31.700	2.765	1.492	46.088	410.729	76.968	562.987	67.117	3.879	0.256	0.455	4.136	0.132	0.696	404.098
ICE 20-39	Dacite	32.02	2.76	1.76	73.76	209.45	82.45	546.60	74.96	5.06	0.24	0.46	5.98	0.22	1.29	600.37
		31.69	2.56	1.78	77.32	236.95	80.52	475.42	72.56	4.14	0.29	0.36	5.80	0.23	1.22	577.98
		31.85	2.66	1.77	75.54	223.20	81.49	511.01	73.76	4.60	0.27	0.41	5.89	0.23	1.25	589.17
ICE 20-32	Dacite	32.114	2.547	1.534	76.755	235.747	83.945	480.691	71.256	4.142	0.213	0.348	5.941	0.206	1.206	591.405
ICE 20-33	Rhyolite	30.785	2.255	1.581	89.702	93.445	74.883	301.976	84.108	4.966	0.139	0.322	7.176	0.255	1.386	703.228

Table 2 (continued)

Sample	TAS rock type	La (ppm)	Ce (ppm)	Pr (ppm)	Nd (ppm)	Sm (ppm)	Eu (ppm)	Gd (ppm)	Tb (ppm)	Dy (ppm)	Ho (ppm)	Er (ppm)	Tm (ppm)	Yb (ppm)	Lu (ppm)
ICE 20-31	Basalt	13.176	30.969	4.193	18.526	4.513	1.603	4.881	0.745	4.269	0.837	2.178	0.293	1.852	0.262
ICE 20-28	Basalt	23.516	54.891	7.460	32.722	7.945	2.705	8.409	1.308	7.548	1.492	3.900	0.544	3.432	0.487
ICE 20-27	Basalt	23.186	53.969	7.375	31.814	7.690	2.639	8.213	1.272	7.407	1.483	3.882	0.543	3.411	0.489
ICE 20-37	Basalt	23.607	55.163	7.511	32.867	7.748	2.682	8.370	1.285	7.553	1.492	3.922	0.545	3.475	0.492
ICE 20-41	Basalt	24.911	58.498	7.993	34.660	8.391	2.856	8.901	1.374	7.914	1.570	4.094	0.568	3.589	0.509
ICE 20-22	Basalt	21.142	52.197	6.708	29.381	7.215	2.473	7.665	1.175	6.940	1.404	3.652	0.521	3.234	0.465
ICE 20-36	Basalt	20.805	50.002	6.648	29.115	6.970	2.437	7.509	1.154	6.771	1.353	3.497	0.497	3.061	0.433
ICE 20-45	Basalt	39.412	94.625	12.266	52.616	12.328	4.088	13.197	2.010	11.427	2.318	6.090	0.858	5.385	0.761
ICE 20-40	Basaltic andesite	51.42	121.95	15.73	66.90	15.41	4.80	16.16	2.44	14.04	2.83	7.41	1.05	6.60	0.95
		50.95	121.61	15.72	67.01	15.42	4.80	16.19	2.44	14.04	2.81	7.36	1.04	6.59	0.94
		51.19	121.78	15.72	66.95	15.41	4.80	16.18	2.44	14.04	2.82	7.38	1.04	6.60	0.94
ICE 20-44	Basaltic andesite	47.92	117.95	14.56	62.19	14.27	4.56	15.12	2.29	13.14	2.65	6.96	0.99	6.27	0.89
		52.03	125.74	16.05	68.69	15.98	5.05	16.85	2.58	14.71	2.94	7.83	1.10	6.91	1.01
		49.97	121.85	15.30	65.44	15.13	4.81	15.98	2.44	13.92	2.79	7.40	1.04	6.59	0.95
ICE 20-34	Basaltic andesite	51.592	120.872	15.463	65.472	15.079	4.768	15.692	2.373	13.700	2.760	7.240	1.019	6.466	0.927
ICE 20-19	Basaltic andesite	50.439	122.419	15.195	64.407	14.836	4.687	15.573	2.361	13.526	2.743	7.265	1.023	6.456	0.926
ICE 20-23	Basaltic andesite	48.11	121.05	14.69	62.36	14.57	4.62	15.36	2.35	13.63	2.71	7.26	1.03	6.56	0.94
		47.28	117.35	14.40	61.71	14.24	4.53	15.12	2.32	13.39	2.70	7.17	1.02	6.41	0.92
		47.69	119.20	14.54	62.03	14.41	4.57	15.24	2.33	13.51	2.71	7.22	1.02	6.49	0.93
ICE 20-24	Andesite	45.61	115.77	14.04	59.87	13.88	4.40	14.59	2.23	12.80	2.59	6.85	0.98	6.12	0.90
		51.51	126.15	15.63	65.81	15.11	4.82	15.96	2.44	14.06	2.85	7.53	1.08	6.79	0.97
		48.56	120.96	14.83	62.84	14.50	4.61	15.27	2.33	13.43	2.72	7.19	1.03	6.46	0.93
ICE 20-35	Andesite	56.739	129.687	16.205	66.845	15.023	4.774	15.665	2.397	13.919	2.850	7.593	1.091	6.932	1.017
ICE 20-39	Dacite	64.84	154.29	17.22	67.49	14.58	3.78	15.23	2.42	14.49	3.01	8.41	1.25	8.22	1.20
		67.36	151.67	17.36	66.93	14.51	3.67	14.91	2.36	13.86	2.89	7.93	1.20	7.80	1.13
		66.10	152.98	17.29	67.21	14.54	3.73	15.07	2.39	14.17	2.95	8.17	1.22	8.01	1.16
ICE 20-32	Dacite	71.872	156.433	18.216	70.292	15.013	3.644	15.512	2.438	14.548	3.014	8.301	1.240	8.223	1.185
ICE 20-33	Rhyolite	63.907	170.501	16.010	61.110	12.991	2.441	13.520	2.131	12.667	2.649	7.267	1.105	7.252	1.025

Table 2 (continued)

Sample	TAS rock type	Hf (ppm)	Ta (ppm)	W (ppm)	Tl (ppm)	Pb (ppm)	Th (ppm)	U (ppm)
ICE 20-31	Basalt	3.285	1.106	0.221	0.015	0.983	1.047	0.312
ICE 20-28	Basalt	5.568	2.130	0.213	0.015	1.501	1.841	0.543
ICE 20-27	Basalt	5.891	1.949	0.220	0.015	1.634	1.872	0.554
ICE 20-37	Basalt	5.950	1.983	0.224	0.016	1.626	1.857	0.554
ICE 20-41	Basalt	6.103	2.218	0.291	0.021	1.564	1.885	0.564
ICE 20-22	Basalt	5.663	1.929	0.246	0.013	1.597	1.616	0.537
ICE 20-36	Basalt	5.391	1.819	0.313	0.013	1.575	1.624	0.528
ICE 20-45	Basalt	9.526	3.180	0.303	0.022	2.626	3.206	0.972
ICE 20-40	Basaltic andesite	10.63	3.47	0.26	0.03	3.43	4.38	1.29
		10.65	3.49	0.27	0.03	3.38	4.39	1.30
		10.64	3.48	0.27	0.03	3.41	4.39	1.29
ICE 20-44	Basaltic andesite	11.03	3.59	0.30	0.03	3.46	3.93	1.33
		12.07	3.95	0.32	0.03	3.65	3.77	1.16
		11.55	3.77	0.31	0.03	3.56	3.85	1.25
ICE 20-34	Basaltic andesite	11.040	3.576	0.324	0.028	3.483	4.672	1.362
ICE 20-19	Basaltic andesite	11.669	3.646	0.327	0.027	3.530	4.341	1.370
ICE 20-23	Basaltic andesite	12.27	3.77	0.32	0.03	3.50	4.31	1.28
		11.82	3.65	0.29	0.02	3.59	4.43	1.43
		12.05	3.71	0.31	0.03	3.54	4.37	1.35
ICE 20-24	Andesite	11.30	3.55	0.29	0.03	3.31	4.00	1.21
		11.63	3.70	0.30	0.00	3.62	4.57	1.43
		11.46	3.63	0.30	0.01	3.46	4.28	1.32
ICE 20-35	Andesite	12.638	3.820	0.324	0.030	4.281	5.773	1.671
ICE 20-39	Dacite	13.86	4.46	0.45	0.06	6.72	9.88	2.71
		12.10	4.21	0.46	0.06	6.71	9.55	2.60
		12.98	4.33	0.46	0.06	6.72	9.72	2.65
ICE 20-32	Dacite	12.334	4.191	0.461	0.058	6.920	9.635	2.647
ICE 20-33	Rhyolite	10.215	4.933	0.474	0.065	7.699	10.450	2.891

3. Results

Table 2 and Table 3 list the chemical compositions and Cd isotope compositions of the samples. Based on their compositions for major elements, we can notice at least 3 anomalous samples, all being basalts: ICE 20-31, 20-22 and 20-36. The first of them, circled in black in Figure 1, is characterized by a slight excess in Al, Ca and Si and a strong Fe and Ti deficit compared to the trend defined by most of the other basalts. The two other outliers share similar behaviors, with slight Fe and Ti enrichments but more importantly by important K and Na depletion. They are highlighted by a red ellipse on Figure 1.

Table 3: Cadmium concentrations and isotopic compositions of the Hekla lavas

Sample	TAS rock type	Cd (ppb)	2SD	δ^{113}Cd (‰)	2SD	δ^{114}Cd (‰)	2SD	n
ICE 20-31	Basalt	112		0.015	0.096	0.044	0.098	7
ICE 20-28	Basalt	136		0.157	0.039	0.217	0.047	5
ICE 20-27	Basalt	138		0.194	0.033	0.284	0.070	4
ICE 20-37	Basalt	136		0.213	0.039	0.327	0.060	5
ICE 20-41	Basalt	142		0.241	0.020	0.318	0.049	7
		147						
		145	**7**	**0.241**	**0.020**	**0.318**	**0.049**	**7**
ICE 20-22	Basalt	94		0.212	0.034	0.298	0.042	5
ICE 20-36	Basalt	119		0.285	0.047	0.355	0.050	3
		120		0.203	0.056	0.277	0.030	5
		120	**1**	**0.244**	**0.116**	**0.316**	**0.110**	**2**
ICE 20-45	Basalt	175		0.276	0.006	0.373	0.060	3
		181						
		178	**8**	**0.276**	**0.006**	**0.373**	**0.060**	**3**
ICE 20-40	Basaltic andesite	193		0.190	0.023	0.252	0.045	7
ICE 20-44	Basaltic andesite	189		0.124	0.025	0.197	0.052	5
ICE 20-34	Basaltic andesite	175		0.243	0.032	0.354	0.043	5
ICE 20-19	Basaltic andesite	180		0.165	0.054	0.250	0.170	4
ICE 20-23	Basaltic andesite	149		0.661	0.031	0.917	0.047	6
		162		0.555	0.043	0.739	0.062	5
		156	**18**	**0.608**	**0.150**	**0.828**	**0.251**	**2**
ICE 20-24	Andesite	191		0.149	0.076	0.210	0.083	7
		186		0.139	0.065	0.202	0.072	5
		189	**7**	**0.144**	**0.014**	**0.206**	**0.011**	**2**
ICE 20-35	Andesite	203		0.118	0.062	0.176	0.132	6
ICE 20-39	Dacite	208		0.055	0.156	0.123	0.064	7
ICE 20-32	Dacite	194		0.113	0.035	0.169	0.025	7
ICE 20-33	Rhyolite	227		0.033	0.099	0.077	0.079	7

Lines in bold font display the mean compositions calculated when replicates were analyzed.

Figure 2 displays the evolutions of Cd concentrations in the differentiating magma. The previously noted three outliers are again out of trend, because of an anomalously high silica content in the first case and because of Cd-depletion for the two others. Another outlier can be found among the basaltic andesites, with ICE 20-23 (circled in green) being Cd-depleted compared to the basaltic andesites or the andesites. This sample did not stand out during the major elements analysis, suggesting that the depleting mechanism is distinct from that affecting the other three outliers.

Apart from these 4 outliers, the Cd concentrations of the samples increase with magmatic evolution toward silicic compositions (see Figure 2), with a good agreement between the Cd vs. MgO and the Cd vs. SiO_2 trends. Two distinct linear trends are visible on this figure, one fitting the basalts and one fitting all the other samples, both being characterized by good R^2 parameter. The basaltic trend is the one with the biggest slope, indicating that Cd is accumulated more slowly in non-basaltic samples than in basaltic ones. This could be caused either by higher rates of Cd crystallization in basaltic andesite to rhyolite melts compared to basaltic magmas or by dilution of the basalts by a Cd-depleted magma coupled with an increasing Cd concentration caused by fractional crystallization.

Table 3 lists the Cd concentrations and isotope compositions for the analyzed samples. We find that there are significant isotope variations between the samples (see Figure 3). The basalts are all characterized by a constant δ^{114}Cd value of 0.319 ± 0.061 ‰ (2SD, n = 6), despite important variations in chemical compositions. Only the black-circled outlier has a significantly distinct Cd isotope composition, the red-circled ones fitting perfectly in the trend. From basaltic andesites to rhyolites, the isotope compositions of the samples get steadily enriched in light Cd isotopes, with a final rhyolitic Cd isotope composition that is close to that of the Si-rich, black-circled outlier basalt. There is a very good negative linear correlation between the Cd isotope compositions of non-basaltic samples and their Cd concentrations. The green-circled outlier is

isotopically much heavier than any other sample in this set. Finally we note that the Cd isotope compositions of the dacites and rhyolites are similar to that of MORB ($\delta^{114}Cd = 0.07 \pm 0.10$ ‰) (Devos et al., 2024) and distinct from the basaltic isotope composition. For the rest of the discussion, we will consider ICE 20-39 as the dacitic end-member as it is the Cd-richest dacite and the one with the most distinct isotope composition ($\delta^{114}Cd = 0.123 \pm 0.064$ ‰).

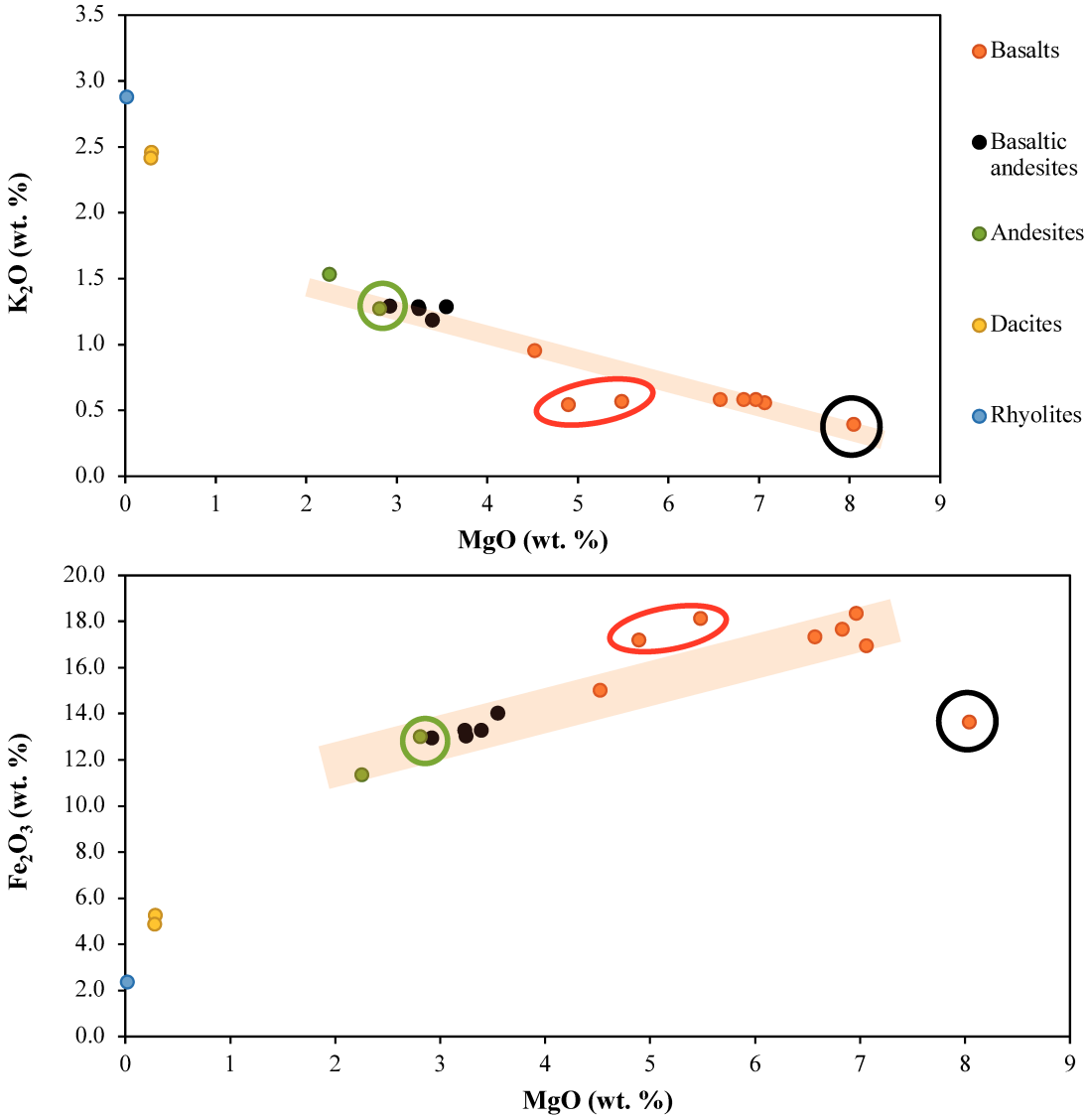


Figure 1: Fe_2O_3 and K_2O concentration as functions of the samples' MgO contents. The overall trend defined by the basalts is materialized by an orange bar while the outliers are circled in black (ICE 20-31), in red (ICE 20-22 and 20-36) or in green (ICE 20-23).

4. Discussion

4.1. What caused the outliers compositions?

As exposed previously, we did isolate four different outliers that we grouped in three distinct categories based on their compositions. We will here discuss further the scenarios that could explain the observed chemical and isotopic compositions of these samples:

- *ICE 20-31 (black-circled):* The sample is significantly distinct chemically from all of the others. Its Fe and Ti depletions and the absence of intermediary compositions between it and the rest of the basalts make it seem improbable for this outlier to be related in any manner to the other Hekla samples. Another independent analysis of this sample did not find anomalous silica and MgO concentrations as we do, but did confirm that this sample is significantly depleted in K compared to the other basalts (Wang et al., 2023). We propose that this sample is either not related to the other basalts or altered to such a degree that its use would be difficult. Since its Cd isotope composition is similar to that of MORB, we could propose that it is related to these lavas.
- *ICE 20-22 and 20-36 (red-circled):* These samples are characterized by a significant depletion in volatile elements (Na, K, Cd), which could indicate a volatilization occurrence. However, their Cd isotope compositions are similar to that of normal basalts. This indicates that any Cd vaporization process did not produce significant isotope fractionation. This could be obtained if Cd diffuses very slowly in the melt, creating a totally Cd-depleted outer layer and a Cd-rich core with minimal isotope compositions variation. Alternatively, the basaltic magma could have been diluted by a volatile-depleted magma. None of these explanations is fully satisfying as even low amounts of Cd volatilization should produce visible isotopic variations (see

next paragraph and chapter 5) and we expect that magma mixing should produce more evident traces than a volatile depletion. Nevertheless, since the isotope compositions of these samples are similar to that of the other basalts, we will use them in the discussion of the isotope fractionation processes.

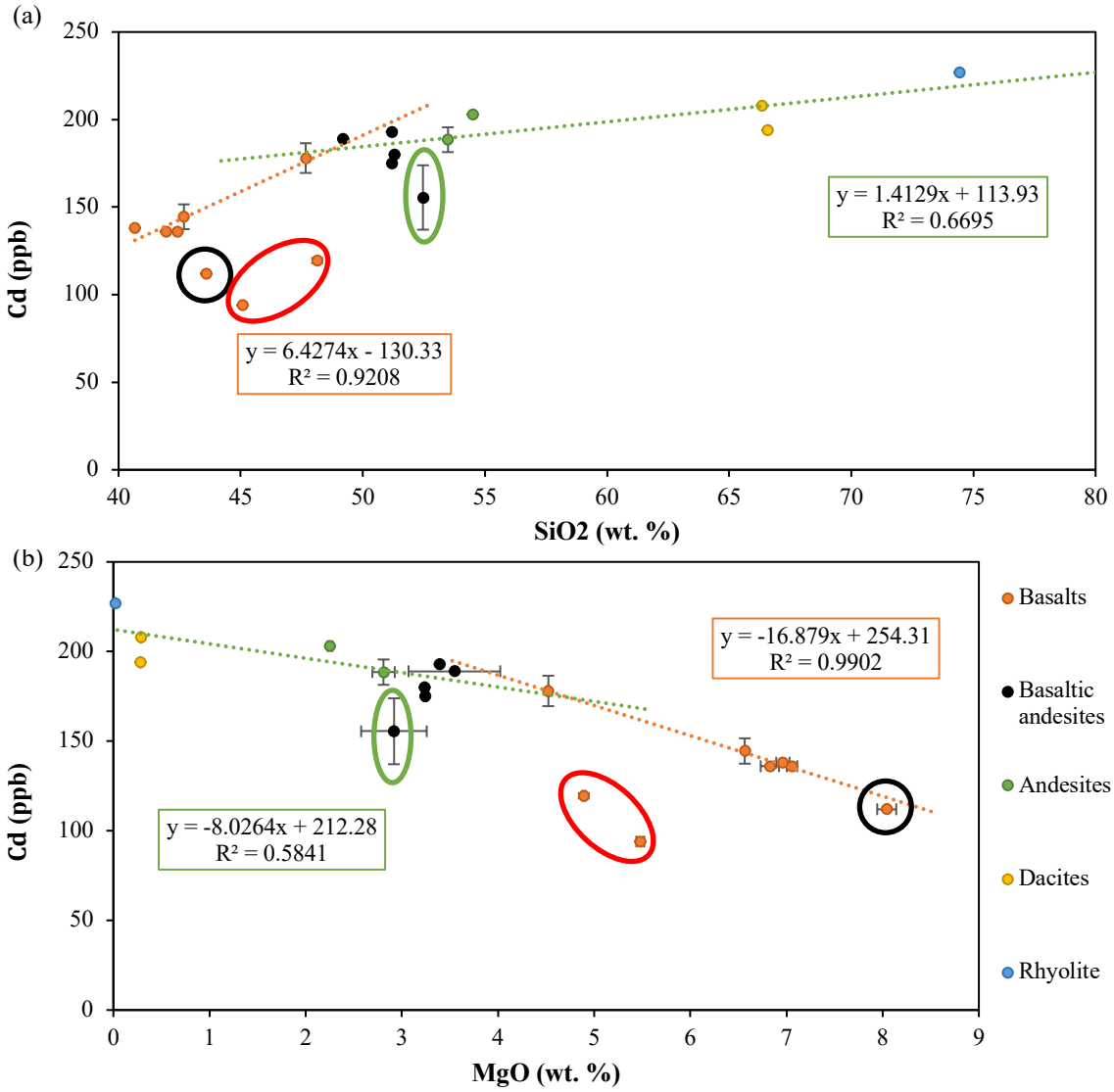


Figure 2: Cadmium concentrations in Hekla samples as a function of their MgO or SiO_2 contents. The orange dotted line materializes the linear trend followed by all basalts, except the three outliers. The green dotted line materializes the linear trend followed by basaltic andesites (except for one outlier), andesites, dacites and rhyolites. The outliers are circled with similar colors than in the Figure 1.

- *ICE 20-23 (green-circled):* This sample is specifically Cd-depleted, with no significant deviation from the chemical compositions of comparable samples. The

Cd depletion is coupled to a heavy Cd isotopes enrichment. This fits well Cd volatilization. Using the most evolved basalts as a starting point, we determine that we can form the observed Cd composition by a 13 % depletion, with a reasonnable 0.9966 α kinetic factor in the Rayleigh distillation law:

$$\Delta^{114}Cd = \delta^{114}Cd_{sample} - \delta^{114}Cd_{initial}$$

$$\Delta^{114}Cd = 10^3 \times \left(\frac{[Cd]_{sample}}{[Cd]_{initial}}\right)^{\alpha-1} - 10^3$$

The fact that a significant isotope fractionation occurs for such a low Cd depletion stands against a possible vaporization without isotope fractionation for the red-circled outliers (respectively depleted by 47 and 33 %). We do not know why this basalt is the only one that experienced Cd vaporization.

4.2.Cadmium during fractional crystallization

4.2.1. Forming the basalts and the rhyolites

Regardless of the model, authors agree on the fact that the basalts evolve into basaltic andesites mainly by fractional crystallization. The fact that the Cd concentrations in the basalts increase with the evolution of the magma confirms that Cd is incompatible, although it does not imply that no Cd is crystallized but rather that the Cd remains mostly in the melt. Since no significant isotope variations are observed for Cd in basalts, we can deduce that no significant amount of Cd crystallizes during the fractional crystallization process occurring in the basaltic melt. Alternatively, we could propose that a Cd-bearing mineral does form but that it has similar isotope composition than the melt, which seems unlikely. Unlike for dacites and rhyolites, the isotope composition of the basalts is significantly heavier than that of MORB (0.07 ± 0.10 ‰) or that of the mantle (0.11 ± 0.10 ‰) (Devos et al., 2024). This heavy Cd composition could be the result of isotope fractionation caused by low degrees of partial melting, which is

characteristic of OIB. In this case, the melts would preferentially collect the heaviest Cd isotopes, similarly to what is known to happen for Zn (Day et al., 2022).

Similarly to the basalts, the formation of the rhyolites by fractional crystallization from the dacites is accepted by most authors. In our case, the rhyolite sample is significantly richer in Cd than the dacites but have similar isotope compositions. Thus, we assess that Cd do not crystallize significantly during the fractional crystallization forming the rhyolites from the dacites.

4.2.2. From the basaltic andesites to the dacites

This step is the most debated one, with some authors stating that it occurs thank to fractional crystallization only (Geist et al., 2021) while other argue that input of an external silicic melt is needed (Sigmarsson et al., 1992) or that both play a role (Chekol et al., 2011). The samples are still significantly enriched in Cd with increasing silica content but the slope of this trend is lesser than for the basalts. According to the fractional crystallization model, this could indicate that, although Cd remains mainly incompatible, a new Cd-bearing phase crystallizes. Alternatively, the pure mixing model would interpret this as showing mixing between a basaltic melt and a dacitic one that is richer in Cd. Finally, if both mixing and fractional crystallization occur, the dacitic melt would need to be Cd-depleted compared to the basaltic one to counterbalance the increase in Cd associated with fractional crystallization.

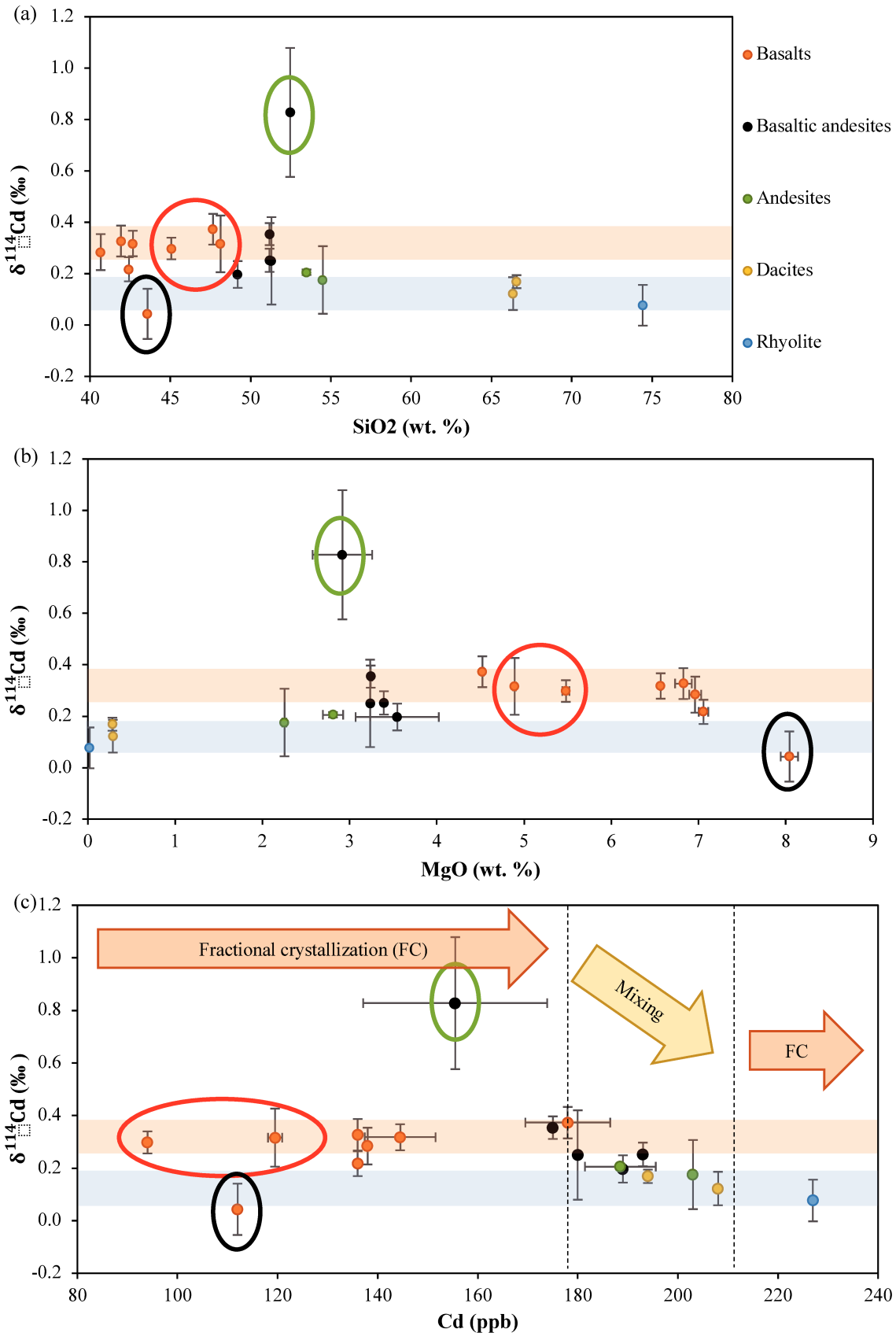


Figure 3: Cadmium isotope compositions of the samples as a function of their SiO_2 (a), MgO (b) or of their Cd concentrations (c). The signification of the symbol's colors is the same than for the previous figure. The blue horizontal bar materializes the

Cd isotope composition of the most pristine dacite while the orange one shows the mean Cd isotope composition for Hekla basalts.

Isotope compositions for samples comprised between basaltic andesites and dacites are negatively correlated with their Cd and Si contents. All of the isotope compositions are comprised between that of the most evolved basalts and that of the reference dacite. Thus, we cannot discriminate between simple mixing of dacitic and basaltic melts, and fractional crystallization of an isotopically heavy Cd-bearing phase. However, the fractional crystallization-only model does not propose that a new mineral crystallizes at the basalt-basaltic andesite transition (Geist et al., 2021). Thus, we find it improbable, although not impossible, that the Cd would suddenly crystallize in a phase in which it did not crystallize before. It is also possible that Cd is integrated in a minor phase that was not modelized. Since we found that fractional crystallization in the basalts and in the dacites do not cause significant Cd isotope fractionation, we assess that it is improbable for such a process to cause the isotope variations between basalts and dacites. Thus, it is our belief that mixing between an OIB basaltic magma and an isotopically MORB-like dacitic one, with or without fractional crystallization occurring, better explains our observations concerning Cd.

5. Conclusion

We analyzed a set of 18 lavas from the Hekla volcano. The samples Cd concentrations are increasing along magma differentiation, with a point of inflexion at the transition between basalts and basaltic andesites. The Cd isotope compositions of the Hekla samples are distributed between two main compositions: dacitic and rhyolitic lavas have a MORB-like δ^{114}Cd value of 0.123 ± 0.064 ‰ while basaltic lavas are isotopically heavier than MORB or than the mantle with a δ^{114}Cd = 0.319 ± 0.061. We propose that this heavy isotope composition of the basalts is caused by isotope fractionation between the melt and its mantellic source during low degrees

of partial melting characteristic of OIB. In such a model, the melts formed by low degrees of partial melting would be isotopically heavier than their mantle source, as is known to occur for Zn.

In the most plausible model, the data can be accounted for by the mixing of two magmas with distinct isotopic composition: an isotopically heavy basaltic melt and an isotopically lighter dacitic one assimilated from the surrounding crust. Since all basalts have similar Cd isotope compositions, we assess that fractional crystallization in basalt does not produce significant Cd isotope variability. The intermediary compositions (basaltic andesites, andesites and dacites) can be formed by mixing of the two magmas. If fractional crystallization plays a significant role in this differentiation process, we assess that it has no impact over the Cd isotope compositions of the samples. Finally, we determine that fractional crystallization occurring between the dacites and rhyolites does not result in significant isotope variations. Thus, we propose that Cd remains mostly unaltered by fractional crystallization, and that no significant Cd-bearing mineral is crystallized during this process for Hekla magmas.

6. References

Bai, R., Jackson, M.G., Huang, F., Moynier, F., Devos, G., Halldórsson, S.A., Lisiecki, L., Yin, H., Peng, Y., Nan, X., 2022. Barium isotopes in ocean island basalts as tracers of mantle processes. Geochim. Cosmochim. Acta 336, 436–447. https://doi.org/10.1016/j.gca.2022.08.023

Baldridge, W.S., McGetchin, T.R., Frey, F.A., Jarosewich, E., 1973. Magmatic evolution of Hekla, Iceland. Contrib. Mineral. Petrol. 42, 245–258. https://doi.org/10.1007/BF00371589

Chekol, T.A., Kobayashi, K., Yokoyama, T., Sakaguchi, C., Nakamura, E., 2011. Timescales of magma differentiation from basalt to andesite beneath Hekla Volcano, Iceland: Constraints from U-series disequilibria in lavas from the last quarter-millennium flows. Geochim. Cosmochim. Acta 75, 256–283. https://doi.org/10.1016/j.gca.2010.10.001

Chen, H., Savage, P.S., Teng, F.-Z., Helz, R.T., Moynier, F., 2013. Zinc isotope fractionation during magmatic differentiation and the isotopic composition of the bulk Earth. Earth Planet. Sci. Lett. 369–370, 34–42. https://doi.org/10.1016/j.epsl.2013.02.037

Day, J.M.D., Moynier, F., Ishizuka, O., 2022. A partial melting control on the Zn isotope composition of basalts. Geochem. Perspect. Lett. 23, 11–16. https://doi.org/10.7185/geochemlet.2230

Deng, Z., Chaussidon, M., Savage, P., Robert, F., Pik, R., Moynier, F., 2019. Titanium isotopes as a tracer for the plume or island arc affinity of felsic rocks. Proc. Natl. Acad. Sci. 116, 1132–1135. https://doi.org/10.1073/pnas.1809164116

Devos, G., Moynier, F., Creech, J., Liu, D., Puchtel, I.S., Bizzarro, M., 2024. Cadmium isotope composition of the Earth's mantle inferred from analysis of oceanic basalts and komatiites. Chem. Geol. 650, 121996. https://doi.org/10.1016/j.chemgeo.2024.121996

Dostal, J., Elson, C., Dupuy, C., 1979. Distribution of lead, silver and cadmium in some igneous rocks and their constituent minerals. Can. Mineral. 17, 561–567.

Geist, D., Harpp, K., Oswald, P., Wallace, P., Bindeman, I., Christensen, B., 2021. Hekla Revisited: Fractionation of a Magma Body at Historical Timescales. J. Petrol. 62, egab001. https://doi.org/10.1093/petrology/egab001

Greaney, A.T., Rudnick, R.L., Helz, R.T., Gaschnig, R.M., Piccoli, P.M., Ash, R.D., 2017. The behavior of chalcophile elements during magmatic differentiation as observed in Kilauea Iki lava lake, Hawaii. Geochim. Cosmochim. Acta 210, 71–96. https://doi.org/10.1016/j.gca.2017.04.033

Inglis, E.C., Moynier, F., Creech, J., Deng, Z., Day, J.M.D., Teng, F.-Z., Bizzarro, M., Jackson, M., Savage, P., 2019. Isotopic fractionation of zirconium during magmatic differentiation and the stable isotope composition of the silicate Earth. Geochim. Cosmochim. Acta 250, 311–323. https://doi.org/10.1016/j.gca.2019.02.010

Jakobsson, S.P., 1979. Petrology of recent basalts of the Eastern Volcanic Zone, Iceland.

Lucic, G., Berg, A., Stix, J., 2016. Water-rich and volatile-undersaturated magmas at Hekla volcano, Iceland. Geochem. Geophys. Geosystems 17, 3111–3130. https://doi.org/10.1002/2016GC006336

Oskarsson, N., Sigvaldason, G.E., Steinthorsson, S., 1982. A dynamic model of rift zone petrogenesis and the regional petrology of Iceland. J. Petrol. 23, 28–74. https://doi.org/10.1093/petrology/23.1.28

Prytulak, J., Brett, A., Webb, M., Plank, T., Rehkämper, M., Savage, P.S., Woodhead, J., 2017a. Thallium elemental behavior and stable isotope fractionation during magmatic processes. Chem. Geol. 448, 71–83. https://doi.org/10.1016/j.chemgeo.2016.11.007

Prytulak, J., Sossi, P.A., Halliday, A.N., Plank, T., Savage, P.S., Woodhead, J.D., 2017b.

Stable vanadium isotopes as a redox proxy in magmatic systems? Geochem. Perspect. Lett. 75–84. https://doi.org/10.7185/geochemlet.1708

Ranta, E., Halldórsson, S.A., Barnes, J.D., Jónasson, K., Stefánsson, A., 2021. Chlorine isotope ratios record magmatic brine assimilation during rhyolite genesis. Geochem. Perspect. Lett. 16, 35–39. https://doi.org/10.7185/geochemlet.2101

Savage, P.S., Georg, R.B., Williams, H.M., Burton, K.W., Halliday, A.N., 2011. Silicon isotope fractionation during magmatic differentiation. Geochim. Cosmochim. Acta 75, 6124–6139. https://doi.org/10.1016/j.gca.2011.07.043

Schuessler, J.A., Schoenberg, R., Sigmarsson, O., 2009. Iron and lithium isotope systematics of the Hekla volcano, Iceland — Evidence for Fe isotope fractionation during magma differentiation. Chem. Geol. 258, 78–91. https://doi.org/10.1016/j.chemgeo.2008.06.021

Sigmarsson, O., Condomines, M., Fourcade, S., 1992. A detailed Th, Sr and O isotope study of Hekla: differentiation processes in an Icelandic Volcano. Contrib. Mineral. Petrol. 112, 20–34. https://doi.org/10.1007/BF00310953

Thorarinsson, S., 1967. The eruption of Hekla in historical times, eruption of Hekla 1947–1948. Visindafelag Isl. 1–183.

Thorarinsson, S., 1950. The eruption of Mt. Hekla 1947 – 1948. Bull. Volcanol. 10, 157–168. https://doi.org/10.1007/BF02596085

Tuller-Ross, B., Savage, P.S., Chen, H., Wang, K., 2019. Potassium isotope fractionation during magmatic differentiation of basalt to rhyolite. Chem. Geol. 525, 37–45. https://doi.org/10.1016/j.chemgeo.2019.07.017

Vincent, E.A., Bilefield, L.I., 1960. Cadmium in rocks and minerals from the Skaergaard intrusion, East Greenland. Geochim. Cosmochim. Acta 19, 63–69.

https://doi.org/10.1016/0016-7037(60)90126-5

Wang, B., Moynier, F., Jackson, M.G., Huang, F., Hu, X., Ari Halldórsson, S., Dai, W., Devos, G., 2023. Rubidium isotopic fractionation during magmatic processes and the composition of the bulk silicate Earth. Geochim. Cosmochim. Acta 354, 38–50. https://doi.org/10.1016/j.gca.2023.05.021

Yang, J., Siebert, C., Barling, J., Savage, P., Liang, Y.-H., Halliday, A.N., 2015. Absence of molybdenum isotope fractionation during magmatic differentiation at Hekla volcano, Iceland. Geochim. Cosmochim. Acta 162, 126–136. https://doi.org/10.1016/j.gca.2015.04.011

Yuan, Y., Guo, J.-L., Zong, K., Feng, L., Wang, Z., Moynier, F., Zhang, W., Hu, Z., Xu, H., 2022. Stable zirconium isotopic fractionation during alkaline magma differentiation: Implications for the differentiation of continental crust. Geochim. Cosmochim. Acta 326, 41–55. https://doi.org/10.1016/j.gca.2022.03.035

Chapter 5 – Cadmium composition of chondrites, a window to the primitive Solar System

1. Introduction

Among meteorites, chondrites stand out as the only primitive samples available, as they are the only ones that did not experience significant melting. Samples that did undergo extensive melting lost their initial texture and had their chemical composition fractionated between different envelops. These processes are coupled to the establishment of a radial structure composed at least of a metallic core surrounded by a rocky mantle during a process called the planetary differentiation. Thus, chondrites still retain their original heterogeneous texture, composed of a mixture of chondrules (small silicate beads composed of igneous minerals caught in glass), refractory inclusions (mainly Ca-Al inclusions - CAI - and amoeboid olivine aggregates - AOA) and fine-grained matrix in varying proportions. Chondrules can be almost absent, but even then, remnants can be found most of the time. Chondrules and refractory inclusions are depleted in moderately volatile elements (200 K < T_{50} < 1287 K) while the matrix is comparatively richer (Hezel et al., 2018). Chondrules and CAI were formed during the first Ma of the Solar System existence (Bollard et al., 2017; Connelly et al., 2012; Grossman, 1972). Thus, study of chondrites allows for the characterization of the conditions that prevailed in the primitive Solar System.

Chondrites can be classified following multiple criteria. One of the most common classification relies on the so-called petrological types, first proposed by Van Schmus and Wood (1967). This is a scale, ranging from 1 to 6 (although some authors have proposed a type 7) and express the degree to which the original chemical and mineralogical compositions of the meteorite have been altered by secondary processes occurring in the parent body. Originally, type 1 samples were supposed to be pristine (Wiik, 1956) and types 2 to 6 were reflecting increasing degrees of metamorphism. This classification was later modified with type 3 taking the “pristine sample” mantle (McSween, 1979). In this new paradigm, types 2 and 1 underwent

increasing aqueous alteration while types 4 to 6 have textures and compositions mainly determined by thermal metamorphism. Types 2 to 1 are characterized by the increasing disappearance of chondrules as they are altered by reaction with water at low temperatures. In types 4 to 6 samples, minerals have gone through chemical equilibration and recrystallization, producing coarse grained-textures and losing chondrules.

Another relevant criterium when analyzing meteorites is the circumstances of their discovery. Two situations are possible here: either the fall of the meteorite has been witnessed and the object has been retrieved in a matter of hours or days after touching the ground (these samples will be hereafter dubbed "falls"), or the meteorite was found without witness of its fall. These last meteorites, hereafter referred as "finds", are usually recovered during systematic surveys in deserts (notably in Atacama or Antarctica) where they can stay for long periods with minimal alteration due to a lack of interaction with water. A few of these samples were discovered in private collections without indications on the potential observation of a fall. The case of the Paris chondrite is a good example of this, as it was discovered during an auction, in Paris, in 2001. Although its Na/K ratio and the freshness of its fusion crust suggest that it was possibly an observed fall (Hewins et al., 2014), it is regarded as a find. Since finds spent an unknown (but potentially significant) time at the surface of the Earth, they are susceptible to present compositions that were modified by surficial processes. Thus, whenever possible, characterization of falls is preferred to that of finds. These terrestrial alteration processes might be especially significant for elements as mobile as cadmium.

Finally, a last chondrite classification can be made based on their chemical, mineralogical and isotopic compositions (Weisberg et al., 2006):

- *Ordinary chondrites (OC):* These are the most common chondrites, representing 94 % of all known chondrites (Grady, 2022). They display high abundances of chondrules (60-80 vol %), low matrix content (10-15 vol %) and almost no

refractory inclusions. They are also characterized by relatively large chondrules (15-30 mm in diameter). Chemically, they are slightly depleted in refractory lithophile elements compared to the mean composition of the Solar System. Finally, their oxygen isotope compositions are distinct from that of carbonaceous chondrites when plotted in a $\delta^{17}O$ vs. $\delta^{18}O$ (Sears and Weeks, 1983). The OC are spread on a large range of petrological types from 3 to 7 (Grady, 2022). This group is subdivided in three subgroups (although some intermediary samples exist), initially based on the Fe content of the meteorites:

- *H chondrites ("high iron content"):* These are the Fe-richest of the OC (25 to 31 wt. %), this is accompanied by high metal content (around 8 vol %). They contain the smallest chondrules of the OC, with diameters generally under 20 mm. Equilibrated H chondrites have usually olivines composed at 19.3 mol % of fayalite. Finally, the Co content of their kamacite and fayalite minerals allows for distinction from L group (Rubin, 1990).
- *L chondrites ("low iron content"):* These samples contain less metal (around 4 vol %) and iron (20-25 wt. %) than H chondrites. They also have specific siderophile elements patterns (Sears and Weeks, 1983). Equilibrated L chondrites are characterized by higher fayalitic content: 25.2 mol % of the olivines.
- *LL chondrites ("low iron content, low metal content"):* They contain the least metal of the OC (less than 2 vol %) and have similar to lower Fe content than L chondrites (19-22 wt. %). Finally, equilibrated LL chondrites have usually olivines composed at 31.3 mol % of fayalite. The different groups can also be differentiated based on their siderophile abundances (Kallemeyn et al., 1989; Sears et al., 1991).

- *Carbonaceous chondrites (CC):* These chondrites owe their name to their original characterization as carbon-rich. This definition, however, has been abandoned as carbon-poor CC were discovered. The current main criteria for determining if a chondrite belongs in the CC family relies on the abundances of refractory lithophile elements. For CC, these elements have normalized abundances superior or equal to that of the Sun photosphere. Numerous subgroups have been proposed based on their chemical, mineral and isotopic compositions, we will review here the main categories that will be encountered in this work:
    - *CI (Ivuna type):* Only five samples of this category are known and they all are of petrological type 1 (Grady, 2022). These chondrites are known for their chemical composition, which is strikingly similar to that of the Sun photosphere (approximating the mean composition of the Solar System). The similarity is such that CI chondrites are widely used as proxies for the Solar System mean chemical composition. These meteorites are very altered and hydrated, they are heavily brecciated and show almost no chondrule or CAI.
    - *CM (Mighei type):* These are the most common CC, representing 29 % of the total. They are characterized by significant aqueous alteration, with petrological types ranging from 1 to 2 (Grady, 2022). This alteration partially to totally replaced CAI and AOA by phyllosilicates, depending on the sample (Browning et al., 1996; Mcsween, 1979). They are characterized by small chondrules (diameters around 300 μm). The proportions of chondrules and matrix are very variable and they have low metal abundances (Weisberg et al., 2006). Clasts of CM chondrites are commonly

found in other meteorite types, which attest of a wide distribution in the Solar System (Zolensky et al., 1996).

- *CO (Ornans type):* Ornans type chondrites are generally characterized by low degrees of metamorphism, as their petrologic types range from 3 to 3.7 (Grady, 2022). They have relatively high chondrule (around 48 vol %) and low matrix (30-45 vol %) abundances. The chondrules in this category of chondrites are small (around 0.15 mm in diameter) (Rubin, 1989). Finally, the oxygen isotope compositions of these samples fall on the CCAM (carbonaceous chondrites-anhydrous minerals) linear trend. Some authors have proposed that CM and CO are related (Kallemeyn and Wasson, 1982).
- *CV (Vigarano type):* They are characterized by mm-sized chondrules, a high abundance of large CAI and AOA and relatively high abundances of matrix. They span across petrological types 2 to 3.3 (Grady, 2022). Finally, their oxygen isotope compositions also fall on the CCAM line.
- *CK (Karoonda type):* These chondrites petrological types range from 3 to 6 (Grady, 2022). They have similar abundances of chondrules, CAI and matrix than CV. Their chondrules are also mm-sized and their oxygen isotope compositions fall on the CCAM line. These similarities between CV and CK chondrites have led some authors to propose that they form a clan of their own (Greenwood et al., 2010). However, CK chondrites are more oxidized than CV, causing high abundance of fayalite (29-33 mol % of the olivines), low amounts of metal and significant presence of oxides like magnetite. They are also more depleted in MVE than CV or CO (Kallemeyn et al., 1991).

- *CR (Renazzo type):* Renazzo type chondrites are all of petrological type 2 (Grady, 2022), they present few CAI or AOA but are matrix-rich (40-70 vol %). The main difference with the other types of CC is the low MVE content of the CR, and their unique oxygen isotope compositions. Indeed, CR chondrites do not fall on the CCAM but follow their own trend, approximated by a line of slope 0.7.
- *CL (Loongana type):* This group was established recently and is constituted by only a few samples (Metzler et al., 2021). All samples are of petrological types 3.9 or 4, with almost equilibrated olivines (12.5 to 14.7 mol % fayalites). The metal content of this type is close to that of CR. It has low CAI abundances (around 1.4 vol %), and has very low matrix abundance (17 to 21 vol %) which cause it to be extremely MVE-depleted. Finally, its isotope compositions fall on the CCAM line.

- *Enstatite chondrites (EC):* This type of chondrites has formed under reduced conditions (Keil, 1968). This is reflected by relatively high metal abundances, often Si-enriched, and by Fe-poor silicates (mostly enstatites). Because of this reduced nature, some elements (Mn, Mg, Ca, Na, K) that act as lithophile in CC and OC behave like chalcophile in EC. The oxygen isotope compositions of enstatite chondrites fall on the terrestrial fractionation line, close to Earth and Moon compositions. These are the only chondrites to overlap with the Earth O isotope composition (Clayton et al., 1984). They are subdivided in two categories based notably on the compositions of their sulfides.
  - *EH ("high iron content"):* These are the most reduced chondrites. This is shown by the presence of niningerite and alkali sulfides (Keil, 1968). They span over a range of petrological types, going from 3 to 6 (Grady, 2022).

They are also characterized by higher amounts of silicon in the metal phases (2-3 wt. %) and by tinier chondrules.

- *EL ("low iron content"):* The presence of alabandite is characteristic. Their Si abundance in metal phases is lower (around 1 wt. %). They span the same range of petrological types than EH (Grady, 2022).

It is believed that all rocky bodies in the solar system are derived from chondritic objects that underwent planetary differentiation. This melting is thought to have been triggered by the heat dissipation during the radioactive disintegration of short-lived radionuclides (mainly ^{26}Al) (Van Kooten et al., 2016). Thus, the chemical and isotopic compositions of bulk terrestrial bodies should be reflective of a mixing of different chondrites or chondritic components. No mixing formula, however, has yet been able to account for all elemental and isotopic constraints related to the Earth. This quest for the determination of the accretion formula has generated numerous studies centered on chondrites. Moreover, the analysis of chondrite components allows for the constraining of the processes at play in chondrites forming reservoirs during the first Ma of the Solar System.

Because of their long history, chondrites can be exposed to numerous composition- or texture-altering processes. We detailed previously the potential influences of thermal metamorphism and aqueous alteration, occurring in the parent body and expressed as petrological types, and of the terrestrial alteration in the case of finds. Apart from these, we know at least two processes that can alter the meteorites Cd abundances and isotope compositions: neutron capture and high-temperature volatilization.

Cosmic rays interaction with solid matter produce, among other, neutrons that can interact with atomic nuclei, altering the isotopic compositions in the reacting objects. Cadmium isotopes do not generally react with such neutrons, as their thermal cross sections are below 1 barn for most of them, with only ^{110}Cd, ^{112}Cd and ^{113}Cd being characterized by bigger ones (Gicking et

al., 2019; Grinyer et al., 2005). Although ^{110}Cd (10.999 barns) and ^{112}Cd (2.198 barns) have slightly bigger thermal cross sections than the other isotopes, they remain mainly unaffected by neutron capture. On the other hand, ^{113}Cd has a thermal cross section at least two thousand times bigger than the other Cd isotopes (20 615 ± 400 barns) (Mughabghab, 2006). Thus, neutron capture transmuting ^{113}Cd into ^{114}Cd should occur in samples exposed to cosmic rays. This would create mass-independent isotope compositions for Cd as samples would be depleted in ^{113}Cd and enriched in ^{114}Cd. Such neutron capture has indeed been observed on lunar meteorites and soils with related isotope fractionation being as high as 3 ‰ per amu (Sands et al., 2001a; Schediwy et al., 2006; Wombacher et al., 2008). However, lunar samples exposed to cosmic rays for less than 30 Ma (Arvidson et al., 1975) are not characterized by significant neutron capture on ^{113}Cd (Schediwy et al., 2006), suggesting a low production rate. To this day, no neutron capture have been detected on non-lunar meteorites (Rosman and De Laeter, 1978; Wombacher et al., 2008). Nevertheless, any chondrite isotopic study will need to check for such processes occurring.

Finally, meteorites are known to experience superficial melting during their atmospheric entry due to air friction. This results in the formation of a fusion crust at the surface of the meteorite. Cadmium being an MVE, it can be significantly depleted by volatilization occurring during heating processes. This depletion would be coupled to a mass-dependent isotope fractionation caused by the preferential loss of lighter Cd isotopes in the gas (Wombacher et al., 2004, 2003). Previous studies of the fusion crust of chondrites have revealed no significant isotope fractionation between the crust and the bulk chondrite (Wombacher et al., 2008).

Volatilization processes can be approached by studying tektites, i.e., impact glasses that result from the ejection of molten crustal material during an asteroid impact. During their ballistic trip in the Earth atmosphere, tektites are hot enough to be subjected to significant MVE volatilization, producing isotope fractionation (Creech et al., 2019; Moynier et al., 2010, 2009;

Wombacher et al., 2003). To this day five tektites strewn fields are known (Australasian, Ivoirian, Central-European, North-American and Central-American) (Rochette et al., 2021), each linked to a singular source crater (although the Australasian crater remains undiscovered). Known tektite strewn fields are quite young, with the oldest (the North American one) being close to 36 Ma (Koeberl et al., 1996) and the other ones ranging in age from 14 Ma to less than 1 Ma (Di Vincenzo and Skála, 2009; Koeberl et al., 1997; Lee and Wei, 2000; Rochette et al., 2021).

2. Samples

In order to complete the characterization of the isotope fractionation occurring during Cd volatilization, which was investigated in Wombacher et al. (2004, 2003), we analyzed a set of two tektites and two impact glasses. Both of the studied tektites come from the Australasian strewn field, with one Australite (A-2018-1) and one Indochinite (I-F-16). Since these samples are from the same strewn field as the only other tektite characterized for Cd (a Muong Nong sample from Laos) (Wombacher et al., 2003), we expect them to fall on a similar trend of Cd depletion and isotope fractionation. The impact glasses (AT1 and AT2) were collected from a recently discovered strewn field in the Atacama desert (Devouard et al., 2014; Gattacceca et al., 2021; Koeberl et al., 2019). Impact glasses differ from tektites in that they are not pure terrestrial material but incorporated a fraction of the impactor.

Apart from the impact glasses, we analyzed a set of 17 chondrites composed of 8 CC, 7 OC and 2 EC. Among these, 14 samples (6 CC, 7 OC and 1 EC) were not previously characterized for both Cd concentrations and isotope compositions. Thus, our data set basically doubles the amount of CC and OC fully characterized for Cd to a total of 13 and 15 respectively. In detail, we analyzed bulk samples of Allende (CV3), Coolidge (CL4), Jbilet Winselwan (CM2), Murchison (CM2), NWA 13689 (ungrouped 3), Sahara 00177 (ungrouped 3.9), Sahara 99544

(CO3) and Tarda (ungrouped 2) carbonaceous chondrites. For ordinary chondrites, bulk samples of Bjurböle (L/LL4), Bruderheim (L6), Guarena (H6), Katol (L6), Kernouvé (H6), Lancon (H6), Olivenza (LL5) and St Séverin (LL6) were analyzed. Finally, Indarch (EH4) and Sahara 97096 (EH3) enstatite chondrites were characterized.

3. Methods

Tektite samples were crushed using agate mortar and pestle, in order to limit any potential input from the grinding material. The acid digestion, spiking, chemical purification and analysis protocol are detailed in Devos et al. (2024) and in the method chapter of this manuscript.

To summarize, we digested the samples using a mixture of concentrated HF and HNO_3 to break the silicate bonds. After total digestion, we evaporated the solution and dissolved the sample in concentrated HCl and refluxed it until total conversion of the fluorides into chloride form. The samples were then spiked using a ^{106}Cd-^{111}Cd double spike (DS) and homogenized at high temperatures. Purified Cd fractions were obtained using a Bio-Rad AG 1X8 200-400 mesh anion exchange resin with HBr-based loading and matrix removing and a HNO_3-based Cd elution protocol.

The solutions were analyzed on a *ThermoFischer Neptune* or *Neptune Plus* MC-ICP-MS, at the IPGP facility, Paris, France, equipped with nickel Jet and H skimmer cones and coupled to an ESI IR Apex desolvation system. The sample was introduced in the system using a 100 μL/min probe. We monitored ^{106}Cd, ^{110}Cd, ^{111}Cd, ^{113}Cd, and ^{114}Cd as well as ^{115}In and ^{118}Sn to correct for potential isobaric interferences from In or Sn.

Deconvolution of the obtained results was conducted using the IsoSpike algorithm (Creech and Paul, 2015). This process, necessitating 4 isotopes, was performed using ^{106}Cd, ^{110}Cd, ^{111}Cd, and either ^{113}Cd or ^{114}Cd. The obtained isotope compositions are expressed in permil deviations from the NIST 3108 Cd standard solution, as detailed hereafter:

$$\delta^{114}Cd = \left[\frac{\left({}^{114}Cd/{}_{110}Cd \right)_{sample}}{\left({}^{114}Cd/{}_{110}Cd \right)_{NIST\ SRM\ 3108}} - 1 \right] \times 10^3$$

The δ^{114}Cd and δ^{113}Cd values have been determined for every sample, to check for mass-dependency. Some samples were found to plot above the mass-dependency line in a δ^{114}Cd vs. δ^{113}Cd field. Such isotope compositions can be caused either by interferences (mainly Pd and Zr on chondrites) or by neutron capture (NC) on ^{113}Cd. We checked for potential NC influence by plotting our samples in a $^{113.5}$Cd/^{110}Cd vs. ^{114}Cd/^{113}Cd field. The $^{113.5}$Cd/^{110}Cd ratio is defined as the sum of ^{113}Cd/^{110}Cd and ^{114}Cd/^{110}Cd, which is insensitive to NC (Sands et al., 2001b), while ^{114}Cd/^{113}Cd is very sensitive to NC. No significant NC effect was observed, indicating that its potential influence should be minimal. This could be explained by the fact that cosmic rays interactions (thus, NC) only affect surface layers of samples, which have been largely lost during atmospheric heating. Moreover, bulk analyses would dilute NC-affected material in pristine one from the core of the meteorite. Lunar samples, are all surficial and did not went through atmospheric heating, which could explain why NC traces were found there. Instead, the mass-independent isotope compositions are coherent with isobaric or polyatomic interferences, either by Pd or by Zr which both cause significant alterations of the measured δ^{113}Cd and δ^{114}Cd for concentrations higher than around 1 % of that of Cd. Zirconium and Palladium are generally present in chondrites at concentrations ranging from 1 to 10 ppm (Barrat et al., 2014) and from 0.1 to 1 ppm respectively (Horan et al., 2003). Thus, Zr interferences are more probable than Pd ones and we corrected the measured deltas for this influence, using the Zr interferences assessment performed in Devos et al. (2024). Because of interferences on ^{114}Cd for I-F-16, the δ^{114}Cd for this sample was re-calculated based on its δ^{113}Cd measured value, assuming a natural mass-dependency.

4. Results

Cadmium concentrations and isotope compositions for all the analyzed samples are listed in Table 1. All the CC are characterized by Cd concentrations ranging from 10 to 500 ppb, while the OC compositions range from less than 1 ppb to more than 3 ppm. One OC (Katol), was so Cd-poor that no detection was possible on the ICP-MS. Enstatite chondrites can contain almost 1 ppm of Cd. Except for Jbilet Winselwan, which is enriched in heavy Cd isotopes, CC isotope compositions are contained in a small range of values (with δ^{114}Cd ranging from 0.150 to 0.652 ‰). Ordinary chondrites are much more isotopically variable, with δ^{114}Cd ranging from -8.411 to +6.955 ‰. Enstatite chondrite have intermediary compositions, with lightest composition being of -3.478 ‰ and heaviest one being of 0.267 ‰. The impact glasses are quite Cd-poor, with concentrations generally under 10 ppb and only one sample being characterized by 23 ppb Cd concentration. They are also isotopically heavy, with δ^{114}Cd being comprised between 1 and 4 ‰.

Table 1: Chondrites and impact glasses Cd compositions as determined in this work

Sample name	Chondrite group	Petrological type	Fall / Find	Cd (ppb)	2SD	δ^{113}Cd (‰)	2SD	δ^{114}Cd (‰)	2SD	n	Analysis conc (ppb)
Carbonaceous											
Jbilet Winselwan	CM	2	Find	402		1.027	0.052	1.369	0.069	1	10
				399		1.034	0.025	1.379	0.033	14	25
				401	**4**	**1.030**	**0.010**	**1.374**	**0.014**	**2**	
Murchison	CM	2	Fall	424		0.238	0.024	0.317	0.032	9	25
Allende	CV	3	Fall	215		0.171	0.014	0.228	0.019	5	25
				198		0.489	0.007	0.652	0.010	5	25
				207	**25**					**2**	
Sahara 99544	CO	3	Find	130		0.113	0.001	0.150	0.001	8	25
Coolidge	CL	4	Find	10		0.303	0.017	0.404	0.022	1	10
NWA 13689	Ungrouped	3	Find	336		0.238	0.020	0.318	0.027	20	25
				422		0.264	0.035	0.352	0.046	20	25
				379	**122**	**0.251**	**0.037**	**0.335**	**0.049**	**2**	
Sahara 00177	Ungrouped	3.9	Find	16		0.231	0.017	0.308	0.022	1	10
Tarda	Ungrouped	2	Fall	405		0.360	0.024	0.480	0.032	8	25
Ordinary											
Olivenza	LL	5	Fall	110		-6.308	0.013	-8.411	0.018	17	25
				288		-0.364	0.031	-0.486	0.042	14	25
St Séverin	LL	6	Fall	24		5.280	0.128	7.040	0.171	2	10
				24		5.153	0.017	6.870	0.022	1	10
				24	**1**	**5.216**	**0.180**	**6.955**	**0.240**	**2**	
Bjurböle	L/LL	4	Fall	2		-1.295	0.052	-1.727	0.069	1	10
				2		-0.005	0.098	-0.007	0.130	1	5
				2	**0.1**					**2**	
Bruderheim	L	6	Fall	0.7		0.480	0.828	0.640	1.104	8	0.1
				0.8		3.199	4.875	4.265	6.500	1	0.1
				1	**0.1**					**2**	
Katol	L	6	Fall	<<1							
Guarena	H	6	Fall	66		-0.094	0.015	-0.125	0.019	7	25
Kernouvé	H	6	Fall	2036		-0.304	0.017	-0.406	0.023	14	25
Lancon	H	6	Fall	3251		-0.684	0.028	-0.911	0.037	21	25
Enstatite											
Indarch	EH	4	Fall	27		-0.192	0.052	-0.256	0.069	1	10
				926		0.200	0.036	0.267	0.048	18	25
Sahara 97096	EH	3	Find	209		-0.348	0.004	-0.463	0.005	13	25
				220		-2.609	0.027	-3.478	0.036	13	25
				215	**15**					**2**	
Impact glasses											
A-2018-1	Australite	Tektite		7		2.546	1.900	4.014	1.200	2	1
I-F-16	Indochinite	Tektite		23		1.853	0.150	2.470	0.200		10
AT1	Atacamaite	Impact glass		8		0.684	0.250	1.026	0.240	1	5
AT2	Atacamaite	Impact glass		5		1.203	0.250	1.733	0.240	1	5

The "n" column lists the number of measurements performed to obtain the given isotope composition. Whenever only one or two measurements were performed, the displayed isotope composition 2SD corresponds to the biggest 2SD obtained for another sample in the same conditions during the same analysis run. The last column lists the Cd concentration of the analyzed

solution, which determined for good part the precision of the measurement. Low concentration samples like Bruderheim chondrite or A-2018-1 tektite are characterized by very high uncertainties. Bold lines display the mean values obtained for samples that does replicate correctly for Cd concentrations or isotope compositions. Most chondrite replicates give up different compositions, be it distinct concentrations (NWA 13689), isotope compositions (Allende, Bjurböle and Sahara 97096) or both (Olivenza and Indarch). Only Jbilet Winselwan, Bruderheim (although the wide uncertainties make the interpretation difficult) and St Séverin replicates show good agreement. This points toward significantly heterogeneous compositions of chondrites for Cd, which persist even when big amounts of sample are mixed to homogenize them.

5. Discussion

5.1. Impact glasses, a study of Cd volatilization

Tektites and impact glasses can be used to constrain the isotope fractionation occurring during volatilization events occurring in the Earth atmosphere (Creech et al., 2019; Moynier et al., 2010, 2009). This, however, requires knowledge of the composition of the initial impacted material, which can be difficult in cases like Australasian tektites for which the generating crater is still to be found. Fortunately, the Earth surface is quite homogeneous for Cd isotope compositions. Upper continental crust isotope composition, approximated by loesses, is of δ^{114}Cd = 0.06 ± 0.14 ‰ (2SD, n = 13) (Pickard et al., 2022); while MORB return a 0.07 ± 0.10 ‰ (2SD, n = 23) for the oceanic crust (Devos et al., 2024). Similarly, the Cd concentrations overlap, with 90 ± 40 ppb (2SD) for the upper continental crust (Rudnick and Gao, 2014) and 126 ± 45 ppb (2SD, n = 23) for the oceanic crust (Devos et al., 2024). These values are very distinct from that of the analyzed tektites and impact glasses, which are good conditions for the assessment of the impact of Cd volatilization.

Figure 1 shows the correlation between the Cd depletion and the sample isotope composition. As shown previously (Wombacher et al., 2004), Cd volatilization causes a drift toward isotopically heavy compositions. This process can be modelized by a Rayleigh distillation law, which is described by the following equations:

$$\Delta^{114}Cd = \delta^{114}Cd_{sample} - \delta^{114}Cd_{initial}$$

$$\Delta^{114}Cd = 10^3 \times \left(\frac{[Cd]_{sample}}{[Cd]_{initial}}\right)^{\alpha-1} - 10^3$$

which gives:

$$\alpha = \frac{log\left(\frac{\Delta^{114}Cd + 1000}{1000}\right)}{log\left(\frac{[Cd]_{sample}}{[Cd]_{initial}}\right)} + 1$$

with $[Cd]_{initial}$ being the Cd concentration of the sample before volatilization, $\delta^{114}Cd_{initial}$ its isotope composition at the same time and α the kinetic fractionation factor. We assume that the occurring isotope fractionation is mass-dependent and took the upper continental crust as starting material. The α parameters used to calculate the trends for each sample group ($\alpha_{atacamaites}$ = 0.9995, $\alpha_{Australasian\ tektites}$ = 0.9995) are mean values of individual α determined for each sample of the trend, using the previous equation. The two tektites analyzed in this study and the one analyzed previously (Wombacher et al., 2003) give coherent compositions.

Theoretical isotope fractionation occurring for purely kinetic Rayleigh distillation can also be calculated, using the square root of the ratio of the mass of the volatized species (Cd or CdO) as α. The obtained trends are displayed in black on Figure 1. Such processes are found to create much more intense isotope fractionation than observed. This is in agreement with previous observations for Cd, and other volatile elements (Creech et al., 2019; Moynier et al., 2010,

2009; Wombacher et al., 2003). These observations have led authors to propose a model in which the depletion and isotope fractionation are controlled by diffusion of the species in the molten droplet during evaporation (Moynier et al., 2010, 2009). In this model, most of the available material at the surface of the droplet is efficiently evaporated, which creates a depleted layer. Diffusion then takes place in the melt, from the concentrated core to the depleted external layer. According to this model, elements characterized by low diffusivity in the melt should experience less isotope fractionation than those characterized by high diffusivity. We compared the literature results for Cu (Moynier et al., 2010), Zn (Moynier et al., 2009) and Sn (Creech et al., 2019) to our Cd measurements to determine which element diffuses the quickest in the melt. For this, we calculated the mean $\alpha_{normalized}$ parameter for Australasian samples, with mass difference-normalized isotope compositions (expressed in ‰ per amu), as given by the following formula for δ^{114}Cd:

$$\alpha_{normalized} = \frac{log\left(\frac{\Delta^{114/110}Cd}{\frac{m_{^{114}Cd} - m_{^{110}Cd}}{1000}} + 1000\right)}{log\left(\frac{[Cd]_{sample}}{[Cd]_{initial}}\right)} + 1$$

with $m_{^{114}Cd}$ being the atomic mass of the ^{114}Cd isotope. We only took into account the samples characterized by distinct isotope composition from that of the initial composition, which significantly affected the obtained result for Cu. We obtained the following $\alpha_{normalized}$ values: Sn (0.9998) > Cd (0.9996) ≥ Zn (0.9995) > Cu (0.9991), where elements with low $\alpha_{normalized}$ are characterized by high diffusivity in the melt and by intensely fractionated isotope compositions. Since the $\alpha_{normalized}$ values for Zn and Cd are essentially similar, we can assess that the elements diffusion speeds in the melt are mainly determined by their chemical group, hence by their chemical properties. This stands in agreement with our

understanding that diffusivity is partly related to the electric charge of the diffusing ion ($Cu^{+/2+}$, Zn^{2+} and Cd^{2+}, $Sn^{2+/4+}$).

The difference in isotope compositions between atacamaites and Australasian tektites could be explained either by an initial composition for atacamaites that is poorer in Cd than the upper continental crust. In such a case, the real $\alpha_{atacamaites}$ could be similar to that of tektites. A second possibility is that the impactor material that mixed with the melted crust was characterized by a light Cd isotopes-enriched composition that significantly altered the impact glasses compositions. Such compositions are known to exist in OC and EC (see later). Finally, it is possible that the chemical and physical parameters in the atacamaites melt (chemical composition, temperature, degree of polymerization…) affected the effective diffusivity of Cd compared to Australasian tektites melt.

The fact that the actual samples that underwent significant Cd volatilization are characterized by significantly lighter isotope composition than what would be expected of a purely kinetic theoretical Rayleigh distillation is confirmed by lunar samples analyses (Sands et al., 2001b; Schediwy et al., 2006). According to the current models, the Moon has formed after a giant impact between the proto-Earth and the Theia impactor that ejected important amounts of molten terrestrial material in space. The Moon would have accreted this material, explaining the observed chemical relationship between the Earth and the Moon. Such a process should be the ideal setting for massive Cd volatilization to occur in lunar material. Since lunar soils Cd compositions are strongly altered by meteoritical inputs, they are not fitting to determine the influence of lunar Cd volatilization over its isotope composition (Sands et al., 2001b; Schediwy et al., 2006). Lunar basalts might be more reliable, as they are thought to sample the Moon mantle. To our knowledge only one lunar basalt Cd composition has ever been reported. It is characterized by extremely depleted Cd content, with only 9 ppb of Cd (75 % depletion from the BSE), and is undistinguishable from the BSE isotope composition, with

a δ^{114}Cd of 1.2 ± 3.6 ‰ (Schediwy et al., 2006). As a point of comparison, a 75 % loss should result in a δ^{114}Cd of more than +20‰, according to theoretical Rayleigh distillation for Cd (g) or CdO (g). This proves that, even with an intense Cd depletion compared to the BSE, the real isotope fractionation is limited, which fits well with the tektites results.

This study of impact glasses indicate that efficient Cd volatilization can occur in molten samples exposed to the Earth atmosphere. This depletion is coupled to a significant isotope fractionation that can alter the bulk isotope composition of the sample, at least for objects as small as impact glasses. During the atmospheric entry of meteorites, the intense heating usually melts the surface layer of the object, creating what is known as a fusion crust. We expect this layer to experience the same kind of Cd volatilization as impact glasses. However, in conformity with the exposed model, we do not expect significant isotope fractionation to occur as only a thin layer of the meteorite melts, preventing any diffusion-driven process to be significant. Thus, we expect that the Cd isotope composition of meteorites that were not melted during their atmospheric journey should remain unchanged by it. The fusion crust is expected to be almost totally Cd-depleted and to have generally unfractionated Cd isotope composition, which is generally what was observed in previous study (Wombacher et al., 2008). Hence, unmelted meteorite bulk isotope composition can be studied without correcting for potential Cd volatilization effects.

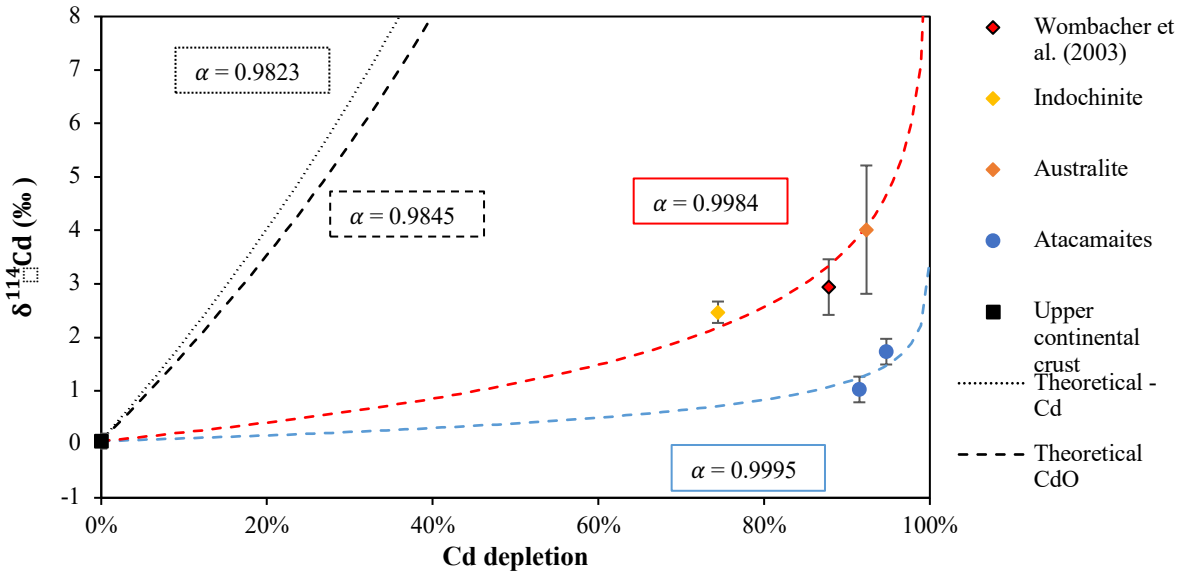


Figure 1: Isotope compositions of tektites and atacamaites vs. their Cd depletion. The samples get isotopically heavier as they become more Cd-depleted. Two trends can be identified: one in red for the Australasian samples (diamonds) and one in blue for the atacamaites. We also included trends for theoretical Rayleigh distillation of both Cd and CdO as gas. The starting composition has been approximated by that of the upper continental crust. We also plotted the only other tektite that was characterized for Cd (Wombacher et al., 2003).

5.2. Cadmium compositions of chondrites

5.2.1. Compositional and isotopic heterogeneities in chondrites

One of the main characteristics of chondrites is their structural and mineralogical heterogeneity, as they did not experience homogenization during melting. However, this heterogeneity implies that, in order to perform bulk analyses, a significant mass of sample must be grounded and mixed. Otherwise, chemical heterogeneities are likely to be reflected in the analysis and the result may be unfit for the characterization of a bulk composition.

To our knowledge, only a handful of chondrites have been independently analyzed multiple times for Cd concentrations. We know of 11 CC samples for which replicates were analyzed, this number falls to 9 for OC and to 3 for EC (see Table 1, Table 2, Table 3 and Table 4). Among these samples, around half do present significant Cd concentrations variability between replicates: Orgueil, Jbilet Winselwan, Murchison, Mighei, NWA 13689 and Allende for CC,

Bishunpur, Parnallee, Bruderheim, Dimmit and Olivenza for OC and Abee and Indarch for EC. This variability is not determined by the fall / find nature of the sample as both are represented in the set.

Similar ratios can be found for isotope compositions, with 7 CC, 8 OC and 3 EC analyzed multiple times, among which 4 CC, 2 OC and 2 EC present significant isotopic variability (see Table 1 and Table 3). These heterogeneous samples are Allende, Colony, Leoville and Orgueil for CC, Bjurböle and Olivenza for OC and Indarch and Sahara 97096 for EC. Similarly to Cd concentrations, this ensemble contains both falls and finds. These results highlight the fact that heterogeneities in chondrites are a prevalent reality for Cd, which could prevent the effective use of bulk compositions.

Carbonaceous chondrites

We analyzed a set of 6 CC for which no Cd isotope composition was already existing in the literature, and two CC that have received important attention in previous works to compare our results (Allende and Murchison). While our Murchison analysis (424 ppb; δ^{114}Cd = 0.317 ± 0.032 ‰; 2SD) agrees perfectly with the previously proposed Cd concentrations and isotope compositions (429 ± 99 ppb; δ^{114}Cd = 0.316 ± 0.071 ‰; 2SD), Allende exhibits more variability.

For Allende, multiple independent analyses have agreed on two compositions: the fraction conserved at the Natural History Museum, London, having a Cd concentration of 224 ± 44 ppb (2SD, n = 7) (Baker et al., 2010; Braukmüller et al., 2018; Loss et al., 1984; Rosman and De Laeter, 1974; Wombacher et al., 2003; This work) while the one from the Smithsonian Institute, USA, is characterized by a Cd concentration of 473 ± 25 ppb (2SD, n = 4) (Braukmüller et al., 2020, 2018; Wang et al., 2015; Wolf et al., 1980). Our proposed Cd concentration of 207 ± 25 ppb (2SD, n = 2), is in good agreement with the proposed compositions for the Allende fraction

from the Natural History Museum, London. Since the observed compositions do not form a continuum but are strictly bimodal, it is probable that Allende formed by aggregation of two homogeneous objects characterized by distinct Cd compositions.

We are not aware of any isotope composition proposed for the Cd-rich fraction of Allende. However, out of our two digestions for the bulk Cd-poor fraction of Allende, only one was characterized by an isotope composition similar to what was previously proposed ($\delta^{114}Cd_{\text{This work}}$ = 0.228 ± 0.019 ‰ vs. $\delta^{114}Cd$ = 0.22 ± 0.12 ‰; 2SD). Our replicate gave a significantly heavier isotope composition of $\delta^{114}Cd$ = 0.652 ± 0.010 ‰; 2SD) despite having similar Cd concentration. Since the isotopically heavier replicate is also slightly poorer in Cd, one could propose that a volatilization mechanism is at the origin of the composition difference. However, this would require an α parameter of 0.9949, much lower than what was found on tektites. Nevertheless, since such a volatilization would occur in the near vacuum of space, it would probably be much more efficient than for tektites; thus, such mechanism cannot be totally dismissed. A more probable scenario is that Allende is isotopically heterogeneous at the scale of our samples. Such heterogeneity could be caused by local variations in the chondrules over matrix ratio, as previous works have shown that chondrules and matrix are isotopically lighter and heavier respectively than the bulk chondrite (Wombacher et al., 2008), similarly to what is observed for Zn (Pringle et al., 2017).

The last CC sample for which we have replicates, NWA 13689, has a homogeneous isotope composition but presents some variability for its Cd concentration. Since the isotope composition of this sample is constant, we propose that the Cd content variation mainly reflects variable dilution of the Cd-bearing phase.

Ordinary chondrites

Ordinary chondrites also display significant heterogeneities for Cd, although their discussion is rendered harder by the fact that we have no isotope compositions in the literature for the samples we analyzed. However, we analyzed replicates for 4 of our samples (Bjurböle, Bruderheim, Olivenza and St Séverin). The Cd concentrations obtained for different digestions showed good agreement for Bjurböle, Bruderheim and St Séverin. However, similar isotope compositions were only found for Bruderheim and St Séverin although low Cd concentrations in Bruderheim led us to conduct very low concentration analyses (with concentrations as low as 0.1 ppb), resulting in wide uncertainties which complicate any comparison.

The Olivenza chondrite is an interesting case. We analyzed two replicates of this chondrite (GD 4-26 and GD 4-27), both sampled from the same powder and with large masses: 1.61g and 1.14g respectively. These two replicates, however, displayed distinct chemical compositions, with GD 4-26 being characterized by a Cd concentration of 110 ppb while GD 4-27 Cd concentration was of 288 ppb. Since these two replicates were sampling the same powder, that was previously mixed to ensure homogeneity, we cannot propose a large-scale heterogeneity as encountered with Allende. We explain our diverging data by a nugget effect in GD 4-27. The Cd-rich particle must be uncommon enough not to be present in the sampled 1.61g of GD 4-26. If the composition of GD 4-26 is representative of the bulk meteorite, nuggets excluded, and if the mass of the particle is negligible, we can determine that the particle should contain around 200 ng of Cd, which is considerable. To this point, the nature of such a particle remains undetermined. Let's finally note that a recent article proposed a Cd concentration of 40 ppb for Olivenza (Palk et al., 2018), showing that this sample is probably composed of very heterogeneous fractions or that nugget effect is very common in this sample.

The Olivenza replicates are not only characterized by very distinct Cd concentrations but also by variable isotope compositions. The replicate which presumably contained a Cd-rich

nugget is characterized by a much heavier isotope composition than the other one, leading to the conclusion that the potential nugget is isotopically heavy. Based on our previous estimation of the Cd input by the nugget, we can determine that it should be characterized by a δ^{114}Cd of 4.40 ‰, which is in the range spanned by ordinary chondrites.

Finally, Bjurböle replicates provided a similar Cd concentration but very distinct isotope compositions. In both cases, we sampled important masses (1.35 and 1.37g) to ensure maximal homogeneity. Since no difference is found in the Cd concentrations for these two samples, these isotopic variations must reflect isotopic heterogeneity in the meteorite.

Enstatite chondrites

The EC dataset presented in this study is much smaller than for OC or CC, with only two analyzed samples, and replicates being analyzed for both. Among these, only Indarch chondrite Cd composition was already characterized (Palk et al., 2018; Wombacher et al., 2008). Again, our replicates compositions are not similar to each other nor are they similar to some of the literature values, highlighting again the probable heterogeneity of chondrites for Cd.

Cadmium concentrations determined for Indarch (27 and 926 ppb) are significantly distinct from the literature value of 659 ± 14 ppb (Palk et al., 2018). Our proposed Cd isotope compositions are slightly distinct; however, they are similar to the composition of -0.28 ± 0.57 ‰ proposed by Wombacher et al. (2008). In our case, the most Cd-rich replicate is also isotopically the heaviest. This suggest that Indarch did not experience significant Cd volatilization. Part of the composition might be explained by the input of a Cd-rich, isotopically heavy phase, like for Olivenza although in a less intense manner. Since the composition determined by Palk et al. (2018) is less concentrated in Cd but isotopically heavier, we have to suggest the input of a Cd-rich, isotopically light, fraction to produce the compositions observed in our work.

The Sahara 97096 replicates have roughly similar Cd concentrations but very distinct isotope compositions. Because of the similarity in Cd concentrations, the isotope composition difference cannot be accounted for by any volatilization event or Cd input by a concentrated phase. It is possible that a Cd-poor phase happening to have a strongly fractionated isotope composition could produce the observed difference. However, this would require an input of around 12 ng of Cd with an isotope composition of -62 ‰, which is much more fractionated than any known sample. Thus, this scenario is unlikely. We propose that this heterogeneity reflects that of the chondrites-forming regions in the solar nebula.

5.2.2. Carbonaceous chondrites

Comparison between falls and finds

Carbonaceous chondrites are characterized by relatively low Cd concentration, ranging from 1 ppb to 1 ppm. Three categories can be devised based on a comparison between the Cd concentrations of fall and find samples (see Figure 2). The first group comprises CI, CV and CR; in these types of CC, the find samples are significantly Cd-depleted compared to the falls. This depletion can be explained by the fact that the Cd-bearing phase is probably easy to weather, readily releasing its Cd during terrestrial water leaching. Figure 3 displays the isotope compositions for the characterized CC samples. We do not have any data for CI finds nor for CR falls. However, we observe that Cd-depleted CV find is isotopically heavier than the CV falls. The alteration process should not be weathering, as it has been shown to preferentially leach the heaviest Cd isotopes contrarily to what happened in this case (Devos et al., 2024; Zhang et al., 2016; Zhu et al., 2018). This isotope composition can be modelized by an 85 % Cd-depletion using a Rayleigh distillation model with a reasonable 0.9996 kinetic factor. However, volatilization is improbable on Earth so that the observed composition could be either the result of non-terrestrial processes, like vaporization, or of a non-characterized terrestrial alteration process. The CR find sample has a similar isotope composition than the rest of the

CC, potentially indicating resilience to isotope fractionation during alteration or short lifetime at the surface of the Earth. The fact that the two other known isotope compositions for CR finds (Acfer 209, $\delta^{114}Cd = 0.32 \pm 0.28$ ‰, and EET 92042, $\delta^{114}Cd = 0.11 \pm 0.05$ ‰) (Baker et al., 2010; Wombacher et al., 2008) are similar suggests that CR isotope compositions are resilient to alteration.

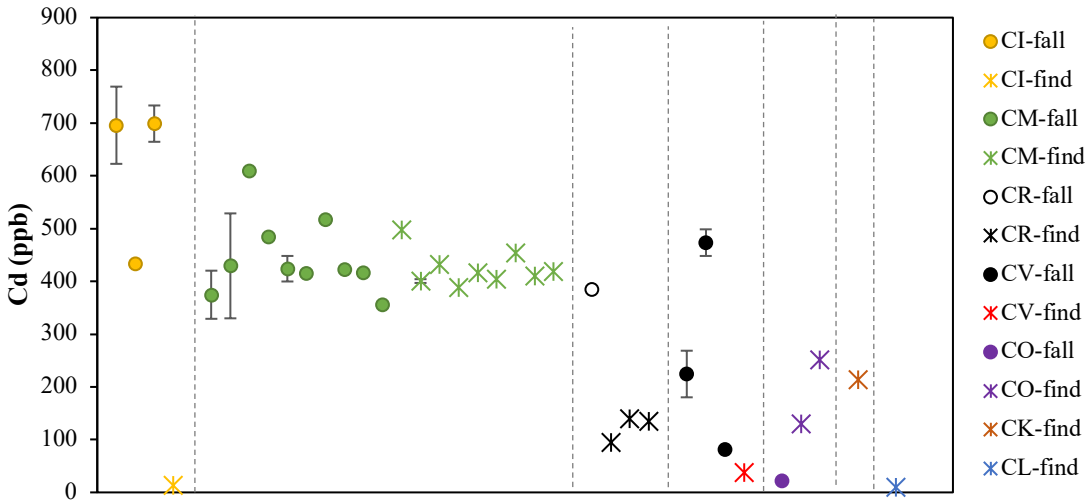


Figure 2: Comparison of Cd concentrations for fall and find CC. The Cd concentrations of find CI, CV and CR are generally inferior to those of fall chondrites, indicating that Cd is probably concentrated in an easily leachable phase. For these samples, it is probably better to only study falls as finds seem to have significantly altered Cd content. CM chondrites Cd concentrations are similar for falls and finds, indicating a good resilience to alteration. The sample of fall CO is Cd-poor, the find CO, however, are enriched in Cd, indicating a terrestrial Cd pollution. Data are exposed in Table 2.

The second group is composed only of CM chondrites, it is characterized by the fact that falls and finds display similar Cd concentrations. This indicates that, in CM samples, Cd is probably mainly concentrated in almost unalterable phases. The only CM find we analyzed is characterized by an isotopically heavy Cd composition and similar Cd concentration to that of falls. This could reflect a complex coupling between Cd depletion and input from a terrestrial source, allowing for a stable Cd concentration, or simply an unusual initial isotope composition.

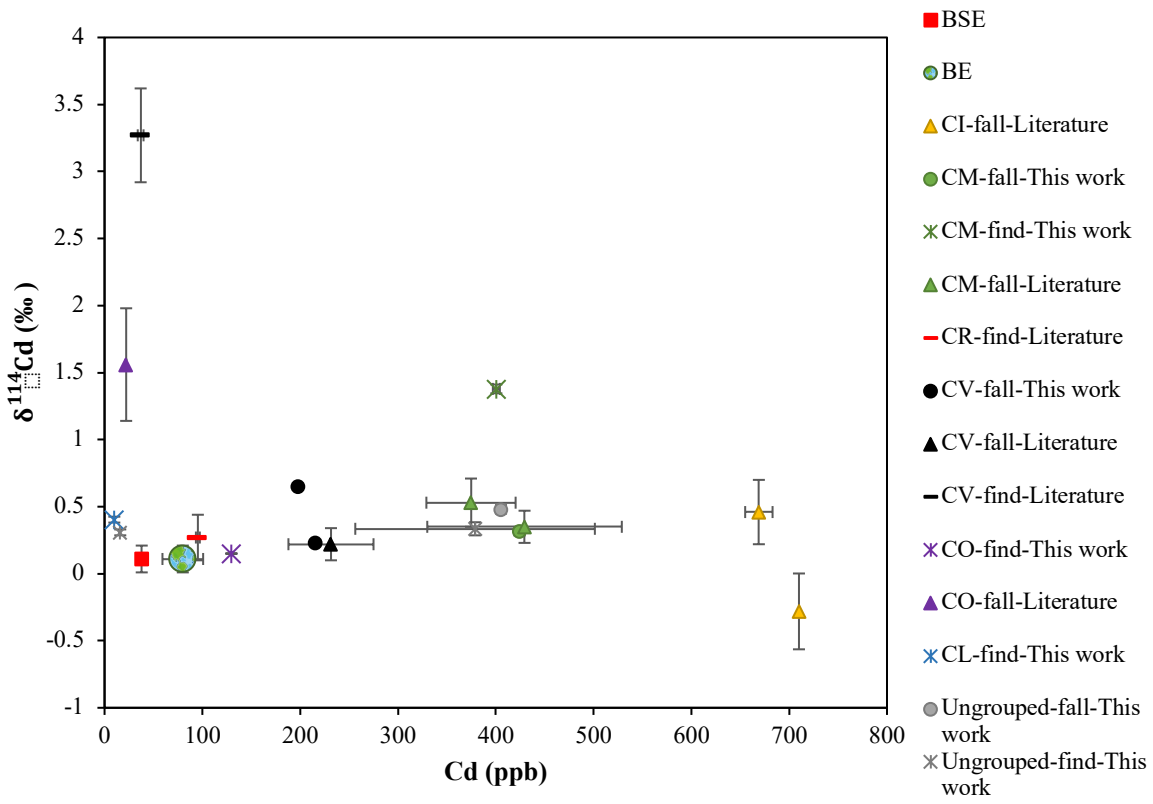


Figure 3: Cadmium isotope compositions for CC as a function of their Cd concentrations. Results from this study are displayed as dots or crosses for falls and finds samples respectively. Literature data are represented by triangles for falls and horizontal bars for finds. The symbol color indicates the sample CC group. BSE and BE compositions are materialized by a red square and a small Earth disk respectively. Their compositions are proposed in Devos et al. (2024) and Wang et al. (2018). Error bars materialize 2SD uncertainties. Whenever multiple distinct compositions were determined for a sample, they were plotted as different points (as an example, both CV points for this study refer to Allende and both CI points from the Literature refer to different compositions for Orgueil). Data are detailed in Table 1 and Table 4. Except for four samples (one fall CI, one fall CO, one find CM and one find CV), the CC isotope compositions are very consistent and globally comprised between 0 and 0.65 ‰. A slight positive correlation between Cd concentrations and isotope compositions can be found for CM, CV and possibly CI, CR and CL.

The last group is composed of CO chondrites, which seem to be characterized by a very low Cd concentration in falls and slightly higher concentrations in finds. The fact that the find samples are enriched in Cd compared to fall ones indicates that terrestrial processes can not only leach Cd out but also inject terrestrial Cd in the altered sample. The fall sample is isotopically heavy, indicating that the Cd input fluid is concentrated in light isotopes.

Characterization of the Cd-bearing phase

The Figure 4 plots Cd concentrations for bulk chondrites against their individual matrix and chondrule contents. The highest Cd concentrations are obtained for CI samples, chondrites that are almost only composed of matrix, indicating that Cd is mainly borne by this phase. However, CC samples with matrix content ranging from more than 80 vol % to less than 50 vol % share similar Cd concentrations. This cannot be accounted for by a model mixing a CI-like matrix with Cd-poor chondrules and refractory inclusions, and suggests a Cd input in chondrules and/or refractory inclusions.

Moreover, analyses of chondrules and CAI in Allende have shown that they can be as concentrated as 300 ppb and 1200 ppb respectively (Wombacher et al., 2008) while the bulk Cd concentration of the sample is of 220 ppb (Wombacher et al., 2003), which suggests that the matrix Cd concentration is below 200 ppb. This suggests that chondrules are a significant Cd-bearing phase and that the matrix can evolve from a CI-like Cd-rich composition to a more Cd-depleted one.

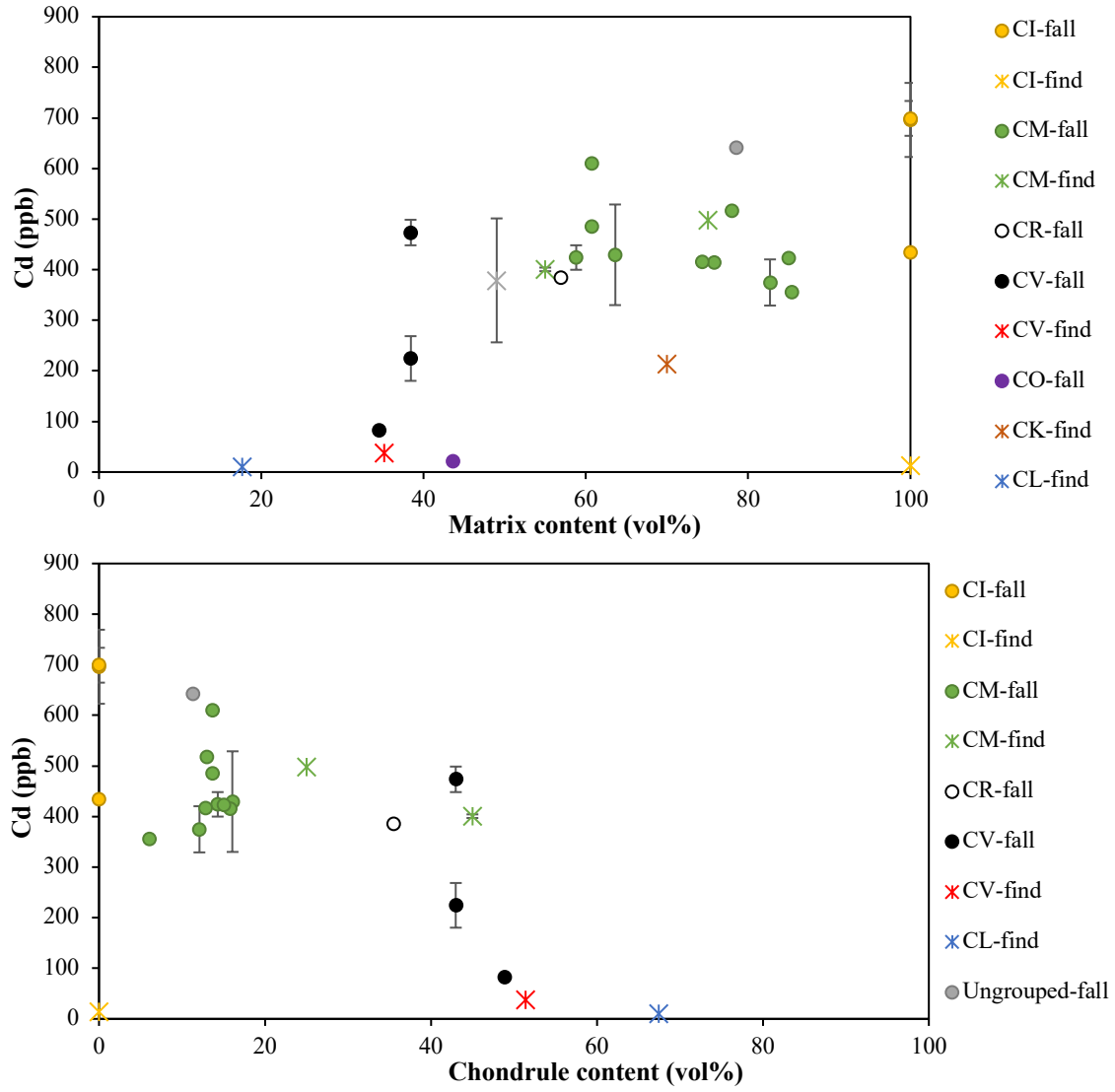


Figure 4: Carbonaceous chondrites Cd concentration as a function of their matrix content (top) and of their chondrule content (bottom). Although the most Cd-rich samples are CI chondrites, indicating that Cd is mainly present in matrix, samples with matrix contents ranging from 50 to 80 vol % maintain almost constant Cd concentrations. This can be explained by leaching of Cd out of the matrix and recrystallization in the chondrules. Data are exposed in Table 2.

Finally, Figure 5 shows a clear linear correlation between Zn and Cd concentrations in CC. This is most probably caused by the fact that these two elements are similarly mainly concentrated in the matrix (before secondary alteration). A loose negative correlation was found between Cd concentrations and metal or sulfide contents, indicating that, despite Cd siderophility and chalcophility, it is not mainly contained in these phases.

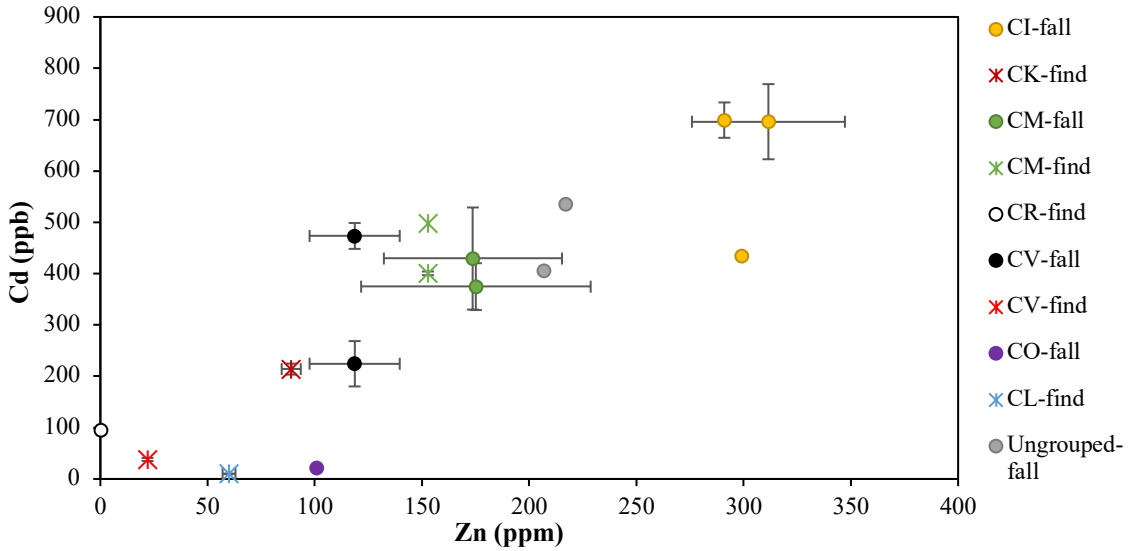


Figure 5: Comparison between Cd and Zn concentrations in carbonaceous chondrites. There is a clear linear correlation between these two elements, indicating that, in CC, Cd behaves similarly than Zn and is probably concentrated in the same phases. Data are exposed in Table 2.

A CC correlation between the Cd contents and isotope compositions?

Figure 3 displays the CC sample's isotope compositions versus their Cd concentrations. Apart from four isotopically fractionated samples, all the compositions are comprised in a small range of isotope compositions (between 0 and 0.65 ‰). We find that there is a weak correlation between Cd concentrations and isotope compositions for CM (falls and finds), CV (falls only) and some ungrouped fall and find chondrites like NWA 13689, Sahara 00177 and Tarda. This correlation could be extended to CR and CL samples if the analyzed finds have similar isotope compositions than the falls and to CI chondrites if they are well represented by the isotopically heaviest replicate of Orgueil. Finally, if Kainsaz isotope composition is representative of the CO falls, very Cd-depleted CC might be significantly enriched in heavy Cd isotopes, following a new trend. The main trend can be explained by a mix between an isotopically heavy matrix and isotopically lighter chondrules (Wombacher et al., 2008) while CO compositions might reflect Cd volatilization. This is similar to the isotopic trend observed for Zn in CC, which testifies of the similarity in behavior connecting these two elements. Let's add that no CC have

similar Cd concentration than the BE. Similarly, its proposed δ^{114}Cd of 0.11 ± 0.10 ‰ is significantly lighter than most CC compositions, except for CV and some CI. Two of the outliers are find samples: one CM with similar Cd content than the related fall and one intensely Cd-depleted CV.

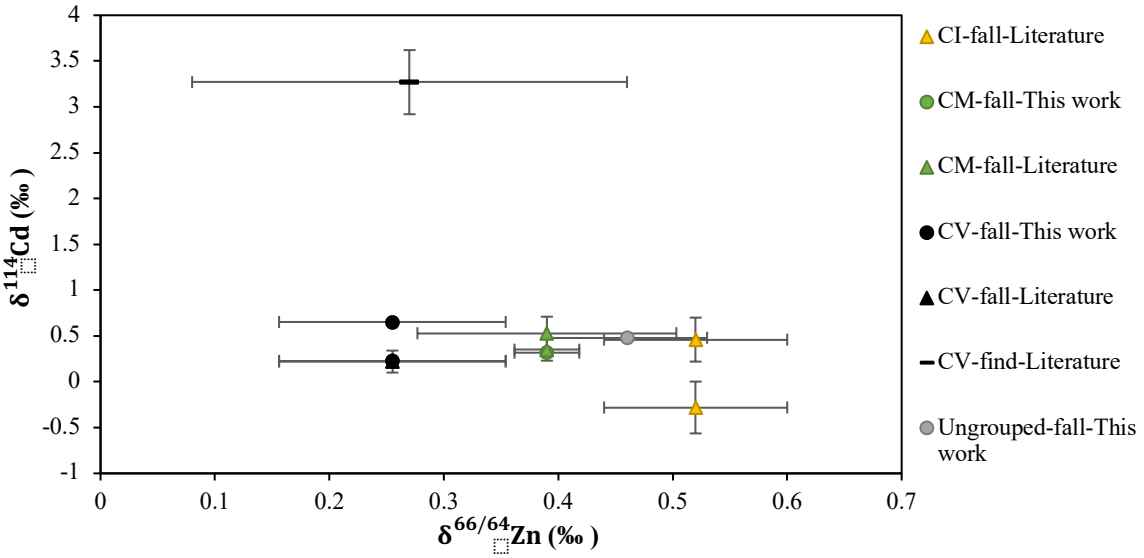


Figure 6: Comparison of the CC isotope compositions for Cd and Zn. The symbols are the same than for the previous figure. Because of the lack of variability in Cd isotope compositions, we find no significant correlation with Zn isotope compositions. This stands in stark contrast with the good correlation occurring between the concentrations of these elements in the same samples. Thus it seems that, although Cd and Zn behave similarly when crystallizing, leading to a concentrations coupling, they are not isotopically fractionnated by the same processes. Data are detailed in Table 1 and Table 4.

Despite the good correlation observed between Cd and Zn contents in CC, Figure 6 shows no significant coupling between their isotope compositions, due to the lack of isotope compositions variation for Cd. Since we know that Cd is isotopically fractionated by vaporization events and that it is more volatile than Zn, we can postulate that no significant MVE volatilization occurred in CC.

Table 2: Cadmium and Zinc concentrations, coupled with matrix and chondrule content for carbonaceous chondrites

Sample name	Group	Type	Fall / Find	Cd (ppb)	2SD	Reference	Zn (ppm)	2SD	Reference	Matrix (Vol. %)	Chondrules (Vol. %)	Reference
Alais	CI	1	Fall	**434**		Krähenbül et al. (1973)	**299**		Krähenbühl et al. (1973)	**100**	**0**	Weisberg et al. (2006)
Ivuna	CI	1	Fall	677	17	Krähenbül et al. (1973)	304		Krähenbühl et al. (1973)	100	0	Weisberg et al. (2006)
				722	4	Loss et al. (1984)	291		Luck et al. (2005)			
				709	4	Loss et al. (1984)						
				691	10	Wang et al. (2015)						
				696		Braukmuller et al. (2018)						
				699	**34**	**Mean**	**298**	**18**	**Mean**	**100**	**0**	**Mean**
Orgueil	CI	1	Fall	661	36	Krähenbül et al. (1973)	303		Krähenbühl et al. (1973)	100	0	Weisberg et al. (2006)
				770		Rosman and De Laeter (1974)	301		Luck et al. (2005)			
				710	25	Loss et al. (1984)	298		Barrat et al. (2012)			
				708		Rosman and De Laeter (1988)	337		Braukmüller et al. (2018)			
				710		Wombacher et al. (2003)	311		Braukmüller et al. (2020)			
				669	14	Baker et al. (2010)						
				695	12	Wang et al. (2015)						
				697		Braukmuller et al. (2018)						
				644	7	Braukmuller et al. (2020)						
				696	**73**	**Mean**	**310**	**32**	**Mean**	**100**	**0**	**Mean**
Y-980115	CI	1	Find	**13**		Braukmuller et al. (2018)				**100**	**0**	Weisberg et al. (2006)
MET 01070	CM	1	Find	**419**		Braukmuller et al. (2018)						
SCO 06043	CM	1	Find	**410**		Braukmuller et al. (2018)						
ALH 85013	CM	2	Find	**389**		Braukmuller et al. (2018)						
Boriskino	CM	2	Fall	**415**		Wolf et al. (1980)				**76**	**16**	McSween (1979)
Cold Bokkeveld	CM	2	Fall	395		Wolf et al. (1980)	204		Wolf et al. (1980)	74	12	McSween (1979)
				350	8	Baker et al. (2010)	162		Luck et al. (2005)	83		Greenwood et al. (1994)
				379		Braukmuller et al. (2018)	145		Pringle et al. (2017)			
							190		Braukmüller et al. (2018)			
				375	**46**	**Mean**	**175**	**54**	**Mean**	**78**	**12**	**Mean**

Table 2 (continued)

Sample name	Group	Type	Fall / Find	Cd (ppb)	2SD	Reference	Zn (ppm)	2SD	Reference	Matrix (Vol. %)	Chondrules (Vol. %)	Reference
EET 96029	CM	2	Find	**416**		Braukmuller et al. (2018)						
Erakot	CM	2	Fall	**517**		Wolf et al. (1980)				**78**	**13**	McSween (1979)
Haripura	CM	2	Fall	**423**		Wolf et al. (1980)				**85**	**15**	Wood (1967)
Jbilet Winselwan	CM	2	Find	498		Braukmuller et al. (2018)	153		Friend et al. (2018)	**75**	**25**	Friend et al. (2018)
				401	4	This study	172		Creech and Moynier (2019)	**55**	**45**	Friend et al. (2018)
				449	**138**	**Mean**	**162**	**27**	**Mean**			
LON 94101	CM	2	Find	**405**		Braukmuller et al. (2018)						
LON 94102	CM	2	Find	**454**		Braukmuller et al. (2018)						
Mighei	CM	2	Fall	**610**		Krähenbül et al. (1973)	**187**		Krähenbühl et al. (1973)	**61**	**14**	McSween (1979)
				485		Braukmuller et al. (2018)						
Murchison	CM	2	Fall	379		Krähenbül et al. (1973)	144		Luck et al. (2005)	**64**	**16**	McSween (1979)
				442		Rosman and De Laeter (1974)	160		Wang and Lipschutz (2005)			
				440		Wombacher et al. (2003)	186		Pringle et al. (2017)			
				427	28	Wang & Lipschutz (2005)	192		Braukmüller et al. (2018)			
				387	8	Baker et al. (2010)	187		Braukmüller et al. (2020)			
				538	8	Wang et al. (2015)						
				422		Braukmuller et al. (2018)						
				400	5	Braukmuller et al. (2020)						
				429	**99**	**Mean**	**174**	**42**	**Mean**	**64**	**16**	**Mean**
Murray	CM	2	Fall	416		Krähenbül et al. (1973)				59	14	McSween (1979)
				416		Rosman and De Laeter (1974)						
				420	3	Loss et al. (1984)						
				445	4	Loss et al. (1984)						
				423		Braukmuller et al. (2018)						
				424	**24**	**Mean**				**59**	**14**	**Mean**
Nogoya	CM	2	Fall	**356**		Braukmuller et al. (2018)				**85**	**6**	McSween (1979)
Paris	CM	2	Find	**432**		Braukmuller et al. (2018)						
Santa Cruz	CM	2	Fall	**416**		Wolf et al. (1980)				**74**	**13**	McSween (1979)
Al Rais	CR	2	Fall	**385**		Wolf et al. (1980)				**57**	**36**	McSween (1977)

Table 2 (continued)

Sample name	Group	Type	Fall / Find	Cd (ppb)	2SD	Reference	Zn (ppm)	2SD	Reference	Matrix (Vol. %)	Chondrules (Vol. %)	Reference
GRA 95229	CR	2	Find	**140**		Braukmuller et al. (2018)						
LAP 02342	CR	2	Find	**135**		Braukmuller et al. (2018)						
NWA 801	CR	2	Find	**95**	**2**	Baker et al. (2010)	**0**		Van kooten et al. (2022)			
Allende	CV	3	Fall	235		Rosman and De Laeter (1974)	134		Wolf et al. (1980)	38	43	McSween (1977)
				474		Wolf et al. (1980)	104		Rubin et al. (1985)			
				207	52	Loss et al. (1984)	122		Luck et al. (2005)			
				220		Wombacher et al. (2003)	110		Pringle et al. (2017)			
				231	6	Baker et al. (2010)	123		Braukmüller et al. (2018)			
				463	7	Wang et al. (2015)	119		Braukmüller et al. (2020)			
				265		Braukmuller et al. (2018)						
				491		Braukmuller et al. (2018)						
				466	7	Braukmuller et al. (2020)						
				215		This study						
				198		This study						
				224	**44**	**Mean**	**119**	**21**	**Mean**	**38**	**43**	**Mean**
				473	**25**	**Mean**						
Leoville	CV	3	Find	39		Rosman and De Laeter (1974)	22		Van kooten et al. (2022)	35	51	McSween (1977)
				37	1	Baker et al. (2010)						
				38	**3**	**Mean**	**22**		**Mean**	**35**	**51**	**Mean**
Vigarano	CV	3	Fall	**82**		Braukmuller et al. (2018)	**93**		Luck et al. (2005)	**35**	**49**	McSween (1977)
ALHA 77307	CO	3	Find	**251**		Braukmuller et al. (2018)						
Kainsaz	CO	3	Fall	22		Braukmuller et al. (2018)	101		Braukmüller et al. (2018)	44		Rubin et al. (1985)
				22		Baker et al. (2010)						
				22	**0**	**Mean**	**101**		**Mean**	**44**		**Mean**
SAH 99544	CO	3	Find	**130**		This study						
ALH 85002	CK	4	Find	**214**		Braukmuller et al. (2018)	**89**		Kallemeyn et al. (1991)	**70**		Aponte et al. (2017)

Table 2 (continued)

Sample name	Group	Type	Fall / Find	Cd (ppb)	2SD	Reference	Zn (ppm)	2SD	Reference	Matrix (Vol. %)	Chondrules (Vol. %)	Reference
Coolidge	CL	4	Find	**10**		This study	**60**		Kallemeyn and Rubin (1995)	**18**	**67**	McSween (1977)
Tagish Lake	Ungrouped	2	Fall	**536**		Braukmuller et al. (2018)	**217**		Luck et al. (2005)			
Tarda	Ungrouped	2	Fall	**405**		This study	**207**		Marrocchi et al. (2021)			
SAH 00177	Ungrouped	3.9	Find	**16**		This study						
Essebi	Ungrouped	2	Fall	**642**		Wolf et al. (1980)				**79**	**11**	McSween (1979)
NWA 13689	Ungrouped	3	Find	**379**	**122**	This study				**49**		Prestgard et al. (2022)

This table presents all the data that we know of regarding the Cd concentrations of CC. Along Cd concentrations are presented Zn concentrations as well as matrix and chondrule amounts. Bold lines present either the mean value or the reference value for the sample. In some cases, like for Mighei or Allende, significantly different compositions led us to propose two reference value (in bold). (Aponte et al., 2017; Baker et al., 2010; Barrat et al., 2012; Braukmüller et al., 2020, 2018; Creech and Moynier, 2019; Friend et al., 2018; Greenwood et al., 1994; Kallemeyn et al., 1991; Kallemeyn and Rubin, 1995; Krähenbühl et al., 1973; Loss et al., 1984; Luck et al., 2005; Marrocchi et al., 2021; Mcsween, 1979, 1977; Prestgard et al., 2022; Pringle et al., 2017; Rosman and De Laeter, 1988, 1974; Rubin et al., 1985; Van Kooten et al., 2022; Wang and Lipschutz, 2005; Wang et al., 2015; Weisberg et al., 2006; Wolf et al., 1980; Wombacher et al., 2003; Wood, 1967)

Table 3: Literature Cd concentrations and isotope compositions of chondrites and tektites

Sample name	Chondrite group	Petrological type	Fall / Find	Cd (ppb)	2SD	δ^{114}Cd (‰)	2SD	References
Carbonaceous								
Orgueil	CI	1	Fall	661	36			Krähenbül et al. (1973)
				770				Rosman and De Laeter (1974)
				710	25			Loss et al. (1984)
				708				Rosman and De Laeter (1988)
				710		-0.281	0.226	Wombacher et al. (2003)
						-0.281	0.283	Wombacher et al. (2008)
				669	14	0.460	0.240	Baker et al. (2010)
				695	12			Wang et al. (2015)
				697				Braukmuller et al. (2018)
				644	6.9			Braukmuller et al. (2020)
				696	**73**			**Mean**
Cold Bokkeveld	CM	2	Fall	395				Wolf et al. (1980)
				350	8	0.530	0.180	Baker et al. (2010)
				379				Braukmuller et al. (2018)
				375	**46**	**0.530**	**0.180**	**Mean**
Jbilet Winselwan*	CM	2	Find	**498**				Braukmuller et al. (2018)
Murchison*	CM	2	Fall	379				Krähenbül et al. (1973)
				442				Rosman and De Laeter (1974)
				440		0.279	0.520	Wombacher et al. (2003)
				427	28			Wang & Lipschutz (2005)
						0.319	0.430	Wombacher et al. (2008)
				387	8	0.350	0.120	Baker et al. (2010)
				538	8			Wang et al. (2015)
				422				Braukmuller et al. (2018)
				400	5			Braukmuller et al. (2020)
				429	**99**	**0.316**	**0.071**	**Mean**
Acfer 209	CR	2	Find			**0.319**	**0.283**	wombacher et al. (2008)
EET 92042	CR	2	Find			**0.110**	**0.050**	Baker et al. (2010)
NWA 801	CR	2	Find	**95**	**2**	**0.270**	**0.170**	Baker et al. (2010)
Allende*	CV	3	Fall	474				Wolf et al. (1980)
				463	7			Wang et al. (2015)
				466	7			Braukmuller et al. (2020)
				468	11			Mean
				235				Rosman and De Laeter (1974)
				207	52			Loss et al. (1984)
				220		-0.161	0.440	Wombacher et al. (2003)
						-0.181	0.430	Wombacher et al. (2008)
				231	6	0.220	0.120	Baker et al. (2010)
				265				Braukmuller et al. (2018)
				232	**43**	**0.220**	**0.120**	**Mean**
Leoville	CV	3	Find	39				Rosman and De Laeter (1974)
						1.719	0.430	Wombacher et al. (2008)
				37	1	3.270	0.350	Baker et al. (2010)
				38	**3**			**Mean**
Colony	CO	3	Find			**1.219**	**0.566**	Wombacher et al. (2008)
						0.280	**0.130**	Baker et al. (2010)
Dar al Gani 005	CO	3	Find			**4.419**	**0.430**	Wombacher et al. (2008)
Kainsaz	CO	3.2	Fall	**22**		**1.560**	**0.420**	Baker et al. (2010)

Table 3 (continued)

Sample name	Chondrite group	Petrological type	Fall / Find	Cd (ppb)	2SD	δ^{114}Cd (‰)	2SD	References
Dar al Gani 275	CK	4	Find			**-1.081**	**0.430**	Wombacher et al. (2008)
Dar al Gani 412	CK	5	Find			**-0.881**	**0.430**	Wombacher et al. (2008)
Watson 002	CK	3	Find			**0.369**	**0.141**	Wombacher et al. (2008)
Acfer 094	Ungrouped	2	Find			**-0.431**	**0.141**	Wombacher et al. (2008)
Ordinary								
Bishunpur	LL	3	Fall	365				Rosman and De Laeter (1988)
						11.119	0.905	Wombacher et al. (2003)
								Wang & Lipschutz (2005)
						11.319	0.849	Wombacher et al. (2008)
				291	29			Palk et al. (2018)
				328	**105**	**11.219**	**0.283**	**Mean**
Dar al Gani 022	LL	3	Find			**0.619**	**0.430**	Wombacher et al. (2008)
Olivenza*	LL	5	Fall	**40**	**4**			Palk (2018)
Semarkona	LL	3	Fall	1248				Rosman and De Laeter (1988)
				1248		-7.828	0.122	Wombacher et al. (2003)
						-7.881		Wombacher et al. (2008)
				1248	**0**	**-7.854**	**0.075**	**Mean**
Adrar 003	L/LL	3.1	Find			**6.219**	**0.430**	Wombacher et al. (2008)
Sarir Qattusah 001	L/LL	3	Find			14.351	0.762	Wombacher et al. (2003)
						14.569	0.808	Wombacher et al. (2008)
						14.460	**0.308**	**Mean**
Bruderheim*	L	6	Fall	**13**				Rosman and De Laeter (1974)
Dar al Gani 085	L	3.5	Find			**0.286**	**0.577**	Wombacher et al. (2008)
Dar al Gani 216	L	3	Find			**5.619**	**0.430**	Wombacher et al. (2008)
Homestead	L	5	Fall	103				Keays et al. (1971)
						3.119	0.430	Wombacher et al. (2008)
				103		**3.119**	**0.430**	**Mean**
Tanezrouft 039	L	3	Find			**6.519**	**0.430**	Wombacher et al. (2008)
Acfer 171	H	3.7	Find			**-6.181**	**0.430**	Wombacher et al. (2008)
Brownfield 1937	H	3.7	Find	152				Rosman and De Laeter (1974)
				406	55			Rosman et al. (1980)
						10.959		Wombacher et al. (2003)
				408		10.756	0.8	Schediwy et al. (2006)
						11.119	0.43	Wombacher et al. (2008)
				407	**4**	**10.945**	**0.364**	**Mean**
Dimmit	H	3.7	Find	44				Rosman and De Laeter (1974)
				200		7.099	0.509	Wombacher et al. (2003)
						7.019	0.430	Wombacher et al. (2008)
				200		**7.059**	**0.113**	**Mean**
Forest Vale	H	4	Fall	1240				Lingner et al. (1987)
						3.106	0.533	Wombacher et al. (2003)
						3.069	0.707	Wombacher et al. (2008)
				1240		**3.087**	**0.052**	**Mean**
Gladstone	H	4	Find	38				Rosman and De Laeter (1974)
						0.619	0.430	Wombacher et al. (2008)
				38		**0.619**	**0.430**	**Mean**
Ucera	H	5	Fall	110				Lingner et al. (1987)
						-0.381	0.430	Wombacher et al. (2008)
				110		**-0.381**	**0.430**	**Mean**

Table 3 (continued)

Sample name	Chondrite group	Petrological type	Fall / Find	Cd (ppb)	2SD	δ114Cd (‰)	2SD	References
Enstatite								
Abee	EH	4	Fall	1000				Rosman and De Laeter (1974)
				455				Rosman and De Laeter (1974)
				825	82			Wang & Lipschutz (2005)
						-0.381	0.693	Wombacher et al. (2008)
				857	18	0.290	0.050	Palk et al. (2018)
				841	**45**	**0.290**	**0.050**	**Mean**
Indarch*	EH	4	Fall			**-0.281**	**0.566**	Wombacher et al. (2008)
				659	**14**	**0.420**	**0.050**	Palk et al. (2018)
SAH 97166	EH	3	Find			**3.319**	**0.430**	Wombacher et al. (2008)
St Marks	EH	5	Fall	**12.5**	**0.8**	**0.970**	**0.100**	Palk et al. (2018)
Qingzhen	EH	3	Fall	61.6				Kaczaral et al. (1988)
Atlanta	EL	6	Find	**5.7**	**0.8**	**1.040**	**0.130**	Palk et al. (2018)
Hvittis	EL	6	Fall	70				Laul et al. (1973)
						7.519	0.430	Wombacher et al. (2008)
				70		**7.519**	**0.430**	**Mean**
Ilafegh 009	EL	7	Find			**4.219**	**0.430**	Wombacher et al. (2008)
Khairpur	EL	6	Fall	**22**	**1**	**6.570**	**0.090**	Palk et al. (2018)
MAC 02839	EL	3	Find	**286**	**6**	**0.760**	**0.060**	Palk et al. (2018)
NWA 3134	EL	6	Find	**1.8**	**1**	**0.690**	**0.210**	Palk et al. (2018)
PCA 91020	EL	3	Find	**486**	**10**	**7.290**	**0.060**	Palk et al. (2018)
						15.919	0.430	Wombacher et al. (2008)
				125.345		**15.919**	**0.430**	**Mean**
Tektite								
106		Muong Nong		**11**		**2.940**	**0.520**	Wombacher et al. (2003)

*Bold lines display either the mean composition or the prefered composition (when one analysis is obviously better) for samples that were analyzed multiple times, or the only referenced value. Samples with a * after their names are those for which we also propose a composition. Some samples, like Allende or Leoville seem to have fractions with distinct Cd concentrations and/or isotope compositions, which reinforce the constatation of significant heterogeneities we made. We only listed here the samples for which a Cd isotope composition was proposed, or for which we propose one. (Baker et al., 2010; Braukmüller et al., 2020, 2018; Kaczaral et al., 1988; Keays et al., 1971; Krähenbühl et al., 1973; Laul et al., 1973; Lingner et al., 1987; Loss et al., 1984; Palk et al., 2018; Rosman et al., 1980; Rosman and De Laeter, 1988, 1974; Schediwy et al., 2006; Wang and Lipschutz, 2005; Wang et al., 2015; Wolf et al., 1980; Wombacher et al., 2008, 2003)*

5.2.3. Ordinary chondrites

Comparison between falls and finds

Unlike carbonaceous chondrites, which have generally consistent Cd concentration among the falls of a group, ordinary chondrites are characterized by very varied Cd concentrations, even within a single group. As an example, LL falls have Cd concentrations ranging from less than 1 ppb to more than 1 ppm (see Figure 7). Although it is difficult to discuss variations for

such diversified samples, we remark that Cd concentrations of falls and finds usually overlap at least partly. Samples from L/LL and L groups are characterized by finds that are similar or more concentrated in Cd than falls, while H chondrites follow a contrary trend. We expect these behavior differences to reflect the Cd-bearing mineralogy distinction between these groups.

Finds from the H group have similar to heavier Cd isotope compositions compared to falls (see Figure 8). Thus, similarly to what was observed for the CV find, we expect H finds to have experienced a terrestrial Cd-depleting process that drove their compositions toward heavy isotopes enrichment. Such process remains to be characterized. We have no other find sample that were characterized both for Cd concentrations and isotope compositions, however a few are characterized for isotope composition only. However, any discussion of these results is prevented by the wide dispersion of the OC isotope composition within a single group, which makes it difficult to compare the samples.

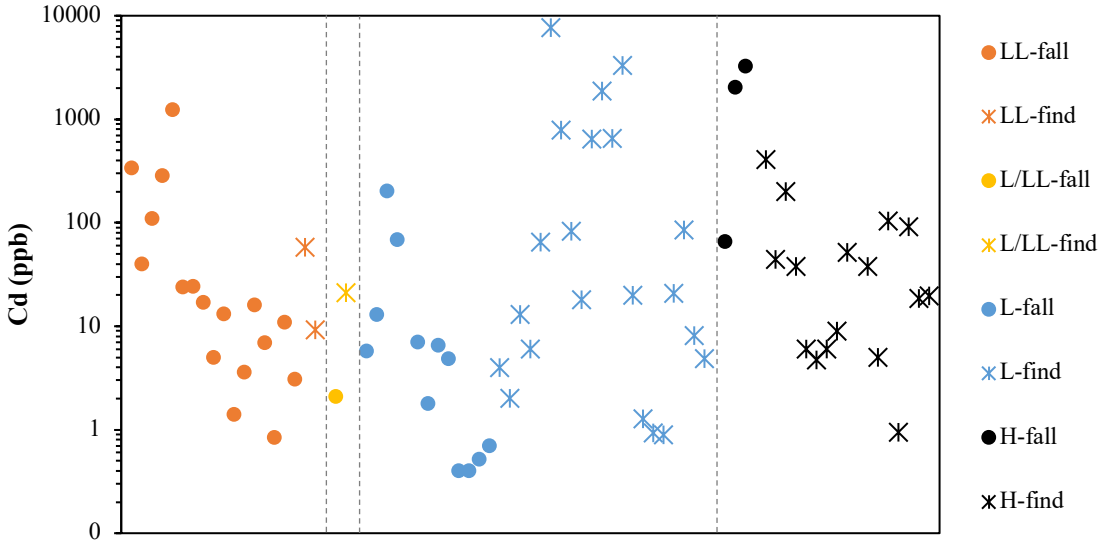


Figure 7: Comparison between fall and find Cd concentrations in OC. The Cd concentrations are comparable for most samples; however, L and L/LL finds can present significantly higher concentrations than the related falls, which suggest a terrestrial Cd pollution. On the contrary, many H finds are characterized by lower concentrations than falls, suggesting leaching. The dataset is detailed in Table 3.

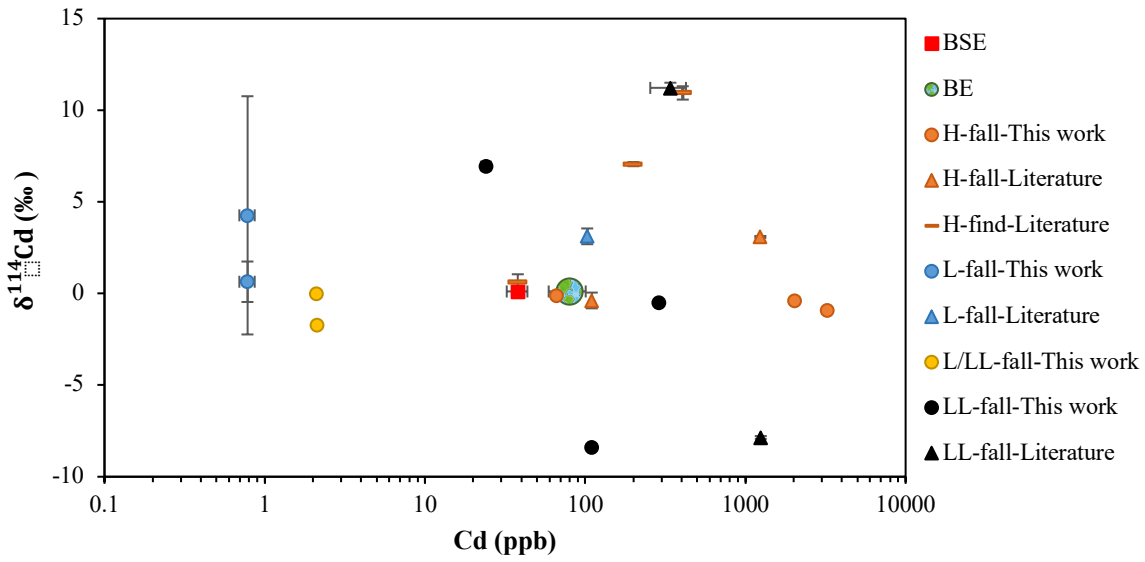


Figure 8: Cadmium concentrations and isotope compositions of ordinary chondrites. The symbols are similar to that of Figure 3. No significant correlation is found for any of the OC groups reviewed here. H fall samples can have similar Cd concentrations and isotope compositions than the BSE and BE. Data are detailed in Table 1 and Table 4.

A correlation to the petrological type?

Cadmium concentrations in ordinary chondrites from LL and L groups seem to be roughly correlated with the petrological type of the sample (see Figure 9). Specifically, the more thermally metamorphosed the sample is, the more Cd-depleted it seems to be. Because of a lack of characterized samples, we cannot argue if a similar trend is at play for H chondrites. Such a depletion pattern could be explained by Cd volatilization during heating or by Cd leaching by hot thermal fluids. Should volatilization have occurred, we expect isotope fractionation to occur. Specifically, we expect Cd-depleted samples (i.e., high petrological type ones) to be characterized by isotopically heavier compositions than type 3 ones. However, OC isotope compositions for Cd do not feature any evident correlation with their petrological types (see Figure 10). This is probably due to the great variability of Cd isotope compositions of the samples, which masks any deviation caused by terrestrial processes.

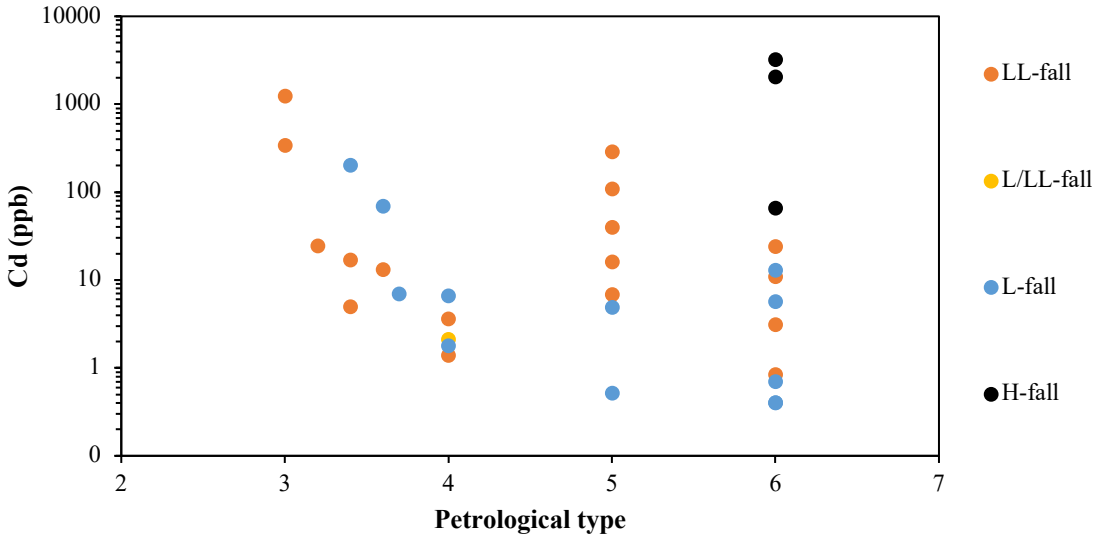


Figure 9: Comparison between the Cd concentrations of fall OC and their respective petrological types. Although the samples Cd concentration variability is great, there seems to be a negative correlation between these two parameters, at least for L and LL samples. This could reflect Cd depletion by volatilization or leaching during thermal processing. The dataset is detailed in Table 3.

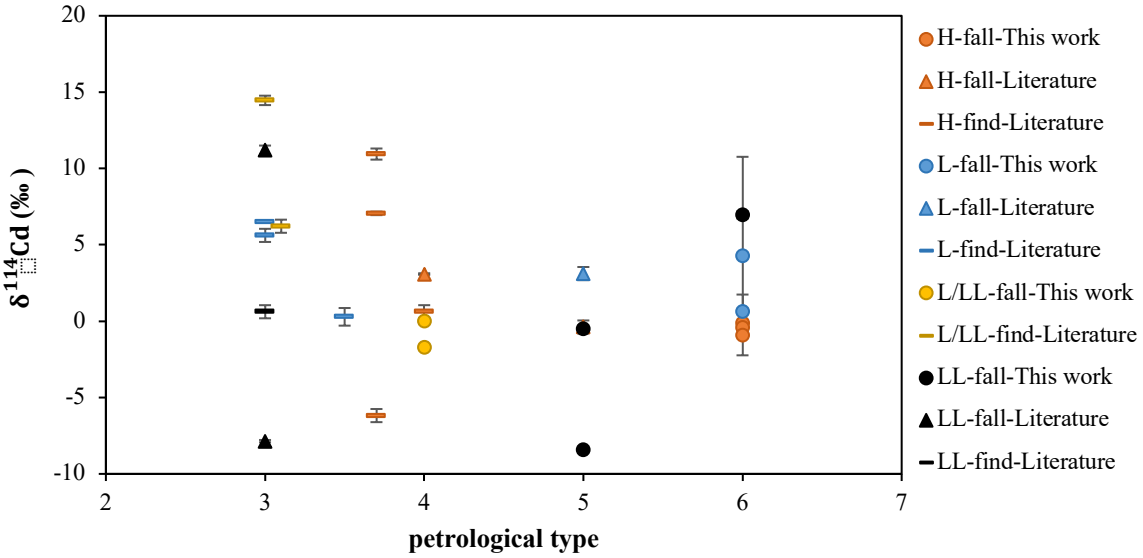


Figure 10: Comparison between the OC isotope compositions and their petrological types. Based on their Cd concentrations, we expected that high petrological type samples would have isotopically heavy compositions because of potential volatilization. However, we do not observe such process as the isotope compositions are scattered across a wide field seemingly at random. Data are detailed in Table 1 and Table 4.

General analysis of the trend

Figure 8 displays the OC isotope compositions plotted against their Cd concentrations. We found no correlation between these parameters as every group presents significantly distinct isotope compositions, that are often strongly enriched in light or heavy Cd isotopes. Nevertheless, it is interesting to note that some H falls are characterized by similar compositions than the Bulk Earth. Few samples show such proximity with terrestrial materials.

Finally, we checked if Cd in OC was correlated with Zn. Unfortunately, not many OC have been characterized both for Cd and Zn concentrations (see Figure 11). This lack of data may cause potential correlations to remain unnoticed. Nevertheless, the few datapoints we have display no real correlation between Cd and Zn concentrations, unlike what was observed in CC. The only noticeable exception might be L samples, for which the three available points are aligned. However, more points would be needed to characterize a trend. The general decorrelation between Zn and Cd indicates that these elements are probably not enriched in the same phases. Similarly, no correlation was observed with the Zn isotope composition (Figure 12).

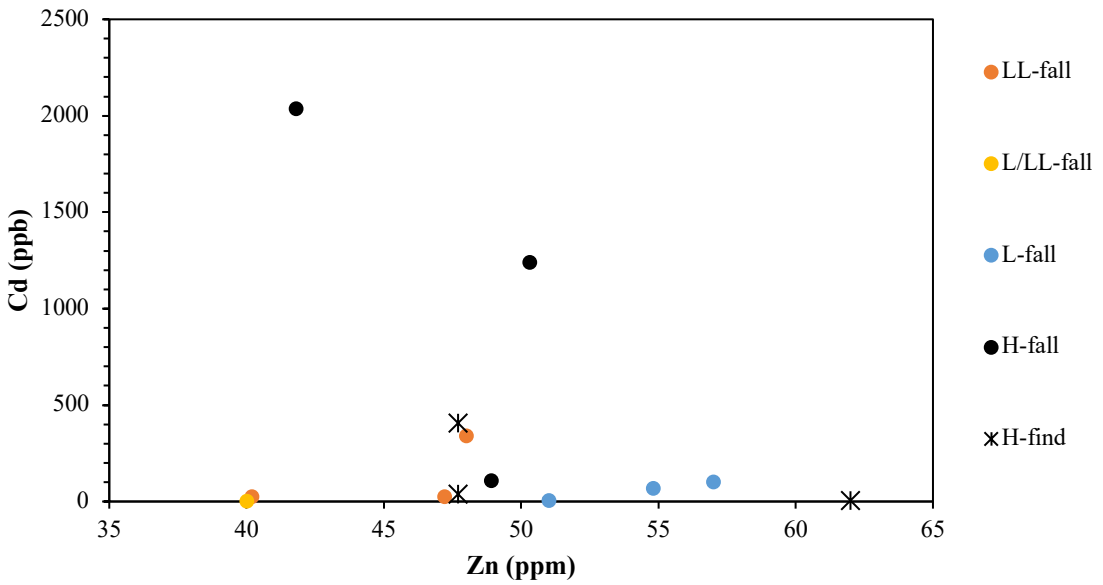


Figure 11: Comparison of Cd and Zn concentrations for OC. No significant correlation was found between these parameters, except maybe a positive correlation for L samples. This decorrelation implies that Cd and Zn are not concentrated in the same phases for OC, unlike what was observed for CC. The dataset is detailed in Table 3.

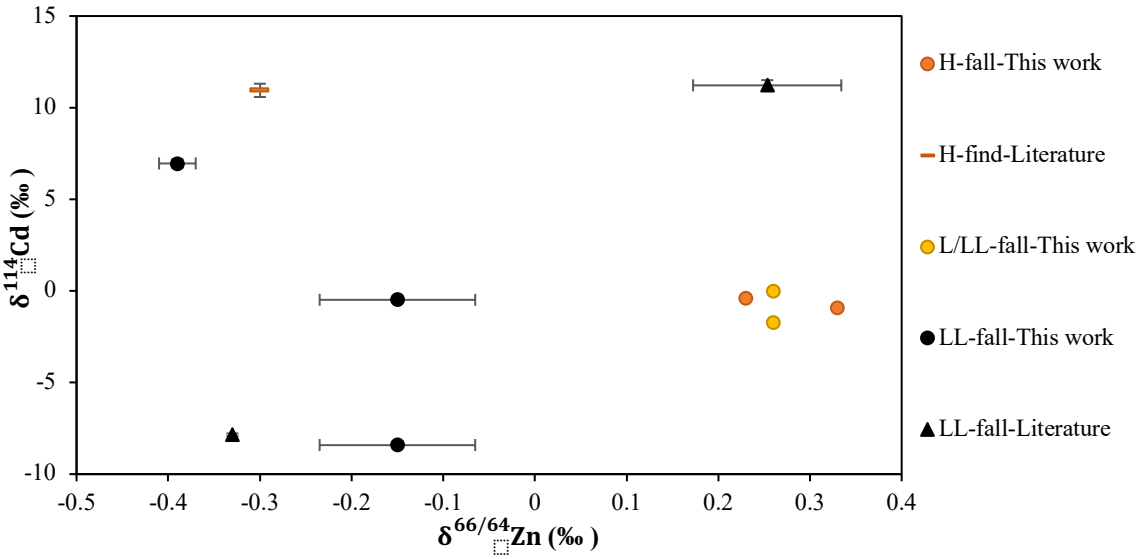


Figure 12: Ordinary chondrites Cd isotope compositions plotted as a function of their Zn isotope compositions. Similarly to the other OC representation, we observe no significant correlation between these two compositions. Data are detailed in Table 1 and Table 4.

Table 4: Cadmium and Zinc concentrations for OC and EC

Sample name	Group	Type	Fall / Find	Cd (ppb)	2SD	Reference	Zn (ppm)	2SD	Reference
Ordinary									
Bishunpur	LL	3	Fall	365		Rosman and De Laeter (1988)	48		Luck et al. (2005)
				365		Wang & Lipschutz (2007)			
				291	29	Palk et al. (2018)			
				340	**85**	**Mean**			
Semarkona	LL	3	Fall	1248		Rosman and De Laeter (1988)			
Krymka	LL	3.2	Fall	25		Wang & Lipschutz (2007)	40		Luck et al. (2005)
ALH A76004	LL	3.3	Find	9		Wang & Lipschutz (2007)			
Chainpur	LL	3.4	Fall	17		Wang & Lipschutz (2007)			
Manych	LL	3.4	Fall	5		Wang & Lipschutz (2007)			
Parnallee	LL	3.6	Fall	25		Wang & Lipschutz (2007)			
				1	0	Palk et al. (2018)			
				13	**33**	**Mean**			
Benares	LL	4	Fall	1	0	Palk et al. (2018)			
Soko-Banja	LL	4	Fall	4	0	Palk et al. (2018)			
Khanpur	LL	5	Fall	16	2	Palk et al. (2018)			
Olivenza	LL	5	Fall	40	4	Baker et al. (2010)			
				110		This study			
				288		This study			
Tuxtuac	LL	5	Fall	7	1	Palk et al. (2018)			
Appley Bridge	LL	6	Fall	1	0	Palk et al. (2018)			
Dhurmsala	LL	6	Fall	11	1	Palk et al. (2018)			
Mangwendi	LL	6	Fall	3	0	Palk et al. (2018)			
Mellenbye	LL	6	Find	58		Rosman and De Laeter (1974)			
St Séverin	LL	6	Fall	24		This study	47		Luck et al. (2005)
				24		This study			
				24	**1**	**Mean**			
EET 96188	L/LL	3.2	Find	21		Wang & Lipschutz (2007)			
Bjurböle	L/LL	4	Fall	2		This study	40		Luck et al. (2005)
				2		This study			
				2	**0**	**Mean**			
EET 90161	L	3.05	Find	7680		Wang & Lipschutz (2007)			

Table 4 (continued)

Sample name	Group	Type	Fall / Find	Cd (ppb)	2SD	Reference	Zn (ppm)	2SD	Reference
QUE 97008	L	3.05	Find	791		Wang & Lipschutz (2007)			
MET 96503	L	3.1	Find	83		Wang & Lipschutz (2007)			
GRO 95544	L	3.2	Find	18		Wang & Lipschutz (2007)			
EET 90628	L	3.4	Find	1870		Wang & Lipschutz (2007)			
Hallingeberg	L	3.4	Fall	203		Wang & Lipschutz (2007)			
LEW 87208	L	3.4	Find	640		Wang & Lipschutz (2007)			
Ioka	L	3.5	Find	21		Wang & Lipschutz (2007)			
LEW 87248	L	3.5	Find	656		Wang & Lipschutz (2007)			
LEW 87284	L	3.5	Find	3300		Wang & Lipschutz (2007)			
MET 96515	L	3.5	Find	65		Wang & Lipschutz (2007)			
Khohar	L	3.6	Fall	69		Wang & Lipschutz (2007)	55		Luck et al. (2005)
Mezö-Madaras	L	3.7	Fall	7	1	Palk et al. (2018)			
Y 74191	L	3.7	Find	20		Wang & Lipschutz (2007)			
WSG 95307	L	3.7	Find	1		Wang & Lipschutz (2007)			
ALH A77216	L	3.8	Find	85		Wang & Lipschutz (2007)			
ALH 84120	L	3.8	Find	1		Wang & Lipschutz (2007)			
ALH A79022	L	3.85	Find	8		Wang & Lipschutz (2007)			
ALH 84205	L	3.9	Find	1		Wang & Lipschutz (2007)			
Carraweena	L	3.9	Find	5		Wang & Lipschutz (2007)			
Dalgety Downs	L	4	Find	6		Rosman and De Laeter (1974)			
Saratov	L	4	Fall	2	0	Palk et al. (2018)			
Tennasilm	L	4	Fall	7	1	Palk et al. (2018)			
Ausson	L	5	Fall	5	1	Palk et al. (2018)			
Barwell	L	5	Fall	1	0	Palk et al. (2018)			
Homestead	L	5	Fall	103		Keays et al. (1971)	57		Keays et al. (1971)

Table 4 (continued)

Sample name	Group	Type	Fall / Find	Cd (ppb)	2SD	Reference	Zn (ppm)	2SD	Reference
Bruderheim	L	6	Fall	13		Rosman and De Laeter (1974)	51		Nishimura and Sandell (1964)
				2		This study			
				2		This study			
				6	**13**	**Mean**			
Calliham	L	6	Find	13		Rosman and De Laeter (1974)			
Lake Brown	L	6	Find	4		Rosman and De Laeter (1974)			
Marion (Iowa)	L	6	Fall	1	0	Palk et al. (2018)			
Mocs 54647	L	6	Fall	0	0	Palk et al. (2018)			
Mocs 54773	L	6	Fall	0	0	Palk et al. (2018)			
Potter	L	6	Find	2		Rosman and De Laeter (1974)			
Woolgorong	L	6	Fall	13		Rosman and De Laeter (1974)			
FRO 84005	H	3	Find	92		Wang & Lipschutz (2007)			
WSG 95300	H	3.3	Find	104		Wang & Lipschutz (2007)			
Brownfield 1937	H	3.7	Find	406	55	Rosman et al. (1980)	48		Luck et al. (2005)
				408		Schediwy et al. (2006)			
				407	**4**	**Mean**			
Dimmit	H	3.7	Find	44		Rosman and De Laeter (1974)			
				200		Wombacher et al. (2003)			
GRA 95208	H	3.7	Find	1		Wang & Lipschutz (2007)			
Grady	H	3.7	Find	6		Rosman and De Laeter (1974)	35		Creech and Moynier (2019)
Prairie dog Creek	H	3.7	Find	19		Wang & Lipschutz (2007)			
RKP A80205	H	3.8	Find	20		Wang & Lipschutz (2007)			
Forest Vale	H	4	Fall	1240		Lingner et al. (1987)	50		Lingner et al. (1987)
Gladstone	H	4	Find	38		Rosman and De Laeter (1974)	62		Nishimura and Sandell (1964)
Cocklebiddy	H	5	Find	5		Rosman and De Laeter (1974)			
Plainview	H	5	Find	9		Rosman and De Laeter (1974)			
Ucera	H	5	Fall	110		Lingner et al. (1987)	49		Lingner et al. (1987)

Table 4 (continued)

Sample name	Group	Type	Fall / Find	Cd (ppb)	2SD	Reference	Zn (ppm)	2SD	Reference
Wellman	H	5	Find	5		Rosman and De Laeter (1974)			
Wildara	H	5	Find	52		Rosman and De Laeter (1974)			
Wiluna	H	5	Find	6		Rosman and De Laeter (1974)			
Guarena	H	6	Fall	66		This study			
Kernouvé	H	6	Fall	2036		This study	42		Luck et al. (2005)
Lancon	H	6	Fall	3251		This study			
Mulga North	H	6	Find	38		Rosman and De Laeter (1974)			
Enstatite									
ALHA 77156	EH	3	Find	73		Wang & Lipschutz (2005)			
ALH 84170	EH	3	Find	465		Wang & Lipschutz (2005)			
ALH 84200	EH	3	Find	154		Wang & Lipschutz (2005)			
ALH 84206	EH	3	Find	401		Wang & Lipschutz (2005)			
EET 83322	EH	3	Find	9837		Wang & Lipschutz (2005)			
PCA 82518	EH	3	Find	23		Wang & Lipschutz (2005)			
Qingzhen	EH	3	Fall	62		Kaczaral et al. (1988)	340		Kaczaral et al. (1988)
Sahara 97096	EH	3	Find	209		This study	309		Creech and Moynier (2019)
				220		This study			
				215	**15**	**Mean**			
Kaidun 03,06	EH	3.5	Find	27		Wang & Lipschutz (2005)			
Abee	EH	4	Fall	1000		Rosman and De Laeter (1974)	730		Nishimura and Sandell (1964)
				455		Rosman and De Laeter (1974)	437		Wang and Lipschutz (2005)
				825	82	Wang & Lipschutz (2005)			
				857	18	Palk et al. (2018)			
				841	**45**	**Mean**			
Indarch	EH	4	Fall	659	14	Palk et al. (2018)	280		Creech and Moynier (2019)
				27		This study	430		Binz et al. (1974)
				926		This study			
QUE 93372	EH	5	Find	1		Wang & Lipschutz (2005)			

Table 4 (continued)

Sample name	Group	Type	Fall / Find	Cd (ppb)	2SD	Reference	Zn (ppm)	2SD	Reference
RKP A80259	EH	5	Find	53		Wang & Lipschutz (2005)			
St Marks	EH	5	Fall	13	1	Palk et al. (2018)	53		Binz et al. (1974)
ALH 85119	EL	3	Find	664		Wang & Lipschutz (2005)			
MAC 02839	EL	3	Find	286	6	Palk et al. (2018)			
MAC 88136	EL	3	Find	360		Wang & Lipschutz (2005)			
PCA 91020	EL	3	Find	486	10	Palk et al. (2018)			
ALH 81021	EL	6	Find	24		Wang & Lipschutz (2005)			
Atlanta	EL	6	Find	6	1	Palk et al. (2018)	8		Binz et al. (1974)
Daniel's Kuil	EL	6	Fall	5	1	Palk et al. (2018)			
GRO 95626	EL	6	Find	9		Wang & Lipschutz (2005)			
Hvittis	EL	6	Fall	70		Laul et al. (1973)	16		Nishimura and Sandell (1964)
Khairpur	EL	6	Fall	22	1	Palk et al. (2018)	8		Laul et al. (1973)
LON 94100	EL	6	Find	6		Wang & Lipschutz (2005)			
North West Forrest	EL	6	Find	19		Rosman and De Laeter (1974)			
NWA 3134	EL	6	Find	2	1	Palk et al. (2018)			
Yilmia	EL	6	Find	16		Rosman and De Laeter (1974)			

This table presents all the data we are aware of regarding the Cd concentrations of OC and EC. Along Cd concentrations are presented Zn concentrations. Bold lines present the mean value. In some cases, like for Abee or Indarch, significantly different compositions prevented us from proposing a reference value. (Baker et al., 2010; Binz et al., 1974; Creech and Moynier, 2019; Kaczaral et al., 1988; Keays et al., 1971; Laul et al., 1973; Lingner et al., 1987; Luck et al., 2005; Nishimura and Sandell, 1964; Palk et al., 2018; Rosman et al., 1980; Rosman and De Laeter, 1988, 1974; Schediwy et al., 2006; Wang and Lipschutz, 2007, 2005; Wombacher et al., 2003)

5.2.4. Enstatite chondrites

Comparison between falls and finds

Enstatite chondrites are unique in our dataset, as finds for both EH and EL can be either richer or poorer in Cd than the falls (see Figure 13). This could result from different alteration mechanisms caused by similarly different climate conditions. However, we did not find any

correlation between the sampling localization of the chondrites and their Cd enrichment or depletion, as Antarctica chondrites are found among the Cd-enriched and Cd-depleted samples.

This enrichment/depletion duality of find samples can be better explained by thermal processing. Figure 14 displays the Cd concentrations of EC versus their petrological types. A significant anti-correlation is found between these two parameters, indicating that samples that experienced intense thermal processing are also the most Cd-depleted. This is similar to what was observed for OC, which we explained by Cd loss by volatilization or by leaching. Although we lack isotopic data to better evaluate any correlation, we observe on Figure 17 that thermally processed EH samples are characterized by significantly lighter isotope compositions than the type 3 ones. This could result from the leaching of isotopically heavy Cd, as is known to occur on Earth.

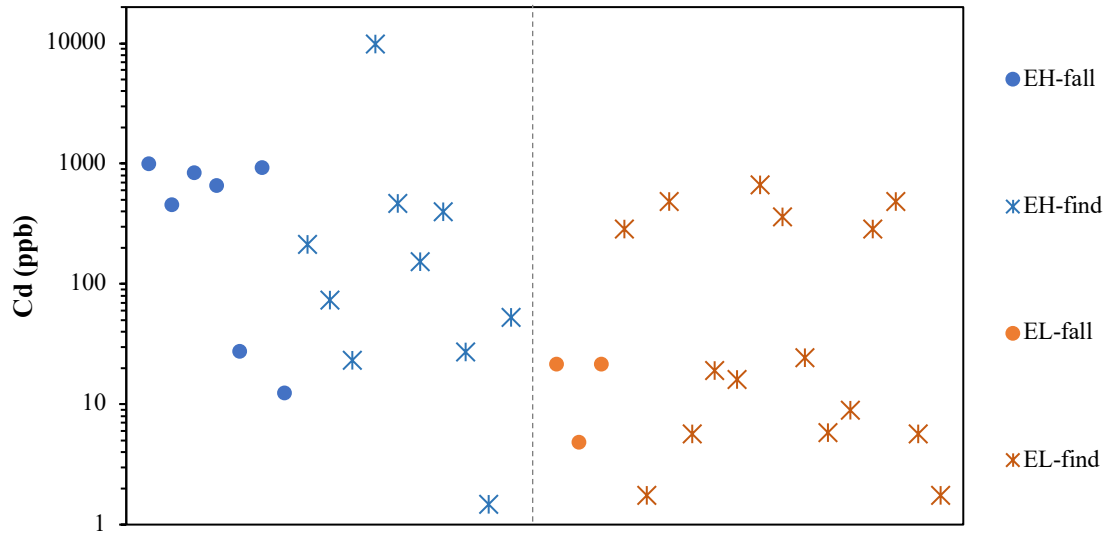


Figure 13: Comparison of the Cd concentrations of fall and find enstatite chondrite. Although most EH find are on the Cd-depleted side of the EH fall compositions, there is general overlap between these two groups. Only two EH find samples do not overlap with the fall compositions: one is significantly Cd-poorer while the other one is Cd-enriched. The dataset is detailed in Table 3.

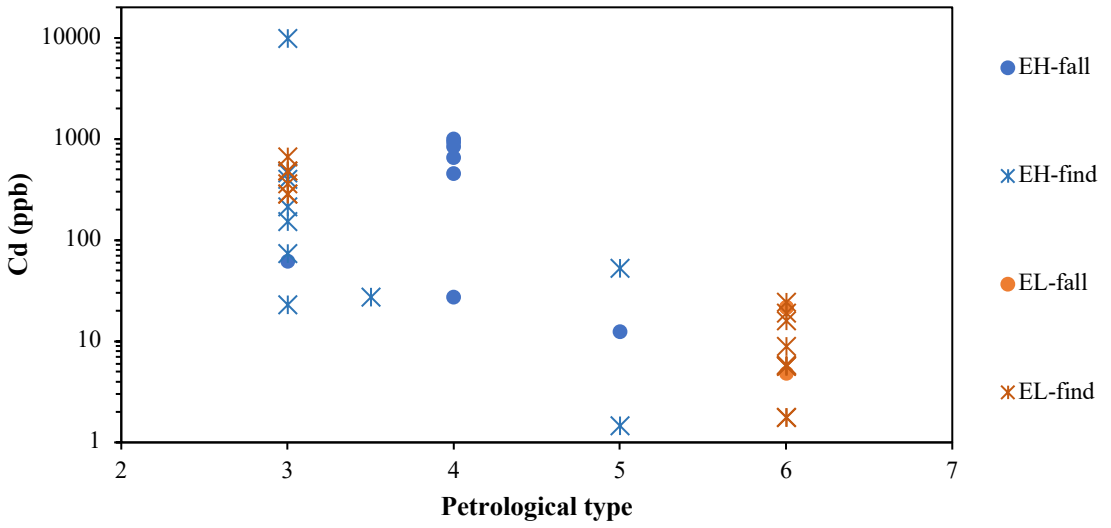


Figure 14: Influence of the petrological type of enstatite chondrites on their Cd content. There is a correlation between these two parameters: samples that underwent thermal processing are depleted in Cd, similarly to what we observed for OC. We observe that the Cd-enriched find samples are of petrologic type close to 3 while the Cd-depleted ones are heavily thermally processed. In that regard it seems that find samples are not significantly distinct from fall ones. The dataset is detailed in Table 3.

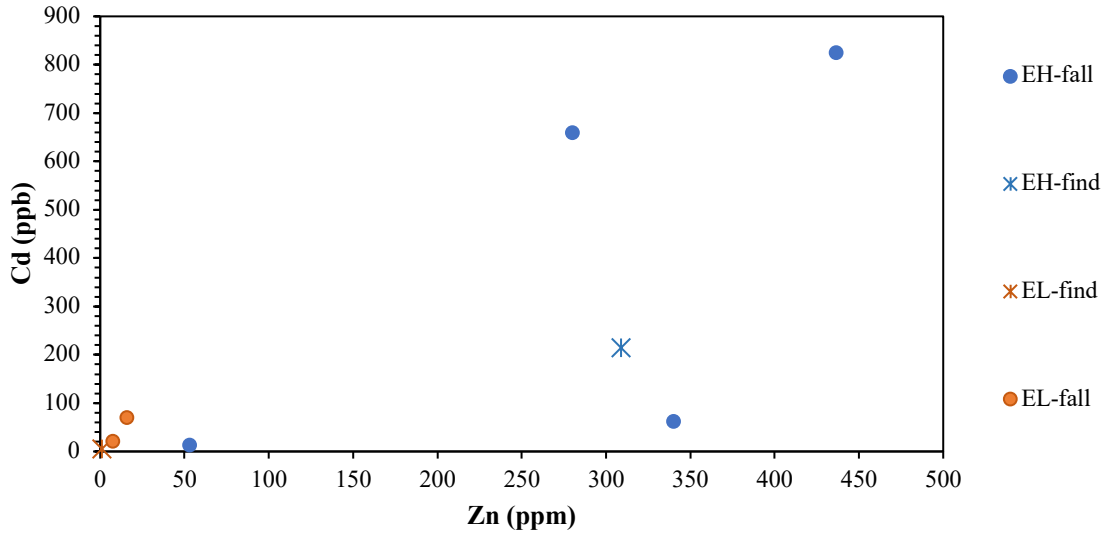


Figure 15: Comparison between the Cd and Zn concentrations of EC samples. There is a positive correlation from which only a few outliers diverge. The dataset is detailed in Table 3.

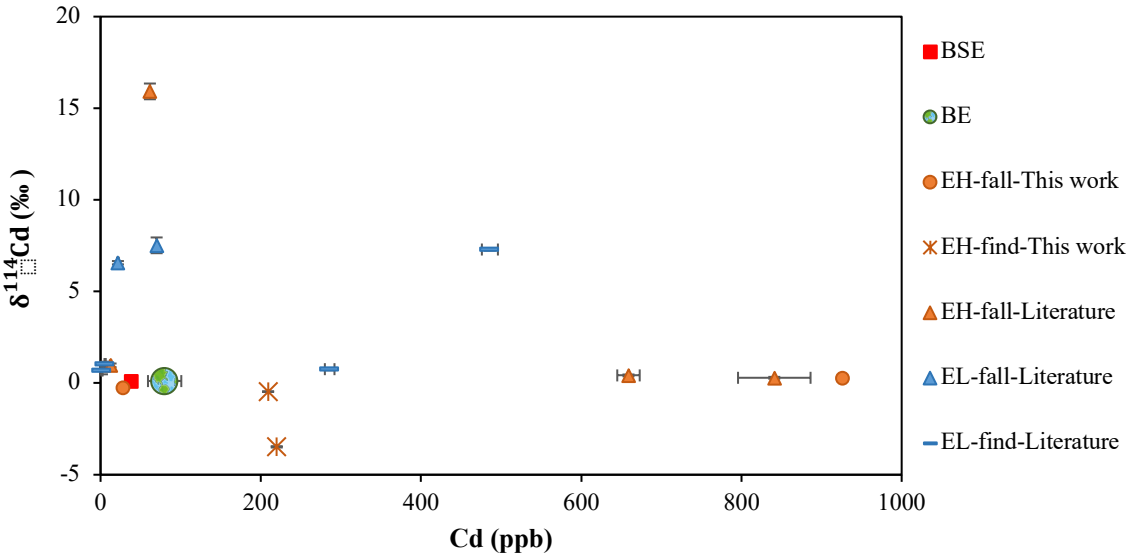


Figure 16: Cadmium isotope composition of EC as a function of their Cd concentration. The symbols are similar to those in previous figures. Except for one outlier, EH fall samples are characterized by generally unfractionated isotope compositions, ranging between -0.5 and +1 ‰, regardless of their C concentrations. These samples display very diverse Cd concentrations, comprised between 1 ppb and 1 ppm. To the contrary, EL fall samples are generally Cd-poor but have very isotopically fractionated compositions. Find samples from both group are isotopically lighter than fall samples, which is coherent with known terrestrial alteration processes. Data are detailed in Table 1 and 4.

General analysis of the trend

Figure 16 displays the relationship between EC isotope compositions and their Cd concentrations. No significant correlation was found as EH fall samples have roughly similar isotope compositions regardless of their Cd concentrations, with one noticeable exception in the Qingzhen chondrite which is the isotopically heaviest known chondrite for Cd. On the other hand, EL fall samples are generally Cd-poor and isotopically heavy; however, the small size of the dataset prevents us from formulating any significant conclusion. The Qingzhen outlier may be explained by its petrological type, as it is the only analyzed type 3 fall EH sample.

Finally, we find a similar Cd-Zn correlation than what was observed for CC (see Figure 15). This indicates again the similarity in behavior between these two elements. However, we lack Zn isotope compositions to determine whether they are correlated to EC Cd isotope compositions.

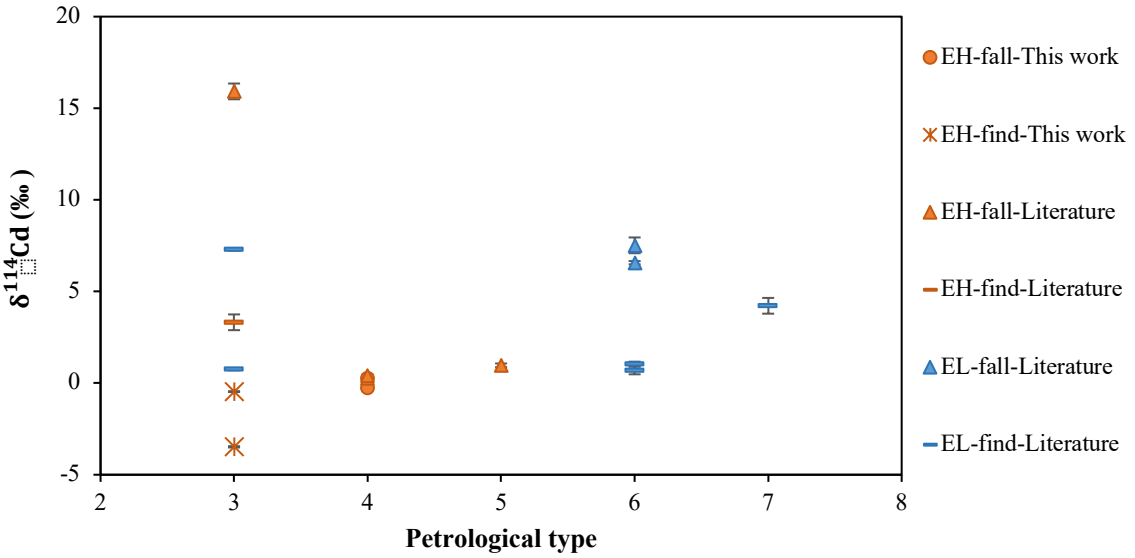


Figure 17: Enstatite chondrites isotope compositions as a function of their petrological types. The symbols are similar to those in previous figures. Pristine EH fall samples seem to be characterized by very heavy isotope compositions while thermally processed ones are much enriched in lightest Cd isotopes. Data are detailed in Table 1 and 4.

6. Conclusion

6.1. Using tektites to assess Cd isotope fractionation during volatilization

We used tektites from the Australasian strewn field and impact glasses from the Atacama Desert to quantify Cd isotopic fractionation during Cd volatilization. Our isotopic data results are in good agreement with the only previously characterized tektite (Wombacher et al., 2003). We propose a Rayleigh distillation kinetic factor of 0.9984 to explain the composition of the Australasian tektites. As would be expected, this is much higher that what a purely kinetic theoretical evaporation into vacuum should produce (0.9823 for Cd gas, or 0.9845 for CdO one), which suggests that the vaporization process is not purely kinetic. This represents the first determination of the Cd isotopic fractionation factor during evaporation that could be used to interpret future natural samples that have suffered evaporation of Cd.

This difference between theory and reality has been previously found to occur for other metal stable isotopes (e.g. Cu, Sn and Zn) (Creech et al., 2019; Moynier et al., 2010, 2009) and

has been interpreted as proof that the volatilization is controlled by elemental diffusion in the melt rather than by volatility (Moynier et al., 2010, 2009). The metals diffusivity in the Australasian melt follows this order: Cu > Zn ≥ Cd > Sn. This order seems to be mainly determined by the ionic charge of these elements.

6.2. Fall versus find chondrites, a sample's validity discussion

Cadmium being a mobile element in fluids, it is expected that compositions of fall and find chondrites are, most of the time, significantly different. It is notably known to be easily leached out rock samples by altering fluids, driving the residue toward Cd-depleted and isotopically light compositions (Zhang et al., 2016; Zhu et al., 2018). Other alteration processes can inject significant amounts of isotopically light Cd in samples (Devos et al., 2024). Leaching of isotopically heavy Cd can be observed for some enstatite chondrites, and light Cd input may be found for CO and EC, but new terrestrial alteration behaviors were also spotted. The first is a drift toward heavy isotope compositions accompanied by a significant loss of Cd (see Leoville CV sample), which is reminding of Cd volatilization processes. The occurrence of such a process on Earth for chondrite samples is unlikely, so that we have to propose either a new alteration process, leaching preferentially the lightest Cd isotopes or the Leoville sample actually underwent Cd volatilization previous to its arrival on Earth. This last possibility implies that Leoville chondrite have had a significantly different history than the other CV samples, that do not show any trace of Cd volatilization. Finally, a few CM and H find meteorites are characterized by heavier Cd isotope compositions than their fall counterparts but cannot be classified as Cd-enriched or -depleted as they have essentially normal Cd concentration (CM) or as the fall compositions span a very large field (H). These could need the intervention of the light Cd isotopes-leaching process described earlier or could require an input of isotopically heavy material to explain their compositions.

Thus, it appears that find samples are subject to multiple composition-altering processes for Cd, and that these influences are not currently characterized enough to be corrected. Because of this, we find it difficult to draw any robust conclusion from find samples concerning their pre-terrestrial histories. It seems to us that the most conservative approach is to consider only fall samples, for which terrestrial alteration can be considered insignificant.

6.3. Chondrite's compositions

Using the detailed Cd compositions of the different fall chondrite groups, we can formulate a few constraints on the history of these objects:

- Carbonaceous chondrites Cd concentrations are determined in comparable amounts by the matrix and chondrule contents of the sample and are strongly correlated with Zn concentrations. This indicates that Cd and Zn are borne by the same phases. However, while the different CC groups have distinct Zn isotope compositions, they are characterized by roughly similar Cd isotope compositions. This lack of important isotope fractionation makes us rule out volatilization events, at least for CI, CM and CV, as even if tektites isotope compositions are lower than expected, they show that significant isotope fractionation occurred. Since Cd has a lower T_{50} than Zn, any volatilization event affecting Zn should leave important footprints on Cd compositions. CO chondrites fractionated isotope compositions might be the result of vaporization events, but we lack a larger set of samples to be sure. The CC isotope compositions are weakly correlated with their Cd concentrations, with the Cd-richest samples being also the isotopically heaviest ones. This can be explained by a mixing of isotopically light chondrules and heavy matrix.
- Ordinary chondrites have very diversified Cd compositions, with concentration and isotope compositions spanning 3 orders of magnitude and around 20‰ respectively

in LL samples. Concentrations are loosely correlated with the petrological type, for LL and L samples, as thermally processed samples have generally a lower Cd concentration than pristine ones. However, due to the high variability of Cd concentrations, a higher number of analyzed samples, ideally type 3 or 4, might be necessary to ensure this point. No correlation was found between petrological type and isotope compositions. Notably, LL samples Cd isotope compositions are scattered seemingly at random, with generally very fractionated compositions. We do not have enough points for H, L or L/LL chondrites to notice any trend related to petrological types. Unlike CC, OC do not present any correlation (either for concentrations or isotope compositions) between Cd and Zn, except maybe for L samples, although more samples would be necessary to qualify a trend. Thus, Cd in OC is apparently not concentrated in the same phases as Zn. We lack the compositional data required to further discuss the nature of the Cd- and Zn-bearing phases in such samples. The OC isotope compositions for Cd are not strongly correlated with their Cd content. Chondrites of the H group are noticeable because, unlike the other OC, they have rather constant isotope compositions despite their wide range of Cd concentrations. Let's finally note that some of the H group OC are characterized by isotope compositions that are close to the Bulk Earth one.

- Enstatite chondrites display a similar correlation between Cd concentrations and petrological types than OC, with high petrological type samples being Cd-depleted compared to type 3 ones. This correlation seems to be coupled to an intense isotope fractionation, as type 4 and 5 samples are 16 ‰ lighter than type 3. This suggest that important loss of heavy Cd isotopes occurs quickly during thermal processing. Such process is similar than what is known to occur during terrestrial alteration. These observations are tempered by the low number of types 3, 5 and 6 samples.

Similarly to CC, EC Cd concentrations are found to be correlated to that of Zn. However, some Cd-depleted outliers exists, indicating that the relationship may be slightly more complicated than expected. We lack Zn isotope compositions for the characterized EC samples; however, 5 out of 6 EH samples have constant Cd isotope compositions, indicating that no correlation would be found with Zn ones. The only EH with a distinct Cd isotope composition, Hvittis, is also the outlier sample in the Cd vs. Zn concentrations trend, indicating that this sample Cd composition might be the result of a low temperature Cd volatilization event that lightly affected its Zn fraction. Again, the lack of isotope fractionation for most EH samples indicate that the samples probably never underwent a significant MVE volatilization event. EL samples are Cd-poor and isotopically heavy, which could indicate Cd vaporization, but we lack enough sample to reasonably make this point.

Producing the Bulk Earth Cd isotope composition by mixing chondrites is possible, as some samples in the CC, OC and EC groups have close isotope compositions that could serve as a basis for establishing the Earth, although most of the analyzed chondrites are isotopically heavier than the Earth. However, few chondrites have Cd concentrations close to that of the Bulk Earth, with most being significantly more Cd-rich than the BE. Since chondrules are both Cd-depleted and isotopically lighter than the bulk chondrites, one can imagine an Earth accretion scenario in which the BE Cd composition is obtained by diluting Cd-rich, isotopically heavy chondrites with Cd-depleted, isotopically light chondrules.

7. References

Aponte, J.C., Abreu, N.M., Glavin, D.P., Dworkin, J.P., Elsila, J.E., 2017. Distribution of aliphatic amines in CO , CV , and CK carbonaceous chondrites and relation to mineralogy and processing history. Meteorit. Planet. Sci. 52, 2632–2646. https://doi.org/10.1111/maps.12959

Arvidson, R., Crozaz, G., Drozd, R.J., Hohenberg, C.M., Morgan, C.J., 1975. Cosmic ray exposure ages of features and events at the apollo landing sites. The Moon 13, 259–276. https://doi.org/10.1007/BF00567518

Baker, R.G.A., Schönbächler, M., Rehkämper, M., Williams, H.M., Halliday, A.N., 2010. The thallium isotope composition of carbonaceous chondrites — New evidence for live 205Pb in the early solar system. Earth Planet. Sci. Lett. 291, 39–47. https://doi.org/10.1016/j.epsl.2009.12.044

Barrat, J.A., Zanda, B., Jambon, A., Bollinger, C., 2014. The lithophile trace elements in enstatite chondrites. Geochim. Cosmochim. Acta 128, 71–94. https://doi.org/10.1016/j.gca.2013.11.042

Barrat, J.A., Zanda, B., Moynier, F., Bollinger, C., Liorzou, C., Bayon, G., 2012. Geochemistry of CI chondrites: Major and trace elements, and Cu and Zn Isotopes. Geochim. Cosmochim. Acta 83, 79–92. https://doi.org/10.1016/j.gca.2011.12.011

Binz, C.M., Kurimoto, R.K., Lipschutz, M.E., 1974. Trace elements in primitive meteorites—V. Abundance patterns of thirteen trace elements and interelement relationships in enstatite chondrites. Geochim. Cosmochim. Acta 38, 1579–1606. https://doi.org/10.1016/0016-7037(74)90175-6

Bollard, J., Connelly, J.N., Whitehouse, M.J., Pringle, E.A., Bonal, L., Jørgensen, J.K., Nordlund, Å., Moynier, F., Bizzarro, M., 2017. Early formation of planetary building blocks

inferred from Pb isotopic ages of chondrules. Sci. Adv. 3, e1700407. https://doi.org/10.1126/sciadv.1700407

Braukmüller, N., Wombacher, F., Bragagni, A., Münker, C., 2020. Determination of Cu, Zn, Ga, Ag, Cd, In, Sn and Tl in geological reference materials and chondrites by isotope dilution ICP-MS. Geostand. Geoanalytical Res. 44, 733–752. https://doi.org/10.1111/ggr.12352

Braukmüller, N., Wombacher, F., Hezel, D.C., Escoube, R., Münker, C., 2018. The chemical composition of carbonaceous chondrites: Implications for volatile element depletion, complementarity and alteration. Geochim. Cosmochim. Acta 239, 17–48. https://doi.org/10.1016/j.gca.2018.07.023

Browning, L.B., McSween, H.Y., Zolensky, M.E., 1996. Correlated alteration effects in CM carbonaceous chondrites. Geochim. Cosmochim. Acta 60, 2621–2633. https://doi.org/10.1016/0016-7037(96)00121-4

Clayton, R.N., Mayeda, T.K., Rubin, A.E., 1984. Oxygen isotopic compositions of enstatite chondrites and aubrites. J. Geophys. Res. Solid Earth 89. https://doi.org/10.1029/JB089iS01p0C245

Connelly, J.N., Bizzarro, M., Krot, A.N., Nordlund, Å., Wielandt, D., Ivanova, M.A., 2012. The Absolute Chronology and Thermal Processing of Solids in the Solar Protoplanetary Disk. Science 338, 651–655. https://doi.org/10.1126/science.1226919

Creech, J.B., Moynier, F., 2019. Tin and zinc stable isotope characterisation of chondrites and implications for early Solar System evolution. Chem. Geol. 511, 81–90. https://doi.org/10.1016/j.chemgeo.2019.02.028

Creech, J.B., Moynier, F., Koeberl, C., 2019. Volatile loss under a diffusion-limited regime in tektites: Evidence from tin stable isotopes. Chem. Geol. 528, 119279.

https://doi.org/10.1016/j.chemgeo.2019.119279

Creech, J.B., Paul, B., 2015. IsoSpike: improved double-spike inversion software. Geostand. Geoanalytical Res. 39, 7–15. https://doi.org/10.1111/j.1751-908X.2014.00276.x

Devos, G., Moynier, F., Creech, J., Liu, D., Puchtel, I.S., Bizzarro, M., 2024. Cadmium isotope composition of the Earth's mantle inferred from analysis of oceanic basalts and komatiites. Chem. Geol. 650, 121996. https://doi.org/10.1016/j.chemgeo.2024.121996

Devouard, B., Rochette, P., Gattacceca, J., Valenzuela, E.M., Alard, O., Balestrieri, M.L., Santos, E.D., Gounelle, M., Jambon, A., Laridhi, N., Shuster, D.L., Warner, M., Warner, M., 2014. A new tektite strewnfield in Atacama, Chile. Presented at the 77th Annual Meteoritical Society Meeting.

Di Vincenzo, G., Skála, R., 2009. 40Ar–39Ar laser dating of tektites from the Cheb Basin (Czech Republic): Evidence for coevality with moldavites and influence of the dating standard on the age of the Ries impact. Geochim. Cosmochim. Acta 73, 493–513. https://doi.org/10.1016/j.gca.2008.10.002

Friend, P., Hezel, D.C., Barrat, J., Zipfel, J., Palme, H., Metzler, K., 2018. Composition, petrology, and chondrule-matrix complementarity of the recently discovered Jbilet Winselwan CM2 chondrite. Meteorit. Planet. Sci. 53, 2470–2491. https://doi.org/10.1111/maps.13139

Gattacceca, J., Devouard, B., Barrat, J.-A., Rochette, P., Balestrieri, M.L., Bigazzi, G., Ménard, G., Moustard, F., Dos Santos, E., Scorzelli, R., Valenzuela, M., Quesnel, Y., Gounelle, M., Debaille, V., Beck, P., Bonal, L., Reynard, B., Warner, M., 2021. A 650 km2 Miocene strewnfield of splash-form impact glasses in the Atacama Desert, Chile. Earth Planet. Sci. Lett. 569, 117049. https://doi.org/10.1016/j.epsl.2021.117049

Gicking, A.M., Takahashi, K., Krane, K.S., 2019. Neutron capture cross sections of stable Cd isotopes. Eur. Phys. J. A 55, 52. https://doi.org/10.1140/epja/i2019-12721-7

Grady, M., 2022. Catalogue of Meteorites. https://doi.org/10.5519/TQFUWLE7

Greenwood, R.C., Franchi, I.A., Kearsley, A.T., Alard, O., 2010. The relationship between CK and CV chondrites. Geochim. Cosmochim. Acta 74, 1684–1705. https://doi.org/10.1016/j.gca.2009.11.029

Greenwood, R.C., Lee, M.R., Hutchison, R., Barber, D.J., 1994. Formation and alteration of CAIs in Cold Bokkeveld (CM2). Geochim. Cosmochim. Acta 58, 1913–1935. https://doi.org/10.1016/0016-7037(94)90424-3

Grinyer, J., Byun, S.H., Chettle, D.R., 2005. In vivo prompt gamma neutron activation analysis of cadmium in the kidney and liver. Appl. Radiat. Isot. 63, 475–479. https://doi.org/10.1016/j.apradiso.2005.05.046

Grossman, L., 1972. Condensation in the primitive solar nebula. Geochim. Cosmochim. Acta 36, 597–619. https://doi.org/10.1016/0016-7037(72)90078-6

Hewins, R.H., Bourot-Denise, M., Zanda, B., Leroux, H., Barrat, J.-A., Humayun, M., Göpel, C., Greenwood, R.C., Franchi, I.A., Pont, S., Lorand, J.-P., Cournède, C., Gattacceca, J., Rochette, P., Kuga, M., Marrocchi, Y., Marty, B., 2014. The Paris meteorite, the least altered CM chondrite so far. Geochim. Cosmochim. Acta 124, 190–222. https://doi.org/10.1016/j.gca.2013.09.014

Hezel, D.C., Harak, M., Libourel, G., 2018. What we know about elemental bulk chondrule and matrix compositions: Presenting the ChondriteDB database. Geochemistry 78, 1–14. https://doi.org/10.1016/j.chemer.2017.05.003

Horan, M.F., Walker, R.J., Morgan, J.W., Grossman, J.N., Rubin, A.E., 2003. Highly siderophile elements in chondrites. Chem. Geol. 196, 27–42. https://doi.org/10.1016/S0009-2541(02)00405-9

Kaczaral, P.W., Dennison, J.E., Verkouteren, R.M., Lipschutz, M.E., 1988. On

volatile/mobile trace element trends in E3 chondrites. https://doi.org/10.15094/00004449

Kallemeyn, G.W., Rubin, A.E., 1995. Coolidge and Loongana 001: A new carbonaceous chondrite grouplet. Meteoritics 30, 20–27. https://doi.org/10.1111/j.1945-5100.1995.tb01207.x

Kallemeyn, G.W., Rubin, A.E., Wang, D., Wasson, J.T., 1989. Ordinary chondrites: Bulk compositions, classification, lithophile-element fractionations and composition-petrographic type relationships. Geochim. Cosmochim. Acta 53, 2747–2767. https://doi.org/10.1016/0016-7037(89)90146-4

Kallemeyn, G.W., Rubin, A.E., Wasson, J.T., 1991. The compositional classification of chondrites: V. The Karoonda (CK) group of carbonaceous chondrites. Geochim. Cosmochim. Acta 55, 881–892. https://doi.org/10.1016/0016-7037(91)90348-9

Kallemeyn, G.W., Wasson, J.T., 1982. The compositional classification of chondrites: III. Ungrouped carbonaceous chondrites. Geochim. Cosmochim. Acta 46, 2217–2228. https://doi.org/10.1016/0016-7037(82)90196-X

Keays, R.R., Ganapathy, R., Anders, E., 1971. Chemical fractionations in meteorites—IV abundances of fourteen trace elements in L-chondrites; implications for cosmothermometry. Geochim. Cosmochim. Acta 35, 337–363. https://doi.org/10.1016/0016-7037(71)90078-0

Keil, K., 1968. Mineralogical and chemical relationships among enstatite chondrites. J. Geophys. Res. 73, 6945–6976. https://doi.org/10.1029/JB073i022p06945

Koeberl, C., Bottomley, R., Glass, B.P., Storzer, D., 1997. Geochemistry and age of Ivory Coast tektites and microtektites. Geochim. Cosmochim. Acta 61, 1745–1772. https://doi.org/10.1016/S0016-7037(97)00026-4

Koeberl, C., Crosta, A.P., Schultz, T., 2019. Geochemical investigation of the atacamaites, a new impact glass occurrence in South America, in: Lunar and Planetary Science Conference. Presented at the 50th Annual Lunar and Planetary Science Conference, p. 1255.

Koeberl, C., Poag, C.W., Reimold, W.U., Brandt, D., 1996. Impact Origin of the Chesapeake Bay Structure and the Source of the North American Tektites. Science 271, 1263–1266. https://doi.org/10.1126/science.271.5253.1263

Krähenbühl, U., Morgan, J.W., Ganapathy, R., Anders, E., 1973. Abundance of 17 trace elements in carbonaceous chondrites. Geochim. Cosmochim. Acta 37, 1353–1370. https://doi.org/10.1016/0016-7037(73)90066-5

Laul, J.C., Ganapathy, R., Anders, E., Morgan, J.W., 1973. Chemical fractionations in meteorites—VI. Accretion temperatures of H-, LL- and E-chondrites, from abundance of volatile trace elements. Geochim. Cosmochim. Acta 37, 329–357. https://doi.org/10.1016/0016-7037(73)90138-5

Lee, M., Wei, K., 2000. Australasian microtektites in the South China Sea and the West Philippine Sea: Implications for age, size, and location of the impact crater. Meteorit. Planet. Sci. 35, 1151–1155. https://doi.org/10.1111/j.1945-5100.2000.tb01504.x

Lingner, D.W., Huston, T.J., Hutson, M., Lipschutz, M.E., 1987. Chemical studies of H chondrites. I: Mobile trace elements and gas retention ages. Geochim. Cosmochim. Acta 51, 727–739. https://doi.org/10.1016/0016-7037(87)90083-4

Loss, R.D., Rosman, K.J.R., De Laeter, J.R., 1984. Mass spectrometric isotope dilution analyses of palladium, silver, cadmium and tellurium in carbonaceous chondrites. Geochim. Cosmochim. Acta 48, 1677–1681. https://doi.org/10.1016/0016-7037(84)90336-3

Luck, J.-M., Othman, D.B., Albarède, F., 2005. Zn and Cu isotopic variations in chondrites and iron meteorites: Early solar nebula reservoirs and parent-body processes. Geochim. Cosmochim. Acta 69, 5351–5363. https://doi.org/10.1016/j.gca.2005.06.018

Marrocchi, Y., Avice, G., Barrat, J.-A., 2021. The Tarda Meteorite: A Window into the Formation of D-type Asteroids. Astrophys. J. Lett. 913, L9. https://doi.org/10.3847/2041-

8213/abfaa3

Mcsween, 1979. Alteration in CM carbonaceous chondrites inferred from modal and chemical variations in matrix. Geochim. Cosmochim. Acta.

McSween, H.Y., 1979. Are carbonaceous chondrites primitive or processed? A review. Rev. Geophys. 17, 1059–1078. https://doi.org/10.1029/RG017i005p01059

Mcsween, H.Y., 1977. Petrographic variations among carbonaceous chondrites of the Vigarano type. Geochim. Cosmochim. Acta 41, 1777–1790. https://doi.org/10.1016/0016-7037(77)90210-1

Metzler, K., Hezel, D.C., Barosch, J., Wölfer, E., Schneider, J.M., Hellmann, J.L., Berndt, J., Stracke, A., Gattacceca, J., Greenwood, R.C., Franchi, I.A., Burkhardt, C., Kleine, T., 2021. The Loongana (CL) group of carbonaceous chondrites. Geochim. Cosmochim. Acta 304, 1–31. https://doi.org/10.1016/j.gca.2021.04.007

Moynier, F., Beck, P., Jourdan, F., Yin, Q.-Z., Reimold, U., Koeberl, C., 2009. Isotopic fractionation of zinc in tektites. Earth Planet. Sci. Lett. 277, 482–489. https://doi.org/10.1016/j.epsl.2008.11.020

Moynier, F., Koeberl, C., Beck, P., Jourdan, F., Telouk, P., 2010. Isotopic fractionation of Cu in tektites. Geochim. Cosmochim. Acta 74, 799–807. https://doi.org/10.1016/j.gca.2009.10.012

Mughabghab, S.F., 2006. Atlas of Neutron Resonnances: Resonnance Parameters and Thermal Cross Sections Z=1-100, 5th ed. Elsevier.

Nishimura, M., Sandell, E.B., 1964. Zinc in meteorites. Geochim. Cosmochim. Acta 28, 1055–1079. https://doi.org/10.1016/0016-7037(64)90060-2

Palk, E., Andreasen, R., Rehkämper, M., Stunt, A., Kreissig, K., Coles, B., Schönbächler,

M., Smith, C., 2018. Variable Tl, Pb, and Cd concentrations and isotope compositions of enstatite and ordinary chondrites—Evidence for volatile element mobilization and decay of extinct ^{205} Pb. Meteorit. Planet. Sci. 53, 167–186. https://doi.org/10.1111/maps.12989

Pickard, H., Palk, E., Schönbächler, M., Moore, R.E.T., Coles, B.J., Kreissig, K., Nilsson-Kerr, K., Hammond, S.J., Takazawa, E., Hémond, C., Tropper, P., Barfod, D.N., Rehkämper, M., 2022. The cadmium and zinc isotope compositions of the silicate Earth – Implications for terrestrial volatile accretion. Geochim. Cosmochim. Acta 338, 165–180. https://doi.org/10.1016/j.gca.2022.09.041

Prestgard, T.J., Bonal, L., Gattacceca, J., Sonzogni, C., Beck, P., 2022. Exploring the connection between CM-CO clan chondrites through anomalous and misclassified members, in: Meteoritics & Planetary Science. Presented at the 85th Annual Meeting of the Meteoritical Society. https://doi.org/10.1111/maps.13901

Pringle, E.A., Moynier, F., Beck, P., Paniello, R., Hezel, D.C., 2017. The origin of volatile element depletion in early solar system material: Clues from Zn isotopes in chondrules. Earth Planet. Sci. Lett. 468, 62–71. https://doi.org/10.1016/j.epsl.2017.04.002

Rochette, P., Beck, P., Bizzarro, M., Braucher, R., Cornec, J., Debaille, V., Devouard, B., Gattacceca, J., Jourdan, F., Moustard, F., Moynier, F., Nomade, S., Reynard, B., 2021. Impact glasses from Belize represent tektites from the Pleistocene Pantasma impact crater in Nicaragua. Commun. Earth Environ. 2, 94. https://doi.org/10.1038/s43247-021-00155-1

Rosman, Barnes, I.L., Moore, L.J., Gramlich, J.W., 1980. Isotope composition of Cd, Ca and Mg in the Brownfield chondrite. Geochem. J. 14, 269–277. https://doi.org/10.2343/geochemj.14.269

Rosman, De Laeter, J.R., 1988. Cadmium mass fractionation in unequilibrated ordinary chondrites. Earth Planet. Sci. Lett. 89, 163–169. https://doi.org/10.1016/0012-821X(88)90168-

Rosman, De Laeter, J.R., 1978. A survey of cadmium isotopic abundances. J. Geophys. Res. 83, 1279. https://doi.org/10.1029/JB083iB03p01279

Rosman, De Laeter, J.R., 1974. The abundance of cadmium and zinc in meteorites. Geochim. Cosmochim. Acta 38, 1665–1677. https://doi.org/10.1016/0016-7037(74)90184-7

Rubin, A.E., 1990. Kamacite and olivine in ordinary chondrites: Intergroup and intragroup relationships. Geochim. Cosmochim. Acta 54, 1217–1232. https://doi.org/10.1016/0016-7037(90)90148-E

Rubin, A.E., 1989. Size-frequency distributions of chondrules in CO3 chondrites. Meteoritics 24, 179–189. https://doi.org/10.1111/j.1945-5100.1989.tb00960.x

Rubin, A.E., James, J.A., Keck, B.D., Weeks, K.S., Sears, D.W.G., Jarosewich, E., 1985. The Colony meteorite and variations in CO3 chondrite properties. Meteoritics 20, 175–196. https://doi.org/10.1111/j.1945-5100.1985.tb00859.x

Rudnick, R.L., Gao, S., 2014. Composition of the continental crust, in: Holland, H.D., Turekian, K.K. (Eds.), Treatise on Geochemistry. Elsevier, pp. 1–51. https://doi.org/10.1016/B978-0-08-095975-7.00301-6

Sands, D.G., De Laeter, J.R., Rosman, K.J.R., 2001a. Measurements of neutron capture effects on Cd, Sm and Gd in lunar samples with implications for the neutron energy spectrum. Earth Planet. Sci. Lett. 186, 335–346. https://doi.org/10.1016/S0012-821X(01)00231-X

Sands, D.G., Rosman, K.J.R., De Laeter, J.R., 2001b. A preliminary study of cadmium mass fractionation in lunar soils. Earth Planet. Sci. Lett. 186, 103–111. https://doi.org/10.1016/S0012-821X(01)00233-3

Schediwy, S., Rosman, K.J.R., de Laeter, J.R., 2006. Isotope fractionation of cadmium in

lunar material. Earth Planet. Sci. Lett. 243, 326–335. https://doi.org/10.1016/j.epsl.2006.01.007

Sears, D.W.G., Hasan, F.A., Batchelor, J.D., Lu, J., 1991. Chemical and physical studies of type 3 chondrites - XI: Metamorphism, pairing, and brecciation of ordinary chondrites. Lunar Planet. Sci. Conf. Proc. 21, 493–512.

Sears, D.W.G., Weeks, K.S., 1983. Chemical and physical studies of type 3 chondrites: 2. Thermoluminescence of sixteen type 3 ordinary chondrites and relationships with oxygen isotopes. J. Geophys. Res. Solid Earth 88. https://doi.org/10.1029/JB088iS01p0B301

Van Kooten, E.M.M.E., Kubik, E., Siebert, J., Heredia, B.D., Thomsen, T.B., Moynier, F., 2022. Metal compositions of carbonaceous chondrites. Geochim. Cosmochim. Acta 321, 52–77. https://doi.org/10.1016/j.gca.2022.01.008

Van Kooten, E.M.M.E., Wielandt, D., Schiller, M., Nagashima, K., Thomen, A., Larsen, K.K., Olsen, M.B., Nordlund, Å., Krot, A.N., Bizzarro, M., 2016. Isotopic evidence for primordial molecular cloud material in metal-rich carbonaceous chondrites. Proc. Natl. Acad. Sci. 113, 2011–2016. https://doi.org/10.1073/pnas.1518183113

Van Schmus, W.R., Wood, J.A., 1967. A chemical-petrologic classification for the chondritic meteorites. Geochim. Cosmochim. Acta 31, 747–765. https://doi.org/10.1016/S0016-7037(67)80030-9

Wang, H.S., Lineweaver, C., Ireland, T., 2018. The elemental abundances (with uncertainties) of the most Earth-like planet. Icarus 299, 460–474. https://doi.org/10.1016/j.icarus.2017.08.024

Wang, M.-S., Lipschutz, M.E., 2007. Trace elements in primitive meteorites—VII Antarctic unequilibrated ordinary chondrites. Geochim. Cosmochim. Acta 71, 1062–1073. https://doi.org/10.1016/j.gca.2006.10.009

Wang, M.-S., Lipschutz, M.E., 2005. Thermal metamorphism of primitive meteorites—

XII. The enstatite chondrites revisited. Environ. Chem. 2, 215–226. https://doi.org/10.1071/EN04075

Wang, Z., Becker, H., Wombacher, F., 2015. Mass fractions of S, Cu, Se, Mo, Ag, Cd, In, Te, Ba, Sm, W, Tl and Bi in geological reference materials and selected carbonaceous chondrites determined by isotope dilution ICP-MS. Geostand. Geoanalytical Res. 39, 185–208. https://doi.org/10.1111/j.1751-908X.2014.00312.x

Weisberg, M.K., McCoy, T.J., Krot, A.N., 2006. Systematics and evaluation of meteorite classification, in: Lauretta, D.S., McSween, H.Y. (Eds.), Meteorites and the Early Solar System II. pp. 19–52.

Wiik, H.B., 1956. The chemical composition of some stony meteorites. Geochim. Cosmochim. Acta 9, 279–289. https://doi.org/10.1016/0016-7037(56)90028-X

Wolf, R., Richter, G.R., Woodrow, A.B., Anders, E., 1980. Chemical fractionations in meteorites—XI. C2 chondrites. Geochim. Cosmochim. Acta 44, 711–717. https://doi.org/10.1016/0016-7037(80)90160-X

Wombacher, F., Rehkämper, M., Mezger, K., 2004. Determination of the mass-dependence of cadmium isotope fractionation during evaporation. Geochim. Cosmochim. Acta 68, 2349–2357. https://doi.org/10.1016/j.gca.2003.12.013

Wombacher, F., Rehkämper, M., Mezger, K., Bischoff, A., Münker, C., 2008. Cadmium stable isotope cosmochemistry. Geochim. Cosmochim. Acta 72, 646–667. https://doi.org/10.1016/j.gca.2007.10.024

Wombacher, F., Rehkämper, M., Mezger, K., Münker, C., 2003. Stable isotope compositions of cadmium in geological materials and meteorites determined by multiple-collector ICPMS. Geochim. Cosmochim. Acta 67, 4639–4654. https://doi.org/10.1016/S0016-7037(03)00389-2

Wood, J.A., 1967. Olivine and pyroxene compositions in type II carbonaceous chondrites. Geochim. Cosmochim. Acta 31, 2095–2108. https://doi.org/10.1016/0016-7037(67)90144-5

Zhang, Y., Wen, H., Zhu, C., Fan, H., Luo, C., Liu, J., Cloquet, C., 2016. Cd isotope fractionation during simulated and natural weathering. Environ. Pollut. 216, 9–17. https://doi.org/10.1016/j.envpol.2016.04.060

Zhu, C., Wen, H., Zhang, Y., Yin, R., Cloquet, C., 2018. Cd isotope fractionation during sulfide mineral weathering in the Fule Zn-Pb-Cd deposit, Yunnan Province, Southwest China. Sci. Total Environ. 616–617, 64–72. https://doi.org/10.1016/j.scitotenv.2017.10.293

Zolensky, M.E., Weisberg, M.K., Buchanan, P.C., Mittlefehldt, D.W., 1996. Mineralogy of carbonaceous chondrite clasts in HED achondrites and the Moon. Meteorit. Planet. Sci. 31, 518–537. https://doi.org/10.1111/j.1945-5100.1996.tb02093.x

Chapter 6 – Synthesis

1. Conclusion

The origin of the MVE depletion pattern in rocky bodies of the solar system remains an open question. This PhD project aimed at providing new insights into this complex field of research, using a non-traditional isotope system: cadmium. Because the number of studies using Cd isotopes to investigate geological processes remains low, some key parameters like the BSE isotope composition are still debated. We conducted analyses in five different directions. The first goal was to assess the accuracy and precision of the data produced with our new purification and analytical protocols as well as determining the potential impact of interferents on the measurements. Once this was done, we focused on determining a new isotope composition for the Earth mantle, which would serve as a reference point to which compare Earth-derived rocks like tektites and extra-terrestrial samples. Thirdly, we characterized the potential isotope fractionation affecting Cd during fractional crystallization in Icelandic lavas. Using tektites and impact glasses, we studied the isotope fractionation of Cd occurring during volatilization in Earth atmosphere. Finally, we analyzed chondritic samples and compared the obtained Cd compositions to the Earth one to assess chondrites role as potential building blocks of the Earth. In total, we analyzed the Cd isotope compositions of a set of 88 individual samples (replicates included), producing more than 1500 datapoints.

Analysis of the pure AAS standard solution gave up a similar Cd isotope composition than what was proposed by previous work. This led us to assess that our DS deconvolution scheme is working satisfactorily. However, because of its lack of matrix, this sample was not processed through the purification protocol. To evaluate the matrix removal efficiency, we processed and analyzed a set of 9 geological and biological standard reference materials. Although we removed any measurement characterized by mass-independent isotope composition, indicating interferences, some of our proposed isotope compositions are on the heavier side of the

published values. This is thought to be caused by isotopically heterogeneous samples. Nonetheless, significant overlap between most of our value and the literature ones provides us with confidence in the ability of our protocol to produce valid data.

In order to determine a new isotope composition for the BSE, we chose to focus on igneous samples. The underlying hypothesis for the use of such samples is that minimal isotope fractionation occurs between the initial peridotite and the derived melt. This assumption is known to be true for melts resulting from high degrees of partial melting, for other elements, but no study of this phenomenon has been conducted for Cd. We analyzed a set of 14 MORB and 12 komatiites, which were completed by previously published data. MORB samples are isotopically very homogeneous, regardless of their origin, being characterized by a mean δ^{114}Cd of 0.07 ± 0.10 ‰ (2SD, n = 23). To the contrary, komatiites display varied Cd concentration and isotope composition values that are correlated with their degree of secondary alteration (approximated by the loss on ignition measurement – LOI). Specifically, Cd concentrations are linearly correlated to LOI, with high-LOI samples being Cd-depleted compared to low-LOI ones. The correlation between LOI and Cd isotope compositions is less clear as some high-LOI samples retain similar isotope compositions than low-LOI ones. Nevertheless, a clear scattering toward isotopically light compositions is visible for many altered samples. This indicates that, although komatiites Cd isotope compositions can be resilient to alteration in some cases, altering fluids leaches preferentially the heaviest Cd isotopes, driving the residue toward isotopically lighter compositions. Thus, conservative estimation of the pristine Cd isotope composition of komatiites should only take into account the least altered samples. We determined a mean Cd isotope composition for the least altered komatiites (LOI < 6%) of 0.14 ± 0.18 ‰ (2SD, n = 5).

Since MORB and komatiites isotope compositions are similar, we assess that isotope fractionation during melting is insignificant for samples with degrees of partial melting similar

or higher than MORB. The great variability in literature isotope compositions for OIB lead us to think that they are affected by partial melting isotope fractionation, contamination by recycled material and/or unrepresentative mantle sources. In any case, these samples are not suited for determination of a BSE isotope composition. Thus, we calculated a mean isotope composition for the Earth mantle, based on MORB and komatiites, of 0.11 ± 0.10 ‰ (2SD, n = 28). Mantle homogeneity for Cd isotopes is thought to have been achieved at least 3549 ± 99 million years ago (the age of the oldest komatiite with pristine Cd isotope composition). This isotope composition is significantly heavier than what was previously proposed, based on peridotites, which could have significant repercussions on the discussion of the nature of Earth building blocks.

In order to determine the potential isotope fractionation occurring for Cd during fractional crystallization, we analyzed a set of lavas from the Hekla volcano, with compositions ranging from basalts to rhyolites. We found that the basalts are characterized by a constant heavy isotope composition that we explained by proposing that low degrees of partial melting preferentially collect the heaviest Cd isotopes. This mirrors what is known to occur for Zn. We found no evidence that there is some isotope fractionation for Cd during fractional crystallization.

We aimed at comparing this BSE isotope composition (which is thought to be also valid for the bulk Earth) to that of chondrites in order to discuss the possibility of accreting the Earth with chondritic building blocks. However, we have first to assess the potential influence of chondrites degassing during their atmospheric trip over their bulk composition. For this, we analyzed two tektites from the Australasian strewn field as well as two impact glasses from the Atacama Desert (hereafter called atacamaites). These samples were melted and projected on a ballistic trajectory by the impact of an asteroid, they are known to have undergone significant MVE volatilization and isotope fractionation. Only one sample was characterized for Cd before this work.

We find that, similarly to what has already been published for other elements, impact glasses are Cd-depleted and isotopically fractionated compared to a mean crustal composition. The isotope composition is correlated with the Cd depletion, following a Rayleigh distillation law that is coherent with Cd volatilization. Atacamaites and Australasian samples follow different trends, characterized by distinct kinetic factors α ($\alpha_{atacamaites} = 0.9995$; $\alpha_{Australasian\ tektites} = 0.9984$). High α factor coincides with rather unfractionated isotope compositions for a given Cd depletion. The observed Cd isotope compositions are significantly less fractionated than what is expected for purely kinetic, theoretical Rayleigh distillation for both Cd and CdO degassing ($\alpha_{Cd} = 0.9823$; $\alpha_{CdO} = 0.9845$). This difference can be explained by the fact that, unlike in a perfect Rayleigh distillation case, the molten tektites are not perfectly homogenized during the evaporation process. Thus, instead of being driven by volatility, Cd vaporization in tektites is probably controlled by diffusivity in the melt, as was found to occur for Cu, Zn and Sn by other authors. Correcting for the isotopic mass difference in the δ notation, we calculated normalized α parameters for these elements to determine which diffuses the most readily in Australasian tektites melt. This high mobility is reflected by highly fractionated isotope compositions. We find the following increasing diffusivity order: Sn (α = 0.9998) > Cd (α = 0.9996) > Zn (α = 0.9995) > Cu (α = 0.9991). We propose that this order is determined mainly by elemental groups, thus by the chemical properties of the element.

The study of impact glasses indicates that melting is important to efficiently depleted a sample from its Cd. Only a superficial layer of chondrites is melted by atmospheric heating. Although it is probable that the obtained fusion crust is significantly Cd-depleted, we do not expect that this thin layer can constitute a significant isotopic pollution for bulk analyses of chondrites.

We analyzed a set of 17 chondrites, composed of 8 carbonaceous chondrites (CC), 7 ordinary chondrites (OC) and 2 enstatite chondrites (EC). Out of these, 14 (6 CC, 7 OC and 1

EC) had not been characterized for their Cd isotope compositions. This ensemble almost doubles the amount of fully characterized (Cd concentrations and isotope compositions) CC and OC. Replicates analyses show that a significant fraction of the chondrites from each group are heterogeneous for Cd.

We found that many chondritic replicates are characterized by significantly distinct isotope compositions while displaying similar Cd concentrations. We can only explain this by local isotopic heterogeneities in different parts of the chondrite and propose that such compositions reflect local condition variations in the nebular region forming the sample. Alongside these samples, some other present distinct Cd concentrations for a same isotope composition. We interpret this as proof of Cd dilution in different parts of the sample. Finally, some chondrites present evidences of Cd input by isotopically fractionated particles, creating a nugget effect.

Another important parameter for the Cd compositions is the collection conditions (falls versus finds), as highly mobile Cd is expected to be affected by terrestrial alteration processes. However, some of the observed compositions cannot be accounted for by typical terrestrial weathering, which preferentially collects the heavy Cd isotopes. Notably, some CC and OC find chondrites are characterized by significantly heavier isotope compositions than their related falls coupled with cd depletion. Thus, it appears that some of the terrestrial alteration processes can produce a depletion of the lightest Cd isotopes that is very close to what is obtained by Cd volatilization. As we consider that Cd vaporization of chondritic material on the Earth surface is very improbable, we have to propose that some yet uncharacterized Cd leaching processes produce similar results. Because of the strong influence of secondary processes on the chondritic Cd compositions, we advise firmly that the next chondritic studies centered on Cd should analyze falls only.

Carbonaceous chondrites Cd isotope compositions from this work and from the literature are weakly correlated to their cd concentrations, with Cd-rich samples being also isotopically

the heaviest. We can explain this correlation by a mixing between Cd-rich, isotopically heavy matrix and Cd-poorer, isotopically light chondrules, which is similar to what is observed for Zn. Only the CO and some CI chondrites seem to be out of this trend. The Kainsaz CO chondrite is Cd-depleted and isotopically heavy, which could be evidences of Cd volatilization. Some Orgueil CI chondrite analyses are out of this trend as well while other for the same material are coherent with the correlation. Thus, we would need to analyze more CI chondrites before being able to be sure that the CC follow only this trend.

No similar trend was found for OC and EC. Ordinary chondrites are characterized by very variable isotope compositions and Cd concentrations, even within a same group. While their Cd concentrations appear to be correlated to their petrological types, with thermally processed samples being Cd-depleted, we found no significant impact of such processes over their cd isotope compositions. This isotopic influence of thermal processing might be masked by the inherent variability of the OC isotope compositions, reflecting the diversity of conditions under which they formed. Enstatite chondrites isotope compositions and Cd concentrations might be explained mainly by their petrological type as well, as type 3 EC are Cd-richer and isotopically heavier than types 4 to 6. Although, more EC samples would be needed before being able to propose a model. We propose that the Earth composition could be obtained by mixing isotopically heavy, Cd-rich chondrites with isotopically light, Cd-depleted chondrules.

2. Future directions

In this work, we proposed a new isotope composition for the Earth mantle that is significantly different from the previously existing one that was based on peridotites. Although we are confident that our composition is correct, a new study re-evaluating the Cd isotope compositions of peridotites is needed to finally reach a conclusion for the Earth mantle. Moreover, should this new study concur with the literature about the peridotite's composition,

we would need to assess which isotopically fractionating processes separate the igneous samples presented in this work from the analyzed peridotites.

Similarly, although a recent study has tackled the subject, more work needs to be done to measure the potential isotope fractionation occurring during the metal-silicate partitioning phase of planetary differentiation. Without this information, the Cd isotope composition of the bulk Earth is out of reach and with it, any comparison to meteorites. Since the Earth core is the terrestrial reservoir containing the most Cd, any minor isotope fractionation occurring between the core and the mantle would cause significant isotope composition deviations.

The current work suggests that, because of their low degrees of partial melting, OIB lavas should have distinct isotope composition than MORB or than their mantle source. Specifically, basalts from the Hekla volcano, Iceland, were interpreted as representative of OIB magmas, leading to the conclusion that low degrees of partial melting cause the formation of magmas that are isotopically heavier than their source. We would welcome a dedicated study of the Cd compositions in OIB samples from all around the world, as it would confirm or infirm this conclusion. Moreover, since many OIB are characterized by crustal recycling or sampling of isotopically distinct mantle domains, such a review would allow for a more nuanced image of the mantle heterogeneities for Cd. The fact that we found that no significant isotope fractionation occurs during fractional crystallization should ease such studies.

Finally, more isotopic data for Cd are needed to discuss the characteristic and isotopic trends of chondrites for Cd. Specifically, we encourage the characterization of fall CI, CO, CR and CL samples, as well as enstatite chondrites. This work could be furthered by analyzing Cd isotope compositions in separated chondrules and matrix, and by trying to chemically map heterogeneous samples for Cd to try to verify our Cd-rich nugget hypothesis. The characterization of achondrites and iron meteorites might also be useful to better understand Cd vaporization processes in the void and Cd partitioning during metal-silicate separation.

Articles as co-author

Geochimica et Cosmochimica Acta 336 (2022) 436–447

Contents lists available at ScienceDirect

Geochimica et Cosmochimica Acta

journal homepage: www.elsevier.com/locate/gca

Barium isotopes in ocean island basalts as tracers of mantle processes

Ruixia Bai [a,*], Matthew G. Jackson [a], Fang Huang [b,c], Frédéric Moynier [d], Gabriel Devos [d], Sæmundur A. Halldórsson [e], Lorraine Lisiecki [a], Haoming Yin [b], Yihang Peng [b], Xiaoyun Nan [b,c]

[a] Department of Earth Science, University of California, Santa Barbara 93106, USA
[b] CAS Key Laboratory of Crust-Mantle Materials and Environments, School of Earth and Space Sciences, University of Science and Technology of China, Anhui 230026, China
[c] CAS Center for Excellence in Comparative Planetology, USTC, Hefei 230026, Anhui, China
[d] Université Paris Cité, Institut de Physique du Globe de Paris, CNRS UMR 7154, 1 rue Jussieu, Paris F-75005, France
[e] NordVulk, Institute of Earth Sciences, University of Iceland, 102 Reykjavík, Iceland

ARTICLE INFO

Article history:
Received 14 February 2022
Accepted 22 August 2022
Available online 28 August 2022
Associate editor: Andreas Stracke

Keywords:
Mantle geochemistry
Ocean island basalts (OIB)
Barium isotopes
Volcanic hotspots
Crustal recycling

ABSTRACT

The compositions of ocean island basalts (OIB) can record signatures of ancient subducted crust that has been recycled through the mantle. Based on their radiogenic isotope, major and trace element compositions, several geochemically-extreme mantle compositions are suggested to host components of recycled crust. Barium (Ba) stable isotopes can serve as a tracer of crustal recycling into the mantle sources of OIB because 1) Ba isotopes are fractionated in surface crustal reservoirs and 2) Ba is highly enriched in crust relative to the mantle. Therefore, the Ba isotopic compositions of the subducted crust could be detected in OIB. Here, we characterized Ba isotopic compositions of fresh OIB from hotspots sampling a range of mantle compositions. We first explore $\delta^{138/134}$Ba (permil deviation of the ^{138}Ba/^{134}Ba ratio from the standard SRM3104a) in a suite of Hekla samples and demonstrate that magmatic differentiation does not impact the $\delta^{138/134}$Ba values of OIB over MgO concentrations from 2.3 to 8.0 wt%, and higher MgO lavas are unlikely to experience $\delta^{138/134}$Ba fractionation. After excluding OIB samples that experienced low-temperature alteration—which may shift the $\delta^{138/134}$Ba values of samples away from their mantle sources—the $\delta^{138/134}$Ba values of Samoan (including EM2 and high ^{3}He/^{4}He) lavas range from -0.07 to 0.07‰, while for Cook-Austral (HIMU) lavas the $\delta^{138/134}$Ba values range from 0.00 to 0.11‰, and for St. Helena (HIMU) samples the $\delta^{138/134}$Ba values range from 0.02 to 0.05‰. High ^{3}He/^{4}He (> 20 Ra, ratio to atmosphere) lavas from Vestfirðir of Iceland (-0.09 to 0.14‰) and Samoa (-0.02 to 0.01‰) also exhibit Ba isotopic variability. An extreme EM2 lava examined here (^{143}Nd/^{144}Nd = 0.512582) has lighter Ba isotopic composition (-0.07 ± 0.02‰, 2SE) than the depleted mantle sampled by MORB (0.05 ± 0.05‰, 2SD). The Samoan lavas show a possible positive trend between $\delta^{138/134}$Ba values and ^{143}Nd/^{144}Nd ratios, and can be modeled as a binary mixing between the high ^{3}He/^{4}He (FOZO) mantle and recycled heterogeneous continental crust. In contrast, the extreme HIMU composition (^{206}Pb/^{204}Pb > 21.7) shows heavier Ba isotope signatures (0.11 ± 0.02‰, 2SE); $\delta^{138/134}$Ba values positively correlate strongly with ^{206}Pb/^{204}Pb ratios in HIMU lavas, consistent with a contribution from recycled oceanic crust.

Published by Elsevier Ltd.

1. Introduction

Ocean island basalts (OIB) are formed by shallow melting within upwelling mantle plumes (Morgan, 1971). The composition of the mantle is influenced by the subduction of surface materials, following 10^8 to > 10^9 years of incubation, which generates heterogeneous compositions with different origins that are identified in OIB erupted at hotspots (Zindler and Hart, 1986; Hofmann, 1997; White, 2015). Geochemical analyses of OIB provide a window into the chemical composition of the deep mantle and reveal the presence of recycled crust in mantle plumes (Zindler and Hart, 1986; Hofmann, 1997; White and Hofmann, 1982; Hofmann and White, 1982; Hauri and Hart, 1993, 1997). Based on different radiogenic isotopic signatures from the ocean island basalts, the OIB-source mantle materials are highly heterogeneous and characterized by five different extreme compositions:

1. Depleted MORB mantle (DMM; Workman and Hart, 2005; Zindler and Hart, 1986; Salters and Stracke, 2004), which is the mantle source of mid-ocean ridge basalts (MORB), characterized by high ^{143}Nd/^{144}Nd and low ^{87}Sr/^{86}Sr, ^{206}Pb/^{204}Pb, ^{207}Pb/ ^{204}Pb, and ^{3}He/^{4}He ratios;

* Corresponding author.
E-mail address: ruixiabai@ucsb.edu (R. Bai).

https://doi.org/10.1016/j.gca.2022.08.023
0016-7037/Published by Elsevier Ltd.

2. Enriched mantle 1 (EM1; Hofmann, 1997; Eisele et al., 2002), characterized by high $^{208}Pb/^{204}Pb$ ratios at a given $^{206}Pb/^{204}Pb$, low $^{206}Pb/^{204}Pb$ and $^{143}Nd/^{144}Nd$, high $^{87}Sr/^{86}Sr$, and low MORB-like $^{3}He/^{4}He$ ratios;
3. Enriched mantle 2 (EM2; White and Hofmann, 1982; Workman et al., 2004), characterized by the highest $^{87}Sr/^{86}Sr$, low $^{143}Nd/^{144}Nd$, intermediate $^{206}Pb/^{204}Pb$ and $^{208}Pb/^{204}Pb$ ratios, and lower-than-MORB $^{3}He/^{4}He$ ratios;
4. High-μ mantle (HIMU, where μ = $^{238}U/^{204}Pb$; Hauri and Hart, 1993, 1997; Hanyu et al., 2014), characterized by high $^{206}Pb/^{204}Pb$, relatively high $^{143}Nd/^{144}Nd$, low $^{87}Sr/^{86}Sr$, and lower-than-MORB $^{3}He/^{4}He$ ratios;
5. Focus zone (FOZO; Hart et al., 1992; Hanan and Graham, 1996), identified by the region of convergence of data arrays of OIB from different hotspots in Sr-Nd-Pb multi-isotope space. FOZO is geochemically depleted—including high $^{143}Nd/^{144}Nd$, low $^{87}Sr/^{86}Sr$, and low $^{206}Pb/^{204}Pb$—and may be characterized by high $^{3}He/^{4}He$ ratios.

In this paper, these compositions (DMM, EM1, EM2, HIMU, and FOZO) are not taken to represent "endmembers" but instead reflect extreme radiogenic isotopic compositions that allow us to investigate potential variability in $\delta^{138/134}Ba$ values in the mantle. These different mantle source materials likely originated from recycling of different types of crustal materials. EM1 and EM2 are generally thought to form from the recycling of continentally-derived materials (White and Hofmann, 1982; Eisele et al., 2002; Jackson et al., 2007a; Moynier et al., 2021), though other explanations for the origin of EM1 have been proposed (for a summary see Garapić et al., 2015). HIMU OIB are likely sourced by ancient recycled oceanic crust (Hofmann and White, 1982), but other origins have been suggested (e.g., Weiss et al., 2015). However, it is important to acknowledge that the exact origins and sources of the different mantle materials remain uncertain.

The sources of different mantle materials can be traced with the elemental and isotopic compositions of fresh OIB lavas. The stable isotopes of barium (Ba) can be used as a sensitive tracer of continental and oceanic crust that have been subducted into the mantle because Ba is a highly incompatible element (Hofmann, 2003; Workman and Hart, 2005; Stracke and Bourdon, 2009) and thus concentrates in melts during mantle melting. As a result, Ba abundances in the continental crust (456 ppm; Rudnick and Gao, 2014) and oceanic crust (29.2 ppm from the "all normal-MORB mean"; Gale et al., 2013) are much higher than in the putative primitive mantle (6.6 ppm; McDonough and Sun, 1995) or the depleted mantle (0.56 ppm for average DMM; Workman and Hart, 2005).

Barium has seven stable isotopes, which are ^{130}Ba (0.11%), ^{132}Ba (0.10%), ^{134}Ba (2.42%), ^{135}Ba (6.59%), ^{136}Ba (7.85%), ^{137}Ba (11.23%), and ^{138}Ba (71.70%) (Eugster et al., 1969). Barium isotope data are usually expressed as:

$$\delta^{13x/134}Ba = \left(\frac{^{13x/134}Ba_{sample}}{^{13x/134}Ba_{standard}} - 1\right) \times 1000\,(\text{expressed as permil, ‰}) \quad (1)$$

where x = 8 in this paper (but x = 7 is used in some previous work) and SRM3104a is the standard (Nan et al., 2015, 2018, 2022; Nielsen et al., 2018, 2020; Li et al., 2020). Barium isotopic variability has been found in many terrestrial reservoirs (summarized in Fig. 1). For example, in continental materials, $\delta^{138/134}Ba$ values of different types of granite range from -1.33 to 0.95‰, which indicates Ba isotopes fractionate during felsic magma genesis and evolution (Nan et al., 2018; Deng et al., 2021; Huang et al., 2021). Other continentally-derived materials, like loess (-0.03 to 0.04‰, Nan et al., 2018) and glacial diamictites (-0.23 to 0.47‰, Nan et al., 2018), also show variable $\delta^{138/134}Ba$ values. Additionally, altered oceanic crust (AOC) exhibits significant Ba isotopic variability (from -0.09 to 0.33‰; Nielsen et al., 2018).

The large Ba concentration contrast between mantle and crust (i.e., both continental and oceanic crust), as well as the large $\delta^{138/134}Ba$ variability among different terrestrial reservoirs, makes Ba isotopes an important and sensitive tracer for crustal material recycling. To our knowledge, with the exception of the United States Geological Survey (USGS) reference materials BHVO-1, BHVO-2 and BIR-1, Ba isotope data have not been reported in OIB lavas. To investigate the source of different mantle materials, and prospect for signatures of Ba isotopic variability imprinted on the mantle from crustal subduction, we analyzed Ba isotopic compositions of OIB from six hotspots and one high $^{3}He/^{4}He$ flood basalt province with the goal of sampling different mantle materials (Fig. 2). We identify $\delta^{138/134}Ba$ variability in OIB (Fig. 1). Based on the relationship between $\delta^{138/134}Ba$ values and radiogenic isotope ratios (i.e., $^{143}Nd/^{144}Nd$ and $^{206}Pb/^{204}Pb$), we show that the Ba isotopic compositions of EM2 lavas can be modeled by a contribution of recycled continental crust with light Ba isotopic compositions ($\delta^{138/134}Ba$ values from 0.00 to -0.80‰), while HIMU lavas can be explained by a contribution of recycled altered oceanic crust with heavy Ba isotopic compositions. Therefore, Ba isotopes potentially provide new insights into the origins of mantle heterogeneity.

2. Samples

As shown in Fig. 3, the $^{206}Pb/^{204}Pb$ and $^{143}Nd/^{144}Nd$ data represented by the samples in this study span the full range of compositions in the global OIB dataset. We analyzed 56 OIB and 4 flood basalt samples from different hotspots including 3 samples from Pitcairn Island (with EM1 signatures; Garapić et al., 2015), 14 samples from the Samoan hotspot (which span lavas with high $^{3}He/^{4}He$ ratios to extreme EM2 signatures; Workman et al., 2004; Jackson et al., 2007a; Hart and Jackson, 2014), 5 samples from St. Helena (which samples HIMU compositions only; Graham et al., 1992; Gaschnig et al., 2021), 8 samples from the Cook-Austral islands—Rurutu, Mangaia, and Tubuai—that are selected to have HIMU compositions only (i.e., $^{206}Pb/^{204}Pb > 20$; Hauri and Hart, 1993, 1997), 3 samples from the Caroline Islands (Jackson et al., 2017), and 27 samples from the Iceland hotspot track. The suite of samples from Iceland includes 7 mid-Miocene Vestfirðir lavas with high $^{3}He/^{4}He$ ratios (up to 43 Ra, Jackson et al., 2020a), and 4 lavas from the Baffin Island flood basalt province that exhibit $^{3}He/^{4}He$ signatures of up to 39.9 Ra in the sample suite explored here (Willhite et al., 2019), but extends up to 50 Ra in samples explored previously (Stuart et al., 2003). The Baffin Island samples examined here were selected to be those that are least affected by continental crust assimilation (Willhite et al., 2019). Additionally, we analyzed Ba isotopic compositions of 16 samples from Hekla volcano in Iceland. Hekla lavas span a large range of MgO concentrations (from 2.3 to 8.0 wt%). Critically, the Hekla igneous suite has remarkably homogeneous radiogenic isotopic compositions of Sr, Nd, and Pb—implying a homogeneous mantle source for radiogenic isotopes—which makes Hekla lavas ideal for evaluating the role of magmatic petrogenesis and evolution in modifying the $\delta^{138/134}Ba$ values of OIB (Jónasson, 2007; Geist et al., 2021; Sigmarsson et al., 2022).

Each of the samples from the Samoa (Workman et al., 2004; Jackson et al., 2007a), Cook-Austral Islands (Hauri and Hart, 1993, 1997; Parai et al., 2009), Caroline (Jackson et al., 2017), Pitcairn (Garapić et al., 2015), and St. Helena (Graham et al., 1992; Gaschnig et al., 2021) hotspots were the subject of prior geochemical work, and there were no notable signatures of oceanic crust assimilation present in any of these lavas. This is not unexpected as the OIB lavas examined here have relatively high MgO concen-

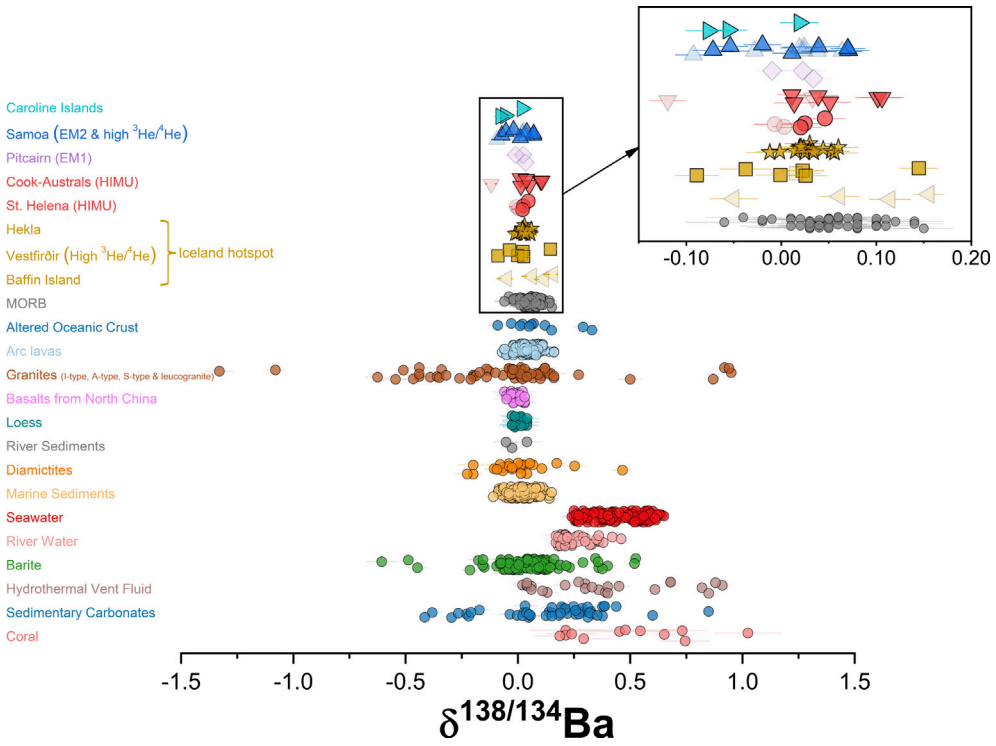


Fig. 1. Ba isotopic compositions of different reservoirs that have been characterized in the literature compared with the new data for hotspot lavas. The freshest (Ba/Rb < 30, Th/U < 4.5) lavas are shown together with altered (Ba/Rb > 30, Th/U > 4.5) hotspots lavas, where the altered lavas that we exclude from further consideration are shown as lighter/more transparent shades of color. The inset provides a closer view of MORB data and the new data. The databases shown include MORB (Nielsen et al., 2018; Nan et al., 2022), altered oceanic crust (Nielsen et al., 2018), arc lavas (Wu et al., 2020), granite (Deng et al., 2021; Nan et al., 2018; Huang et al., 2021), basalts from the North China Craton (Zhao et al., 2021), loess (Nan et al., 2018), river sediments (Nan et al., 2018), diamictites (Nan et al., 2018), marine sediments (Bridgestock et al., 2018; Nielsen et al., 2018, 2020), seawater (Bridgestock et al., 2018; Horner et al., 2015; Hsieh and Henderson, 2017), river water (Gou et al., 2020), barite (Crockford et al., 2019; von Allmen et al., 2010), hydrothermal vent fluid (Hsieh et al., 2020), sedimentary carbonates (Wei et al., 2021), and coral (Pretet et al., 2015).

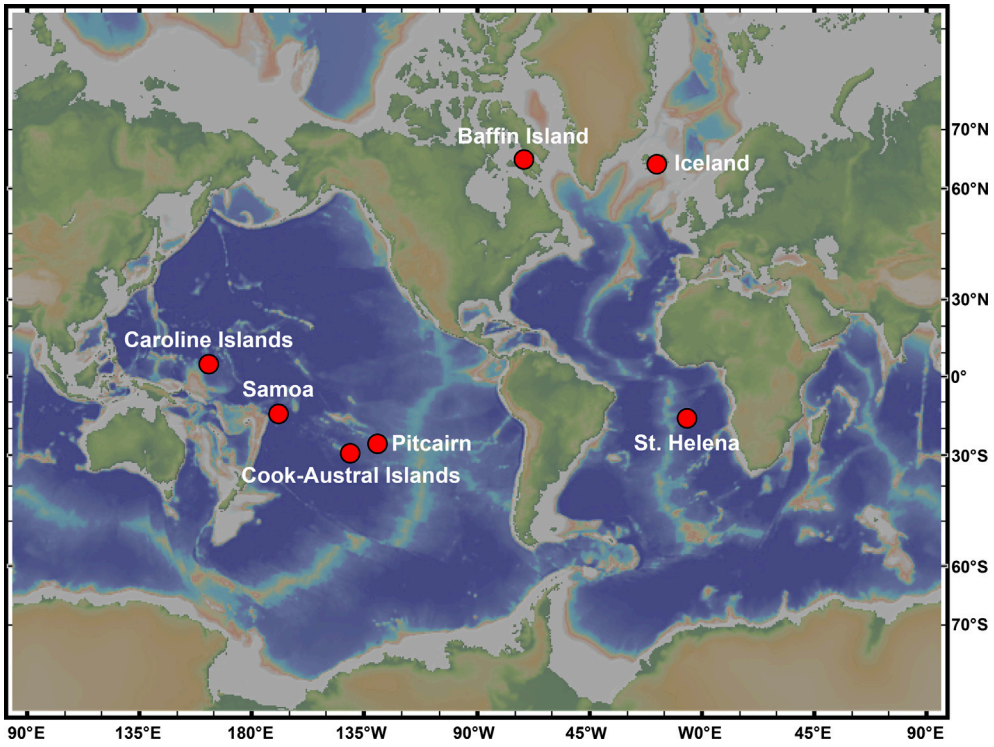


Fig. 2. Sample locations in this study. The red points are the sample locations including Samoa (EM2 and high $^3He/^4He$), Pitcairn (EM1), St. Helena (HIMU), Cook-Austral Islands (HIMU), Caroline Islands, Baffin Island (high $^3He/^4He$), Iceland (high $^3He/^4He$). The map was made using GeoMapApp (http://www.geomapapp.org), where the basemap was generated by Ryan et al. (2009).

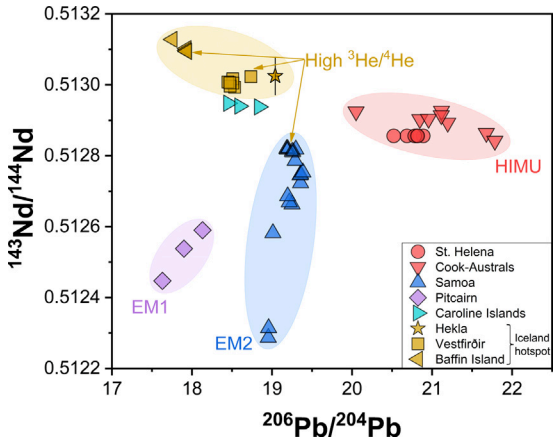


Fig. 3. Nd and Pb isotopic compositions of the samples characterized for Ba isotopic compositions in this study. The samples were chosen to span the range of radiogenic isotopic compositions in the mantle, including EM1, EM2, HIMU, and high $^{3}He/^{4}He$. High $^{3}He/^{4}He$ (>20 Ra, ratio to atmosphere) is found in Baffin Island lavas, Vestfirðir lavas, and a subset of lavas from Samoa that have relatively high $^{143}Nd/^{144}Nd$ ratios (note that EM2 lavas from Samoa have low $^{143}Nd/^{144}Nd$ ratios). Nd and Pb isotope data are not available for the Hekla lavas examined here, but Hekla lavas exhibit homogeneous Nd and Pb isotopic compositions, so an average (and 2SD) from literature data is shown (Bindeman et al., 2012; Carley et al., 2020; Chekol et al., 2011; Gee, 1999; Hémond et al., 1993; Jakobsson, 1979; Park, 1990; Schattel et al., 2014; Sigmarsson et al., 1991, 1992; Thirlwall et al., 2004). While Pb isotope data are available for St. Helena lavas, Nd isotope data are not; because Nd isotopic compositions are relatively homogeneous in St. Helena lavas, we use an average $^{143}Nd/^{144}Nd$ ratio for St. Helena lavas from Hanyu et al. (2014). The Nd and Pb isotopic compositions of Kosrae (Caroline Island) sample KOS-13–4 was not measured, but Kosrae samples show relatively homogeneous radiogenic isotope compositions, so the average radiogenic isotope data for Kosrae lavas from Jackson et al. (2017) are used for this sample.

trations and erupted in oceanic settings where the oceanic crust is both thin and geochemically depleted. Some Hekla lavas may have experienced crustal assimilation due to extreme degrees of crystal fractionation and very thick crust in Iceland, but the geochemical impacts of these issues on the Hekla sample suite examined here are minimized by avoiding the most evolved Hekla lavas with MgO < 2.3 wt% (i.e., the Hekla lavas in this study span MgO concentrations ranging from 2.3 to 8.0 wt%). Additionally, the Baffin Island lavas characterized for Ba isotopes here were carefully evaluated by Willhite et al. (2019) to determine whether continental crust assimilation has occurred. In Willhite et al. (2019), trace element ratios sensitive to continental crust assimilation, Nb/Th and Ce/Pb, were used to exclude Baffin Island lavas that had experienced continental crust assimilation: Baffin Island lavas that have Nb/Th and Ce/Pb ratios that are lower than the "mantle window" (i.e., Nb/Th = 15.6 ± 2.6, Ce/Pb = 24.3 ± 4.3) were considered to have experienced crustal assimilation and excluded from consideration. The four Baffin Island lavas examined here all have high Nb/Th (13.3 to 13.9) and Ce/Pb (21.5 to 24.7) ratios that fall in the mantle window (i.e., they do not exhibit low ratios that would implicate continental crust), and they all have high MgO (19.9 to 21.6 wt %). Thus Willhite et al. (2019) did not consider these four lavas to be impacted by continental crust assimilation.

The samples presented here are well-characterized geochemically, and the new Ba isotope data are presented in **Table S1**. Relevant geochemical characterization of the lavas presented here—including major and trace element concentrations and radiogenic isotopic ratios—is also provided in **Table S1**. However, for the Hekla lavas presented here, radiogenic isotopic data are not available. Nonetheless, published measurements on Hekla lavas reveal remarkably homogeneous radiogenic isotopic compositions and we present average radiogenic isotopic compositions for Hekla lavas from the literature (Jakobsson, 1979; Park, 1990; Sigmarsson et al., 1991, 1992; Hémond et al., 1993; Gee, 1999; Thirlwall et al., 2004; Chekol et al., 2011; Bindeman et al., 2012; Schattel et al., 2014; Carley et al., 2020). While Pb isotope data are available for St. Helena lavas, Nd isotopic analyses are not available, but existing published measurements on St. Helena reveal remarkable Nd isotopic homogeneity. Therefore, in figures showing Nd isotopes, we present the average Nd isotopic composition of St. Helena from Hanyu et al. (2014).

3. Methods

Barium isotope ratios were analyzed in the CAS Key Laboratory of Crust-Mantle Materials and Environments, USTC (University of Science and Technology of China). The chemical separation procedures follow Deng et al. (2021), which are briefly described here. In an ISO 6 cleanroom, the powdered samples were dissolved in Teflon® PFA screw-top beakers (Savillex®) using double-distilled concentrated HF, HNO_3, and HCl. Then the samples were dissolved in 3 mol/L HCl and processed through cation exchange columns with AG50W-X12 resin (200–400 mesh, 2 mL for the 1st column (with column volume equal to 30 mL) and 0.5 mL for the 2nd column (with column volume equal to 2 mL), BioRad, USA) to separate Ba from other matrix elements. After the matrix elements had been eluted in 28 mL 3 mol/L HCl, Ba was collected in 16 mL 3 mol/L HNO_3. Ba was fully separated from other matrix elements and > 99% of total Ba was collected for Ba isotope measurements. The total procedure blank was < 5 ng Ba, which is negligible relative to sample Ba amount (>2 μg). After the column chemistry, the purified samples were dried and re-dissolved in 2 wt% HNO_3 for isotope measurements.

Following column chemistry, a $^{135}Ba/^{136}Ba$ double-spike solution was added to the sample solutions. Ba isotopic compositions were measured by a Thermo-Fisher Scientific® Neptune-Plus multi-collector inductively coupled plasma mass spectrometer (MC-ICP-MS) at USTC (Nan et al., 2015). In low-resolution mode, the Ni sample and Ni X skimmer cones (Thermo Fisher Scientific®) were used during Ba isotope analyses. A dry plasma applying the Aridus-II desolvator (CETAC Technologies) was used to reduce polyatomic ion (e.g., BaO^{+}) formation and obtain higher sensitivity (~30 V/100 ppb for ^{138}Ba). Five Ba isotopes ^{134}Ba, ^{135}Ba, ^{136}Ba, ^{137}Ba and ^{138}Ba were collected by the Faraday cups L2, L1, C, H1, and H2, respectively. Simultaneously, ^{131}Xe and ^{140}Ce were also collected by L4 and H3 Faraday cups to correct the isobaric interferences (i.e., ^{134}Xe, ^{136}Xe, ^{136}Ce, and ^{138}Ce). The background signals of ^{138}Ba were < 0.02 V, which were negligible relative to the sample signals (~30 V on mass 138).

Each new analysis reported on hotspot lavas and USGS reference materials in **Table S1** is an average of 76 measurements (i.e., 76 "cycles" in the Neptune software) of the same solution. Many hotspot lavas were analyzed in duplicate or triplicate to evaluate reproducibility. Five secondary standards were analyzed together with the samples, and they include the following USGS reference materials: AGV-2, BCR-2, BHVO-2, GSP-2, and G-2 (**Table S1**). Note that all replicate analyses of samples and secondary standards were measured on separate dissolutions of powders (dissolved in different beakers) that were processed separately (on different days) by column chemistry, and analyzed for their isotopic compositions during different analytical sessions on the Neptune. All USGS reference materials were run in duplicate, triplicate, or quadruplicate across multiple analytical sessions. The Ba isotopic results of all the USGS reference materials agree with the previously-published values for these materials, and are provided in **Table S1** (Nan et al., 2015, 2018,2022; Bullen and Chadwick, 2016; van Zuilen et al., 2016; Nielsen et al., 2018; Gong et al., 2019; An et al., 2020; Gou et al., 2020; Li et al., 2020;

Wu et al., 2020; Deng et al., 2021; Gu et al., 2021; Huang et al., 2021; Zhao et al., 2021; Fang et al., 2022). The uncertainty of $\delta^{138/134}$Ba values across multiple measurements of the five USGS reference materials is better than 0.017‰ (2SE), indicating excellent reproducibility during analytical sessions associated with this study. The seven basalt unknowns analyzed in duplicate have overall $\delta^{138/134}$Ba uncertainties better than 0.017‰ (2SE).

4. Results

The Ba isotope data from several different hotspots are reported here (Fig. 4, **Table S1**), including Iceland (27 samples), Cook-Austral Islands (8 samples), St. Helena (5 samples), Pitcairn (3 samples), Samoa (14 samples), Caroline Islands (3 samples). Prior to applying any filters for low-temperature alteration, the Iceland hotspot lavas show a wide range of $\delta^{138/134}$Ba values, spanning 0.25‰: Hekla lavas show Ba isotopic compositions from -0.01 to 0.06‰; Baffin Island lavas show Ba isotopic compositions ranging from -0.05 to 0.16‰; mid-Miocene Vestfirðir lavas exhibit Ba isotopic compositions of -0.09 to 0.14‰. The Cook-Austral Islands lavas show $\delta^{138/134}$Ba variability from -0.12 to 0.11‰ (ranging 0.23‰), which is only slightly greater than the variability exhibited by Samoan hotspot lavas which vary from -0.09 to 0.07‰ (ranging 0.16‰). The St. Helena hotspot shows a range of Ba isotopic compositions from -0.01 to 0.05‰ (ranging 0.06 ‰). The Pitcairn lavas show the narrowest range of Ba isotopic compositions, from -0.01 to 0.03‰ (ranging 0.04‰), and the lavas from Caroline Islands show Ba isotopic compositions ranging from -0.08 to 0.02‰ (ranging 0.10‰). Fig. 4b shows the relationship between $\delta^{138/134}$Ba values and 1/Ba values (log scale), and the inset shows the relationship with a normal linear scale. The lavas examined here span a wide range of Ba concentrations (6 to 683 ppm), but no simple mixing relationship is apparent in a plot of $\delta^{138/134}$Ba values versus 1/Ba values (see inset of Fig. 4b).

5. Discussion

5.1. Assessing primary and secondary controls on $\delta^{138/134}$Ba values of OIB

5.1.1. Magmatic Differentiation

Before examining the new Ba isotope data in the context of characterizing the Ba isotopic composition of the mantle, it is important to differentiate between compositions that reflect the mantle sources of the lavas, and the Ba isotopic compositions that have been modified by magmatic differentiation. Barium is a highly incompatible element during mantle melting (partition coefficient $D^{solid/melt}$ for Ba is approximately 0.0001; Hofmann, 2003; Stracke and Bourdon, 2009; Workman and Hart, 2005), which means that, during melting, nearly all Ba is partitioned into the melt phase relative to the solid residue. If we assume > 1% melting (i.e., F > 0.01) in a batch melting model (where the Ba mantle-melt partition coefficient $D^{solid/melt}$ = 0.0001; Stracke and Bourdon, 2009; Workman and Hart, 2005), then > 99% of the Ba is in the melt and, hence, Ba isotope fractionation during melting is not likely. Similarly, as long as there are no fractionating phases in which Ba is compatible, Ba isotope fractionation is not possible. As a result, the Ba isotopic compositions of primary mantle-derived melts should reflect the composition of the mantle source. Similarly, because Ba is highly incompatible in early fractionating magmatic phases (e.g., chromium spinel, olivine, pyroxene), the Ba isotopic composition of a magma will not be modified during moderate degrees of fractional crystallization (Nielsen et al., 2020). However, in more evolved lavas, Ba is compatible in felsic minerals like feldspar and biotite. Crystallization of such phases may modify the Ba isotopic compositions of evolved lavas. Therefore, it is necessary to test whether Ba isotopes fractionate during magmatic differentiation. The Hekla lavas in this study span a large range of MgO concentrations, from 2.3 to 8.0 wt%. While the data do hint at lower $\delta^{138/134}$Ba values in the most evolved Hekla lavas, and there is scatter in the $\delta^{138/134}$Ba values outside of analytical uncertainty (i.e., the $\delta^{138/134}$Ba values vary from -0.01 ± 0.02‰ (2SE) to 0.06 ± 0.02‰ (2SE)), there is no resolvable trend between $\delta^{138/134}$Ba values and MgO concentrations. This suggests the Ba isotopic differences are not related to magmatic fractionation (at least, in lavas with MgO > 2.3 wt%). Furthermore, Ba concentrations increase systematically in the Hekla lavas with decreasing MgO concentrations, which argues for the incompatibility of Ba during magmatic differentiation in Hekla lavas with MgO > 2.3 wt% (see **Supplementary Figure S1**). We infer from the Hekla data that the Ba isotopic compositions of OIB examined in this study (2.3 to 25.5 wt% MgO) are not fractionated during petrogenesis and magmatic differentiation. Future work will explore whether Ba isotopes in highly evolved hotspot lavas (i.e., MgO < 2.3 wt%) are impacted by magmatic differentiation.

5.1.2. Low temperature alteration

Low temperature alteration following basalt eruption is another important factor that may modify the Ba isotopic compositions of

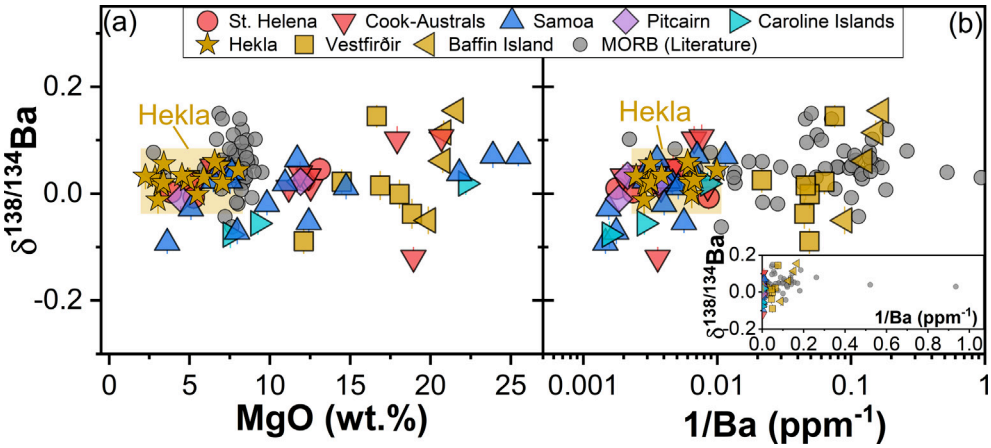


Fig. 4. Ba isotopic compositions of OIB and previously-published MORB as a function of magmatic differentiation (i.e., whole rock MgO concentrations) and Ba concentrations. (a) Samples in this study span a large range in whole rock MgO concentrations (from 2.3 to 25.5 wt%). (b) A plot of Ba isotopic compositions versus 1/Ba values with a log scale. The inset shows the data with a normal linear scale, which reveals no simple binary mixing trend in the dataset.

OIB. However, seawater alteration is unlikely to explain the Ba isotopic variability in OIB lavas. To show this, we first assume the Ba concentration of seawater is 0.015 ppm (Neff, 2002) and the $\delta^{138/134}$Ba value of seawater is 0.44‰ (where the average $\delta^{138/134}$Ba is calculated from Bridgestock et al. (2018), Horner et al. (2015) and Hsieh and Henderson, (2017)), and we also assume that the Sr concentration in seawater is 7.8 ppm (Kuznetsov et al., 2012) and that the seawater $^{87}Sr/^{86}Sr$ ratio is 0.7092 (Mokadem et al., 2015). We also assume that a Ba concentration for OIB of 241 ppm (i.e., the average concentration for OIB presented in this study), a $\delta^{138/134}$Ba value for OIB of 0.00‰, a Sr concentration for OIB of 443 ppm (i.e., the average for OIB in this study), and a $^{87}Sr/^{86}Sr$ ratio for OIB of 0.7030 (i.e., the lower end of values presented in this study). Assuming a binary mixing model and the addition of 99.8% seawater to the rock, the Ba isotopic composition of basalt is increased by just 0.013‰ (which is within the $\delta^{138/134}$Ba measurement uncertainty for this study), while the $^{87}Sr/^{86}Sr$ ratio of the basalt would increase from 0.7030 to 0.7086, which approaches the global seawater value. Because the Sr/Ba ratio in seawater (7.8/0.015 = 520) is much higher than in OIB (443/241 = 1.8), even a slight increase in the $\delta^{138/134}$Ba value of a basalt due to seawater alteration will be made abundantly clear as a substantial increase in the $^{87}Sr/^{86}Sr$ ratio, but this is not observed in the sample suite examined here. In fact, OIB with the highest $^{87}Sr/^{86}Sr$ ratios, from Samoa, have the lowest $\delta^{138/134}$Ba values. Therefore, we exclude seawater alteration as the source of $\delta^{138/134}$Ba variability in the OIB examined here.

Because different elements behave differently during low temperature alteration as a result of different fluid mobility, elemental ratios like Th/U and Ba/Rb have been used to identify OIB samples affected by low temperature alteration (e.g., Workman et al., 2004). During alteration in oxidizing conditions, U(IV) is oxidized into much more fluid mobile U(VI) (Omel'yanenko et al., 2007), and more of the oxidized fluid mobile U will be lost to the fluid compared to relatively immobile Th, leaving the altered OIB samples with higher Th/U ratios. Similarly, Rb is more fluid mobile than Ba, so low temperature alteration will increase the Ba/Rb ratio of the sample since more Rb is lost into the fluid relative to Ba. In this study, we used Th/U > 4.5 and Ba/Rb > 30 as thresholds to identify samples modified by low temperature alteration (altered OIB samples are shown separately from other OIB samples in Fig. 5), and these altered samples with high Th/U and Ba/Rb ratios are not further considered in the following discussion. The canonical Ba/Rb ratio for fresh OIB is ~ 12 (Hofmann and White, 1983), so our filter—following Pietruszka et al. (2013), lavas with Ba/Rb > 30 are considered altered—permits some primary mantle source variability for Ba/Rb ratios in OIB. The Th/U ratios of OIB from Samoa cluster at ~ 4.5 (Workman et al., 2004), and given that this is a hotspot with relatively high primary Th/U ratios, this Th/U threshold will capture alteration resulting in moderate U mobility at this and other hotspots. We acknowledge inherent uncertainty in assigning Ba/Rb and Th/U thresholds for the purposes of filtering out samples impacted by low temperature alteration, and we emphasize that the more stringent the filter, the less data that will be available for interpretation. With this in mind, we approach the new dataset as a first attempt to constrain mantle source $\delta^{138/134}$Ba variability in OIB.

5.2. Mantle source $\delta^{138/134}$Ba signatures

After the exclusion of a role for magmatic differentiation, and following exclusion of samples impacted by low-temperature alteration, the Ba isotopic compositions of the remaining OIB samples should reflect the signatures of the mantle source (and, unless otherwise noted, all data discussed below relate to OIB following filtering for low-temperature alteration). The remaining OIB samples exhibit heterogeneity that we interpret as mantle source heterogeneity: Samoa ($\delta^{138/134}$Ba values from -0.07 to 0.07‰), Cook-Austral Island (0.01 to 0.11‰), St. Helena (0.02 to 0.05‰), Vestfirðir lavas (-0.09 to 0.14‰), Hekla (-0.01 to 0.06‰), and Caroline Islands (-0.08 to 0.02‰).

Fig. 1 includes the Ba isotope signatures of OIB with existing Ba isotope data on igneous rocks—including MORB, altered oceanic crust, arc lavas, granites, and basalts from the North China Craton—and available datasets on sedimentary and low-temperature reservoirs, including loess, river sediments, diamictites, marine sediments, seawater, river water, barite, hydrothermal vent fluids, sedimentary carbonates, and coral. Compared with other reservoirs, the Ba isotopic variability in OIB lavas is relatively limited (Fig. 1). Nonetheless, the Ba isotopic signatures among different hotspots do exhibit resolvable heterogeneity (see Fig. 1 inset).

We compare the Ba isotope data with Nd and Pb radiogenic isotopic compositions in the same samples (Fig. 6), as Nd and Pb isotopes reflect mantle source compositions in OIB. Fig. 6a shows the relationship between $\delta^{138/134}$Ba values and $^{143}Nd/^{144}Nd$ ratios for hotspot lavas and MORB. We first note that the mid-Miocene Vestfirðir lavas from Iceland—which exhibit rather homogeneous $^{143}Nd/^{144}Nd$ and $^{206}Pb/^{204}Pb$ ratios—span a large range in $\delta^{138/134}$Ba values (-0.09 to 0.14‰), which might reflect local Ba isotope heterogeneity that exists in Iceland mantle source that is not reflected in the rather homogeneous Sr, Nd and Pb radiogenic isotopic compositions of the Vestfirðir lavas. If this is the case, we can conclude that there is not always systematic relationships between Ba isotopic and radiogenic isotopic compositions in OIB like that which is observed in, for example, the clear relationship between $\delta^{138/134}$Ba values and $^{206}Pb/^{204}Pb$ ratios presented by HIMU lavas in Fig. 6b (see below). Alternatively, given the relative homogeneity of the radiogenic isotopic compositions in the Vestfirðir lavas, we leave open the possibility that their extreme $\delta^{138/134}$Ba variability may reflect non-primary variability that the trace element filters for low temperature alteration have failed to capture. However, the low temperature alteration mechanism that might cause this $\delta^{138/134}$Ba variation, and why it is a process that does not induce variability in the samples from other hotspots, is not known, but we note that studies exploring the mechanisms for low temperature Ba isotope mobility in basalt are still in their infancy (Gong et al., 2019). Thus, the origin of the significant $\delta^{138/134}$Ba heterogeneity in mid-Miocene Vestfirðir lavas remains an unresolved issue that will be the source of additional future work. Nonetheless, a takeaway observation is that the Samoan dataset on EM2 lavas exhibits a range of $^{143}Nd/^{144}Nd$ ratios and $\delta^{138/134}$Ba values that extend to low values (and the HIMU lavas exhibit heavy $\delta^{138/134}$Ba values, see below), and in the following discussion we show that incorporation of recycled crustal materials can plausibly explain this variability.

Fig. 6b shows the relationship between $\delta^{138/134}$Ba values and $^{206}Pb/^{204}Pb$ ratios of hotspot lavas. Overall, there is no obvious global relationship between $\delta^{138/134}$Ba values and $^{206}Pb/^{204}Pb$ ratios. However, one notable observation from Fig. 6b is the clear positive trend between $\delta^{138/134}$Ba values and $^{206}Pb/^{204}Pb$ ratios in OIB lavas—from St. Helena and Cook-Austral volcanic lineament—that host a HIMU composition (i.e., lavas that have $^{206}Pb/^{204}Pb$ > 20), and below we show that incorporation of recycled oceanic crust materials can plausibly explain this trend.

5.3. Origin of Ba isotope heterogeneity in the mantle

5.3.1. EM2 mantle source

Samoa provides an ideal natural laboratory to test the impact of continental crust recycling on the Ba isotopic composition of the mantle because lavas from the Samoan hotspot have long been

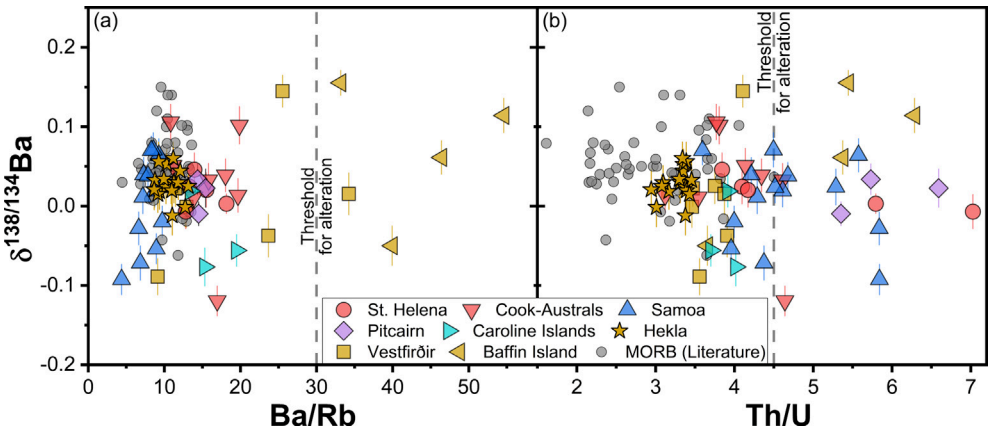


Fig. 5. $\delta^{138/134}$Ba values shown as a function of trace element indicators of alteration. (a) $\delta^{138/134}$Ba values versus Ba/Rb ratios. A threshold of Ba/Rb = 30 is used to identify samples that have experience low-temperature alteration; lavas with Ba/Rb > 30 are excluded in subsequent figures. (b) $\delta^{138/134}$Ba values versus Th/U ratios. A threshold of Th/U = 4.5 is used to identify samples that have experienced low-temperature alteration; samples with Th/U > 4.5 are excluded in subsequent figures.

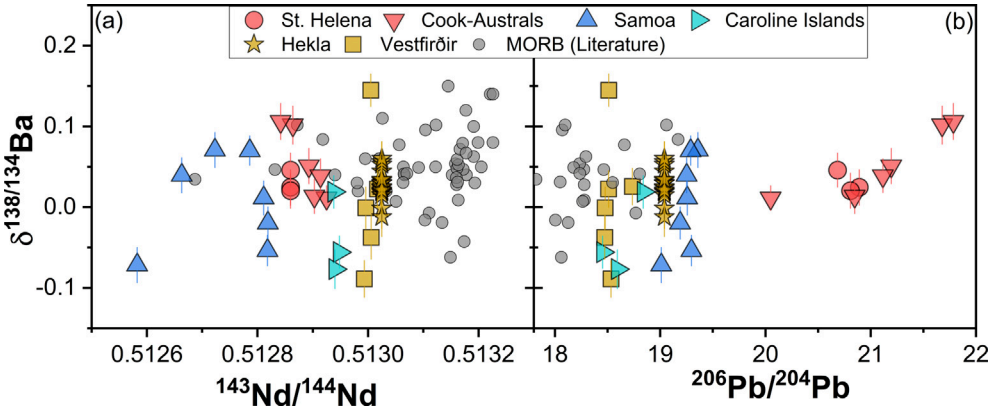


Fig. 6. Ba isotopic compositions versus (a) Nd and (b) Pb isotopes for hotspots lavas in this study and previously-published MORB data. MORB data are from Nielsen et al. (2018) and Nan et al. (2022). Pb isotopes are not available for the MORB lavas characterized for $\delta^{138/134}$Ba data in Nielsen et al. (2018). In both figure panels, samples with Th/U > 4.5 and Ba/Rb > 30 are considered altered and excluded.

argued to sample melts of recycled continental materials derived from upper continental crust (White and Hofmann, 1982; Workman et al., 2004; Jackson et al., 2007a). As indicated above, the Ba isotopic compositions of the freshest (i.e., Ba/Rb < 30 and Th/U < 4.5) Samoan lavas range from -0.07 to + 0.07‰, and the most extreme enriched Samoan EM2 lava (with the largest contribution from recycled continental crust) has the lowest $\delta^{138/134}$Ba value recorded at Samoa (Fig. 6a). In contrast, the Samoan lavas with the highest $\delta^{138/134}$Ba value in this study, AVON3-63–2 and AVON3-74–1 ($\delta^{138/134}$Ba = 0.07‰), have less geochemically-enriched (higher) ^{143}Nd/^{144}Nd, and their $\delta^{138/134}$Ba falls within the MORB mantle range of Ba isotopic compositions (i.e., $\delta^{138/134}Ba_{MORB}$ = 0.05 ± 0.05‰, 2SD (standard deviation), N = 16; Nielsen et al., 2018; Nan et al., 2022). We propose that the low $\delta^{138/134}$Ba value of extreme Samoan EM2 lavas is a result of a contribution of a continental protolith—with a low $\delta^{138/134}$Ba value—to a geochemically depleted mantle domain with a higher $\delta^{138/134}$Ba value. This model is similar to one suggested previously for the formation of Samoan EM2 mantle (Jackson et al., 2007a).

While isotope systems examined in Samoan lavas to date point to involvement of continental crust in their mantle source (e.g., White and Hofmann, 1982; Workman et al., 2004; Jackson et al., 2007a), we acknowledge that Ba isotopes do not provide a unique constraint on the role of continental crust recycling in Samoa. This is because continental rocks exhibit extremely heterogeneous Ba isotopic compositions. For example, different continental materials can have Ba isotopic compositions that range from very low values (down to -0.63‰ in A-type granite from Nan et al. [2018] or even down to -1.33‰ in leucogranite from Huang et al. [2021]) to very high values (up to 0.47‰ in glacial diamictites [Nan et al., 2018] or even 0.95‰ in I type granites [Deng et al., 2021]). Additionally, while some diamictite and sediment samples have $\delta^{138/134}$Ba values that are lower than the lowest values measured in fresh Samoan lavas, they do not exhibit the very low $\delta^{138/134}$Ba values required to successfully model the low $\delta^{138/134}$Ba values in Samoan lavas: prior work has established that the contribution of continental crust material to the Samoan EM2 mantle is relatively small (<7% mass fraction even in the most extreme EM2 samples; Jackson et al., 2007a; Edwards et al., 2019), so the recycled continental protolith requires an extreme isotopic composition that is not reflective of average sediment compositions, a conclusion that was reached in prior work exploring the origin of extreme EM2 Samoan lavas (Jackson et al., 2007a). For example, the average GLOSS [Global Subducting Sediment] composition has Sr (^{87}Sr/^{86}Sr = 0.71730 for GLOSS from Plank and Langmuir, 1998) isotopic compositions that are less geochemically enriched than the most extreme EM2 Samoan lavas (^{87}Sr/^{86}Sr = 0.720469). Therefore, we approach Ba isotope models for Samoan lavas by exploring whether there are continental crust compositions that, with relatively small mass fraction contributions to the Samoan

mantle, can be used to generate the low $\delta^{138/134}$Ba values in Samoan lavas, as described below.

We test the hypothesis that continental crust recycling can generate the negative $\delta^{138/134}$Ba values in Samoan EM2 lavas by generating a suite of mixing models between a depleted mantle composition—represented by the geochemically depleted FOZO (Focus Zone) composition suggested to reside in the Samoan mantle—and a suite of continental crust endmembers with low $\delta^{138/134}$Ba values (i.e., 0.00‰, -0.20‰, -0.40‰, -0.60‰, -0.80‰). This geochemically depleted endmember in the model has also been referred to as the C (Common; Hanan and Graham, 1996) component (Konter et al., 2008), which is analogous to the FOZO common component proposed by Hart et al. (1992). In the mixing model, we mix melts of the continental protolith with solid peridotite. This is because, in an upwelling plume, continental material will cross its solidus before peridotite. We assume in the model that continental material melts quantitatively during upwelling in the mantle plume, and the melt rises and reacts with solid peridotite; the enriched peridotite then melts to generate Samoan lavas. (We note that, for incompatible elements, even if the continental crust does not melt quantitatively, nearly all of the incompatible elements in the crust will enter the melt.) In the model, the FOZO isotopic composition, a peridotite, is assumed to have a $\delta^{138/134}$Ba value of 0.10‰, a value that is slightly higher than the highest $\delta^{138/134}$Ba analyzed in Samoan lavas; the ^{143}Nd/^{144}Nd ratio is chosen to be similar to high ^{3}He/^{4}He Samoan lavas (0.51285; Jackson et al., 2007b) because the various geochemical compositions in Samoa have been shown to exhibit mixing trends with a common Samoan high ^{3}He/^{4}He composition (Jackson et al., 2014); the Ba and Nd concentrations of FOZO are 4.4 ppm and 1.0 ppm, respectively, and they reflect estimates for the trace element concentrations of the high ^{3}He/^{4}He mantle source (Jackson and Jellinek, 2013). While continental crust is highly heterogeneous for Ba isotopic compositions, given that the Samoan array trends to lower $\delta^{138/134}$Ba with an increasing contribution from continental crust (i.e., lower ^{143}Nd/^{144}Nd ratio), the continental protolith contributing to the Samoan hotspot must have low (negative) $\delta^{138/134}$Ba values. Because the Ba isotopic composition of the continental protolith in the Samoan mantle is not well known, we explore how successfully different continental crust endmembers with variable, but low, $\delta^{138/134}$Ba values match the array formed by Samoan basalts. The range of explored $\delta^{138/134}$Ba values (0.00 to -0.80‰) falls within the range of known values for continental materials. We assume that the recycled continental crust protolith (and quantitative melts of the continental crust protolith) in the Samoan plume has a trace element composition similar to the GLOSS II composition of Plank (2014) (i.e., [Ba] = 786 ppm, [Nd] = 27.6 ppm), and we also adopt the ^{143}Nd/^{144}Nd ratio of the continental protolith previously calculated to contribute to the EM2 composition in the Samoan plume (i.e., 0.5117; Jackson et al., 2007a).

The results of the binary mixing model are shown in Fig. 7 and the model input compositions are provided in **Table S2**. While there is no clear correlation between the $\delta^{138/134}$Ba values and ^{143}Nd/^{144}Nd ratios in Samoan lavas, we interpret the rough positive trend between $\delta^{138/134}$Ba values and ^{143}Nd/^{144}Nd ratios in the Samoan dataset to be consistent with mixing between a continental crust protolith (and quantitative melts of the continental crust protolith) and geochemically-depleted FOZO material in the Samoan plume source, where increasing contributions of recycled continental crust result in lower $\delta^{138/134}$Ba values in Samoan lavas. We find that no single $\delta^{138/134}$Ba value for the continental crust endmember in the mixing model can match the range of ^{143}Nd/^{144}Nd ratios and $\delta^{138/134}$Ba values in Samoan lavas, and this might be explained by heterogeneous Ba isotopic compositions in the recycled continental materials hosted within the Samoan plume.

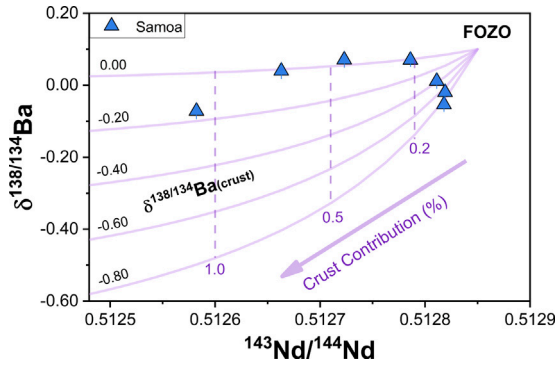


Fig. 7. Binary mixing model for Samoan EM2 lavas. The trend between $\delta^{138/134}$Ba values and ^{143}Nd/^{144}Nd ratios of EM2 can be explained by the mixing between a solid peridotite FOZO mantle (which is known to be geochemically depleted) and quantitative melts of continental crust. The samples with Th/U > 4.5 and Ba/Rb > 30 are considered altered and excluded. Mixing intervals (in percent) are shown on the mixing lines, and the five different mixing lines are shown to explore the impact of different $\delta^{138/134}$Ba crustal values on the mixing model (where the $\delta^{138/134}$Ba value of the crustal endmember explored is shown directly above each mixing line). Model parameters are discussed in the text and shown in **Table S2**.

5.3.2. HIMU mantle source

HIMU mantle domains have long been argued to form from the recycling of altered oceanic crust into the mantle, where subducted oceanic crust may generate highly radiogenic ^{206}Pb/^{204}Pb ratios over time (Hofmann and White, 1982; Kelley et al., 2005). During subduction zone metamorphism, downgoing oceanic crust may lose Pb more efficiently than U, leaving the residual oceanic crust with high U/Pb ratios that are conducive to generating radiogenic ^{206}Pb/^{204}Pb ratios over time (Kelley et al., 2005). Lavas from St. Helena and some localities in the Cook-Austral Islands exhibit radiogenic ^{206}Pb/^{204}Pb ratios that extend to extreme HIMU compositions, which is thought to host a component of recycled ancient oceanic crust (Hofmann and White, 1982; Hauri and Hart, 1993, 1997; Parai et al., 2009). Therefore, we targeted HIMU lavas from these localities for Ba isotopic analysis to characterize how recycled oceanic crust impacts the Ba isotopic composition of the mantle.

When examining only the freshest (i.e., Ba/Rb < 30 and Th/U < 4.5) HIMU lavas from St. Helena and the Cook-Austral islands, the observation that HIMU lavas with increasingly higher ^{206}Pb/^{204}Pb ratios have monotonically heavier Ba isotopic compositions (see Fig. 8) is consistent with a recycled oceanic crust contribution to HIMU because altered oceanic crust has generally elevated Ba isotopic values of -0.09 to 0.33‰ (average = 0.09 ± 0.26‰, 2SD, N = 11; Nielsen et al., 2018). However, the assumption that the Ba isotopic composition of the subducted oceanic crust protolith in the HIMU domain reflects the $\delta^{138/134}$Ba signature of altered oceanic crust (i.e., the $\delta^{138/134}$Ba value of the crust is not modified by subduction zone processes) requires consideration of the influence of subduction metamorphism. Gu et al. (2021) considers whether Ba isotope fractionation might happen during subduction zone metamorphism of eclogite by comparing Ba isotopic compositions between natural eclogite and associated veins, where the veins are assumed to have formed during fluid loss from the eclogite during the subduction process. They found that bulk eclogite sampled distal to the veins has $\delta^{138/134}$Ba that falls in the MORB field, while the veins have higher $\delta^{138/134}$Ba values. Gu et al. (2021) argued that the $\delta^{138/134}$Ba values of the bulk eclogite distal to the veins remains relatively unchanged during subduction metamorphism because the Ba concentrations measured in the veins are low, a result of the presence of Ba-rich phengite that retains Ba, inhibiting Ba loss to the fluid. Thus, Ba isotope fractionation of the slab during subduction metamorphism is limited, and we infer that the elevated $\delta^{138/134}$Ba values in the most extreme HIMU lavas reflects the heavy Ba isotopic compositions of altered oceanic crust.

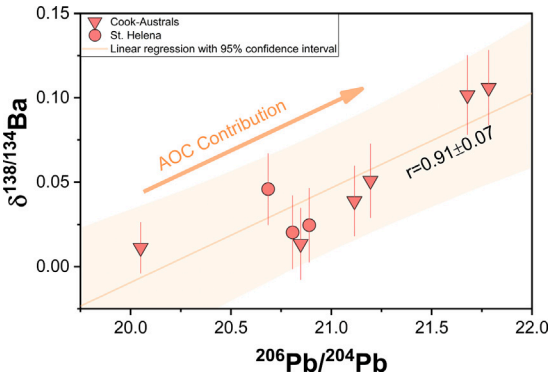


Fig. 8. Correlation between $\delta^{138/134}$Ba values and ^{206}Pb/^{204}Pb for HIMU lavas. The samples with Th/U > 4.5 and Ba/Rb > 30 are considered altered and excluded. When only HIMU (^{206}Pb/^{204}Pb > 20) lavas from the islands of Mangaia, Tubuai, Rurutu, and St. Helena are shown, a clear correlation between Ba and Pb isotopes emerges. The correlation is consistent with an increasing contribution of recycled altered oceanic crust (AOC). See text for calculation of the correlation coefficient.

However, modeling the Pb isotopic evolution of the recycled oceanic crust protolith contributing to HIMU OIB is complicated by a number of issues. For example, the Pb isotope evolution of the mantle is often modeled as a two-stage process: the first stage is assumed to have occurred shortly after terrestrial accretion when there was a U/Pb fractionation event, and the second stage occurred sometime in the Proterozoic. However, this simple two-stage evolution is unrealistic because the Earth's mantle has undergone long-term differentiation resulting from many stages of crustal extraction during its history. This is evidenced by zircon U-Pb ages preserved in the continents that record many stages of crustal extraction over geologic time (Condie and Aster, 2009, Condie et al., 2011; Roberts and Spencer, 2015), which makes a simple two-stage approach to the Pb-isotope evolution of the mantle unreasonable. However, Pb isotope models that invoke more than two stages simply add increasing complexity to the description of an under-constrained system (i.e., the mantle), an approach that we consider unsatisfactory.

Therefore, instead of modeling the long-term Pb isotope evolution of the HIMU mantle, we adopt a simpler approach. We embrace the standard model (e.g., Hofmann and White, 1982; Hauri and Hart, 1993) that the high ^{206}Pb/^{204}Pb HIMU composition sampled by hotspots hosts recycled altered oceanic crust with heavy Ba isotopic compositions, a model that is supported by 1) the heavy Ba isotopic compositions that we report in the most extreme HIMU lavas here, 2) the high $\delta^{138/134}$Ba values observed in altered oceanic crust (0.09 ± 0.26‰, 2SD, N = 11; Nielsen et al., 2018), and 3) the correlation between $\delta^{138/134}$Ba values and ^{206}Pb/^{204}Pb ratios in HIMU lavas (Fig. 8). The $\delta^{138/134}$Ba value of the AOC protolith contributing to HIMU lavas is not well-constrained, but must have a $\delta^{138/134}$Ba of at least 0.11‰ (i.e., the highest $\delta^{138/134}$Ba reported in the study of HIMU lavas), a value that falls in the range of $\delta^{138/134}$Ba signatures in AOC (-0.09 to 0.33‰; Nielsen et al. 2018). The excellent correlation between $\delta^{138/134}$Ba values and ^{206}Pb/^{204}Pb ratios in the HIMU lavas is consistent with an increasing contribution of altered oceanic crust to a depleted mantle or FOZO-like mantle with less radiogenic Pb isotopic composition and lower $\delta^{138/134}$Ba value that is at least as low as 0.01‰ (i.e., the lowest $\delta^{138/134}$Ba value recorded in the HIMU lavas shown in Fig. 8), a relatively light value that is consistent with the range for depleted mantle compositions reported in the literature ($\delta^{138/134}Ba_{MORB}$ = 0.05 ± 0.05‰, 2SD, N = 16; Nielsen et al., 2018; Nan et al., 2022). A geochemically-depleted mantle source has been observed in Cook-Austral hotspot lavas (Lassiter et al., 2003; Jackson et al., 2020b), and this geochemically depleted composition has been referred to as the C or FOZO component (Hart et al., 1992; Hanan and Graham, 1996; Konter et al., 2008).

While we do not attempt to estimate the under-constrained compositional endmembers that contribute to the relationship between $\delta^{138/134}$Ba and ^{206}Pb/^{204}Pb in HIMU lavas, we do evaluate the correlation between $\delta^{138/134}$Ba values and ^{206}Pb/^{204}Pb ratios in HIMU lavas by using a permutation test (Lehmann and Romano, 1986) to resample the data randomly over 10^6 iterations, and the null hypothesis that the Ba and Pb isotope data are uncorrelated was rejected at the 95% confidence interval. We calculate the correlation coefficient (r) using the following formula:

$$r_{x,y} = \frac{\sum \left(x_i - \bar{x}\right)\left(y_i - \bar{y}\right)}{(n-1)\sigma_x\sigma_y} \quad (2)$$

where x represents the ^{206}Pb/^{204}Pb ratio, y represents the $\delta^{138/134}$Ba value, $\bar{x}$ and $\bar{y}$ represent the average values of ^{206}Pb/^{204}Pb ratios and $\delta^{138/134}$Ba values, respectively, n represents the number of HIMU samples considered in the correlation calculation, and σ_x and σ_y represent the standard deviations of ^{206}Pb/^{204}Pb ratios and $\delta^{138/134}$Ba values, respectively. We employed a bootstrap test to resample the data over 10^6 iterations to calculate the error of the correlation coefficient (Mudelsee, 2003). We find that r = 0.91 ± 0.07 (2SD). The strong correlation between $\delta^{138/134}$Ba values and ^{206}Pb/^{204}Pb ratios supports the hypothesis that HIMU lavas host a component of recycled ancient oceanic crust, where an increasing contribution of altered oceanic crust yields both higher $\delta^{138/134}$Ba and ^{206}Pb/^{204}Pb in the lavas.

5.3.2.1. Crustal recycling and $\delta^{138/134}$Ba variability of the Earth's mantle. Surface crustal reservoirs host highly heterogeneous Ba isotopic compositions, and given the extreme incompatibility of Ba during mantle melting, surface crustal reservoirs (in particular continental crust) host a significant fraction of the Ba in the silicate Earth. As a result of the high concentrations of Ba in subducted crust and the low concentrations of Ba in the mantle, and the highly heterogeneous Ba isotopic compositions of crustal reservoirs, subduction and recycling of crust is expected to be manifested as heterogeneous $\delta^{138/134}$Ba values in OIB sampling recycled crustal reservoirs. We find that the relatively limited variability in $\delta^{138/134}$Ba values observed in in the freshest OIB (down to -0.07‰ in extreme EM2 Samoan and up to 0.11‰ in extreme HIMU lavas from the Cook Islands) is consistent with the addition of recycled continental and oceanic crust to the Earth's mantle. However, the recycled crust $\delta^{138/134}$Ba signal in OIB is rather muted: given the extreme heterogeneous Ba isotopic compositions in continental crust reservoirs, for example, we might expect somewhat more extreme $\delta^{138/134}$Ba signatures in OIB. This may be a result of a small fraction of recycled crust in OIB, and/or a result of limited homogenization of recycled crustal signatures during mantle mixing.

There are 46 oceanic hotspots that have some degree of geochemical characterization (Jackson et al., 2021), but only a small fraction of them have been explored for Ba isotopic compositions in this study. Therefore, it is possible that larger-magnitude $\delta^{138/134}$Ba signatures remain to be identified. Below, we also speculate that EM lavas may not always have negative $\delta^{138/134}$Ba values, and that HIMU lavas may not always have positive $\delta^{138/134}$Ba values.

While Samoan EM2 lavas exhibit negative $\delta^{138/134}$Ba values, we do not necessarily expect EM lavas from other hotspots to exhibit negative $\delta^{138/134}$Ba values. Given the extreme $\delta^{138/134}$Ba varibility in continental crust samples that spans both extreme negative $\delta^{138/134}$Ba values (down to -1.33‰ in leucogranite [Huang et al., 2021]) to extreme positive values (up to 0.95‰ in I type granites [Deng et al., 2021]), we might anticipate some EM OIB sampling recycled continental crust to exhibit positive values. Analysis of

$\delta^{138/134}$Ba values from extreme EM lavas from different hotspots (e.g., Societies, Marquesas, Pitcairn, etc.) will be important to evaluate whether both positive and negative $\delta^{138/134}$Ba values in continental crust is manifested as positive and negative $\delta^{138/134}$Ba values in EM hotspot lavas. Perhaps these EM hotspots will exhibit a wider range of $\delta^{138/134}$Ba signatures, both positive and negative, that reflect the extreme variability identified in continental crust.

By the same token, not all AOC samples have positive $\delta^{138/134}$Ba values. There are hints of negative $\delta^{138/134}$Ba values in published AOC samples, which are as low as -0.09‰ in Nielsen et al. (2018). Even more negative $\delta^{138/134}$Ba values in AOC, down to -0.20‰, are suggested in Nan et al. (2017), but the frequency of such low values in AOC was not provided by the authors. Nonetheless, we cannot exclude the possibility that recycled oceanic crust may present as negative $\delta^{138/134}$Ba values in hotspot lavas. Future work targeting additional HIMU localities (e.g., Bermuda; Mazza et al., 2019) will be important for clarifying whether HIMU lavas consistently have positive $\delta^{138/134}$Ba, as indicated by the relationship identified in Fig. 8, or whether HIMU can exhibit lower, or perhaps even negative, $\delta^{138/134}$Ba values.

6. Conclusions

Due to the extreme incompatibility of Ba during mantle melting, Ba budgets in the Earth are likely to be dominated by oceanic and continental crust reservoirs. Therefore, in this study, we present new Ba isotope data of lavas sampling the different canonical mantle compositions, including EM1, EM2, HIMU, and high ^{3}He/^{4}He, because the EM1, EM2, and HIMU compositions are thought to host components of recycled oceanic and continental crust. The Ba isotope study of Hekla lavas indicates that Ba isotope compositions are not affected by petrogenesis and magmatic differentiation of relatively undifferentiated lavas (i.e., MgO > 2.3 wt%). Because Ba is a fluid mobile element, Ba isotope signatures may be modified by low temperature alteration processes, and lavas with Ba/Rb ratios > 30 and Th/U ratios > 4.5—which are considered to have suffered loss of fluid-mobile elements—were excluded from consideration. After excluding lavas impacted by low temperature alteration, we consider the remaining lavas to have Ba isotopic compositions that reflect the signatures of the mantle source: we identify resolvable variability in the Ba isotope signatures among different mantle radiogenic isotope compositions. EM2 lavas show lower $\delta^{138/134}$Ba values (down to -0.07‰ in the freshest lava with the lowest ^{143}Nd/^{144}Nd ratio) relative to depleted mantle (0.05 ± 0.05‰, 2SD, as indicated by MORB signatures). HIMU lavas show heavier Ba isotopic signatures (up to 0.11‰ in the freshest lavas with ^{206}Pb/^{204}Pb > 21.7). The EM2 lava with the lowest ^{143}Nd/^{144}Nd ratio can be explained by binary mixing between continental crust protolith with a low (negative) $\delta^{138/134}$Ba value and a geochemically depleted FOZO composition with slightly positive $\delta^{138/134}$Ba value (0.1‰). We find a strong correlation (r = 0.91 ± 0.07, 2SD) between $\delta^{138/134}$Ba values and ^{206}Pb/^{204}Pb ratios in HIMU lavas (i.e., St. Helena, Tubuai, Rurutu and Mangaia lavas with ^{206}Pb/^{204}Pb > 20). The compositions of the most extreme HIMU lavas can be explained by the recycling of ancient altered oceanic crust (with positive $\delta^{138/134}$Ba values that overlap with values measured in modern oceanic crust) into a depleted mantle composition that may be similar to FOZO. The variations of $\delta^{138/134}$Ba values in the different mantle compositions examined here highlight the potential of Ba isotopes to trace the heterogeneity of the mantle resulting from crustal subduction and recycling.

Data availability

The data are included as supplemental materials.

Declaration of Competing Interest

The authors declare that they have no known competing financial interests or personal relationships that could have appeared to influence the work reported in this paper.

Acknowledgements

We thank Stan Hart and the late Erik Hauri for trace element data on sample MGA-B-25. MGJ acknowledges partial support from OCE-1912931. XN acknowledges partial support from the National Nature Science Foundation of China (42073007).

Appendix A. Supplementary material

Supplementary material to this article can be found online at https://doi.org/10.1016/j.gca.2022.08.023.

References

An, Y., Li, X., Zhang, Z., 2020. Barium Isotopic Compositions in Thirty-Four Geological Reference Materials Analysed by MC-ICP-MS. Geostand. Geoanal. Res. 44, 183–199.

Bindeman, I., Gurenko, A., Carley, T., Miller, C., Martin, E., Sigmarsson, O., 2012. Silicic magma petrogenesis in Iceland by remelting of hydrothermally altered crust based on oxygen isotope diversity and disequilibria between zircon and magma with implications for MORB. Terra Nova 24, 227–232.

Bridgestock, L., Hsieh, Y.-T., Porcelli, D., Homoky, W.B., Bryan, A., Henderson, G.M., 2018. Controls on the barium isotope compositions of marine sediments. Earth Planet. Sci. Lett. 481, 101–110.

Bullen, T., Chadwick, O., 2016. Ca, Sr and Ba stable isotopes reveal the fate of soil nutrients along a tropical climosequence in Hawaii. Chem. Geol. 422, 25–45.

Carley, T.L., Miller, C.F., Fisher, C.M., Hanchar, J.M., Vervoort, J.D., Schmitt, A.K., Economos, R.C., Jordan, B.T., Padilla, A.J., Banik, T.J., 2020. Petrogenesis of silicic magmas in Iceland through space and time: The isotopic record preserved in zircon and whole rocks. J. Geol. 128, 1–28.

Chekol, T.A., Kobayashi, K., Yokoyama, T., Sakaguchi, C., Nakamura, E., 2011. Timescales of magma differentiation from basalt to andesite beneath Hekla Volcano, Iceland: Constraints from U-series disequilibria in lavas from the last quarter-millennium flows. Geochim. Cosmochim. Acta 75, 256–283.

Condie, K.C., Aster, R.C., 2009. Zircon age episodicity and growth of continental crust. *EOS, Trans. Am. Geophys. Union* 90. 364–364.

Condie, K.C., Bickford, M.E., Aster, R.C., Belousova, E., Scholl, D.W., 2011. Episodic zircon ages, Hf isotopic composition, and the preservation rate of continental crust. Bulletin 123, 951–957.

Crockford, P.W., Wing, B.A., Paytan, A., Hodgskiss, M.S.W., Mayfield, K.K., Hayles, J.A., Middleton, J.E., Ahm, A.-S.-C., Johnston, D.T., Caxito, F., 2019. Barium-isotopic constraints on the origin of post-Marinoan barites. Earth Planet. Sci. Lett. 519, 234–244.

Deng, G., Kang, J., Nan, X., Li, Y., Guo, J., Ding, X., Huang, F., 2021. Barium isotope evidence for crystal-melt separation in granitic magma reservoirs. Geochim. Cosmochim. Acta 292, 115–129.

Edwards, M.A., Jackson, M.G., Kylander-Clark, A.R.C., Harvey, J., Hagen-Peter, G.A., Seward, G.G.E., Till, C.B., Adams, J.V., Cottle, J.M., Hacker, B.R., Spera, F.J., 2019. Extreme enriched and heterogeneous ^{87}Sr/^{86}Sr ratios recorded in magmatic plagioclase from the Samoan hotspot. Earth Planet. Sci. Lett. 511, 190–201.

Eisele, J., Sharma, M., Galer, S.J.G., Blichert-Toft, J., Devey, C.W., Hofmann, A.W., 2002. The role of sediment recycling in EM-1 inferred from Os, Pb, Hf, Nd, Sr isotope and trace element systematics of the Pitcairn hotspot. Earth Planet. Sci. Lett. 196, 197–212.

Eugster, O., Tera, F., Wasserburg, G.J., 1969. Isotopic analyses of barium in meteorites and in terrestrial samples. J. Geophys. Res. 74, 3897–3908.

Fang, L., Moynier, F., Huang, F., Deng, G., Tian, L., 2022. Barium stable isotopic composition of chondrites and its implication for the Earth. Chem. Geol. 604, 120923.

Gale, A., Dalton, C.A., Langmuir, C.H., Su, Y., Schilling, J., 2013. The mean composition of ocean ridge basalts. Geochem. Geophys. Geosyst. 14, 489–518.

Garapić, G., Jackson, M.G., Hauri, E.H., Hart, S.R., Farley, K.A., Blusztajn, J.S., Woodhead, J.D., 2015. A radiogenic isotopic (He-Sr-Nd-Pb-Os) study of lavas from the Pitcairn hotspot: Implications for the origin of EM-1 (enriched mantle 1). Lithos 228, 1–11.

Gaschnig, R.M., Reinhard, C.T., Planavsky, N.J., Wang, X., Asael, D., Jackson, M.G., 2021. The impact of primary processes and secondary alteration on the stable isotope composition of ocean island basalts. Chem. Geol. 581, 120416.

Gee, M.A.M., 1999. Volcanology and geochemistry of Reykjanes Peninsula: plume-mid-ocean ridge interaction. Doctoral dissertation. University of London, Royal Holloway.

Geist, D., Harpp, K., Oswald, P., Wallace, P., Bindeman, I., Christensen, B., 2021. Hekla revisited: fractionation of a magma body at historical timescales. J. Petrol. 62, egab001.

Gong, Y., Zeng, Z., Zhou, C., Nan, X., Yu, H., Lu, Y., Li, W., Gou, W., Cheng, W., Huang, F., 2019. Barium isotopic fractionation in latosol developed from strongly weathered basalt. Sci. Total Environ. 687, 1295–1304.
Gou, L.-F., Jin, Z., Galy, A., Gong, Y.-Z., Nan, X.-Y., Jin, C., Wang, X.-D., Bouchez, J., Cai, H.-M., Chen, J.-B., 2020. Seasonal riverine barium isotopic variation in the middle Yellow River: Sources and fractionation. Earth Planet. Sci. Lett. 531, 115990.
Graham, D.W., Humphris, S.E., Jenkins, W.J., Kurz, M.D., 1992. Helium isotope geochemistry of some volcanic rocks from Saint Helena. Earth Planet. Sci. Lett. 110, 121–131.
Gu, X.-F., Guo, S., Yu, H.-M., Xu, J., Huang, F., 2021. Behavior of barium isotopes during high-pressure metamorphism and fluid evolution. Earth Planet. Sci. Lett. 575, 117176.
Hanan, B.B., Graham, D.W., 1996. Lead and helium isotope evidence from oceanic basalts for a common deep source of mantle plumes. Science 272, 991–995.
Hanyu, T., Kawabata, H., Tatsumi, Y., Kimura, J.-I., Hyodo, H., Sato, K., Miyazaki, T., Chang, Q., Hirahara, Y., Takahashi, T., 2014. Isotope evolution in the HIMU reservoir beneath St. Helena: Implications for the mantle recycling of U and Th. Geochim. Cosmochim. Acta 143, 232–252.
Hart, S.R., Hauri, E.H., Oschmann, L.A., Whitehead, J.A., 1992. Mantle plumes and entrainment: isotopic evidence. Science 256, 517–520.
Hart, S.R., Jackson, M.G., 2014. Ta'u and Ofu/Olosega volcanoes: The "twin sisters" of Samoa, their P, T, X melting regime, and global implications. Geochem. Geophys. Geosyst. 15, 2301–2318.
Hauri, E.H., Hart, S.R., 1993. ReOs isotope systematics of HIMU and EMII oceanic island basalts from the south Pacific Ocean. Earth Planet. Sci. Lett. 114, 353–371.
Hauri, E.H., Hart, S.R., 1997. Rhenium abundances and systematics in oceanic basalts. Chem. Geol. 139, 185–205.
Hémond, C., Arndt, N.T., Lichtenstein, U., Hofmann, A.W., Oskarsson, N., Steinthorsson, S., 1993. The heterogeneous Iceland plume: Nd-Sr-O isotopes and trace element constraints. J. Geophys. Res. Solid Earth 98, 15833–15850.
Hofmann, A.W., 1997. Mantle geochemistry: the message from oceanic volcanism. Nature 385, 219–229.
Hofmann, A.W., 2003. Sampling mantle heterogeneity through oceanic basalts: isotopes and trace elements. Treat. Geochem. 2, 568.
Hofmann, A.W., White, W.M., 1982. Mantle plumes from ancient oceanic crust. Earth Planet. Sci. Lett. 57, 421–436.
Hofmann, A.W., White, W.M., 1983. Ba, Rb and Cs in the Earth's mantle. Zeitschrift für Naturforschung A 38, 256–266.
Horner, T.J., Kinsley, C.W., Nielsen, S.G., 2015. Barium-isotopic fractionation in seawater mediated by barite cycling and oceanic circulation. Earth Planet. Sci. Lett. 430, 511–522.
Hsieh, Y.-T., Bridgestock, L., Scheuermann, P.P., Seyfried Jr, W.E., Henderson, G.M., 2020. Barium isotopes in mid-ocean ridge hydrothermal vent fluids: a source of isotopically heavy Ba to the ocean. Geochim. Cosmochim. Acta.
Hsieh, Y.-T., Henderson, G.M., 2017. Barium stable isotopes in the global ocean: Tracer of Ba inputs and utilization. Earth Planet. Sci. Lett. 473, 269–278.
Huang, F., Bai, R., Deng, G., Liu, X., Li, X., 2021. Barium isotope evidence for the role of magmatic fluids in the origin of Himalayan leucogranites. Sci. Bull. 66, 2329–2336.
Jackson, M.G., Blichert-Toft, J., Halldórsson, S.A., Mundl-Petermeier, A., Bizimis, M., Kurz, M.D., Price, A.A., Harðardóttir, S., Willhite, L.N., Breddam, K., 2020a. Ancient helium and tungsten isotopic signatures preserved in mantle domains least modified by crustal recycling. Proc. Natl. Acad. Sci. 117, 30993–31001.
Jackson, M.G., Becker, T.W., Steinberger, B., 2021. Spatial characteristics of recycled and primordial reservoirs in the deep mantle. Geochem. Geophys Geosyst. 22. e2020GC009525.
Jackson, M.G., Hart, S.R., Koppers, A.A.P., Staudigel, H., Konter, J., Blusztajn, J., Kurz, M., Russell, J.A., 2007a. The return of subducted continental crust in Samoan lavas. Nature 448, 684–687.
Jackson, M.G., Halldórsson, S.A., Price, A., Kurz, M.D., Konter, J.G., Koppers, A.A.P., Day, J.M.D., 2020b. Contrasting Old and Young Volcanism from Aitutaki, Cook Islands: Implications for the Origins of the Cook-Austral Volcanic Chain. J. Petrol. 61. egaa037.
Jackson, M.G., Hart, S.R., Konter, J.G., Kurz, M.D., Blusztajn, J., Farley, K.A., 2014. Helium and lead isotopes reveal the geochemical geometry of the Samoan plume. Nature 514, 355–358.
Jackson, M.G., Jellinek, A.M., 2013. Major and trace element composition of the high $^{3}He/^{4}He$ mantle: Implications for the composition of a nonchonditic Earth. Geochem. Geophys. Geosyst. 14, 2954–2976.
Jackson, M.G., Kurz, M.D., Hart, S.R., Workman, R.K., 2007b. New Samoan lavas from Ofu Island reveal a hemispherically heterogeneous high $^{3}He/^{4}He$ mantle. Earth Planet. Sci. Lett. 264, 360–374.
Jackson, M.G., Price, A.A., Blichert-Toft, J., Kurz, M.D., Reinhard, A.A., 2017. Geochemistry of lavas from the Caroline hotspot, Micronesia: Evidence for primitive and recycled components in the mantle sources of lavas with moderately elevated $^{3}He/^{4}He$. Chem. Geol. 455, 385–400.
Jakobsson, S.P., 1979. Petrology of recent basalts of the Eastern Volcanic Zone. Iceland Acta Nat. Islandica 26, 1–103.
Jónasson, K., 2007. Silicic volcanism in Iceland: Composition and distribution within the active volcanic zones. J. Geodyn. 43, 101–117.
Kelley, K.A., Plank, T., Farr, L., Ludden, J., Staudigel, H., 2005. Subduction cycling of U, Th, and Pb. Earth Planet. Sci. Lett. 234, 369–383.
Konter, J.G., Hanan, B.B., Blichert-Toft, J., Koppers, A.A.P., Plank, T., Staudigel, H., 2008. One hundred million years of mantle geochemical history suggest the retiring of mantle plumes is premature. Earth Planet. Sci. Lett. 275, 285–295.
Kuznetsov, A.B., Semikhatov, M.A., Gorokhov, I.M., 2012. The Sr isotope composition of the world ocean, marginal and inland seas: Implications for the Sr isotope stratigraphy. Stratigr. Geol. Correl. 20, 501–515.
Lassiter, J.C., Blichert-Toft, J., Hauri, E.H., Barsczus, H.G., 2003. Isotope and trace element variations in lavas from Raivavae and Rapa, Cook-Austral islands: constraints on the nature of HIMU-and EM-mantle and the origin of mid-plate volcanism in French Polynesia. Chem. Geol. 202, 115–138.
Lehmann, E.L., Romano, J.P., 1986. Testing statistical hypotheses **2**. Wiley, New York.
Li, W.-Y., Yu, H.-M., Xu, J., Halama, R., Bell, K., Nan, X.-Y., Huang, F., 2020. Barium isotopic composition of the mantle: Constraints from carbonatites. Geochim. Cosmochim. Acta 278, 235–243.
Mazza, S.E., Gazel, E., Bizimis, M., Moucha, R., Béguelin, P., Johnson, E.A., McAleer, R. J., Sobolev, A.V., 2019. Sampling the volatile-rich transition zone beneath Bermuda. Nature 569, 398–403.
McDonough, W.F., Sun, S.-S., 1995. The composition of the Earth. Chem. Geol. 120, 223–253.
Mokadem, F., Parkinson, I.J., Hathorne, E.C., Anand, P., Allen, J.T., Burton, K.W., 2015. High-precision radiogenic strontium isotope measurements of the modern and glacial ocean: Limits on glacial–interglacial variations in continental weathering. Earth Planet. Sci. Lett. 451, 111–120.
Morgan, W.J., 1971. Convection plumes in the lower mantle. Nature 230, 42–43.
Moynier, F., Jackson, M.G., Zhang, K., Cai, H., Halldorsson, S.A., Pik, R., Day, J.M.D., Chen, J., 2021. The Mercury Isotopic Composition of Earth's Mantle and the Use of Mass Independently Fractionated Hg to Test for Recycled Crust. Geophys. Res Lett. 48. e2021GL094301.
Mudelsee, M., 2003. Estimating Pearson's correlation coefficient with bootstrap confidence interval from serially dependent time series. Math. Geol. 35, 651–665.
Nan, X., Wu, F., Zhang, Z., Hou, Z., Huang, F., Yu, H., 2015. High-precision barium isotope measurements by MC-ICP-MS. J. Anal. Atom. Spectrom. 30, 2307–2315.
Nan, X., Yu, H., Gao, Y., 2017. Barium isotope composition of altered oceanic crust from the IODP Site 1256 at the East Pacific Rise. In: In: *AGU Fall Meeting Abstracts*, pp. V33C–0534.
Nan, X., Yu, H., Kang, J., Huang, F., 2022. Re-visiting barium isotope compositions of mid-ocean ridge basalts and the implications. JUSTC 52. 1–1.
Nan, X.-Y., Yu, H.-M., Rudnick, R.L., Gaschnig, R.M., Xu, J., Li, W.-Y., Zhang, Q., Jin, Z.-D., Li, X.-H., Huang, F., 2018. Barium isotopic composition of the upper continental crust. Geochim. Cosmochim. Acta 233, 33–49.
Neff, J.M., 2002. Barium in the ocean. Bioaccumulation in marine organisms, 79–87.
Nielsen, S.G., Horner, T.J., Pryer, H.V., Blusztajn, J., Shu, Y., Kurz, M.D., le Roux, V., 2018. Barium isotope evidence for pervasive sediment recycling in the upper mantle. Sci Adv 4. eaas8675.
Nielsen, S.G., Shu, Y., Auro, M., Yogodzinski, G., Shinjo, R., Plank, T., Kay, S.M., Horner, T.J., 2020. Barium isotope systematics of subduction zones. Geochim. Cosmochim. Acta 275, 1–18.
Omel'yanenko, B.I., Petrov, V.A., Poluektov, V.v., 2007. Behavior of uranium under conditions of interaction of rocks and ores with subsurface water. Geol. Ore Depos. 49, 378–391.
Parai, R., Mukhopadhyay, S., Lassiter, J.C., 2009. New constraints on the HIMU mantle from neon and helium isotopic compositions of basalts from the Cook-Austral Islands. Earth Planet. Sci. Lett. 277, 253–261.
Park, K.H., 1990. Strontium, neodymium and lead isotope studies of ocean island basalts: constraints on their origin and evolution. Doctoral dissertation. Columbia University.
Pietruszka, A.J., Norman, M.D., Garcia, M.O., Marske, J.P., Burns, D.H., 2013. Chemical heterogeneity in the Hawaiian mantle plume from the alteration and dehydration of recycled oceanic crust. Earth Planet. Sci. Lett. 361, 298–309.
Plank, T., 2014. The chemical composition of subducting sediments. In Elsevier.
Plank, T., Langmuir, C.H., 1998. The chemical composition of subducting sediment and its consequences for the crust and mantle. Chem. Geol. 145, 325–394.
Pretet, C., van Zuilen, K., Nägler, T.F., Reynaud, S., Böttcher, M.E., Samankassou, E., 2015. Constraints on barium isotope fractionation during aragonite precipitation by corals. The Depositional Record 1, 118–129.
Roberts, N.M., Spencer, C.J., 2015. The zircon archive of continent formation through time. Geological Society, London, Special Publications 389, 197–225.
Rudnick, R.L., Gao, S., 2014. Composition of the continental crust. In: Rudnick, R.L. (Ed.), Treatise on Geochemistry, vol 4, The crust **3**, 1–64. second ed. Elsevier, Oxford.
Ryan, W.B.F., Carbotte, S.M., Coplan, J.O., O'Hara, S., Melkonian, A., Arko, R., Weissel, R.A., Ferrini, V., Goodwillie, A., Nitsche, F., Bonczkowski, J., 2009. Global multi-resolution topography synthesis. Geochem. Geophys. Geosyst. 10.
Salters, V.J., Stracke, A., 2004. Composition of the depleted mantle. Geochem. Geophys. Geosyst. 5.
Schattel, N., Portnyagin, M., Golowin, R., Hoernle, K., Bindeman, I., 2014. Contrasting conditions of rift and off-rift silicic magma origin on Iceland. Geophys. Res. Lett. 41, 5813–5820.
Sigmarsson, O., Hémond, C., Condomines, M., Fourcade, S., Oskarsson, N., 1991. Origin of silicic magma in Iceland revealed by Th isotopes. Geology 19, 621–624.
Sigmarsson, O., Condomines, M., Fourcade, S., 1992. A detailed Th, Sr and O isotope study of Hekla: differentiation processes in an Icelandic volcano. Contrib. Miner. Petrol. 112, 20–34.
Sigmarsson, O., Bergþórsdóttir, I.A., Devidal, J.-L., Larsen, G., Gannoun, A., 2022. Long or short silicic magma residence time beneath Hekla volcano, Iceland? Contrib. Miner. Petrol. 177, 1–15.

Stracke, A., Bourdon, B., 2009. The importance of melt extraction for tracing mantle heterogeneity. Geochim. Cosmochim. Acta 73, 218–238.
Stuart, F.M., Lass-Evans, S., Fitton, J.G., Ellam, R.M., 2003. High $^{3}He/^{4}He$ ratios in picritic basalts from Baffin Island and the role of a mixed reservoir in mantle plumes. Nature 424, 57–59.
Thirlwall, M.F., Gee, M.A.M., Taylor, R.N., Murton, B.J., 2004. Mantle components in Iceland and adjacent ridges investigated using double-spike Pb isotope ratios. Geochim. Cosmochim. Acta 68, 361–386.
van Zuilen, K., Nägler, T.F., Bullen, T.D., 2016. Barium isotopic compositions of geological reference materials. Geostand. Geoanal. Res. 40, 543–558.
von Allmen, K., Böttcher, M.E., Samankassou, E., Nägler, T.F., 2010. Barium isotope fractionation in the global barium cycle: First evidence from barium minerals and precipitation experiments. Chem. Geol. 277, 70–77.
Wei, W., Zeng, Z., Shen, J., Tian, L.-L., Wei, G.-Y., Ling, H.-F., Huang, F., 2021. Dramatic changes in the carbonate-hosted barium isotopic compositions in the Ediacaran Yangtze Platform. Geochim. Cosmochim. Acta 299, 113–129.
Weiss, Y., McNeill, J., Pearson, D.G., Nowell, G.M., Ottley, C.J., 2015. Highly saline fluids from a subducting slab as the source for fluid-rich diamonds. Nature 524, 339–342.
White, W.M., 2015. Isotopes, DUPAL, LLSVPs, and anekantavada. Chem. Geol. 419, 10–28.
White, W.M., Hofmann, A.W., 1982. Sr and Nd isotope geochemistry of oceanic basalts and mantle evolution. Nature 296, 821–825.
Willhite, L.N., Jackson, M.G., Blichert-Toft, J., Bindeman, I., Kurz, M.D., Halldórsson, S. A., Harðardóttir, S., Gazel, E., Price, A.A., Byerly, B.L., 2019. Hot and heterogenous high-$^{3}He/^{4}He$ components: New constraints from proto-Iceland plume lavas from Baffin Island. Geochem. Geophys. Geosyst. 20, 5939–5967.
Workman, R.K., Hart, S.R., Jackson, M., Regelous, M., Farley, K.A., Blusztajn, J., Kurz, M., Staudigel, H., 2004. Recycled metasomatized lithosphere as the origin of the Enriched Mantle II (EM2) end-member: Evidence from the Samoan Volcanic Chain. Geochem. Geophys. Geosyst. 5.
Workman, R.K., Hart, S.R., 2005. Major and trace element composition of the depleted MORB mantle (DMM). Earth Planet. Sci. Lett. 231, 53–72.
Wu, F., Turner, S., Schaefer, B.F., 2020. Mélange versus fluid and melt enrichment of subarc mantle: A novel test using barium isotopes in the Tonga-Kermadec arc. Geology.
Zhao, Y.-P., Tang, Y.-J., Xu, J., Zeng, Z., Ying, J.-F., Tian, H.-C., Huang, F., 2021. Barium isotope evidence for recycled crustal materials in the mantle source of continental basalts. Lithos 390, 106111.
Zindler, A., Hart, S., 1986. Chemical geodynamics. Annu. Rev. Earth Planet. Sci. 14, 493–571.

Geochimica et Cosmochimica Acta 354 (2023) 38–50

Contents lists available at ScienceDirect

Geochimica et Cosmochimica Acta

journal homepage: www.elsevier.com/locate/gca

Rubidium isotopic fractionation during magmatic processes and the composition of the bulk silicate Earth

Baoliang Wang [a,*], Frederic Moynier [a], Matthew G. Jackson [b], Fang Huang [c], Xia Hu [c], Sæmundur Ari Halldórsson [d], Wei Dai [a], Gabriel Devos [a]

[a] Université Paris Cité, Institut de Physique du Globe de Paris, CNRS, 1 Rue Jussieu, 75005 Paris, France
[b] Department of Earth Science, University of California, Santa Barbara 93106, USA
[c] CAS Key Laboratory of Crust-Mantle Materials and Environments, School of Earth and Space Sciences, University of Science and Technology of China, Hefei, Anhui 230026, China
[d] Nordic Volcanological Center, Institute of Earth Sciences, University of Iceland, Reykjavík, Iceland

ARTICLE INFO

Associate editor: Julie Prytulak

Keywords:
Rb isotopes
Hekla volcano
Magmatic evolution
MORB
Earth's mantle

ABSTRACT

Rubidium is a moderately volatile element with high incompatibility and fluid mobility. Its stable isotopes have great potential in tracing various geological processes. For example, lunar rocks are isotopically heavier than terrestrial ones, suggesting volatile loss by evaporation during or following the formation of the Moon. However, these studies rely on a poorly constrained estimate for the composition of the Earth's mantle and a poor understanding of high-temperature processes which may act to fractionate stable Rb isotopes. It is therefore important to precisely characterize different rock types that sample the Earth's mantle as well as to evaluate the importance of key isotopic fractionation processes. In order to address these issues, we established a high precision analytical method for Rb isotopic measurements using the Nu Sapphire CC-MC-ICP-MS (collision-cell multi-collector inductively coupled plasma mass spectrometer). In addition, we present a series of Rb isotopic data of volcanic rocks from Hekla volcano (Iceland) and MORB (mid-ocean ridge basalt) samples. We show that our method returns a high Rb sensitivity (~500 V/μg·g^{-1} for ^{85}Rb) and a long-term reproducibility of 0.03‰ on δ^{87}Rb (the permil deviation of the ^{87}Rb/^{85}Rb ratio from the SRM 984 standard). This method uses a 2 ng/g Rb solution for analyses, allowing us to consume about 10 times less Rb to achieve similar or better precision than previous studies. Using this method, seven geostandards and one synthetic standard return Rb isotopic data consistent with previous work. Twenty-one Hekla volcanic rocks, spanning compositions from basalt to rhyolite, show limited Rb isotopic variation, with δ^{87}Rb values varying from −0.17‰ to −0.07‰, demonstrating that magmatic evolution has an insignificant effect on Rb isotope ratios. A set of MORB samples (n = 15) from different mid-ocean ridges also span a limited Rb isotopic variation, displaying a range similar to the Hekla rock suite (−0.19 to −0.02‰). Combining our new data together with previously reported OIB data gives an average δ^{87}Rb value of −0.12 ± 0.08‰ (2SD, n = 25), representing the current best estimate of the mantle's isotopic composition. Considering the δ^{87}Rb values of the upper continental crust (−0.14 ± 0.01‰, 2SE, n = 73), as inferred from recent measurements of granites, loess and sediments, and assuming this value represents the whole crust, the revised Rb isotopic composition of the bulk silicate Earth (and by extension the bulk Earth, assuming no Rb partitioned into the core) is −0.13 ± 0.06‰ (2SD).

1. Introduction

Rubidium (Rb) is a univalent lithophile alkali metal element. Due to its high incompatibility, Rb is enriched in crustal materials compared to the mantle. The estimated Rb abundances of the lower, middle, and upper continental crust are 11 μg/g, 65 μg/g and 84 μg/g, respectively (Rudnick et al., 2003), while that in the primitive mantle is only 0.6 μg/g (McDonough and Sun, 1995), and the depleted upper mantle is 0.05 μg/g (Workman and Hart, 2005). Rubidium is a fluid-mobile element (Han et al., 2021; Hu et al., 2022a) and it is moderately volatile with a 50%

Abbreviations: MORB, mid-ocean ridge basalt.

* Corresponding author.
E-mail address: bwang@ipgp.fr (B. Wang).

https://doi.org/10.1016/j.gca.2023.05.021
Received 3 January 2023; Accepted 29 May 2023
Available online 3 June 2023
0016-7037/© 2023 Elsevier Ltd. All rights reserved.

condensation temperature (T_c^{50}) of 800 K (Lodders, 2003). Similar to other moderately volatile elements (MVE) such as K, Cu, Zn, Cd, Cl, S and Se (Luck et al., 2005; Wombacher et al., 2008; Paniello et al. 2012; Boyce et al., 2015, 2018; Wing and Farquhar, 2015; Pringle et al., 2017; Barnes et al., 2019; Tian et al., 2019, 2021; Gargano et al., 2020; Van Kooten et al., 2020; Vollstaedt et al., 2020; Hu et al., 2022b; Paquet et al. 2022), Rb stable isotopes show promise for studying mechanisms of volatile depletion processes in the inner Solar System.

Rubidium has two naturally occurring isotopes: the stable isotope ^{85}Rb (72.17%) and the radioactive isotope ^{87}Rb (27.83%) (Berglund and Wieser, 2011). However, ^{87}Rb is also considered as a stable isotope due to its long half-life (4.97×10^{10} y, where ^{87}Rb decays to ^{87}Sr) (Nebel et al., 2011b). Previous applications of Rb stable isotopes mainly focused on cosmochemical processes. For example, tektites were analyzed for Rb isotopes in order to explore the influence of impact melting (Nebel et al., 2005). Nebel et al. (2011a) reported Rb isotopic compositions of chondrites and observed resolvable variations on the order of ±1‰ δ^{87}Rb in some meteorites. Pringle and Moynier (2017) established a high-precision analytical method and reported Rb isotopic data of a series of terrestrial and extraterrestrial samples, including chondrites, achondrites and lunar samples. The results show significant Rb isotopic differences among these samples, especially lunar samples, which exhibit Rb isotopic compositions that are heavier than the Earth's mantle by ~0.2 permil. Subsequent measurements employing a different analytical method, have also found heavier Rb isotopic signatures in lunar rocks compared to terrestrial samples (Nie and Dauphas, 2019). All these studies show that Rb isotope can be used as a powerful tool to study planetary evolution.

However, these planetary studies rely on the Earth's composition estimated by Pringle and Moynier (2017), and very few studies have applied Rb isotopes to terrestrial samples. Pringle and Moynier (2017) estimated the Rb isotopic composition of the bulk silicate Earth (BSE) (δ^{87}Rb = −0.12 ± 0.06‰, 2SD) based on only 6 samples, including one mid-ocean ridge basalt (MORB) from the Atlantic ridge, two ocean island basalts (OIB) (Galapagos and Hawaii), one continental flood basalt (BCR-2), one andesite (AGV-2) and one granite (GS-N). X. Hu et al. (2022) constrained the composition of the upper continental crust (UCC) to be −0.14 ± 0.01‰ (2SE, n = 73) based on an extensive sample set of granites, loess and sediments. A few additional igneous geostandards have also been analyzed for Rb stable isotopes (Zhang et al., 2018; Nie and Dauphas, 2019; Nie et al., 2021) (see Table 1).

Since the estimation of the Rb isotopic composition of the mantle is a key parameter for inter-planetary comparison, the limited set of data obtained from mantle-derived materials calls for a more comprehensive characterization. The very low Rb contents (~0.05 μg/g; Workman and Hart, 2005) makes it relatively difficult to directly analyze depleted peridotites (e.g., more than 200 mg of samples are needed with the highest sensitivity to date, i.e., 250 V/μg·g^{-1}, Pringle and Moynier, 2017). In this regard, MORBs are obvious targets as they are generated via partial melting of depleted upper mantle materials, thus providing a straightforward way to constrain the composition of this important reservoir, assuming no isotopic fractionation is generated during partial melting (Hofmann, 2003). Furthermore, magmatic evolution is known to fractionate stable isotopes of various isotopic systems (e.g., Fe, Teng et al., 2008; Sn, Badullovich et al., 2017) and it is important to evaluate this effect on Rb isotopes. Previous Rb isotopic analyses of geostandards with different compositions found that Rb tends to become lighter gradually from mafic to felsic rocks (Zhang et al., 2018; Hu et al., 2021). These isotopic differences observed among the geostandards are relatively minor, typically within the range of approximately 0.2‰. This variability may also be attributed to the mantle source of the analyzed lavas. However, it is worth noting that geostandards are mass-produced and may become contaminated during production as suggested by studies of Mo isotopes (Willbold and Elliott 2017). Therefore, they may not be ideal for accurately estimating magmatic processes on Rb isotopes. In order to better determine the behavior of Rb isotopes during magmatic evolution, it is therefore necessary to investigate a co-genetic rock suite that is largely controlled by magmatic differentiation from a common parental melt. The Hekla volcano produced eruptive materials that range from basalt to rhyolite (Thorarinsson, 1967) and the Hekla suite has been used extensively in recent years to study isotopic fractionation during igneous processes responsible for formation of high-Si igneous rocks for various isotopic systems (e.g., Fe, Li, Schuessler et al., 2009; Si, Savage et al., 2011; V, Prytulak et al., 2016; Zn, Chen et al., 2013; Tl, Prytulak et al., 2017; Ti, Deng et al., 2019; K, Tuller-Ross et al., 2019; Cl, Ranta et al., 2021; Ba, Bai et al., 2022). Hekla is, therefore, well suited for evaluating the behavior of Rb during igneous processes ultimately forming high-Si igneous rocks.

Here, we developed a new analytical method and report the first high precision Rb isotopic data using a Nu Sapphire CC-MC-ICP-MS (collision-cell multi-collector inductively coupled plasma mass spectrometer). We present Rb isotopic compositions for a variety of samples, including 21 igneous rocks from Hekla volcano, and 15 MORBs from different mid-ocean ridge segments, as well as seven different igneous geostandards. Based on these data, we assess the effect of magmatic processes on Rb isotopes and estimate the average Rb isotopic composition of the mantle. Combining our findings from the mantle with the extensive crustal dataset previously reported by Hu et al. (2022a), a more precise constraint on the Rb isotopic composition of the BSE is provided in this study.

Table 1
Rubidium isotopic compositions of standards.

Standard	This study		Reference value		
	δ^{87}Rb (‰)	2SD	δ^{87}Rb (‰)	2SD	Literature
IPGP-Rb	−0.12	0.02	−0.12	0.08	Pringle and Moynier (2017)
BHVO-2	−0.12	0.05	−0.12	0.02	Nie et al. (2021)
			−0.09	0.05	Pringle and Moynier (2017)
			−0.07	0.04	Zhang et al. (2018)
BCR-2	−0.15	0.03	−0.12	0.03	Hu et al. (2021)
			−0.14	0.12	Pringle and Moynier (2017)
			−0.16	0.02	Nie and Dauphas (2019)
W-2a	−0.15	0.02	−0.14	0.05	Hu et al. (2021)
			−0.11	0.02	Zhang et al. (2018)
			−0.15	0.03	Nie and Dauphas (2019)
AGV-2	−0.14	0.02	−0.16	0.12	Pringle and Moynier (2017)
			−0.10	0.06	Zhang et al. (2018)
			−0.15	0.03	Nie and Dauphas (2019)
GSP-2	−0.27	0.01	−0.27	0.02	Hu et al. (2021)
GS-N	−0.11	0.04	−0.14	0.02	Pringle and Moynier, 2017
GA	−0.25	0.01	−0.22	0.03	Nie et al. (2021)

2. Samples

2.1. Geostandards

In order to test the accuracy of our new method, a number of geostandards with compositions ranging from basalt to granite were selected because they have previously been analyzed for their Rb isotopic compositions. The geostandards comprise BHVO-2 (basalt, United

States Geological Survey, USGS), BCR-2 (basalt, USGS), W-2a (diabase, USGS), AGV-2 (andesite, USGS), GSP-2 (granodiorite, USGS), GS-N (granite, Centre de Recherches Pétrographiques et Géochimiques, CRPG), and GA (granite, CRPG). We also mixed pure NIST SRM 984 solution (the Rb isotopic standard) with PCC-1 (peridotite, USGS) to be treated as a synthetic standard to evaluate the accuracy of the measurements.

2.2. Hekla volcano samples

In recent years, the Hekla magma suite has been extensively utilized for investigating isotopic fractionation during magmatic processes (e.g., Savage et al., 2011; Chen et al., 2013; Prytulak et al., 2017; Deng et al., 2019; Tuller-Ross et al., 2019). A set of Hekla volcanic rocks were collected (see sample locations in Bai et al., 2022) and analyzed for Rb isotope in this study. Located at the margin of the propagating South Iceland Volcanic Zone, Hekla volcano is an active central volcano in Iceland that rises nearly 1500 masl (meters above the sea level; Thorarinsson, 1967). It is well-known as a natural laboratory for investigating magmatic processes and the origin of high-Si rocks (Sigmarsson et al., 1992, 2022; Geist et al., 2021). It erupts a series of cogenetic volcanic products, including basalts, basaltic andesites, andesites, dacites and rhyolites. At present, origin of Hekla's wide compositional variability is a matter of debate. Sigmarsson et al. (1992) proposed a three-stage model to explain generation of Hekla's igneous rocks from basalt to rhyolite: (1) The rise of basaltic magma causes partial melting of metabasaltic crust, thus forming dacitic magma. (2) The basaltic magmas undergo fractional crystallization to generate basaltic andesite compositions, and the latter mixes with dacitic liquid to form andesites. (3) Rhyolites are formed from dacitic magma through fractional crystallization. Chekol et al. (2011) suggested that andesitic to more evolved compositions were produced through AFC (assimilation and fractional crystallisation) processes. These studies both advocated the contribution of crustal components to high-Si rocks (i.e., assimilation and/or partial melting of the crust). By contrast, Geist et al. (2021) suggested that the entire Hekla suite is formed by fractional crystallization processes alone, over a period of several tens of thousands of years. A more recent study argued that partial melting of the metabasaltic crust remains the preferred mechanism for petrogenesis of the Hekla silicic rocks, with the time span from silicic magma formation to eruption being less than a few centuries (Sigmarsson et al., 2022).

In this study, we analyzed 9 basalts, 6 basaltic andesites, 2 andesites, 3 dacites and 1 rhyolite from Hekla volcano. Some of these have previously been analyzed for their Ba isotopic composition (Bai et al., 2022). The Hekla rocks studied here are generally fresh, Holocene igneous rocks with little to no visible signs of secondary alteration (Sigmarsson et al., 1992; Chekol et al., 2011; Geist et al., 2021). Furthermore, besides some rare secondary incrustations, formed during solidification, cooling and secondary degassing (Óskarsson, 1981), the vast amount of data published from the Hekla suite does not indicate that secondary alteration affects the chemical and isotopic composition. Thus, the Hekla suite records extensive magmatic evolution of a OIB magma, from basalt through rhyolite, making this suite ideal for studying the effect of magmatic processes on Rb isotopes.

2.3. MORB samples

Sixteen MORB samples from different mid-ocean ridge segments were collected to estimate the Rb isotopic composition of the upper mantle. Among them, nine are from the Atlantic Ocean, four are from the Indian Ocean and three are from the East Pacific Ocean. All MORB samples in this study are fresh glasses (quenched melts), which were not subjected to significant alteration as indicated by the chemical index of alteration (CIA) and loss on ignition (LOI) (She et al., 2023). According to a common classification scheme (Schilling, 1975; Schilling et al., 1983), MORB samples can be divided into Normal-MORBs (N-MORBs, $La/Sm_N < 0.7$), Enriched-MORBs (E-MORBs, $La/Sm_N > 1.8$) and Transitional-MORBs (T-MORBs, with La/Sm_N between N- and E-MORBs). Importantly for the purpose of this study, these MORB samples cover all the different types mentioned above (Amsellem et al., 2018; Deng et al., 2018; Inglis et al., 2019), which allows us to evaluate the role of partial melting and/or mantle source-derived variability on $\delta^{87}Rb$ values.

3. Analytical methods

3.1. Sample dissolution

Sample digestion and chemical purification were conducted at the Institut de Physique du Globe de Paris (IPGP). 18.2 MΩ·cm ultrapure water and distilled high-purity concentrated acids were used throughout the processes. For each Hekla sample, whole-rock powder was made from approximatively 50 g of rock. For MORB samples, fresh glass fragments were handpicked and powdered with an agate mortar (She et al., 2023). 20–60 mg of sample powders were weighed into Savillex PFA Teflon beakers to yield >10 ng Rb for isotopic measurement. A separate 50 mg of Hekla sample powders were weighed for major and trace elements measurement. Samples were first digested with a 3:1 vol mix of concentrated HF and HNO_3 by heating at 130 °C for 48 h on a hotplate. After evaporation of HF-HNO_3, the samples were sequentially treated with aqua regia (concentrated HCl: HNO_3 = 3:1, volume ratio) and 6 mol/L HCl at 120 °C to remove fluoride complexes. Finally, dried samples were re-dissolved in 1 mL 0.5 mol/L HNO_3 for major and trace elements measurements, or re-dissolved in 1 mol/L HNO_3 for subsequent column chemistry.

3.2. Major and trace elements measurement

Full basic geochemical data of the MORB samples has been reported in She et al. (2023). Elemental concentration measurement was performed for all the Hekla samples at IPGP. An aliquot of the digested solution was diluted by a factor of 15,000 for elemental analysis. Major and trace elements were measured using an Agilent quadrupole inductively coupled plasma mass spectrometer (Q-ICP-MS). Two geostandards (i.e, BHVO-2 and BCR-2) were processed with the same procedures to monitor the accuracy. The data are provided in the Supplementary Material.

3.3. Chemical purification and Rb isotopic measurement

Pringle and Moynier (2017) developed a column chemistry procedure of Rb isotopes at IPGP. The procedure consists of four steps, with one column of Eichrom DGA resin (50–100 μm, 1.8 mL) to remove Ca, then two columns of Bio-Rad AG50W-X12 resin (200–400 mesh, 20 mL and 10 mL, respectively) to remove other matrix elements, and finally one column of Bio-Rad AG50W-X8 resin (200–400 mesh, 1 mL) to further separate K. However, this procedure is time-consuming and requires large volumes of acid. Previous studies showed that the separation of Rb and K could be successfully realized by using Sr-spec resin (Zhang et al., 2018; Nie and Dauphas, 2019; Hu et al., 2021). Thus, based on the column chemistry established by Pringle and Moynier (2017), we modified the last step by replacing it with a Sr-spec resin chemistry. The full chemical purification procedure is listed in Supplementary Table 1, in which the first three steps have been described in Pringle and Moynier (2017) and remain the same here. In the text that follows, we provide a detailed description of only the last step (i.e., Sr-spec purification).

After the first three steps of purification, sample elution was dried down and re-dissolved in 3 mol/L HNO_3 for Sr-spec column chemistry. 1 mL Eichrom Sr-spec resin (20–50 μm) was filled into a pre-cleaned homemade heat-shrink Teflon column (0.46 cm inner diameter, 6.5 cm length). The resin was cleaned with 3 mL of 3 mol/L HNO_3 and 2 mL of H_2O successively, and then conditioned with 3 mL 3 mol/L HNO_3

prior to sample loading. Sample was loaded on the resin in 0.25 mL of 3 mol/L HNO_3 and followed by another 0.25 mL of 3 mol/L HNO_3. The Rb was collected with 1 mL 3 mol/L HNO_3 (Supplementary Table 1). Compared to the AG50W-X8 resin method (which required 40 mL of acid to collect Rb) that was previously used by Pringle and Moynier (2017), the Sr-spec in this study used only 1 mL of acid. This greatly simplifies the chemical purification process. Using the Sr-spec method, we can achieve a complete separation of Rb from K (Fig. 1).

The recovery and blank of the whole procedure were carefully evaluated. The yield of each sample was >95%, and the total procedural blank was <0.03 ng, which was negligible (<0.3%) compared to the total Rb in sample (>10 ng).

Rubidium isotopic measurements were performed on CC-MC-ICP-MS Nu Sapphire at IPGP. The Nu Sapphire is a new generation double-focusing MC-ICP-MS which includes both a high energy ion pathway (traditional MC-ICP-MS) and a low energy ion pathway (equipped with a collision cell). For Rb isotopic measurements, we used conventional high energy mode. Sample solution was introduced through an Apex Omega desolvating system using a 100 μL/min PFA nebulizer (Elemental Scientific, Omaha, NE, USA). Rubidium isotopic abundances were analyzed in low resolution mode with standard Ni dry cones ("dry plasma"). The isotopes ^{85}Rb and ^{87}Rb were simultaneously collected on L3 and H1 Faraday cups, respectively, with $10^{11}\Omega$ resistors. Strontium-88 was collected on the H3 Faraday cup ($10^{11}\Omega$ resistor) in order to evaluate ^{87}Sr intensity. The interference of ^{87}Sr on ^{87}Rb is corrected by assuming an $^{87}Sr/^{88}Sr$ value of 0.085, following prior work (Nebel et al., 2005; Pringle and Moynier, 2017; Zhang et al., 2018; Hu et al., 2021). A constant $^{87}Sr/^{88}Sr$ ratio of 0.085 is sufficient for the Sr correction, because the ^{87}Sr interference on ^{87}Rb is insignificant due to efficient Sr removal during column chemistry, and thus the uncertainty on the $^{87}Sr/^{88}Sr$ ratio would have a minor impact. For example, taking two extreme values of $^{87}Sr/^{88}Sr$ (0.083 and 0.089, corresponding to $^{87}Sr/^{86}Sr$ of 0.70 and 0.75, respectively) from the reported range in terrestrial and extraterrestrial rocks and for the sample with the most Sr residue ($^{88}Sr/^{85}Rb = 0.003$), would only affect the correction by only ~0.03‰.

Relevant operating parameters of the instrument are shown in Supplementary Table 2. The sensitivity of ^{85}Rb was ~500 V/μg·g^{-1}. Samples and standard solutions were diluted to 2 ng/g using 0.5 mol/L HNO_3 for analyses. Before each analysis, a 30-second blank measurement was performed in 0.5 mol/L HNO_3. Each sample analysis consisted of 40 cycles of data with an integration time of 5 s per cycle. In order to eliminate potential cross-contamination, the sample introduction system was cleaned 90 s using 0.5 mol/L HNO_3 following each standard and sample analysis. Each sample was measured at least 3 times, bracketed by the international isotopic standard NIST SRM 984. Rubidium isotopic data were reported as $\delta^{87}Rb = [(^{87}Rb/^{85}Rb)_{sample}/(^{87}Rb/^{85}Rb)_{SRM984} - 1] \times 1000$ (‰).

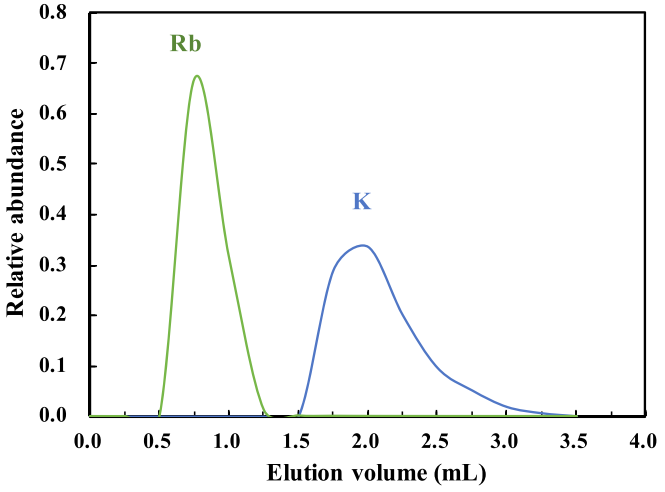


Fig. 1. Elution curves for Rb and K of our Sr-spec column chemistry. The homemade heat-shrink Teflon columns (0.46 cm inner diameter, 6.5 cm length) contain 1 mL of Eichrom Sr-spec resin (20–50 μm) and the elution are realized using 3 mol/L HNO_3. Relevant data see Supplementary Table 3.

4. Results

The pure NIST SRM 984 solution yielded $\delta^{87}Rb$ values between −0.05‰ and +0.04‰, with an average of 0.00 ± 0.03‰ (2SD, n = 23; Fig. 2a and Supplementary Table 4). Rubidium isotopic compositions of one in-house standard (IPGP-Rb, a pure Rb ICP-MS solution), previously used in Pringle and Moynier (2017) and seven geostandards are presented in Table 1, and literature values are also listed for reference. The value of IPGP-Rb (−0.12 ± 0.02‰, 2SD, n = 6) was identical to that (−0.12 ± 0.08‰, 2SD, n = 40) measured by Pringle and Moynier (2017) using a Thermo-Fisher Neptune plus. The $\delta^{87}Rb$ values of geostandards all agree well with previously published data (Fig. 2b). In addition, some of these geostandards are used to test the effect of the measuring concentrations (Fig. 3). These results are discussed in Section 5.1.

Hekla samples data are reported in Table 2. Consistent with previous studies (e.g., Sigmarsson et al., 1992, 2022; Geist et al., 2021), Rb contents of Hekla suite display reasonably good correlations with SiO_2 and MgO contents as well as other incompatible minor (K_2O) and trace elements (La), gradually increasing with the magmatic evolution

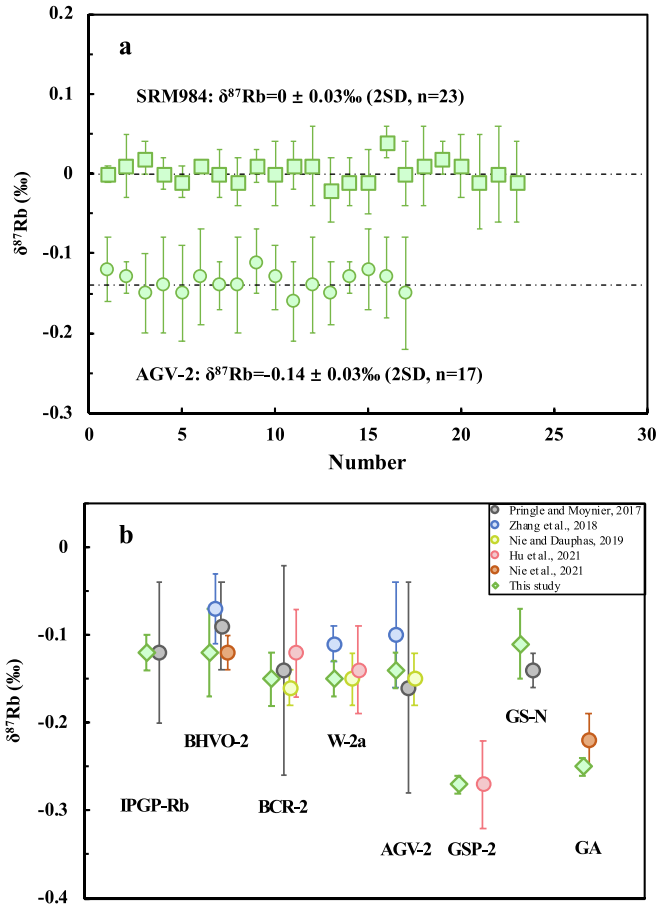


Fig. 2. Rubidium isotopic data of standards. (a): The $\delta^{87}Rb$ of pure NIST SRM 984 solution and AGV-2. The long-term reproducibility of Rb isotopic analyses is 0.03‰ (2SD) based on the repeated measurements of AGV-2; (b): Rubidium isotopic compositions of one in-house standard IPGP-Rb solution and seven geostandards. The data are reported as $\delta^{87}Rb$ relative to the SRM 984 solution. Data from the literature are reported for comparison.

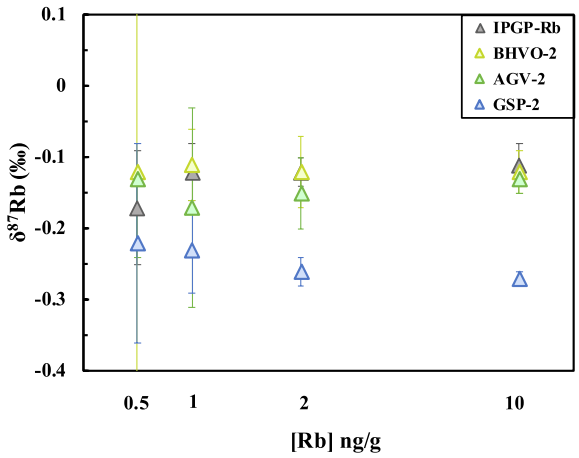


Fig. 3. Effect of Rb testing concentrations on accuracy and precision. Rubidium concentrations decrease from 10 to 0.5 ng/g for a pure Rb standard as well as for three rock standards (BHVO-2, AGV-2, GSP-2). Relevant data are reported in Supplementary Table 5.

(Fig. 6a, b, c and d), which is consistent with its strong incompatibility. The average Rb concentrations of these five rock types—basalts, basaltic andesites, andesites, dacites, and rhyolite—are 10.4 μg/g, 27.2 μg/g, 29.2 μg/g, 55.7 μg/g and 68.3 μg/g, respectively. However, irrespective of Rb contents, all Hekla samples show uniform Rb isotopic composition within uncertainty, with δ^{87}Rb values ranging from −0.17 to −0.07‰ (Fig. 6e and f).

The $(La/Sm)_N$ of MORB samples ranges from 0.4 to 2.0 (Table 3 and Fig. 7a), covering different types of N-MORB, E-MORB and T-MORB (Schilling, 1975; Schilling et al., 1983). Rubidium isotopic compositions of MORBs vary from −0.19 to −0.02‰, with an average of −0.12 ± 0.09‰ (2SD, n = 15). Most of the different types of MORB samples exhibit similar Rb isotope signatures, except one E-MORB sample (CH30 DR 17–03), which has slightly heavier Rb isotopic composition (−0.02 ± 0.02‰, 2SD) than others (Fig. 7a and b). Nevertheless, Rb isotope data of MORB samples in this study shows no obvious trend with Rb and MgO contents, Na_8 and Ba/Th (Fig. 7b, c, d and e).

Table 2
Rubidium isotopic compositions of Hekla volcanic rocks.

Sample	Type	SiO_2 (wt. %)	MgO (wt. %)	K_2O (wt. %)	La (μg/g)	Rb (μg/g)	δ^{87}Rb (‰)	2SD[a]	n
ICE 20-22	Basalt	48.59	4.66	0.56	22.7	9.8	−0.16	0.05	4
ICE 20-25	Basalt	48.60	5.00	0.54	20.1	9.2	−0.15	0.05	4
ICE 20-28	Basalt	46.27	6.00	0.55	24.1	11.2	−0.10	0.02	3
ICE 20-31	Basalt	47.71	6.83	0.39	13.1	6.2	−0.14	0.05	4
ICE 20-36	Basalt	51.44	4.16	0.54	21.4	8.7	−0.07	0.04	3
ICE 20-37	Basalt	45.80	5.80	0.58	24.0	11.9	−0.11	0.02	3
ICE 20-41	Basalt	46.44	5.58	0.58	25.8	11.6	−0.10	0.06	4
ICE 20-45	Basalt	51.20	3.84	0.95	40.5	15.5	−0.11	0.01	3
ICE 20-19	Basaltic Andesite	54.70	2.75	1.28	53.9	20.6	−0.17	0.03	3
ICE 20-23	Basaltic Andesite	55.34	2.58	1.31	48.6	22.7	−0.16	0.02	3
ICE 20-23 (Replicate[b])	Basaltic Andesite	55.34	2.58	1.31	48.6	22.7	−0.17	0.03	3
ICE 20-34	Basaltic Andesite	54.59	2.76	1.27	52.7	19.7	−0.13	0.02	3
ICE 20-40	Basaltic Andesite	54.72	2.88	1.18	52.0	24.7	−0.16	0.02	3
ICE 20-44	Basaltic Andesite	54.27	2.87	1.25	48.0	27.0	−0.17	0.04	3
ICE 20-24	Andesite	57.76	2.42	1.24	48.3	22.4	−0.11	0.03	3
ICE 20-35	Andesite	57.77	1.91	1.53	55.9	34.1	−0.16	0.04	3
ICE 20-32	Dacite	69.21	0.24	2.41	71.6	57.4	−0.16	0.04	3
ICE 20-32 (Replicate[b])	Dacite	69.21	0.24	2.41	71.6	57.4	−0.15	0.05	3
ICE 20-39	Dacite	68.43	0.24	2.49	61.0	52.1	−0.13	0.02	3
ICE 20-33	Rhyolite	76.52	0.02	2.87	64.8	68.3	−0.17	0.04	3

[a] 2SD = 2 times the standard deviation of the population of three repeat measurements of a sample solution;
[b] Replicate = repeat chemical purification and measurement of different aliquots of a stock solution.

Table 3
Rubidium isotopic compositions of MORB samples.

Sample	Location	MgO[a] (wt. %)	$(La/Sm)_N$[a]	Na_8[a] (wt. %)	Ba/Th[a]	Rb[a] (μg/g)	δ^{87}Rb (‰)	2SD	n
CYP78 12-34	East Pacific Ridge	7.53	0.6	2.34	93.2	1.7	−0.09	0.01	4
SEARISE1 DR04	East Pacific Ridge	6.61	0.6	2.08	57.6	1.2	−0.07	0.03	4
SEARISE2 DR03	East Pacific Ridge	7.06	0.5	2.34	48.4	0.5	−0.06	0.03	4
CYP74 31-35	Mid Atlantic Ridge	10.56	1.4	2.86	103.3	4.0	−0.14	0.01	3
ARP 73 13 4	Mid Atlantic Ridge	9.95	1.5	2.66	107.2	4.2	−0.18	0.03	3
ARP 74 9 13C COLUMN	Mid Atlantic Ridge	6.61	1.2	1.53	87.3	4.2	−0.13	0.02	3
ARP 74 7 8 SURFACE	Mid Atlantic Ridge	8.28	1.5	2.03	88.9	5.6	−0.14	0.02	3
DSDP-52-417D-55-2	Mid Atlantic Ridge	5.89	0.4	1.28	45.6	0.4	−0.13	0.02	3
CH30 DR 17-03	Mid Atlantic Ridge	5.15	2.0	1.92	114.0	11.2	−0.02	0.02	3
CH30 DR 17-03 (Replicate)	Mid Atlantic Ridge	5.14	2.0	1.92	114.0	11.2	0.01	0.04	3
CH31-DR12-137	Mid Atlantic Ridge	8.28	1.3	2.21	92.3	3.9	−0.11	0.04	4
EW9309 3D-1g	Mid Atlantic Ridge	6.69	1.8	2.28	131.3	9.8	−0.13	0.03	3
MD57 D6-7	Central Indian Ridge	8.13	0.8	2.76	83.3	3.0	−0.18	0.03	4
MD57 D3-3	Central Indian Ridge	7.48	0.6	2.01	65.4	1.0	−0.19	0.01	3
MD34 D1	Central Indian Ridge	6.52	0.9	2.78	62.8	2.6	−0.14	0.04	3
MD57 D13	Central Indian Ridge	6.76	0.7	2.13	56.9	2.1	−0.16	0.06	3

[a] Major and trace elements data is from She et al. (2023).

5. Discussion

5.1. Validating high precision Rb isotopic measurements using a Nu Sapphire

5.1.1. Accuracy and precision

In order to evaluate the accuracy of our method, we first analyzed the pure NIST SRM 984 solution. Self-bracketing NIST SRM 984 solutions generated the expected δ^{87}Rb values around zero (within the uncertainty), with an average of 0.00 ± 0.03‰ (2SD, n = 23; Fig. 2a). In addition, a synthetic sample (SRM 984+PCC-1, after Rb separation following column chemistry) was also measured to test the matrix separation efficiency of the chemical purification. This peridotite sample, PCC-1 contains almost no Rb (0.07 μg/g, Takazawa et al., 2000; Sossi et al., 2016). Approximately 20 mg of PCC-1 powder was digested and then redissolved into 1 mL of pure SRM 984 solution which contained 25 ng of Rb. Given the mass ratio of Rb contained in SRM 984 and PCC-1 (i.e., 25:1.4), 95% of the Rb of this synthetic sample comes from the pure SRM 984. Due to its low Rb content, the Rb isotopic composition of PCC-1 has never been measured, but assuming that its δ^{87}Rb value is within ±1‰ from SRM 984 (this is reasonable because as a peridotite it should have Rb isotopic characteristics comparable to that of the mantle, i.e., δ^{87}Rb = −0.12 ± 0.06‰, 2SD; Pringle and Moynier, 2017), this synthetic sample should have isotopic composition that is within error of the pure SRM 984 after column chemistry. The results obtained validate this prediction because the average δ^{87}Rb value of the three synthetic samples is −0.01 ± 0.03‰ (2SD, n = 3). This confirms the reliability of matrix separation of our chemistry. The in-house standard IPGP-Rb solution and seven geostandards were analyzed to further test the accuracy of our method (Fig. 2b). All the results presented in this study are consistent with previously published data (Pringle and Moynier, 2017; Zhang et al., 2018; Nie and Dauphas, 2019; Nie et al., 2021; Hu et al., 2021). The long-term reproducibility of our Rb isotopic analyses is 0.03‰ (2SD), as estimated from the repeated measurements of AGV-2 (δ^{87}Rb = −0.14 ± 0.03‰, 2SD, n = 17; Fig. 2a and Supplementary Table 4) during 17 analytical sessions over 3 months (where, in each session, AGV-2 was measured at least 3 times).

5.1.2. Effect of Rb concentration

The Nu sapphire coupled to the Apex Omega allows us to obtain the highest sensitivity (500 V/μg·g^{-1} for ^{85}Rb) ever achieved compared with previous studies, e.g., 100 to ~250 V/μg·g^{-1} in Pringle and Moynier (2017), 50 V/μg·g^{-1} in Zhang et al. (2018) and Nie et al. (2021), and 45 V/μg·g^{-1} in Hu et al. (2021). For the purposes of evaluating the effect of measuring concentrations on accuracy and precision, and examining the lower limit of the analytical concentration on the Nu Sapphire, we measured IPGP-Rb, BHVO-2, GSP-2, and AGV-2 at various Rb concentrations. The concentrations of samples and bracketing standards were set from 10 ng/g, 2 ng/g, 1 ng/g and even 0.5 ng/g. Under different conditions, even if the Rb concentration was as low as 0.5 ng/g, we could obtain accurate values consistent with previously reported data for these standards. However, the analytical precision decreases significantly at the lowest running concentrations. For example, the precisions reported for 10 ng/g and 2 ng/g are within 0.05‰ (2SD), but precision is generally worse and more variable at 1 ng/g (down to 0.14‰, 2SD). At 0.5 ng/g the precision is 0.38‰ (2SD) (Fig. 3 and Supplementary Table 5). Given that at 2 ng/g measurements still provide excellent precision, we set 2 ng/g as the analytical concentration for the rest of this work. This allows us to perform Rb isotopic measurement with only a small amount of sample.

5.1.3. Effects of concentration and acid molarity mismatch

Previous studies demonstrated that a concentration mismatch between standards and samples can have a more significant impact on measurements of K, Ca and Cu isotopes on the Nu Sapphire compared to Neptune or Neptune Plus, and an intensity match within 1% was suggested during analysis (Moynier et al., 2021; Dai et al., 2022; Wang et al., 2022). In order to test the effect of concentration mismatch on Rb isotopic measurements, pure SRM 984 solutions with different Rb concentrations were analyzed as unknown samples. The bracketing standard was kept at 10 ng/g, while samples were run with concentrations varying from ~5 ng/g to 15 ng/g (i.e., the ratio of sample/standard varied from just under 0.5 to a bit over 1.5). Unlike K and Ca isotopes, Rb isotopic analyses on Nu Sapphire are insensitive to the concentration mismatch (Fig. 4a and Supplementary Table 6).

It was also reported that Nu Sapphire measurements may be more sensitive to mismatch of acid molarity between samples and bracketing standard (Moynier et al., 2021; Dai et al., 2022; Chen et al., 2021; Li et al., 2022; Wang et al., 2022; Zheng et al., 2022). The influence of acid molarity mismatch on Rb isotopic measurements was assessed by a series of condition tests. Pure SRM 984 solutions were treated as samples, and measured with the same Rb concentration (i.e., 2 ng/g) as the bracketing standard. However, they were prepared with different molarities of acid. The standard was diluted using 0.5 mol/L HNO_3, while samples were diluted in HNO_3 at various concentrations (from 0.1 mol/L to 1.0 mol/L). The results show that acid molarity mismatch has no obvious effect on the Rb isotopic measurements when analyzed on the Nu Sapphire (Fig. 4b and Supplementary Table 6). Nevertheless, we use the same HNO_3 (0.5 mol/L) to prepare samples and standard solutions during measurements.

5.1.4. Effect of matrix elements

A small amount of matrix residues after column chemistry may also influence isotope measurements. For example, interferences of isobars and polyatomic ions, and influences of matrix on ionization and transmission of target elements, can affect the quality of the isotopic measurements (Tan and Horlick, 1987; Tanner, 1992; Chen et al., 2021). In particular, previous studies have reported that some matrix elements can strongly affect Rb isotopic values during mass spectrometry analysis (Zhang et al., 2018; Nie and Dauphas, 2019; Hu et al., 2021). In this study, we tested these effects on the Nu Sapphire, of Sr, K, Cr, Ga, Ca, Ti, Fe, Mn, Al and Na. Pure standard solutions of various elements were doped into a 2 ng/g SRM 984 to obtain different ratios of [element]/[Rb]. The doped solutions were measured against pure SRM 984 with the same Rb concentration. The results are presented in Fig. 5 and Supplementary Table 7.

Strontium correction with a fixed ^{87}Sr/^{88}Sr value of 0.085 is effective only when there is a very small amount of Sr residue in the Rb solution. The result of our Sr doping test showed that accurate δ^{87}Rb values could be obtained when Sr/Rb ≤ 0.005 (i.e., ^{88}Sr/^{85}Rb intensity ≤ 0.006). In order to minimize the impact of the isobaric interference of ^{87}Sr on ^{87}Rb, all natural samples in this study had ^{88}Sr/^{85}Rb intensity ≤ 0.003 (for most samples the ratio was ≤0.002 or lower) after chemical purification, and therefore the Sr correction did not affect the quality of the δ^{87}Rb data. Because Rb and K have very similar geochemical behavior, a challenge of our method is to achieve complete separation of Rb and K. Previous studies have shown that K affects Rb isotopic measurements, but to different degrees between different instruments. For example, Pringle and Moynier (2017) (Neptune Plus with quartz cyclonic spray chamber or Apex) and Zhang et al. (2018) (Neptune Plus with quartz dual cyclonic-Scott spray chamber) found that the K/Rb ratios must be maintained below 10 and 25, respectively, to obtain accurate δ^{87}Rb values. Nie and Dauphas (2019) (Neptune with quartz dual cyclonic-Scott spray chamber) found that it was sufficient to keep it below 50. A more recent study found that the isotopic measurements were very sensitive to K residue (Neptune Plus with quartz dual cyclonic-Scott spray chamber; Hu et al.,2021) with the δ^{87}Rb values shifted when K/Rb >1.5. Thus, it is necessary to evaluate the effect of K on Rb isotopic measurements on the Nu Sapphire coupled to an Apex Omega. Our doping test results showed that Rb isotopic analyses were not affected by K as long as the K/Rb ratio ≤ 20. Chromium and Ga were doped here to test the effect of some possible impurities, since they are eluted very

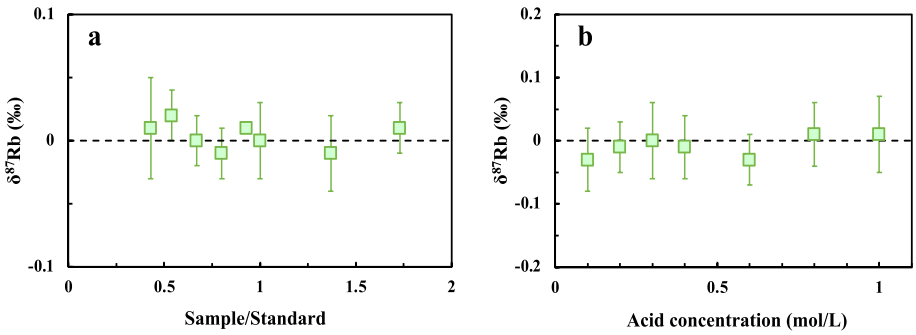


Fig. 4. Effects of concentration and acid molarity mismatch on Rb isotopic measurements. Samples and standards are both pure SRM984 solutions. (a): the bracketing standard was kept at 10 ng/g, samples with different Rb concentrations were prepared to obtain the sample/standard concentration ratio varying from 0.5 to 1.5; (b): samples and bracketing standard were prepared with different molarities of acid. Samples were dissolved in HNO_3 from 0.1 moL/L to 1.0 moL/L, while the standard was diluted in 0.5 moL/L HNO_3.

closely to Rb according to the elution curves presented in Pringle and Moynier (2017). The influence was negligible as long as Cr/Rb was ≤10 and Ga/Rb was ≤20. Other matrix elements (such as Ca, Ti, Fe, Mn, Al and Na) affected Rb isotopic measurements to different extent. $\delta^{87}Rb$ values were modified when Ti/Rb was ≥20, Fe/Rb was ≥20 and Al/Rb was ≥ 10, while Ca, Na and Mn had no obvious influence within the range of concentration ratios set in our doping tests (i.e., [element]/[Rb] ≤ 50).

5.2. Magmatic processes do not fractionate Rb isotopes

Igneous products of the Hekla volcano have been widely used to investigate behaviors of different isotopic systems during magmatic processes. For example, Th, Fe, Si, B and V isotopic compositions of Hekla igneous rocks correlate with SiO_2 contents, suggesting that magmatic evolution has a significant influence on these isotope systems (Sigmarsson et al., 1992; Rose-Koga and Sigmarsson, 2008; Schuessler et al., 2009; Prytulak et al., 2016; Savage et al., 2011). Moreover, highly light Cl isotopic values observed in high-Si rocks from Hekla have been interpreted to reflect the assimilation of magmatic brine (Ranta et al., 2021). However, no isotopic variation was observed in the same set of samples for Li, Zn, Mo, Tl, K and Ba isotopes (Schuessler et al., 2009; Chen et al., 2013; Yang et al., 2015; Prytulak et al., 2017; Tuller-Ross et al., 2019; Bai et al., 2022). A set of igneous rocks from the Hekla volcano were analyzed in this study in order to explore the Rb isotopic behaviors during magmatic evolution. In the following sections, we will systematically evaluate different magmatic processes which have the potential to fractionate Rb isotopes.

5.2.1. Assimilation and/or exsolution of magmatic fluids

As Rb is a fluid-mobile element, hydrothermal fluid activities may lead to its isotopic fractionation. For example, Hu et al. (2022a) reported a highly heavy Rb isotopic signature (−0.29‰ to 1.20‰) in Kampa leucogranites compared to the available data on sedimentary materials of the UCC (−0.31‰ to 0.07‰). After ruling out the influences of source heterogeneity, partial melting, fractional crystallization and chemical weathering, this highly heavy Rb isotopic signature was attributed to the involvement of magmatic fluids (Hu et al., 2022a). This is consistent with previous studies that have also shown that Kampa leucogranite magma was modified by fluids during its evolution (Liu et al., 2020; Huang et al., 2021). Therefore, the influence of assimilation and/or exsolution of magmatic fluids need to be considered.

Previous chlorine isotopes study indicates that the assimilation of magmatic brine plays an important role in generating light chlorine isotopic characteristics evident in Hekla rhyolites (Ranta et al., 2021). However, we do not observe any abnormal signals in high-Si rocks from Hekla, either in terms of Rb concentration or isotopic composition. For example, Rb contents follow a consistent evolution trend when plotted against SiO_2 and MgO contents (Fig. 6a and b). Besides, compared with associated basalts ($\delta^{87}Rb_{average}$ = −0.12 ± 0.06‰, 2SD, n = 8) and basaltic andesites ($\delta^{87}Rb_{average}$ = −0.15 ± 0.06‰, 2SD, n = 6), dacites ($\delta^{87}Rb_{average}$ = −0.15 ± 0.03‰, 2SD, n = 3) and one rhyolite sample ($\delta^{87}Rb$ = −0.17 ± 0.04‰) have similar Rb isotopic compositions. This similarity indicates that the influence of magmatic brine on Rb isotope in our samples is not obvious, if indeed magmatic brines are concentrated in rhyolites relative to basalts and dacites. In addition, fluid exsolution is also unlikely to affect Rb isotopic signature of Hekla rocks, given the identical Li isotopic composition of the different Hekla lavas, which indicates that exsolution of fluids from melt is not significant (Schuessler et al., 2009).

5.2.2. Degassing

Rubidium is a moderately volatile element with a T_c^{50} of 800 K (Lodders, 2003). Previous studies on extraterrestrial samples indicate that volatile loss during evaporation may lead to Rb isotopic fractionation (Pringle and Moynier, 2017; Nie and Dauphas, 2019). Hekla lavas experience significant loss of F, Cl and S during eruptions (Moune et al., 2007; Ranta, et al., 2021). Therefore, Rb isotope fractionation caused by volatile loss during volcanic degassing is possible.

While the Rb isotopic compositions of Hekla rocks are relatively uniform and non-systematic, the total variation observed (~0.10‰) exceeds the precision of our method (0.03‰). Rubidium isotopes can therefore be used to estimate the amount of Rb loss during volcanic degassing at Hekla. Rubidium is evaporated as RbCl gas during degassing, and the theoretical Rayleigh fractionation coefficient (α) can be calculated as the square root of the mass difference between $^{85}RbCl$ and $^{87}RbCl$ [i.e., $(120.3648/122.3622)^{0.5}$ = 0.9838]. Based on this, we can estimate a maximum of 0.6% of Rb is lost during volcanic degassing, which is similar to the loss amount of K (0.8–1.3%) estimated by Tuller-Ross et al. (2019). However, it should be noted that this estimation is based on the assumption that the Rb isotopic variation of Hekla rocks is entirely due to degassing. As a result, the actual loss of Rb during volcanic degassing may be much less than our estimated value. This is supported by the fact that the Rb contents are consistent with the behavior of other non-volatile incompatible elements (e.g., La) during magma evolution (Fig. 6d), indicating that there may be no significant loss of Rb following magma evolution at Hekla. Therefore, we conclude that volatile loss associated with petrogenesis of the Hekla rock suite is unlikely to fractionate Rb isotopes.

5.2.3. Magmatic evolution

The Hekla basaltic to intermediate rocks are commonly considered to be controlled by fractional crystallization process (Sigmarsson et al., 1992, 2022; Geist et al., 2021). Currently, there is an ongoing debate regarding the petrogenesis of the silicic rocks from Hekla. For example, studies of short-lived radiogenic isotopes (Sigmarsson et al., 1992, 2022; Chekol et al., 2011) and B and Cl stable isotopes (Rose-Koga and Sigmarsson, 2008; Ranta et al., 2021) suggest that crustal anatexis and assimilation are important processes for the formation of dacites, from which rhyolites are generated via fractional crystallization. Geist et al. (2021) suggested a “fractional crystallization alone” model, arguing that the evolution of magma at Hekla was primally driven by fractionation

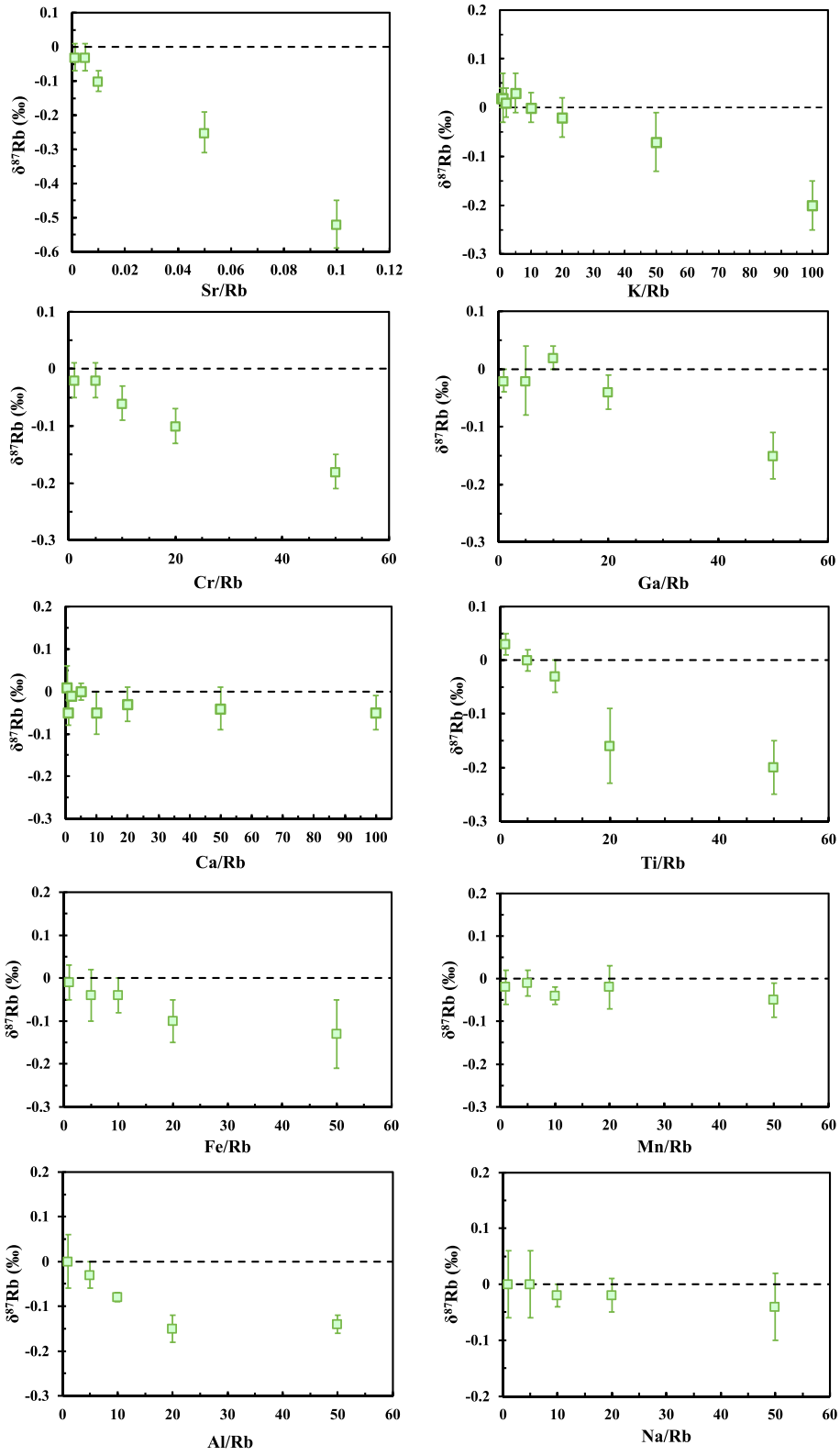


Fig. 5. Matrix effects on Rb isotopic measurements evaluated by doping the solutions with various elements. Rubidium concentrations were set to 2 ng/g, and [element]/[Rb] represents the concentration ratio of different elements to Rb, e.g., [K]/[Rb] = 20 corresponds to K of 40 ng/g.

crystallization based on trends in trace element ratios, as well as oxygen isotopic data, with which they excluded significant contribution from the crust. The Hekla dacites, together with other types of rocks, show a good correlation between their Rb concentrations and SiO_2 as well as MgO contents, strictly following a magmatic differentiation trend (Fig. 6a and b). However, an influence of the crust cannot be ruled out, as partial melting of metabasaltic crust to form dacites also fits the consistent trend of elemental Rb. For example, we can roughly evaluate the contribution of the crust melting by using the equation: $C_1/C_0 = F^{(D-1)}$, where C_1 is the Rb content of the melt (i.e., dacites), C_0 is Rb content

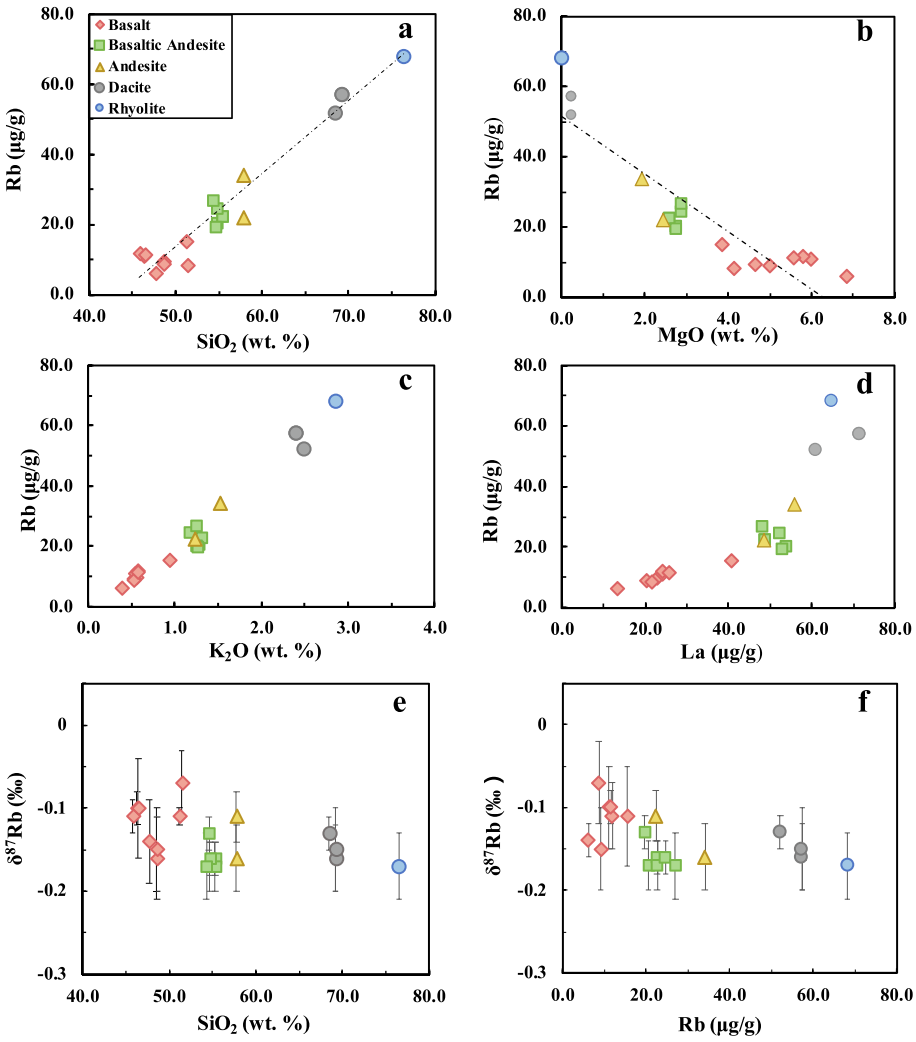


Fig. 6. Rubidium elemental and isotopic characteristics of Hekla volcanic rocks. (a): Rb concentration plotted against SiO_2 content; (b): Rb concentration plotted against MgO content; (c): Rb concentration plotted against K_2O content; (d): Rb concentration plotted against La content; (e): $\delta^{87}Rb$ vs. SiO_2 content; (f): $\delta^{87}Rb$ vs. Rb concentration.

of parent material (i.e., metabasalts), F is the degree of partial melting, and D is bulk partition coefficient of Rb. Using the average Rb concentration of dacites (54.8 μg/g) and basalts (10.5 μg/g) to represent C_1 and C_0 respectively. And assuming that the distribution coefficient of Rb during partial melting of the metabasalts is between 0 and 0.2 (which is the highest Rb partitioning of the dominant phenocryst phases in Hekla rocks according to Geist et al., 2021), it is estimated that the dacites can be formed by 13% to 19% partial melting of metabasalts. This is consistent with previous estimates using elemental Th and U (10–20%, Sigmarsson et al., 1992, 2022) as well as Tl (16%, Prytulak et al., 2017).

In cases where traditional major and trace elements analyses fail to distinguish between competing petrogenesis models, emerging isotope systems may hold potential for providing new insights. Therefore, we aim to investigate whether Rb isotopes can offer new insights into the ongoing debate over the petrogenesis of Hekla. The anhydrous phenocryst assemblage of Hekla lavas is dominated by plagioclase, olivine, clinopyroxene, orthopyroxene, magnetite, apatite, ilmenite and zircon (Sigmarsson et al., 1992, 2022; Geist et al., 2021). Based on partition coefficients from Geist et al. (2021), we anticipate that only a limited amount of Rb would enter these phases during fractional crystallization. This is consistent with what is observed for K (Tuller-Ross et al., 2019). Since Rb and K are both highly incompatible elements and the concentration of these elements correlate in the Hekla samples (Fig. 6c), they must exhibit very similar geochemical behavior during magmatic evolution. Tuller-Ross et al. (2019) proposed that K-bearing minerals were absent when solid phases crystallized from melt at Hekla. Rubidium mainly exists in the form of isomorphic substitution of K, thus Rb would not get incorporated into solid phases during magmatic evolution. This is also supported by the good correlation between Rb and La (Fig. 6d) as well as other trace elements such as Tl, Ba, U, Th and Pb (Sigmarsson et al., 1992; Prytulak et al., 2017; Geist et al., 2021). If considering that the Hekla system undergoes fractional crystallization alone as proposed by Geist et al. (2021), the magmatic process would not lead to significant Rb isotopic fractionation, given that limited Rb enters the solid phases during fractional crystallization. For comparison, we also evaluate the impact in the case of crustal involvement during magmatic evolution. Prytulak et al. (2017) suggested that the contributions of crustal components were highly unlikely to be low temperature altered crust, pelagic clays and/or Fe-Mn sediments, based on the homogeneity of the Tl isotopic compositions across the range of magmatic products at Hekla. A recent study shows that the Rb isotopic composition of the upper continental crust (−0.14 ± 0.01‰, 2SE, n = 73; Hu et al., 2022a) is close to the mantle's composition (−0.12 ± 0.06‰, 2SD, n = 6; Pringle and Moynier, 2017). The possible similarity of the Rb isotopic composition between the crust and mantle implies that even if the origin of dacites is influenced by the crustal contribution, they still have the same Rb isotopic composition as less evolved rocks. The two competing models (i.e., assimilation and/or partial melting of

the crust versus fractional crystallization alone, Sigmarsson et al., 1992, 2022; Chekol et al., 2011; Geist et al., 2021), accordingly, both agree with the absence of resolvable Rb isotopic variation between the dacites ($\delta^{87}Rb_{average} = -0.15 \pm 0.03$‰, 2SD, n = 3) and other less evolved rock types (average δ^{87}Rb value of -0.12 ± 0.06‰, 2SD, n = 8 for basalts and -0.15 ± 0.06‰, 2SD, n = 6 for basaltic andesites). Therefore, the ongoing petrogenesis debate is not resolved with Rb isotopes.

The origin of dacites is still controversial. However, despite this uncertainty, the uniformity of δ^{87}Rb values in the Hekla rock suite suggests that magmatic processes do not significantly modify the Rb isotopic characteristics of the source melt. This is consistent with the prediction made by Zeng et al. (2019) through first-principle calculations. They estimated that the Rb isotopic equilibrium fractionation between silicate melt and mineral would not exceed 0.01‰ at 900–1000 °C, which is within our analytical uncertainty. It is, however, worth noting that Hekla is an anhydrous, tholeiitic system, and the behavior for Rb isotope could be different if a hydrous (e.g., biotite) or K-rich phases are involved during magma evolution.

5.3. Rubidium isotopic composition of the Earth's mantle

Magma emplaced at mid-ocean ridges makes up a major part of terrestrial magma production (White and Klein, 2014; Nan et al., 2022; Wu et al., 2023). MORBs are generated by partial melting of the mantle (Hofmann, 2003; White and Klein, 2014). According to Workman and Hart (2005), the bulk distribution coefficient $D_{solid/melt}$ of Rb during mantle partial melting can be low as 0.00001, and MORBs correspond to melting degrees between 6% and 20%. This means that during the partial melting of the mantle, more than 99% of Rb tends to enter the basaltic melt, and therefore we can safely assume that Rb isotopic fractionation does not occur during partial melting. The lack of correlation between Rb isotopic compositions and the indicator of partial melting degree Na_8 (which is defined as $Na_8 = Na_2O + 0.373 \times MgO - 2.98$; Klein and Langmuir, 1987) of MORB samples in this study (Fig. 7d) is consistent with this assumption. In addition, Rb isotopic fractionation is very limited during magmatic evolution based on no obvious correlation between δ^{87}Rb and MgO contents (Fig. 7c) as well as our observation of Hekla volcanic rocks. Therefore, the Rb isotopic characteristics of MORB samples can reflect the composition of their mantle source.

In this study, various MORB samples with a broad geographical distribution were analyzed for Rb isotopes. All but one of these samples span a limited range of Rb isotopic compositions (−0.19 to −0.07‰) despite different localities. One exception is the E-MORB sample, CH30 DR 17–03, which is found to have a slightly heavier Rb isotopic composition ($\delta^{87}Rb = -0.02 \pm 0.02$‰, Table 3 and Fig. 7a). Previous studies proposed that formation of E-MORBs may be related to the

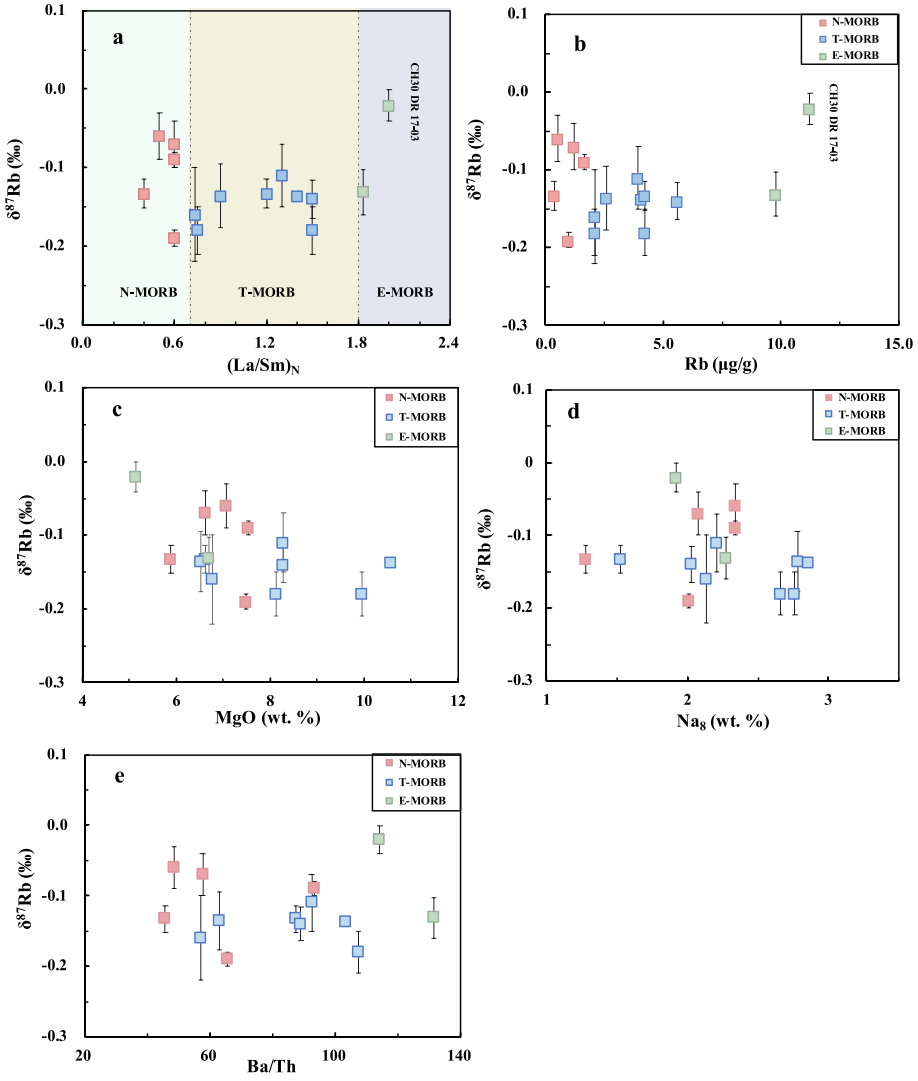


Fig. 7. Correlations between δ^{87}Rb and (a) $(La/Sm)_N$, (b) Rb concentration, (c) MgO content, (d) Na_8 (indicator of partial melting degree which is defined as $Na_8 = Na_2O + 0.373 \times MgO - 2.98$; Klein and Langmuir, 1987), and (e) Ba/Th for MORB samples.

involvement of deep recycling of crustal materials (Hofmann, 2003; Elliott et al., 2006). Although a recent study estimated the Rb isotopic composition of the upper continental crust is −0.14 ± 0.01‰ (2SE, n = 73; Hu et al., 2022a), low temperature alteration process would lead to significant Rb isotopic fractionation (Zhang et al., 2021) thus surface sediments or altered oceanic crust (AOC) may have abnormal Rb isotopic characteristics. Recycling of these materials may cause the inhomogeneity of the local mantle sources of MORBs. This may account for the heavier Rb isotopic characteristic associated with higher Rb content observed in CH30 DR 17–03 (Fig. 7b). However, the addition of abnormal Rb was unlikely via fluid, since extremely high Ba/Th, an indicator of fluid enrichment, is not observed in CH30 DR 17–03 (Fig. 7e). It is therefore, necessary to further test if Rb isotopes can be used to trace subduction recycling into the mantle, for example by targeting altered oceanic crust or sediments. In addition, it is worth noting that N-MORBs show more scattered Rb isotopic compositions compared to T-MORBs (Fig. 7a). A similar scatter for Sn isotopes was also observed in this set of samples (She et al., 2023). The scatter was unlikely caused by secondary modification, as the MORBs in this study did not undergo significant alteration according to the CIA and LOI values (She et al., 2023). Thus, it is more likely related to the diversity of sampling sites as suggested by She et al. (2023), which span locations as diverse as the Atlantic, Indian, and East Pacific Ocean. Nevertheless, Rb isotopic compositions of all MORB samples cluster within a narrow range. Based on the average δ^{87}Rb value of these MORBs, the Rb isotopic composition of the upper mantle is estimated at −0.12 ± 0.09‰ (2SD, n = 15). This value is consistent with the previous estimate (−0.12 ± 0.06‰, 2SD; n = 6) from Pringle and Moynier (2017). If we assume that Rb isotopic compositions of OIBs also reflect the characteristics of their mantle source, we can combine MORBs and Hekla basalts in this study with the OIB data reported in the literature (Pringle and Moynier, 2017) to estimate the Rb isotopic composition of the mantle. This compilation yields a δ^{87}Rb value of −0.12 ± 0.08‰ (2SD, n = 25; Fig. 8).

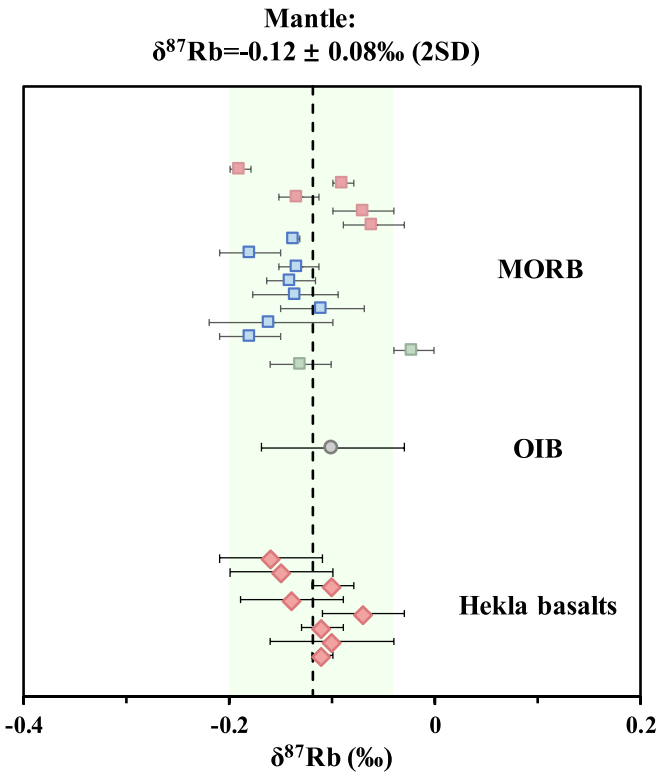


Fig. 8. Average Rb isotopic composition of the Earth's mantle (δ^{87}Rb = −0.12 ± 0.08‰, 2SD) estimated based on MORBs and Hekla basalts in this study as well as previously reported OIB (Pringle and Moynier, 2017).

5.4. Rubidium isotopic composition of the Bulk Silicate Earth

As mentioned above, Rb is a strongly incompatible element, and it can be calculated that the continental crust hosts ~55% of the Earth's Rb budget (Rudnick et al., 2003; Pringle and Moynier, 2017). Thus, the contribution of the continental crust actually plays a major role in the Rb isotopic composition of the BSE. As mantle partial melting and magmatic processes do not produce significant Rb isotopic fractionation (this study), the continental crust should have similar Rb isotopic characteristics to that of the mantle. This is consistent with the similarity between the estimated Rb isotopic composition of the upper continental crust (−0.14 ± 0.01‰, 2SE, n = 73; Hu et al., 2022a) and our estimation of the mantle's composition (−0.12 ± 0.08‰, 2SD; n = 25). Given the relative proportions of the crust and mantle, the Rb isotopic composition of the BSE can be estimated through a mass balance calculation: $\delta^{87}Rb_{BSE} = f \times \delta^{87}Rb_{crust} + (1 - f) \times \delta^{87}Rb_{mantle}$, where f (~55%, Rudnick et al., 2003; Pringle and Moynier, 2017) is the proportion of BSE's Rb budget hosted by the continental crust. The Rb isotopic composition of the continental crust ($\delta^{87}Rb_{crust}$) is assumed to be represented by the average value of the UCC (−0.14 ± 0.09‰, 2SD, n = 73; Hu et al., 2022a), and $\delta^{87}Rb_{mantle}$ to be equal to −0.12 ± 0.08‰ (2SD, n = 25) as discussed above. Using this approach, the Rb isotopic composition of the BSE is estimated to be −0.13 ± 0.06‰ (2SD; propagated error).

6. Conclusions

In this study, we developed a high precision Rb isotope analytical method on CC-MC-ICP-MS Nu Sapphire. Seven geostandards as well as a synthetic sample (PCC-1 + SRM 984) were measured. δ^{87}Rb values reported here for these standards are all in good agreement with reference data, confirming the accuracy of the method. The long-term reproducibility of Rb isotopic analyses is 0.03‰ (2SD) at 2 ng/g running concentration. Based on this high precision method, a series of igneous rocks from Hekla volcano and 15 MORB samples with various localities were measured. Hekla volcanic rocks exhibit very uniform Rb isotopic composition (from −0.17 to −0.07‰) over a wide range of bulk-rock compositions, ranging from basalts to rhyolites, indicating that Rb isotopic fractionation during magmatic evolution is not significant. Similarly, MORB samples also have a narrow Rb isotopic variation range (−0.19 to −0.02‰) regardless of their various localities. Combining basaltic samples (MORBs and Hekla basalts) in this study and previously published OIB data, the Rb isotopic composition of the mantle is estimated at −0.12 ± 0.08‰ (2SD, n = 25). The average composition of the BSE is evaluated to be −0.13 ± 0.06‰ (2SD), and this is a more precise estimate that is consistent with previous studies.

Declaration of Competing Interest

The authors declare that they have no known competing financial interests or personal relationships that could have appeared to influence the work reported in this paper.

Acknowledgement

This work was partly supported by the IPGP analytical platform PARI, Region Ile-de-France SESAME Grants no. 12015908, and DIM ACAV+, the ERC grant agreement No. 101001282 (METAL) (F.M.), the UnivEarthS Labex program (numbers: ANR-10-LABX-0023 and ANR-11-IDEX-0005-02) (F.M.). B.W thanks the support of CSC scholarship (No. 202106340025). We are grateful to the editorial handling of Prof. Jeffrey G. Catalano and Prof. Julie Prytulak and constructive comments from Prof. Julie Prytulak, Prof. Oliver Nebel and two anonymous reviewers.

Appendix A. Supplementary material

Supplementary Tables as well as major and trace elements data of Hekla samples are presented in the supplementary file. The information of chemical purification procedure and instrument operating parameters, as well as data of validating Rb isotope analytical method are provided in the Supplementary Tables. Supplementary material to this article can be found online at https://doi.org/10.1016/j.gca.2023.05.021.

References

Amsellem, E., Moynier, F., Day, J.M., Moreira, M., Puchtel, I.S., Teng, F.-Z., 2018. The stable strontium isotopic composition of ocean island basalts, mid-ocean ridge basalts, and komatiites. Chem. Geol. 483, 595–602.

Badullovich, N., Moynier, F., Creech, J., Teng, F., Sossi, P., 2017. Tin isotopic fractionation during igneous differentiation and Earth's mantle composition. Geochem. Perspect. Lett 5, 24–28.

Bai, R., Jackson, M.G., Huang, F., Moynier, F., Devos, G., Halldórsson, S.A., Lisiecki, L., Yin, H., Peng, Y., Nan, X., 2022. Barium isotopes in ocean island basalts as tracers of mantle processes. Geochim. Cosmochim. Acta 336, 436–447.

Barnes, J.J., Franchi, I.A., McCubbin, F.M., Anand, M., 2019. Multiple reservoirs of volatiles in the Moon revealed by the isotopic composition of chlorine in lunar basalts. Geochim. Cosmochim. Acta 266, 144–162.

Berglund, M., Wieser, M.E., 2011. Isotopic compositions of the elements 2009 (IUPAC Technical Report). Pure Appl. Chem. 83, 397–410.

Boyce, J.W., Treiman, A.H., Guan, Y., Ma, C., Eiler, J.M., Gross, J., Greenwood, J.P., Stolper, E.M., 2015. The chlorine isotope fingerprint of the lunar magma ocean. Sci. Adv. 1, e1500380.

Boyce, J.W., Kanee, S.A., McCubbin, F.M., Barnes, J.J., Bricker, H., Treiman, A.H., 2018. Early loss, fractionation, and redistribution of chlorine in the Moon as revealed by the low-Ti lunar mare basalt suite. Earth Planet. Sci. Lett. 500, 205–214.

Chekol, T.A., Kobayashi, K., Yokoyama, T., Sakaguchi, C., Nakamura, E., 2011. Timescales of magma differentiation from basalt to andesite beneath Hekla Volcano, Iceland: Constraints from U-series disequilibria in lavas from the last quarter-millennium flows. Geochim. Cosmochim. Acta 75, 256–283.

Chen, H., Savage, P.S., Teng, F.-Z., Helz, R.T., Moynier, F., 2013. Zinc isotope fractionation during magmatic differentiation and the isotopic composition of the bulk Earth. Earth Planet. Sci. Lett. 369, 34–42.

Chen, H., Saunders, N.J., Jerram, M., Halliday, A.N., 2021. High-precision potassium isotopic measurements by collision cell equipped MC-ICPMS. Chem. Geol. 578, 120281.

Dai, W., Moynier, F., Paquet, M., Moureau, J., Debret, B., Siebert, J., Gerard, Y., Zhao, Y., 2022. Calcium isotope measurements using a collision cell (CC)-MC-ICP-MS. Chem. Geol. 590, 120688.

Deng, Z., Moynier, F., Sossi, P., Chaussidon, M., 2018. Bridging the depleted MORB mantle and the continental crust using titanium isotopes. Geochem. Perspect. Lett 9, 11–15.

Deng, Z., Chaussidon, M., Savage, P., Robert, F., Pik, R., Moynier, F., 2019. Titanium isotopes as a tracer for the plume or island arc affinity of felsic rocks. Proc. Natl. Acad. Sci. 116, 1132–1135.

Elliott, T., Thomas, A., Jeffcoate, A., Niu, Y., 2006. Lithium isotope evidence for subduction-enriched mantle in the source of mid-ocean-ridge basalts. Nature 443, 565–568.

Gargano, A., Sharp, Z., Shearer, C., Simon, J.I., Halliday, A., Buckley, W., 2020. The Cl isotope composition and halogen contents of Apollo-return samples. Proc. Natl. Acad. Sci. 117, 23418–23425.

Geist, D., Harpp, K., Oswald, P., Wallace, P., Bindeman, I., Christensen, B., 2021. Hekla revisited: fractionation of a magma body at historical timescales. J. Petrol. 62, egab001.

Han, J., Chen, H., Hollings, P., Wang, J., Zhang, D., Zhang, L., Zeng, T., Ma, J., Ai, Y., 2021. Efficient enrichment of Rb during the magmatic-hydrothermal transition in a highly evolved granitic system: Implications from mica chemistry of the Tiantangshan Rb-Sn-W deposit. Chem. Geol. 560, 120020.

Hofmann, A., 2003. Sampling mantle heterogeneity through oceanic basalts: isotopes and trace elements. Treat. Geochem. 2, 568.

Hu, Y., Moynier, F., Bizzarro, M., 2022b. Potassium isotope heterogeneity in the early Solar System controlled by extensive evaporation and partial recondensation. Nat. Commun. 13, 1–10.

Hu, X., Nan, X.-Y., Yu, H.-M., Huang, F., 2021. High precision Rb isotope measurements by MC-ICP-MS. J. Anal. At. Spectrom. 36, 2744–2755.

Hu, X., Nan, X., Liu, X., Huang, F., 2022a. Rubidium isotope compositions of the average upper continental crust and the Himalayan leucogranites: Implications for magmatic-fluid interaction. Geochim. Cosmochim. Acta 336, 165–176.

Huang, F., Bai, R., Deng, G., Liu, X., Li, X., 2021. Barium isotope evidence for the role of magmatic fluids in the origin of Himalayan leucogranites. Sci. Bull. 66, 2329–2336.

Inglis, E.C., Moynier, F., Creech, J., Deng, Z., Day, J.M., Teng, F.-Z., Bizzarro, M., Jackson, M., Savage, P., 2019. Isotopic fractionation of zirconium during magmatic differentiation and the stable isotope composition of the silicate Earth. Geochim. Cosmochim. Acta 250, 311–323.

Klein, E.M., Langmuir, C.H., 1987. Global correlations of ocean ridge basalt chemistry with axial depth and crustal thickness. J. Geophys. Res. Solid Earth 92 (B8), 8089–8115.

Li, W., Cui, M., Pan, Q., Wang, J., Gao, B., Liu, S., Yuan, M., Su, B., Zhao, Y., Teng, F.-Z., 2022. High-precision potassium isotope analysis using the Nu Sapphire collision cell (CC)-MC-ICP-MS. Sci. China Earth Sci. 65, 1510–1521.

Liu, Z., Liu, X., Yu, L., Wang, J., 2020. Highly fractionated origin and magmatic-hydrothermal evolution of the Kampa leucogranites in the Tethyan Himalaya. J. Nanjing Univ. Nat. Sci. 56, 800–814.

Lodders, K., 2003. Solar system abundances and condensation temperatures of the elements. Astrophys. J. 591, 1220.

Luck, J.-M., Othman, D.B., Albarède, F., 2005. Zn and Cu isotopic variations in chondrites and iron meteorites: early solar nebula reservoirs and parent-body processes. Geochim. Cosmochim. Acta 69, 5351–5363.

McDonough, W.F., Sun, S.-S., 1995. The composition of the Earth. Chem. Geol. 120, 223–253.

Moune, S., Sigmarsson, O., Thordarson, T., Gauthier, P.-J., 2007. Recent volatile evolution in the magmatic system of Hekla volcano, Iceland. Earth Planet. Sci. Lett. 255, 373–389.

Moynier, F., Hu, Y., Wang, K., Zhao, Y., Gérard, Y., Deng, Z., Moureau, J., Li, W., Simon, J.I., Teng, F.-Z., 2021. Potassium isotopic composition of various samples using a dual-path collision cell-capable multiple-collector inductively coupled plasma mass spectrometer, Nu instruments. Sapphire. Chem. Geol. 571, 120144.

Nan, X., Yu, H., Kang, J., Huang, F., 2022. Re-visiting barium isotope compositions of mid-ocean ridge basalts and the implications. Justc 52, 1-1–1-8.

Nebel, O., Mezger, K., Scherer, E., Münker, C., 2005. High precision determinations of 87Rb/85Rb in geologic materials by MC-ICP-MS. Int. J. Mass Spectrom. 246, 10–18.

Nebel, O., Mezger, K., van Westrenen, W., 2011a. Rubidium isotopes in primitive chondrites: Constraints on Earth's volatile element depletion and lead isotope evolution. Earth Planet. Sci. Lett. 305, 309–316.

Nebel, O., Scherer, E.E., Mezger, K., 2011b. Evaluation of the 87Rb decay constant by age comparison against the U-Pb system. Earth Planet. Sci. Lett. 301, 1–8.

Nie, N.X., Dauphas, N., 2019. Vapor Drainage in the Protolunar Disk as the Cause for the Depletion in Volatile Elements of the Moon. Astrophys. J. 884, L48.

Nie, N.X., Dauphas, N., Hopp, T., Hu, J.Y., Zhang, Z.J., Yokochi, R., Ireland, T.J., Tissot, F.L., 2021. Chromatography purification of Rb for accurate isotopic analysis by MC-ICPMS: a comparison between AMP-PAN, cation-exchange, and Sr resins. J. Anal. At. Spectrom. 36, 2588–2602.

Óskarsson, N., 1981. The chemistry of Icelandic lava incrustations and the latest stages of degassing. J. Volcanol. Geotherm. Res. 10, 93–111.

Paniello, R.C., Day, J., Moynier, F., 2012. Zinc isotopic evidence for the origin of the Moon. Nature 490, 376–379.

Paquet, M., Moynier, F., Yokoyama, T., Dai, W., Hu, Y., Abe, Y., Aléon, J., Alexander, C. M.O'D., Amari, S., Amelin, Y., 2022. Contribution of Ryugu-like material to Earth's volatile inventory by Cu and Zn isotopic analysis. Nat. Astron. 7, 182–189.

Pringle, E.A., Moynier, F., 2017. Rubidium isotopic composition of the Earth, meteorites, and the Moon: Evidence for the origin of volatile loss during planetary accretion. Earth Planet. Sci. Lett. 473, 62–70.

Pringle, E.A., Moynier, F., Beck, P., Paniello, R., Hezel, D.C., 2017. The origin of volatile element depletion in early solar system material: Clues from Zn isotopes in chondrules. Earth Planet. Sci. Lett. 468, 62–71.

Prytulak, J., Sossi, P., Halliday, A., Plank, T., Savage, P., Woodhead, J., 2016. Stable vanadium isotopes as a redox proxy in magmatic systems. Geochem. Perspect. Lett 3, 75–84.

Prytulak, J., Brett, A., Webb, M., Plank, T., Rehkämper, M., Savage, P., Woodhead, J., 2017. Thallium elemental behavior and stable isotope fractionation during magmatic processes. Chem. Geol. 448, 71–83.

Ranta, E.J., Halldórsson, S.A., Barnes, J., Jónasson, K., Stefánsson, A., 2021. Chlorine isotope ratios record magmatic brine assimilation during rhyolite genesis. Geochem. Perspect. Lett. 16, 35–39.

Rose-Koga, E.F., Sigmarsson, O., 2008. B-O–Th isotope systematics in Icelandic tephra. Chem. Geol. 255, 454–462.

Rudnick, R., Gao, S., Holland, H., Turekian, K., 2003. Treatise on Geochemistry. Elsevier, Amsterdam, pp. 1–64.

Savage, P.S., Georg, R.B., Williams, H.M., Burton, K.W., Halliday, A.N., 2011. Silicon isotope fractionation during magmatic differentiation. Geochim. Cosmochim. Acta 75, 6124–6139.

Schilling, J.G., 1975. Rare-earth variations across 'normal segments' of the Reykjanes Ridge, 60–53 N, Mid-Atlantic Ridge, 29 S, and East Pacific Rise, 2–19 S, and evidence on the composition of the underlying low-velocity layer. J. Geophys. Res. 80, 1459–1473.

Schilling, J., Zajac, M., Evans, R., Johnston, T., White, W., Devine, J., Kingsley, R., 1983. Petrologic and geochemical variations along the Mid-Atlantic Ridge from 29 degrees N to 73 degrees N. Am. J. Sci. 283, 510–586.

Schuessler, J.A., Schoenberg, R., Sigmarsson, O., 2009. Iron and lithium isotope systematics of the Hekla volcano, Iceland—evidence for Fe isotope fractionation during magma differentiation. Chem. Geol. 258, 78–91.

She, J.-X., Kubik, E., Li, W., Moynier, F., 2023. Stable Sn isotope signatures of Mid-ocean ridge basalts. Chem. Geol. 622, 121347.

Sigmarsson, O., Condomines, M., Fourcade, S., 1992. A detailed Th, Sr and O isotope study of Hekla: differentiation processes in an Icelandic volcano. Contrib. Mineral. Petrol. 112, 20–34.

Sigmarsson, O., Bergþórsdóttir, I.A., Devidal, J.-L., Larsen, G., Gannoun, A., 2022. Long or short silicic magma residence time beneath Hekla volcano, Iceland? Contrib. Mineral. Petrol. 177, 13.

Sossi, P.A., Eggins, S.M., Nesbitt, R.W., Nebel, O., Hergt, J.M., Campbell, I.H., O'Neill, H. S.C., Van Kranendonk, M., Davies, D.R., 2016. Petrogenesis and geochemistry of Archean komatiites. J. Petrol. 57, 147–184.
Takazawa, E., Frey, F., Shimizu, N., Obata, M., 2000. Whole rock compositional variations in an upper mantle peridotite (Horoman, Hokkaido, Japan): are they consistent with a partial melting process? Geochim. Cosmochim. Acta 64, 695–716.
Tan, S.H., Horlick, G., 1987. Matrix-effect observations in inductively coupled plasma mass spectrometry. J. Anal. At. Spectrom. 2, 745–763.
Tanner, S.D., 1992. Space charge in ICP-MS: calculation and implications. Spectrochim. Acta Part B At. Spectrosc. 47, 809–823.
Teng, F.-Z., Dauphas, N., Helz, R.T., 2008. Iron isotope fractionation during magmatic differentiation in Kilauea Iki lava lake. Science 320, 1620–1622.
Thorarinsson, S., 1967. The eruption of Hekla 1947–48: the eruption of Hekla in historical times. Soc. Sci. Isl. 1, 1–170.
Tian, Z., Chen, H., Fegley Jr, B., Lodders, K., Barrat, J.-A., Day, J.M., Wang, K., 2019. Potassium isotopic compositions of howardite-eucrite-diogenite meteorites. Geochim. Cosmochim. Acta 266, 611–632.
Tian, Z., Magna, T., Day, J.M., Mezger, K., Scherer, E.E., Lodders, K., Hin, R.C., Koefoed, P., Bloom, H., Wang, K., 2021. Potassium isotope composition of Mars reveals a mechanism of planetary volatile retention. Proc. Natl. Acad. Sci. 118, e2101155118.
Tuller-Ross, B., Savage, P.S., Chen, H., Wang, K., 2019. Potassium isotope fractionation during magmatic differentiation of basalt to rhyolite. Chem. Geol. 525, 37–45.
Van Kooten, E.M., Moynier, F., Day, J.M., 2020. Evidence for transient atmospheres during eruptive outgassing on the Moon. Planet. Sci. J. 1, 67.
Vollstaedt, H., Mezger, K., Leya, I., 2020. The selenium isotope composition of lunar rocks: Implications for the formation of the Moon and its volatile loss. Earth Planet. Sci. Lett. 542, 116289.
Wang, J., Su, B.-X., Tang, D.-M., Yuan, Q.-H., Li, W.-J., Gao, B.-Y., Bao, Z.-A., Zhao, Y., 2022. High-precision copper isotopic analysis using a Nu Sapphire MC-ICP-MS. J. Anal. At. Spectrom. 37, 2589–2598.
White, W., Klein, E., 2014. 4.13-Composition of the oceanic crust. Treatise on Geochemistry (second edition), 457–496.
Willbold, M., Elliott, T., 2017. Molybdenum isotope variations in magmatic rocks. Chem. Geol. 449, 253–268.
Wing, B.A., Farquhar, J., 2015. Sulfur isotope homogeneity of lunar mare basalts. Geochim. Cosmochim. Acta 170, 266–280.
Wombacher, F., Rehkämper, M., Mezger, K., Bischoff, A., Münker, C., 2008. Cadmium stable isotope cosmochemistry. Geochim. Cosmochim. Acta 72, 646–667.
Workman, R.K., Hart, S.R., 2005. Major and trace element composition of the depleted MORB mantle (DMM). Earth Planet. Sci. Lett. 231, 53–72.
Wu, F., Turner, S., Hoernle, K., Hauff, F., Schaefer, B.F., Kokfelt, T., Bindeman, I., 2023. Barium isotope composition of depleted MORB mantle constrained by basalts from the South Mid-Atlantic Ridge (5–11° S) with implication for recycled components in the convecting upper mantle. Geochim. Cosmochim. Acta 340, 85–98.
Yang, J., Siebert, C., Barling, J., Savage, P., Liang, Y.-H., Halliday, A.N., 2015. Absence of molybdenum isotope fractionation during magmatic differentiation at Hekla volcano, Iceland. Geochim. Cosmochim. Acta 162, 126–136.
Zeng, H., Rozsa, V.F., Nie, N.X., Zhang, Z., Pham, T.A., Galli, G., Dauphas, N., 2019. Ab initio calculation of equilibrium isotopic fractionations of potassium and rubidium in minerals and water. ACS Earth Space Chem. 3, 2601–2612.
Zhang, Z., Ma, J., Zhang, L., Liu, Y., Wei, G., 2018. Rubidium purification via a single chemical column and its isotope measurement on geological standard materials by MC-ICP-MS. J. Anal. At. Spectrom. 33, 322–328.
Zhang, Z., Ma, J., Wang, Z., Zhang, L., He, X., Zhu, G., Zeng, T., Wei, G., 2021. Rubidium isotope fractionation during chemical weathering of granite. Geochim. Cosmochim. Acta 313, 99–115.
Zheng, X.-Y., Chen, X.-Y., Ding, W., Zhang, Y., Charin, S., Gérard, Y., 2022. High precision analysis of stable potassium (K) isotopes by the collision cell MC-ICP-MS "Sapphire" and a correction method for concentration mismatch. J. Anal. At. Spectrom. 37, 1273–1287.

Cadmium abundances and isotope compositions in Earth and chondrites

Par Gabriel Devos

• Résumé

Ce travail s'est focalisé sur le développement d'un nouveau protocole d'analyses isotopiques de haute précision pour l'élément cadmium et sur son application à différents domaines actifs de la géochimie moderne. Nous avons notamment déterminé une nouvelle composition isotopique pour le manteau terrestre. Pour cela nous avons caractérisé des basaltes de dorsales océaniques, lesquels présentent une homogénéité isotopique remarquable, ainsi que des komatiites. Les komatiites ont des valeurs de concentration en Cd et de compositions isotopiques bien plus variables que les basaltes. Nous avons mis en évidence le fait que les compositions isotopiques des komatiites sont principalement influencées par le degré d'altération de la roche. Ces analyses nous ont permis de proposer une composition isotopique pour le manteau bien plus lourde que ce que de précédentes études supposaient.

La deuxième étape de ce travail a consisté en la caractérisation du fractionnement isotopique ayant lieu lors de la différentiation magmatique par cristallisation fractionnée. Nous nous sommes basés pour cela sur des échantillons du volcan islandais Hekla, connu pour former des roches allant des basaltes aux rhyolites. Nous n'avons trouvé aucune influence de la cristallisation fractionnée sur les compositions isotopiques mesurées.

L'étude de tectites et de verres d'impacts nous a permis de compléter la caractérisation du fractionnement isotopique se produisant lors d'évènements de vaporisation du Cd. Nous avons confirmé le résultat préexistant indiquant que le fractionnement isotopique réel est significativement inférieur à celui prédit par une distillation de Rayleigh théorique.

Enfin nous avons analysé un jeu de 17 chondrites, réparti entre chondrites carbonées (8), ordinaires (7) et à enstatite (2). Nos résultats principaux indiquent que ces échantillons sont, pour bonne partie, caractérisés par des compositions hétérogènes pour le Cd. Ainsi les réplicats mesurés pour un même échantillon indiquent parfois des concentrations ou des compositions isotopiques très distinctes. Les chondrites carbonées sont caractérisées par des compositions isotopiques corrélées à leurs concentrations, contrairement aux chondrites ordinaires ou à enstatite.

• Mots clés

Cadmium ; isotopes stables ; double spike ; échantillons standard ; manteau terrestre ; bulk silicate Earth ; MORB ; komatiites ; tectites ; chondrites ; MC-ICP-MS

IPGP Université Paris Cité